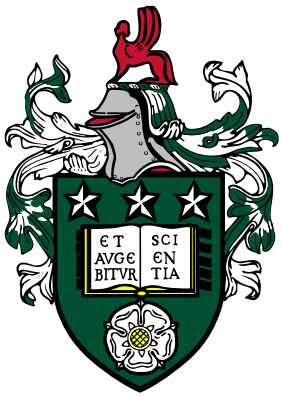
Using perturbed parameter ensembles to explore the behaviour of mixed-phase cold-air outbreak clouds



Xinyi Huang

Submitted in accordance with the requirements for the degree of
Doctor of Philosophy

The University of Leeds
School of Earth, Environment and Sustainability

October 2026

Declaration of Authorship

I confirm that the work submitted is my own, except where work which has formed part of jointly authored publications has been included. My contribution and the contributions of the other authors to this work have been explicitly indicated below. I confirm that appropriate credit has been given within the thesis where reference has been made to the work of others.

Chapter 2 is based on the following paper, which is already published in the journal *Atmospheric Chemistry and Physics*:

Huang, X., Field, P. R., Murray, B. J., Grosvenor, D. P., van den Heuvel, F., and Carslaw, K. S. (2025). Different responses of cold-air outbreak clouds to aerosol and ice production depending on cloud temperature. *Atmospheric Chemistry and Physics*, 25(18), 11363–11406. https://doi.org/10.5194/acp-25-11363-2025.

In this paper, I carried out the model simulations, analysed the model output, and performed the model–observation comparison using satellite retrievals. I wrote the original draft of the manuscript, which was edited by all co-authors. PRF, BJM and KSC contributed to the design of the work. PRF and DPG provided help and advice on running the model simulations. DPG, FvdH and KSC provided guidance on the comparison between model output and satellite retrievals, including the interpretation of the model-observation comparison results. KSC, BJM, DPG and FvdH are the supervisors of my PhD project and provided general guidance, advice and feedback throughout this work.

Chapter 3 is based on the following paper, which has been accepted for final production in the journal *Atmospheric Chemistry and Physics*:

Huang, X., Field, P. R., Herbert, R. J., Murray, B. J., van den Heuvel, F., Grosvenor, D. P., Sansom, R. W. N., and Carslaw, K. S. (2026). Interacting effects of droplet number and ice formation processes on mixed-phase cold-air outbreak clouds. *EGUsphere*, 2026, 1–49. https://doi.org/10.5194/egusphere-2026-311.

In this paper, I designed the experiments, performed the regional perturbed parameter ensemble simulations, developed the Gaussian process emulators from the model

simulations, and carried out the analysis of both the numerical model and emulator output. I wrote the original draft of the manuscript, which was edited by all co-authors. RJH provided the ice-nucleating particle parameterisation from a global model, which was then used in the regional model. PRF, BJM and KSC contributed to the design of the study. PRF and DPG provided guidance on the model setup. KSC and FvdH provided guidance on the design of the training, validation and testing of the Gaussian process emulators. RWNS provided advice on the interpretation of the emulator results. KSC, BJM, DPG and FvdH are the supervisors of my PhD project and provided general guidance, advice and feedback throughout this work.

Chapter 4 is based on the following paper, which is developed and formatted to be submitted to the *Journal of Geophysical Research: Atmospheres*:

Huang, X., Field, P. R., Murray, B. J., Grosvenor, D. P., van den Heuvel, F., and Carslaw, K. S. Identification of model inconsistencies using perturbed parameter ensembles and aircraft observations of mixed-phase cold-air outbreak clouds.

In this paper, I designed and developed the experiments, processed and analysed both the observational datasets from aircraft measurements and from satellite retrievals, and performed the model-observation comparison. I wrote the original draft of the manuscript, which was edited by all co-authors. PRF, BJM and KSC contributed to the design of the work. DPG provided guidance on model-observation comparison with the satellite retrievals. KSC, PRF, BJM and FvdH provided guidance on model-observation comparison with the aircraft measurements. KSC, BJM, DPG and FvdH are the supervisors of my PhD project and provided general guidance, advice and feedback throughout this work.

Chapter 5 is based on the following paper, which is developed and formatted to be submitted to the *Proceedings of the National Academy of Sciences*:

Huang, X., Field, P. R., Murray, B. J., Grosvenor, D. P., van den Heuvel, F., and Carslaw, K. S. The importance of aerosols and ice formation for the response of mixed-phase clouds to warming.

In this paper, I designed the idealised model simulations, performed the analysis of environmental conditions during cold-air outbreak events with the Coupled Model Intercomparison Project Phase 6 (CMIP6) data from the UK Earth System Model version 1, trained and tested the Gaussian Process emulators, sampled the parameter space with cold-air outbreak conditions from the CMIP6 model and with my designs on the aerosols and secondary ice production parameter space, and performed the data analysis. I wrote the original draft, which was edited by co-authors. KSC and PRF provided guidance on the design of the experiments and methods. PRF provided guidance on the setup of the idealised simulations. KSC, PRF and BJM provided

guidance on the interpretation of the emulator results. KSC, BJM, DPG and FvdH are the supervisors of my PhD project and provided general guidance, advice and feedback throughout this work.

This thesis is presented in an alternative format because the research undertaken during my PhD has produced a coherent body of work that addresses a unified research question and is suitable for publication. This format allows me to preserve the integrity of each work, but also to demonstrate how they collectively make an original contribution to my research topic.

The thesis is constructed as follows: an introduction chapter describing the research topic, rationale, general methods and approach for my PhD research, four article manuscripts of which one is published, one has been submitted and received permission to revise, and two have been developed and formatted to be ready for submission, and a conclusions chapter summarising the work from all four manuscripts and discussing potential future work.

This copy has been supplied on the understanding that it is copyright material and that no quotation from the thesis may be published without proper acknowledgement.

The right of Xinyi Huang to be identified as Author of this work has been asserted by Xinyi Huang in accordance with the Copyright, Designs and Patents Act 1988.

Copyright © 2026 The University of Leeds and Xinyi Huang

Acknowledgements

First and foremost, I would like to express my sincere gratitude to all my supervisors: Ken Carslaw, Ben Murray, Dan Grosvenor and Floor van den Heuvel. Thank you for your support, guidance, encouragement and patience throughout my PhD. I am especially grateful for your insightful suggestions and feedback, which have helped shape this thesis and my development as a researcher. I feel very fortunate to have been supervised by you and to have learned so much from every single discussion we had. I would also like to thank Paul Field for his generous support on my PhD and guidance on modelling and cloud microphysics. I am particularly thankful for his support during my 3-month placement at the UK Met Office, which is a valuable part of my PhD experience.

I am grateful to the NERC SENSE CDT for funding my PhD project and for providing excellent training opportunities. I am also grateful to the UK Met Office for being my CASE partner and for supporting this work through a CASE studentship. I would like to acknowledge Monsoon and JASMIN for providing the computational resources, data storage and analysis facilities used to produce the results presented in this thesis.

I would like to thank everyone in the Aerosol, Clouds and Climate group, the Ice Nucleation Group, and SEE Office 11.121. Thank you for the group meetings, conversations, social events, coffee and tea time, and all the laughter that we shared. These moments have formed a very meaningful part of my time in Leeds.

My thanks must also go to my friends, who have been wonderful company throughout my PhD and my life. Yue, thank you for walking with me from the train station every Friday morning, and for being one of the few people who has shared my journey in Leeds since our master's degree. Feiyu, thank you for being there with me for over a decade since our high school days, and for listening to me through all the ups and downs.

I would like to thank my family for their unconditional love and support. Mum, I could not have completed this journey without your support and trust in me. Your encouragement has always been with me whenever I doubted myself, giving me the

strength to face all the challenges. Dad, thank you for always telling me to be happy and strong, and I hope you knew how deeply I appreciated you.

Finally, I would like to thank my partner, Ziyu. Thank you for your continuous love, patience and support. Thank you for standing by me through the happiness, sadness, celebrations, stress, deadlines, and all the special moments of this journey. Thank you for reminding me to stay healthy, and for dragging me to exercise after long days of work. I feel very lucky to have you.

Abstract

Cloud feedback remains one of the largest uncertainties in estimating climate sensitivity and future climate change, with the representation of mixed-phase clouds playing a key role in recent assessments. Mixed-phase clouds contain both liquid droplets and ice particles, and their properties are strongly controlled by microphysical processes that determine the formation and evolution of these hydrometeors. Aerosol-cloud interactions through cloud condensation nuclei (CCN), primary ice production through ice-nucleating particles (INPs), and secondary ice production (SIP) can strongly influence mixed-phase cloud properties. However, these processes are often investigated and evaluated individually, and their effects on the responses of mixed-phase clouds to warming remain poorly quantified. This thesis aims to advance understanding of how aerosol-cloud interactions and ice formation processes influence mixed-phase clouds and their responses to warming using perturbed parameter ensemble (PPE) simulations with a high-resolution regional model. Rather than assessing mixed-phase clouds globally, this thesis focuses on marine cold-air outbreaks (CAOs), which provide strongly forced meteorological conditions with extensive mixed-phase cloud formation.

In Chapter 2, following the introduction, the thesis first investigates the sensitivities of mixed-phase CAO clouds to droplet number concentration, INP concentration, and the efficiency of the Hallett-Mossop (HM) SIP process using a one-at-a-time approach in two contrasting CAO cases. The results show that these sensitivities depend strongly on environmental conditions, especially cloud temperature, and liquid-ice partitioning in the clouds. Increasing INP concentration reduces cloud cover and albedo in a warm, liquid-dominated case, but increases cloud cover and albedo in a cold, ice-dominated case. Changes in droplet number concentration and HM process efficiency exert strong influences only in the liquid-dominated case.

Building on these findings, in Chapter 3, PPE simulations and model emulation are applied to the liquid-dominated case to investigate the joint effects of droplet number concentration, INP concentration, three SIP parameters, and a parameter controlling liquid-ice overlap within a model grid box. The results reveal strong non-linear interactions among these parameters, indicating that the cloud response to one parameter depends on the values of others. Different parameter combinations can also produce

similar cloud properties through compensating effects, leading to equifinality when modelled cloud properties are evaluated against observations.

In Chapter 4, the same PPE simulations are evaluated against multiple aircraft observations from the M-Phase aircraft campaign to determine whether observations are able to constrain uncertainties in the model. It is found that different observational constraints identify inconsistent subsets of plausible ensemble members, and constraining one cloud property does not necessarily improve agreement with others. This demonstrates that agreement with a single observed variable does not guarantee that the underlying mixed-phase cloud microphysics are correctly represented. The identified model inconsistencies also point to potential structural weaknesses in the model.

Finally, in Chapter 5, emulators trained on idealised high-resolution PPE simulations are used to sample thousands of present-day and future CAO cases, extending the analysis beyond individual present-day case studies. These results show that the processes controlling present-day mixed-phase CAO cloud properties are not the same as those controlling their responses to warming. A key finding is that ice formation processes and future changes in aerosols can strongly affect cloud radiative responses to warming.

Contents

Declaration of Authorship ii

Acknowledgements v

Abstract vii

List of Figures xiii

List of Tables xxi

List of Abbreviations xxiii

1 Introduction 1

1.1 Clouds and cloud feedback . . . 1

1.1.1 Clouds in the Earth system . . . 1

1.1.2 Decomposition of cloud feedback . . . 2

1.1.3 Mixed-phase clouds and cloud-phase feedback . . . 4

1.2 Microphysical controls on mixed-phase clouds . . . 5

1.2.1 Aerosol-cloud interactions . . . 6

1.2.2 Primary ice production . . . 7

1.2.3 Secondary ice production . . . 9

1.3 Mixed-phase clouds in cold-air outbreaks . . . 10

1.3.1 Microphysical controls on mixed-phase CAO clouds . . . 11

1.3.2 Environmental controls on mixed-phase CAO clouds . . . 13

1.4 High-resolution regional modelling . . . 15

1.5 Perturbed parameter ensemble and Gaussian Processes emulator . . . 16

1.6 Research objectives and thesis overview . . . 17

1.6.1 Chapter 2: Quantify the responses of mixed-phase CAO clouds to aerosol-cloud interactions and ice formation processes under different environmental conditions . . . 18

1.6.2 Chapter 3: Explore the interacting effects of aerosol-cloud interactions and ice formation processes on mixed-phase CAO clouds 18

1.6.3 Chapter 4: Assess the representation of mixed-phase CAO clouds in a high-resolution model using multiple observations . . . 19

1.6.4 Chapter 5: Quantify the role of aerosols and ice formation processes in the responses of mixed-phase CAO clouds to a warming climate . . . 20
References . . . 21

2 Different responses of cold-air outbreak clouds to aerosol and ice production depending on cloud temperature 37
2.1 Abstract . . . 38
2.2 Introduction . . . 39
2.3 Methods . . . 40
2.3.1 Case description . . . 41
2.3.2 Model set-up . . . 41
2.3.3 Perturbed parameters and the selection of their values . . . 43
2.3.4 Satellite data . . . 46
2.4 Results . . . 47
2.4.1 Control simulations . . . 47
2.4.2 Responses of cloud properties to perturbed parameters . . . 50
2.4.3 Responses of CAO cloud field development to perturbed parameters 55
2.4.4 Overall comparison of the cloud responses to perturbed parameters between the cases . . . 57
2.4.5 Comparison with satellite retrievals . . . 60
2.5 Discussion and Conclusions . . . 66
Appendix . . . 70
References . . . 95

3 Interacting effects of droplet number and ice formation processes on mixed-phase cold-air outbreak clouds 105
3.1 Abstract . . . 106
3.2 Introduction . . . 107
3.3 Methods . . . 109
3.3.1 Model setup and case description . . . 109
3.3.2 Perturbed parameters and PPE design . . . 110
3.3.3 Gaussian Process (GP) emulators . . . 117
3.4 Results . . . 118
3.4.1 Example response from PPE simulations: TOA albedo . . . 118
3.4.2 Emulated model response surface . . . 119
3.4.3 Dependence of individual parameter sensitivities on other parameters . . . 123
3.5 Discussion and Conclusions . . . 126
Appendix . . . 133
References . . . 152

4 Identification of model inconsistencies using perturbed parameter ensembles and aircraft observations of mixed-phase cold-air outbreak clouds 165
4.1 Abstract . . . 166
4.2 Introduction . . . 167
4.3 Methods and Data . . . 169
4.3.1 Campaign and case description . . . 169
4.3.2 Aircraft measurements . . . 170
4.3.3 Model simulations . . . 172
4.3.4 Preprocessing of aircraft measurements and model output . . . 173
4.3.5 Implausibility measure for model-observation comparison . . . 176
4.3.6 Satellite retrievals . . . 177
4.4 Results and Discussion . . . 178
4.4.1 Representativeness of aircraft measurements . . . 178
4.4.2 Inconsistency in model-observation comparison . . . 180
4.4.3 Effects of constraining *in-situ* cloud variables on bulk cloud properties . . . 187
4.5 Conclusions . . . 192
Appendix . . . 195
References . . . 204

5 The importance of aerosols and ice formation for the response of mixed-phase clouds to warming 211
5.1 Abstract . . . 212
5.2 Introduction . . . 213
5.3 Results and Discussion . . . 215
5.3.1 Effect of aerosols on cloud albedo, cover and longwave radiation 216
5.3.2 Effect of aerosols on SW and LW cloud radiative effects . . . 218
5.3.3 Importance of secondary ice production . . . 221
5.3.4 The cloud microphysical component of feedback uncertainty . . . 223
5.3.5 Effect from changes in aerosol in the future climate . . . 225
5.4 Conclusions . . . 227
5.5 Materials and Methods . . . 230
5.5.1 Identification of cold-air outbreak initialising points in CMIP6 . 230
5.5.2 Model configuration . . . 231
5.5.3 Design of perturbed parameter ensemble . . . 232
5.5.4 Preprocessing of albedo in idealised simulations . . . 232
5.5.5 Gaussian Process emulation . . . 233
5.5.6 Sampling of N_d, S_{INP} and SIP processes for each CAO event . . 234
5.5.7 Calculation of SW fluxes . . . 234

Appendix 236
References 254

6 Conclusions and Future Work **261**
6.1 Summary of main findings 261
6.1.1 Chapter 2: Different responses of cold-air outbreak clouds to aerosol and ice production depending on cloud temperature . . . 261
6.1.2 Chapter 3: Interacting effects of droplet number and ice formation processes on mixed-phase cold-air outbreak clouds 263
6.1.3 Chapter 4: Identification of model inconsistencies using perturbed parameter ensembles and aircraft observations of mixed-phase cold-air outbreak clouds 264
6.1.4 Chapter 5: The importance of aerosols and ice formation for the response of mixed-phase clouds to warming 267
6.2 Implications and Recommendations for future studies 269
References 271

List of Figures

1.1 Assessed values of individual cloud feedbacks and the total cloud feedback from Sherwood et al. (2020) 3

1.2 Schematic diagram of cloud microphysics in a typical two-moment cloud microphysics scheme adapted from Randall et al. (2018) 6

1.3 Satellite imagery of a cold-air outbreak event over the Labrador Sea on 14 March 2022 12

2.1 The UK Met Office surface analysis charts at 1200 UTC on 15 March 2022 and 24 October 2022 41

2.2 Perturbed INP range in Chapter 2 compared to INP measurements at high-latitude regions in the Northern Hemisphere from literature data and INP measurements from each flight during the M-Phase aircraft campaign 45

2.3 Satellite retrievals for CAO events over the Labrador Sea on 15 March 2022 and 24 October 2022 47

2.4 In-cloud cloud water path (CWP) from the control UM-CASIM simulations and MODIS retrievals on 15 March 2022 and 24 October 2022. 50

2.5 Cross-section mean cloud properties from the 15 March 2022 and the 24 October 2022 control simulations. 51

2.6 Responses of cross-section mean CAO cloud properties to the three perturbed parameters on 15 March 2022 at 16:45 UTC 54

2.7 Responses of cross-section mean CAO cloud properties to the three perturbed parameters on 24 October 2022 at 17:00 UTC 55

2.8 The cloud field homogeneity parameter and the fraction of cumulus-capped boundary layer in cloudy pixels for simulations with perturbed N_{d}, S_{INP} and E_{HM} on 15 March 2022 58

2.9 The cloud field homogeneity parameter and the fraction of cumulus-capped boundary layer in cloudy pixels for simulations with perturbed N_{d}, S_{INP} and E_{HM} on 24 October 2022 59

2.10 Fractional changes of cloud properties in the perturbed parameter simulations relative to the control simulations for the 15 March 2022 and the 24 October 2022 cases 61
2.11 Vertical profiles for in-cloud properties in the 15 March 2022 case . . 62
2.12 Vertical profiles for in-cloud properties in the 24 October 2022 case . 63
2.13 Model output compared with satellite retrievals of all-sky liquid water path (LWP) from AMSR-2, shortwave radiation and longwave radiation at the top-of-atmosphere from CERES for simulations with different S_{INP} on 15 March 2022 64
2.14 Model output compared with satellite retrievals of all-sky liquid water path (LWP) from AMSR-2, shortwave radiation and longwave radiation at the top-of-atmosphere from CERES for simulations with different S_{INP} on 24 October 2022 65
2.15 A schematic diagram for explaining the different sensitivities of CAO cloud properties to perturbations of INPs in ice-dominant and liquid-dominant clouds 69
A2.1 Monthly distribution for cloud top temperature of low-level, mixed-phase CAO clouds over the Labrador Sea in January, February, March, October, November and December 2022 72
A2.2 Nested model domains and the selected sub-domains for analysis for 15 March 2022 and 24 October 2022 74
A2.3 Cloud top temperature (CTT) from the control simulation of the 15 March 2022 case and the MODIS onboard Aqua satellite. 79
A2.4 Comparison of the cloud top temperature (CTT) distributions of 15 March 2022 between the CTT retrieved from the MODIS onboard the Aqua satellite and the CTT extracted from the control simulation of the March case using different total water content thresholds 79
A2.5 Comparison of temperature and IWC (ice water content) profiles from CALIOP onboard CALIPSO satellite and the control simulation of 15 March 2022 80
A2.6 Information of the M-Phase C322 and C323 flights used for the validation of the control simulation on 24 October 2022 81
A2.7 Model-observation comparison of the control simulation against M-Phase C322 and C323 measurements on 24 October 2022 81
A2.8 Cross-section mean cloud properties from the 15 March 2022 and the 24 October 2022 control simulations in the sub-domain 82
A2.9 Cross-section mean environmental conditions from the 15 March 2022 and the 24 October 2022 control simulations in the sub-domain . . . 83

A2.10 Cross-section mean vertical profiles from the sub-domain of bulk cloud volume fraction and in-cloud total water content (TWC) for the 15 March 2022 case and the 24 October 2022 case in the control simulations 84
A2.11 Sub-domain mean CAO cloud properties from the beginning of the cloud system to the end of the cloud system for 15 March 2022 at 16:45 UTC 85
A2.12 Sub-domain mean CAO cloud properties from the beginning of the cloud system to the end of the cloud system for 24 October 2022 at 17:00 UTC 86
A2.13 Boundary layer type fractions for all the simulations of 15 March 2022 and 24 October 2022 87
A2.14 The cloud field homogeneity parameter with the fraction of cumulus-capped boundary layer in cloudy pixels and cloud cover from simulations with perturbed S_{INP} for default setup, no precipitation (sedimentation of all hydrometeors) setup, no evaporation and sublimation setup, and no-all (no precipitation, evaporation and sublimation) for the 15 March 2022 case 88
A2.15 Boundary layer type fractions from simulations with perturbed S_{INP} for default setup, no precipitation (sedimentation of all hydrometeors) setup, no evaporation and sublimation setup, and no-all (no precipitation, evaporation and sublimation) for the 15 March 2022 case . . . 89
A2.16 Vertical profiles of in-cloud LWC (liquid water content), in-cloud IWC (ice water content), $N_{\mathrm{ice}} + N_{\mathrm{snow}}$ and equivalent spherical radius for stratocumulus-dominated and cumulus-dominated regions in the 15 March 2022 CAO case with different N_{d} and E_{HM} 90
A2.17 Vertical profiles of in-cloud LWC (liquid water content), in-cloud IWC (ice water content), $N_{\mathrm{ice}} + N_{\mathrm{snow}}$ and equivalent spherical radius for stratocumulus-dominated and cumulus-dominated regions in the 24 October 2022 CAO case with different N_{d} and E_{HM}. 91
A2.18 Model output compared with satellite retrievals for simulations with different N_{d} and E_{HM} on 15 March 2022 92
A2.19 Model output compared with satellite retrievals for simulations with different N_{d} and E_{HM} on 24 October 2022 93
A2.20 Modelled cloud fraction compared to cloud fraction retrieved from MODIS onboard the Aqua satellite with different N_{d}, S_{INP} and E_{HM} on 15 March 2022 94
A2.21 Modelled cloud fraction compared to cloud fraction retrieved from MODIS onboard the Aqua satellite with different N_{d}, S_{INP} and E_{HM} on 24 October 2022 94

3.1 Flight tracks, nested model domains and model analysis domains for the Sc region and the Cu region on 24 October 2022 over the Labrador Sea . . . 111
3.2 Key processes among the five CASIM hydrometeors . . . 112
3.3 Comparison between the perturbed range and the measurements for N_{d} and N_{INP} . . . 116
3.4 Paired combinations of parameters perturbed in Chapter 3. . . . 117
3.5 Responses of TOA albedo for the Sc region ordered according to N_{d} and N_{INP}^{-15} and the Cu region ordered according to N_{d} and mpof . . . 120
3.6 Distributions of cloud variables from 1 million combinations of parameter values for all-sky TOA albedo, cloud cover, all-sky LWP, all-sky IWP, and all-sky TWP. . . . 124
3.7 Emulated mean model responses of all-sky TOA albedo to paired parameters in the Sc region and the Cu region . . . 130
3.8 Emulated mean model responses of all-sky LWP to paired parameters in the Sc region and the Cu region . . . 131
3.9 Distributions of the cloud property changes resulting from an increase of individual parameters one-at-a-time (OAT) in multiple OAT tests for all-sky TOA albedo, cloud cover, all-sky LWP, all-sky IWP, all-sky TWP and cloud top temperature . . . 132
A3.1 Empirical soil-dust parameterisation of $n_{s,\mathrm{soil}}(T)$ . . . 133
A3.2 Kernel selection and testing results of the GP emulators on TOA albedo, cloud cover, and LWP in the Sc model analysis region . . . 138
A3.3 Kernel selection and testing results of the GP emulators on IWP, TWP and cloud top temperature in the Sc model analysis region. . . . 139
A3.4 Kernel selection and testing results of the GP emulators on TOA albedo, cloud cover, and LWP in the Cu model analysis region. . . . 140
A3.5 Kernel selection and testing results of the GP emulators on IWP, TWP and cloud top temperature in the Cu model analysis region. . . . 141
A3.6 Convergence test results ($RMSE$) by using different number of training points over the Sc region and the Cu region for all variables . . . 142
A3.7 Flowchart for methods involved in Chapter 3 . . . 143
A3.8 A simple illustration of linear and non-linear joint effects between two parameters . . . 144
A3.9 Projected mean model responses of cloud cover to paired parameters in the Sc region and the Cu region . . . 145
A3.10 Projected mean model responses of all-sky IWP (ice water path) to paired parameters in the Sc region and the Cu region . . . 146
A3.11 Projected mean model responses of all-sky TWP (total water path) to paired parameters in the Sc region and the Cu region . . . 147

A3.12 Projected mean model responses of cloud top temperature to paired parameters in the Sc region and the Cu region 148
A3.13 Sensitivity indices of all the perturbed parameters for all variables in the Sc and the Cu regions 151

4.1 Flight tracks, nested model domains and model analysis domain for Flight C322 and Flight C323 in the M-Phase aircraft campaign . . . 170
4.2 Time-series of measurements during Flight C322 and Flight C323 in the M-Phase aircraft campaign 171
4.3 Domain-mean vertical profiles of ambient temperature, cloud fractions, in-cloud cloud water contents, N_{CDP}, and N_{HI} from aircraft measurements for Flight C322 and Flight C323 175
4.4 The number of aircraft measurements per model grid box and the number of valid grid boxes per model height level for cloud properties assessed in Chapter 4 for Flight C322 and Flight C323 180
4.5 Vertical profiles in the C322 Sc region for cloud properties from aircraft observations and model output, along with the distribution of I and the number of plausible ensemble members with $|I| \leq 2$ 183
4.6 Vertical profiles in the C323 Cu region for cloud properties from aircraft observations and model output, along with the distribution of I and the number of plausible ensemble members with $|I| \leq 2$ 184
4.7 Comparison of using different observational constraints in the C322 Sc region 187
4.8 Comparison of using different observational constraints in the C323 Cu region 188
4.9 Percentage of constrained variables that are consistent with observations for each ensemble member and number of ensemble members that are consistent with all observational constraints, against different multiples of the original representation uncertainty ($Var(\mathrm{R})$) 189
4.10 Effects of applying observational constraint on one cloud variable (constrained variable) to other cloud variables (affected variable) . . . 189
4.11 Effects of applying observational constraint on one *in-situ* cloud variable to bulk cloud properties including cloud cover, all-sky LWP (liquid water path) and TOA (top-of-the-atmosphere) albedo 191
A4.1 Comparison of using different measurements from aircraft observations to identify in-cloud measurements 195
A4.2 Comparison in vertical profiles of ambient temperatures from aircraft measurements and PPE simulations 195
A4.3 Representation uncertainties in compositing domain-mean vertical profiles in the C322 Sc region 196

A4.4 Representation uncertainties in compositing domain-mean vertical profiles in the C323 Cu region 197

A4.5 Dependency of representation uncertainty (σ) in compositing domain-mean vertical profiles on the number of valid model grid boxes at one model level in the C322 Sc region 198

A4.6 Dependency of representation uncertainty (σ) in compositing domain-mean vertical profiles on the number of valid model grid boxes at one model level in the C323 Cu region 198

A4.7 Binary maps for PPE members with observational constraints on different cloud properties in the C322 Sc region 199

A4.8 Binary maps for PPE members with observational constraints on different cloud properties in the C323 Cu region 199

A4.9 Distributions of parameter ranges from the PPE members retained by observational constraints on different cloud properties in the C322 Sc region for cloud fraction, liquid cloud fraction, in-cloud LWC, in-cloud N_{d}, and in-cloud N_{d}/LWC 200

A4.10 Distributions of parameter ranges from the PPE members retained by observational constraints on different cloud properties in the C322 Sc region for ice cloud fraction, in-cloud IWC, in-cloud N_{ice} and in-cloud N_{ice}/IWC 201

A4.11 Distributions of parameter ranges from the PPE members retained by observational constraints on different cloud properties in the C323 Cu region for cloud fraction, liquid cloud fraction, in-cloud N_{d}, and in-cloud N_{d}/LWC 202

A4.12 Distributions of parameter ranges from the PPE members retained by observational constraints on different cloud properties in the C323 Cu region for ice cloud fraction, in-cloud N_{ice}, and in-cloud N_{ice}/IWC 203

5.1 A simplified illustration of sampling environmental factors and cloud microphysical parameters over the parameter space. 215

5.2 Effects of N_{d} and S_{INP} in the SH on cloud cover, cloud albedo, cloud longwave flux and changes of these three cloud properties between the warming climate (2090s) and the present-day climate (2020s) 219

5.3 Effects of N_{d} and S_{INP} in the NH on cloud cover, cloud albedo, cloud longwave flux and changes of these three cloud properties between the warming climate (2090s) and the present-day climate (2020s) 220

5.4 Effects of N_{d} and N_{INP} on the decomposition terms for SWCRE and LWCRE 221

5.5 Effects from N_d, S_{INP} and three SIP parameters (E_{HM}, E_{BR} and E_{DS}) using slope from linear fit between the decomposition terms and standardized values of parameters 223
5.6 The central 90% range of changes in SWCRE (ΔR^{SW}_{CRE}), LWCRE (ΔR^{LW}_{CRE}) and net CRE (ΔR^{net}_{CRE}) by sampling N_d, N_{INP} and all three SIP uncertainties, and the first-order sensitivities on the changes of CREs from these parameters 225
5.7 Comparison of the central 90% range of the changes in net CRE (ΔR^{net}_{CRE}) for no future changes of aerosols, and including future changes of aerosols in the warmer climate, along with different constraints on present-day and future N_d and N_{INP} 228
A5.1 Distributions of environmental conditions in CAO events in present-day climate (2020s) and warmer climate (2090s) for the Southern Hemisphere and Northern Hemisphere 236
A5.2 Distributions from varying N_d, N_{INP} and SIP processes on the variations of cloud-state variables and the change of cloud states in the SH 237
A5.3 Distributions from varying N_d, N_{INP} and SIP processes on the variations of cloud-state variables and the change of cloud states in the NH 238
A5.4 Effects from N_d, N_{INP} and three SIP parameters (E_{HM}, E_{BR} and E_{DS}) using slope from linear fit between the cloud properties and standardized values of parameters 239
A5.5 Monthly ranges (5% quantile, median and 95% quantile) of the feedback decomposition terms 240
A5.6 Distributions of SW, LW and net fluxes changes by varying N_d, N_{INP} and SIP processes across the parameter space 241
A5.7 Comparison of the central 90% range of the changes in SWCRE (ΔR^{SW}_{CRE}) for no future changes of aerosols, and including future changes of aerosols in the warmer climate, along with different constraints on present-day and future N_d and N_{INP} 242
A5.8 Comparison of the central 90% range of the changes in LWCRE (ΔR^{LW}_{CRE}) for no future changes of aerosols, and including future changes of aerosols in the warmer climate, along with different constraints on present-day and future N_d and N_{INP} 243
A5.9 Scatter plots of changes in SWCRE, LWCRE and net CRE against N_d and $log(S_{INP})$ for the Southern Hemisphere and Northern Hemisphere 247
A5.10 Examples of CAO initialising points identified over the Northern Hemisphere (2025-01-01) and the Southern Hemisphere (2025-07-02) . . . 248
A5.11 Initial profiles and external forcings for the control simulation 249

A5.12 Time-series of model output in the one-at-a-time sensitivity test for using different initial SSTs (SST_0) 250
A5.13 Examples of raw and adjusted albedos, and the predicted cloud albedo using ridge regression from PPE member 30 251
A5.14 Testing results for GP emulators 252
A5.15 Sampling of N_d, S_{INP} and SIP processes over the parameter space . . 252
A5.16 Number of valid CAO cases for analysis in each latitude-month bin for the Southern Hemisphere and the Northern Hemisphere. 253

List of Tables

2.1 Configurations of simulations for both the 15 March 2022 and the 24 October 2022 case studies 44

A2.1 Satellite products used in Chapter 2, their retrieval times and selected model time points for comparison in the sub-domains 70

A3.1 Polynomial coefficients used in Eq. A3.1 134

A5.1 Statistics for ΔR_{CRE} between present-day (2020s) and warmer (2090s) climates 242

A5.2 Statistics for $\Delta R_{\mathrm{CRE}}^{\mathrm{SW}}$ between present-day (2020s) and warmer (2090s) climates for different aerosol assumptions in the SH 244

A5.3 Statistics for $\Delta R_{\mathrm{CRE}}^{\mathrm{SW}}$ between present-day (2020s) and warmer (2090s) climates for different aerosol assumptions in the NH 244

A5.4 Statistics for $\Delta R_{\mathrm{CRE}}^{\mathrm{LW}}$ between present-day (2020s) and warmer (2090s) climates for different aerosol assumptions in the SH 245

A5.5 Statistics for $\Delta R_{\mathrm{CRE}}^{\mathrm{LW}}$ between present-day (2020s) and warmer (2090s) climates for different aerosol assumptions in the NH 245

A5.6 Statistics for $\Delta R_{\mathrm{CRE}}^{\mathrm{net}}$ between present-day (2020s) and warmer (2090s) climates for different aerosol assumptions in the SH 246

A5.7 Statistics for $\Delta R_{\mathrm{CRE}}^{\mathrm{net}}$ between present-day (2020s) and warmer (2090s) climates for different aerosol assumptions in the NH 246

A5.8 Parameters perturbed and their descriptions 248

List of Abbreviations

2D-S	Two-Dimensional Stereoscopic probe
ACAO	Arctic Cold-Air Outbreak campaign
ACTIVATE	Aerosol Cloud meTeorology Interactions oVer the western ATlantic Experiment
AMSR-2	Advanced Microwave Scanning Radiometer 2
BR	ice-ice collisional breakup
CAESAR	Cold Air outbreak Experiment in the Sub-Arctic Region
CALIOP	Cloud-Aerosol Lidar with Orthogonal Polarization
CALIPSO	Cloud-Aerosol Lidar and Infrared Pathfinder Satellite Observations
CAO	cold-air outbreak
CASIM	Cloud AeroSol Interacting Microphysics
CCN	cloud condensation nuclei
CDP	Cloud Droplet Probe
CERES	Clouds and the Earth's Radiant Energy System
CMIP5	Coupled Model Intercomparison Project Phase 5
CMIP6	Coupled Model Intercomparison Project Phase 6
CNT	classical nucleation theory
COMBLE	Cold-Air Outbreaks in the Marine Boundary Layer Experiment
CPM	Convection-Permitting Model

CRE cloud radiative effect

CRM Cloud-Resolving Model

CTH cloud-top height

CTP cloud-top pressure

CTT cloud-top temperature

Cu cumulus

CWP cloud water path

DS droplet shattering

ECS equilibrium climate sensitivity

EIS estimated inversion strength

ERA5 ECMWF ReAnalysis version 5

FAAM Facility for Airborne Atmospheric Measurements

GCM Global Climate Model/ General Circulation Model

GCOM-W Global Change Observation Mission - Water

GP Gaussian Process

HALO-(AC)^3 High Altitude and Long Range Research Aircraft Project on Arctic Amplification Climate Relevant Atmospheric and Surface Processes and Feedback Mechanisms

HM Hallett-Mossop process

INP ice-nucleating particle

IWC ice water content

IWP ice water path

LAM Limited-Area Model

LES Large Eddy Simulation

LHS Latin hypercube sampling

LTS	lower-tropospheric stability
LW	longwave
LWCRE	longwave cloud radiative effect
LWC	liquid water content
LWP	liquid water path
MAE	mean absolute error
MODIS	Moderate Resolution Imaging Spectroradiometer
M-PACE	Mixed-Phase Arctic Cloud Experiment
NH	Northern Hemisphere
NWP	numerical weather prediction
OAT	one-at-a-time
PIP	primary ice production
PPE	perturbed parameter ensemble
PSD	particle size distribution
RBF	radial basis function
RH	relative humidity
RMSE	root mean square error
Sc	stratocumulus
ScenarioMIP	Scenario Model Intercomparison Project
SCT	stratocumulus-to-cumulus transition
SH	Southern Hemisphere
SIP	secondary ice production
SOC	Southern Ocean Clouds campaign
SOCRATES	Suite Of Community Radiative Transfer codes based on Edwards and Slingo

SSA sea-spray aerosol

SSF Single Scanner Footprint

SSP Shared Socioeconomic Pathway

SST sea surface temperature

STABLE Springtime Atmospheric Boundary Layer Experiment

SW shortwave

SWCRE shortwave cloud radiative effect

SZA solar zenith angle

TOA top of atmosphere

TWC total water content

TWP total water path

UKCA UK Chemistry and Aerosol

UKESM UK Earth System Model

UM Unified Model

Chapter 1

Introduction

1.1 Clouds and cloud feedback

1.1.1 Clouds in the Earth system

Clouds cover approximately 70% of the Earth's surface (Stubenrauch et al., 2013) and play an important role in the Earth system. They consist of liquid water droplets, ice crystals, or a mixture of both. Through the formation of precipitation and the redistribution of water, clouds exert a strong control on the global hydrological cycle. By influencing both the shortwave (SW) and longwave (LW) radiation budgets at the top-of-the-atmosphere (TOA), clouds also act as important modulators of the Earth's energy budget. In the absence of clouds, 47 W m^{-2} less SW radiation would be reflected back to space due to the loss of cloud albedo effect, while 28 W m^{-2} more LW radiation would be emitted to space due to the loss of cloud greenhouse effect (Khain et al., 2015; Wild et al., 2019; Forster et al., 2021). In addition to the TOA radiation budget, clouds affect the energy fluxes in the atmosphere through the vertical redistribution of latent heat. This includes the release of latent heat through condensation and deposition of water vapour, as well as the consumption of latent heat through evaporation and sublimation of cloud hydrometeors.

Cloud radiative effect (CRE) is defined as the difference between the radiative flux under all-sky conditions and the corresponding clear-sky flux, representing the effect of clouds on the TOA radiation budget. A negative CRE indicates that clouds reduce the net downward radiative flux and therefore exert a cooling effect on the climate system, whereas a positive CRE indicates that clouds increase the net downward radiative flux and therefore exert a warming effect. The net CRE is determined by the relative effects of the SW cloud radiative effect (SWCRE) and the LW cloud radiative effect (LWCRE). The relative importance of these two effects varies with cloud type, altitude, optical depth and location (Dhuria et al., 1990; Chen et al., 2000). Low-level clouds generally

have a negative net CRE because they are often optically thick and hence produce a strong negative SWCRE, while their small temperature contrast with the surface results in a relatively weak positive LWCRE, and therefore exert a net cooling effect on the climate system (Klein et al., 1993). However, the net effect changes when the surface beneath these clouds switches from low-albedo surface such as ocean, to highly reflective surface such as snow (e.g. Shupe et al., 2004), as the SWCRE is reduced. Cirrus clouds and deep convective clouds both fall into high-level clouds, but they have different net CREs. Thin cirrus clouds are generally semi-transparent to incoming SW radiation but they have a strong temperature contrast to the surface, so their CRE is dominated by their LWCRE, leading to a positive net CRE (Lee et al., 2009). Deep convective clouds also have a strong LWCRE, but they are optically thick and have a strong SWCRE, resulting in a near-neutral net CRE (Kiehl, 1994).

Increasing greenhouse-gas concentrations in the atmosphere from human activities have warmed the climate system, leading to changes in cloud properties and their radiative effects at TOA. The change in TOA radiative flux associated with cloud responses to warming is known as cloud feedback. Cloud feedback is one of the climate feedbacks, with others including water-vapour and temperature lapse-rate feedback, surface albedo feedback and Planck feedback. Among the major climate feedbacks, cloud feedback remains one of the largest sources of uncertainty in estimating climate sensitivity and future climate change (Sherwood et al., 2020; Forster et al., 2021). This uncertainty arises because cloud radiative effects depend on many factors as shown above, but also many of the physical processes controlling clouds are poorly parameterised in climate and atmospheric models (Sherwood et al., 2020).

1.1.2 Decomposition of cloud feedback

Cloud feedbacks have been studied over several decades. In the late 1980s and early 1990s, cloud feedbacks started to be examined with General Circulation Models (GCMs) to a perturbation in sea surface temperature (SST) which serves as a surrogate climate change (Cess et al., 1988; Cess et al., 1990). Using a surrogate climate change benefits the intercomparison and examination of climate feedbacks among GCMs without significant differences in the geographical distributions of the simulated warming (Cess et al., 1988; Cess et al., 1990). These early studies showed that, including cloud feedback in the assessment, the variation of climate sensitivity increases by a factor of three, with a large spread of estimated cloud feedbacks among the assessed models (Cess et al., 1990).

To further understand the mechanisms behind cloud feedbacks, several methods have been used since the early 2000s, including separating the thermodynamic and dynamic components (Bony et al., 2004; Bony et al., 2005; Wyant et al., 2006) and separating the SW and LW cloud feedback components (Webb et al., 2006). Zelinka

et al. (2012) later proposed the cloud radiative kernel method to quantify the cloud feedbacks in each regime of clouds based on the cloud top pressure and optical depth. Many studies have since been using this framework for the assessment and decomposition of cloud feedback, including the AR5 (the Fifth Assessment Report) (Boucher et al., 2013) and the AR6 (Forster et al., 2021) from the Intergovernmental Panel on Climate Change (IPCC).

Based on cloud types (location and altitude) and the physical mechanisms behind the cloud feedbacks (changes of cloud altitude, amount and optical depth), six individual cloud feedbacks were assessed by Sherwood et al. (2020) using multiple lines of evidence and seven feedbacks with the additional Arctic cloud feedback were assessed by IPCC AR6 (Forster et al., 2021). Figure 1.1 shows the assessed values of individual cloud feedbacks and the total cloud feedback from Sherwood et al. (2020). The total cloud feedback is positive with a value of +0.45 W m^{-2} K^{-1} ($\pm$ 0.33 W m^{-2} K^{-1}). This suggests that cloud responses to the warming climate are very likely to amplify the global warming.

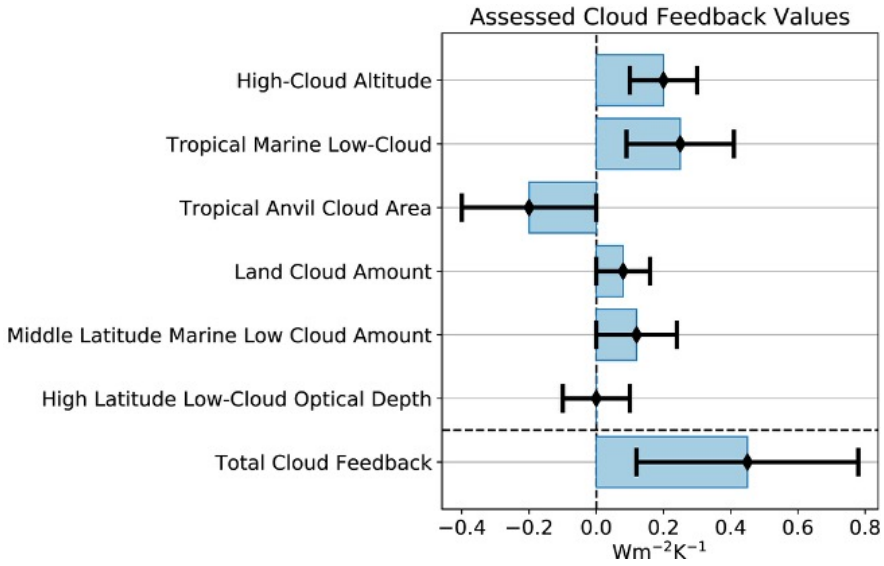


Figure 1.1: Assessed values of individual cloud feedbacks and the total cloud feedback. Black diamonds represent the maximum likelihood values, and the black uncertainty bars represent the $\pm$ 1-sigma likelihood values. This figure is from Sherwood et al. (2020).

The majority of the assessed individual cloud feedback components are also positive, and only one of these feedbacks is negative. For example, the amount of land cloud is expected to reduce as the relative humidity and surface water availability decreases with the warming of land surfaces (Bretherton, 2015), leading to a positive land cloud amount feedback. Changes in tropical low clouds associated with the increasing SST and estimated inversion strength (EIS) also result in a positive feedback (Klein et al., 2017). The only negative feedback is from the reduction of tropical anvil cloud area, which leads to more LW radiation being emitted to space. However, large uncertainties

still remain for the estimates of these feedbacks and the value of 0 (a neutral feedback) is within one standard deviation of the maximum likelihood value for all the feedbacks mentioned above.

Among the assessed individual cloud feedbacks, the high-latitude low-cloud optical depth feedback is unique because both its sign and magnitude remain highly uncertain. This uncertainty is particularly important because a more positive estimate of this feedback is one of the major reasons why many Coupled Model Intercomparison Project phase 6 (CMIP6) models show substantially higher climate sensitivity than CMIP5 models (Zelinka et al., 2020). The positive shift of this feedback has been linked to the improved representations of low-level mixed-phase clouds in CMIP6 models (Zelinka et al., 2020). This highlights the key role of mixed-phase clouds in reducing the uncertainties of cloud feedback estimates. Therefore, mixed-phase clouds and their response to a warming climate are the central focuses of this thesis.

1.1.3 Mixed-phase clouds and cloud-phase feedback

Mixed-phase clouds contain both liquid droplets and ice particles at the same time, and typically exist at temperatures between approximately 0°C and −38°C (Pruppacher et al., 1996). They are ubiquitous globally and occur throughout all seasons, spanning a wide range of meteorological environments and cloud types (Korolev et al., 2017).

A key property of mixed-phase clouds is the partitioning between liquid and ice, which strongly affects the cloud radiative properties, precipitation and lifetime (Pruppacher et al., 1996; Korolev et al., 2017). For the same amount of condensed water, mixed-phase clouds containing more liquid droplets are typically more reflective for SW radiation than those composed of fewer but larger ice crystals (Korolev et al., 2017). This is because smaller liquid droplets provide a larger total surface area for scattering SW radiation. The liquid-ice partitioning also controls precipitation formation because ice particles can grow rapidly by vapour deposition, riming, and aggregation, producing larger hydrometeors with higher fall speeds than cloud droplets (Pruppacher et al., 1996). A shift from liquid-dominated mixed-phase clouds towards ice-dominated mixed-phase clouds can therefore enhance precipitation and cloud water depletion, reduce cloud optical depth, shorten cloud lifetime, and hence lead to less SW radiation being reflected.

Liquid-ice partitioning is directly relevant to mixed-phase cloud feedback (e.g., McCoy et al., 2015), as it strongly affects the radiative properties of mixed-phase clouds. One mechanism of the cloud optical depth feedback is the change in cloud phase of mixed-phase clouds under the warming climate (Ceppi et al., 2017), which is called the cloud-phase feedback (Mitchell et al., 1989). As the atmosphere warms, mixed-phase clouds tend to contain more liquid water and less ice. Such a shift increases

the cloud optical depth and exerts a negative cloud-phase feedback (Storelvmo et al., 2015). Using observational constraints on climate models improves the representation of liquid-ice partitioning in present-day mixed-phase clouds and leads to a weaker negative cloud feedback and a corresponding higher climate sensitivity (Tan et al., 2016). This is because models with too little present-day supercooled liquid water have more scope for an ice-to-liquid transition under warming and can then produce a too strong negative cloud-phase feedback.

Temperature is not the only control on liquid-ice partitioning in mixed-phase clouds. Cloud microphysical processes that lead to ice formation and the subsequent depletion of cloud liquid water also play an important role in liquid-ice partitioning and radiative properties of these clouds (Pruppacher et al., 1996; Khain et al., 2018). In addition, liquid-ice partitioning alone does not fully capture the properties and complex interactions of cloud hydrometeors at the microphysical scale. Thus, understanding cloud-phase feedback in mixed-phase clouds requires not only quantifying changes in liquid-ice partitioning, but also investigating the influences from microphysical processes that control the formation and properties of liquid droplets and ice crystals in mixed-phase clouds.

1.2 Microphysical controls on mixed-phase clouds

Cloud microphysics refers to the microscale processes that control the formation and development of cloud hydrometeors. Figure 1.2 shows a schematic diagram of common cloud microphysical processes. These processes occur over spatial scales ranging from sub-micrometre to centimetre, which are much smaller than the grid spacing of most atmospheric and climate models, from metres in Large Eddy Simulations (LES) to tens or hundreds of kilometres in GCMs. Therefore, cloud microphysical processes cannot be explicitly resolved and have to be parameterised in the models. The poor representation of cloud microphysical processes remains a major source of uncertainty in estimating cloud feedbacks from GCMs (Sherwood et al., 2020). Even in Cloud-Resolving Models (CRMs), cloud microphysical processes are still subject to large uncertainties due to their highly parameterised and complex nature (Khain et al., 2015; Morrison et al., 2020b).

Rather than assessing the sensitivity of mixed-phase clouds to all microphysical processes, this thesis focuses on two major sources of uncertainty: aerosol-cloud interactions, and ice formation processes including primary ice production (PIP) and secondary ice production (SIP).

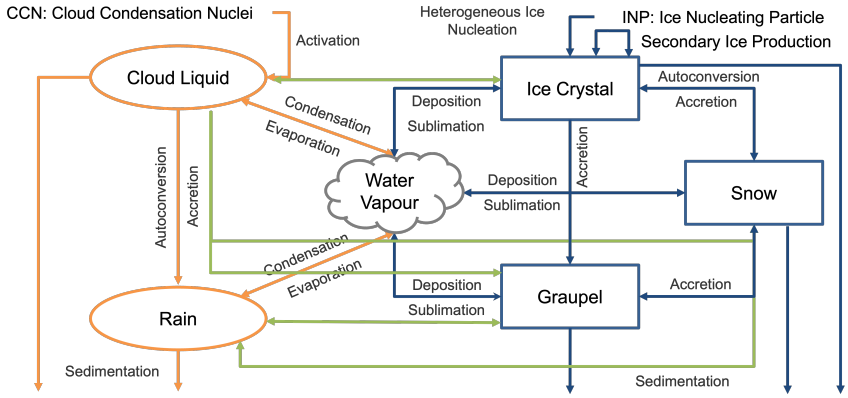


Figure 1.2: Schematic diagram of cloud microphysics in a typical two-moment cloud microphysics scheme. Interactions between hydrometeors in liquid-only clouds are shown in orange, those in ice-only clouds are shown in blue and additional interactions in mixed-phase clouds are shown in green. This figure is adapted from Randall et al. (2018).

1.2.1 Aerosol-cloud interactions

Aerosol is a suspension of particles in air, with its size ranging more than four orders of magnitude from nanometre to tens of micrometres. Aerosol can be emitted at the Earth's surface from both natural and anthropogenic sources, or form directly through gas-to-particle conversion in the atmosphere (Carslaw, 2022).

Aerosol exerts radiative effects on the Earth energy budget directly through scattering, absorbing and emitting radiation, and indirectly through aerosol-cloud interactions. Aerosol-cloud interactions occur when aerosol acts as cloud condensation nuclei (CCN), which serves as the initial site for water vapour condensation and leads to the formation of cloud droplets, or as ice-nucleating particles (INPs), which enable ice formation in supercooled clouds. As INPs are discussed in detail in the next section for PIP, this section mainly focuses on the role of aerosol as CCN in aerosol-cloud interactions.

Cloud droplets form when water vapour condenses onto CCN as air rises and reaches saturation. Soluble or hydrophilic aerosol particles compete and consume water vapour through hygroscopic growth and form aqueous solution droplets. Dissolved solutes reduce the saturation vapour pressure over these droplets through the Raoult effect, allowing them to grow at lower supersaturations compared to that required for a pure water droplet. At the same time, the curvature of small droplets increases their saturation vapour pressure through the Kelvin effect. The Köhler theory combines these two competing effects and describes a critical supersaturation at which an aerosol particle activates into a cloud droplet. When the ambient supersaturation exceeds this critical supersaturation, the aerosol particle is activated into a cloud droplet. The droplet activation with CCN depends on various factors, including updraught speed, aerosol composition, vertical velocity and supersaturation (Carslaw, 2022). Uncertainties and challenges remain regarding the representations of these properties in current climate

and atmospheric models (e.g., the treatment of supersaturation in models and see Gordon et al. (2020) for a detailed discussion), as well as in the parameterisation of aerosol activation.

With the same liquid water content, a higher CCN concentration can lead to a higher droplet number concentration (N_d) and smaller cloud droplets, resulting in a stronger reflection of SW radiation. This is the famous Twomey effect (Twomey, 1977), which is also called the first indirect aerosol effect (Houghton et al., 2001) and is instantaneous. An increase in N_d can also suppress precipitation (warm rain) by reducing the cloud droplet size, hence maintaining clouds. This is the Albrecht effect (Albrecht, 1989), also called the second indirect aerosol effect (Houghton et al., 2001) or cloud adjustment (Boucher et al., 2013). Other cloud adjustments to changes in N_d include, but are not limited to, the sedimentation-entrainment and evaporation-entrainment feedbacks (Ackerman et al., 2004) and cloud invigoration (Andreae et al., 2004; Khain et al., 2005; Koren et al., 2005; Rosenfeld et al., 2008; Koren et al., 2014).

1.2.2 Primary ice production

Primary ice production (PIP) refers to the initial formation of ice crystals in a cloud through ice nucleation, which can occur either through homogeneous freezing of supercooled water or through heterogeneous freezing mediated by ice-nucleating particles (INPs).

In the atmosphere, liquid water droplets can remain supercooled below 0 °C to as low as -38 °C. This is because the phase transition from liquid to ice requires the initial formation of a stable ice embryo, which involves overcoming a Gibbs free-energy barrier. Therefore, freezing is kinetically limited even though ice is thermodynamically favoured at sub-zero temperatures (Pruppacher et al., 1996; Lohmann et al., 2016). When temperature decreases, the Gibbs free-energy barrier decreases and the probability of ice nucleation increases. Eventually, near approximately -38 °C, supercooled liquid droplets freeze spontaneously through homogeneous ice nucleation without the requirement of a foreign substance.

At temperatures warmer than the homogeneous freezing temperature, ice formation requires heterogeneous nucleation on a subset of aerosols called INPs (Murray et al., 2012; Kanji et al., 2017). INPs facilitate freezing by reducing the Gibbs free-energy barrier required for the formation of a stable ice embryo. There are different modes of heterogeneous ice nucleation, including deposition freezing, contact freezing, immersion freezing and condensation freezing (Vali, 1985; Murray et al., 2012; Kanji et al., 2017). In mixed-phase clouds, immersion freezing is considered as the most significant mechanism for the ice crystal formation (Kanji et al., 2017), where INPs are immersed in supercooled water droplets.

The characteristics and abundance of INPs are important for mixed-phase clouds, as well as the responses of mixed-phase clouds to the warming climate. As the saturation vapour pressure over ice is lower than the one over liquid, vapour tends to deposit onto ice crystals at the expense of evaporating liquid droplets, which is the famous Wegener-Bergeron-Findeisen (WBF) process (Wegener, 1911; Bergeron, 1935; Findeisen, 1938; Findeisen et al., 1943). An increase in INP concentration can enhance ice formation in mixed-phase clouds and deplete supercooled liquid water through the WBF process and accretion, hence leading to a reduction in cloud optical depth and less SW radiation being reflected by the cloud (e.g. Vergara-Temprado et al., 2018). It is also suggested that the strength and even sign of cloud-phase feedback can vary with different present-day INP concentrations and potential INP changes in the warming future (Murray et al., 2021).

Parametrisations of heterogeneous ice nucleation and INPs are therefore important for representing mixed-phase clouds in climate and atmospheric models. Heterogeneous ice nucleation is commonly described in two ways: the classical nucleation theory (CNT) and the singular theory (Pruppacher et al., 1996; Murray et al., 2012). The CNT treats freezing as a stochastic process in which the probability of nucleation depends on thermodynamic conditions, particle surface properties and time. In contrast, singular theory ignores time dependence and assumes that aerosol particles contain active sites with characteristic freezing temperatures. Freezing occurs when the temperature reaches the activation temperature of a given site in the singular theory. In climate models, traditional approaches are based on thermodynamic state variables, such as temperature and ice supersaturation. For example, the Cooper parameterisation provides a temperature-dependent estimate of ice crystal number concentration (Cooper, 1986), while the Bigg parameterisation describes the freezing of supercooled raindrops as a temperature-dependent stochastic process (Bigg, 1953). Although these traditional approaches do not explicitly consider the properties or concentrations of INPs, they are computationally cheap and are still actively used in climate and atmospheric models.

Improved understanding of INP sources and laboratory measurements of ice-nucleating abilities from different aerosols have enabled more aerosol-aware parameterisation of heterogeneous ice nucleation in models. Mineral dust is considered as an important source of INPs globally, with different minerals having different ice-nucleating abilities. In particular, laboratory studies have shown that feldspar minerals, especially K-rich feldspars, can dominate the ice-nucleating ability of mineral dust despite representing only a small fraction of the emitted dust mass (Atkinson et al., 2013; Harrison et al., 2016; Harrison et al., 2019). In models, INP parameterisations based on mineral dust have been developed over a decade, such as linking INP concentration directly to desert dust concentration (DeMott et al., 2015) or through the surface active site density (n_s) measured in laboratory experiments (Niemand et al., 2012; Atkinson et al., 2013; Har-

rison et al., 2019). Primary marine organic aerosols associated with sea spray aerosols have also been shown to contribute to INP populations, particularly in remote marine environments (Wilson et al., 2015; Vergara-Temprado et al., 2017; McCluskey et al., 2018; McCluskey et al., 2019). Different model parameterisations for marine organic INPs have also been developed, such as deriving INP concentrations based on the total organic carbon mass concentration (Wilson et al., 2015) or through n_s (McCluskey et al., 2018; McCluskey et al., 2019). However, despite these improvements, challenges remain in simulating INP concentrations and their spatial and temporal variability in climate models (Burrows et al., 2022). Large uncertainties in INP parameterisations can propagate into uncertainties in simulating ice formation in mixed-phase clouds, and hence radiative effects from these clouds on the Earth energy budget.

1.2.3 Secondary ice production

Secondary ice production (SIP) refers to the formation of new ice crystals based on the presence of pre-existing ice, which is also known as ice multiplication. Observed ice crystal number concentrations in mixed-phase clouds often exceed the INP concentrations by several orders of magnitude, suggesting that PIP alone is frequently insufficient to explain cloud ice concentrations (Field et al., 2017a; Korolev et al., 2020). There are a number of mechanisms for SIP processes which occur at various thermodynamic and microphysical conditions.

The best-known mechanism is rime splintering, also called the Hallett-Mossop (HM) process (Hallett et al., 1974). This process produces small ice splinters when supercooled cloud droplets freeze during riming onto graupel or snow. This process is active within a temperature range between -3 °C and -8 °C, and requires the presence of supercooled liquid droplets with appropriate sizes. The HM process is also the most frequently, and sometimes the only, implemented SIP process in climate and atmospheric models (Field et al., 2017a). A common approach is using a temperature-dependent function which peaks at -5 °C to modulate the rate of the HM process and assume a constant number of splinters produced per milligram of rimed liquid (e.g., Cotton et al., 1986; Ferrier, 1994; Sullivan et al., 2018; Field et al., 2023). Despite over decades of research on the HM process, the rates of splinter production in the HM process still remain uncertain (Field et al., 2017a). Recent works on SIP in Arctic mixed-phase clouds have also suggested that HM process alone is not sufficient to represent SIP processes (Sotiropoulou et al., 2020; Pasquier et al., 2022).

Ice-ice collision is another important SIP mechanism, in which ice fragments are produced during collisions between ice particles (Vardiman, 1978; Takahashi et al., 1995). Unlike the HM process, ice-ice collision does not require the existence of liquid. One parameterisation of ice-ice collision in models is the temperature-dependent approach in which the process rate peaks at -21 °C using the fragment numbers mea-

sured by Takahashi et al. (1995). Such an approach is highly simplified and a more physically-based parameterisation was recently proposed by Phillips et al. (2017) which estimates the rate of ice-ice collision based on collisional kinetic energy and separates the calculations of process rates between ice categories. However, due to the lack of laboratory studies, the efficiency of ice-ice collision still remains highly uncertain (Field et al., 2017a; Korolev et al., 2020; Morrison et al., 2020b).

The third mechanism is droplet shattering, which produces ice splinters from large supercooled droplets freezing and breaking apart (Latham et al., 1961; Dye et al., 1968; Johnson et al., 1968; Leisner et al., 2014). Historically, droplet shattering was the first mechanism proposed for explaining SIP in clouds. During the freezing of large droplets, internal pressure can build up when an ice shell forms around the droplet, leading to mechanical breakup and the release of ice splinters. This process is most active between -10 °C and -15 °C (Leisner et al., 2014). A commonly used parameterisation for the droplet shattering is based on a shattering probability from droplet levitation experiments by Leisner et al. (2014), which is given by a normal distribution with peaks at -10 °C or -15 °C.

In addition to these three SIP processes, three other SIP processes have also been identified, including ice particle fragmentation due to thermal shock (Koenig, 1963; Gold, 1963), fragmentation of sublimating ice (Oraltay et al., 1989) and activation of INP in high transient supersaturation areas around freezing drops (Gagin, 1972). However, these processes are less studied with little implementation in atmospheric and climate models, hence are not further investigated in this thesis.

1.3 Mixed-phase clouds in cold-air outbreaks

Rather than examining mixed-phase clouds globally, this thesis focuses on mixed-phase clouds formed during cold-air outbreak (CAO) events. This is because CAOs are strongly forced meteorological events, and CAO clouds are generally in mixed-phase state due to the low ambient temperature (Fowler et al., 1996), providing a natural laboratory to understand the role of cloud microphysics in the behaviour of mixed-phase clouds. Additionally, strong CAO events are usually associated with the cold air sector of extratropical cyclones (Fletcher et al., 2016a) and clouds formed in the cold sector of extratropical cyclone systems have been shown important to the radiation bias over the Southern Ocean (SO) (Bodas-Salcedo et al., 2014; Bodas-Salcedo et al., 2016), suggesting improvements on the representation of mixed-phase CAO clouds in climate models are required.

CAOs occur when cold and dry airmass travels from polar regions, mid- or high-latitude continents to open and warm ocean. The temperature contrast between sea surface and air produces strong turbulent fluxes of heat and moisture from the ocean

to the atmosphere, leading to rapid boundary layer deepening and extensive cloud formation (Brümmer, 1996; Kolstad et al., 2008; Kolstad et al., 2009; Fletcher et al., 2016a; Fletcher et al., 2016b). CAOs are common in high-latitude regions for both hemispheres and have a clear seasonal cycle in their frequencies of occurrence (Fletcher et al., 2016a). Regions with a high frequency of CAO events include the Labrador Sea, the Norwegian Sea, the Kuroshio, the Bering Sea, the Gulf Stream and the North Atlantic in the Northern Hemisphere, and the Agulhas Current, the Indian polar front, the Indian subtropical front, the north Ross Sea, the north Bellingshausen Sea and the Brazil Current in the Southern Hemisphere (Fletcher et al., 2016a).

A typical CAO cloud field begins with cloud streets, which are roll clouds associated with roll-like circulations (Brümmer, 1999), and stratocumulus clouds near the sea-ice edge or coast. Then the cloud field transits to open-cell convection and broken cumulus clouds farther downstream. Figure 1.3 shows the satellite imagery of cloud field in a CAO event over the Labrador Sea. This stratocumulus-to-cumulus transition (SCT) in the development of CAO cloud field has important radiative impacts as stratocumulus generally has higher cloud cover and albedo than broken cumulus (McCoy et al., 2017). Many dedicated field campaigns have been conducted to observe and measure boundary-layer structures, airmass and clouds during CAOs, such as M-PACE (the Mixed-Phase Arctic Cloud Experiment) on the North Slope of Alaska (Verlinde et al., 2007), STABLE (the Springtime Atmospheric Boundary Layer Experiment) in the Fram Strait and over Svalbard (Michaelis et al., 2022), COMBLE (The Cold-Air Outbreaks in the Marine Boundary Layer Experiment) in northern Scandinavia and on Bear Island (Geerts et al., 2022), ACTIVATE (the Aerosol Cloud MeTeorology Interactions oVer the western ATlantic Experiment) (Sorooshian et al., 2023), ACAO (Arctic Cold-Air Outbreak campaign) over the Norwegian and Barents seas (Raif et al., 2024), M-Phase over the Labrador Sea (Clarke et al., 2025), HALO-AC^3 (High Altitude and Long Range Research Aircraft Project on Arctic Amplification Climate Relevant Atmospheric and Surface Processes and Feedback Mechanisms) in northern Sweden (Wendisch et al., 2024), and CAESAR (the Cold Air outbreak Experiment in the Sub-Arctic Region) over the Greenland/Norwegian Seas (Zuidema et al., 2026).

1.3.1 Microphysical controls on mixed-phase CAO clouds

Studies have shown that microphysical controls from aerosol-cloud interactions and ice formation processes are very important for the morphology and radiative properties of CAO clouds, especially for precipitation which is shown as the key to SCT in CAO events (Abel et al., 2017).

Changes in CCN or droplet number concentration can strongly affect cloud properties through their control on precipitation and the removal of liquid water in clouds. Using sensitivity tests with different prescribed droplet number concentrations in seven

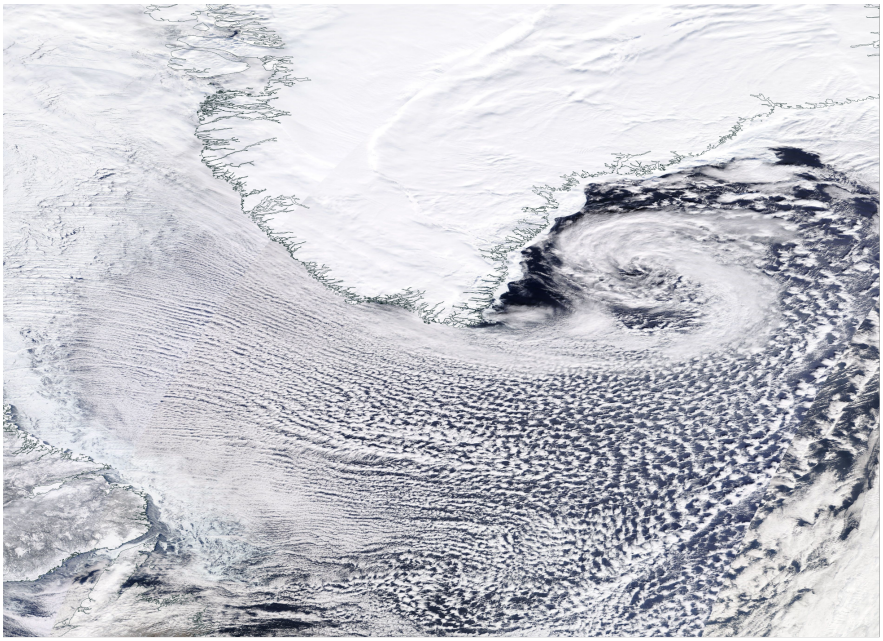


Figure 1.3: Satellite imagery of a cold-air outbreak event over the Labrador Sea on 14 March 2022. The imagery was obtained from the NASA Worldview using the retrievals from the Moderate Resolution Imaging Spectroradiometer (MODIS) instrument onboard the Aqua satellite (MODIS Characterization Support Team (MCST), 2017).

LES models, de Roode et al. (2019) show that reducing prescribed droplet number concentration generally produces larger droplets, stronger precipitation, smaller liquid water path (LWP), and an earlier breakup of the stratocumulus deck. The reduction in cloud water associated with smaller droplet number concentration can also lead to weaker cloud-top entrainment because less available cloud water reduces the evaporative cooling rate (de Roode et al., 2019). A study by Tornow et al. (2021) further shows that precipitation can deplete aerosol and CCN in CAO clouds, producing a feedback in which lower CCN concentrations lead to larger droplets, enhanced precipitation, and stronger reductions in LWP, thereby mediating SCT. Such decreasing trends in CCN or droplet number concentration from upwind to downwind during CAO events are also consistent with observations (Field et al., 2017b; Abel et al., 2017; Tornow et al., 2022; Murray-Watson et al., 2023). A more recent LES study by Li et al. (2023) found that aerosol particle size distribution (PSD) and hygroscopicity can strongly affect droplet number concentration, droplet effective radius, and LWP in CAO clouds, which is further supported by the work from Tornow et al. (2025) using LES to assess the impact of having observationally-constrained PSD in simulating mixed-phase CAO clouds. Combining trajectories of CAOs and satellite retrievals, Murray-Watson et al. (2023) find that CAO clouds with a higher initial aerosol load have a delayed transition and slower decreasing trend of cloud cover, and hence a bigger TOA albedo and more SW flux reflected at TOA.

INPs affect mixed-phase CAO clouds by controlling the efficiency of PIP, precipitation and LWP, hence influencing the development of CAO cloud field and the radiative properties of mixed-phase clouds. Using different INP parameterisations in high-resolution simulations, Vergara-Temprado et al. (2018) shows that an increase in INP concentration strongly reduces LWP and SW reflectivity of mixed-phase CAO clouds, especially when INP concentration is over 1 L^{-1}. An increase in INP concentration can also progressively accelerate the SCT in CAOs (Tornow et al., 2021; Wu et al., 2025). Besides modelling studies, *in-situ* aircraft measurements suggest that INP concentrations can vary substantially in a CAO event (Raif et al., 2024). Murray-Watson et al. (2024) uses airmass trajectories collocated with satellite retrievals and suggests that the CAO cloud phase evolution is linked with the history of air-mass which can affect the INP conditions in CAOs. Along with the importance of INPs to CAO clouds mentioned above, these results indicate the need for a good representation of INP sources and processing in models to simulate the behaviours of CAO clouds.

Secondary ice production (SIP) can also affect mixed-phase CAO clouds through ice multiplication, enhancement of precipitation and strong removal of liquid water. Using high-resolution simulations with three SIP mechanisms tested, Karalis et al. (2022) found that increasing SIP efficiencies enhances ice precipitation and a stronger decoupling in the boundary layer, hence accelerating the breakup of clouds. Work by Possner et al. (2024) with idealised simulations similarly showed that SIP can enhance ice production and interact with mesoscale cloud organisation, in addition to a better agreement with the observed ice number concentration through the inclusion of SIP processes. Observational evidence from the M-Phase campaign (Biggart et al., 2026) found ice particle concentrations frequently exceeding measured INP concentrations, with peak ice number concentration at the temperature zone for the HM process, further supporting the importance of SIPs for the properties of mixed-phase clouds during CAO events.

In addition to the direct investigation on INPs and SIPs discussed above, modelling studies have also tested the influences from different treatments of ice microphysics on mixed-phase CAO clouds. Field et al. (2017a) found that changing the temperature at which heterogeneous freezing begins and the PSD of ice in their model can affect the LWP and SW flux in their CAO case. Permitting ice in the model also accelerates the SCT and reduces cloud cover in CAOs (Abel et al., 2017; de Roode et al., 2019). These results further indicate the key role of ice formation processes in controlling the morphology and properties of mixed-phase CAO clouds.

1.3.2 Environmental controls on mixed-phase CAO clouds

Besides cloud microphysics, environmental conditions, or cloud-controlling factors, have also been investigated in many previous studies for their controls on mixed-phase CAO

clouds.

CAO index, which is defined as the difference in potential temperatures between the sea surface and a selected pressure level, is an important indicator of the strength of CAO and has long been used to identify CAOs (Kolstad et al., 2008; Kolstad et al., 2009; Fletcher et al., 2016a). Based on satellite data and CAO index from reanalysis data with a grid-by-grid approach, Fletcher et al. (2016b) shows that clouds formed during stronger CAOs have higher cloud fraction and optical thickness (Fletcher et al., 2016a). McCoy et al. (2017) finds that CAO index has a strong positive correlation with the frequency of open-cell clouds, and a negative correlation with the frequency of closed-cell clouds in marine CAOs. Wu et al. (2022) further suggests that in the region of CAO cloud breaking up, the CAO cloud areas and the CAO index both reach the local maxima in the case studied. By analysing a large number of CAO trajectories with satellite retrievals, Murray-Watson et al. (2023) find stronger CAOs have a generally higher LWP, a higher cloud fraction at the beginning of CAOs but a quicker and stronger reduction of cloud fraction later in the cloud field evolution.

Sea surface temperature (SST) has also been shown to strongly affect CAO cloud development through its controls on the sea-air temperature contrast, the sensible and latent heat fluxes. Using simulations with different SSTs, Chen et al. (2022) shows that a larger domain-mean SST and/or stronger SST gradient increase the hydrometeor water paths, and reduce cloud fraction which is associated with stronger entrainment of dry air above clouds. A recent work from Wu et al. (2025) tested the influence of SST on SCT in CAOs using LES with a case study. They find that a higher SST (+2 K to the control SST) leads to a faster deepening of boundary layer and accelerates cloud breakup in their case, which is similar to the effect of SST on SCT in warm, liquid clouds (e.g. Wyant et al., 1997; Sandu et al., 2010).

Wind conditions also play an important role in controlling the CAO cloud field development. By comparing the simulated cloud streets in a CAO event with different wind-direction shear conditions, Chen et al. (2022) show that wind-direction shear is important for reproducing the observed mesoscale morphology of cloud streets during their case, and a stronger wind-direction shear leads to a higher fraction of roll clouds and more cloud streets. A recent work with analysis on observational data from Klingebiel et al. (2025) further shows that wind speed is also vital for CAO cloud morphology, with a lower wind speed disrupting the formation of cloud streets and accelerating the SCT.

Although CAO clouds are usually in mixed-phase state, which is different from the shallow warm clouds, cloud-controlling factors may affect mixed-phase CAO clouds in ways similar to their effects on warm clouds. These include some of the cloud-controlling factors not yet mentioned, such as lower-tropospheric stability, estimated

inversion strength, free tropospheric humidity, and large-scale subsidence (Wood et al., 2006).

1.4 High-resolution regional modelling

Numerical modelling provides an essential tool for investigating cloud processes and their effects on climate, but different types of model represent clouds and cloud microphysics at different levels of complexity. Global Climate Models or General Circulation Models (GCMs) are designed to simulate the large-scale climate system over long timescales, but their relatively coarse horizontal grid spacing (over 10–20 km) means that clouds cannot be explicitly resolved and convection has to be parameterised (Khain et al., 2018). In addition, cloud microphysics in GCMs is often represented using relatively simple bulk schemes, in which the mass mixing ratio of each hydrometeor species is predicted, while hydrometeor number concentration is prescribed or diagnosed. These simplified representations of processes allow GCMs to remain computationally feasible, but they treat cloud processes in a crude manner, which is not sufficient for the aim of this thesis.

Convection-Permitting Models (CPMs) are regional models that provide a much finer horizontal grid spacing (less than 4 km) compared to the ones in GCM. At these resolutions, convection is explicitly resolved and parameterisation of convection is no longer required (Prein et al., 2015). Processes that are important to cloud evolution, such as thermodynamics, radiation and microphysical processes, can also be better represented in CPMs (Khain et al., 2018). Large Eddy Simulation (LES) with even finer resolutions (5-500 m) can explicitly resolve large-scale turbulent eddies and provide a valuable tool for process-level understanding of cloud behaviours (Khain et al., 2018). However, high computational cost of LES usually restricts the simulations to smaller domains and more idealised boundary conditions than regional models.

The aim of this thesis is to investigate the sensitivities of mixed-phase CAO clouds to aerosol-cloud interactions and ice formation processes while retaining large-scale synoptic and mesoscale forcing during CAOs. A high-resolution regional model is therefore used in this thesis to provide both realistic large-scale meteorological conditions and a sufficient representation of cloud processes. In particular, the high-resolution regional simulation is performed with a horizontal grid spacing of 1.5 km in this thesis, as previous work from Field et al. (2017b) has shown that this grid spacing can reproduce the general features of the CAO cloud system. In addition, a double-moment bulk cloud microphysics scheme is used within the high-resolution regional model, which predicts the mass mixing ratio and number concentration of each hydrometeor. The cloud microphysics parameters investigated in this thesis are from the cloud microphysics scheme and are perturbed simultaneously in perturbed parameter ensemble (PPE) simulations,

which are introduced in the next section.

1.5 Perturbed parameter ensemble and Gaussian Processes emulator

In Section 1.3, it is shown that the properties and morphology of mixed-phase CAO clouds can be affected by many factors including cloud microphysics and environmental conditions. However, most of the modelling studies shown above use a one-at-a-time (OAT) approach for sensitivity tests on how these factors affect CAO clouds. Such an OAT test only allows the responses of CAO cloud properties around a control simulation to be quantified, lacking full exploration of the parameter space and interactions among the parameters. Exploring and assessing interactions among parameters and processes are important for mixed-phase clouds, as complex interactions occur between liquid droplets and ice crystals, and the bulk cloud properties and behaviours are strongly dependent on the properties of these hydrometeors (Pruppacher et al., 1996). In addition, different combinations of parameter values may result in the same value of simulated cloud properties, which is called equifinality (Beven, 2006; Lee et al., 2016; Carslaw et al., 2026). Perturbing each parameter individually to match observations may fall into the problem of equifinality because it would result in a single and overly confident estimate of a parameter value rather than a range. Therefore, perturbed parameter ensemble (PPE) and Gaussian Process (GP) emulator are used in this thesis to explore the behaviour of mixed-phase clouds to these factors over the whole parameter space.

A PPE is a set of model simulations in which various parameters are perturbed simultaneously (Carslaw et al., 2026). PPEs have been widely used in climate and numerical weather prediction (NWP) models for quantifying model uncertainties. In this thesis, depending on how the model is set, the perturbed parameters can be measurable physical quantities (e.g., cloud droplet number concentration (N_d), ice crystal number concentration and hydrometeor density), physical process rates (e.g., autoconversion and accretion rates), coefficients in parameterisations (e.g., INP parameterisation coefficients), as well as initial environmental conditions (e.g., SST and CAO index). In addition, perturbing multiple parameters simultaneously has the advantage of investigating the interactions between perturbed parameters, which is important for cloud microphysics as many processes can act at the same time and interact with each other (Figure 1.2).

Traditional PPE uses the Monte Carlo method to design and perform simulations over the whole parameter space. This is extremely computationally expensive when the dimension of the parameter space increases and with high-resolution simulations. Therefore, this thesis also follows the statistical emulation approach proposed by Lee et al. (2011) in which they investigated the modelled CCN to uncertain parameters

in a complex global aerosol model using the Gaussian process (GP) emulators (Oakley et al., 2002; O'Hagan, 2006) and variance-based sensitivity analysis (Saltelli et al., 2000). Gaussian Process (GP) emulation is a non-parametric supervised machine learning method that learns the relationship between model input parameters and outputs of interest (Oakley et al., 2002; O'Hagan, 2006). In this approach, GP emulators are constructed on the output from the PPE simulations and act as statistical "surrogate" models for the computationally-expensive numerical models. The GP emulators enabled efficient exploration of the entire parameter space with dense sampling, allowing for construction of multi-dimensional response surfaces and a variance-based sensitivity analysis to assess the importance of the perturbed parameters to the cloud variables. Detailed methodologies and explanations on building GP emulators for climate and atmospheric models can be found in Lee et al. (2011) and Johnson et al. (2015).

The PPE and GP emulator approach has been recently applied in many complex climate and atmospheric models, including understanding the magnitude and causes of uncertainty in aerosol radiative forcing (Lee et al., 2011; Lee et al., 2012; Lee et al., 2013; Regayre et al., 2014; Regayre et al., 2015; Regayre et al., 2018; Lee et al., 2016; Johnson et al., 2018; Marshall et al., 2019), assessing potential model simplification of cloud microphysics in GCMs (Proske et al., 2022; Proske et al., 2023), constraining model parametric uncertainties with observations (Johnson et al., 2020; Regayre et al., 2023), identifying the potential existence of structural deficiencies (Regayre et al., 2023; Prévost et al., 2025). Besides global models, this approach has also been used in regional models such as investigating the environmental controls on sea breeze circulations (Igel et al., 2018; Park et al., 2020), understanding the controls of cloud properties for deep convective clouds (Johnson et al., 2015; Wellmann et al., 2018; Wellmann et al., 2020; Hawker et al., 2021) and stratocumulus clouds (Glassmeier et al., 2019; Sansom, 2021; Sansom et al., 2024; Sansom et al., 2025).

In the world of cloud microphysics, Morrison et al. (2020a) have recently developed a Bayesian approach for the statistical-physical bulk parameterisation of rain microphysics, which uses observations to constrain process-level microphysics. This approach is able to explore both the structural and parametric uncertainties simultaneously. However, it has currently only been developed for rain microphysics, while mixed-phase clouds require a much more complex setup, and is therefore not applied in this thesis.

1.6 Research objectives and thesis overview

Large uncertainties exist in estimating cloud-phase feedback for predicting future global warming, with cloud microphysics being one of the main sources of uncertainties. Clouds formed during CAO events provide a natural laboratory to investigate the role

of aerosol-cloud interactions and ice formation processes in mixed-phase clouds, but no studies have systematically investigated the responses of mixed-phase CAO clouds to perturbations of these cloud microphysical parameters and processes, as well as under different environmental conditions.

This thesis uses high-resolution modelling, PPE and GP emulators to quantify the role of key cloud microphysics parameters and processes in controlling the properties of mixed-phase CAO clouds, and their responses under a warming climate. Observational data including aircraft measurements and satellite retrievals are also used to assess the model representation of mixed-phase clouds. Research objectives and overview for each chapter are shown below.

1.6.1 Chapter 2: Quantify the responses of mixed-phase CAO clouds to aerosol-cloud interactions and ice formation processes under different environmental conditions

Mixed-phase CAO clouds are strongly influenced by aerosol-cloud interactions and ice formation processes, but their responses to these processes may vary with environmental conditions. No study has compared the sensitivities of mixed-phase CAO clouds to these processes under different environmental conditions. In this chapter, I use high-resolution, regional model simulations to compare two CAO cases over the Labrador Sea with contrasting environmental conditions, especially in terms of CAO strength and cloud temperature. I perform sensitivity tests with prescribed droplet number concentration, INP concentration from a temperature-dependent INP parametrisation, and efficiency of the HM process using the OAT approach.

The specific questions addressed by Chapter 2 are:

(a) How do aerosol-cloud interactions and ice formation processes affect the properties of mixed-phase CAO clouds under different environmental conditions?

(b) What is the relative importance of droplet number concentration, INP concentration and the HM SIP process on mixed-phase CAO clouds in a one-at-a-time test?

1.6.2 Chapter 3: Explore the interacting effects of aerosol-cloud interactions and ice formation processes on mixed-phase CAO clouds

OAT tests limit the exploration of the parameter space and the complex interactions of model parameters and processes. This is particularly important for the aim of this thesis because these processes can interact with each other, which is not captured by

the OAT tests in Chapter 2. In Chapter 3, I use PPE simulations and GP emulators on a case study over the Labrador Sea, with six parameters perturbed at the same time. The six parameters include three parameters that have been tested before in Chapter 2 and three additional parameters for the efficiencies of two newly added SIP mechanisms and a parameter controlling the spatial overlap between liquid and ice in a model grid-box. Two new SIP mechanisms are added in this chapter because previous studies have shown that including the HM process alone in models is often insufficient to reproduce observed ice number concentrations in mixed-phase clouds (e.g. Sullivan et al., 2018; Sotiropoulou et al., 2020; Karalis et al., 2022). The two new SIP mechanisms have also been shown to be important for LWP and morphology of mixed-phase CAO clouds (Karalis et al., 2022). It is also suggested that changing the degree of spatial overlap between liquid and ice can exert a strong influence on LWP and radiative properties of mixed-phase CAO clouds (Abel et al., 2017; Evans et al., 2025), hence the parameter controlling this spatial overlap is also included in this chapter.

The specific questions addressed by Chapter 3 are:

(a) What is the effect on the properties of mixed-phase CAO clouds of simultaneously perturbing parameters controlling aerosol-cloud interactions and ice formation processes?

(b) What is the relative importance of these parameters in controlling the properties of mixed-phase CAO clouds over the whole parameter space?

1.6.3 Chapter 4: Assess the representation of mixed-phase CAO clouds in a high-resolution model using multiple observations

Previous studies suggested that the high-resolution model used in the thesis generally has a low LWP bias in mixed-phase CAO clouds and this bias can be reduced by perturbing some parameters in the model (Field et al., 2017b; Abel et al., 2017; Van Weverberg et al., 2023). However, compensating effects may exist among model parameters and different combinations of parameter values may result in the same value of simulated cloud properties (the equifinality problem). In Chapter 4, I will use the PPE simulations from Chapter 3 and compare multiple modelled cloud properties against *in-situ* observations from the M-Phase aircraft campaign and satellite retrievals to assess the representation of mixed-phase clouds in these PPE simulations.

The specific questions addressed by Chapter 4 are:

(a) Do aircraft measurements, which are sparse point data, provide enough information for model-observation comparison against model output, which are grid-box mean data?

(b) Can the model simultaneously simulate all cloud properties well?

1.6.4 Chapter 5: Quantify the role of aerosols and ice formation processes in the responses of mixed-phase CAO clouds to a warming climate

The importance of aerosols and ice formation processes for the states of mixed-phase clouds has been studied extensively, but few studies so far have quantitatively examined how they affect mixed-phase cloud properties in a warming climate, i.e., how aerosols affect the strength of cloud feedback. GCMs provide the primary framework for estimating cloud feedbacks, but the coarse resolution and simplified cloud microphysics limit their ability to resolve the cloud-scale processes that are vital to mixed-phase clouds (Ceppi et al., 2017; Sherwood et al., 2020). High-resolution regional simulations, such as CRMs and LES, can represent these processes more explicitly (Bretherton, 2015), but their computational cost means that they are usually restricted to case studies, missing a wide range of environmental conditions that can vary the aerosol and thermodynamic conditions relevant for cloud microphysics substantially. In addition, to fully understand the role of these processes, PPE with a large number of simulations is required to understand the interactions and compensation among these processes in the model (Carslaw et al., 2026), which can further increase the requirement of computational resource.

In Chapter 5, I use idealised, high-resolution PPE simulations on CAO clouds with both cloud microphysics parameters and environmental (cloud-controlling) parameters perturbed together to train GP emulators. Thousands of CAO cases from both present-day (2020s) and future (2090s) climates are sampled from a climate model output. For each of these several thousand cases, I further sample over 10,000 combinations of the cloud microphysical parameters for droplet number concentration, INP concentration and SIP efficiencies which have been investigated in the case studies in Chapters 2 and 3.

The specific questions addressed by Chapter 5 are:

(a) How do environmental conditions change for CAO events in the warming climate?

(b) How do aerosols and ice formation processes affect the responses of mixed-phase CAO clouds to the warming climate?

(c) How much do future changes in aerosol affect the response of mixed-phase CAO clouds to the warming climate?

References

Abel, S. J., Boutle, I. A., Waite, K., Fox, S., Brown, P. R. A., Cotton, R., Lloyd, G., Choularton, T. W., and Bower, K. N. (2017). "The Role of Precipitation in Controlling the Transition from Stratocumulus to Cumulus Clouds in a Northern Hemisphere Cold-Air Outbreak". In: *Journal of the Atmospheric Sciences* 74.7, pp. 2293–2314.

Ackerman, A. S., Kirkpatrick, M. P., Stevens, D. E., and Toon, O. B. (2004). "The impact of humidity above stratiform clouds on indirect aerosol climate forcing". In: *Nature* 432.7020, pp. 1014–1017.

Albrecht, B. A. (1989). "Aerosols, Cloud Microphysics, and Fractional Cloudiness". In: *Science* 245.4923, pp. 1227–1230.

Andreae, M. O., Rosenfeld, D., Artaxo, P., Costa, A. A., Frank, G. P., Longo, K. M., and Silva-Dias, M. A. F. (2004). "Smoking Rain Clouds over the Amazon". In: *Science* 303.5662, pp. 1337–1342.

Atkinson, J. D., Murray, B. J., Woodhouse, M. T., Whale, T. F., Baustian, K. J., Carslaw, K. S., Dobbie, S., O'Sullivan, D., and Malkin, T. L. (2013). "The importance of feldspar for ice nucleation by mineral dust in mixed-phase clouds". In: *Nature* 498.7454, pp. 355–358.

Bergeron, T. (1935). "On the physics of clouds and precipitation". In: *Proces Verbaux de l'Association de Météorologie*, pp. 156–178.

Beven, K. (2006). "A manifesto for the equifinality thesis". In: *Journal of Hydrology* 320.1, pp. 18–36.

Bigg, E. K. (1953). "The formation of atmospheric ice crystals by the freezing of droplets". In: *Quarterly Journal of the Royal Meteorological Society* 79.342, pp. 510–519.

Biggart, M., Choularton, T. W., Gallagher, M. W., Bower, K. N., Lloyd, G., Connolly, P. J., Murray, B. J., Tarn, M. D., Raif, E. N., and Abel, S. J. (2026). "Secondary ice production within shallow, mixed-phase clouds in cold air outbreaks over the Labrador Sea". In: *EGUsphere* 2026, pp. 1–41.

Bodas-Salcedo, A., Andrews, T., Karmalkar, A. V., and Ringer, M. A. (2016). "Cloud liquid water path and radiative feedbacks over the Southern Ocean". In: *Geophysical Research Letters* 43.20, pp. 10938–10946.

Bodas-Salcedo, A., Williams, K. D., Ringer, M. A., Beau, I., Cole, J. N. S., Dufresne, J.-L., Koshiro, T., Stevens, B., Wang, Z., and Yokohata, T. (2014). "Origins of the Solar Radiation Biases over the Southern Ocean in CFMIP2 Models". In: *Journal of Climate* 27.1, pp. 41–56.

Bony, S. and Dufresne, J. L. (2005). "Marine boundary layer clouds at the heart of tropical cloud feedback uncertainties in climate models". In: *Geophysical Research Letters* 32, p. L20806.

Bony, S., Dufresne, J. L., Le Treut, H., Morcrette, J. J., and Senior, C. (2004). "On dynamic and thermodynamic components of cloud changes". In: *Climate Dynamics* 22, pp. 71–86.

Boucher, O., Randall, D., Artaxo, P., Bretherton, C., Feingold, G., Forster, P., Kerminen, V.-M., Kondo, Y., Liao, H., Lohmann, U., Rasch, P., Satheesh, S. K., Sherwood, S., Stevens, B., and Zhang, X. Y. (2013). "Clouds and Aerosols". In: *Climate Change 2013: The Physical Science Basis. Contribution of Working Group I to the Fifth Assessment Report of the Intergovernmental Panel on Climate Change*. Ed. by T. F. Stocker, D. Qin, G.-K. Plattner, M. Tignor, S. K. Allen, J. Boschung, A. Nauels, Y. Xia, V. Bex, and P. M. Midgley. Cambridge, United Kingdom and New York, NY, USA: Cambridge University Press. Chap. 7, pp. 571–657.

Bretherton, C. S. (2015). "Insights into low-latitude cloud feedbacks from high-resolution models". In: *Philosophical Transactions of the Royal Society A: Mathematical, Physical and Engineering Sciences* 373.2054, p. 20140415.

Brümmer, B. (1996). "Boundary-layer modification in wintertime cold-air outbreaks from the Arctic sea ice". In: *Boundary-Layer Meteorology* 80.1, pp. 109–125.

— (1999). "Roll and Cell Convection in Wintertime Arctic Cold-Air Outbreaks". In: *Journal of the Atmospheric Sciences* 56.15, pp. 2613–2636.

Burrows, S. M., McCluskey, C. S., Cornwell, G., Steinke, I., Zhang, K., Zhao, B., Zawadowicz, M., Raman, A., Kulkarni, G., China, S., Zelenyuk, A., and DeMott, P. J. (2022). "Ice-Nucleating Particles That Impact Clouds and Climate: Observational and Modeling Research Needs". In: *Reviews of Geophysics* 60.2, e2021RG000745.

Carslaw, K. S., Regayre, L. A., Proske, U., Gettelman, A., Sexton, D. M. H., Qian, Y., Marshall, L. R., Wild, O., van Lier-Walqui, M., Oertel, A., Peatier, S., Yang, B., Johnson, J. S., Li, S., McCoy, D. T., Sanderson, B. M., Williamson, C. J., Elsaesser, G. S., Yamazaki, K., and Booth, B. B. B. (2026). "Opinion: The importance and future development of perturbed parameter ensembles in climate and atmospheric science". In: *Atmospheric Chemistry and Physics* 26.7, pp. 4651–4667.

Carslaw, K. S. (2022). *Aerosols and Climate*. Elsevier.

Ceppi, P., Brient, F., Zelinka, M. D., and Hartmann, D. L. (2017). "Cloud feedback mechanisms and their representation in global climate models". In: *WIREs Climate Change* 8.4, e465.

Cess, R. D., Potter, G. L., Blanchet, J. P., Boer, G. J., Del Genio, A. D., Déqué, M., Dymnikov, V., Galin, V., Gates, W. L., Ghan, S. J., Kiehl, J. T., Lacis, A. A., Le Treut, H., Li, Z.-X., Liang, X.-Z., McAvaney, B. J., Meleshko, V. P., Mitchell, J. F. B., Morcrette, J.-J., Randall, D. A., Rikus, L., Roeckner, E., Royer, J. F., Schlese, U., Sheinin, D. A., Slingo, A., Sokolov, A. P., Taylor, K. E., Washington, W. M., Wetherald, R. T., Yagai, I., and Zhang, M.-H. (1990). "Intercomparison and interpretation of climate feedback processes in 19 atmospheric general circulation

models". In: *Journal of Geophysical Research: Atmospheres* 95.D10, pp. 16601–16615.

Cess, R. D. and Potter, G. L. (1988). "A methodology for understanding and intercomparing atmospheric climate feedback processes in general circulation models". In: *Journal of Geophysical Research: Atmospheres* 93.D7, pp. 8305–8314.

Chen, J., Wang, H., Li, X., Painemal, D., Sorooshian, A., Thornhill, K. L., Robinson, C., and Shingler, T. (2022). "Impact of Meteorological Factors on the Mesoscale Morphology of Cloud Streets during a Cold-Air Outbreak over the Western North Atlantic". In: *Journal of the Atmospheric Sciences* 79.11, pp. 2863–2879.

Chen, T., Rossow, W. B., and Zhang, Y. (2000). "Radiative Effects of Cloud-Type Variations". In: *Journal of Climate* 13.1, pp. 264–286.

Clarke, S. J., Abel, S. J., Nott, G. J., Raif, E. N., Tarn, M. D., Biggart, M., Wu, H., Ashmore, D. W., Barr, S. L., Barrett, P. A., Bower, K. N., Bowles, J., Connolly, P. J., Cotton, R., Evans, M. D., Flynn, M., Foster, P. B., Fox, S., Gallagher, M. W., Hu, K., Kent, J., Lloyd, G., Marsden, N. A., McQuaid, J. B., Robinson, J., Tiddeman, D., Wilson, A., Wivell, K., Field, P. R., Choularton, T. W., and Murray, B. J. (2025). "Marine cold-air outbreaks over the Norwegian-Barents and Labrador seas: observational datasets from the ACAO and M-Phase aircraft campaigns". Manuscript submitted for publication.

Cooper, W. (1986). "Ice Initiation in Natural Clouds". In: *Precipitation Enhancement—A Scientific Challenge, Meteorological Monographs.*

Cotton, W. R., Tripoli, G. J., Rauber, R. M., and Mulvihill, E. A. (1986). "Numerical Simulation of the Effects of Varying Ice Crystal Nucleation Rates and Aggregation Processes on Orographic Snowfall". In: *Journal of Applied Meteorology and Climatology* 25.11, pp. 1658–1680.

de Roode, S. R., Frederikse, T., Siebesma, A. P., Ackerman, A. S., Chylik, J., Field, P. R., Fricke, J., Gryschka, M., Hill, A., Honnert, R., Krueger, S. K., Lac, C., Lesage, A. T., and Tomassini, L. (2019). "Turbulent Transport in the Gray Zone: A Large Eddy Model Intercomparison Study of the CONSTRAIN Cold Air Outbreak Case". In: *Journal of Advances in Modeling Earth Systems* 11.3, pp. 597–623.

DeMott, P. J., Prenni, A. J., McMeeking, G. R., Sullivan, R. C., Petters, M. D., Tobo, Y., Niemand, M., Möhler, O., Snider, J. R., Wang, Z., and Kreidenweis, S. M. (2015). "Integrating laboratory and field data to quantify the immersion freezing ice nucleation activity of mineral dust particles". In: *Atmospheric Chemistry and Physics* 15.1, pp. 393–409.

Dhuria, H. L. and Kyle, H. L. (1990). "Cloud Types and the Tropical Earth Radiation Budget". In: *Journal of Climate* 3.12, pp. 1409–1434.

Dye, J. E. and Hobbs, P. V. (1968). "The Influence of Environmental Parameters on the Freezing and Fragmentation of Suspended Water Drops". In: *Journal of Atmospheric Sciences* 25.1, pp. 82–96.

Evans, M. D., Abel, S. J., Field, P. R., Finney, D. L., Lloyd, G., Cotton, R. J., Smith, D. K., Murray, B. J., and Huang, X. (2025). "Characterising the spatial overlap between liquid and ice in mixed-phase clouds". In: *Quarterly Journal of the Royal Meteorological Society*, e5041.

Ferrier, B. S. (1994). "A Double-Moment Multiple-Phase Four-Class Bulk Ice Scheme. Part I: Description". In: *Journal of Atmospheric Sciences* 51.2, pp. 249–280.

Field, P. R., Lawson, R. P., Brown, P. R. A., Lloyd, G., Westbrook, C., Moisseev, D., Miltenberger, A., Nenes, A., Blyth, A., Choularton, T., Connolly, P., Buehl, J., Crosier, J., Cui, Z., Dearden, C., DeMott, P., Flossmann, A., Heymsfield, A., Huang, Y., Kalesse, H., Kanji, Z. A., Korolev, A., Kirchgaessner, A., Lasher-Trapp, S., Leisner, T., McFarquhar, G., Phillips, V., Stith, J., and Sullivan, S. (2017a). "Secondary Ice Production: Current State of the Science and Recommendations for the Future". In: *Meteorological Monographs* 58, pp. 7.1–7.20.

Field, P. R., Brožková, R., Chen, M., Dudhia, J., Lac, C., Hara, T., Honnert, R., Olson, J., Siebesma, P., de Roode, S., Tomassini, L., Hill, A., and McTaggart-Cowan, R. (2017b). "Exploring the convective grey zone with regional simulations of a cold air outbreak". In: *Quarterly Journal of the Royal Meteorological Society* 143.707, pp. 2537–2555.

Field, P. R., Hill, A., Shipway, B., Furtado, K., Wilkinson, J., Miltenberger, A., Gordon, H., Grosvenor, D. P., Stevens, R., and Van Weverberg, K. (2023). "Implementation of a Double Moment Cloud Microphysics Scheme in the UK Met Office Regional Numerical Weather Prediction Model". In: *Quarterly Journal of the Royal Meteorological Society*.

Findeisen, W. (1938). "Kolloid-meteorologische Vorgänge bei Niederschlagsbildung". In: *Meteorologische Zeitschrift* 55, pp. 121–133.

Findeisen, W. and Findeisen, E. (1943). "Untersuchungen über die Eissplitterbildung an Reifschichten (Ein Beitrag zur Frage der Entstehung der Gewitterelektrizität und zur Mikrostruktur der Cumulonimben)". In: *Meteorologische Zeitschrift* 60, pp. 145–154.

Fletcher, J., Mason, S., and Jakob, C. (2016a). "The Climatology, Meteorology, and Boundary Layer Structure of Marine Cold Air Outbreaks in Both Hemispheres". In: *Journal of Climate* 29.6, pp. 1999–2014.

Fletcher, J. K., Mason, S., and Jakob, C. (2016b). "A Climatology of Clouds in Marine Cold Air Outbreaks in Both Hemispheres". In: *Journal of Climate* 29.18, pp. 6677–6692.

Forster, P., Storelvmo, T., Armour, K., Collins, W., Dufresne, J. L., Frame, D., Lunt, D. J., Mauritsen, T., Palmer, M. D., Watanabe, M., Wild, M., and Zhang, H. (2021). "The Earth's Energy Budget, Climate Feedbacks, and Climate Sensitivity". In: *Climate Change 2021: The Physical Science Basis. Contribution of Working Group I to the Sixth Assessment Report of the Intergovernmental Panel on Climate*

Change. Ed. by V. Masson-Delmotte, P. Zhai, A. Pirani, S. L. Connors, C. Péan, S. Berger, N. Caud, Y. Chen, L. Goldfarb, M. I. Gomis, M. Huang, K. Leitzell, E. Lonnoy, J. B. R. Matthews, T. K. Maycock, T. Waterfield, O. Yelekçi, R. Yu, and B. Zhou. Cambridge, United Kingdom and New York, NY, USA: Cambridge University Press. Chap. 7.

Fowler, L. D., Randall, D. A., and Rutledge, S. A. (1996). "Liquid and Ice Cloud Microphysics in the CSU General Circulation Model. Part 1: Model Description and Simulated Microphysical Processes". In: *Journal of Climate* 9.3, pp. 489–529.

Gagin, A. (1972). "The effect of supersaturation on the ice crystal production by natural aerosols". In: *Journal de Recherches Atmospheriques*, pp. 175–185.

Geerts, B., Giangrande, S. E., McFarquhar, G. M., Xue, L., Abel, S. J., Comstock, J. M., Crewell, S., DeMott, P. J., Ebell, K., Field, P., Hill, T. C. J., Hunzinger, A., Jensen, M. P., Johnson, K. L., Juliano, T. W., Kollias, P., Kosovic, B., Lackner, C., Luke, E., Lüpkes, C., Matthews, A. A., Neggers, R., Ovchinnikov, M., Powers, H., Shupe, M. D., Spengler, T., Swanson, B. E., Tjernström, M., Theisen, A. K., Wales, N. A., Wang, Y., Wendisch, M., and Wu, P. (2022). "The COMBLE Campaign: A Study of Marine Boundary Layer Clouds in Arctic Cold-Air Outbreaks". In: *Bulletin of the American Meteorological Society* 103.5, E1371–E1389.

Glassmeier, F., Hoffmann, F., Johnson, J. S., Yamaguchi, T., Carslaw, K. S., and Feingold, G. (2019). "An emulator approach to stratocumulus susceptibility". In: *Atmospheric Chemistry and Physics* 19.15, pp. 10191–10203.

Gold, L. W. (1963). "CRACK FORMATION IN ICE PLATES BY THERMAL SHOCK". In: *Canadian Journal of Physics* 41.10, pp. 1712–1728.

Gordon, H., Field, P. R., Abel, S. J., Barrett, P., Bower, K., Crawford, I., Cui, Z., Grosvenor, D. P., Hill, A. A., Taylor, J., Wilkinson, J., Wu, H., and Carslaw, K. S. (2020). "Development of aerosol activation in the double-moment Unified Model and evaluation with CLARIFY measurements". In: *Atmospheric Chemistry and Physics* 20.18, pp. 10997–11024.

Hallett, J. and Mossop, S. C. (1974). "Production of secondary ice particles during the riming process". In: *Nature* 249, pp. 26–28.

Harrison, A. D., Whale, T. F., Carpenter, M. A., Holden, M. A., Neve, L., O'Sullivan, D., Vergara Temprado, J., and Murray, B. J. (2016). "Not all feldspars are equal: a survey of ice nucleating properties across the feldspar group of minerals". In: *Atmospheric Chemistry and Physics* 16.17, pp. 10927–10940.

Harrison, A. D., Lever, K., Sanchez-Marroquin, A., Holden, M. A., Whale, T. F., Tarn, M. D., McQuaid, J. B., and Murray, B. J. (2019). "The ice-nucleating ability of quartz immersed in water and its atmospheric importance compared to K-feldspar". In: *Atmospheric Chemistry and Physics* 19.17, pp. 11343–11361.

Hawker, R. E., Miltenberger, A. K., Johnson, J. S., Wilkinson, J. M., Hill, A. A., Shipway, B. J., Field, P. R., Murray, B. J., and Carslaw, K. S. (2021). "Model

emulation to understand the joint effects of ice-nucleating particles and secondary ice production on deep convective anvil cirrus". In: *Atmospheric Chemistry and Physics* 21.23, pp. 17315–17343.

Houghton, J. T., Ding, Y., Griggs, D. J., Noguer, M., van der Linden, P. J., Dai, X., Maskell, K., and Johnson, C. A. (2001). "Aerosols, Their Direct and Indirect Effects". In: *Climate Change 2001: The Scientific Basis. Contribution of Working Group I to the Third Assessment Report of the Intergovernmental Panel on Climate Change*. Cambridge, United Kingdom and New York, NY, USA: Cambridge University Press, pp. 289–348.

Igel, A. L., van den Heever, S. C., and Johnson, J. S. (2018). "Meteorological and Land Surface Properties Impacting Sea Breeze Extent and Aerosol Distribution in a Dry Environment". In: *Journal of Geophysical Research: Atmospheres* 123.1, pp. 22–37.

Johnson, D. A. and Hallett, J. (1968). "Freezing and shattering of supercooled water drops". In: *Quarterly Journal of the Royal Meteorological Society* 94.402, pp. 468–482.

Johnson, J. S., Cui, Z., Lee, L. A., Gosling, J. P., Blyth, A. M., and Carslaw, K. S. (2015). "Evaluating uncertainty in convective cloud microphysics using statistical emulation". In: *Journal of Advances in Modeling Earth Systems* 7.1, pp. 162–187.

Johnson, J. S., Regayre, L. A., Yoshioka, M., Pringle, K. J., Turnock, S. T., Browse, J., Sexton, D. M. H., Rostron, J. W., Schutgens, N. A. J., Partridge, D. G., Liu, D., Allan, J. D., Coe, H., Ding, A., Cohen, D. D., Atanacio, A., Vakkari, V., Asmi, E., and Carslaw, K. S. (2020). "Robust observational constraint of uncertain aerosol processes and emissions in a climate model and the effect on aerosol radiative forcing". In: *Atmospheric Chemistry and Physics* 20.15, pp. 9491–9524.

Johnson, J. S., Regayre, L. A., Yoshioka, M., Pringle, K. J., Lee, L. A., Sexton, D. M. H., Rostron, J. W., Booth, B. B. B., and Carslaw, K. S. (2018). "The importance of comprehensive parameter sampling and multiple observations for robust constraint of aerosol radiative forcing". In: *Atmospheric Chemistry and Physics* 18.17, pp. 13031–13053.

Kanji, Z. A., Ladino, L. A., Wex, H., Boose, Y., Burkert-Kohn, M., Cziczo, D. J., and Krämer, M. (2017). "Overview of Ice Nucleating Particles". In: *Meteorological Monographs* 58, pp. 1.1–1.33.

Karalis, M., Sotiropoulou, G., Abel, S. J., Bossioli, E., Georgakaki, P., Methymaki, G., Nenes, A., and Tombrou, M. (2022). "Effects of secondary ice processes on a stratocumulus to cumulus transition during a cold-air outbreak". In: *Atmospheric Research* 277, p. 106302.

Khain, A., Rosenfeld, D., and Pokrovsky, A. (2005). "Aerosol impact on the dynamics and microphysics of deep convective clouds". In: *Quarterly Journal of the Royal Meteorological Society* 131.611, pp. 2639–2663.

Khain, A. P., Beheng, K. D., Heymsfield, A., Korolev, A., Krichak, S. O., Levin, Z., Pinsky, M., Phillips, V., Prabhakaran, T., Teller, A., van den Heever, S. C., and Yano, J.-I. (2015). "Representation of microphysical processes in cloud-resolving models: Spectral (bin) microphysics versus bulk parameterization". In: *Reviews of Geophysics* 53.2, pp. 247–322.

Khain, A. P. and Pinsky, M. (2018). *Physical Processes in Clouds and Cloud Modeling*. Cambridge University Press.

Kiehl, J. T. (1994). "On the Observed Near Cancellation between Longwave and Shortwave Cloud Forcing in Tropical Regions". In: *Journal of Climate* 7.4, pp. 559–565.

Klein, S. A., Hall, A., Norris, J. R., and Pincus, R. (2017). "Low-Cloud Feedbacks from Cloud-Controlling Factors: A Review". In: *Surveys in Geophysics* 38.6, pp. 1307–1329.

Klein, S. A. and Hartmann, D. L. (1993). "The Seasonal Cycle of Low Stratiform Clouds". In: *Journal of Climate* 6.8, pp. 1587–1606.

Klingebiel, M., Ehrlich, A., Gryschka, M., Risse, N., Maherndl, N., Schirmacher, I., Rosenburg, S., Hörnig, S., Moser, M., Jäkel, E., Schäfer, M., Deneke, H., Mech, M., Voigt, C., and Wendisch, M. (2025). "Airborne observations of cloud properties during their evolution from organized streets to isotropic cloud structures along an Arctic cold-air outbreak". In: *Atmospheric Chemistry and Physics* 25.17, pp. 9787–9801.

Koenig, L. R. (1963). "The Glaciating Behavior of Small Cumulonimbus Clouds". In: *Journal of Atmospheric Sciences* 20.1, pp. 29–47.

Kolstad, E. W. and Bracegirdle, T. J. (2008). "Marine cold-air outbreaks in the future: an assessment of IPCC AR4 model results for the Northern Hemisphere". In: *Climate Dynamics* 30.7, pp. 871–885.

Kolstad, E. W., Bracegirdle, T. J., and Seierstad, I. A. (2009). "Marine cold-air outbreaks in the North Atlantic: temporal distribution and associations with large-scale atmospheric circulation". In: *Climate Dynamics* 33.2, pp. 187–197.

Koren, I., Kaufman, Y. J., Rosenfeld, D., Remer, L. A., and Rudich, Y. (2005). "Aerosol invigoration and restructuring of Atlantic convective clouds". In: *Geophysical Research Letters* 32.14, p. L14828.

Koren, I., Dagan, G., and Altaratz, O. (2014). "From aerosol-limited to invigoration of warm convective clouds". In: *Science* 344.6188, pp. 1143–1146.

Korolev, A. and Leisner, T. (2020). "Review of experimental studies of secondary ice production". In: *Atmospheric Chemistry and Physics* 20.20, pp. 11767–11797.

Korolev, A., McFarquhar, G., Field, P. R., Franklin, C., Lawson, P., Wang, Z., Williams, E., Abel, S. J., Axisa, D., Borrmann, S., Crosier, J., Fugal, J., Krämer, M., Lohmann, U., Schlenczek, O., Schnaiter, M., and Wendisch, M. (2017). "Mixed-Phase Clouds: Progress and Challenges". In: *Meteorological Monographs* 58, pp. 5.1–5.50.

Latham, J., Mason, B. J., and Blackett, P. M. S. (1961). "Generation of electric charge associated with the formation of soft hail in thunderclouds". In: *Proceedings of the Royal Society of London. Series A. Mathematical and Physical Sciences* 260.1303, pp. 537–549.

Lee, J., Yang, P., Dessler, A. E., Gao, B.-C., and Platnick, S. (2009). "Distribution and Radiative Forcing of Tropical Thin Cirrus Clouds". In: *Journal of the Atmospheric Sciences* 66.12, pp. 3721–3731.

Lee, L. A., Carslaw, K. S., Pringle, K. J., and Mann, G. W. (2012). "Mapping the uncertainty in global CCN using emulation". In: *Atmospheric Chemistry and Physics* 12.20, pp. 9739–9751.

Lee, L. A., Carslaw, K. S., Pringle, K. J., Mann, G. W., and Spracklen, D. V. (2011). "Emulation of a complex global aerosol model to quantify sensitivity to uncertain parameters". In: *Atmospheric Chemistry and Physics* 11.23, pp. 12253–12273.

Lee, L. A., Pringle, K. J., Reddington, C. L., Mann, G. W., Stier, P., Spracklen, D. V., Pierce, J. R., and Carslaw, K. S. (2013). "The magnitude and causes of uncertainty in global model simulations of cloud condensation nuclei". In: *Atmospheric Chemistry and Physics* 13.17, pp. 8879–8914.

Lee, L. A., Reddington, C. L., and Carslaw, K. S. (2016). "On the relationship between aerosol model uncertainty and radiative forcing uncertainty". In: *Proceedings of the National Academy of Sciences* 113.21, pp. 5820–5827.

Leisner, T., Pander, T., Handmann, P., and Kiselev, A. (2014). "Secondary ice processes upon heterogeneous freezing of cloud droplets". In: *Proceedings of the 14th Conference on Cloud Physics 14th Conference on Atmospheric Radiation*. Presented Monday, 7 July 2014, 11:00 AM, Essex Center/South (Westin Copley Place). American Meteorological Society. Boston, MA, USA.

Li, X.-Y., Wang, H., Chen, J., Endo, S., Kirschler, S., Voigt, C., Crosbie, E., Ziemba, L. D., Painemal, D., Cairns, B., Hair, J. W., Corral, A. F., Robinson, C., Dadashazar, H., Sorooshian, A., Chen, G., Ferrare, R. A., Kleb, M. M., Liu, H., Moore, R., Scarino, A. J., Shook, M. A., Shingler, T. J., Thornhill, K. L., Tornow, F., Xiao, H., and Zeng, X. (2023). "Large-Eddy Simulations of Marine Boundary Layer Clouds Associated with Cold-Air Outbreaks during the ACTIVATE Campaign. Part II: Aerosol–Meteorology–Cloud Interaction". In: *Journal of the Atmospheric Sciences* 80.4, pp. 1025–1045.

Lohmann, U., Lüönd, F., and Mahrt, F. (2016). *An Introduction to Clouds: From the Microscale to Climate*. Cambridge: Cambridge University Press.

Marshall, L., Johnson, J. S., Mann, G. W., Lee, L., Dhomse, S. S., Regayre, L., Yoshioka, M., Carslaw, K. S., and Schmidt, A. (2019). "Exploring How Eruption Source Parameters Affect Volcanic Radiative Forcing Using Statistical Emulation". In: *Journal of Geophysical Research: Atmospheres* 124.2, pp. 964–985.

McCluskey, C. S., DeMott, P. J., Ma, P.-L., and Burrows, S. M. (2019). "Numerical Representations of Marine Ice-Nucleating Particles in Remote Marine Environments Evaluated Against Observations". In: *Geophysical Research Letters* 46.13, pp. 7838–7847.

McCluskey, C. S., Hill, T. C. J., Humphries, R. S., Rauker, A. M., Moreau, S., Strutton, P. G., Chambers, S. D., Williams, A. G., McRobert, I., Ward, J., Keywood, M. D., Harnwell, J., Ponsonby, W., Loh, Z. M., Krummel, P. B., Protat, A., Kreidenweis, S. M., and DeMott, P. J. (2018). "Observations of Ice Nucleating Particles Over Southern Ocean Waters". In: *Geophysical Research Letters* 45.21, pp. 11989–11997.

McCoy, D. T., Hartmann, D. L., Zelinka, M. D., Ceppi, P., and Grosvenor, D. P. (2015). "Mixed-phase cloud physics and Southern Ocean cloud feedback in climate models". In: *Journal of Geophysical Research: Atmospheres* 120.18, pp. 9539–9554.

McCoy, I. L., Wood, R., and Fletcher, J. K. (2017). "Identifying Meteorological Controls on Open and Closed Mesoscale Cellular Convection Associated with Marine Cold Air Outbreaks". In: *Journal of Geophysical Research: Atmospheres* 122.21, pp. 11678–11702.

Michaelis, J., Schmitt, A. U., Lüpkes, C., Hartmann, J., Birnbaum, G., and Vihma, T. (2022). "Observations of marine cold-air outbreaks: a comprehensive data set of airborne and dropsonde measurements from the Springtime Atmospheric Boundary Layer Experiment (STABLE)". In: *Earth System Science Data* 14.4, pp. 1621–1637.

Mitchell, J. F. B., Senior, C. A., and Ingram, W. J. (1989). "C02 and climate: a missing feedback?" In: *Nature* 341.6238, pp. 132–134.

MODIS Characterization Support Team (MCST) (2017). *MODIS 1km Calibrated Radiances Product*. MODIS Adaptive Processing System, Goddard Space Flight Center, USA.

Morrison, H. C., van Lier-Walqui, M., Kumjian, M. R., and Prat, O. P. (2020a). "A Bayesian approach for statistical-physical bulk parameterization of rain microphysics, Part I: Scheme description". In: *J. Atmos. Sci.* 77.3, pp. 1019–1041.

Morrison, H., van Lier-Walqui, M., Fridlind, A. M., Grabowski, W. W., Harrington, J. Y., Hoose, C., Korolev, A., Kumjian, M. R., Milbrandt, J. A., Pawlowska, H., Posselt, D. J., Prat, O. P., Reimel, K. J., Shima, S.-I., van Diedenhoven, B., and Xue, L. (2020b). "Confronting the Challenge of Modeling Cloud and Precipitation Microphysics". In: *Journal of Advances in Modeling Earth Systems* 12.8, e2019MS001689.

Murray, B. J., Carslaw, K. S., and Field, P. R. (2021). "Opinion: Cloud-phase climate feedback and the importance of ice-nucleating particles". In: *Atmospheric Chemistry and Physics* 21.2, pp. 665–679.

Murray, B. J., O'Sullivan, D., Atkinson, J. D., and Webb, M. E. (2012). "Ice nucleation by particles immersed in supercooled cloud droplets". In: *Chemical Society Reviews* 41.19, pp. 6519–6554.

Murray-Watson, R. J. and Gryspeerdt, E. (2024). "Air mass history linked to the development of Arctic mixed-phase clouds". In: *Atmospheric Chemistry and Physics* 24.19, pp. 11115–11132.

Murray-Watson, R. J., Gryspeerdt, E., and Goren, T. (2023). "Investigating the development of clouds within marine cold-air outbreaks". In: *Atmospheric Chemistry and Physics* 23.16, pp. 9365–9383.

Niemand, M., Möhler, O., Vogel, B., Vogel, H., Hoose, C., Connolly, P., Klein, H., Bingemer, H., DeMott, P., Skrotzki, J., and Leisner, T. (2012). "A Particle-Surface-Area-Based Parameterization of Immersion Freezing on Desert Dust Particles". In: *Journal of the Atmospheric Sciences*.

O'Hagan, A. (2006). "Bayesian analysis of computer code outputs: A tutorial". In: *Reliability Engineering and System Safety* 91.10, pp. 1290–1300.

Oakley, J. and O'Hagan, A. (2002). "Bayesian inference for the uncertainty distribution of computer model outputs". In: *Biometrika* 89.4, pp. 769–784.

Oraltay, R. and Hallett, J. (1989). "Evaporation and melting of ice crystals: A laboratory study". In: *Atmospheric Research* 24.1, pp. 169–189.

Park, J. M., van den Heever, S. C., Igel, A. L., Grant, L. D., Johnson, J. S., Saleeby, S. M., Miller, S. D., and Reid, J. S. (2020). "Environmental Controls on Tropical Sea Breeze Convection and Resulting Aerosol Redistribution". In: *Journal of Geophysical Research: Atmospheres* 125.6, e2019JD031699.

Pasquier, J. T., Henneberger, J., Ramelli, F., Lauber, A., David, R. O., Wieder, J., Carlsen, T., Gierens, R., Maturilli, M., and Lohmann, U. (2022). "Conditions favorable for secondary ice production in Arctic mixed-phase clouds". In: *Atmospheric Chemistry and Physics* 22.23, pp. 15579–15601.

Phillips, V. T. J., Yano, J.-I., Formenton, M., Ilotoviz, E., Kanawade, V., Kudzotsa, I., Sun, J., Bansemer, A., Detwiler, A. G., Khain, A., and Tessendorf, S. A. (2017). "Ice Multiplication by Breakup in Ice–Ice Collisions. Part II: Numerical Simulations". In: *Journal of the Atmospheric Sciences* 74.9, pp. 2789–2811.

Possner, A., Pfannkuch, K., and Ramadoss, V. (2024). "Cloud-Resolving ICON Simulations of Secondary Ice Production in Arctic Mixed-Phase Stratocumuli Observed during M-PACE". In: *Journal of the Atmospheric Sciences* 81.2, pp. 417–434.

Prein, A. F., Langhans, W., Fosser, G., Ferrone, A., Ban, N., Goergen, K., Keller, M., Tölle, M., Gutjahr, O., Feser, F., Brisson, E., Kollet, S., Schmidli, J., van Lipzig, N. P. M., and Leung, L. R. (2015). "A review on regional convection-permitting climate modeling: Demonstrations, prospects, and challenges". In: *Reviews of Geophysics* 53.2, pp. 323–361.

Prévost, L. M. C., Regayre, L. A., Johnson, J. S., McNeall, D., Milton, S., and Carslaw, K. S. (2025). "Detection of structural deficiencies in a global aerosol model to explain limits in parametric uncertainty reduction". In: *EGUsphere* 2025, pp. 1–65.

Proske, U., Ferrachat, S., Klampt, S., Abeling, M., and Lohmann, U. (2023). "Addressing Complexity in Global Aerosol Climate Model Cloud Microphysics". In: *Journal of Advances in Modeling Earth Systems* 15.5, e2022MS003571.

Proske, U., Ferrachat, S., Neubauer, D., Staab, M., and Lohmann, U. (2022). "Assessing the potential for simplification in global climate model cloud microphysics". In: *Atmospheric Chemistry and Physics* 22.7, pp. 4737–4762.

Pruppacher, H. and Klett, J. (1996). *Microphysics of Clouds and Precipitation*. Atmospheric and Oceanographic Sciences Library. Springer Netherlands.

Raif, E. N., Barr, S. L., Tarn, M. D., McQuaid, J. B., Daily, M. I., Abel, S. J., Barrett, P. A., Bower, K. N., Field, P. R., Carslaw, K. S., and Murray, B. J. (2024). "High ice-nucleating particle concentrations associated with Arctic haze in springtime cold-air outbreaks". In: *EGUsphere* 2024, pp. 1–38.

Randall, D. A., Bitz, C. M., Danabasoglu, G., Denning, A. S., Gent, P. R., Gettelman, A., Griffies, S. M., Lynch, P., Morrison, H., Pincus, R., and Thuburn, J. (2018). "100 Years of Earth System Model Development". In: *Meteorological Monographs* 59, pp. 12.1–12.66.

Regayre, L. A., Deaconu, L., Grosvenor, D. P., Sexton, D. M. H., Symonds, C., Langton, T., Watson-Paris, D., Mulcahy, J. P., Pringle, K. J., Richardson, M., Johnson, J. S., Rostron, J. W., Gordon, H., Lister, G., Stier, P., and Carslaw, K. S. (2023). "Identifying climate model structural inconsistencies allows for tight constraint of aerosol radiative forcing". In: *Atmospheric Chemistry and Physics* 23.15, pp. 8749–8768.

Regayre, L. A., Pringle, K. J., Booth, B. B. B., Lee, L. A., Mann, G. W., Browse, J., Woodhouse, M. T., Rap, A., Reddington, C. L., and Carslaw, K. S. (2014). "Uncertainty in the magnitude of aerosol-cloud radiative forcing over recent decades". In: *Geophysical Research Letters* 41.24, pp. 9040–9049.

Regayre, L. A., Johnson, J. S., Yoshioka, M., Pringle, K. J., Sexton, D. M. H., Booth, B. B. B., Lee, L. A., Bellouin, N., and Carslaw, K. S. (2018). "Aerosol and physical atmosphere model parameters are both important sources of uncertainty in aerosol ERF". In: *Atmospheric Chemistry and Physics* 18.13, pp. 9975–10006.

Regayre, L. A., Pringle, K. J., Lee, L. A., Rap, A., Browse, J., Mann, G. W., Reddington, C. L., Carslaw, K. S., Booth, B. B. B., and Woodhouse, M. T. (2015). "The Climatic Importance of Uncertainties in Regional Aerosol–Cloud Radiative Forcings over Recent Decades". In: *Journal of Climate* 28.17, pp. 6589–6607.

Rosenfeld, D., Lohmann, U., Raga, G. B., O'Dowd, C. D., Kulmala, M., Fuzzi, S., Reissell, A., and Andreae, M. O. (2008). "Flood or Drought: How Do Aerosols Affect Precipitation?" In: *Science* 321.5894, pp. 1309–1313.

Saltelli, A., Chan, K., and Scott, E. (2000). *Sensitivity Analysis*. Vol. 134.

Sandu, I., Stevens, B., and Pincus, R. (2010). "On the transitions in marine boundary layer cloudiness". In: *Atmospheric Chemistry and Physics* 10.5, pp. 2377–2391.

Sansom, R. W. N., Johnson, J. S., Regayre, L. A., Lee, L. A., and Carslaw, K. S. (2025). "Strong control of the stratocumulus-to-cumulus transition time by aerosol: analysis of the joint roles of several cloud-controlling factors using Gaussian process emulation". In: *EGUsphere* 2025, pp. 1–30.

Sansom, R. (2021). "Demystifying the complex nature of stratocumulus clouds with machine learning". In: *Weather* 76.6, pp. 185–191.

Sansom, R. W. N., Carslaw, K. S., Johnson, J. S., and Lee, L. (2024). "An Emulator of Stratocumulus Cloud Response to Two Cloud-Controlling Factors Accounting for Internal Variability". In: *Journal of Advances in Modeling Earth Systems* 16.9, e2023MS004179.

Sherwood, S. C., Webb, M. J., Annan, J. D., Armour, K. C., Forster, P. M., Hargreaves, J. C., Hegerl, G., Klein, S. A., Marvel, K. D., Rohling, E. J., Watanabe, M., Andrews, T., Braconnot, P., Bretherton, C. S., Foster, G. L., Hausfather, Z., von der Heydt, A. S., Knutti, R., Mauritsen, T., Norris, J. R., Proistosescu, C., Rugenstein, M., Schmidt, G. A., Tokarska, K. B., and Zelinka, M. D. (2020). "An Assessment of Earth's Climate Sensitivity Using Multiple Lines of Evidence". In: *Reviews of Geophysics* 58.4, e2019RG000678.

Shupe, M. D. and Intrieri, J. M. (2004). "Cloud Radiative Forcing of the Arctic Surface: The Influence of Cloud Properties, Surface Albedo, and Solar Zenith Angle". In: *Journal of Climate* 17.3, pp. 616–628.

Sorooshian, A., Alexandrov, M. D., Bell, A. D., Bennett, R., Betito, G., Burton, S. P., Buzanowicz, M. E., Cairns, B., Chemyakin, E. V., Chen, G., Choi, Y., Collister, B. L., Cook, A. L., Corral, A. F., Crosbie, E. C., van Diedenhoven, B., DiGangi, J. P., Diskin, G. S., Dmitrovic, S., Edwards, E.-L., Fenn, M. A., Ferrare, R. A., van Gilst, D., Hair, J. W., Harper, D. B., Hilario, M. R. A., Hostetler, C. A., Jester, N., Jones, M., Kirschler, S., Kleb, M. M., Kusterer, J. M., Leavor, S., Lee, J. W., Liu, H., McCauley, K., Moore, R. H., Nied, J., Notari, A., Nowak, J. B., Painemal, D., Phillips, K. E., Robinson, C. E., Scarino, A. J., Schlosser, J. S., Seaman, S. T., Seethala, C., Shingler, T. J., Shook, M. A., Sinclair, K. A., Smith Jr., W. L., Spangenberg, D. A., Stamnes, S. A., Thornhill, K. L., Voigt, C., Vömel, H., Wasilewski, A. P., Wang, H., Winstead, E. L., Zeider, K., Zeng, X., Zhang, B., Ziemba, L. D., and Zuidema, P. (2023). "Spatially coordinated airborne data and complementary products for aerosol, gas, cloud, and meteorological studies: the NASA ACTIVATE dataset". In: *Earth System Science Data* 15.8, pp. 3419–3472.

Sotiropoulou, G., Sullivan, S., Savre, J., Lloyd, G., Lachlan-Cope, T., Ekman, A. M. L., and Nenes, A. (2020). "The impact of secondary ice production on Arctic stratocumulus". In: *Atmospheric Chemistry and Physics* 20.3, pp. 1301–1316.

Storelvmo, T., Tan, I., and Korolev, A. V. (2015). "Cloud Phase Changes Induced by CO2 Warming—a Powerful yet Poorly Constrained Cloud-Climate Feedback". In: *Current Climate Change Reports* 1.4, pp. 288–296.

Stubenrauch, C. J., Rossow, W. B., Kinne, S., Ackerman, S., Cesana, G., Chepfer, H., Di Girolamo, L., Getzewich, B., Guignard, A., Heidinger, A., Maddux, B. C., Menzel, W. P., Minnis, P., Pearl, C., Platnick, S., Poulsen, C., Riedi, J., Sun-Mack, S., Walther, A., Winker, D., Zeng, S., and Zhao, G. (2013). "Assessment of Global Cloud Datasets from Satellites: Project and Database Initiated by the GEWEX Radiation Panel". In: *Bulletin of the American Meteorological Society* 94.7, pp. 1031–1049.

Sullivan, S. C., Barthlott, C., Crosier, J., Zhukov, I., Nenes, A., and Hoose, C. (2018). "The effect of secondary ice production parameterization on the simulation of a cold frontal rainband". In: *Atmospheric Chemistry and Physics* 18.22, pp. 16461–16480.

Takahashi, T., Nagao, Y., and Kushiyama, Y. (1995). "Possible High Ice Particle Production during Graupel–Graupel Collisions". In: *Journal of Atmospheric Sciences* 52.24, pp. 4523–4527.

Tan, I., Storelvmo, T., and Zelinka, M. D. (2016). "Observational constraints on mixed-phase clouds imply higher climate sensitivity". In: *Science* 352.6282, pp. 224–227.

Tornow, F., Ackerman, A. S., and Fridlind, A. M. (2021). "Preconditioning of overcast-to-broken cloud transitions by riming in marine cold air outbreaks". In: *Atmospheric Chemistry and Physics* 21.15, pp. 12049–12067.

Tornow, F., Ackerman, A. S., Fridlind, A. M., Cairns, B., Crosbie, E. C., Kirschler, S., Moore, R. H., Painemal, D., Robinson, C. E., Seethala, C., Shook, M. A., Voigt, C., Winstead, E. L., Ziemba, L. D., Zuidema, P., and Sorooshian, A. (2022). "Dilution of Boundary Layer Cloud Condensation Nucleus Concentrations by Free Tropospheric Entrainment During Marine Cold Air Outbreaks". In: *Geophysical Research Letters* 49.11, e2022GL098444.

Tornow, F., Crosbie, E. C., Fridlind, A. M., Ackerman, A. S., Ziemba, L. D., Elsaesser, G., Cairns, B., Painemal, D., Chellappan, S., Zuidema, P., Voigt, C., Kirschler, S., and Sorooshian, A. (2025). "High Accumulation Mode Aerosol Concentration and Moderate Aerosol Hygroscopicity Limit Impacts of Recent Particle Formation on Northwest Atlantic Post-Frontal Clouds". In: *Geophysical Research Letters* 52.18, e2025GL116020.

Twomey, S. (1977). "The Influence of Pollution on the Shortwave Albedo of Clouds". In: *Journal of Atmospheric Sciences* 34.7, pp. 1149–1152.

Vali, G. (1985). "Nucleation Terminology". In: *Bulletin of the American Meteorological Society* 66, pp. 1426–1427.

Van Weverberg, K., Giangrande, S., Zhang, D., Morcrette, C. J., and Field, P. R. (2023). "On the Role of Macrophysics and Microphysics in Km-Scale Simulations of Mixed-Phase Clouds During Cold Air Outbreaks". In: *Journal of Geophysical Research: Atmospheres* 128.11, e2022JD037854.

Vardiman, L. (1978). "The generation of secondary ice particles in clouds by crystal–crystal collisions". In: *J. Atmos. Sci.* 35, pp. 2168–2180.

Vergara-Temprado, J., Murray, B. J., Wilson, T. W., O'Sullivan, D., Browse, J., Pringle, K. J., Ardon-Dryer, K., Bertram, A. K., Burrows, S. M., Ceburnis, D., DeMott, P. J., Mason, R. H., O'Dowd, C. D., Rinaldi, M., and Carslaw, K. S. (2017). "Contribution of feldspar and marine organic aerosols to global ice nucleating particle concentrations". In: *Atmospheric Chemistry and Physics* 17.5, pp. 3637–3658.

Vergara-Temprado, J., Miltenberger, A. K., Furtado, K., Grosvenor, D. P., Shipway, B. J., Hill, A. A., Wilkinson, J. M., Field, P. R., Murray, B. J., and Carslaw, K. S. (2018). "Strong control of Southern Ocean cloud reflectivity by ice-nucleating particles". In: *Proceedings of the National Academy of Sciences* 115.11, pp. 2687–2692.

Verlinde, J., Harrington, J. Y., McFarquhar, G. M., Yannuzzi, V. T., Avramov, A., Greenberg, S., Johnson, N., Zhang, G., Poellot, M. R., Mather, J. H., Turner, D. D., Eloranta, E. W., Zak, B. D., Prenni, A. J., Daniel, J. S., Kok, G. L., Tobin, D. C., Holz, R., Sassen, K., Spangenberg, D., Minnis, P., Tooman, T. P., Ivey, M. D., Richardson, S. J., Bahrmann, C. P., Shupe, M., DeMott, P. J., Heymsfield, A. J., and Schofield, R. (2007). "The Mixed-Phase Arctic Cloud Experiment". In: *Bulletin of the American Meteorological Society* 88.2, pp. 205–222.

Webb, M. J., Senior, C. A., Sexton, D. M. H., Ingram, W. J., Williams, K. D., Ringer, M. A., McAvaney, B. J., Colman, R., Soden, B. J., Gudgel, R., Knutson, T., Emori, S., Ogura, T., Tsushima, Y., Andronova, N., Li, B., Musat, I., Bony, S., and Taylor, K. E. (2006). "On the contribution of local feedback mechanisms to the range of climate sensitivity in two GCM ensembles". In: *Climate Dynamics* 27.1, pp. 17–38.

Wegener, A. (1911). *Thermodynamik der Atmosphäre*. Leipzig: J. A. Barth. 331 pp.

Wellmann, C., Barrett, A. I., Johnson, J. S., Kunz, M., Vogel, B., Carslaw, K. S., and Hoose, C. (2018). "Using Emulators to Understand the Sensitivity of Deep Convective Clouds and Hail to Environmental Conditions". In: *Journal of Advances in Modeling Earth Systems* 10.12, pp. 3103–3122.

Wellmann, C., Barrett, A. I., Johnson, J. S., Kunz, M., Vogel, B., Carslaw, K. S., and Hoose, C. (2020). "Comparing the impact of environmental conditions and microphysics on the forecast uncertainty of deep convective clouds and hail". In: *Atmospheric Chemistry and Physics* 20.4, pp. 2201–2219.

Wendisch, M., Crewell, S., Ehrlich, A., Herber, A., Kirbus, B., Lüpkes, C., Mech, M., Abel, S. J., Akansu, E. F., Ament, F., Aubry, C., Becker, S., Borrmann, S., Bozem, H., Brückner, M., Clemen, H.-C., Dahlke, S., Dekoutsidis, G., Delanoë, J., De La Torre Castro, E., Dorff, H., Dupuy, R., Eppers, O., Ewald, F., George, G., Gorodetskaya, I. V., Grawe, S., Groß, S., Hartmann, J., Henning, S., Hirsch, L., Jäkel, E., Joppe, P., Jourdan, O., Jurányi, Z., Karalis, M., Kellermann, M., Klingebiel, M., Lonardi, M., Lucke, J., Luebke, A. E., Maahn, M., Maherndl, N., Maturilli, M., Mayer, B., Mayer, J., Mertes, S., Michaelis, J., Michalkov, M., Mioche, G., Moser, M., Müller, H., Neggers, R., Ori, D., Paul, D., Paulus, F. M., Pilz, C., Pithan,

F., Pöhlker, M., Pörtge, V., Ringel, M., Risse, N., Roberts, G. C., Rosenburg, S., Röttenbacher, J., Rückert, J., Schäfer, M., Schaefer, J., Schemann, V., Schirmacher, I., Schmidt, J., Schmidt, S., Schneider, J., Schnitt, S., Schwarz, A., Siebert, H., Sodemann, H., Sperzel, T., Spreen, G., Stevens, B., Stratmann, F., Svensson, G., Tatzelt, C., Tuch, T., Vihma, T., Voigt, C., Volkmer, L., Walbröl, A., Weber, A., Wehner, B., Wetzel, B., Wirth, M., and Zinner, T. (2024). "Overview: quasi-Lagrangian observations of Arctic air mass transformations – introduction and initial results of the HALO–$(\mathcal{AC})^3$ aircraft campaign". In: *Atmospheric Chemistry and Physics* 24.15, pp. 8865–8892.

Wild, M., Hakuba, M. Z., Folini, D., Dörig-Ott, P., Schär, C., Kato, S., and Long, C. N. (2019). "The cloud-free global energy balance and inferred cloud radiative effects: an assessment based on direct observations and climate models". In: *Climate Dynamics* 52.7, pp. 4787–4812.

Wilson, T. W., Ladino, L. A., Alpert, P. A., Breckels, M. N., Brooks, I. M., Browse, J., Burrows, S. M., Carslaw, K. S., Huffman, J. A., Judd, C., Kilthau, W. P., Mason, R. H., McFiggans, G., Miller, L. A., Nájera, J. J., Polishchuk, E., Rae, S., Schiller, C. L., Si, M., Temprado, J. V., Whale, T. F., Wong, J. P. S., Wurl, O., Yakobi-Hancock, J. D., Abbatt, J. P. D., Aller, J. Y., Bertram, A. K., Knopf, D. A., and Murray, B. J. (2015). "A marine biogenic source of atmospheric ice-nucleating particles". In: *Nature* 525.7568, pp. 234–238.

Wood, R. and Bretherton, C. S. (2006). "On the relationship between stratiform low cloud cover and lower-tropospheric stability". In: *J. Climate* 19, pp. 6425–6432.

Wu, P. and Ovchinnikov, M. (2022). "Cloud Morphology Evolution in Arctic Cold-Air Outbreak: Two Cases During COMBLE Period". In: *Journal of Geophysical Research: Atmospheres* 127.10, e2021JD035966.

Wu, P., Ovchinnikov, M., Xiao, H., Lackner, C. P., Geerts, B., Tornow, F., and Elsaesser, G. (2025). "Effect of Ice Number Concentration on the Evolution of Boundary Layer Clouds During Arctic Marine Cold-Air Outbreaks". In: *Journal of Geophysical Research: Atmospheres* 130.3, e2024JD041282.

Wyant, M. C., Bretherton, C. S., Bacmeister, J. T., Kiehl, J. T., Held, I. M., Zhao, M., Klein, S. A., and Soden, B. J. (2006). "A comparison of low-latitude cloud properties and responses in AGCMs sorted into regimes using mid-tropospheric vertical velocity". In: *Climate Dynamics* 27, pp. 261–279.

Wyant, M. C., Bretherton, C. S., Rand, H. A., and Stevens, D. E. (1997). "Numerical Simulations and a Conceptual Model of the Stratocumulus to Trade Cumulus Transition". In: *Journal of the Atmospheric Sciences* 54.1, pp. 168–192.

Zelinka, M. D., Klein, S. A., and Hartmann, D. L. (2012). "Computing and Partitioning Cloud Feedbacks Using Cloud Property Histograms. Part I: Cloud Radiative Kernels". In: *Journal of Climate* 25.11, pp. 3715–3735.

Zelinka, M. D., Myers, T. A., McCoy, D. T., Po-Chedley, S., Caldwell, P. M., Ceppi, P., Klein, S. A., and Taylor, K. E. (2020). "Causes of Higher Climate Sensitivity in CMIP6 Models". In: *Geophysical Research Letters* 47.1, e2019GL085782.

Zuidema, P., Geerts, B., McFarquhar, G., Bailey, A., Cassano, J., Doyle, J., French, J., DeMott, P. J., Dzambo, A., Grasmick, C., Jarvinen, E., Romashkin, P., Rosky, E., Wolff, C., and Zietlow, D. (2026). "Flying into the Cold: The NSF Cold Air outbreak Experiment in the Sub-Arctic (CAESAR)". In: *ESS Open Archive*.

Chapter 2

Different responses of cold-air outbreak clouds to aerosol and ice production depending on cloud temperature

Chapter 2 is based on the paper published in the journal *Atmospheric Chemistry and Physics*: Huang, X., Field, P. R., Murray, B. J., Grosvenor, D. P., van den Heuvel, F., and Carslaw, K. S. (2025). Different responses of cold-air outbreak clouds to aerosol and ice production depending on cloud temperature. *Atmospheric Chemistry and Physics*, 25(18), 11363–11406. https://doi.org/10.5194/acp-25-11363-2025.

Authors: Xinyi Huang[1], Paul R. Field[1,2], Benjamin J. Murray[1], Daniel P. Grosvenor[1,2], Floortje van den Heuvel[3], and Kenneth S. Carslaw[1]

[1]Institute for Climate and Atmospheric Science, School of Earth and Environment, University of Leeds, Leeds LS2 9JT, UK

[2]Met Office, Exeter EX1 3PB, UK

[3]British Antarctic Survey, Cambridge CB3 0ET, UK

2.1 Abstract

Aerosol-cloud interactions and ice production processes are important factors that influence mixed-phase cold-air outbreak (CAO) clouds and their contribution to cloud-phase feedback. Recent case studies of CAO events suggest that increases in ice-nucleating particle (INP) concentrations cause a reduction in cloud total water content and albedo at the top of the atmosphere. However, no study has compared the sensitivities of the CAO cloud to these processes under different environmental conditions. Here, we use a high-resolution nested model to quantify and compare the responses of cloud microphysics and dynamics in cloud droplet number concentration (N_{d}), INP concentration and efficiency of the Hallett-Mossop (HM) secondary ice production process in two CAO events over the Labrador Sea, representing intense (cold, March) and weaker (warmer, October) mixed-phase conditions. Our results show that variations in INP concentrations strongly influence both cases, while changing N_{d} and the HM process efficiency affect only the warmer October case. With a higher INP concentration, cloud cover and albedo at the top of the atmosphere increase in the cold March case, while the opposite responses were found in the warm October case. We suggest that the CAO cloud response to the parameters is different in ice-dominated and liquid-dominated regimes, and the determination of the regime is strongly controlled by the cloud temperature and the characteristics of ambient INP, which both control the glaciation of clouds. This study provides an instructive perspective to understand how these cloud microphysics affect CAO clouds under different environmental conditions and serves as an important basis for future exploration of cloud microphysics parameter space.

2.2 Introduction

During cold-air outbreak (CAO) events, cold and dry air masses are drawn from high-latitude continental or sea-ice-covered regions to the warm and open ocean, leading to extensive formation of boundary layer clouds (Brümmer, 1996; Brümmer, 1999; Renfrew et al., 1999; Kolstad et al., 2008; Kolstad et al., 2009; Fletcher et al., 2016a; Fletcher et al., 2016b). CAO clouds, which form mainly over extra-tropical regions and are generally in a mixed-phase state, play an important role in cloud feedback under a warming climate (Ceppi et al., 2017; Sherwood et al., 2020; Zelinka et al., 2020; Murray et al., 2021) and different physical representations of clouds are a key reason why models in CMIP6 (Coupled Model Intercomparison Project phase 6) have a higher climate sensitivity compared to models in CMIP5 (Zelinka et al., 2020).

Poor representation of mixed-phase CAO clouds is one of the major reasons for radiative flux biases in global climate models (GCMs) compared to observations, especially in the Southern Ocean (Bodas-Salcedo et al., 2014; Bodas-Salcedo et al., 2016). As CAO clouds are often in a mixed-phase state, where both cloud liquid and ice are present at the same time, cloud liquid can be rapidly removed by ice through the Wegener-Bergeron-Findeisen (WBF) process (Wegener, 1911; Bergeron, 1935; Findeisen, 1938; Findeisen et al., 1943) and accretion processes. Therefore, the interactions between liquid and ice hydrometeors as well as their properties are important for mixed-phase clouds, which are strongly controlled by cloud microphysics processes. However, large uncertainties still exist when simulating the behaviour of these mixed-phase clouds under a warming climate because of the poorly represented cloud microphysics in GCMs (Bodas-Salcedo et al., 2019; Sherwood et al., 2020). Recent studies show that using satellite observations of mixed-phase clouds to constrain GCMs result in a higher climate sensitivity (Tan et al., 2016; Hofer et al., 2024), suggesting the importance of having a good representation of mixed-phase clouds in GCMs for future climate prediction. Even within cloud-resolving models, cloud microphysical processes have large uncertainties due to their complicated and highly parameterised nature (Morrison et al., 2020). Aerosol-cloud interactions and ice production processes are the main sources of these uncertainties (Khain et al., 2015; Morrison et al., 2020), as demonstrated in simulations of cloud properties and cloud field development using high-resolution models (Field et al., 2014; Abel et al., 2017; Vergara-Temprado et al., 2018; de Roode et al., 2019; Tornow et al., 2021; Karalis et al., 2022).

Adjustment of various microphysical processes in models has been shown to improve agreement with observations for CAO clouds. Field et al. (2014) found that an improvement of LWP (liquid water path) and radiation bias can be achieved by modifying the boundary layer parameterization and by inhibiting heterogeneous ice formation in CAO clouds. It is also found by Vergara-Temprado et al. (2018) that changes in the INP

(ice-nucleating particle) concentration can strongly modulate the freezing behaviour of cloud droplets and the albedo of CAO clouds through changing the liquid-ice partitioning in mixed-phase CAO clouds, and hence affects the cloud-phase feedback (Storelvmo et al., 2015; Murray et al., 2021). Stratocumulus-to-cumulus transition (SCT) in CAOs have an important influence on the radiative properties of CAO clouds, and recent studies have shown that SCT in CAO events is sensitive to aerosol loadings including CCN (cloud condensation nuclei) (de Roode et al., 2019; Tornow et al., 2021), INP concentrations (Tornow et al., 2021) and secondary ice production (SIP) (Karalis et al., 2022), which influence precipitation (Abel et al., 2017) and hence affect the radiative properties of the CAO clouds. These studies highlight the importance of cloud microphysical processes for the modelling of mixed-phase CAO clouds. However, they were mainly focused on the sensitivity of single CAO cases to these uncertain cloud microphysical properties and processes, with limited work on understanding the role of environmental conditions.

Our study aims to improve our understanding of the responses of mixed-phase CAO clouds to CCNs (through changing the droplet number concentration), INPs and the secondary ice production process. We use a convection-permitting numerical weather prediction model with a horizontal grid spacing of 1.5 km over a 1500 km domain and compare two CAO cases over the Labrador Sea that occurred under different environmental conditions – one in spring that was cold and one in autumn that was comparatively warm, with the one in Autumn corresponding to the period of the M-Phase field campaign (Murray et al., 2024; Tarn et al., 2025). The selected cases also have different marine CAO strengths, which have been found to affect the CAO cloud properties and cloud field morphology by previous studies using satellite and reanalysis data (Fletcher et al., 2016b; McCoy et al., 2017; Wu et al., 2022; Murray-Watson et al., 2023).

This paper is structured as follows. In Section 2.3, we describe the two CAO cases, the default model setup, the selection of model parameters including their values for each sensitivity test, and the satellite data used for model-observation comparison. In Section 2.4, we present the results showing how these parameters affect the CAO cloud properties differently in each case, as well as the comparison between model output and satellite retrievals. In Section 2.5, we discuss the reasons behind the responses of two CAO events to these tested cloud microphysical processes, along with the limitations and future work.

2.3 Methods

The overall approach of this study is using high-resolution, convection-permitting regional model simulations to understand and compare the sensitivity of mixed-phase

CAO cloud properties in two CAO cloud events over the Labrador Sea to droplet number concentration, INP concentration and efficiency of the Hallett-Mossop secondary ice production process.

2.3.1 Case description

Two CAO events were selected over the Labrador Sea: 15 March 2022 and 24 October 2022, with the latter one coinciding with the M-Phase aircraft campaign (Murray et al., 2024; Tarn et al., 2025). Figure 2.1 shows the UK Met Office surface analysis charts for both cases. There were strong north-westerly flows over the Labrador Sea region during both cases, which is a typical feature during CAO events in this region. A low-pressure system was located to the south-east of Greenland in March, drawing the CAO system around the Greenland. Compared with the March case, the October CAO event was at an earlier stage, generally weaker and only for approximately 2 days (compared to approximately 4 days of the March CAO event). The October case was also accompanied with warmer environmental conditions (see Section 2.3.4 for cloud top temperatures from satellite).

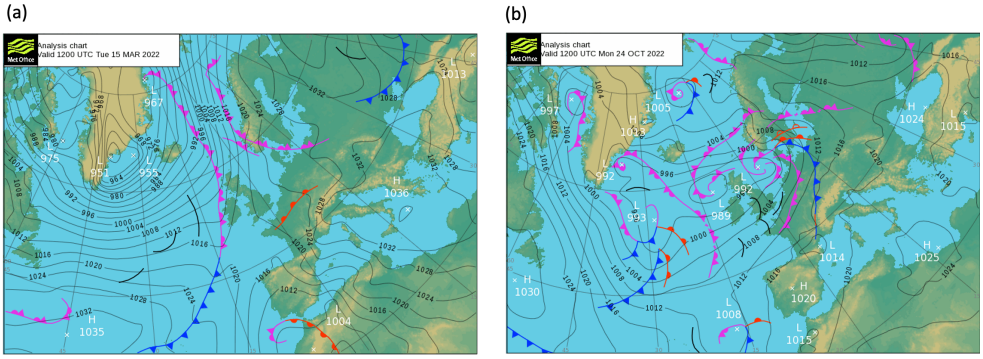


Figure 2.1: The UK Met Office surface analysis charts at 1200 UTC on (a) 15 March 2022 and (b) 24 October 2022.

2.3.2 Model set-up

The Met Office Unified Model (UM) (Brown et al., 2012) version 13.0 with Regional Atmosphere and Land (RAL) 3.2 configuration (Bush et al., 2020; Bush et al., 2022) was used in this study. A 1500 km by 1500 km regional domain with 1.5 km grid spacing and centred at 59 °N, 52 °W was nested within a global model (N216, $\simeq$ 60 km grid spacing near the mid-latitudes) with Global Atmosphere and Land (GAL) 6.1 configuration (Walters et al., 2017). The nested model domains are shown in Appendix 2.3. Using a 1.5 km grid spacing has shown a good ability to reproduce the general features of the CAO cloud system (e.g., the stratus and cumulus regions) from Field et al. (2017b). Such design of the regional domain balances sufficient coverage of the CAO cloud system and the computational cost. There were 70 vertical levels in the

nested region up to 40 km (28 model levels below 3 km where most of the cloud are in both cases) and the time step is 60 seconds for the regional model. The lateral boundary is provided to the regional model from the global model every hour. The simulations were initialized from archived global model analysis at 0000 UTC on the case date and run for 24 hours. The first 12 hours were excluded from the analysis due to model spin-up.

Cloud microphysics are parametrized with the double-moment bulk Cloud AeroSol Interacting Microphysics (CASIM) scheme (Shipway et al., 2012; Grosvenor et al., 2017; Field et al., 2023). There are five hydrometeor species in CASIM: cloud liquid, rain, cloud ice, snow and graupel, with a generalized gamma distribution for the particle size distributions (PSD). CASIM provides two options to calculate the droplet number concentration (N_d), prescribing a fixed in-cloud N_d or deriving N_d from the background aerosol. The prescribed fixed N_d option was selected in this study for an easier perturbation of N_d and interpretation of the results. However, it is worth noting that using fixed in-cloud N_d instead of having aerosols involved can remove potential feedbacks between aerosols and clouds, for example, precipitation formed in clouds can remove aerosols/CCNs which can enhance the precipitation and further remove the aerosols. Details on the selection of parameter values are shown in Section 2.3.3 below. For heterogeneous ice nucleation on INPs (primary ice production, PIP), we use the parameterization of Cooper (1986). The Cooper approach is a parameterization for ice crystal number concentration (N_ice), but because we assume that one INP can produce one ice crystal, the Cooper approach is treated as an INP parameterization in this study. Heterogeneous ice nucleation is assumed to occur in grid boxes with temperatures lower than -8 °C, and higher than -38 °C when homogeneous ice nucleation can occur. Bigg's parameterization for rain freezing (Bigg, 1953) was switched off in this study to avoid potentially unrealistic formation of graupel in convective clouds. The secondary ice production (SIP) process implemented in CASIM is the Hallett-Mossop (HM) process (Hallett et al., 1974), which produces ice splinters through riming between -2.5 °C and -7.5 °C with a peak efficiency at -5 °C. The rates are calculated from cloud liquid accreted by graupel and snow with a default efficiency of 350 ice splinters produced per milligram-rimed cloud liquid. Other SIP mechanisms, such as collision fragmentation (Vardiman, 1978; Takahashi et al., 1995) and droplet shattering (Latham et al., 1961), are currently in development and hence not available for use in this study. When both ice and liquid exist in the same grid box, the overlap mixed-phase fraction is calculated, with a fixed mixed-phase overlap factor of 0.5 (Field et al., 2023). The mixed-phase overlap factor controls a function that quantifies the overlap during the run time of the model rather than being a fixed mixed-phase overlap in a model grid box. If the overlap factor is set to 1, then the subgrid liquid and ice cloud are maximally overlapped. If the overlap factor is 0, then the subgrid liquid and ice are not overlapped as long as

$CF_{\mathrm{liq}} + CF_{\mathrm{ice}} < 1$, where CF refers to cloud volume fraction. Once the combined cloud fraction goes above 1, there will be overlap. For an overlap factor of 0, the overlap is minimised. Values of the overlap factor in between lead to increasing overlap, but once either the liquid or ice cloud fraction reaches 1, then mixed-phase overlap is maximum whatever the overlap factor is set to. See Section A.6 in the documentation of CASIM implementation in UM from Field et al. (2023) for more information.

The cloud parameterization in the nested UM is a diagnostic cloud scheme that uses skewed and bi-modal probability density function for sub-grid saturation departure. This Bimodal Cloud scheme diagnoses the cloud volume fractions and condensed liquid water amounts in each grid box and passes them to CASIM. It is the Bimodal Cloud scheme that handles the condensation and evaporation between water vapour and cloud liquid via a saturation adjustment approach justified by the long model timestep (approx. 60 s) compared to the timescales of saturation adjustment (approx. 1 s). This process happens at a different point of the time step from CASIM. A detailed technical explanation of coupling CASIM to the cloud schemes in UM is discussed in Field et al. (2023).

The radiative processes in the simulations are represented by SOCRATES (Suite Of Community Radiative Transfer codes based on Edwards and Slingo) (Edwards et al., 1996; Manners et al., 2023), which calculates radiative fluxes using the two-stream method and radiance using spherical harmonics. The single-scattering properties of water droplets are dependent on the mass mixing ratio of liquid water and the effective radius of the droplets (Slingo et al., 1982). In this study, the single-scattering properties of ice crystals are calculated using an equivalent mass spherical radius with both the ice water mass mixing ratio and ice hydrometeor number concentration (N_{ice}) from CASIM. This allows a Twomey-like effect to be included from changes in N_{ice}.

2.3.3 Perturbed parameters and the selection of their values

Three model input parameters are perturbed in this study: the prescribed fixed in-cloud droplet number concentration (N_{d}), the scale factor of INP concentration (S_{INP}), and the ice multiplication efficiency of the Hallett-Mossop process (E_{HM}). Table 2.1 shows the values used for each simulation and the selection of parameter values are explained below.

2.3.3.1 Droplet number concentration (N_{d})

CASIM provides two options for calculating N_{d}. Here we use fixed in-cloud N_{d} to allow an easier interpretation of results instead of deriving N_{d} from background aerosol. The grid-box mean N_{d} is calculated by multiplying the fixed in-cloud N_{d} with the liquid cloud fraction in the grid box from the Bimodal Cloud scheme. The default value of

Table 2.1: Configurations of simulations for both case studies. Cell content marked by "-" means that the value used for the parameter is the same as the configuration in the control simulation.

Model Configuration	Fixed N_{d} (cm^{-3})	S_{INP}	E_{HM} (mg^{-1})
Control	150	1	350
low N_{d}	10	-	-
high N_{d}	500	-	-
low S_{INP}	-	0.0001	-
high S_{INP}	-	100	-
low E_{HM}	-	-	10
high E_{HM}	-	-	7000

the fixed in-cloud N_{d} is 150 cm^{-3}, and we selected 10 cm^{-3} for low N_{d} and 500 cm^{-3} for high N_{d} simulations based on values from (Wood, 2012) for general stratocumulus clouds. This range also covers the observations from the M-Phase measurements (Murray et al., 2024; Tarn et al., 2025) and warm cloud N_{d} derived from satellite retrievals (Grosvenor et al., 2018) in this region.

2.3.3.2 Scale factor of INP concentration (S_{INP})

The INP parameterization used in this study is the default heterogeneous ice nucleation parameterization from Cooper (1986) assuming that one INP produces one ice crystal. Here we use a scale factor S_{INP} (unitless) to change the INP concentration from the default Cooper parameterization:

$$N_{\mathrm{INP}}(T) = S_{\mathrm{INP}}(5e^{-0.304(T_0-T)}), \tag{2.1}$$

The unit of $N_{\mathrm{INP}}(T)$ is m^{-3}. The default value of S_{INP} is 1.0. T_0 is 273.15 K and T is the ambient temperature (K). 265.15 K (-8 °C) was chosen as the warmest condition for ice nucleation, meaning there are no INPs at temperature higher than -8 °C. We selected 0.0001 for low S_{INP} and 100 for high S_{INP} simulations to cover the majority of the INP measurements at high latitude regions of the Northern Hemisphere (Figure 2.2a) and the INP measurements from the M-Phase aircraft campaign (Figure 2.2b; Murray et al., 2024; Tarn et al., 2025). There is also a parameter in the Cooper parameterization that defines the dependence of N_{INP} on temperature. Although it has been shown important for deep convective anvil cirrus (Hawker et al., 2021a; Hawker et al., 2021b), it plays a secondary role in the CAO clouds of interest here as the CAO clouds are generally thin (Fletcher et al., 2016b) and the slope in the default Cooper approach matches reasonably well with most of the M-Phase measurements in Figure 2.2b.

2.3.3.3 Efficiency of the Hallett-Mossop Process (E_{HM})

The Hallett-Mossop (HM) process is included as the only SIP process in this study with a default efficiency of 350 ice splinters produced per milligram of rimed cloud liquid (Hallett et al., 1974; Field et al., 2023):

$$P_{\mathrm{HM}} = E_{\mathrm{HM}}(P_{\mathrm{gacw}} + P_{\mathrm{sacw}})f(T)M_{\mathrm{I0}}, \tag{2.2}$$

where P_{HM} is the mass of ice produced from the HM process, E_{HM} is the HM process efficiency perturbed in this study with a default value of 350 mg^{-1}, P_{gacw} is the rate at which graupel accretes cloud water, P_{sacw} is the rate at which snow accretes cloud water, M_{I0} is the produced splinter mass of 10^{-18} kg, and $f(T)$ is a triangular function between -2.5 °C and -7.5 °C with peak at -5 °C when $f(T) = 1$. Clouds formed in the October case span this range of temperatures, while cloud temperatures in the March case are much colder with few clouds formed in this range of temperatures (Section 2.3.1).

We selected 10 mg^{-1} for low E_{HM} and 7000 mg^{-1} for high E_{HM} simulations. The high E_{HM} value was selected following the studies by Young et al. (2019) and Sotiropoulou et al. (2020) to show good agreement with observed N_{ice} when only the HM process is implemented in the model. The low E_{HM} was selected to test the effects of reducing the HM process but not completely removing it. It is worth noticing here that self-limiting feedback may exist when using high E_{HM} (Field et al., 2017a) which can potentially limit the increase of ice splinters produced by increasing the E_{HM} through stronger removal of liquid for riming.

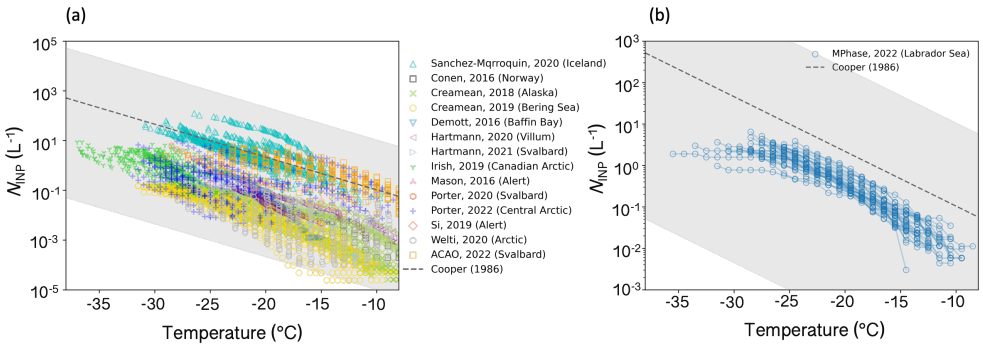


Figure 2.2: Perturbed INP range in this study compared to INP measurements at high-latitude regions in the Northern Hemisphere from (a) literature data (Sanchez-Marroquin et al., 2020; Conen et al., 2016; Creamean et al., 2018; Creamean et al., 2019; DeMott et al., 2016; Hartmann et al., 2020; Hartmann et al., 2021; Irish et al., 2019; Mason et al., 2016; Porter et al., 2020; Porter et al., 2022; Si et al., 2019; Welti et al., 2020; Raif et al., 2024) and (b) M-Phase aircraft campaign (Tarn et al., 2025). INP measurements from each flight during the M-Phase aircraft campaign are connected with lines to compare the INP concentration slope with the default Cooper parameterization slope. The top and bottom boundary of the shaded area are the upper and lower perturbed range of INP concentration in the sensitivity test.

2.3.4 Satellite data

Multiple satellite data products were used in this study to compare model output with observations. Figure 2.3 shows the satellite data products for the two CAO cases including RGB composites (a and e) using bands 1 (620-670 nm), 3 (459-479 nm) and 4 (545-565 nm) from MODIS (Moderate Resolution Imaging Spectroradiometer) Level 1B Calibrated Radiances Product (Collection 6.1) (MODIS Characterization Support Team (MCST), 2017); the Single Scanner Footprint (SSF) of top-of-atmosphere shortwave flux ($F_{\mathrm{SW}}^{\mathrm{TOA}}$, b and f) and longwave flux ($F_{\mathrm{LW}}^{\mathrm{TOA}}$, c and g) from the CERES (Clouds and the Earth's Radiant Energy System) instrument (Edition 4A) (Su et al., 2015a; Su et al., 2015b); and the cloud top temperature (CTT; d and h) from the MODIS Atmosphere Level 2 Cloud Product (Collection 6.1) (Platnick et al., 2015). All-sky liquid water path (LWP) with 0.25° spatial resolution retrieved from the AMSR-2 (Advanced Microwave Scanning Radiometer) columnar cloud liquid water product (version 8.2) (Wentz et al., 2014) and cloud water path (CWP) for both liquid and ice and cloud cover from MODIS Atmosphere Level 2 Cloud Product (Collection 6.1) (Platnick et al., 2015) were also used for model-observation comparison, shown in the Results Section below. A table of retrieval time and selected model time points for each satellite product is shown in Appendix 2.1.

The MODIS and CERES instruments are onboard NASA's Aqua satellite and the AMSR-2 instrument is onboard the JAXA's (The Japan Aerospace Exploration Agency) GCOM-W (Global Change Observation Mission – Water) satellite. Both polar-orbiting satellites have the same equator crossing time of 1:30 p.m. while ascending, and similar altitudes for their orbits. This means satellite retrievals can be made close to each other in time. Geostationary satellite products are not used in this study due to large uncertainties in retrievals for high-latitude regions (Seethala et al., 2010).

Although the two selected CAO events shared similar synoptic situations as shown in Figure 2.1, the cloud top temperatures of them were strongly different. The March case had much colder cloud top temperatures with peak around -30 °C, compared to the ones in the October case with peak around -10 °C. Monthly distributions for cloud top temperature of low-level, mixed-phase clouds during CAO events over the Labrador Sea in 2022 are shown in Appendix 2.2 using the ERA5 (ECMWF ReAnalysis version 5) (Hersbach et al., 2020) dataset and CTT retrieved from MODIS. The CTTs in the March case are near the colder end of the shown distributions, while the ones in the October case are more close to the warmer end, which suggests that these two CAO cases are nicely contrasting from each other in terms of CTTs and sit near the boundaries of CTT ranges in CAO clouds over the Labrador Sea. These two cases were chosen on the basis that they represent end members of the temperature range of mixed-phase CAO clouds. Detailed information for the method of analysis is shown in Appendix 2.2.

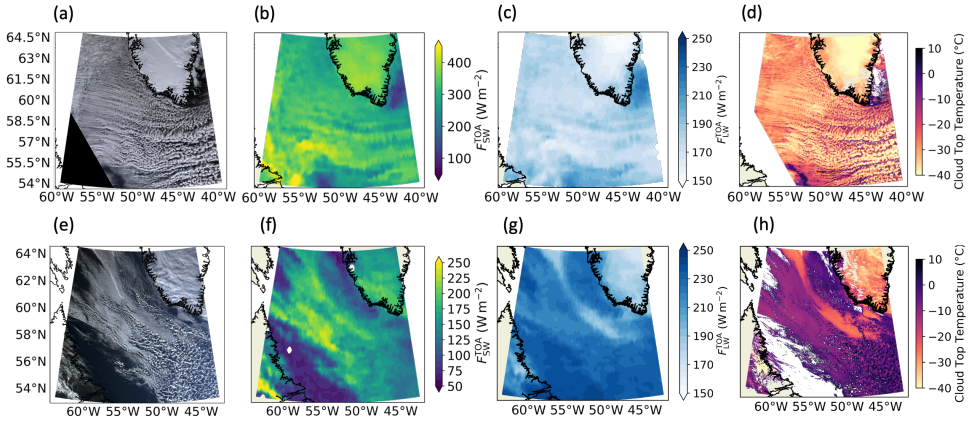


Figure 2.3: Satellite retrievals for CAO events over the Labrador Sea on 15 March 2022 (top) and 24 October 2022 (bottom): RGB imagery (a, e), top-of-atmosphere shortwave flux (b, f), top-of-atmosphere longwave flux (c, g), and cloud top temperature (d, h). Note that the scales of the colour bars for the shortwave radiation flux are different for these two cases due to different satellite retrieval times.

2.4 Results

2.4.1 Control simulations

Control simulations with the default model set-up are introduced and compared in this section. Figure 2.4 shows the modelled in-cloud cloud water path (CWP), which is the sum of the in-cloud liquid water path (LWP) and the in-cloud ice water path (IWP), for both cases compared with MODIS retrieved in-cloud CWP. This comparison acts as a qualitative check of whether our model can simulate the main synoptic features of the CAO cloud system. MODIS-retrieved CWP data were re-gridded to the same spatial resolution as the modelled CWP (1.5 km) using the nearest-neighbour method. The satellite retrieval time and selected model output time point are shown in Appendix 2.1.

In general, the March CAO event has a less broken cloud field with higher CWP compared to the October CAO event. For both cases, the control simulations capture the cloud regimes (e.g., stratus and open cells) during the CAO event, and reproduce the large-scale synoptic structures and the locations of the CAO event well compared with the MODIS retrievals. In the March case, the model struggles with reproducing the fine structures of cloud streets to the east of 54 °W in the sub-domain. This is because the effective horizontal resolution (between 5 times to 10 times of the grid spacing) in our model cannot fully resolve the cloud streets at the beginning of the CAO event. With the clouds moving into the convective region and the boundary layer getting deepened (to the west of 54 °W), the scales of cloud street grow and

can then be resolved in the model. A better representation of the cloud streets at the beginning of the CAO event requires higher model resolution (Field et al., 2017b) and therefore much higher computational resources to conduct the sensitivity test, hence are not further investigated here. Our control simulations generally have higher in-cloud CWP compared with the MODIS, which may be because of different definitions of cloudy pixels between model output and satellite products, uncertainties in the MODIS-retrieved CWP for high-latitude mixed-phase clouds (Khanal et al., 2018), as well as potential overestimation of CWP from our model.

Note that the CWP comparison is only qualitative here, and quantitative model-observation comparisons of the control simulations with satellite retrievals of cloud top temperature from MODIS, temperature and IWC (ice water content) from CALIOP for the March case, and M-Phase aircraft measurements of temperature, cloud water content and liquid water fraction for the October case are shown and discussed in Appendix 2.4. Quantitative comparisons of all-sky LWP, shortwave (SW) and longwave (LW) fluxes between model output from all simulations (control and sensitivity test simulations) and satellite retrievals are shown later in Section 2.4.5.

Cross-section mean cloud properties within the highlighted sub-domain (yellow parallelogram) in Figure 2.4 of both cases are presented and compared in Figure 2.5, with supplementary information shown in Appendix 2.5. The sub-domain was selected to be aligned with directions of wind and cloud movements, and the cross-section mean is calculated by averaging along the y-axis of the sub-domain parallelogram. The locations of the sub-domains in the nested model domains are shown in Appendix 2.3. The whole sub-domain in the March case and most of the sub-domain (except the small northwestern part) of the October case are sufficiently distant from the boundaries of the nested model domain, hence not affected by the boundary effects from fields entering from the global model. A detailed discussion on the boundary effects is shown in Appendix 2.3.

Both cases experience a general west-to-east reducing trend of cloud cover (Figure 2.5a) in the sub-domain along the direction of cloud movements to the open ocean, with the March case having a generally higher cloud cover (>0.9 for most of the cross-section) compared to the one in October. The in-cloud LWP (Figure 2.5b) is much higher in October, with the peak LWP happening around 150 g m^{-2} near 56 °W in October and less than 20 g m^{-2} near the eastern boundary of the sub-domain in March. The trend of LWP changing from the west to the east of the sub-domain is different in these two cases: a general increasing trend in March while the LWP first increases to the peak value and then reduces in October. The in-cloud IWP (Figure 2.5c) is much higher in the March case with the peak around 750 g m^{-2} near 50 °W. The in-cloud IWP starts at a low level in October and generally increases from west to east with the peak value slightly lower than 300 g m^{-2} near the eastern boundary of the

sub-domain. Liquid water fraction, the ratio of LWP to CWP, is calculated to show the liquid-ice partitioning in both cases (Appendix 2.5). The dominant cloud water are in ice-phase in the March case, while the liquid-phase dominates at the western region in the October and later ice-phase dominates when clouds move towards east. Both cases experience little precipitation in the western region and enhanced precipitation when clouds move to further east (Figure 2.5d), with the dominant type of precipitation in March being snow and rain in October (Appendix 2.5).

As the SW radiation dominates cloud radiative effects in shallow mixed-phase clouds, here we use albedo at the top-of-the-atmosphere (TOA) in Figure 2.5e to investigate the CAO cloud radiative properties. The outgoing shortwave and longwave flux are shown in Appendix 2.5. The overall trend of albedo changing from the west to the east of the sub-domain is very similar in these two cases, with the albedo slightly higher in October. By comparing the trend with other cloud properties mentioned above, it is shown that albedo is strongly affected by the cloud cover in both of the two cases, but influenced more from in-cloud IWP in March, while more from in-cloud LWP in October. This is due to the variation of the liquid-ice partitioning in their control simulations, and the liquid-ice partitioning is strongly controlled by the cloud temperature with a same temperature-dependent INP parameterization (as well N_{d} and E_{HM}). Cross-section mean for cloud profiles (cloud volume fraction and total water content) with ambient temperature are shown in Appendix 2.5. Most of the clouds in the March case in the sub-domain are between -15 °C and -35 °C, while the ones in the October case having a much warmer ambient temperature most between 0 °C and -15 °C. Such temperature difference can directly lead to different efficiencies of many temperature-dependent cloud microphysics processes including the INP concentration and HM efficiency perturbed in this study during these two cases.

Meteorological variables and environmental conditions of boundary layer are also shown and compared for the control simulations of these cases as shown in Figure A2.9 of Appendix 2.5. The SST (sea surface temperature) increases as clouds move eastward, with the SST lower in the March case (2-3 °C) compared to the one in the October case (4-7 °C). Note that the SST was prescribed based on daily forecasting analyses in all our model simulations. The March case is a much stronger CAO event with the highest CAO index at 800 hPa (M_{800}, defined as the difference between the potential temperature at the surface skin and that at 800 hPa) almost reaching 20 K at the western boundary of the sub-domain, while the highest M_{800} is around 1.5 K in the October case. The more unstable boundary layer in the March case is consistent with a lower LTS (lower tropospheric stability) compared to the one in the October case. Both cases experience an EIS (estimated inversion strength) over 5 K at the western boundary of their sub-domain with a decreasing trend to the east.

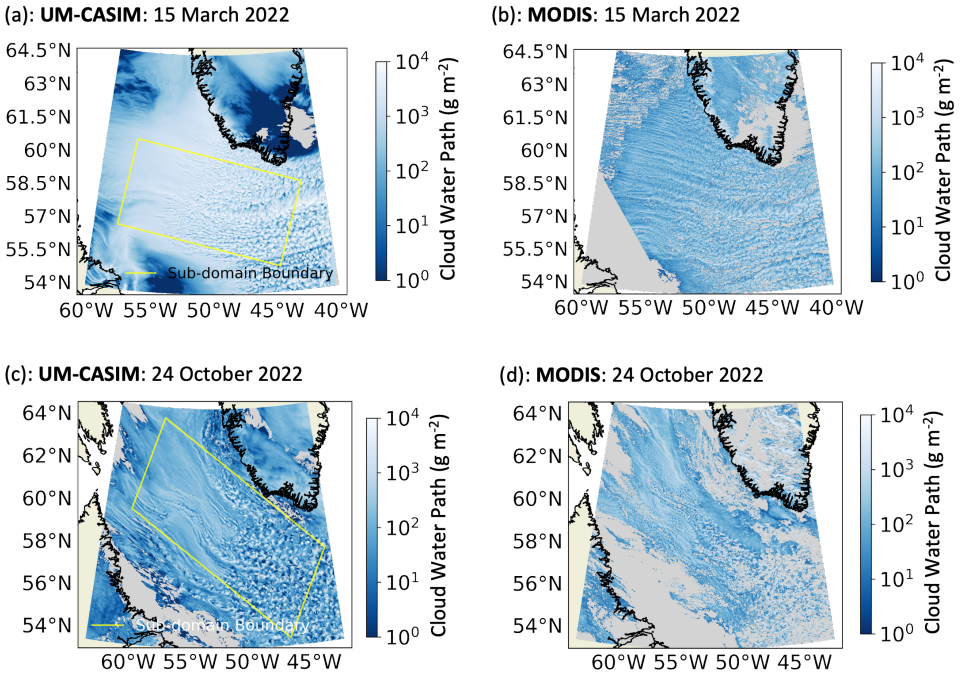


Figure 2.4: In-cloud cloud water path (CWP) from the control UM-CASIM simulations and MODIS retrievals on 15 March 2022 (a,b) and 24 October 2022 (c,d). The model reproduces the general CAO cloud system in both case studies well when compared to satellite retrievals. In-cloud cloud water path retrieved from MODIS is not used for a quantitative comparison due to its large uncertainties. Sub-domains of interest for both cases are highlighted in yellow. Model output pixels with less than 20% cloud cover are excluded before calculating the in-cloud values. The grey shading represents no-cloud conditions (cloud water path less than 1 gm^{-2}). Times of model output and satellite retrieval time are shown in Appendix 2.1.

2.4.2 Responses of cloud properties to perturbed parameters

In this section, the responses of the cloud properties to the perturbations in droplet number concentration (N_d), the INP concentration (S_INP) and the efficiency of the HM process (E_HM) are compared between the two cases. An overall comparison between the two cases as well as the cloud profiles are shown later in Section 2.4.4.

2.4.2.1 15 March 2022

Here we first present the responses of cloud cover, in-cloud LWP, in-cloud IWP, surface precipitation rate, and TOA albedo in Figure 2.6 for the March case, as well as other properties shown in Appendix 2.6 (Figure A2.11). There is limited influence from perturbing N_d (left panel) and E_HM (right panel) on the cloud properties in March. Effects from these parameters are small due to little water in the control simulation and most of the clouds are out of the active temperature range for the HM process in March as shown in Figure A2.10 of Appendix 2.5.

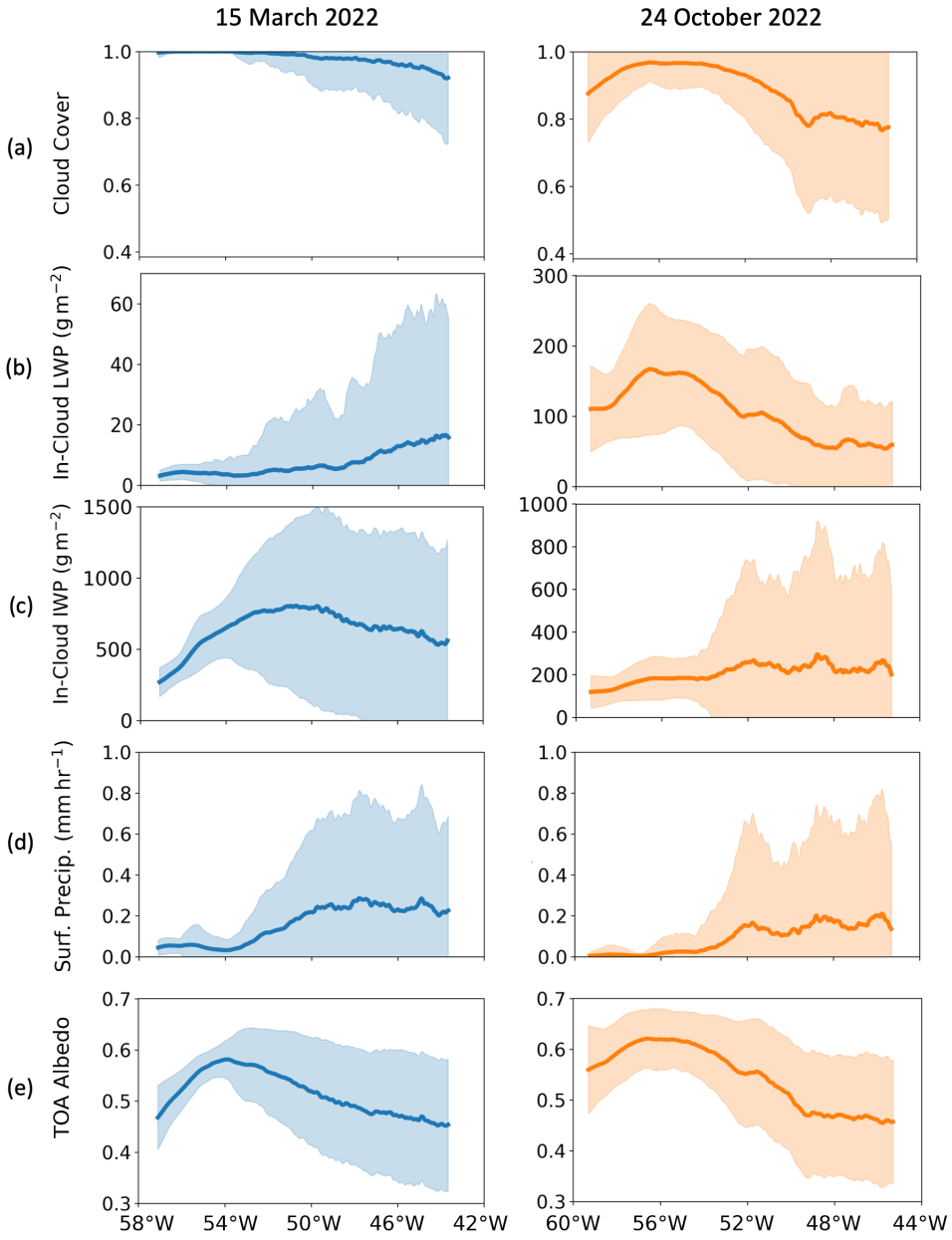


Figure 2.5: Cross-section mean (averaging along y-axis of the sub-domain parallelogram shown in Figure 2.4) cloud properties from the March (left panel) and the October (right panel) control simulations: (a) cloud cover, (b) in-cloud liquid water path (LWP), (c) in-cloud ice water path (IWP), (d) surface precipitation, and (e) albedo at the top-of-the-atmosphere (TOA albedo). The time points selected are 16:45 UTC for the March case and 17:00 UTC for the October case, which are consistent with the corresponding CERES measurement times. Grid boxes with cloud cover smaller than 20% were removed before averaging for calculation of the in-cloud LWP and in-cloud IWP. The shaded area indicates the range of ± 1 standard deviation.

Perturbing S_{INP} (middle column of panels) has a much stronger influence on all the column cloud properties shown here than perturbing N_{d} or E_{HM}. With a higher INP concentration, the modelled CAO clouds experience a higher cloud cover from

around 54 °W to the eastern boundary of the sub-domain and a higher in-cloud IWP throughout the sub-domain (stronger increase in the eastern region) along with a lower surface precipitation. The in-cloud LWP decreases only slightly because there is so little liquid water in the control simulation, with a similar change for the liquid cloud fraction (Appendix 2.5). The limited influence from lower in-cloud LWP is then offset by the higher cloud cover and higher in-cloud IWP, resulting in a general higher TOA albedo in the high INP concentration simulation.

The responses of in-cloud LWP, IWP and liquid water fraction are consistent with previous studies (Abel et al., 2017; Tornow et al., 2021), but the responses of cloud cover, surface precipitation and TOA albedo differ from the previous studies, where the CAO cloud cover becomes smaller with a higher INP concentration (Tornow et al., 2021). Similarly, Abel et al. (2017) found that cloud cover was increased when they prevented ice formation. In this March case, the increase in cloud cover with higher INP concentration is due to the small amount of liquid water in the control simulation so that the increase in ice concentrations has only a small effect on the further removal of liquid water. In addition, with a higher INP concentration, there is a higher ice number concentration and the autoconversion from ice crystals to snow becomes slower, as well as the mean ice hydrometeor particle size becomes smaller resulting in a lower mean fallspeed and reduced sedimentation flux. These effects lead to less precipitation and slower removal of cloud water, resulting in a greater cloud cover. The responses here to a higher INP concentration are similar to what we would expect in cirrus clouds.

With a lower INP concentration, a strong increase in the in-cloud LWP is seen in the western sub-domain, with the peak value over 300 g m^{-2}. However, a sharp reduction of in-cloud LWP follows around 53 °W to 52 °W as well as a strong surface precipitation at the same location. This strong removal of liquid water from clouds limits the influence of decreasing INP on increasing the in-cloud LWP in the rest of the sub-domain. Compared to the control simulation, lower INP concentration has limited influence on the cloud cover and leads to a generally lower in-cloud IWP throughout the sub-domain. The change of TOA albedo is slightly complex: in the western sub-domain before the liquid water being rapidly removed, a higher albedo is seen by having a much higher LWP; after the strong removal of LWP, the albedo reduces quickly and becomes lower than the one in the control simulation, which is a result of the lower in-cloud IWP. While the enhanced reflectivity with decreased INP is confined to the beginning of the sub-domain, the response to INP in the rest of the sub-domain extends over a massive area stretching out into the Atlantic and dominates the radiative effect of the INP over the sub-domain region as a whole.

2.4.2.2 24 October 2022

A similar analysis for the October CAO case is shown both in Figure 2.7 and Appendix 2.6 (Figure A2.12). Unlike the March case where only the S_{INP} simulation strongly influences the cloud properties, all three perturbed parameters show clear and various influences in this October case, and some responses of cloud properties vary in the CAO development from west to east.

Perturbing N_{d} now has a strong influence on CAO cloud cover, in-cloud LWP and TOA albedo in this October case. A low N_{d} leads to lower cloud cover and LWP along with a higher surface precipitation, which is consistent with the Albrecht effect (Albrecht, 1989). With a high N_{d}, there is limited influence on cloud cover at the beginning of the CAO cloud system, and this is because the precipitation rate is very small in the control simulation at this location, hence cannot be further suppressed with a higher N_{d}. The responses of the TOA albedo to both low and high N_{d} are the strongest among all the sensitivity test simulations in October, and is consistent with the Twomey effect (Twomey, 1977).

The responses of cloud properties to the perturbation of S_{INP} from the western boundary to around 50 °W are similar to the CAO cloud responses to INP concentration or ice in previous studies (Abel et al., 2017; Tornow et al., 2021). The responses become complex and some even non-monotonic near the eastern end of the sub-domain. Until around 50 °W, a higher INP concentration results in lower cloud cover, in-cloud LWP and TOA albedo, with higher in-cloud IWP and surface precipitation, and vice versa for lower INP concentrations.

Various responses of cloud properties are also seen when perturbing E_{HM}. With a high E_{HM}, which means a more efficient HM process in the simulation, the cloud cover, surface precipitation and TOA albedo are only affected strongly close to the eastern end of the sub-domain. This is because the HM process in the model is dependent on the processes of cloud water accretion onto graupel and snow, while ice is very limited in the stratocumulus-dominated region but a higher IWP is seen after SCT. A high E_{HM} leads to a higher cloud cover, a lower surface precipitation rate and a higher TOA albedo. This is because although the HM process is the source of ice crystals, it is also the sink for graupel and snow which can accrete and remove water through precipitation in the model. A high E_{HM} results in a lower amount of graupel and snow, hence leading to a smaller precipitation. The responses of in-cloud LWP and in-cloud IWP are consistent throughout the sub-domain, with a high E_{HM} resulting in lower in-cloud LWP (through riming) and higher in-cloud IWP (slow snow autoconversion with a high ice crystal number concentration). These influences become stronger in the eastern region. Although low E_{HM} has a limited influence compared to the ones from high E_{HM}, one might notice that the responses of surface precipitation to E_{HM}

become complicated and non-monotonic (e.g., the default model output is outside the low and high model output range) near the end of the sub-domain where cumulus clouds dominate. For example, low E_{HM} results in a stronger surface precipitation from 52 °W to 50 °W, but a weaker surface precipitation around 46 °W, compared to the precipitation from the control simulation. This may be because precipitation rate is a state-dependent variable, and a low E_{HM} leads to an earlier peak of precipitation when clouds move eastward compared to the one from the control simulation, followed by a lower precipitation rate later as less cloud water exists.

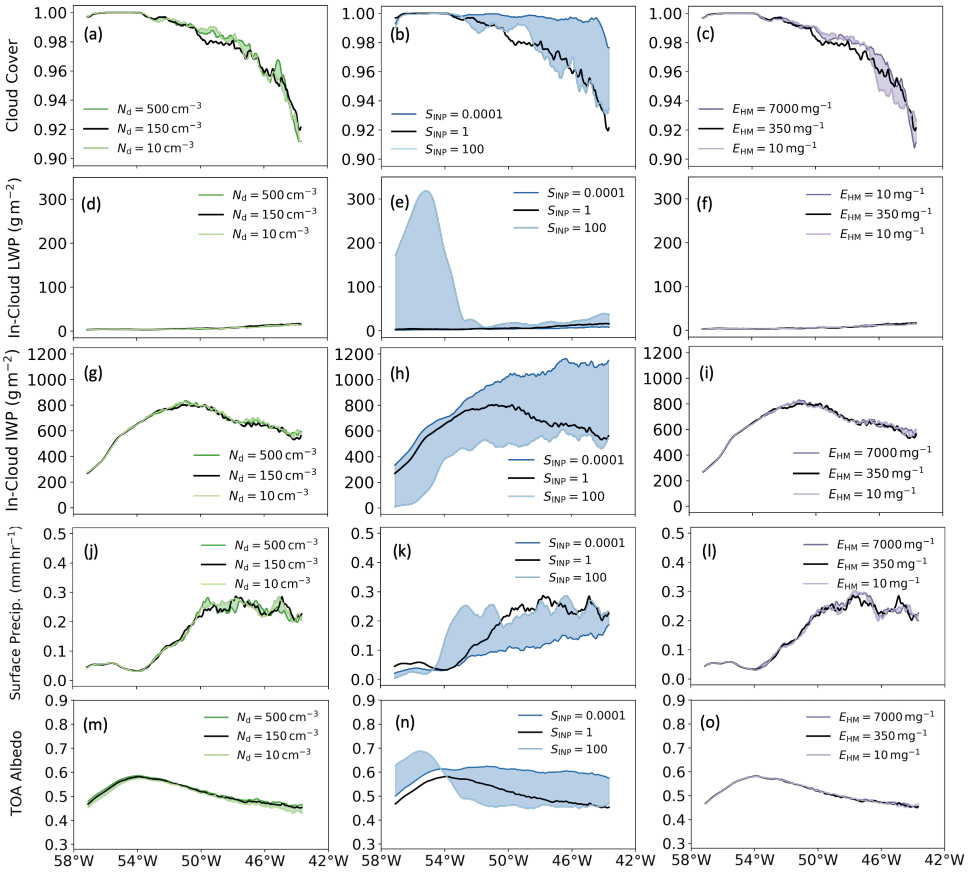


Figure 2.6: Responses of cross-section mean CAO cloud properties to the three perturbed parameters on 15 March 2022 at 16:45 UTC: (a)-(c) cloud cover, (d)-(f) in-cloud liquid water path (LWP), (g)-(i) in-cloud ice water path (IWP), (j)-(l) surface precipitation, and (m)-(o) albedo at the top-of-the-atmosphere (TOA albedo). Grid boxes with cloud cover smaller than 20% were removed before calculating in-cloud LWP and IWP. 16:45 UTC was chosen for the corresponding CERES measurements of radiation on 15 March 2022. Space between the variable data from the high and low simulations is filled to highlight the range of variables and identify non-monotonic behaviours (e.g., data from the control simulation are not in the shaded space).

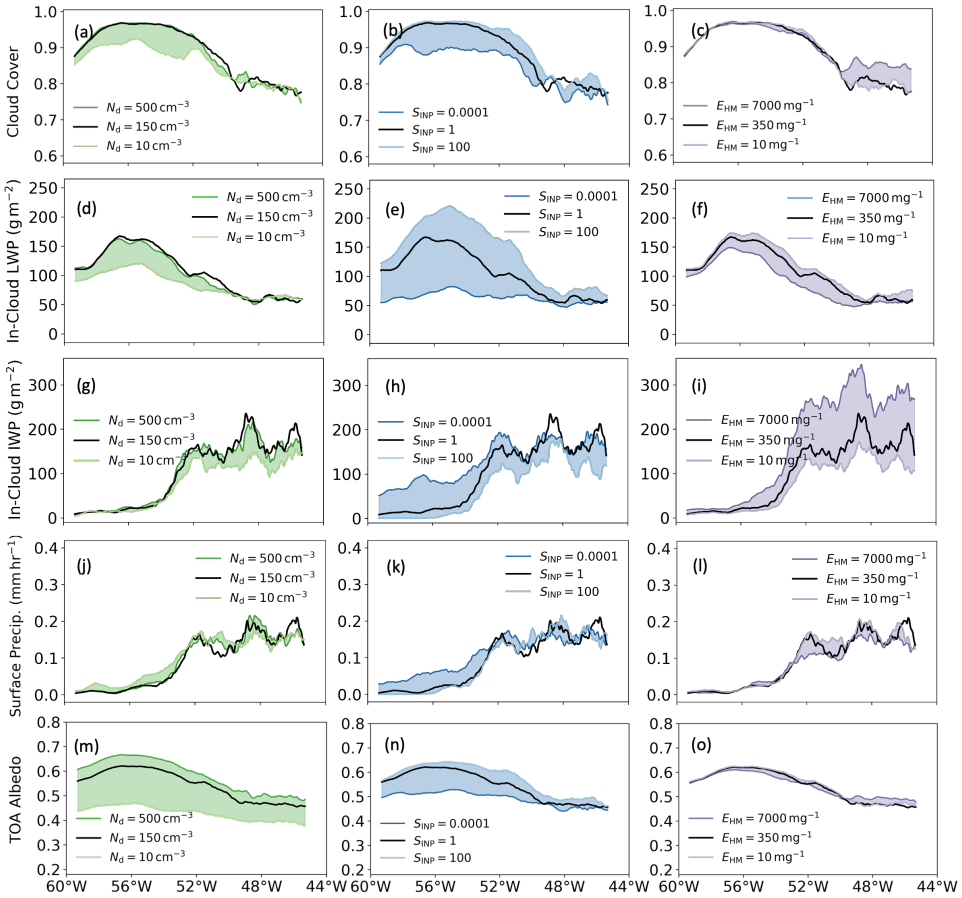


Figure 2.7: Responses of cross-section mean CAO cloud properties to the three perturbed parameters on 24 October 2022 at 17:00 UTC: (a)-(c) cloud cover, (d)-(f) in-cloud liquid water path (LWP), (g)-(i) in-cloud ice water path (IWP), (j)-(l) surface precipitation, and (m)-(o) albedo at the top-of-the-atmosphere (TOA albedo). Grid boxes with cloud cover smaller than 20% were removed before calculating in-cloud LWP and IWP. 17:00 UTC was chosen for the corresponding CERES measurements of radiation on 24 October 2022. Space between the variable data from the high and low simulations is filled to highlight the range of variables and identify non-monotonic behaviours (e.g., data from the control simulation are not in the shaded space).

2.4.3 Responses of CAO cloud field development to perturbed parameters

Cloud field development including stratocumulus-to-cumulus transition (SCT) is important for the radiative properties of CAO clouds. In this section, we use the cloud field homogeneity parameter (ν) calculated using in-cloud cloud water path (CWP), which has been successfully used for identifying cloud field transition from satellite retrievals (Wood, 2012; Wu et al., 2022), to understand how the perturbed parameters affect the cloud field development in the two selected cases. The cloud field homogeneity parameter (ν) is calculated using the squared ratio of the mean ($\bar{x}$) to the standard deviation (σ) for CWP over 20 by 20 grids: $\nu = (\frac{\bar{x}}{\sigma})^2$.

Figures shown in this section are the cross-section mean of the cloud field homogeneity parameter in the selected sub-domain. A sharp decrease in the cloud field homogeneity parameter generally implies a transition from stratocumulus clouds (Sc) to cumulus clouds (Cu). We also qualitatively determine the stratocumulus-dominated, transition and cumulus-dominated regions by using the trends of the cloud field homogeneity parameter and the fraction of the 20 by 20 grids that are of the cumulus-capped boundary layer type. The methods for determining boundary layer type in the UM are shown in Lock (2001). A quantitative determination of where the transition happens is not conducted in this study and requires further research on using the cloud field homogeneity parameter for model output. Note that we did not define the regions for different simulations individually to avoid any location effects. A detailed description of how we qualitatively define these regions can be found in the captions of Figure 2.8 and Figure 2.9 .

Figure 2.8 shows the evolution of cloud morphology (in terms of the spatial distribution of CWP) together with the homogeneity parameter and the cumulus-capped boundary layer fraction in the March case. The contribution of other boundary layer types for all the simulations is shown in Appendix 2.7. Figure 2.8d shows the CWP field with different S_{INP} and the stratocumulus-dominated, transition and cumulus-dominated regions are separated by dashed grey lines.

Similar to the cloud properties shown in Figure 2.6, the overall development of the cloud field in March is only strongly influenced by S_{INP}. With a higher INP concentration, the CAO cloud field begins with a more heterogeneous stratocumulus-dominated region, a higher cumulus-capped boundary layer fraction, and a slightly earlier transition to cumulus-dominated region, indicated by an earlier sharp decrease of the cloud field homogeneity parameter and increase of the cumulus-capped boundary layer fraction.

To test whether the effect of INP on cloud field homogeneity and boundary layer types is caused by modifications to precipitation through the precipitation-induced SCT mechanism from Abel et al. (2017), we performed additional simulations in which precipitation, or evaporation and sublimation of precipitation were turned off, and a simulation without precipitation, evaporation or sublimation (denoted "no-all") shown in Appendix 2.8. Most of the difference in cloud field development is removed in the no-precipitation and no-all simulations, with limited influence from the no-evaporation-and-sublimation simulations. This shows that the influence of INP on the March case's cloud field morphology and boundary layer structure is mainly through precipitation evolution that acts as a sink of moisture from the cloud layer.

Figure 2.9 shows a similar analysis for the October case. Compared to the cloud field in the March case above, the CAO cloud field in the October case is more heterogeneous,

and the cumulus clouds begin to show even at the western boundary of the sub-domain (Appendix 2.7). Perturbing both N_{d} and S_{INP} now have strong influences on the cloud field. Despite the dependence of cloud properties on E_{HM} in the October case discussed above (Figure 2.7), there are limited effects on the cloud field development from perturbing E_{HM}.

With a higher S_{INP}, the October CAO cloud field also has an earlier transition to cumulus-dominated region, a more heterogeneous cloud field across all of the CAO domain, and a higher surface precipitation rate (shown in Figure 2.7k). An earlier transition to cumulus-dominated region is also seen with low N_{d} in the October case here. Both high S_{INP} and low N_{d} simulations experience earlier and more intense precipitation at the early stage of the CAO cloud shown in Figure 2.7, and this is consistent with the precipitation-induced SCT mechanism in CAO clouds from Abel et al. (2017). Such influence of low N_{d} on SCT is not seen in the March case, as there is limited influence of changing N_{d} on precipitation due to the very limited amount of liquid cloud in the control simulation. Note that the stratocumulus-dominated region in the October case is very limited here due to the cumulus starting to show up at a very early stage of the sub-domain.

Several other factors may influence SCT during CAO events but they were not examined in this study. These include sea surface temperature (SST), which can impact convection and turbulence, as well as boundary layer stability, inversion layer strength and humidity. Additionally, this work focused on only three cloud microphysics parameters, whereas other microphysical processes could also potentially affect SCT. Future research should aim to explore the influence of these additional factors to gain a more comprehensive understanding of factors controlling SCT in CAO events.

The regions identified here are used for the overall comparison of cloud properties in the sub-domain as well as in different regions between the March and the October case in the next section.

2.4.4 Overall comparison of the cloud responses to perturbed parameters between the cases

In this section, the responses of cloud properties are compared in terms of the fractional change relative to the default simulation (Figure 2.10). We compared the fractional changes between the stratocumulus-dominated region (Figure 2.10a), cumulus-dominated region (Figure 2.10b), and the overall domain that includes the previous two regions and the transition region (Figure 2.10c). Mean cloud profiles (grid-box with in-cloud total water content $> 10^{-6}$ kg kg^{-1}) for the stratocumulus-dominated region and the cumulus-dominated region for each case are shown in Figure 2.11 and Figure 2.12 to illustrate the responses of in-cloud properties to the perturbed S_{INP}.

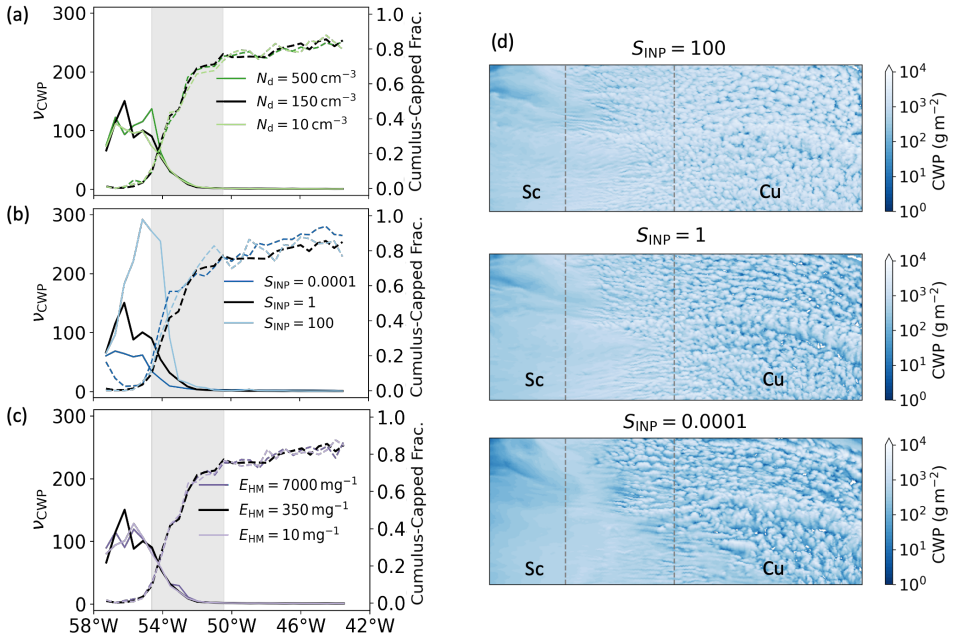


Figure 2.8: The cloud field homogeneity parameter (ν, solid lines) and the fraction of cumulus-capped boundary layer (dashed lines) in cloudy pixels (cloud cover $\geq 20\%$) for simulations with perturbed N_d (a), S_{INP} (b) and E_{HM} (c) on 15 March 2022, and (d) shows the 2D fields of cloud water path for simulations with perturbed S_{INP}. Grey-shaded areas in (a)-(c) as well as the region between grey dashed lines in (d) are the general stratocumulus to cumulus transition regions selected using both the cloud field homogeneity parameter (ν) and the fraction of cumulus-topped boundary layer. Note that we did not define the regions for different simulations individually to avoid any location effects. The stratocumulus-dominated region is determined to be located before the sharp decrease of the cloud homogeneity parameter and before the sharp increase of cumulus-capped boundary layer fraction; the cumulus-dominated region is determined to be where both the cloud homogeneity parameter and the cumulus-capped boundary layer fraction become stable; and the rest is determined as the transition region.

The responses of in-cloud properties to N_d and E_{HM} are shown in Appendix 2.9 and will not be further discussed in detail here.

The strengths of the cloud responses to high S_{INP} and low S_{INP} are different in the two cases in the stratocumulus-dominated regions. Low S_{INP} has the strongest effect in March, while high S_{INP} has the strongest effect in October. This is because the March control simulation has low liquid water (Figure 2.11b and c) to be further removed when S_{INP} increases , while the October control simulation has a very high liquid fraction (Figure 2.12b and c), so a high S_{INP} can strongly convert the liquid to ice with subsequent ice removal through accretion. This is similar when considering the influence of low S_{INP} for the two cases.

Responses of cloud cover to S_{INP} perturbations are opposite in these two cases in the cumulus-dominated region: a high S_{INP} results in a higher cloud cover in March, but a lower one in October. The response in October is similar to the previous studies,

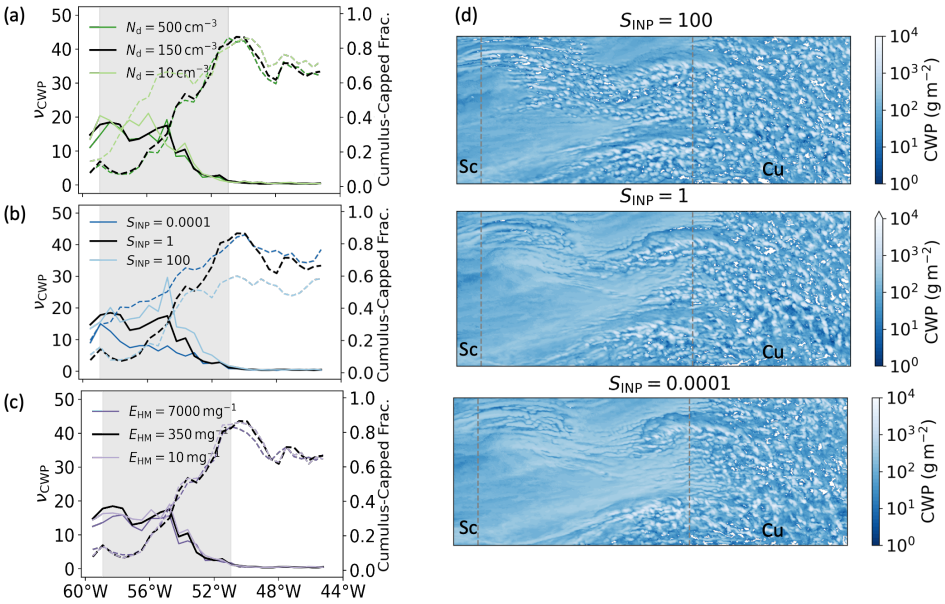


Figure 2.9: The cloud field homogeneity parameter (ν, solid lines) and the fraction of cumulus-capped boundary layer (dashed lines) in cloudy pixels (cloud cover $\geq 20\%$) for simulations with perturbed N_d (a), S_{INP} (b) and E_{HM} (c) on 24 October 2022, and (d) shows the 2D fields of cloud water path for simulations with perturbed S_{INP}. Grey-shaded areas in (a)-(d) as well as the region between grey dashed lines are the general stratocumulus to cumulus transition regions selected using both the cloud field homogeneity parameter (ν) and the fraction of cumulus-topped boundary layer. Note that we did not define the regions for different simulations individually to avoid the location effect. The stratocumulus-dominated region is determined as before the sharp decrease of the cloud homogeneity parameter and the sharp increase of cumulus-capped boundary layer fraction, the cumulus-dominated region is determined by the trend of cloud homogeneity parameter and the overall cumulus-capped boundary layer fraction becoming stable, and the rest is determined as the transition region.

hence not further discussed here. The higher cloud cover in March from a higher S_{INP} is the result of a slower snow autoconversion and smaller ice hydrometeor size (Figure 2.11j) for lower fallspeed hence a lower precipitation rate. As there is very limited liquid in the control simulation already, and the dominant precipitation type (the main way to remove cloud water) in March is snow. Therefore, the impact of having more ice to remove more liquid is very limited in March, and instead, we see a similar influence from having more INPs in precipitating mixed-phase clouds to the one from having more CCNs in precipitating liquid-only clouds (the Albrecht effect). Such response is also expected to see in cirrus clouds with more INPs. This also explains why there is no such influence in the stratocumulus-dominated region as the precipitation rate is very low.

The influence of S_{INP} on in-cloud LWP in the March cumulus-dominated region is also suppressed when compared to the one in the stratocumulus-dominated region. This is due to the liquid water being rapidly removed during SCT as shown in Figure

2.6h. We also find lower S_{INP} leads to higher LWP but lower albedo at the top of the atmosphere in the March cumulus-dominated region. This is the result of the compensation between a slightly increased LWC (Figure 2.11g) near cloud top and a decrease in the albedo of ice through increasing ice size (Figure 2.11j) - a "Twomey-like" effect from INPs.

Most responses of the cloud properties to N_{d} in both cases and all regions have the same direction (same sign of the fractional changes), but the influence of perturbing N_{d} on the October CAO clouds are much stronger. This can also be explained by the different liquid-ice partitioning in control simulations of the two cases, with the October case having a much higher in-cloud LWP.

The strongest influence of perturbing E_{HM} on cloud properties is in the cumulus-dominated region of the October case. There are limited effects of perturbing E_{HM} in March and this is because the ambient temperature for the March case is too cold and outside of the HM active range (Figure 2.11a and f). In the cumulus-dominated region of the October case, both high and low E_{HM} simulations result in a higher reflected radiation, but the underlying reasons are different. For the simulation with high E_{HM}, the higher albedo comes from a higher cloud cover, while for the simulation with low E_{HM}, it comes from a higher in-cloud LWP.

The responses of cloud properties in the overall domain are not just determined by the responses in stratocumulus- and cumulus-dominated regions, but also the size of these two regions and the SCT region. As the selected domains of CAO clouds in two cases both have bigger cumulus-dominated regions than the stratocumulus-dominated regions, the overall responses of cloud properties shown here are more similar to the ones in cumulus-dominated regions, with some influences from the stratocumulus-dominated regions.

2.4.5 Comparison with satellite retrievals

In this section, we explore the extent to which the changes in INP, droplet number and secondary ice production alter the comparison with multiple satellite-retrieved cloud properties (all-sky LWP, top-of-atmosphere shortwave flux, and top-of-atmosphere longwave flux) in Figure 2.13 for March and Figure 2.14 for October. The satellite retrieval time and the selected corresponding model output time are concluded in Appendix 2.1. Figures shown in the main text only include model output with different S_{INP}, comparison to simulations with N_{d} and E_{HM} are shown in Figures A2.18 and A2.19 of Appendix 2.10. Cloud fractions retrieved from MODIS were also used for model-observation comparison shown in Figures A2.20 and A2.21. As the cloud fractions from MODIS were calculated by the percentage of cloudy pixel from finer resolution in a 5 km resolution pixel, we created a cloud mask from our model (1.5 km grid spacing)

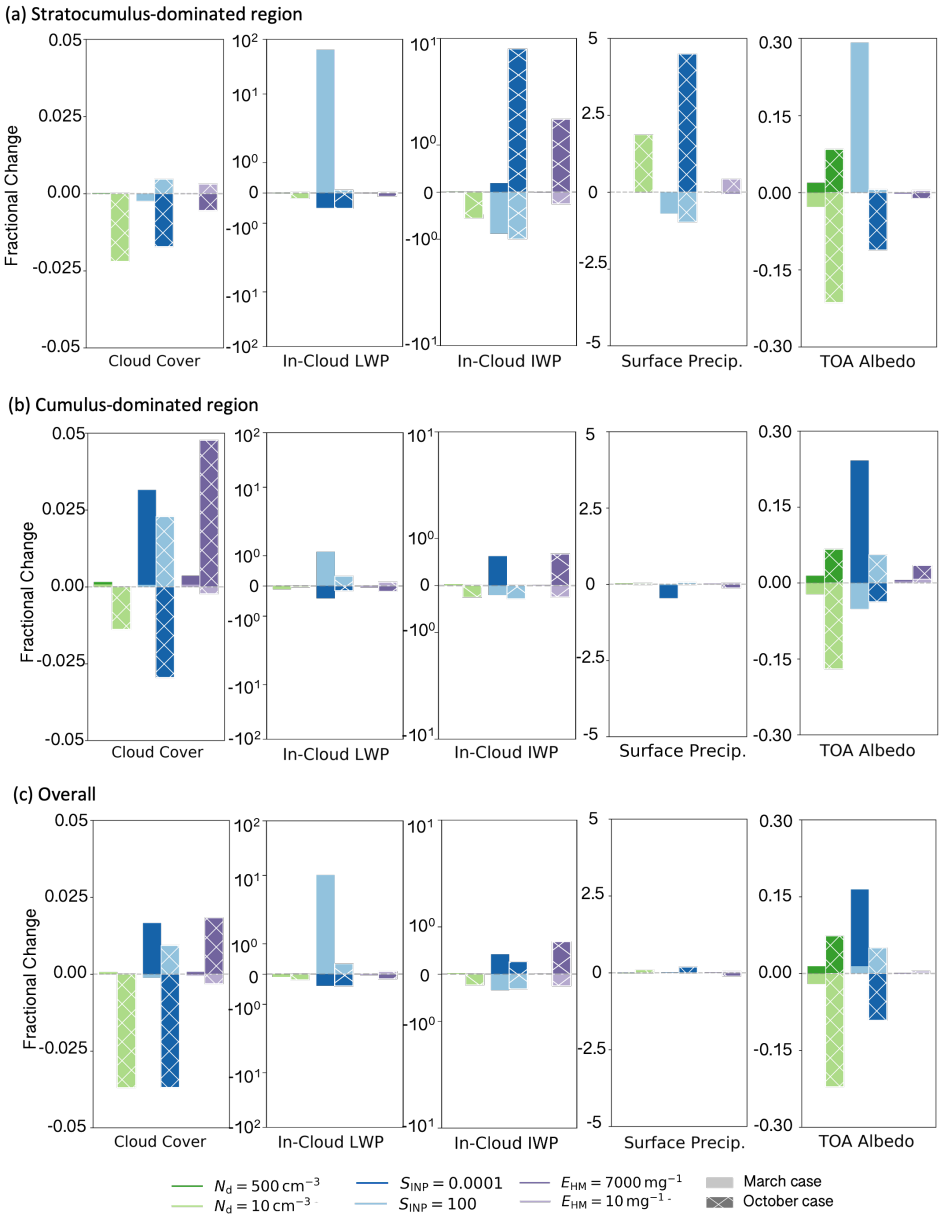


Figure 2.10: Fractional changes of cloud properties in the perturbed parameter simulations relative to the control simulations for the 15 March 2022 (solid shading) and the 24 October 2022 (hatched shading) cases, separated into the (a) stratocumulus-dominated domain, (b) cumulus-dominated domain and (c) overall domain. Cross-section means of the sub-domain are shown in Figures 2.6 and 2.7, and the determination of stratocumulus- and cumulus-dominated domains is described in Section 2.3.3. Note that the fractional change in the sub-domain is not just influenced by the fraction changes in stratocumulus-dominated and cumulus-dominated regions, but also the proportion of each region.

using 20% cloud cover as a threshold and then derive the cloud fraction using the percentage of cloudy grids in each corresponding MODIS cloud fraction grid.

For all the comparisons, our model output was first regridded to the same spatial resolution as the satellite retrieval and we only focused on the data within the sub-

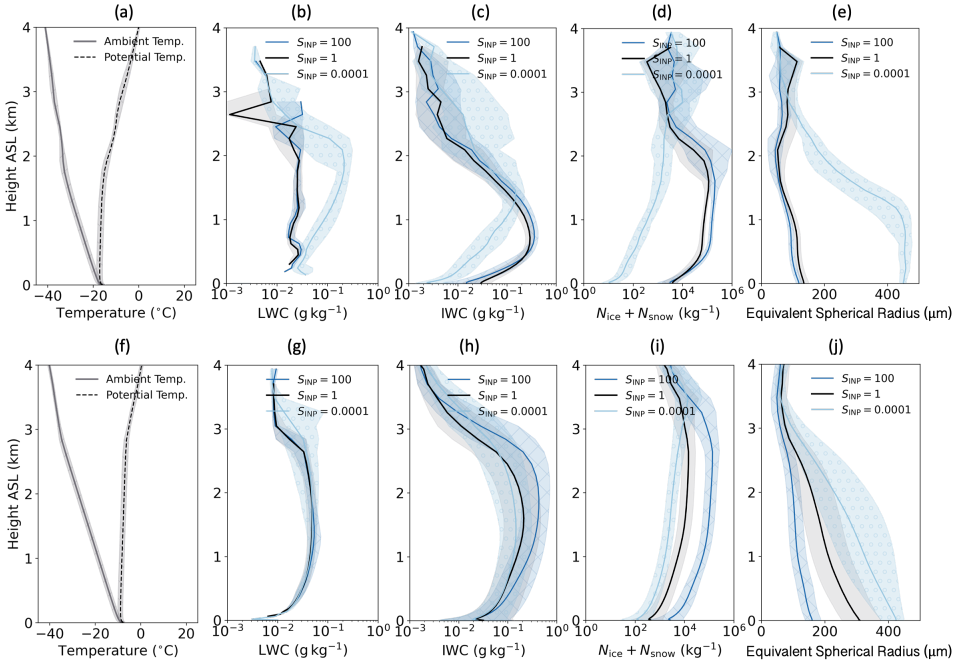


Figure 2.11: Vertical profiles for in-cloud properties in the March case: ambient temperature (default configuration), potential temperature (default configuration), in-cloud liquid water content (LWC), in-cloud ice water content (IWC), $N_{\text{ice}} + N_{\text{snow}}$ and equivalent spherical radius for stratocumulus-dominated (a-e) and cumulus-dominated (f-j) regions in the 15 March 2022 CAO case with different S_{INP}. The solid lines are medians, and the shaded areas were values between 25% quantile and 75% quantile. For the cloud properties plots, grids with lower than 10^{-6} kg kg^{-1} total water content are removed. For hydrometeor number concentrations, cloudy grids with lower than 1 m^{-3} are removed.

domain as shown in Figure 2.4(a) and Figure 2.4(c) for model-observation comparison. The normalized frequency and cross-section mean (± 1 standard deviation) are used for the comparison. MODIS-retrieved LWP is not used for quantitative comparison here due to its high mixed-phase cloud bias (Khanal et al., 2018).

In the March case, the control simulation shows reasonably good agreements of SW and LW fluxes at the top-of-the-atmosphere compared with other sensitivity test simulations, however underestimates the all-sky LWP from approximately 54 °W to 46 °W (approx. 10 g m^{-2} lower for the domain-mean LWP compared to the AMSR-2 retrievals (Figure 2.13)). With low S_{INP}, a higher all-sky LWP is produced but leads to a very large overestimation of all-sky LWP at the beginning of the CAO cloud field. Small underestimation of SW flux and overestimation of LW flux are also seen near the eastern boundary of the sub-domain in the control simulation, which may be due to the cloud cover and IWP in the control simulation being slightly lower than the observed.

Although our model underestimates the LWP, the LWP from AMSR-2 retrievals suggests that the liquid water was very small in this March case (domain mean around 17 gm^{-2}). Clouds in the March case were dominated by ice with a high IWP (modelled

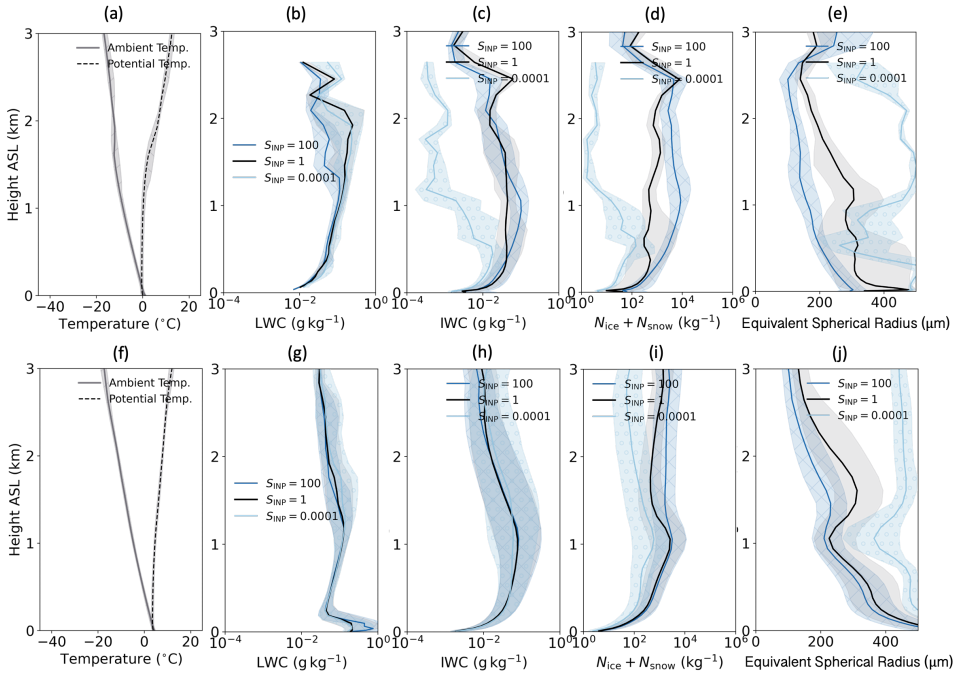


Figure 2.12: Vertical profiles for in-cloud properties in the October case: ambient temperature (default configuration), potential temperature (default configuration), in-cloud liquid water content (LWC), in-cloud ice water content (IWC), $N_{\mathrm{ice}} + N_{\mathrm{snow}}$ and equivalent spherical radius for stratocumulus-dominated (a-e) and cumulus-dominated (f-j) regions in the 24 October 2022 CAO case with different S_{INP}. The solid lines are medians, and the shaded areas were values between 25% quantile and 75% quantile. For the cloud properties plots, grids with lower than 10^{-6} kg kg^{-1} total water content are removed. For hydrometeor number concentrations, cloudy grids with lower than 1 m^{-3} are removed.

domain mean around 632 gm^{-2}) and the control simulation shows good agreement of IWC against CALIOP retrievals (Appendix 2.4). Therefore, we suggest that our model agrees with the observations on the liquid-ice partitioning and that the CAO clouds in this March case were dominated by ice, on which we based our conclusions.

The simulation with a high S_{INP} in the October case agrees with all satellite retrievals from approximately 56 °W to 46 °W(Figure 2.14), but strongly underestimates the LWP for the region from 60 °W to 56 °W and overestimates the LWP for the eastern end of the region. The simulations with default and low S_{INP} reproduce the LWP for the region from 60 °W to 56 °W, but overestimates the LWP for the rest of the region. Such overestimation of LWP in the cumulus-dominated region for the control simulation may come from the overestimation of LWC and underestimation of IWC in Figure A2.7 when model output are compared to measurements from M-Phase flight C323 (a research flight with the FAAM BAe-146 aircraft during the M-Phase campaign; see Appendix 2.4). Similar biases are seen for SW flux which may be the results of LWP bias from the simulations. The overestimation of SW flux can be reduced by using a low N_{d} as shown in Figure A2.19 of Appendix 2.10, but such change

has limited influence on the all-sky LWP bias. Based on the INP measurements from the M-Phase aircraft campaign, it is known that the measured INP concentrations in this October case are within the range of INP concentrations from default S_{INP} and low S_{INP}, but both simulations show clear overestimation of LWP and SW flux here. This inconsistency may come from the fact that we are only doing a sensitivity test here instead of exploring the whole parameter space, missing the output from different combinations of the parameter values; there are other processes (e.g., mixing and other cloud microphysics processes) which are not investigated in this study; the INP concentrations are temperature dependent but not directly derived from the background aerosols, and potentially missing variations of INPs through CAO cloud development.

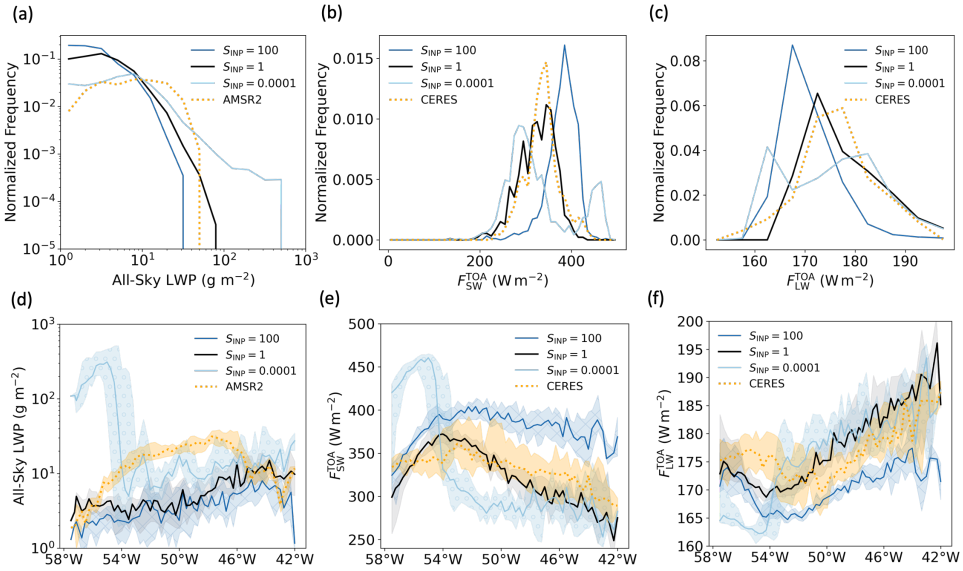


Figure 2.13: Model output compared with satellite retrievals of all-sky liquid water path (LWP) from AMSR-2, shortwave radiation and longwave radiation at the top-of-atmosphere from CERES for simulations with different S_{INP} on 15 March 2022 : (a)-(c) are the normalized frequency, and (d)-(f) are the cross-section median and quantile comparisons. All the comparisons were done within the selected sub-domain with model output and satellite retrievals regridded to the same resolution. The times of model output were selected as the closest quarter to the satellite retrieval times.

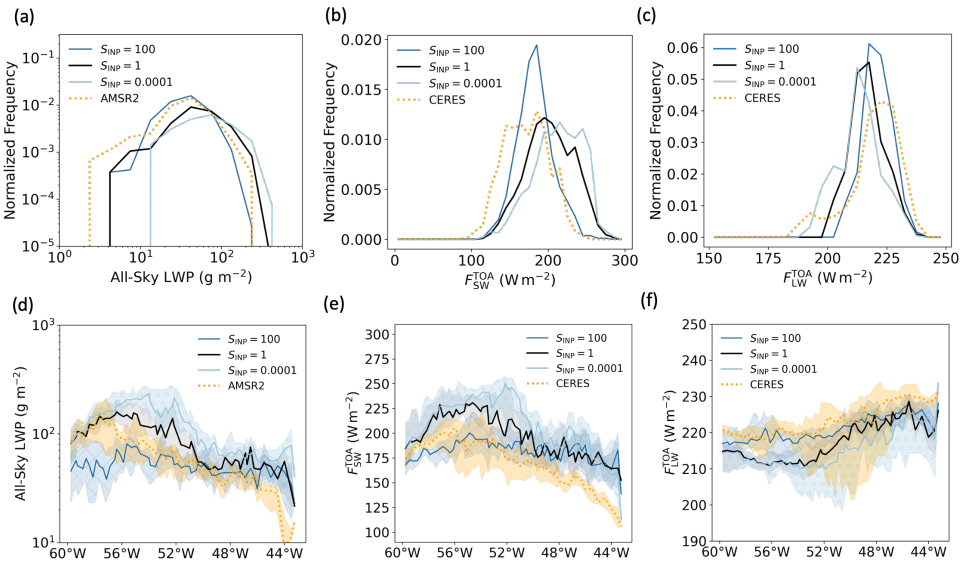


Figure 2.14: Model output compared with satellite retrievals of all-sky liquid water path (LWP) from AMSR-2, shortwave radiation and longwave radiation at the top-of-atmosphere from CERES for simulations with different S_{INP} on 24 October 2022 : (a)-(c) are the normalized frequency, and (d)-(f) are the cross-section median and quantile comparisons. All the comparisons were done within the selected sub-domain with model output and satellite retrievals regridded to the same resolution. The times of model output were selected as the closest quarter to the satellite retrieval times.

2.5 Discussion and Conclusions

We illustrate in the Results section above that the responses of modelled CAO cloud properties to the perturbations of N_{d}, S_{INP} and E_{HM} are different or even opposite in the two selected CAO cases over the Labrador Sea. Clouds in the October case respond similarly to increases in INP concentration (or ice concentration) compared to previous studies, which is a reduction in reflected SW flux and albedo at the top-of-the-atmosphere (Vergara-Temprado et al., 2018) and an earlier transition from stratocumulus to cumulus (Abel et al., 2017; Tornow et al., 2021). However, the March case differs strongly from the existing literature. We explain this difference in behaviour by categorising the March case as an ice-dominated regime and the October case as a liquid-dominated regime (Figure 2.15).

Cloud temperatures are very different in the March and the October CAO cases, with the mixed-phase CAO clouds in March being in a much colder environment (approximately 15 °C to 20 °C lower). Such temperature difference leads to a strong difference in primary ice production through INP as the INP concentration increases exponentially with decreasing temperature using the same parameterization (approximately 2 orders of magnitude for 20 °C difference). A higher primary ice production (colder cloud temperatures) means a greater portion of the condensed cloud water is converted to ice, resulting in a lower liquid water fraction in March, and vice versa for lower primary ice production (warmer cloud temperatures) in October.

The March CAO event is in an ice-dominated regime with a low liquid water fraction. In such an ice-dominated regime, increasing INP concentration leads to a higher number concentration of ice (N_{ice}), slows down the snow autoconversion rate and reduces the ice hydrometeor size and fallspeed, which then reduces the precipitation and restricts the removal of cloud water. This is more obvious in the cumulus-dominated region as it experiences stronger precipitation than the stratocumulus-dominated region. Such influence leads to higher cloud cover and IWP in March, and consequently a higher TOA albedo and SW flux, which is further enhanced by the higher single-scattering albedo from high N_{ice} (Twomey-like effect). These behaviours are similar to the aerosol first (Twomey, 1977) and second (Albrecht, 1989) indirect effects on liquid clouds through changes in cloud condensation nuclei concentrations, but in this March case acting through INP concentrations. As the clouds are dominated by ice, there is also very little water available for liquid-phase processes, therefore changes in N_{d} have only a small influence on the cloud. Furthermore, because the cloud temperatures are cold (approx. -15 °C to -35 °C for cloudy grids) and the Hallett-Mossop process is assumed to occur only in the temperature range from -2.5 to -7.5 °C, changing E_{HM} has only a small influence on the clouds.

The response of TOA albedo to increased S_{INP} simulation in March identifies a

possible new mechanism of negative cloud-phase feedback if INP concentrations increase in the future, besides the original three mechanisms suggested in Murray et al. (2021). For ice-dominated cloud with increasing INP concentrations from the warming climate, it will respond to the higher INP concentration with radiative responses similar to those seen in liquid clouds when CCN increases (i.e., an INP-driven first and second indirect effect), leading to a higher SW flux at the top of the atmosphere and negative cloud-phase feedback, competing with the effect of warming these cloud systems.

With low INP concentrations in the March CAO event, different responses are seen in stratocumulus-dominated and cumulus-dominated regions. In the stratocumulus-dominated region, a higher in-cloud LWP and a lower surface precipitation with no obvious change in cloud cover result in a higher reflected radiation. In the cumulus-dominated region, as the cloud liquid is rapidly removed during SCT, the increase of in-cloud LWP from low INP concentration is therefore very limited. Instead, lower IWP and lower ice albedo from the "Twomey-like" effect result in a lower SW reflection, compensating the limited increase of LWP.

Contrary to the March case, the warmer October case is in a liquid-dominated regime with a high liquid water fraction in general (apart from the end of the CAO cloud system). In this liquid-dominated regime, increases in INP concentration lead to higher N_{ice} and therefore a higher collection of liquid water from ice hydrometeors, and consequently more precipitation, stronger removal of cloud water and lower cloud cover, opposite to the March case. Together with lower LWP, increasing INP concentration in such a liquid-dominated regime leads to a lower SW flux at the top-of-atmosphere. As the liquid water fraction is high, there is also a strong influence from changing N_{d} and consequently a larger effect on the SW flux from changes in liquid water than in March. Because the temperatures are relatively warm, more clouds are in the active temperature range for the HM process and there is enough liquid water available for riming, hence we see a strong influence from changing E_{HM}.

The occurrence of liquid- and ice-dominated clouds, which controls their response to INP, N_{d} and E_{HM}, is not controlled only by temperature, but also by the ambient INP concentration: for example, the cloud is liquid-dominated at the beginning of the March CAO cloud system in the low S_{INP} simulation. This suggests that there could be an interaction between INP concentrations and other cloud properties, such as a strong effect of N_{d} on cloud properties at very low INP concentrations but a weak dependence at high INP concentrations when the cloud is ice-dominated. This illustrates one of the limitations of this study since we have only explored the effects of individual parameters. A full PPE (perturbed parameter ensemble) that explores potential co-variations in inputs and interactive effects would be needed to explore this further. In addition, we only compared two cases and their environmental conditions in this study, and a more robust and systematic investigation of the influence of environmental conditions can

also be carried out using a PPE in which environmental/initial conditions are varied using idealised simulations.

Other secondary ice production (SIP) mechanisms are not included in our model when this work is conducted, while the non-included SIP mechanisms such as droplet shattering and ice-ice collision have been shown important to SCT in CAO events (Karalis et al., 2022). These two SIP mechanisms can take place at a colder temperature than the existing HM process, which could have some impacts on the CAO cloud properties and responses in the cold March case (e.g., higher ice number concentrations and smaller ice hydrometeor sizes). Future modelling work will include other SIP mechanisms when these become available in the model. In addition, fixed in-cloud N_{d} was used in this study for the easier interpretation of sensitivity test results, but such a setup can lead to the neglect of potential feedbacks between cloud and aerosols/CCNs. Future work will also include aerosol-derived N_{d} and cloud processing of aerosols where possible for a better representation of aerosol-cloud interactions.

In general, this comparative sensitivity study reveals different or even opposite responses of the CAO cloud properties to aerosols including CCNs (through changing N_{d}) and INPs and SIP (the Hallett-Mossop process) when the cloud temperatures are different by comparing two CAO events over the Labrador Sea. The main findings and conclusions drawn from this study are shown below.

1. Cloud temperature and INP concentrations control the liquid-ice partitioning in the control simulations and thereby affect their responses to the perturbed parameters. The two cases have different liquid-ice partitioning and hence are categorized into ice-dominated (the cold March case) and liquid-dominated (the warm October case) regimes.

2. In the liquid-dominated, warm October case, increasing INP concentration leads to lower cloud cover and in-cloud LWP, hence a lower albedo, consistent with findings from previous studies.

3. In the ice-dominated, cold March case, increasing INP concentration leads to higher cloud cover and in-cloud IWP, hence resulting in a higher albedo and SW flux at the top-of-atmosphere. Such response is more prominent in the cumulus clouds. This influence of increasing INP concentration is opposite to the one in the liquid-dominated October case, and is potentially a new mechanism of negative cloud-phase feedback in ice-dominated CAO clouds if INP concentrations increase in the future due to the warming climate, additional to the original three cloud-phase feedback mechanisms suggested by Murray et al. (2021).

4. Stronger influences from changing N_{d} and the Hallett-Mossop efficiency are seen in the liquid-dominated October case as more liquid is available and cloud tem-

perature in October spans the HM active temperature range (-2.5 to -7.5 °C).

Future work with a full exploration of the parameter space (including other SIP mechanisms), systematically perturbed environmental conditions or other important cloud microphysics parameters will be beneficial to our understanding and modelling of these mixed-phase CAO clouds and their responses to the warming climate.

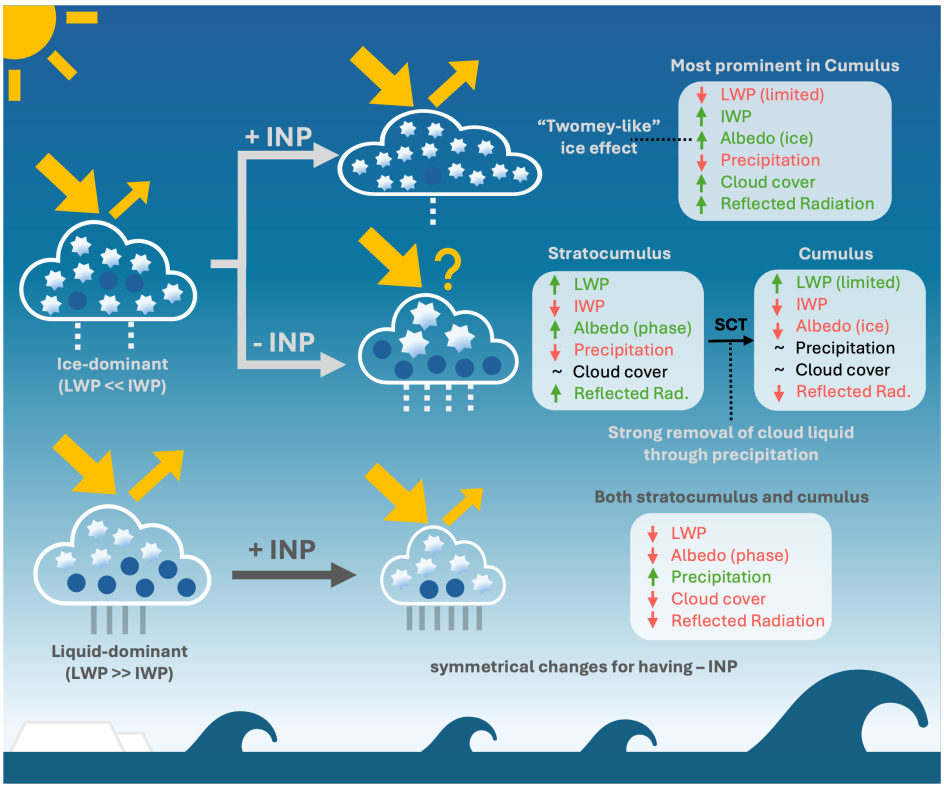


Figure 2.15: A schematic diagram for explaining the different sensitivities of CAO cloud properties to perturbations of INPs in ice-dominant and liquid-dominant clouds.

Appendix

A2.1 Retrieval time and selected model timepoint for satellite data used in this study

		15 March 2022		24 October 2022	
Instrument	Satellite Products	Retrieval time (UTC)	Selected model timepoint (UTC)	Retrieval time (UTC)	Selected model timepoint (UTC)
AMSR-2	LWP	16:48	16:45	16:18	16:15
CERES	SW,LW Fluxes	16:45	16:45	17:00	17:00
MODIS	Band1,3,4, CTT, CWP	15:15	15:15	17:00	17:00
CALIOP	IWC, temperature	16:13	16:15	N/A	N/A

Table A2.1: The satellite products used in this study, their retrieval times and selected model time points for comparison in the sub-domains. LWP: liquid water path, SW: shortwave, LW: longwave, CTT: cloud top temperature, CWP: cloud water path, IWC: ice water content.

A2.2 Monthly distribution of cloud top temperature over the Labrador Sea in 2022

Monthly distribution of cloud top temperature of low-level (cloud top pressure > 700 hPa) and mixed-phase (cloud top temperature ranging from -40 °C to 0 °C) CAO cloud over the Labrador Sea in 2022 are shown here in Figure A2.1.

Daily-mean CAO index at 800 hPa (M_{800}) (Kolstad et al., 2008; Fletcher et al., 2016a), which is the difference between potential temperature at surface skin (θ_{skin}) and potential temperature at 800 hPa (θ_{800}): $M_{800} = \theta_{\text{skin}} - \theta_{800}$, was calculated using the ERA5 dataset (Hersbach et al., 2020). Grids with $M_{800} > 0$ K, which is a compulsory condition for CAO identification and an indicator of unstable atmosphere, were defined as CAO grids. We use θ_{800} in this study because more high-latitude CAOs can be identified by using θ_{800} compared with using θ_{700} (potential temperature at 700 hPa) (Fletcher et al., 2016a). Cloud top pressure (CTP) and cloud top temperature (CTT) from MODIS were used to filter low-level (CTP > 700 hPa), mixed-phase (-40 °C < CTT < 0°C) clouds.

CTTs of low-level, mixed-phase CAO clouds in January, February and March are generally colder with CTT peaks between -20 °C to -25 °C, while the ones in October, November and December are warmer with CTT peaks between -10 °C and -15 °C. Other months were not included due to low density of CAO events in those time of the year. The cold March case in this study located near the colder end of the CTT climatology while the warm October case located near the warmer end, providing contrasting CTT conditions for this sensitivity test and a study range covering most of the range from the shown CTT climatology.

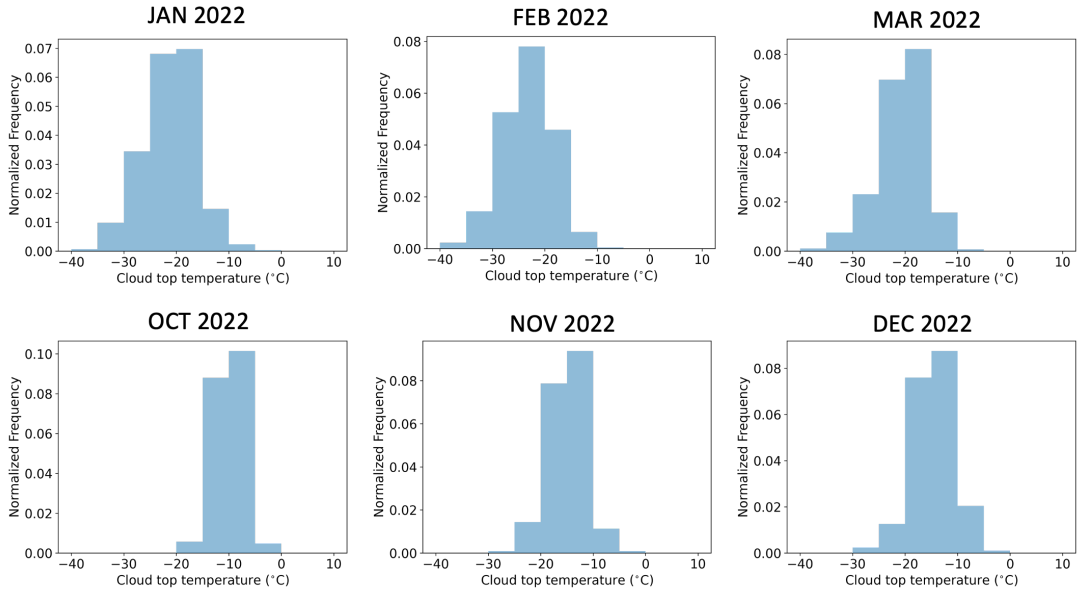


Figure A2.1: Monthly distribution for cloud top temperature of low-level, mixed-phase CAO clouds over the Labrador Sea in January, February, March, October, November and December 2022. Clouds with cloud top pressure smaller than 700 hPa and cloud top temperature warmer than 0 °C and colder than -40 °C were excluded.

A2.3 Maps for the nested model domains and the sub-domains for analysis

Figure A2.2 shows the nested model domains and the sub-domains for analysis of both cases. The sub-domains were chosen to be away from the boundaries of the nested model domains to avoid the boundary effects. In both cases, due to the winds and airmasses from north-west direction, the fields generated from the coarser global model require a few hours to spin-up once entering the nested model domains.

The timescales for spinning up the boundary layer structure in the nested model domain is $\frac{L}{\sigma_w}$, where L is the boundary layer depth (approx. 1000 m at the beginning of the CAO events) and σ_w is the standard deviation of the w component of wind. For the March case, the mean σ_w between the western boundaries of the nested model domain and the sub-domain is around 0.83 ms^{-1}, which requires about 20 minutes to spin up. For the October case, the mean σ_w between the northwestern ends of the nested model domain and the sub-domain is around 0.39 ms^{-1}, which requires about 45 minutes to spin up.

We examined whether the boundary effects can reach the sub-domains by using simple calculations of how long it takes the airmasses to reach the western boundary of each sub-domain. The distances were estimated based on the mean direction of wind. For the March case, the distance between the middle of the western boundary of the nested model domain to the middle of the western boundary of the sub-domain is around 430 km. The mean wind speed from surface to 2 km height above sea level is 13.0 ms^{-1} (46.8 kmhr^{-1}). Therefore, it takes around 9 hours for the airmasses to travel in the March case. For the October case, the distance between the north-west point of the nested model domain to the middle of the western boundary of the sub-domain is around 500 km. The mean wind speed from surface to 2 km height above sea level is 16.5 ms^{-1} (59.4 kmhr^{-1}), so it takes around 8.5 hours for the airmasses to travel in the October case. Some airmass travelling into northwestern part of the sub-domain may have less time to spin up and be affected by the boundary effects, however, we choose to keep this part of the sub-domain for capturing more earlier stage CAO clouds as the clouds broke up into cumulus clouds very soon in the October case.

For the whole sub-domain in the March case and most of the sub-domain (except the small northwestern part) of the October case, the time and distance required for the airmasses to reach the sub-domains are sufficient to avoid the boundary effects propagate into the sub-domain.

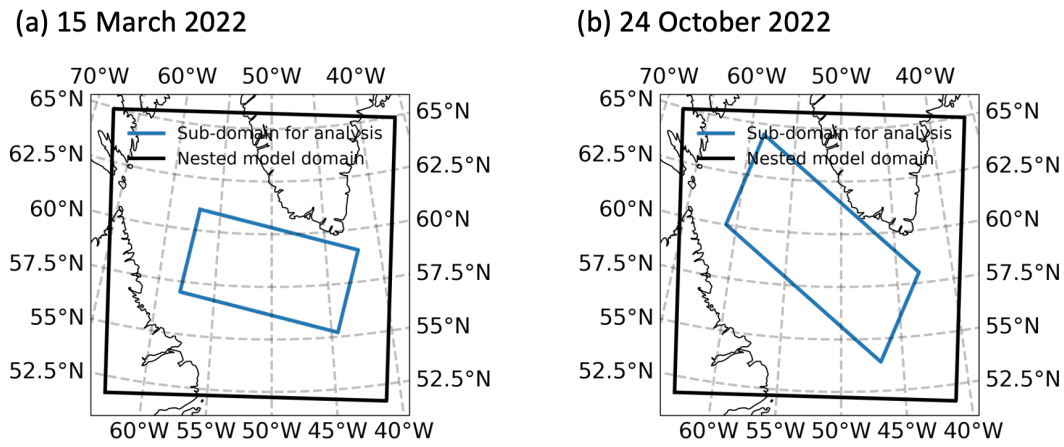


Figure A2.2: Nested model domains (black) and the selected sub-domains for analysis (blue) for (a) 15 March 2022, (b) 24 October 2022.

A2.4 Model-observation comparison for control simulations

In this appendix, we validate our control simulations using satellite retrievals for the March case (as there is no aircraft campaign for this case) shown in Figures A2.3, A2.4 and A2.5, and M-Phase aircraft measurements for the October case shown in Figure A2.7 from two flights (M-Phase C322 and C323) with the flight tracks shown in Figure A2.6. The results of model-observation comparison for the March case are shown first, followed by the results for the October case.

A2.4.1 15 March 2022

For the March case studied in this work, we evaluate our model against cloud top temperature (CTT) from MODIS onboard the Aqua satellite, as well as temperature and ice water content (IWC) from CALIOP onboard the CALIPSO satellite (Level-2 1 km Cloud Layer Data for temperature and Level-2 5 km Cloud Layer Data for IWC, version 4-51).

Figure A2.3 shows the CTT from model output and MODIS retrievals. As a satellite simulator was not available for regional simulations in our model, the extraction of modelled CTT relied on the definition of cloudy grids. Here we used two thresholds of grid-box mean TWC (total water content) for determining whether a grid in our model output is cloudy or non-cloudy. The threshold 10^{-5} kgkg^{-1} has been used before for comparing model water content with *in-situ* aircraft measurements (e.g. Abel et al., 2017), and the threshold 10^{-4} kgkg^{-1} was selected for a stricter definition of cloudy grids as passive satellite retrievals can be less sensitive compared to aircraft measurements. As there is no high clouds in the domain of interest, the cloud top for each column of model grids is defined as the highest grid passing the selected threshold of TWC. The MODIS data (1 km) were regridded to model resolution (1.5 km) using the nearest-neighbour method.

The cloud top height (CTH) retrieved from MODIS is around 5 km for low-level clouds (not shown), which is unreasonable as the CALIPSO satellite retrievals of temperature and IWC in Figure A2.5 suggest that the cloud top is around 3 km. Therefore, CTH from MODIS is not further used for validating CTH in the control simulation. This may be because the MODIS CTH over the sea level is not directly retrieved but calculated using observed SST (sea surface temperature), CTT, and a zonal mean lapse rate (Platnick et al., 2016), but the CTT in the March case is much colder compared to climatology.

The distributions of CTTs within the sub-domain shown in Figures A2.3(a),(b) and (c) are compared in Figure A2.4. Using a threshold of 10^{-5} kgkg^{-1} resulted in a much colder CTT (peak near -40 °C) compared to the MODIS-retrieved CTT (peak near -30 °C). Using a threshold of 10^{-4} kgkg^{-1} reduces the cold bias strongly and leads to

a similar peak temperature of CTT (near -30 °C) to the one from MODIS. However, small cold bias still exists with the modelled CTT using the 10^{-4} kgkg^{-1} threshold having higher frequency at colder temperatures and lower frequency at warmed temperatures compared to satellite retrieved CTT. Note that the grid-to-grid bias was not calculated here due to potential double-penalty problem when compared model data with observations.

Temperature and IWC profiles from CALIOP onboard CALIPSO were also used to evaluate the control simulation of the March case. Figure A2.5 shows the selected CALIPSO track (a), comparison of the temperature and IWC distributions (b,c) as well as the along-track profiles (d-g). The modelled profile was extracted by finding the closest model grid for each footprint from the CALIPSO data. The CALIPSO temperature has a higher resolution (1 km) and therefore was regridded to the model resolution (1.5 km), while the modelled IWC has a higher resolution compared to the CALIPSO IWC resolution (5 km) therefore the modelled IWC was regridded to the CALIPSO IWC resolution. Due to the nature of lidar attenuation for clouds at lower levels, grids which had no CALIPSO data or model data were excluded when comparing the distributions and plotting the profiles.

There is also a small cold bias for the temperature but the overall temperature distribution from our model agrees well with the one from CALIPSO. This is also shown for the whole profile statistics: the median temperature from the modelled profile is -30.9 °C (interquartile range (IQR): -34.3 °C to -25.8 °C) and the median temperature from the CALIPSO profile is -30.2 °C (IQR: -33.7 °C to -25.1 °C).

The distributions of IWC from model and CALIPSO have similar peak IWC values. However, the modelled IWC has higher frequencies both at the low (0.01 to 0.02 gm^{-3}) and high (0.5 to 1 gm^{-3}) ends of the IWC bins, and lower frequencies for the IWC bins in the middle. Based on the profile statistics, the model slightly overestimates the IWC (median: 0.19 gm^{-3}, IQR:0.08 gm^{-3} to 0.39 gm^{-3}) compared to the CALIPSO IWC (median: 0.17 gm^{-3}, IQR:0.08 gm^{-3} to 0.33 gm^{-3}). However, such bias (0.02 gm^{-3}) is considered low and acceptable.

To summarize the model-observation comparison above for the March case, our modelled CTTs are slightly colder compared to the MODIS-retrieved CTTs when using the 10^{-4} kgkg^{-1} threshold. Similarly, the temperature comparison between modelled profile and CALIPSO profile shows that our model has small cold bias of the temperature (-0.7 °C), but such bias is acceptable and suggests temperatures from our model are reasonably comparable with the satellite retrievals. Our model overestimates the IWC by 0.02 gm^{-3} compared to the CALIPSO IWC, but such bias is also relatively small and acceptable, suggesting the control simulation can also reproduce the IWC reasonably well.

A2.4.2 24 October 2022

For the October case, we evaluate the control simulations by comparing the temperature, grid-box mean TWC (total water content), liquid water fraction (LWC / TWC), grid-box mean LWC (liquid water content) and grid-box mean IWC (ice water content) with the aircraft measurements from two flights (C322 and C323) during the M-Phase aircraft campaign. The flight tracks and time-series plots of temperature and height for each flight are shown in Figure A2.6. Results of comparison for the variables mentioned above are shown in Figure A2.7. The water content measurements were from Nevzorov probes onboard the aircraft.

Preprocessing of the aircraft data (1 Hz resolution) and the model data was performed for a like-for-like comparison. Each point of the observation data was assigned to the nearest model grid (longitude,latitude and altitude) and the mean of all the observed data points within each model grid was calculated for the later comparison with model data. The model data were extracted using the flight track with grids within 10.5 km around each point of the flight tracks also included. Considering the issues including a model may not simulate the same cloud at a same location as the real world, and the aircraft measurements may not be representative enough for comparison with grid-box mean value from the model, we did not calculate the grid-by-grid bias directly, but compared them using the composited vertical profile of each flight.

For the model-observation comparison with measurements from M-Phase C322, where the dominant type of clouds are stratocumulus clouds, our modelled temperature are colder than the observed temperature above 1000 m (Figure A2.7(a)) and has a higher inversion layer. This may be the reason why that the locations of the clouds simulated from our control simulation are higher compared to the observed clouds (Figure A2.7(b). Before the calculation of bias, we shifted the modelled clouds lower to match the peaks of the observed cloud profile and modelled cloud profile. The control simulation slightly overestimates the TWC, LWC and IWC with the profile mean bias of 0.048 gm^{-3}, 0.047 gm^{-3} and 0.0003 gm^{-3}, but is consistent with the observations on the liquid water fraction that most of the clouds were dominated by liquid. Some ice-free conditions were not simulated in our model (Figure A2.7(e)), but such bias needs further model-observation comparison with more cases to investigate and is beyond the scope of this work.

For the model-observation comparison with measurements from M-Phase C323, where the dominant type of clouds were cumulus clouds, our model shows good agreement of the temperature profile with the observed one (Figure A2.7(g)). Our model did not simulate some high clouds (around 2500 m), however these clouds were very thin with the majority of their TWC around 0.001 gm^{-3} (Figure A2.7(i)). Our model reproduced the grid-box mean TWC with a profile mean bias of 0.004 gm^{-3}. The LWC

is overestimated with a bias of 0.018 gm^{-3}, while the IWC is underestimated with a bias of -0.003 gm^{-3}, resulting in higher liquid water fraction in our model. For clouds ranging from 1500 m to 2000 m, our model captured the TWC but making too much liquid and too little ice, resulting a much higher liquid water fraction. The overestimation of LWC and liquid water fraction here may be the reason for the overestimation of all-sky LWP shown in Figure 2.14 in the October case.

To summarize the model-observation comparison of the October case, in the C322 region where stratocumulus clouds dominated, the heights of our modelled clouds were higher for around 500 m, potentially due to the cold bias of temperature above 1000 m and a higher modelled inversion layer. The grid-box mean TWC, LWC and liquid water fraction generally agreed with the observation if the modelled clouds shifted to the heights matching with the observed clouds. The modelled IWC biased high compared to the observed IWC, but remained as a very small part of the cloud water similar to the observation. In the C323 region where cumulus clouds dominated, our model captured the temperature profile but missed some thin (TWC around 0.001 gm^{-3}), high (around 2500 m) clouds. For clouds ranging from 1500 m to 2000 m, our model overestimates the LWC and underestimates the IWC, this is also seen for clouds below 1500 m but with much smaller bias, which can lead to the overestimation of all-sky LWP shown in Figure 2.14 in the October case.

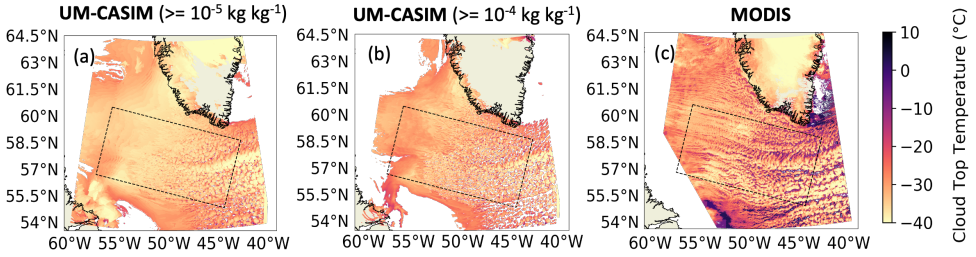


Figure A2.3: Cloud top temperature (CTT, a-c) from the control simulation of the March case and the MODIS onboard Aqua satellite. Two TWC (total water content) thresholds were used for determine whether a model grid is cloudy or not which are TWC $\geq 10^{-5}$ kgkg^{-1} (a) and TWC $\geq 10^{-4}$ kgkg^{-1} (b). Regions marked with grey dashed lines in (a) - (c) are the sub-domains (same as the sub-domains shown in the main content) for the comparison of CTT distributions in Figure A2.4.

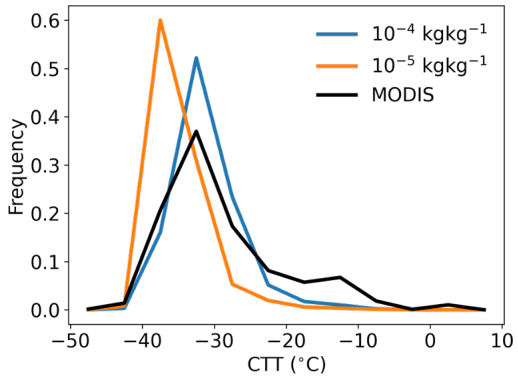


Figure A2.4: Comparison of the cloud top temperature (CTT) distributions of 15 March 2022 between the CTT retrieved from the MODIS onboard the Aqua satellite (black) and the CTT extracted from the control simulation of the March case using different total water content thresholds: TWC $\geq 10^{-5}$ kgkg^{-1} (orange) and TWC $\geq 10^{-4}$ kgkg^{-1} (blue).

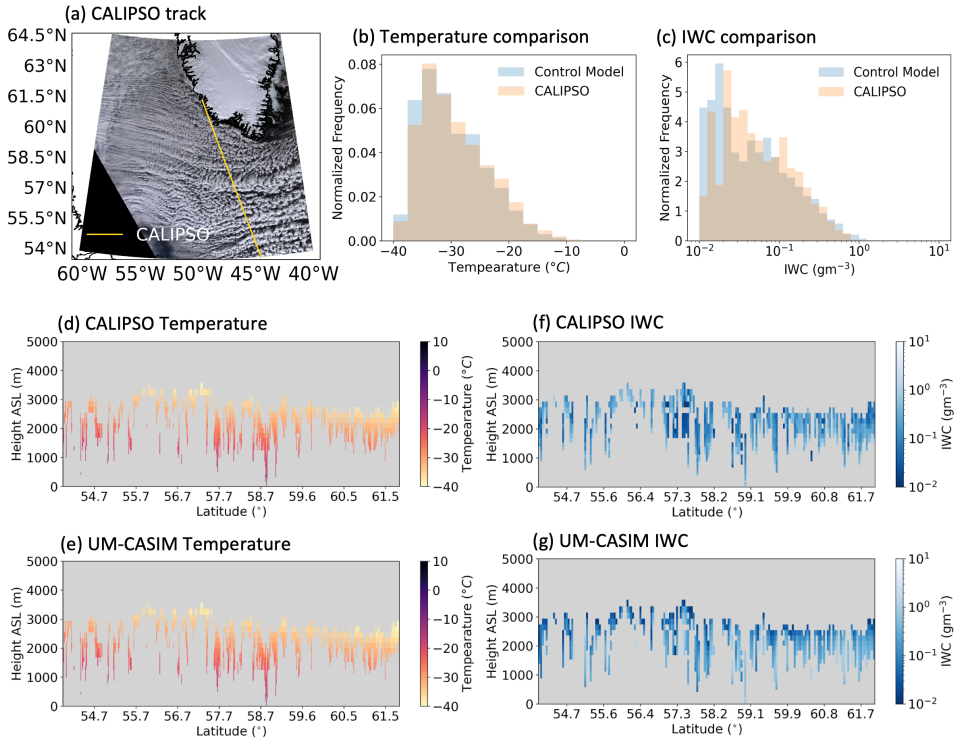


Figure A2.5: Comparison of temperature and IWC (ice water content) profiles from CALIOP onboard CALIPSO satellite and the control simulation of 15 March 2022: (a) the selected CALIPSO track, (b) distributions of temperature, (c) distributions of IWC, (d) regridded CALIPSO temperature profile, (e) modelled temperature profile, (f) CALIPSO IWC profile, and (g) regridded modelled IWC profile. Note that for the comparison and individual profiles, grids without valid CALIOP data or model data are removed.

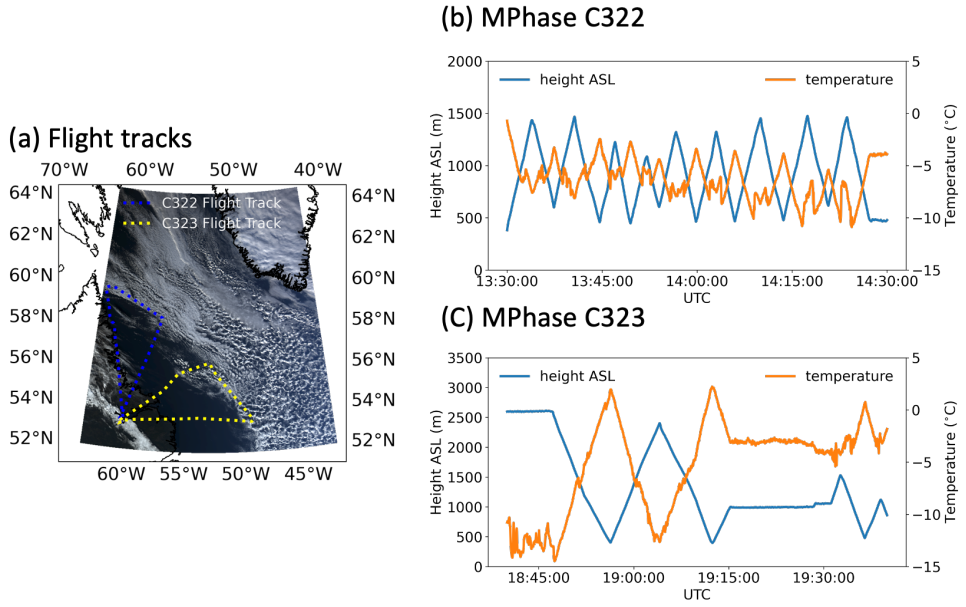


Figure A2.6: Information of the M-Phase C322 and C323 flights used for the validation of the control simulation on 24 October 2022: (a) flight tracks, (b) height and temperature profiles for cloud measurements during M-Phase C322, (c) height and temperature profiles for cloud measurements during M-Phase C323.

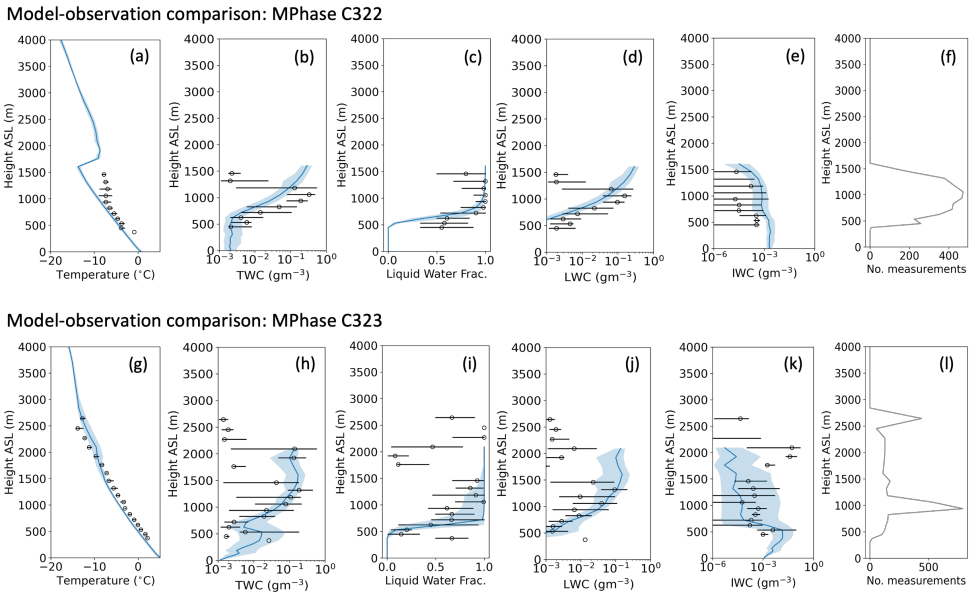


Figure A2.7: Model-observation comparison of the control simulation against M-Phase C322 and C323 measurements on 24 October 2022: (a,g) temperature, (b,h) grid-box mean TWC (total water content), (c-i) liquid water fraction (LWC / TWC), (d-j) grid-box mean LWC (liquid water content), (e-k) grid-box mean IWC (ice water content). Figures (f) and (l) show the number of measurements from each flight. Model data are shown in blue lines (medians) with the IQR (interquartile) ranges coloured in light blue. Observation data are shown in black unfilled circles (medians) with the IQR ranges shown in black solid lines.

A2.5 Supplementary figures for Figure 2.5

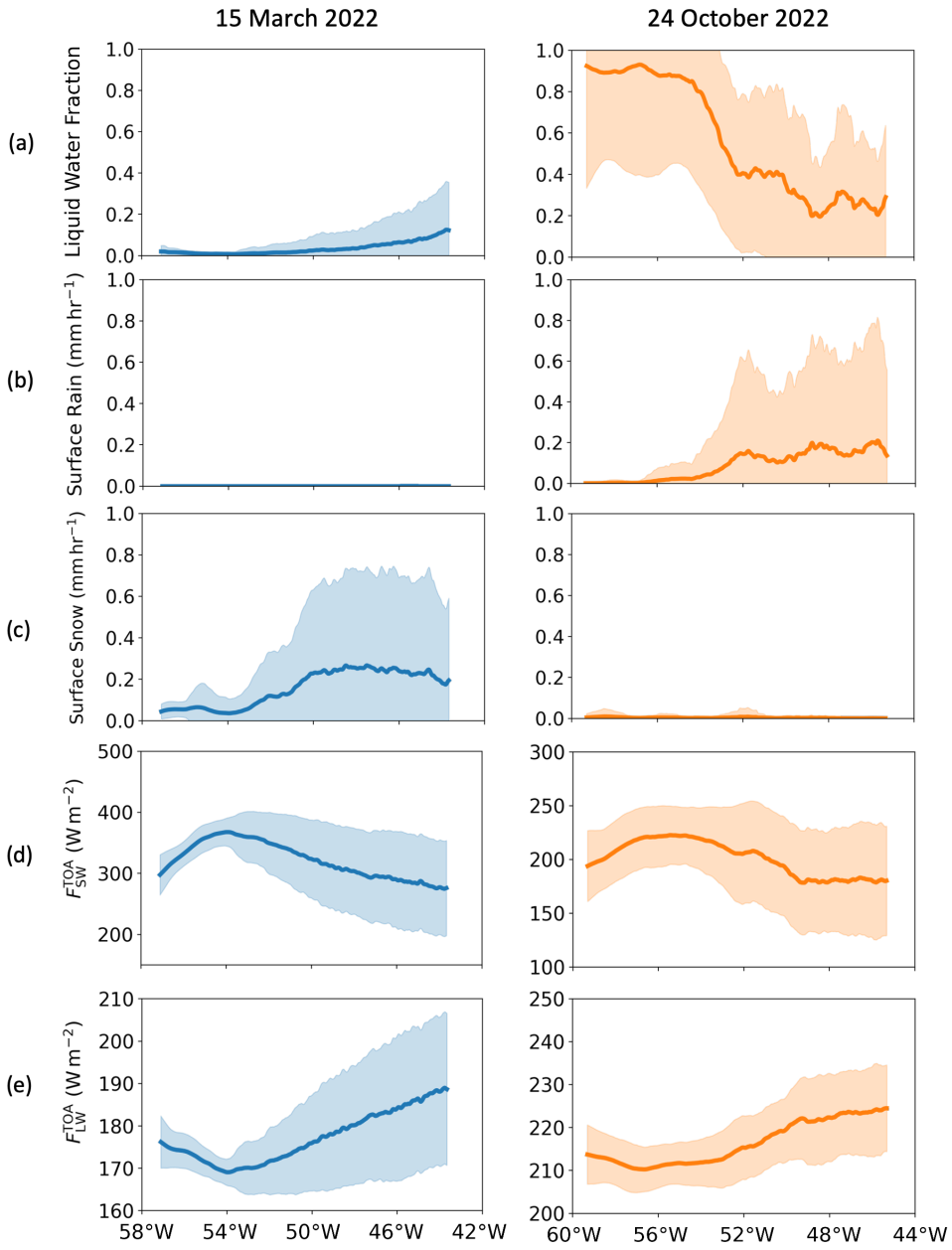


Figure A2.8: Cross-section mean cloud properties from the March (left panel) and the October (right panel) control simulations in the sub-domain: (a) liquid water fraction (LWP/CWP), (b) surface rain rate, (c) surface snow rate, (d) shortwave (SW) radiation flux at the top of atmosphere, and (e) longwave (LW) radiation flux at the top of atmosphere. The shaded area indicates the range of ± 1 standard deviation. The time points selected are 16:45 UTC for the March case and 17:00 UTC for the October case, which are consistent with the corresponding CERES measurement times.

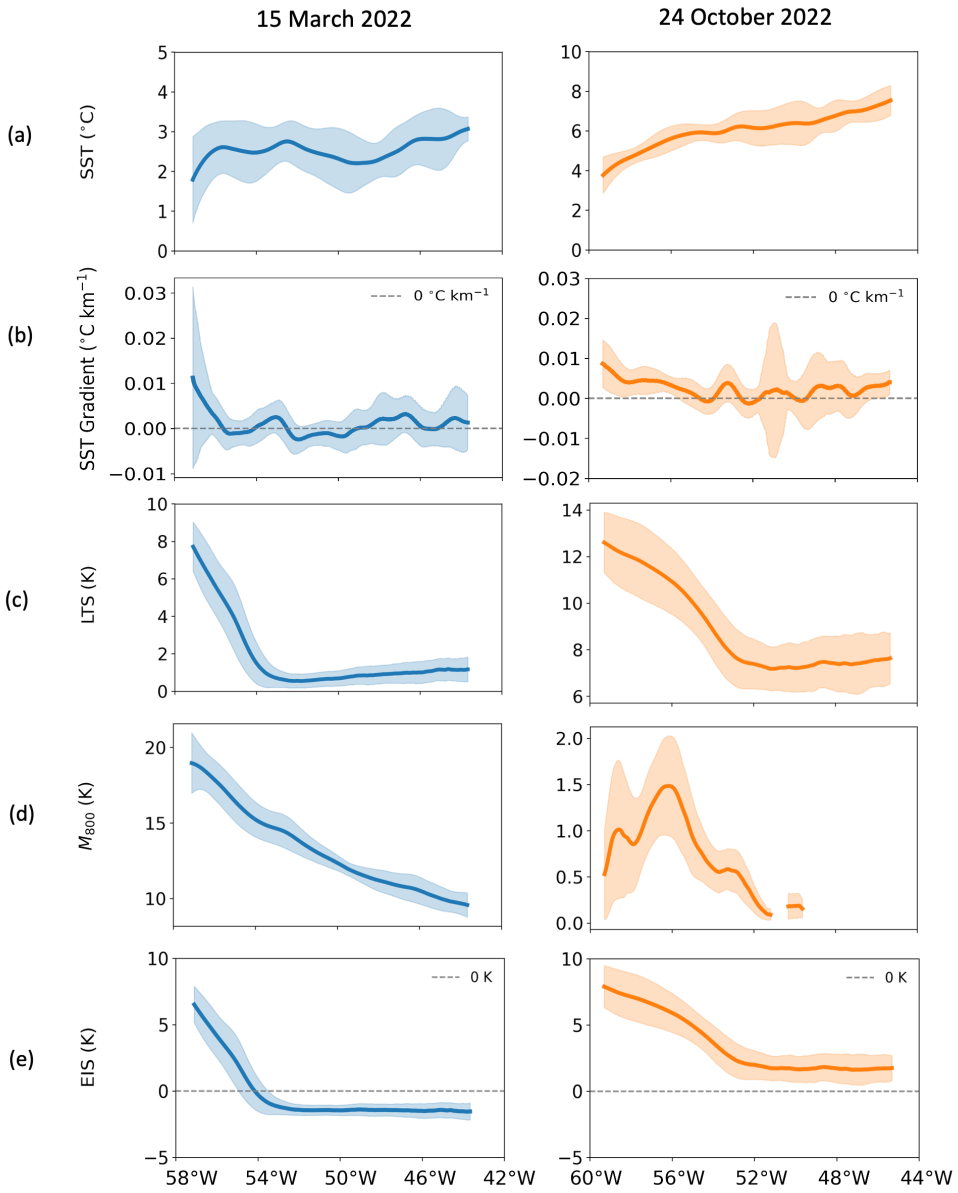


Figure A2.9: Cross-section mean environmental conditions from the March (left panel) and the October (right panel) control simulations in the sub-domain: (a) sea surface temperature (SST), (b) SST gradient, (c) lower tropospheric stability (LTS), (d) CAO index at 800 hPa (M_{800}), and (e) estimated inversion layer strength (EIS). The shaded area indicates the range of $\pm$ 1 standard deviation. The time points selected are 16:45 UTC for the March case and 17:00 UTC for the October case, which are consistent with the corresponding CERES measurement times.

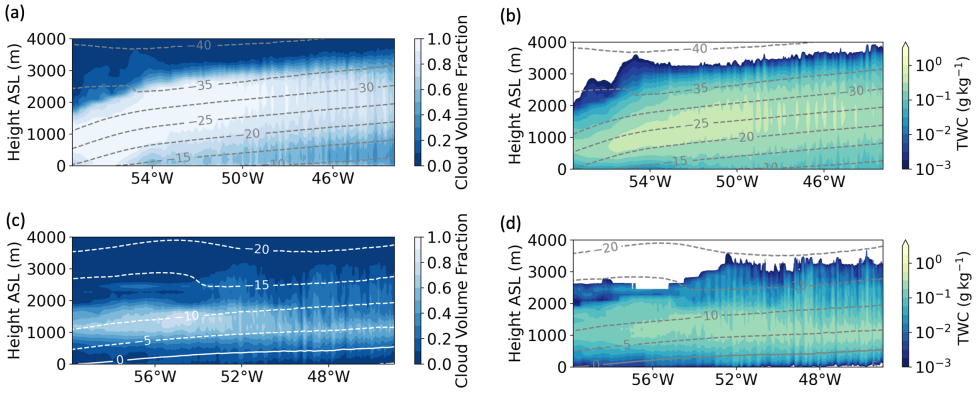


Figure A2.10: Cross-section mean vertical profiles from the sub-domain of bulk cloud volume fraction and in-cloud total water content (TWC) for the March case (a,b) and the October case (c,d) in the control simulations. Dashed lines in all figures are the ambient temperature contour lines in °C. To calculate the mean of the in-cloud total TWC, grid boxes with cloud volume fractions lower than 5% and total in-cloud TWC less than 1 gkg^{-1} are excluded. The time points selected are 16:45 UTC for the March case and 17:00 UTC for the October case, which are consistent with the corresponding CERES measurement times.

A2.6 Supplementary figures for Figures 2.6 and 2.7

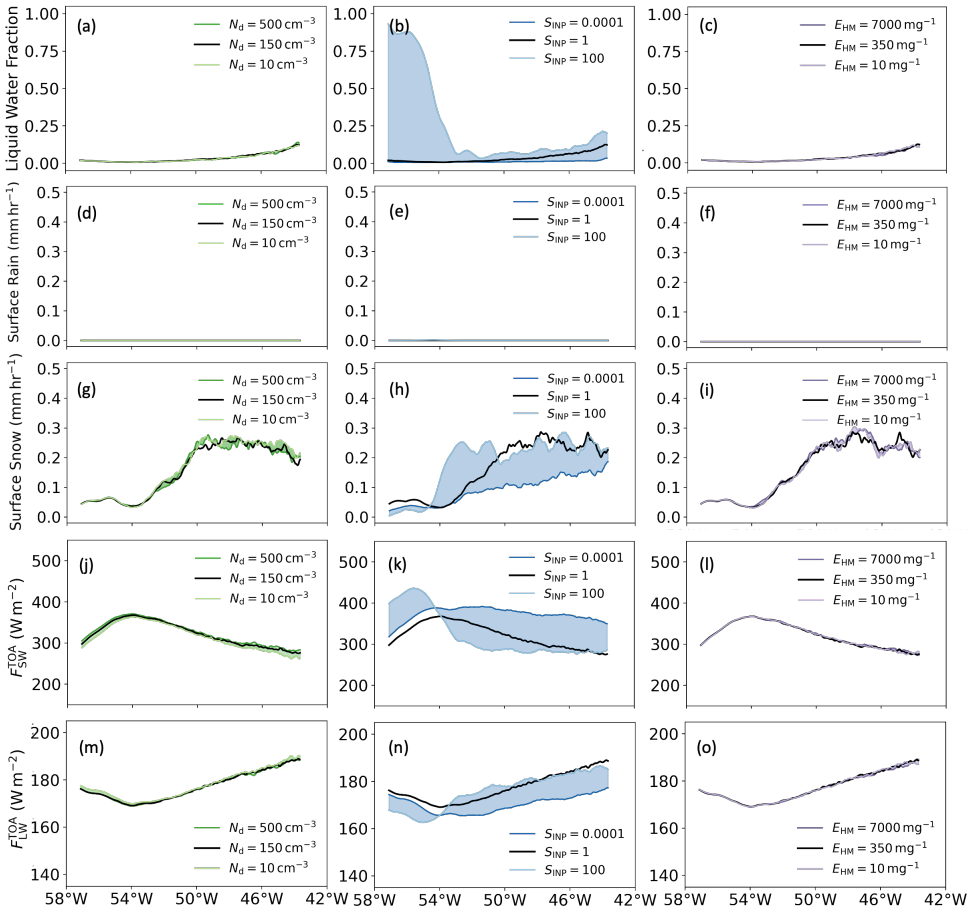


Figure A2.11: Sub-domain mean CAO cloud properties from the beginning of the cloud system to the end of the cloud system for 15 March 2022 at 16:45 UTC: (a)-(c) liquid water fraction (LWP/CWP), (d)-(f) surface rain, (g)-(i) surface snow, (j)-(l) shortwave radiation flux at the top of atmosphere, and (m)-(o) longwave radiation flux at the top of atmosphere. Grid boxes with cloud cover smaller than 20% were removed before averaging. 16:45 UTC was chosen for the relative CERES (onboard the Aqua satellite) measurement time.

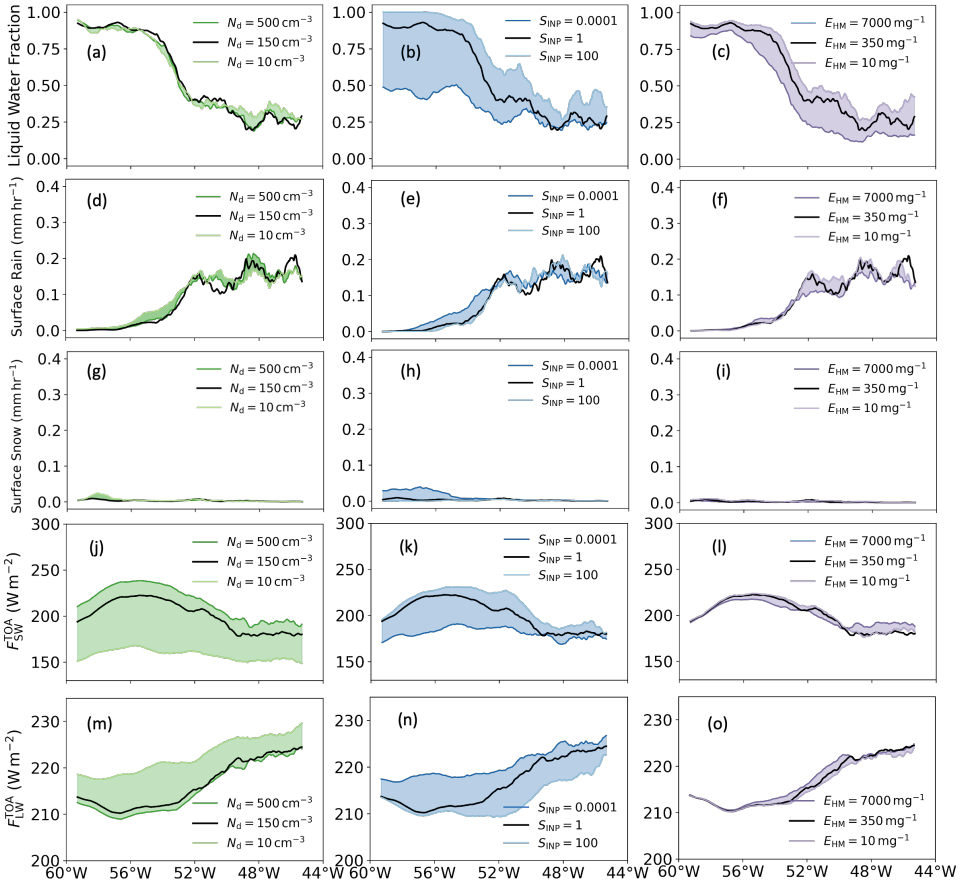


Figure A2.12: Sub-domain mean CAO cloud properties from the beginning of the cloud system to the end of the cloud system for 24 October 2022 at 17:00 UTC: (a)-(c) liquid water fraction (LWP/CWP), (d)-(f) surface rain, (g)-(i) surface snow, (j)-(l) shortwave radiation flux at the top of atmosphere, and (m)-(o) longwave radiation flux at the top of atmosphere. Grid boxes with cloud cover smaller than 20% were removed before averaging. 17:00 UTC was chosen for the relative CERES (onboard the Aqua satellite) measurement time.

A2.7 Boundary layer type fractions for all the simulations

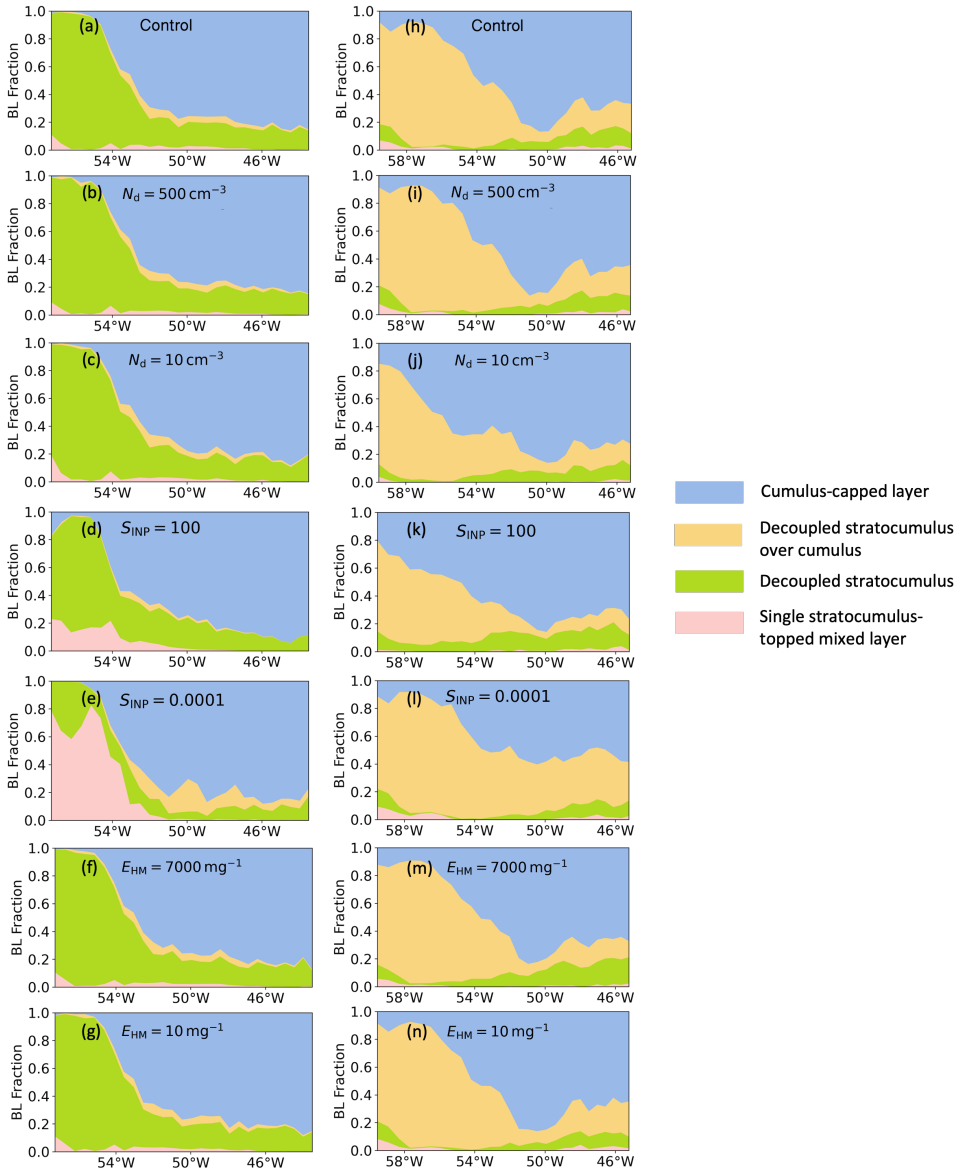


Figure A2.13: Boundary layer type fractions for all the simulations of 15 March 2022 (a-g) and 24 October 2022 (h-n). Four major boundary layer types are shown here: pink – single stratocumulus-topped mixed-payer, green - decoupled stratocumulus, orange – decoupled stratocumulus over cumulus, and blue – cumulus-capped layer. Only pixels with cloud cover higher than or equal to 20% are included for analysis.

A2.8 Results of model simulations with different precipitation, evaporation and sublimation setup for the March case

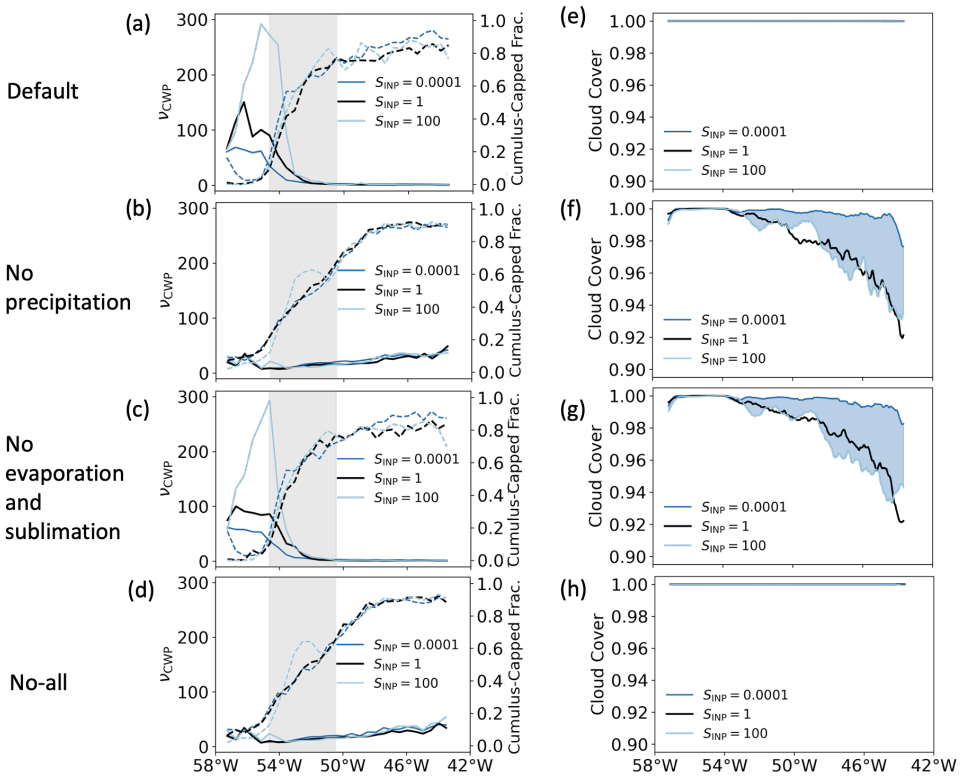


Figure A2.14: The cloud field homogeneity parameter (ν, solid lines) with the fraction of cumulus-capped boundary layer (dashed lines) in cloudy pixels (cloud cover $\geq$ 20%) (a-d) and cloud cover (e-h) from simulations with perturbed S_{INP} for (a,e) default setup, (b,f) no precipitation (sedimentation of all hydrometeors) setup, (c,g) no evaporation and sublimation setup, and (d) no-all (no precipitation, evaporation and sublimation) for the March case.

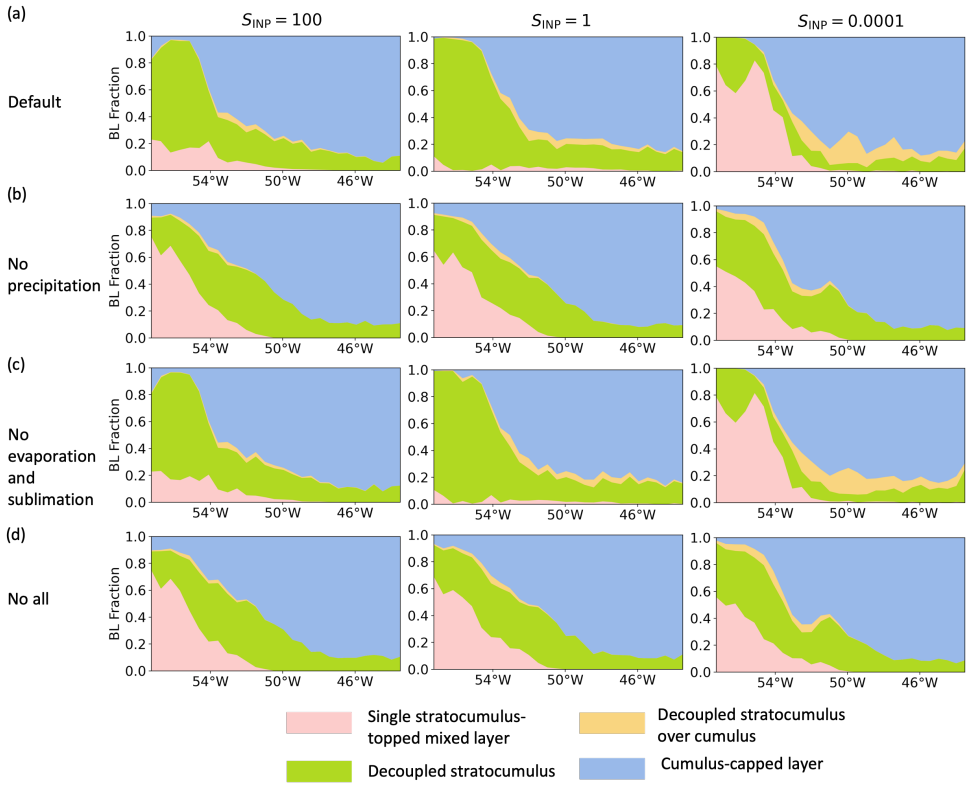


Figure A2.15: Boundary layer type fractions from simulations with perturbed S_{INP} for (a) default setup, (b) no precipitation (sedimentation of all hydrometeors) setup, (c) no evaporation and sublimation setup, and (d) no-all (no precipitation, evaporation and sublimation) for the March case.

A2.9 Vertical profiles of in-cloud properties for simulations with different N_d and E_{HM}

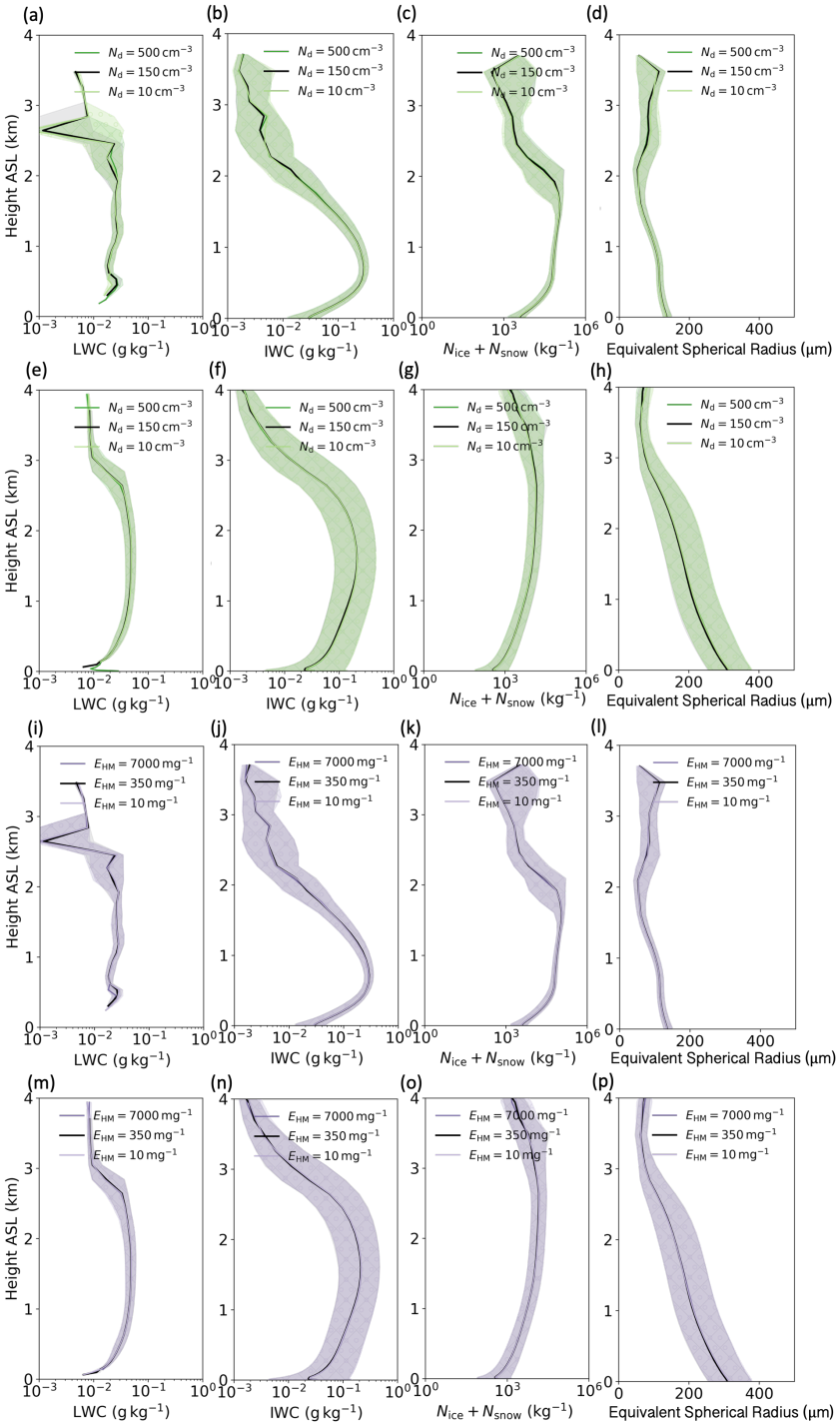


Figure A2.16: Vertical profiles of in-cloud LWC (liquid water content), in-cloud IWC (ice water content), $N_{ice} + N_{snow}$ and equivalent spherical radius for stratocumulus-dominated (a-d, i-l) and cumulus-dominated (e-h, m-p) regions in the 15 March 2022 CAO case with different N_d (a-h) and E_{HM} (i-p).

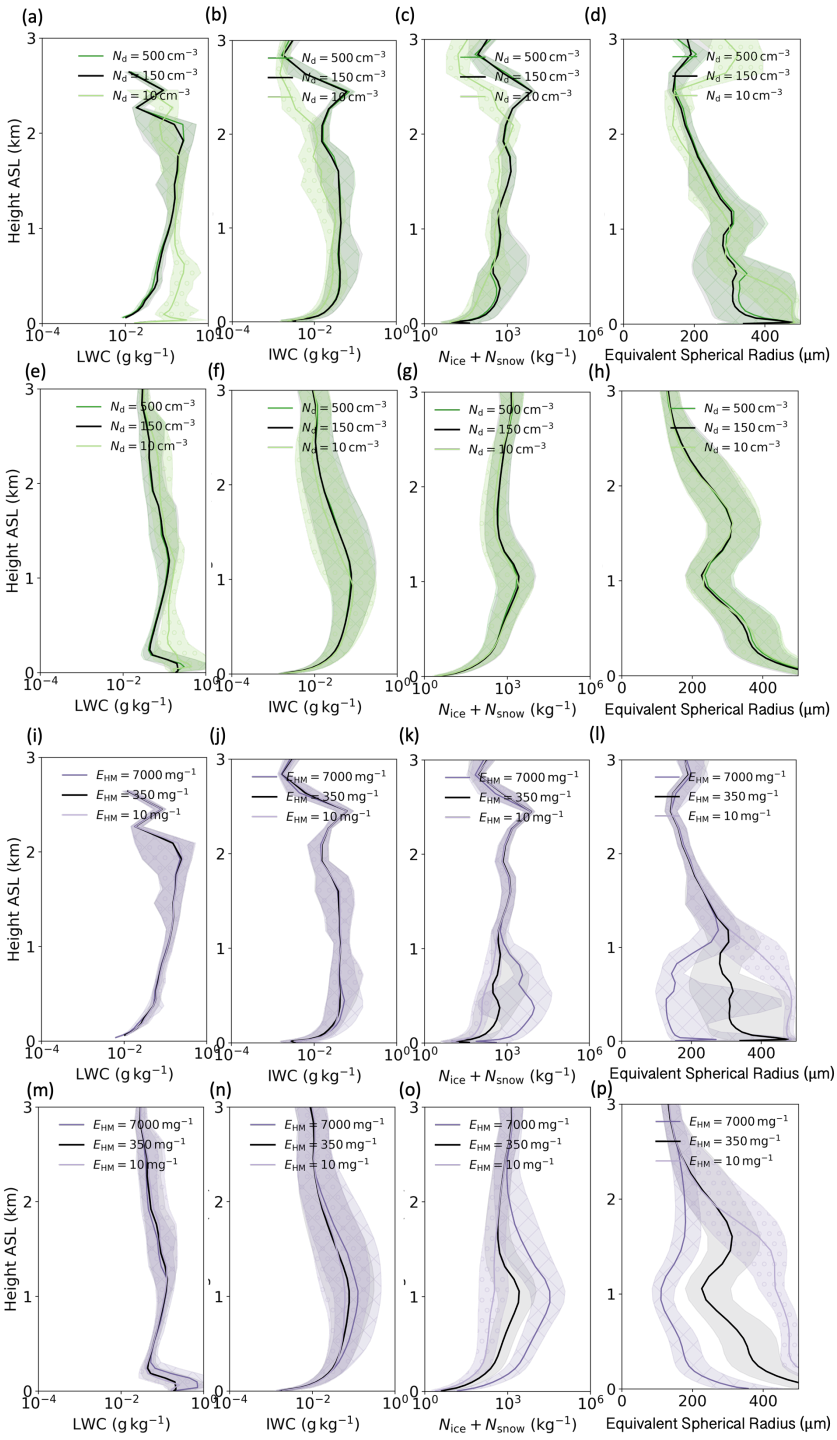


Figure A2.17: Vertical profiles of in-cloud LWC (liquid water content), in-cloud IWC (ice water content), $N_{\mathrm{ice}} + N_{\mathrm{snow}}$ and equivalent spherical radius for stratocumulus-dominated (a-d, i-l) and cumulus-dominated (e-h, m-p) regions in the 24 October 2022 CAO case with different N_{d} (a-h) and E_{HM} (i-p).

A2.10 Supplementary figures for model output compared to satellite retrievals

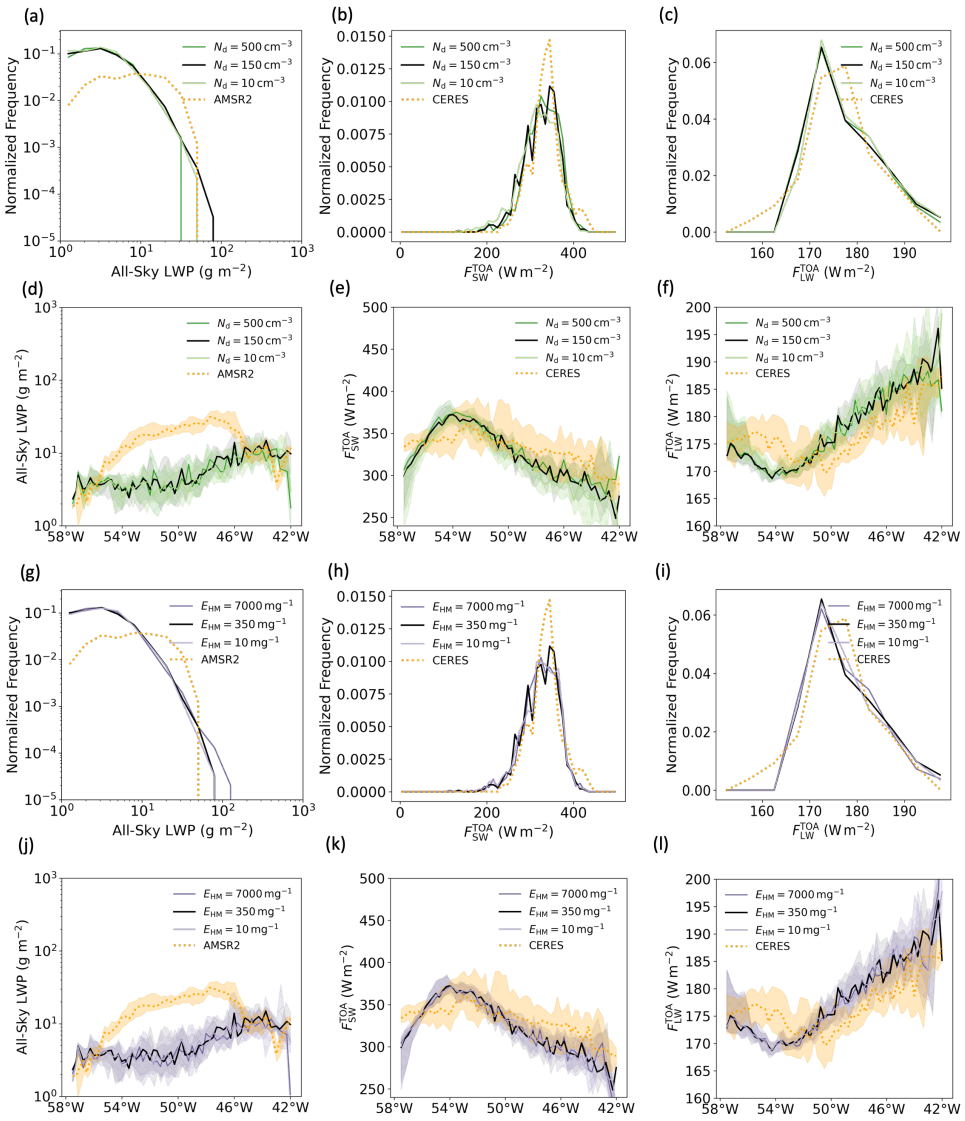


Figure A2.18: Model output compared with satellite retrievals for simulations with different N_d (a-f) and E_{HM} (g-l) on 15 March 2022: the normalized frequency of all-sky liquid water path (LWP) from AMSR-2 (left column), shortwave radiation at the top-of-atmosphere (middle column) and longwave radiation at the top-of-atmosphere from CERES (right column).

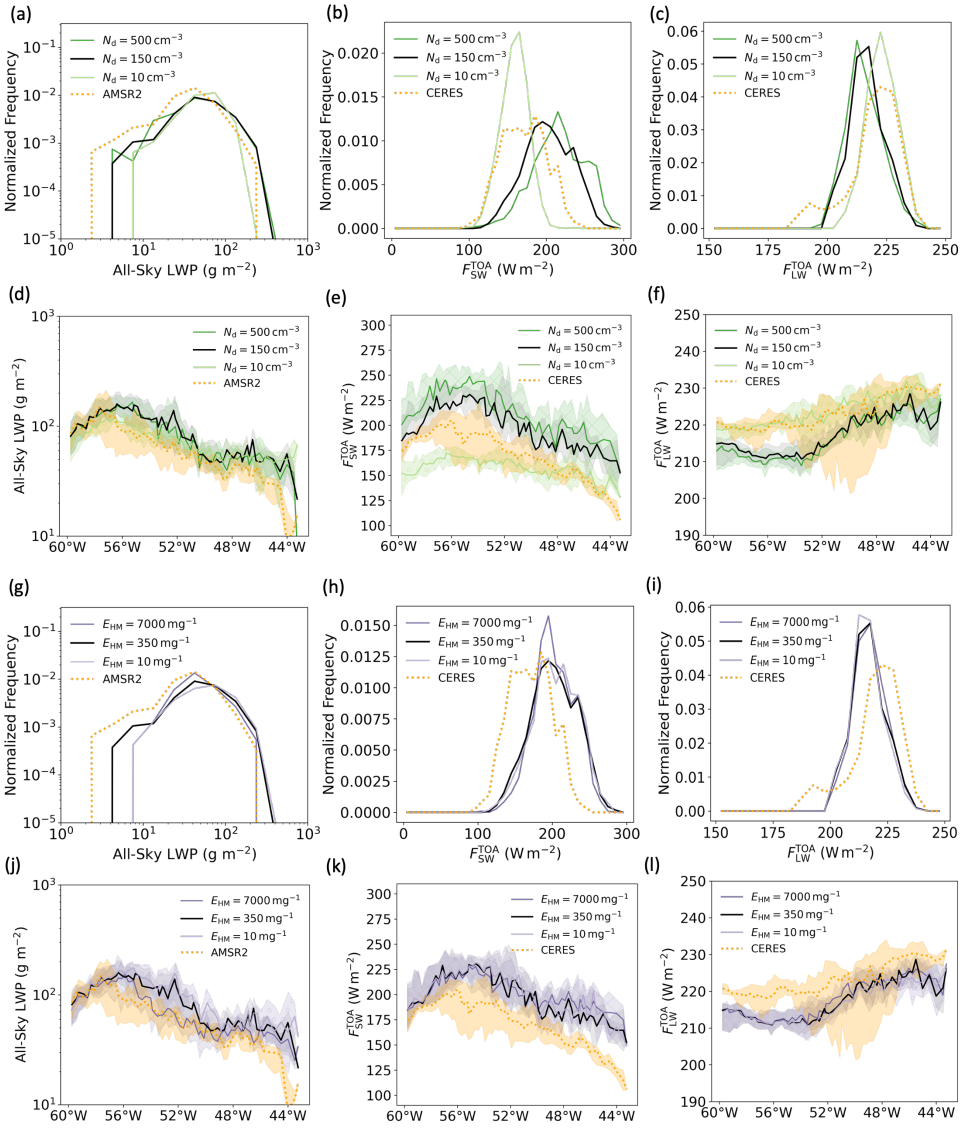


Figure A2.19: Model output compared with satellite retrievals for simulations with different N_d (a-f) and E_{HM} (g-l) on 24 October 2022: the normalized frequency of all-sky liquid water path (LWP) from AMSR-2 (left column), shortwave radiation at the top-of-atmosphere (middle column) and longwave radiation at the top-of-atmosphere from CERES (right column).

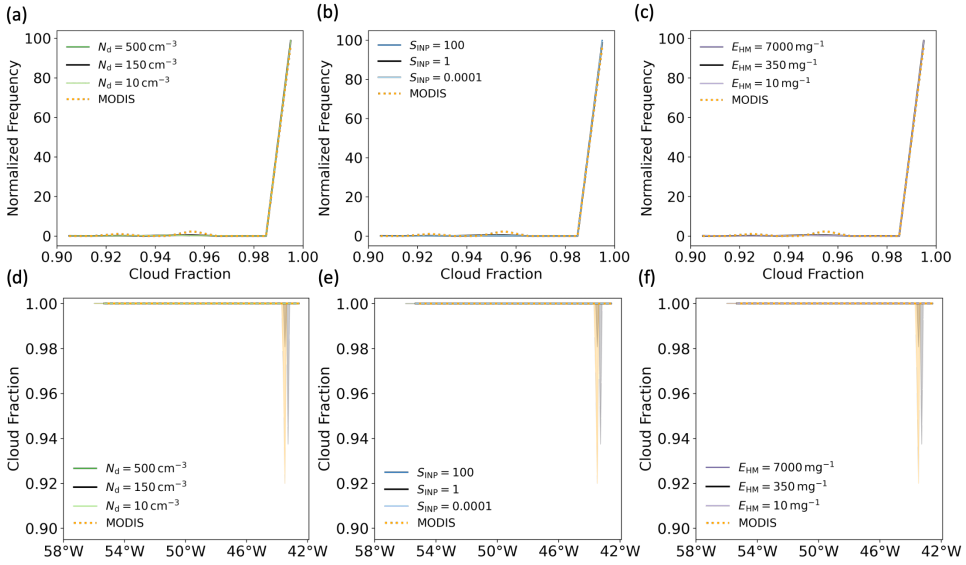


Figure A2.20: Modelled cloud fraction compared to cloud fraction retrieved from MODIS onboard the Aqua satellite with different N_d (a,d), S_{INP} (b,e) and E_{HM} (g-l) on 15 March 2022. Cloud fractions from the model were calculated using the percentage of model grids with cloud cover larger than 20% in each coarser MODIS grid. Lines in Figures (d), (e) and (f) are the cross-section medians and the shaded area indicates the IQR (interquartile) range.

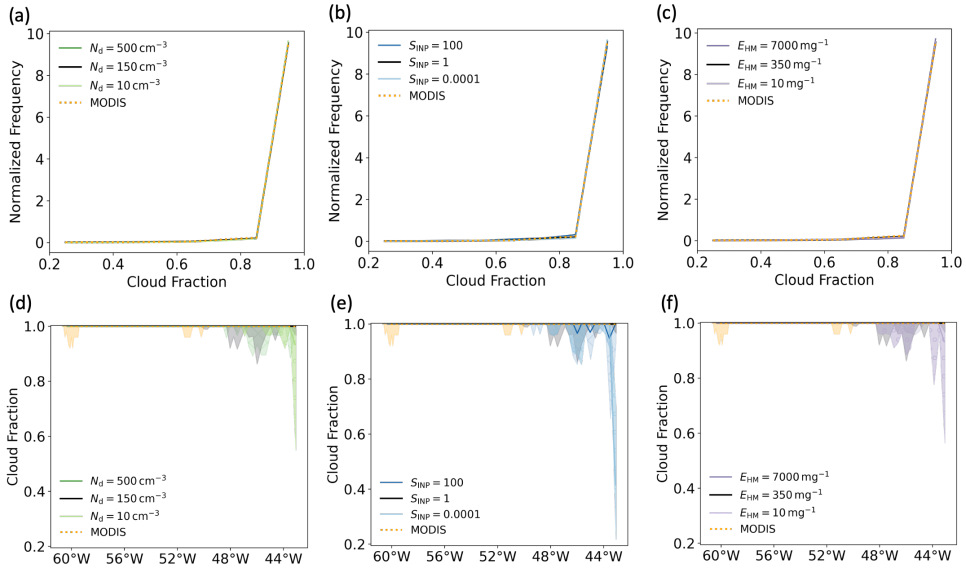


Figure A2.21: Modelled cloud fraction compared to cloud fraction retrieved from MODIS onboard the Aqua satellite with different N_d (a,d), S_{INP} (b,e) and E_{HM} (g-l) on 24 October 2022. Cloud fractions from the model were calculated using the percentage of model grids with cloud cover larger than 20% in each coarser MODIS grid. Lines in Figures (d), (e) and (f) are the cross-section medians and the shaded area indicates the IQR (interquartile) range.

References

Abel, S. J., Boutle, I. A., Waite, K., Fox, S., Brown, P. R. A., Cotton, R., Lloyd, G., Choularton, T. W., and Bower, K. N. (2017). "The Role of Precipitation in Controlling the Transition from Stratocumulus to Cumulus Clouds in a Northern Hemisphere Cold-Air Outbreak". In: *Journal of the Atmospheric Sciences* 74.7, pp. 2293–2314.

Albrecht, B. A. (1989). "Aerosols, Cloud Microphysics, and Fractional Cloudiness". In: *Science* 245.4923, pp. 1227–1230.

Bergeron, T. (1935). "On the physics of clouds and precipitation". In: *Proces Verbaux de l'Association de Météorologie*, pp. 156–178.

Bigg, E. K. (1953). "The formation of atmospheric ice crystals by the freezing of droplets". In: *Quarterly Journal of the Royal Meteorological Society* 79.342, pp. 510–519.

Bodas-Salcedo, A., Andrews, T., Karmalkar, A. V., and Ringer, M. A. (2016). "Cloud liquid water path and radiative feedbacks over the Southern Ocean". In: *Geophysical Research Letters* 43.20, pp. 10938–10946.

Bodas-Salcedo, A., Mulcahy, J. P., Andrews, T., Williams, K. D., Ringer, M. A., Field, P. R., and Elsaesser, G. S. (2019). "Strong Dependence of Atmospheric Feedbacks on Mixed-Phase Microphysics and Aerosol-Cloud Interactions in HadGEM3". In: *Journal of Advances in Modeling Earth Systems* 11.6, pp. 1735–1758.

Bodas-Salcedo, A., Williams, K. D., Ringer, M. A., Beau, I., Cole, J. N. S., Dufresne, J.-L., Koshiro, T., Stevens, B., Wang, Z., and Yokohata, T. (2014). "Origins of the Solar Radiation Biases over the Southern Ocean in CFMIP2 Models". In: *Journal of Climate* 27.1, pp. 41–56.

Brown, A., Milton, S., Cullen, M., Golding, B., Mitchell, J., and Shelly, A. (2012). "Unified Modeling and Prediction of Weather and Climate: A 25-Year Journey". In: *Bulletin of the American Meteorological Society* 93.12, pp. 1865–1877.

Brümmer, B. (1996). "Boundary-layer modification in wintertime cold-air outbreaks from the Arctic sea ice". In: *Boundary-Layer Meteorology* 80.1, pp. 109–125.

— (1999). "Roll and Cell Convection in Wintertime Arctic Cold-Air Outbreaks". In: *Journal of the Atmospheric Sciences* 56.15, pp. 2613–2636.

Bush, M., Allen, T., Bain, C., Boutle, I., Edwards, J., Finnenkoetter, A., Franklin, C., Hanley, K., Lean, H., Lock, A., Manners, J., Mittermaier, M., Morcrette, C., North, R., Petch, J., Short, C., Vosper, S., Walters, D., Webster, S., Weeks, M., Wilkinson, J., Wood, N., and Zerroukat, M. (2020). "The first Met Office Unified Model–JULES Regional Atmosphere and Land configuration, RAL1". In: *Geoscientific Model Development* 13.4, pp. 1999–2029.

Bush, M., Boutle, I., Edwards, J., Finnenkoetter, A., Franklin, C., Hanley, K., Jayakumar, A., Lewis, H., Lock, A., Mittermaier, M., Mohandas, S., North, R., Porson,

A., Roux, B., Webster, S., and Weeks, M. (2022). "The second Met Office Unified Model/JULES Regional Atmosphere and Land configuration, RAL2". In: *Geoscientific Model Development Discussions*, pp. 1–35.

Ceppi, P., Brient, F., Zelinka, M. D., and Hartmann, D. L. (2017). "Cloud feedback mechanisms and their representation in global climate models". In: *WIREs Climate Change* 8.4, e465.

Conen, F., Stopelli, E., and Zimmermann, L. (2016). "Clues that decaying leaves enrich Arctic air with ice nucleating particles". In: *Atmospheric Environment* 129, pp. 91–94.

Cooper, W. (1986). "Ice Initiation in Natural Clouds". In: *Precipitation Enhancement—A Scientific Challenge, Meteorological Monographs*.

Creamean, J. M., Cross, J. N., Pickart, R., McRaven, L., Lin, P., Pacini, A., Hanlon, R., Schmale, D. G., Ceniceros, J., Aydell, T., Colombi, N., Bolger, E., and DeMott, P. J. (2019). "Ice Nucleating Particles Carried From Below a Phytoplankton Bloom to the Arctic Atmosphere". In: *Geophysical Research Letters* 46.14, pp. 8572–8581.

Creamean, J. M., Kirpes, R. M., Pratt, K. A., Spada, N. J., Maahn, M., de Boer, G., Schnell, R. C., and China, S. (2018). "Marine and terrestrial influences on ice nucleating particles during continuous springtime measurements in an Arctic oilfield location". In: *Atmospheric Chemistry and Physics* 18.24, pp. 18023–18042.

de Roode, S. R., Frederikse, T., Siebesma, A. P., Ackerman, A. S., Chylik, J., Field, P. R., Fricke, J., Gryschka, M., Hill, A., Honnert, R., Krueger, S. K., Lac, C., Lesage, A. T., and Tomassini, L. (2019). "Turbulent Transport in the Gray Zone: A Large Eddy Model Intercomparison Study of the CONSTRAIN Cold Air Outbreak Case". In: *Journal of Advances in Modeling Earth Systems* 11.3, pp. 597–623.

DeMott, P. J., Hill, T. C. J., McCluskey, C. S., Prather, K. A., Collins, D. B., Sullivan, R. C., Ruppel, M. J., Mason, R. H., Irish, V. E., Lee, T., Hwang, C. Y., Rhee, T. S., Snider, J. R., McMeeking, G. R., Dhaniyala, S., Lewis, E. R., Wentzell, J. J. B., Abbatt, J., Lee, C., Sultana, C. M., Ault, A. P., Axson, J. L., Diaz Martinez, M., Venero, I., Santos-Figueroa, G., Stokes, M. D., Deane, G. B., Mayol-Bracero, O. L., Grassian, V. H., Bertram, T. H., Bertram, A. K., Moffett, B. F., and Franc, G. D. (2016). "Sea spray aerosol as a unique source of ice nucleating particles". In: *Proceedings of the National Academy of Sciences* 113.21, pp. 5797–5803.

Edwards, J. M. and Slingo, A. (1996). "Studies with a flexible new radiation code. I: Choosing a configuration for a large-scale model". In: *Quarterly Journal of the Royal Meteorological Society* 122.531, pp. 689–719.

Field, P. R., Cotton, R. J., McBeath, K., Lock, A. P., Webster, S., and Allan, R. P. (2014). "Improving a convection-permitting model simulation of a cold air outbreak". In: *Quarterly Journal of the Royal Meteorological Society* 140.678, pp. 124–138.

Field, P. R., Lawson, R. P., Brown, P. R. A., Lloyd, G., Westbrook, C., Moisseev, D., Miltenberger, A., Nenes, A., Blyth, A., Choularton, T., Connolly, P., Buehl, J., Crosier, J., Cui, Z., Dearden, C., DeMott, P., Flossmann, A., Heymsfield, A., Huang, Y., Kalesse, H., Kanji, Z. A., Korolev, A., Kirchgaessner, A., Lasher-Trapp, S., Leisner, T., McFarquhar, G., Phillips, V., Stith, J., and Sullivan, S. (2017a). "Secondary Ice Production: Current State of the Science and Recommendations for the Future". In: *Meteorological Monographs* 58, pp. 7.1–7.20.

Field, P. R., Brožková, R., Chen, M., Dudhia, J., Lac, C., Hara, T., Honnert, R., Olson, J., Siebesma, P., de Roode, S., Tomassini, L., Hill, A., and McTaggart-Cowan, R. (2017b). "Exploring the convective grey zone with regional simulations of a cold air outbreak". In: *Quarterly Journal of the Royal Meteorological Society* 143.707, pp. 2537–2555.

Field, P. R., Hill, A., Shipway, B., Furtado, K., Wilkinson, J., Miltenberger, A., Gordon, H., Grosvenor, D. P., Stevens, R., and Van Weverberg, K. (2023). "Implementation of a Double Moment Cloud Microphysics Scheme in the UK Met Office Regional Numerical Weather Prediction Model". In: *Quarterly Journal of the Royal Meteorological Society*.

Findeisen, W. (1938). "Kolloid-meteorologische Vorgänge bei Niederschlagsbildung". In: *Meteorologische Zeitschrift* 55, pp. 121–133.

Findeisen, W. and Findeisen, E. (1943). "Untersuchungen über die Eissplitterbildung an Reifschichten (Ein Beitrag zur Frage der Entstehung der Gewitterelektrizität und zur Mikrostruktur der Cumulonimben)". In: *Meteorologische Zeitschrift* 60, pp. 145–154.

Fletcher, J., Mason, S., and Jakob, C. (2016a). "The Climatology, Meteorology, and Boundary Layer Structure of Marine Cold Air Outbreaks in Both Hemispheres". In: *Journal of Climate* 29.6, pp. 1999–2014.

Fletcher, J. K., Mason, S., and Jakob, C. (2016b). "A Climatology of Clouds in Marine Cold Air Outbreaks in Both Hemispheres". In: *Journal of Climate* 29.18, pp. 6677–6692.

Grosvenor, D. P., Field, P. R., Hill, A. A., and Shipway, B. J. (2017). "The relative importance of macrophysical and cloud albedo changes for aerosol-induced radiative effects in closed-cell stratocumulus: insight from the modelling of a case study". In: *Atmospheric Chemistry and Physics* 17.8, pp. 5155–5183.

Grosvenor, D. P., Sourdeval, O., Zuidema, P., Ackerman, A., Alexandrov, M. D., Bennartz, R., Boers, R., Cairns, B., Chiu, J. C., Christensen, M., Deneke, H., Diamond, M., Feingold, G., Fridlind, A., Hünerbein, A., Knist, C., Kollias, P., Marshak, A., McCoy, D., Merk, D., Painemal, D., Rausch, J., Rosenfeld, D., Russchenberg, H., Seifert, P., Sinclair, K., Stier, P., van Diedenhoven, B., Wendisch, M., Werner, F., Wood, R., Zhang, Z., and Quaas, J. (2018). "Remote Sensing of Droplet Number

Concentration in Warm Clouds: A Review of the Current State of Knowledge and Perspectives". In: *Reviews of Geophysics* 56.2, pp. 409–453.

Hallett, J. and Mossop, S. C. (1974). "Production of secondary ice particles during the riming process". In: *Nature* 249, pp. 26–28.

Hartmann, M., Adachi, K., Eppers, O., Haas, C., Herber, A., Holzinger, R., Hünerbein, A., Jäkel, E., Jentzsch, C., van Pinxteren, M., Wex, H., Willmes, S., and Stratmann, F. (2020). "Wintertime Airborne Measurements of Ice Nucleating Particles in the High Arctic: A Hint to a Marine, Biogenic Source for Ice Nucleating Particles". In: *Geophysical Research Letters* 47.13, e2020GL087770.

Hartmann, M., Gong, X., Kecorius, S., van Pinxteren, M., Vogl, T., Welti, A., Wex, H., Zeppenfeld, S., Herrmann, H., Wiedensohler, A., and Stratmann, F. (2021). "Terrestrial or marine – indications towards the origin of ice-nucleating particles during melt season in the European Arctic up to 83.7° N". In: *Atmospheric Chemistry and Physics* 21.15, pp. 11613–11636.

Hawker, R. E., Miltenberger, A. K., Johnson, J. S., Wilkinson, J. M., Hill, A. A., Shipway, B. J., Field, P. R., Murray, B. J., and Carslaw, K. S. (2021a). "Model emulation to understand the joint effects of ice-nucleating particles and secondary ice production on deep convective anvil cirrus". In: *Atmospheric Chemistry and Physics* 21.23, pp. 17315–17343.

Hawker, R. E., Miltenberger, A. K., Wilkinson, J. M., Hill, A. A., Shipway, B. J., Cui, Z., Cotton, R. J., Carslaw, K. S., Field, P. R., and Murray, B. J. (2021b). "The temperature dependence of ice-nucleating particle concentrations affects the radiative properties of tropical convective cloud systems". In: *Atmospheric Chemistry and Physics* 21.7, pp. 5439–5461.

Hersbach, H., Bell, B., Berrisford, P., Hirahara, S., Horányi, A., Muñoz-Sabater, J., Nicolas, J., Peubey, C., Radu, R., Schepers, D., Simmons, A., Soci, C., Abdalla, S., Abellan, X., Balsamo, G., Bechtold, P., Biavati, G., Bidlot, J., Bonavita, M., De Chiara, G., Dahlgren, P., Dee, D., Diamantakis, M., Dragani, R., Flemming, J., Forbes, R., Fuentes, M., Geer, A., Haimberger, L., Healy, S., Hogan, R. J., Hólm, E., Janisková, M., Keeley, S., Laloyaux, P., Lopez, P., Lupu, C., Radnoti, G., de Rosnay, P., Rozum, I., Vamborg, F., Villaume, S., and Thépaut, J.-N. (2020). "The ERA5 global reanalysis". In: *Quarterly Journal of the Royal Meteorological Society* 146.730, pp. 1999–2049.

Hofer, S., Hahn, L. C., Shaw, J. K., McGraw, Z. S., Bruno, O., Hellmuth, F., Pietschnig, M., Mostue, I. A., David, R. O., Carlsen, T., and Storelvmo, T. (2024). "Realistic representation of mixed-phase clouds increases projected climate warming". In: *Communications Earth & Environment* 5.1, p. 390.

Irish, V. E., Hanna, S. J., Willis, M. D., China, S., Thomas, J. L., Wentzell, J. J. B., Cirisan, A., Si, M., Leaitch, W. R., Murphy, J. G., Abbatt, J. P. D., Laskin, A., Girard, E., and Bertram, A. K. (2019). "Ice nucleating particles in the marine bound-

ary layer in the Canadian Arctic during summer 2014". In: *Atmospheric Chemistry and Physics* 19.2, pp. 1027–1039.

Karalis, M., Sotiropoulou, G., Abel, S. J., Bossioli, E., Georgakaki, P., Methymaki, G., Nenes, A., and Tombrou, M. (2022). "Effects of secondary ice processes on a stratocumulus to cumulus transition during a cold-air outbreak". In: *Atmospheric Research* 277, p. 106302.

Khain, A. P., Beheng, K. D., Heymsfield, A., Korolev, A., Krichak, S. O., Levin, Z., Pinsky, M., Phillips, V., Prabhakaran, T., Teller, A., van den Heever, S. C., and Yano, J.-I. (2015). "Representation of microphysical processes in cloud-resolving models: Spectral (bin) microphysics versus bulk parameterization". In: *Reviews of Geophysics* 53.2, pp. 247–322.

Khanal, S. and Wang, Z. (2018). "Uncertainties in MODIS-Based Cloud Liquid Water Path Retrievals at High Latitudes Due to Mixed-Phase Clouds and Cloud Top Height Inhomogeneity". In: *Journal of Geophysical Research: Atmospheres* 123.19, pp. 11154–11172.

Kolstad, E. W. and Bracegirdle, T. J. (2008). "Marine cold-air outbreaks in the future: an assessment of IPCC AR4 model results for the Northern Hemisphere". In: *Climate Dynamics* 30.7, pp. 871–885.

Kolstad, E. W., Bracegirdle, T. J., and Seierstad, I. A. (2009). "Marine cold-air outbreaks in the North Atlantic: temporal distribution and associations with large-scale atmospheric circulation". In: *Climate Dynamics* 33.2, pp. 187–197.

Latham, J., Mason, B. J., and Blackett, P. M. S. (1961). "Generation of electric charge associated with the formation of soft hail in thunderclouds". In: *Proceedings of the Royal Society of London. Series A. Mathematical and Physical Sciences* 260.1303, pp. 537–549.

Lock, A. P. (2001). "The Numerical Representation of Entrainment in Parameterizations of Boundary Layer Turbulent Mixing". In: *Monthly Weather Review* 129.5, pp. 1148–1163.

Manners, J., Edwards, J. M., Hill, P., and Thelen, J.-C. (2023). *SOCRATES Technical Guide Suite Of Community RAdiative Transfer codes based on Edwards and Slingo.* Met Office, FitzRoy Rd, Exeter EX1 3PB.

Mason, R. H., Si, M., Chou, C., Irish, V. E., Dickie, R., Elizondo, P., Wong, R., Brintnell, M., Elsasser, M., Lassar, W. M., Pierce, K. M., Leaitch, W. R., MacDonald, A. M., Platt, A., Toom-Sauntry, D., Sarda-Estève, R., Schiller, C. L., Suski, K. J., Hill, T. C. J., Abbatt, J. P. D., Huffman, J. A., DeMott, P. J., and Bertram, A. K. (2016). "Size-resolved measurements of ice-nucleating particles at six locations in North America and one in Europe". In: *Atmospheric Chemistry and Physics* 16.3, pp. 1637–1651.

McCoy, I. L., Wood, R., and Fletcher, J. K. (2017). "Identifying Meteorological Controls on Open and Closed Mesoscale Cellular Convection Associated with Marine

Cold Air Outbreaks". In: *Journal of Geophysical Research: Atmospheres* 122.21, pp. 11678–11702.

MODIS Characterization Support Team (MCST) (2017). *MODIS 1km Calibrated Radiances Product*. MODIS Adaptive Processing System, Goddard Space Flight Center, USA.

Morrison, H., van Lier-Walqui, M., Fridlind, A. M., Grabowski, W. W., Harrington, J. Y., Hoose, C., Korolev, A., Kumjian, M. R., Milbrandt, J. A., Pawlowska, H., Posselt, D. J., Prat, O. P., Reimel, K. J., Shima, S.-I., van Diedenhoven, B., and Xue, L. (2020). "Confronting the Challenge of Modeling Cloud and Precipitation Microphysics". In: *Journal of Advances in Modeling Earth Systems* 12.8, e2019MS001689.

Murray, B. J., Carslaw, K. S., and Field, P. R. (2021). "Opinion: Cloud-phase climate feedback and the importance of ice-nucleating particles". In: *Atmospheric Chemistry and Physics* 21.2, pp. 665–679.

Murray, B. J. and the M-Phase Team (2024). "Ice production in northern hemisphere cold air-outbreak clouds: two contrasting aircraft campaigns". In: EGU General Assembly 2024, Vienna, Austria, 14–19 Apr 2024, EGU24-11598.

Murray-Watson, R. J., Gryspeerdt, E., and Goren, T. (2023). "Investigating the development of clouds within marine cold-air outbreaks". In: *Atmospheric Chemistry and Physics* 23.16, pp. 9365–9383.

Platnick, S., Ackerman, S., and King, M. (2015). *MODIS Atmosphere L2 Cloud Product*. MODIS Adaptive Processing System, Goddard Space Flight Center, USA.

Platnick, S., Meyer, K., King, M. D., Wind, G., Amarasinghe, N., Marchant, B., Arnold, G. T., Zhang, Z., Hubanks, P. A., Holz, R. E., Yang, P., Ridgway, W. L., and Riedi, J. (2016). "2017: The MODIS cloud optical and microphysical products: Collection 6 updates and examples from Terra and Aqua". In: *IEEE Trans. Geosci. Remote Sens.* 55, pp. 502–525.

Porter, G. C. E., Sikora, S. N. F., Adams, M. P., Proske, U., Harrison, A. D., Tarn, M. D., Brooks, I. M., and Murray, B. J. (2020). "Resolving the size of ice-nucleating particles with a balloon deployable aerosol sampler: the SHARK". In: *Atmospheric Measurement Techniques* 13.6, pp. 2905–2921.

Porter, G. C. E., Adams, M. P., Brooks, I. M., Ickes, L., Karlsson, L., Leck, C., Salter, M. E., Schmale, J., Siegel, K., Sikora, S. N. F., Tarn, M. D., Vüllers, J., Wernli, H., Zieger, P., Zinke, J., and Murray, B. J. (2022). "Highly Active Ice-Nucleating Particles at the Summer North Pole". In: *Journal of Geophysical Research: Atmospheres* 127.6, e2021JD036059.

Raif, E. N., Barr, S. L., Tarn, M. D., McQuaid, J. B., Daily, M. I., Abel, S. J., Barrett, P. A., Bower, K. N., Field, P. R., Carslaw, K. S., and Murray, B. J. (2024). "High ice-nucleating particle concentrations associated with Arctic haze in springtime cold-air outbreaks". In: *EGUsphere* 2024, pp. 1–38.

Renfrew, I. A. and Moore, G. W. K. (1999). "An Extreme Cold-Air Outbreak over the Labrador Sea: Roll Vortices and Air–Sea Interaction". In: *Monthly Weather Review* 127.10, pp. 2379–2394.

Sanchez-Marroquin, A., Arnalds, O., Baustian-Dorsi, K. J., Browse, J., Dagsson-Waldhauserova, P., Harrison, A. D., Maters, E. C., Pringle, K. J., Vergara-Temprado, J., Burke, I. T., McQuaid, J. B., Carslaw, K. S., and Murray, B. J. (2020). "Iceland is an episodic source of atmospheric ice-nucleating particles relevant for mixed-phase clouds". In: *Science Advances* 6.26, eaba8137.

Seethala, C. and Horváth, A. (2010). "Global assessment of AMSR-E and MODIS cloud liquid water path retrievals in warm oceanic clouds". In: *Journal of Geophysical Research: Atmospheres* 115.D13.

Sherwood, S. C., Webb, M. J., Annan, J. D., Armour, K. C., Forster, P. M., Hargreaves, J. C., Hegerl, G., Klein, S. A., Marvel, K. D., Rohling, E. J., Watanabe, M., Andrews, T., Braconnot, P., Bretherton, C. S., Foster, G. L., Hausfather, Z., von der Heydt, A. S., Knutti, R., Mauritsen, T., Norris, J. R., Proistosescu, C., Rugenstein, M., Schmidt, G. A., Tokarska, K. B., and Zelinka, M. D. (2020). "An Assessment of Earth's Climate Sensitivity Using Multiple Lines of Evidence". In: *Reviews of Geophysics* 58.4, e2019RG000678.

Shipway, B. J. and Hill, A. A. (2012). "Diagnosis of systematic differences between multiple parametrizations of warm rain microphysics using a kinematic framework". In: *Quarterly Journal of the Royal Meteorological Society* 138.669, pp. 2196–2211.

Si, M., Evoy, E., Yun, J., Xi, Y., Hanna, S. J., Chivulescu, A., Rawlings, K., Veber, D., Platt, A., Kunkel, D., Hoor, P., Sharma, S., Leaitch, W. R., and Bertram, A. K. (2019). "Concentrations, composition, and sources of ice-nucleating particles in the Canadian High Arctic during spring 2016". In: *Atmospheric Chemistry and Physics* 19.5, pp. 3007–3024.

Slingo, A. and Schrecker, H. M. (1982). "On the Shortwave Radiative Properties of Stratiform Water Clouds". In: *Quarterly Journal of the Royal Meteorological Society* 108, pp. 407–426.

Sotiropoulou, G., Sullivan, S., Savre, J., Lloyd, G., Lachlan-Cope, T., Ekman, A. M. L., and Nenes, A. (2020). "The impact of secondary ice production on Arctic stratocumulus". In: *Atmospheric Chemistry and Physics* 20.3, pp. 1301–1316.

Storelvmo, T., Tan, I., and Korolev, A. V. (2015). "Cloud Phase Changes Induced by CO2 Warming—a Powerful yet Poorly Constrained Cloud-Climate Feedback". In: *Current Climate Change Reports* 1.4, pp. 288–296.

Su, W., Corbett, J., Eitzen, Z., and Liang, L. (2015a). "Next-generation angular distribution models for top-of-atmosphere radiative flux calculation from CERES instruments: methodology". In: *Atmospheric Measurement Techniques* 8.2, pp. 611–632.

Su, W., Corbett, J., Eitzen, Z., and Liang, L. (2015b). "Next-generation angular distribution models for top-of-atmosphere radiative flux calculation from CERES instruments: validation". In: *Atmospheric Measurement Techniques* 8.8, pp. 3297–3313.

Takahashi, T., Nagao, Y., and Kushiyama, Y. (1995). "Possible High Ice Particle Production during Graupel–Graupel Collisions". In: *Journal of Atmospheric Sciences* 52.24, pp. 4523–4527.

Tan, I., Storelvmo, T., and Zelinka, M. D. (2016). "Observational constraints on mixed-phase clouds imply higher climate sensitivity". In: *Science* 352.6282, pp. 224–227.

Tarn, M., Foster, P., McQuaid, J., Robinson, J., Clarke, S., Raif, E., Choularton, T., Gallagher, M., Bower, K., Field, P., and Murray, B. (2025). *Ice-nucleating particle measurements from the M-Phase 2022 flight campaign*.

Tornow, F., Ackerman, A. S., and Fridlind, A. M. (2021). "Preconditioning of overcast-to-broken cloud transitions by riming in marine cold air outbreaks". In: *Atmospheric Chemistry and Physics* 21.15, pp. 12049–12067.

Twomey, S. (1977). "The Influence of Pollution on the Shortwave Albedo of Clouds". In: *Journal of Atmospheric Sciences* 34.7, pp. 1149–1152.

Vardiman, L. (1978). "The generation of secondary ice particles in clouds by crystal–crystal collisions". In: *J. Atmos. Sci.* 35, pp. 2168–2180.

Vergara-Temprado, J., Miltenberger, A. K., Furtado, K., Grosvenor, D. P., Shipway, B. J., Hill, A. A., Wilkinson, J. M., Field, P. R., Murray, B. J., and Carslaw, K. S. (2018). "Strong control of Southern Ocean cloud reflectivity by ice-nucleating particles". In: *Proceedings of the National Academy of Sciences* 115.11, pp. 2687–2692.

Walters, D., Boutle, I., Brooks, M., Melvin, T., Stratton, R., Vosper, S., Wells, H., Williams, K., Wood, N., Allen, T., Bushell, A., Copsey, D., Earnshaw, P., Edwards, J., Gross, M., Hardiman, S., Harris, C., Heming, J., Klingaman, N., Levine, R., Manners, J., Martin, G., Milton, S., Mittermaier, M., Morcrette, C., Riddick, T., Roberts, M., Sanchez, C., Selwood, P., Stirling, A., Smith, C., Suri, D., Tennant, W., Vidale, P. L., Wilkinson, J., Willett, M., Woolnough, S., and Xavier, P. (2017). "The Met Office Unified Model Global Atmosphere 6.0/6.1 and JULES Global Land 6.0/6.1 configurations". In: *Geoscientific Model Development* 10.4, pp. 1487–1520.

Wegener, A. (1911). *Thermodynamik der Atmosphäre*. Leipzig: J. A. Barth. 331 pp.

Welti, A., Bigg, E. K., DeMott, P. J., Gong, X., Hartmann, M., Harvey, M., Henning, S., Herenz, P., Hill, T. C. J., Hornblow, B., Leck, C., Löffler, M., McCluskey, C. S., Rauker, A. M., Schmale, J., Tatzelt, C., van Pinxteren, M., and Stratmann, F. (2020). "Ship-based measurements of ice nuclei concentrations over the Arctic, Atlantic, Pacific and Southern oceans". In: *Atmospheric Chemistry and Physics* 20.23, pp. 15191–15206.

Wentz, F., T. Meissner, C., Gentemann, K., and Hilburn, J. S. (2014). *Remote Sensing Systems GCOM-W1 AMSR2 Environmental Suite on 0.25 deg grid*. Remote Sensing Systems, Santa Rosa, CA.

Wood, R. (2012). "Stratocumulus Clouds". In: *Monthly Weather Review* 140.8, pp. 2373–2423.

Wu, P. and Ovchinnikov, M. (2022). "Cloud Morphology Evolution in Arctic Cold-Air Outbreak: Two Cases During COMBLE Period". In: *Journal of Geophysical Research: Atmospheres* 127.10, e2021JD035966.

Young, G., Lachlan-Cope, T., O'Shea, S. J., Dearden, C., Listowski, C., Bower, K. N., Choularton, T. W., and Gallagher, M. W. (2019). "Radiative Effects of Secondary Ice Enhancement in Coastal Antarctic Clouds". In: *Geophysical Research Letters* 46.4, pp. 2312–2321.

Zelinka, M. D., Myers, T. A., McCoy, D. T., Po-Chedley, S., Caldwell, P. M., Ceppi, P., Klein, S. A., and Taylor, K. E. (2020). "Causes of Higher Climate Sensitivity in CMIP6 Models". In: *Geophysical Research Letters* 47.1, e2019GL085782.

Chapter 3

Interacting effects of droplet number and ice formation processes on mixed-phase cold-air outbreak clouds

Chapter 3 is based on the paper accepted for final production in the journal *Atmospheric Chemistry and Physics*: Huang, X., Field, P. R., Herbert, R. J., Murray, B. J., van den Heuvel, F., Grosvenor, D. P., Sansom, R. W. N., and Carslaw, K. S. (2026). Interacting effects of droplet number and ice formation processes on mixed-phase cold-air outbreak clouds. *EGUsphere*, 2026, 1–49. https://doi.org/10.5194/egusphere-2026-311.

Authors: Xinyi Huang[1], Paul R. Field[1,2], Ross J. Herbert[1], Benjamin J. Murray[1], Floortje van den Heuvel[3], Daniel P. Grosvenor[1,2], Rachel W. N. Sansom [1], and Kenneth S. Carslaw[1]

[1]Institute for Climate and Atmospheric Science, School of Earth and Environment, University of Leeds, Leeds LS2 9JT, UK

[2]Met Office, Exeter EX1 3PB, UK

[3]British Antarctic Survey, Cambridge CB3 0ET, UK

3.1 Abstract

Shallow, mixed-phase clouds associated with cold-air outbreak (CAO) events are natural laboratories for studying mixed-phase cloud processes which are important for estimating cloud-phase feedback in the warming climate. Recent studies show that CAO clouds are sensitive to aerosol-cloud interactions and ice formation processes, but many modelling studies perturbed model parameters individually, limiting the investigation of joint effects from multiple processes on cloud properties. Here we investigated how six cloud microphysics parameters jointly affect CAO cloud properties by building model emulators trained on output from perturbed parameter ensembles of a high-resolution regional model. The parameters are cloud droplet number concentration (N_d), ice-nucleating particle concentration (N_INP), efficiencies of three secondary ice production processes, as well as the mixed-phase overlap factor (mpof). For the CAO case studied, N_d and N_INP most strongly control the cloud radiative properties in the stratocumulus region; whereas in the cumulus region, effects from varying N_d and mpof are the strongest. Our results show that these parameters have non-linear joint effects such that the magnitude and even sign of cloud responses to a parameter are highly dependent on the values of other parameters. For example, the sensitivity of cloud albedo to increases in N_INP varies between near zero to strongly negative across the sampled parameter space. Therefore, perturbing parameters individually is an inadequate method for determining the cloud responses to model parameters. This work demonstrates the power of model emulation and the importance of a full exploration of parameter space in order to understand the factors controlling cloud properties.

3.2 Introduction

Low-level, mixed-phase clouds at mid and high latitudes play a key role in the low-cloud optical depth feedback through their phase changes in a warming climate and affect the Earth's radiation budget (Ceppi et al., 2017), which is referred to as the cloud-phase feedback (Mitchell et al., 1989; Storelvmo et al., 2015; Ceppi et al., 2017; Murray et al., 2021). In these mixed-phase clouds, liquid and ice hydrometeors exist at the same time, and the radiative properties of these clouds are strongly controlled by the characteristics and interactions of these hydrometeors at the microphysical scale (Wegener, 1911; Bergeron, 1935; Findeisen, 1938; Findeisen et al., 1943; Pruppacher et al., 1996; Korolev et al., 2017). However, because current global climate models are generally poor in representing mixed-phase cloud microphysics (Bodas-Salcedo et al., 2019; Sherwood et al., 2020), uncertainties persist in both the direction and magnitude of the cloud-phase feedback (Sherwood et al., 2020; Zelinka et al., 2020; Forster et al., 2021; Murray et al., 2021). In fact, cloud microphysical processes are subject to large uncertainties due to their highly parametrized and complicated nature (Morrison et al., 2020), even within high-resolution models such as cloud-resolving models and large-eddy simulations.

In this study, we focused on a specific synoptic-scale meteorological event called a cold-air outbreak (CAO). During a CAO event, air masses flow from cold and dry high-latitude continents or ice-covered regions to the warm, open and sea-ice free ocean, leading to instability of the marine boundary layer and strong atmospheric convection for cloud formation (Brümmer, 1996; Brümmer, 1999; Renfrew et al., 1999; Kolstad et al., 2008; Kolstad et al., 2009; Fletcher et al., 2016a; Fletcher et al., 2016b). As the temperature during CAO events is low and normally below 0 °C, extensive mixed-phase clouds form. These mixed-phase CAO clouds have a well-defined flow, which makes them ideal natural laboratories for understanding the mixed-phase processes that are important for modelling the behaviour of mixed-phase clouds under the warming climate. The CAO clouds usually begin with a form of "cloud street" or stratocumulus-like clouds, and then transition into cumulus-like clouds downwind (Brümmer, 1999; McCoy et al., 2017), which can have very different radiative properties (McCoy et al., 2017).

Cloud microphysics strongly controls mixed phase CAO cloud properties. Several high-resolution modelling studies have been conducted to understand the effect of various cloud microphysics processes and parameters on CAO clouds (Field et al., 2014; Abel et al., 2017; Vergara-Temprado et al., 2018; de Roode et al., 2019; Tornow et al., 2021; Karalis et al., 2022; Li et al., 2023; Possner et al., 2024; Huang et al., 2025, Chapter 2). These studies show that the cloud properties are very sensitive to aerosols including those that can act as cloud condensation nuclei (CCN) and ice-nucleating

particles (INPs), as well as ice formation processes including primary ice production and secondary ice production (SIP). However, all of these studies were conducted by perturbing parameters individually, often called a one-at-a-time (OAT) sensitivity approach. Such an OAT test only allows the responses of cloud properties around a control simulation to be quantified, lacking full exploration of the parameter space and interactions between the parameters. For example, Johnson et al. (2015) has shown that the responses of modelled precipitation in deep convective clouds to the concentration of Aitken and accumulation modes of aerosols and the collection efficiency of drops by graupel are strongly dependent on the values of each other.

A large number of simulations are needed to explore multiple combinations of parameters, which is computationally expensive and impractical for a large number of parameters. To obtain the responses of model variables over the whole parameter space, we applied the approach of model emulation with Gaussian Process (GP) emulators, which is a Bayesian machine learning approach that statistically learns the relationship between model inputs and outputs and acts as a surrogate model of the complex numerical model (Oakley et al., 2002; O'Hagan, 2006). The training data are produced by running PPE (perturbed parameter ensemble) simulations of a numerical model, where parameters are perturbed in combinations that are well-designed for training the emulators. The model emulation approach has been recently applied in many complex climate and atmospheric models, including understanding the magnitude and causes of uncertainty in aerosol radiative forcing (Lee et al., 2011; Lee et al., 2012; Lee et al., 2013; Regayre et al., 2014; Regayre et al., 2015; Regayre et al., 2018; Lee et al., 2016; Johnson et al., 2018; Marshall et al., 2019), assessing potential model simplification of cloud microphysics in global climate models (Proske et al., 2022; Proske et al., 2023), constraining model parametric uncertainties with observations (Johnson et al., 2020; Regayre et al., 2023), identifying the potential existence of structural deficiencies (Regayre et al., 2023; Prévost et al., 2025) and parameter calibration (Elsaesser et al., 2025) in climate models . Besides global models, this approach has also been used in regional models such as investigating the environmental controls on sea breeze circulations (Igel et al., 2018; Park et al., 2020), understanding the controls of cloud properties for deep convective clouds (Johnson et al., 2015; Wellmann et al., 2018; Wellmann et al., 2020; Hawker et al., 2021) and stratocumulus clouds (Glassmeier et al., 2019; Sansom, 2021; Sansom et al., 2024; Sansom et al., 2025). With the model response surface generated from the GP emulators, a variance-based sensitivity analysis (Saltelli et al., 2000) can be applied to quantify the sensitivities of model variables to the investigated parameters.

Here we focus on the influences of aerosol-cloud interactions and ice formation processes on a CAO cloud system over the Labrador Sea on 24 October 2022. This is the warmer case studied in our previous OAT test work (Huang et al., 2025, Chapter 2),

which showed similar cloud responses to previous studies of aerosol-cloud interactions and ice formation processes in CAO clouds. We explore the joint effects of 6 parameters: (1) fixed in-cloud droplet number concentration, (2) INP concentration, (3-5) three parameters from SIP processes including the Hallett-Mossop process, ice-ice collision and droplet shattering, as well as (6) a parameter controlling the extent of spatial overlap between liquid and ice clouds. The parameters for ice-ice collision, droplet shattering and the extent of spatial overlap between liquid and ice clouds are additional to the parameters studied in Huang et al. (2025, Chapter 2). All three SIP mechanisms have been shown to be important for CAO cloud morphology (Karalis et al., 2022) and ice crystal number concentrations in Arctic stratocumulus clouds (Sotiropoulou et al., 2020). It is also suggested that changing the degree of spatial overlap between liquid and ice, which can be estimated with observations, can exert a strong influence on the liquid water path (LWP) and radiative properties of mixed-phase CAO clouds (Abel et al., 2017; Evans et al., 2025).

This paper is structured as follows. In Section 3.3, we describe the numerical model setup, PPE design, training, validation and testing of the GP emulators. In Section 3.4, we present the results starting with example PPE output, and then emulated model responses from the emulators, as well as the multiple OAT tests across the whole parameter space from emulators, followed by summary and discussion on the results of our study compared to previous work, limitations of this study and potential future work in Section 3.5.

3.3 Methods

Our overall approach was to use PPEs (perturbed parameter ensembles) and GP (Gaussian Process) emulators to understand the joint effects of six cloud microphysics parameters at different stages of a CAO (cold-air outbreak) event. A flow chart of methods involved in this work is shown in Appendix 3.4.

3.3.1 Model setup and case description

The nested UM (Unified Model) (Brown et al., 2012) from the UK Met Office was coupled with a double-moment cloud microphysics scheme CASIM (Cloud AeroSol Interacting Microphysics) (Field et al., 2023). We used UM version 13.0 with the RAL (Regional Atmosphere and Land) 3.2 configuration (Bush et al., 2025). The boundary conditions of the nested domains were provided hourly by a global model (N216) with the GAL (Global Atmosphere and Land) 6.1 configuration (Walters et al., 2017). The cloud parameterisation in the nested model was from the bimodal cloud scheme (Van Weverberg et al., 2021b; Van Weverberg et al., 2021a). This approach uses subgrid turbulent kinetic energy to diagnose the subgrid humidity distribution and

hence cloudy fraction. The cloud cover was derived using cloud fractions in a column with the maximum-random overlap assumption. The radiative processes were from SOCRATES (Suite Of Community Radiative Transfer codes based on Edwards and Slingo) (Manners et al., 2023), and mass mixing ratio and number concentration of ice hydrometeors were both considered when calculating the single-scattering albedo of ice in SOCRATES (Baran et al., 2025). The parameterisation of boundary layer processes in our model is from Lock et al. (2000).

The selected CAO event occurred on 24 October 2022 over the Labrador Sea, which coincided with two flights (C322 and C323) during the M-Phase aircraft campaign (Murray et al., 2024; Clarke et al., 2025). Figure 3.1 shows the tracks of both flights, the corresponding nested model domains, and the analysis domains. Flight C322 measured regions dominated by stratocumulus (Sc) clouds, while Flight C323 focused on regions dominated by cumulus (Cu) clouds.

Both nested model domains contain 500 × 500 gridpoints with a horizontal grid spacing of 1.5 km, centred at 60 °N, 60.5 °W for capturing the early stage and Sc region and 56 °N, 51 °W for the Cu region. Field et al. (2017) has demonstrated that this grid spacing is capable of reproducing the general cloud features of a CAO event. The nested model domains were designed to ensure the model analysis domains remained sufficiently distant from the domain boundaries, allowing cloud fields to fully develop when they leave the ice edge and before entering the model analysis domains. At this point, the model has already spun up from the boundaries. The regional model has 90 vertical levels capped at 40 km with 16 model levels below 1 km and 28 model levels below 3 km.

The simulations were initialized at 0000 UTC and performed for 24 hours, with the model output from the first 12 hours excluded from the analysis due to model spin-up.

3.3.2 Perturbed parameters and PPE design

Six parameters were investigated in this study: N_{d} (cloud droplet number concentration), N_{INP}^{-15} (INP concentration at -15 °C), E_{HM} (efficiency of the Hallett-Mossop process), E_{BR} (leading coefficient controlling the efficiency of the ice-ice collisional breakup process), E_{DS} (efficiency of the droplet shattering process), and mpof (mixed-phase overlap factor). All the parameters are within the CASIM scheme. A description of each perturbed parameter and the selection of their perturbed ranges are introduced in this section. The combinations of the six parameter values were designed with the maximin Latin hypercube sampling method. The single OAT test was performed for every parameter before running the PPEs to investigate the effects of perturbing each parameter individually around the control simulation (not shown).

Figure 3.2 shows the main processes in CASIM with relevant processes for the

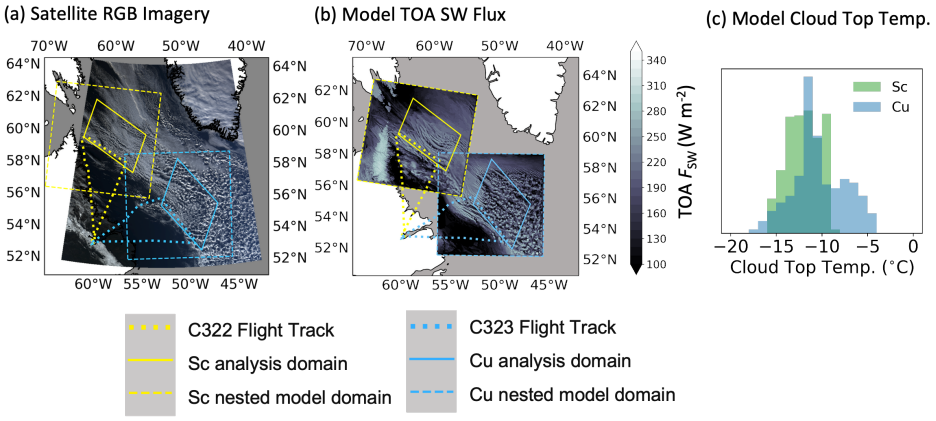


Figure 3.1: Flight tracks (dotted line), nested model domains (dashed squares) and model analysis domains (solid rectangles) for the Sc region (yellow) and the Cu region (blue) on 24 October 2022 over the Labrador Sea: (a) the RGB satellite imagery created using bands 1 (620-670 nm), 3 (459-479 nm) and 4 (545-565 nm) from MODIS (Moderate Resolution Imaging Spectroradiometer) Level 1B Calibrated Radiances Product (Collection 6.1) (MODIS Characterization Support Team (MCST), 2017) onboard the Aqua satellite, (b) the SW (shortwave) reflectance at the top-of-the-atmosphere from the control simulations. The selected model time is the same as the satellite retrieval time at 17:00 UTC and the model output fields are instantaneous. Cloud top temperatures in the two analysis domains are shown in (c). The cloud top temperatures were derived using the air temperature at the highest model grid in a column, with a cloudy grid defined using total cloud water content $\geq 10^{-6}$ kg kg^{-1}. The model output time for CTT in the Sc region is 14:00 UTC and is 19:00 UTC in the Cu region for the corresponding times of flights. The temperature profiles were evaluated in our previous work (Huang et al., 2025, Chapter 2).

perturbed parameters in this work highlighted. Not all processes in CASIM are shown here (e.g., self-collection, sedimentation, evaporation and sublimation); see Field et al. (2023) for a complete description of CASIM implementation in the UM. To keep the consistency of symbols, we used the same symbol for mass tendency (P) and number tendency (N) in the description of parameters below.

3.3.2.1 N_d (cloud droplet number concentration)

N_d is a fixed vertical profile of in-cloud droplet number concentration set in CASIM if aerosols are not used for deriving the cloud droplet number concentration. We did not select the option to use aerosol-derived N_d in this study to avoid extra complexity for parameter perturbation and model output interpretation. N_d was set to 35 cm^{-3} in the control simulation and perturbed over the range from 5 cm^{-3} to 75 cm^{-3} in the PPE design to cover the observed N_d ranges calculated using satellite retrievals from MODIS instrument onboard the Aqua satellite with the method from Grosvenor et al. (2018) (Figure 3.3a). The satellite-derived N_d ranges agree well with the N_d ranges from the CDP (cloud droplet probe) instrument onboard M-Phase C322 and C323 (Figure 3.3a). The 1 Hz CDP measurements were averaged to match the model resolution (1.5 km) and those with N_d less than 1 cm^{-3} were removed before averaging.

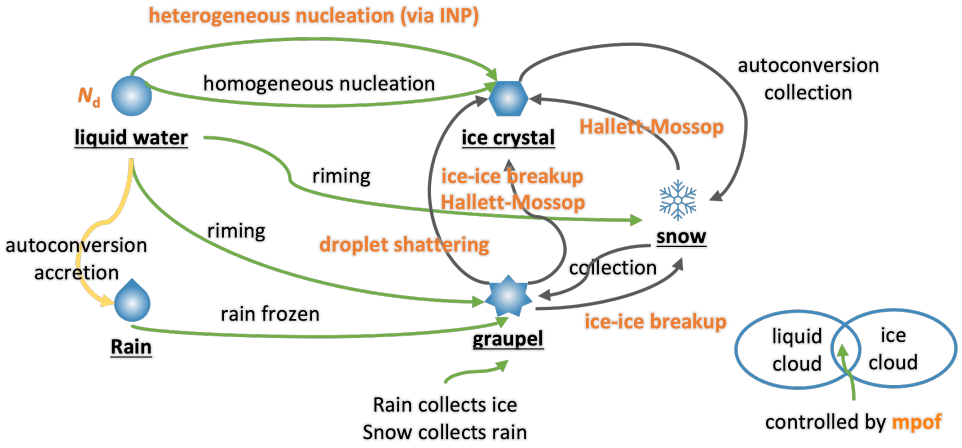


Figure 3.2: Key processes among the five CASIM hydrometeors: liquid water, rain, ice crystal, snow and graupel. Processes which contain the parameters investigated in this work are highlighted in orange. Liquid-liquid processes are highlighted in yellow, mixed-phase processes are highlighted in green and ice-ice processes are in dark grey. Details of the treatment of SIP processes are shown in the Methods section. Not all the cloud microphysical processes in CASIM are shown here; see Field et al. (2023) for detailed information about the implementation of CASIM in the UM.

The range of N_d was chosen to understand how much the variation of N_d in a CAO event affects the cloud properties, which arises from the natural variability of aerosols and limited by the fixed N_d setup. We did not select the bigger range as in Huang et al. (2025, Chapter 2) because the domain-mean N_d can be constrained approximately from satellite retrievals (e.g. Grosvenor et al., 2018).

3.3.2.2 N_INP^{-15} (INP concentration at -15 °C)

INP concentration (N_INP) was perturbed by scaling a temperature-dependent INP parameterisation as shown in Figure 3.3b and 3.3c. The temperature-dependent INP parameterisation over the Labrador Sea region was derived based on $n_s(T)$ (active site density) parameterisations for sea-spray aerosols (McCluskey et al., 2018) and soil dusts (see Appendix 3.1) that accounts for the biogenic component associated with the dust (Herbert et al., 2025). The sea-spray aerosol and dust concentrations from a separate global model over the Labrador Sea region during the M-Phase aircraft campaign period were used with the above parameterisations to derive the temperature-dependent INP parameterisation in this study. The global model used for the aerosol concentrations was performed with a global configuration of the UM (Brown et al., 2012) version 12.1 which includes Global Atmosphere version 8.0 and Global Land model version 9.0 (Willett et al., 2020). Appendix 3.2 shows the details of the global model and the INP concentration in the control simulation, which agrees well with INP measurements from the M-Phase aircraft campaign as in Figure 3.3c.

N_{INP} in the regional model was directly linked to the number concentration of ice crystals produced by heterogenous ice nucleation, assuming that one INP produces one ice crystal. No aerosols were included for the INP calculation in the regional model. Therefore, when perturbing N_{d} and N_{INP}, we are effectively directly changing cloud hydrometeor concentrations rather than explicitly modelling the interaction between evolving aerosol fields and clouds. We chose to not use aerosol-interactive N_{d} and N_{INP} in this study to reduce the complexity of interpretation over the multi-dimensional parameter space and the computational resources required for running a large number of simulations for PPEs. However, there are several limitations of such choice (e.g., missing potential feedback with aerosol processing) which are further discussed in the Discussion and Conclusions.

INP concentrations were perturbed by the same scale factor at all temperatures. For ease of reference to typical values we define the parameter in the PPE as N_{INP}^{-15} (INP concentration at -15 °C, L^{-1}), which is around 0.17 L^{-1} (170 m^{-3}) in the control simulation. The range of N_{INP}^{-15} in the PPE is shown in Figure 3.3b. The N_{INP}^{-15} were perturbed with a range from 1.7×10^{-5} L^{-1} (0.017 m^{-3}) to 17 L^{-1} (17000 m^{-3}) (factor of 0.0001 – 100 relative to the control value).

Such a large range of INP concentration (six orders of magnitude) was selected to represent the range of possible INPs based on our knowledge prior to the *in-situ* measurements of INPs from the aircraft campaign. This is because, unlike N_{d}, the INP concentration cannot be constrained using satellite retrievals or other remote-sensing observations. The ranges for N_{d} and N_{INP} were therefore based on different sources of information available before the aircraft campaign. The aim was to examine how these natural ranges in these two quantities interactively affect CAO clouds.

3.3.2.3 E_{HM} (efficiency of the Hallett-Mossop process)

The Hallett-Mossop process (also called rime splintering) produces small ice splinters during the riming of liquid droplets onto existing ice hydrometeors (Hallett et al., 1974). The efficiency of the Hallett-Mossop process (E_{HM}) is defined as the number of splinters produced per milligram of rimed liquid, with the mass of each splinter (M_{I0}) set as 10^{-18} kg. The mass tendency of ice created by the Hallett-Mossop process in CASIM (P_{ihal}) is based on the mass tendencies of graupel-cloud water (P_{gacw}) and snow-cloud water riming (P_{sacw}) with the number of splinters per milligram of rime varying according to a triangular function ($f(T)$) between -2.5 °C and -7.5 °C (outside of which the value is zero) with the peak at -5 °C (Field et al., 2023).

$$P_{\mathrm{ihal}} = E_{\mathrm{HM}} M_{\mathrm{I0}} (P_{\mathrm{gacw}} + P_{\mathrm{sacw}}) f(T) \tag{3.1}$$

E_{HM} was set to 350 mg^{-1} in the control simulation and perturbed from 35 mg^{-1} to 3500 mg^{-1} (factor of 0.1 – 10). This range was defined based on previous findings that simulations with a factor of 10 higher efficiency than the default value agree well with observed ice crystal number concentrations (Young et al., 2019). The lower limit was chosen to ensure that the default value remains sufficiently distant from the boundary of the parameter space, where emulator predictions are typically subject to higher uncertainties. The multiple OAT test (Section 3.4.3) and global sensitivity analysis (Appendix 3.7) were performed with a different range of E_{HM} from the range of PPE design, which is from 350 mg^{-1} to 3500 mg^{-1} rather than from 35 mg^{-1} to 3500 mg^{-1}.

3.3.2.4 E_{BR} (coefficient controlling the efficiency of the ice-ice collisional breakup)

E_{BR} is a coefficient controlling the efficiency of the ice-ice collisional breakup (χ_{BR}), which is the number of fragments produced from hydrometeor collisions. The number tendency of ice-ice collisional breakup ($N_{\mathrm{iics,xy}}$, where x denotes the colliding hydrometeor and y the hydrometeor being collided with) used in this study follows the temperature-dependent approach in Takahashi et al. (1995) and Sullivan et al. (2018).

$$N_{\mathrm{iics,xy}} = -\chi_{\mathrm{BR}} N_{xacy} \tag{3.2}$$

$$\chi_{\mathrm{BR}} = E_{\mathrm{BR}}(T - T_{\mathrm{min}})^{1.2} \exp\left[-\frac{(T - T_{\mathrm{min}})}{\gamma_{\mathrm{BR}}}\right] \tag{3.3}$$

The minimum temperature (T_{min}) for ice-ice break-up is set at -21 °C and a decay rate (γ_{BR}) of fragment number at warmer subzero temperatures is set to 5. The collisions involve ice and snow particles breaking up through collisions with graupel. N_{xacy} are the existing number tendencies from graupel collecting ice and graupel collecting snow. Detailed description of mixed-phase and cold-phase collection between particles of different hydrometeors in CASIM can be found in Field et al. (2023).

E_{BR} was set to 280 in the control simulation and perturbed with a range from 2.8 to 2800 (factor of 0.01 – 10 relative to the control value). The lower limit of the perturbation range is similar to the scaling factors in Sotiropoulou et al. (2020), considering that the original value from Takahashi et al. (1995) overestimates the number of fragments as their experiments were conducted with hails. Although the upper limit is highly unlikely for ice and snow particles due to the excessive number of fragments it implies, it was retained to ensure that the default value remains sufficiently distant from the boundary of the parameter space, where emulator predictions are generally associated with greater uncertainties. The multiple OAT test (Section 3.4.3) and global sensitivity analysis (Appendix 3.7) were performed with the realistic range of E_{BR} from

2.8 to 280.

Compared to the parameterisation from Phillips et al. (2017), which is based on collision kinetic energy, our approach here is simplified and only considered the broad type II of collision with graupel. Such choice was made to avoid extra complexity for parameter perturbation of the ice-ice collision process and future work is recommended to investigate with the parametrization from Phillips et al. (2017) for a more comprehensive understanding of the role of ice-ice breakup.

3.3.2.5 E_{DS} (efficiency of the droplet shattering process)

During the freezing of large supercooled droplets, the pressure inside the freezing droplets increases which can lead to the breakup of the frozen droplets and ice crystal formation (Leisner et al., 2014). Our approach follows the droplet shattering parameterisation from Sullivan et al. (2018), in which the droplet shattering tendency is dependent on the number of fragments produced for each droplet shattering (E_{DS}), a temperature-dependent shattering probability (p_{DS}) and the Bigg droplet freezing rate (Bigg, 1953) (N_{Bigg}). The equation below shows the calculation of the number tendency of ice (N_{idps}) from the droplet shattering process. Details on p_{DS} can be found in Sullivan et al. (2018) and the Bigg droplet freezing in CASIM can be found in Field et al. (2023).

$$N_{\mathrm{idps}} = (1 + p_{\mathrm{DS}} E_{\mathrm{DS}}) N_{\mathrm{Bigg}} \tag{3.4}$$

The shattering probability was set to the same as the default one in Sullivan et al. (2018) with the shattering probability centred at -15 °C and the maximum probability set at 20%. E_{DS} was set to 5 in the control simulation with a perturbed range from 2 to 10 in the PPE design, following the sensitivity test values in Sullivan et al. (2018).

3.3.2.6 mpof (mixed-phase overlap factor)

When both ice and liquid clouds exist in the same model grid box, the mpof (mixed-phase overlap factor) is used for determining the extent to which ice and liquid co-exist in the same air in CASIM, which is important for mixed-phase processes (Field et al., 2023; Evans et al., 2025). We followed the naming of this parameter the same as in Field et al. (2023) and Evans et al. (2025) for consistency.

The mpof controls a function that quantifies the fractional overlap during the run time of the model rather than being a fixed value in a model grid box. When mpof is 1, the sub-grid liquid and ice cloud are maximally overlapped. When mpof is 0, the sub-grid liquid and ice are not overlapped as long as $CF_{\mathrm{liq}} + CF_{\mathrm{ice}} < 1$, where CF refers to cloud volume fraction in a model grid box. Once the combined cloud fraction

goes above 1, there will be overlap. For an mpof of 0, the overlap is minimised. Values of mpof in between lead to increasing overlap, but once either the liquid or ice cloud fraction reaches 1, then mixed-phase overlap is maximum whatever mpof is set to. See Section A.6 in the documentation of CASIM implementation in the UM from Field et al. (2023) for more information. The mpof was set to 0.5 in the control simulation with a perturbed range from 0 to 1 in the PPE design.

3.3.2.7 Parameter design of PPE members

The maximin Latin hypercube sampling method was used to generate random combinations of parameter values across the 6-dimensional space for PPE simulations. The ranges of each parameter are discussed above. The maximin design maximizes the minimum distances between the points in parameter space. Each PPE contains 66 members following the guidance from Loeppky et al. (2009) that at least 10 × n (where n is the number of parameters) simulations are required for training GP emulators. Two 6-member testing sets of simulations were also performed with parameter values from another maximin Latin hypercube sampling design. The testing simulations were used for assessing the performance of emulators trained with PPE output. The values of parameters in the testing simulations were different from the ones in the PPE simulations which were used for training the emulators. Figure 3.4 shows the PPE and testing set input values.

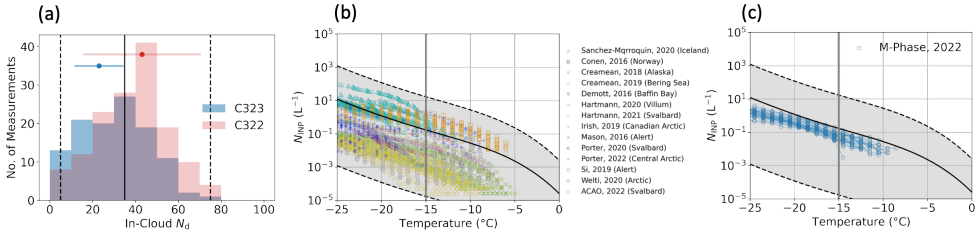


Figure 3.3: Comparison between the perturbed range and the measurements: (a) N_d with measured in-cloud N_d from M-Phase C322 and C323 using the CDP (cloud droplet probe) onboard, and N_d (mean ± one standard deviation) calculated based on retrievals from MODIS instrument onboard the Aqua satellite; (b) perturbed temperature-dependent N_{INP} ranges compared to INP measurements at high latitudes in the Northern Hemisphere (Sanchez-Marroquin et al., 2020; Conen et al., 2016; Creamean et al., 2018; Creamean et al., 2019; DeMott et al., 2016; Hartmann et al., 2020; Hartmann et al., 2021; Irish et al., 2019; Mason et al., 2016; Porter et al., 2020; Porter et al., 2022; Si et al., 2019; Welti et al., 2020; Raif et al., 2024); (c) perturbed temperature-dependent N_{INP} ranges compared to all INP measurements from the M-Phase campaign (Tarn et al., 2025). Boundaries of each perturbed range (maximum and minimum values) are shown with dashed black lines, and the values used for the control simulations are shown with solid black lines. Cloud top temperatures are around -15 °C for the CAO clouds in this case and -15 °C is marked with bold gray solid line in (b) and (c).

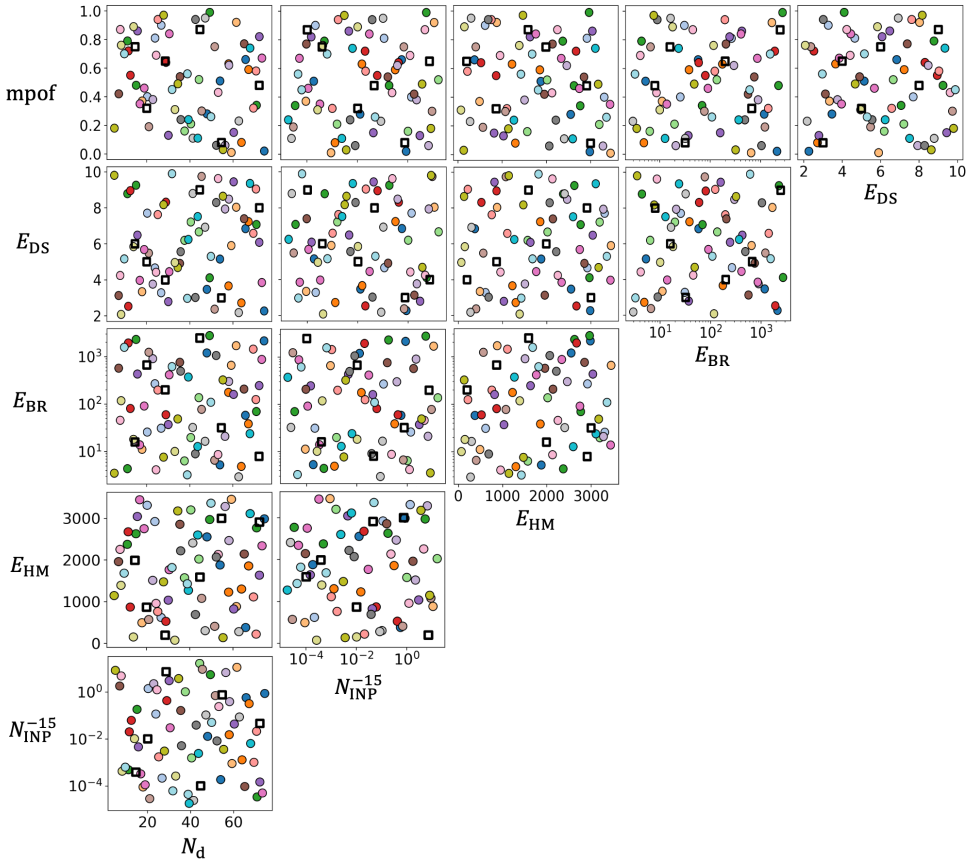


Figure 3.4: Paired combinations of parameters perturbed in this study. Colour filled circles are the 66 PPE members used for training the GP emulators, and the unfilled squares are the six testing members used for testing the trained GP emulators. Each colour suggests a set of parameter values. Results of kernel selection, validation and testing are shown in Appendix 3.3.

3.3.3 Gaussian Process (GP) emulators

Gaussian Process (GP) emulation is a non-parametric supervised machine learning method that learns the relationship between model input parameters and outputs of interest (Oakley et al., 2002; O'Hagan, 2006). GP emulators were constructed on the output from the PPE simulations and acted as a statistical "surrogate" model for the computationally-expensive numerical model. The GP emulators enabled efficient exploration of the entire parameter space with dense sampling, allowing for construction of multi-dimensional response surfaces and a variance-based sensitivity analysis to assess the importance of the perturbed parameters to the cloud variables. Detailed methodologies and explanations on building GP emulators for climate and atmospheric models can be found in Lee et al. (2011) and Johnson et al. (2015).

A GP emulator consists of a mean function and a covariance function, also called the kernel. To obtain a good GP emulator of each variable of interest we tested four commonly-used stationary kernels: the Radial Basis Function (RBF) kernel and three

Matérn kernels with different smoothness parameters: the Matérn12 kernel (0.5), the Matérn32 kernel (1.5) and the Matérn52 kernel (2.5), implemented in the GP Jax Python library for Gaussian processes (Pinder et al., 2022). When the smoothness parameter becomes infinite in a Matérn kernel, it becomes equivalent to the RBF kernel. For each variable, we conducted cross-validation by dividing the 66 PPE members into 11 sets with 60 training and 6 validation data points per set. The cross-validation was used here to maximise the use of our limited data due to the high computational cost of running the numerical simulations. Emulator performance was assessed with graphical diagnostics including individual standardized error plots and Q-Q plots following the guidance from Bastos et al. (2009), as well as the RMSE (root mean squared error) and R^2 (coefficient of determination). The kernel selection was mainly based on the RMSE values, with the Q-Q plots and R^2 for supporting the assessment. Once the best-performing kernel was selected for each variable, we trained the GP emulator with the best kernel on all 66 PPE members and tested it with the corresponding testing set. Appendix 3.3 describes and discusses the emulator performances from the kernel selection and testing steps, as well as the dependency of the RMSE on the different numbers of training points.

3.4 Results

3.4.1 Example response from PPE simulations: TOA albedo

Before analysing emulated response surfaces of domain-mean outputs in the next section, we first illustrate the strength of perturbing parameters in a PPE design and use TOA albedo here as an example in Figure 3.5. Note that the emulators (Section 3.4.2) define the relationship between input parameters and mean output variables (e.g., domain-mean albedo) and cannot describe the specific cloud patterns shown here, hence why we start by showing the results of some PPE members. We selected two parameters to demonstrate the PPE results: N_d and N_INP^{-15} for the Sc region, and N_d and mpof for the Cu region. These parameter pairs were chosen only for illustration because, as we show in Section 3.4.2, they have the strongest joint effects on cloud albedo in each region.

Figure 3.5 shows the maps of TOA albedo in 25 of the 66 PPE simulations over the two regions. The intervals between each PPE output are not equal in Figure 3.5 because of the Latin hypercube design method used for sampling the parameter space, and the subplots shown in Figure 3.5 are only ordered using the values of the selected parameters with the values of other four parameters ignored.

In both regions, the selected parameters jointly affect the TOA albedo. For example, in the Sc region (Figure 3.5a), low N_d and high N_INP^{-15} (top left subplot) result in the lowest TOA albedo, while high N_d and low N_INP^{-15} (bottom right subplot) result in the

highest TOA albedo. With PPE simulations, we can see clear joint effects of parameters on cloud properties. However, the number of simulations is too small to identify whether the joint effects are linear (combined effects) that could be predicted from combinations of OAT simulations, or non-linear (interactive effects) (Sansom, 2023). See Appendix 3.5 for a simple illustration of linear and non-linear joint effects between two parameters. Using the emulators enables a much denser sampling of the parameter space and, as we show in Section 3.4.2, exposure of non-linear effects (interactions) of combinations of parameters that are not apparent in Figure 3.5.

3.4.2 Emulated model response surface

The PPE members provide considerable information about cloud behaviour across the 6-D parameter space, but the data sparseness (just 66 points in 6-D space) limits our ability to visualise joint parameter effects or to perform statistical analysis. Therefore, we built emulators of temporally and spatially averaged cloud properties, which enable 6-D continuous response surfaces to be created. The time of averaging for variables (except the cloud top temperature) is from 12 UTC to 19 UTC, and the domains of averaging are shown as analysis domains in Figure 3.1. Cloud top temperature (CTT) is derived from the air temperature at the highest model level in a column with total cloud water content $\geq 10^{-6}$ kgkg^{-1}. The model output is taken at 14:00 UTC for the Sc region and 19:00 UTC for the Cu region, corresponding to the times of the M-Phase C322 and C323 flights respectively. An evaluation of modelled air temperature against aircraft measurements can be found in Huang et al. (2025, Chapter 2). The response surfaces were generated by predicting one million output values from the emulators across the parameter space.

Figure 3.6 shows the distributions of TOA albedo, cloud cover, all-sky LWP (liquid water path), all-sky IWP (ice water path), all-sky TWP (total water path) and CTT from one million combinations of parameters drawn from the GP emulators. By perturbing all 6 parameters in the Sc region, the TOA albedo ranges from 0.43 to 0.54 (inter-percentile range from 5% to 95%), cloud cover from 0.84 to 0.91, LWP from 74.5 g m^{-2} to 149.5 g m^{-2}, IWP from 0.0 g m^{-2} to 38.1 g m^{-2}, TWP from 97.6 g m^{-2} to 148.4 g m^{-2} and CTT from -12.3 °C to -11.2 °C. In the Cu region, the TOA albedo ranges from 0.37 to 0.44, cloud cover from 0.78 to 0.84, LWP from 47.9 g m^{-2} to 98.4 g m^{-2}, IWP from 71.3 g m^{-2} to 186.1 g m^{-2}, TWP from 147.8 g m^{-2} to 244.4 g m^{-2} and CTT from -11.0 °C to -9.3 °C.

Figures 3.7 and 3.8 show the joint effects of each combination of two parameters with the other parameter effects averaged for TOA albedo and all-sky LWP, which are two key properties for cloud-phase feedback, respectively over the two selected regions. These are known as “paired projections”. Paired projections for cloud cover, all-sky IWP, all-sky TWP and CTT are shown in Appendix 3.6. The values shown on the

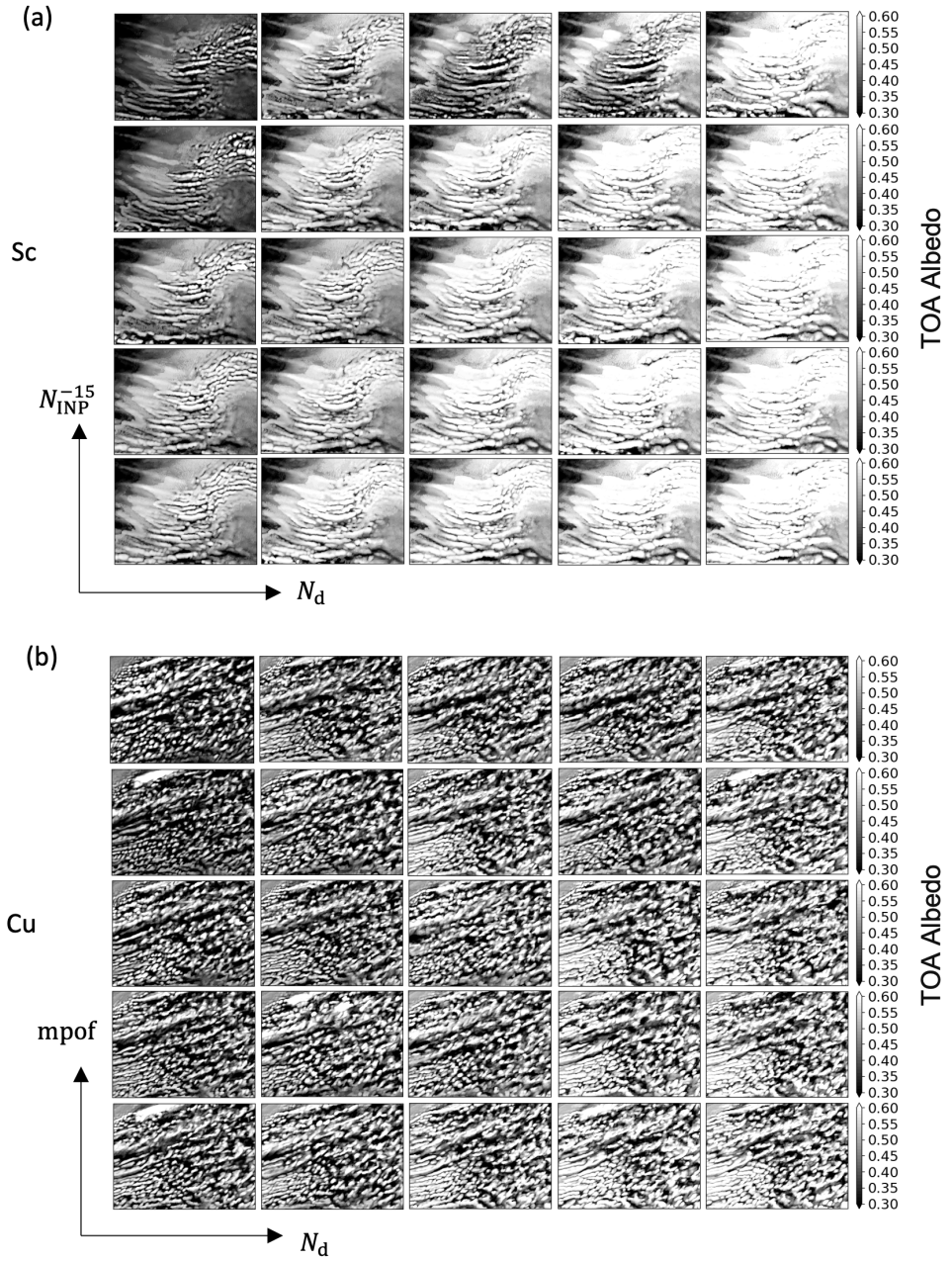


Figure 3.5: Responses of TOA albedo for maps of (a) the Sc region ordered according to N_{d} and N_{INP}^{-15} and (b) the Cu region ordered according to N_{d} and mpof. The selected model output time is 16:00 UTC. The selected domains are the same as the regions shown in Figure 3.1. Note that each image shows a different simulation, and only 25 out of the 66 PPE parameters are shown here. Because of the Latin hypercube design method used for sampling the parameter space, the subplots shown here are only ordered using the values of the selected two parameters with the values of other four parameters ignored and the intervals between of these subplots for each parameter are not the same.

paired projection plots are calculated by averaging over the other four dimensions, and therefore describe the mean response of each variable to each paired parameter set.

Using the paired projections, we are able to qualitatively identify key parameters controlling the cloud properties over the parameter space in this CAO event. In the Sc region, N_{d} and N_{INP}^{-15} exert the strongest effects on TOA albedo and LWP. All parameters from SIP processes and mpof only show weak effects across the projections due to the liquid-dominated nature of these clouds, demonstrating limited effects in the Sc region. In the Cu region, N_{d} maintains its strong influence on TOA albedo and LWP, while the second strongest effect is now from varying mpof. The perturbation of mpof now results in a stronger effect on cloud properties compared to in the Sc region and to N_{INP}^{-15} in the Cu region. A reduction in mpof leads to less interactions of liquid and ice particles, which weakens the removal of liquid water through accretion. The increasing effect from mpof in the Cu region compared to in the Sc region comes from an increasing ice formation in Cu clouds when the cloud top deepens and more mixing between ice and liquid hydrometeors. The effects from mpof in the Sc region are also limited by a large liquid cloud fraction with little ice cloud fraction, as the extent to which liquid and ice interacts in a model grid box is not just determined by mpof but also cloud fraction.

All three SIP parameters have a relatively weak effect on TOA albedo and LWP in both Sc and Cu regions in this case, even though the cloud temperature covers most of the active temperature range of the HM process. Note that a low sensitivity does not imply that SIP is unimportant, only that the cloud properties are fairly insensitive to its precise value. Although the influences from varying SIP processes on albedo and LWP are small in both regions, the effect of each parameter is specific to this case study and is not representative of all mixed-phase CAO clouds. The HM process has a much stronger effect on IWP and TWP in the Cu region (Appendix 3.6), but such influence is weakly transferred to the radiative properties (TOA albedo). When ice formation processes are stronger (e.g., a higher N_{INP}^{-15} or E_{HM}), the reduction in cloud liquid is less than the increase in cloud ice, leading to a net increase of total water path (Figure A3.11). This is because the increase of IWP is not only from the direct conversion of liquid to ice, but also a stronger vapour deposition onto ice compared to liquid at the same temperature.

The influences of N_{INP}^{-15} and mpof on TOA albedo are weaker compared to their influences on LWP in both regions. This is because perturbing N_{d} alters cloud albedo both directly via the Twomey effect (reduced effective radius at fixed liquid water path), and indirectly via adjustments to liquid water path and cloud fraction. As a result, the effect of perturbing N_{INP}^{-15} and mpof on TOA albedo becomes smaller than their effects on LWP. There are also non-monotonic responses of LWP to the perturbation of N_{INP}^{-15} at lower N_{INP}^{-15} values in the Sc region. An increase in N_{INP}^{-15} does not lead to a monotonic decrease in LWP; instead, LWP initially increases with increasing N_{INP}^{-15}, followed by a decrease at higher N_{INP}^{-15}. This may be because the removal of liquid

through warm rain processes is first reduced when increasing N_{INP}^{-15} as the amount of liquid is reduced, hence leading to a higher LWP; but with further increases in INPs, the removal of liquid is then dominated by the mixed-phase processes rather than the warm rain processes, hence leading to a lower LWP eventually. One can also see that, as N_{d} increases, the warm rain processes reduce due to less rain autoconversion, and the value of N_{INP}^{-15} required to let mixed-phase processes start dominating the water removal process (where the increasing LWP becomes decreasing LWP with increases in INP) decreases. To further test this, one can compare different model response surfaces between N_{d} and N_{INP}^{-15} with and without the warm rain and cold rain processes.

In this CAO case, CTT is strongly controlled by N_{d} in both regions, with stronger effects from N_{INP}^{-15} and mpof in the Cu region. SIP processes have limited influences on CTT in both regions. A reduction in N_{d} or an increase in N_{INP}^{-15} leads to a higher (warmer) CTT, and hence a shallower vertical development of clouds. Both the reduction of N_{d} and the increase of N_{INP}^{-15} can lead to an enhancement of precipitation, as shown in our previous work (Huang et al., 2025, Chapter 2) for this CAO case. This response of CTT to the change of precipitation is consistent with previous work from Tornow et al. (2021) on CAO clouds, which show that enhancement of precipitation can stabilise the boundary layer during CAO event and lead to less vertical development of clouds. The limited cloud vertical development from a high N_{INP}^{-15} can also prevent the effects of converting liquid to ice, as the INP concentration is temperature-dependent.

For most of the paired projections, non-linear joint effects (interactions) of the parameters on the cloud properties can be identified. Here we use the projections between N_{d} and N_{INP}^{-15} in the Sc region and the ones between N_{d} and mpof in the Cu region as examples. Parameter interactions are apparent when the sensitivity of a cloud property to a parameter perturbation depends on the value of another parameter - i.e., the number of contours across for the same change of a parameter differs when the value of another parameter changes. Using LWP in the Sc region as an example, by perturbing N_{d} from low to high values and keeping N_{INP}^{-15} low (less than 0.01 L^{-1}), the LWP ranges from approximately 90 $\mathrm{g\,m^{-2}}$ to 140 $\mathrm{g\,m^{-2}}$; if the N_{INP}^{-15} is high (more than 1 L^{-1}), the LWP ranges approximately from 70 $\mathrm{g\,m^{-2}}$ to 95 $\mathrm{g\,m^{-2}}$. In the Cu region, the LWP ranges from 70 $\mathrm{g\,m^{-2}}$ to 90 $\mathrm{g\,m^{-2}}$ for low to high N_{d} values when mpof is low (less than 0.2), but from 50 $\mathrm{g\,m^{-2}}$ to 60 $\mathrm{g\,m^{-2}}$ when mpof is high (more than 0.6).

Another example of parameter interactions is that the local sensitivity of a parameter can vary across the parameter space. In the Sc region, the LWP is insensitive to N_{INP}^{-15} when N_{d} is lower than approximately 20 cm^{-3} and N_{INP}^{-15} less than 0.1 L^{-1}, while it becomes very sensitive to N_{INP}^{-15} when N_{d} is higher than approximately 50 cm^{-3}. The relative importances of SIP processes and mpof in the Sc region also depend on the values of N_{d} and N_{INP}^{-15}, despite the perturbations of SIP parameters and mpof hav-

ing limited effect on cloud radiative properties in this region. When N_{d} is higher than about 40 cm^{-3} or N_{INP}^{-15} lower than 0.01 L^{-1}, the influence on LWP is strongly enhanced by SIP processes and mpof. It is worth noting that the effects of SIP processes and mpof on LWP are still quite small, so although they strongly affect the change in LWP in that part of the parameter space, their importance over the whole parameter space is small compared to N_{d} and N_{INP}^{-15}. Such interdependency between the parameters shows that a single OAT test is insufficient to draw conclusions about the importance of a parameter or a process, and the results from the OAT test are highly dependent on the default values of the parameters in the control simulation.

Figures 3.6–3.8 also show that different combinations of parameter values may result in the same value of cloud properties, which is called equifinality (Beven, 2006; Lee et al., 2016; Carslaw et al., 2026). For example, the mode TOA albedo in the Sc region is 0.54, meaning a large number of model variants with different parameter values produce the same albedo of 0.54. The equifinality is also visible in the filled contour plots in the paired projections shown in Figures 3.7 and 3.8 - each contour colour defines parameter combinations that produce equifinal model output. Equifinality becomes important when model output is compared to observations, because model output from different combinations of parameters will agree equally well with observations. Perturbing each parameter individually to match observations may fall into the problem of equifinality because it would result in a single and overly confident estimate of a parameter value rather than a range. Here we use TOA albedo as an example. The observed, domain-mean TOA albedo from CERES onboard the Aqua satellite is around 0.48 in the Sc region and around 0.39 for the Cu region at 17:00 UTC. There are more than 70,000 model variants out of the 1 million model variants that produce this value of TOA albedo ($\pm$ 0.005) in the Sc region, and more than 90,000 model variants in the Cu region. There would also be many more equifinal variants when accounting for observation uncertainty. Such equifinality problem suggests that using a single variable to constrain the parameter space is not sufficient, and multiple variables for different cloud properties are needed. A key question is whether there exists a single part of parameter space for which all the variables agree well with observations, which will be shown in our subsequent paper comparing the PPE simulations shown in this work with multiple observations (*in-situ* and satellite).

3.4.3 Dependence of individual parameter sensitivities on other parameters

The response surfaces in the previous section show that the sensitivity of cloud properties to a change in a parameter depends strongly on the setting of the other parameters. However, these paired projections neglect variations in the other four parameters and therefore only present the mean response of each model variable to each paired param-

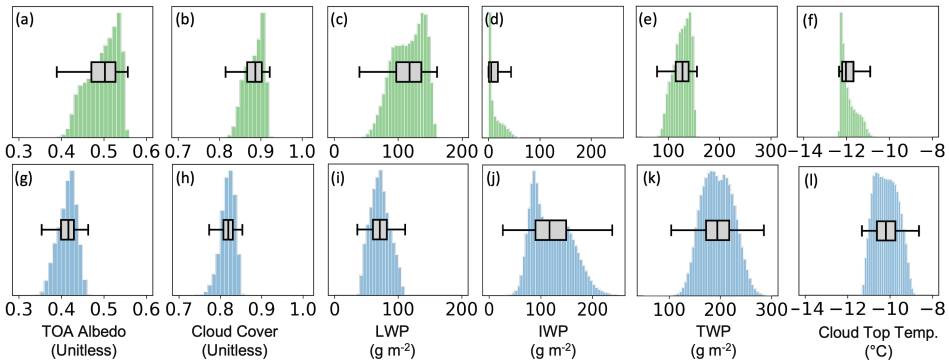


Figure 3.6: Distributions of cloud variables from 1 million combinations of parameter values for (a,g) all-sky TOA albedo (unitless), (b,h) cloud cover (unitless), (c,i) all-sky LWP ($\mathrm{g\,m^{-2}}$); (d,j) all-sky IWP ($\mathrm{g\,m^{-2}}$), (e,k) TWP ($\mathrm{g\,m^{-2}}$) which is the sum of LWP and IWP, and (f,l) cloud top temperature (°C). Separate distributions are shown for the Sc (top row) and Cu (bottom row) regions.

eter set. Therefore, to understand how much the sensitivities of cloud properties vary within the parameter space, we present the results from multiple OAT tests across the parameter space in Figure 3.9.

We performed a large number OAT tests using the trained GP emulators for each model variable with different starting points. To design the starting points, three values were selected for each parameter: low (25% of the perturbed range), mid (50% of the perturbed range), and high (75% of the perturbed range). For N parameters each with M values, the number of possible parameter combinations are M^N. Hence, there were 729 starting points (control sets of parameter values) across the 6-D parameter space in the multiple OAT tests. For each OAT test, the parameters were perturbed to the high-end (95% of the perturbed range) and the low-end (5% of the perturbed range) individually. The responses of cloud properties were the change from high-end parameter value output to the low-end parameter value output. The perturbed ranges in the multiple OAT tests were smaller than the perturbed parameter range in the PPE design to avoid the high uncertainties of emulators near boundaries of the parameter space. As for each parameter, we perturbed the value from low-end to high-end without directly including the emulator output from the control simulation, the number of output points from the emulator for each variable is $2 \times M^{N-1}$. Therefore, for each model variable in one domain (one subplot in Figure 3.9), the total number of investigated model variants is 2916. A compact distribution in Figure 3.9 means that the sensitivity of the cloud property to that parameter is not strongly dependent on the setting of the other parameters.

The magnitudes of cloud responses to individual parameter perturbations are sometimes strongly dependent on the values of other parameters. For example, in the Sc region, the increase in LWP (Figure 3.9e) by perturbing N_d from low to high values

ranges from +31 $\mathrm{g\,m^{-2}}$ to +65 $\mathrm{g\,m^{-2}}$, and the decrease in LWP by perturbing N_{INP}^{-15} from low to high values ranges from -73 $\mathrm{g\,m^{-2}}$ to -29 $\mathrm{g\,m^{-2}}$. In the Cu region, the decrease in LWP (Figure 3.9f) by perturbing mpof from low to high values ranges from -39 $\mathrm{g\,m^{-2}}$ to -15 $\mathrm{g\,m^{-2}}$. Although the projection plots suggest clouds are not very sensitive to variations of SIP processes, the multiple OAT tests here show that in some parameter space, varying SIP processes can have same or even stronger effects on cloud cover, IWP and TWP in the Cu region than N_{d} and N_{INP}^{-15}. In addition, due to the existence of dominant parameters across the parameter space (e.g., N_{d}), the effects from SIP processes may be obscured through averaging in the paired projections. The relative importance of each parameter across the parameter space can also be quantitively compared by using the statistics of the sensitivities from the multiple OAT test (e.g. mean or mode), which shows similar results to those from a global sensitivity analysis in Appendix 3.7. Similar to the other variables discussed above, parameter interactions are also identified here for CTT, particularly in the Cu region. Across different parts of the parameter space, an increase in N_{d} can reduce CTT from about -0.5 °C to nearly -2 °C in the Cu region. An increase in N_{INP}^{-15} can lead to an increase in CTT ranging from nearly 0 °C to about +1.5 °C. This dependence of individual parameter sensitivities on other parameters indicates that these parameters also jointly affect cloud vertical development in CAO clouds and may therefore influence cloud field evolution, such as the transition from stratocumulus to cumulus. It is therefore important to explore the full parameter space when assessing the effects of aerosols and ice-production processes on cloud evolution during CAO events.

The direction (or sign) of the cloud response can also depend on the control values of the parameters. For example, changes in SIP parameters in this case can cause either increases or decreases in cloud cover (Figures 3.9c and 3.9d) depending on the other parameters (primarily N_{d} and N_{INP}^{-15} which dominate the sensitivities). In the Cu region, increasing N_{INP}^{-15} does not consistently lead to a reduction of the TOA albedo (Figure 3.9b). For most OAT tests with N_{INP}^{-15} perturbations, increasing N_{INP}^{-15} causes cloud cover to increase (Figure 3.9d), but also leads to a reduction in LWP (Figure 3.9f). These two effects compensate each other for the effect of increasing N_{INP}^{-15} on TOA albedo. Therefore, the influence from a high N_{INP}^{-15} on TOA albedo in Cu region is controlled by multiple cloud properties, and these cloud properties can have different responses to changing N_{INP}^{-15} at different part of the parameter space.

In summary, the sensitivities of modelled cloud properties to each individual perturbed parameter depend on the starting point in the parameter space; this includes both the magnitudes and sign of responses. Results from our multiple OAT tests across the parameter space demonstrate that using a single OAT test is inadequate for determining the magnitude and even sign of the cloud response to model parameters. It is therefore important to investigate the whole parameter space for a more comprehensive

understanding of the effects from these parameters.

3.5 Discussion and Conclusions

We present here the first analysis of mixed-phase CAO cloud responses to combinations of six key cloud microphysics parameters related to aerosol-cloud interactions and ice formation processes. The perturbed ranges of these parameters either match the observed ranges when available, or were chosen based on uncertain ranges suggested by previous studies. The full 6-dimensional parameter space of cloud responses was explored using PPEs, GP emulators, and multiple OAT tests across the whole parameter space. The properties we investigated included all-sky TOA albedo, all-sky LWP, cloud cover, all-sky IWP and all-sky TWP, which are key properties that influence the radiative effects of mixed-phase clouds (Ceppi et al., 2017). Model simulations were based on a CAO event case over the Labrador Sea on 24 October 2022, focused on Sc and Cu cloud regimes and covering the routes of two research flights from the M-Phase aircraft campaign (Murray et al., 2024; Clarke et al., 2025).

In this CAO case, where the liquid phase dominates with cloud top temperatures of around -15 °C, N_d exerts the strongest controls on TOA albedo and LWP in both regions with the Twomey effect (Twomey, 1977) and the Albrecht effect (Albrecht, 1989). The effects of N_d on mixed-phase CAO clouds in these simulations are also consistent with previous simulations from de Roode et al. (2019) who reported that higher N_d leads to a higher LWP and cloud cover, and vice versa. However, we further show that the effect of changing N_d varies strongly across the parameter space. Perturbing N_d from low to high in different parts of the parameter space leads to TOA albedo responses ranging from +0.08 to +0.11 and LWP responses ranging from +31 $\mathrm{g\,m^{-2}}$ to +65 $\mathrm{g\,m^{-2}}$ in the Sc region, and TOA albedo responses ranging from +0.02 to +0.07 and LWP responses ranging from near-zero (+2 $\mathrm{g\,m^{-2}}$) to +24 $\mathrm{g\,m^{-2}}$ in the Cu region. Thus, although the effect of N_d on albedo and LWP are dominating, there are strong variations depending on other parameters. Such variation demonstrates the importance of performing simulations across a joint parameter space to avoid incomplete conclusions or overly confident estimates of sensitivities.

An increase in N_INP^{-15} leads to a reduction in TOA albedo and LWP in the Sc region in this case, which is consistent with the results from previous studies on the influences of different INP concentrations (Tornow et al., 2021) or ice treatment in models (Abel et al., 2017). However, the sampling of parameter space using PPEs and emulators shows that the magnitude and even sign of response to N_INP^{-15} perturbations depends on the setting of other parameters, even within the single environment represented by the case we studied. It is seen in the Sc region that the modelled TOA albedo is not sensitive to N_INP^{-15} when N_d is low (less than approximately 20 $\mathrm{cm^{-3}}$). A similar weak

sensitivity of clouds to changes in N_{INP}^{-15} was found by the study from McCluskey et al. (2024) over the Southern Ocean, where they found that the modelled IWP was relatively insensitive to the representation of INP under low N_{d} condition. It is shown that their model underestimates CCN concentration (Niu et al., 2025) over the Southern Ocean, which could account for the weak INP sensitivity consistent with our results. We also find that in the Cu region, the sensitivity of clouds to N_{INP}^{-15} is relatively weaker and the sign of the cloud response as a function of N_{INP}^{-15} varies over the parameter space. For example, an increase in N_{INP}^{-15} can lead to both increases and decreases of TOA albedo (from -0.02 to +0.03) and cloud cover (from -0.02 to +0.08) when the values of other parameters are changed. The pronounced variation in the modelled cloud sensitivity to INP concentrations highlights the importance of having good representations of other microphysical processes in the model and the necessity of a full exploration of the parameter space, including other cases, to understand the role of INPs in mixed-phase CAO clouds.

Our results show that, for this CAO case, N_{d} and N_{INP} strongly control the radiative properties of mixed-phase clouds in the Sc region, but with large uncertainty in the sensitivities depending on other poorly quantified model parameters. The strong sensitivity of this CAO case to changes in N_{d} highlights the importance of accurately representing and treating CCN in models in order to better simulate mixed-phase CAO clouds. Our results also show that cloud sensitivities to N_{d} can depend on N_{INP}. Because measurements of INP concentrations are sparse and cannot be obtained from satellite retrievals or other remote-sensing observations, the sensitivity of clouds to CCN can remain difficult to constrain without knowing INP concentrations. Improved temporal and spatial coverage of INP measurements is therefore also needed to better constrain the properties and sensitivities of mixed-phase CAO clouds, together with improved representation of INPs in atmospheric and climate models.

The SIP parameters generally have a weak effect on the radiative properties (TOA albedo) of the studied CAO clouds. Our results on the effect from SIP processes on LWP are generally consistent with previous work from Karalis et al. (2022) who showed that an enhancement of SIP can lead to the reduction of LWP. However, we show that the magnitude of LWP (and other cloud properties) responses to perturbations of all three SIP parameters vary across the parameter space, with strong dependency on the other parameters such as N_{d} and N_{INP}^{-15}. Compared to the results from Karalis et al. (2022), the relative importance of each of the SIP processes differs between our study and theirs. In Karalis et al. (2022), the droplet shattering process was more effective than the Hallett-Mossop process in the Cu region, while the Hallett-Mossop process exerts stronger effects on LWP in our case. Such differences may occur because the environmental conditions vary between cases, which will affect the efficiencies of SIP processes. In addition, Karalis et al. (2022) used alternative parameterisations for the

droplet-shattering and ice-ice breakup processes which follow Phillips et al. (2017). Therefore, it is worth noting that our conclusions are potentially specific to this CAO case and may be dependent on the CAO case being simulated, and may be influenced by the model setup or choice of parameterisations.

The influence of mpof in this case is more prominent in the Cu region where an increase in mpof leads to a reduction in LWP and cloud cover, and therefore a lower TOA albedo. These responses of cloud properties to changes in the mpof value are similar to the results from Abel et al. (2017). However, the sensitivity of LWP as a function of mpof in our work is weaker in the Sc region than seen in Abel et al. (2017) where they also modified the cloud liquid and ice overlap. Although our case here has similar cloud temperature as the case investigated in Abel et al. (2017), the overlap parameter used in their work is from the bulk cloud scheme, while the mpof in our work is within the cloud microphysics scheme. This suggests that different model setups can also lead to potentially different sensitivities of cloud properties to the parameters. Similar to the other parameters, the effect from mpof on the investigated cloud properties vary across the parameter space and interactively affect the influence of the other parameters.

We expect the large, non-linear joint effects of cloud microphysical parameters on CAO clouds will be a feature of CAOs in other meteorological environments, but the sensitivities are likely to vary. By limiting our analysis to a single case study, we are able to fully explore the sensitivity of the CAO clouds to six key parameters without the confounding effects of environmental conditions. The sensitivity of mixed-phase CAO clouds to the parameters investigated here may be substantially different in a different CAO event. For example, in previous work we showed that the sensitivities of mixed-phase CAO clouds to INP concentration can differ in magnitude and sign between warm and cold cases (Huang et al., 2025, Chapter 2). Previous studies have shown that CAO cloud properties depend strongly on environmental conditions (Fletcher et al., 2016b; McCoy et al., 2017; Wu et al., 2022; Murray-Watson et al., 2023), including factors such as CAO strength and wind conditions. This environmental dependence is likely to modify CAO cloud sensitivities to the parameters examined here. Future work should therefore investigate how different environmental conditions influence CAO clouds and how those influences interact with key cloud microphysical parameters.

In this first PPE study of a high-resolution regional model of mixed-phase clouds, we have made several simplifying assumptions in the cloud microphysics processes, including the use of fixed N_{d} and temperature-dependent N_{INP}, rather than aerosol-interactive CCN and INP. This choice was made to reduce the complexity of the model result interpretation and to have a direct understanding of N_{d} and N_{INP} interactions which is the main objective of this study. However, this approach omits several potentially important processes, including interactions of aerosols and cloud hydrometeors,

feedbacks associated with aerosol and in-cloud processing of CCN and INP, and the influence of different aerosol sources. These processes could alter the sensitivities of CAO clouds to aerosols and to other microphysical parameters. Future work should therefore include aerosol-interactive CCN and INP in order to provide a more complete representation of aerosol effects and their interactions in mixed-phase CAO clouds. In addition, our analysis does not include all potentially important parameters and processes, such as boundary-layer mixing (Field et al., 2014) and cloud fraction schemes (cloud macrophysics) (Van Weverberg et al., 2023). Future studies should extend the analysis to include these additional parameters in order to provide a more comprehensive quantification of uncertainty in CAO cloud properties.

To conclude, this work illustrates the power of using PPEs and model emulation for systematically identifying important non-linear joint effects of multiple cloud microphysical parameters on mixed-phase CAO clouds. These interactions of parameters cannot be revealed using single OAT tests, which may therefore lead to misleading or overly confident estimates of the key factors controlling mixed-phase CAO cloud properties. Exploration of the entire parameter space is necessary to fully understand the influences on CAO clouds from these uncertain model parameters, and to constrain the effect of the uncertainties on the estimation of cloud-phase feedback.

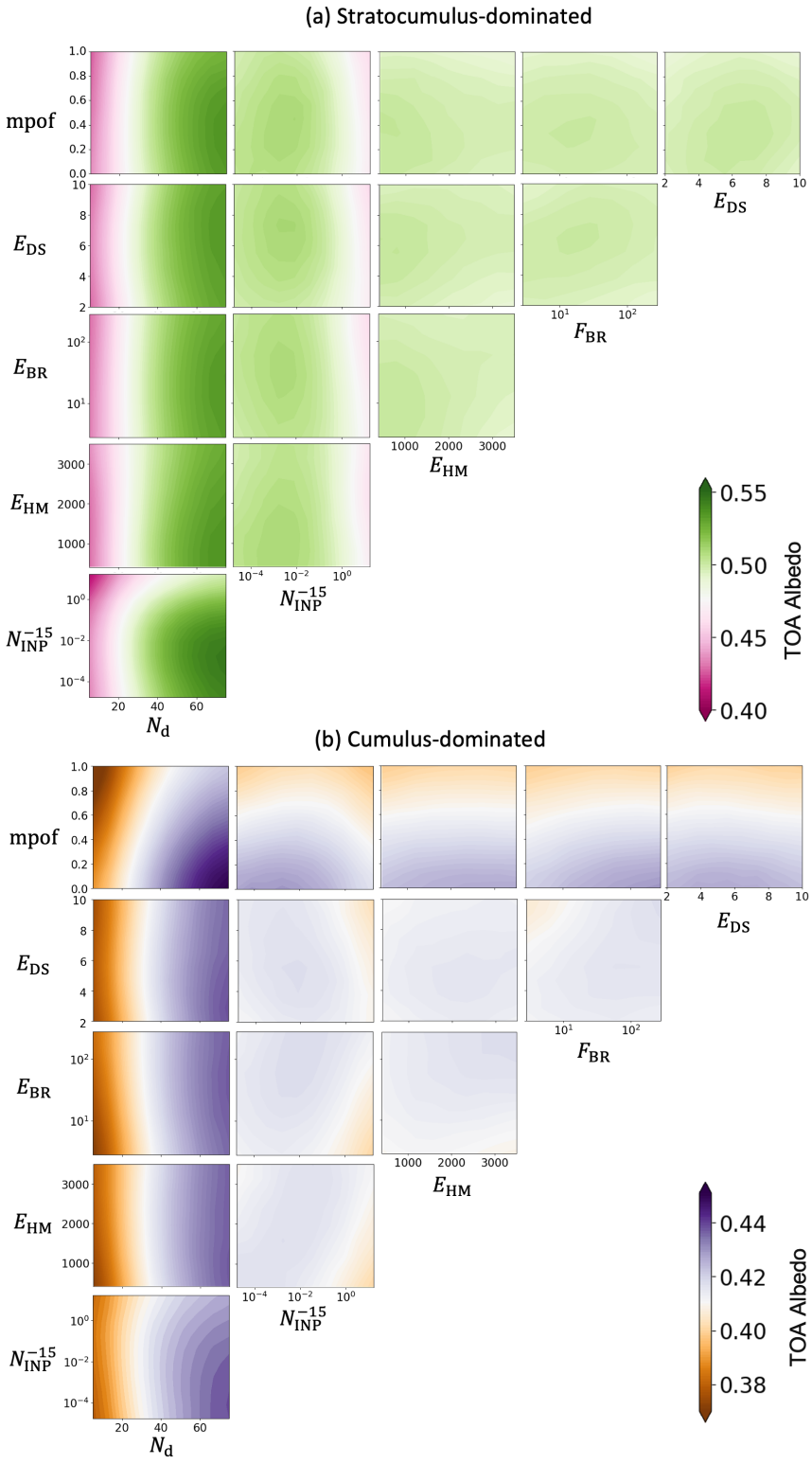


Figure 3.7: Emulated mean model responses of all-sky TOA albedo to paired parameters in (a) the Sc region and (b) the Cu region. The values shown on the paired projection plots are calculated by averaging over the other four dimensions, and therefore describe the mean response of each variable to each paired parameter set.

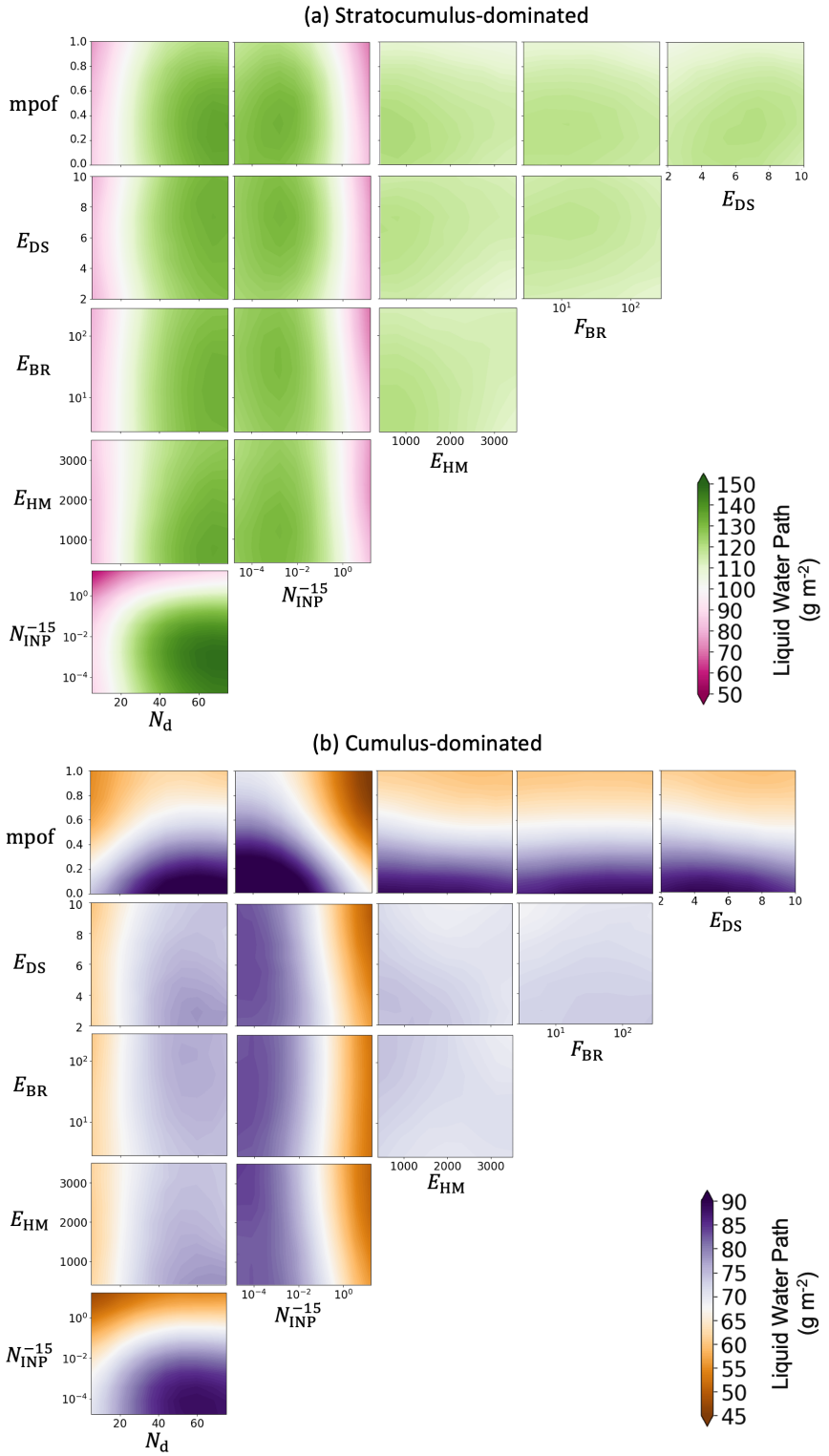


Figure 3.8: Emulated mean model responses of all-sky LWP to paired parameters in (a) the Sc region and (b) the Cu region. The values shown on the paired projection plots are calculated by averaging over the other four dimensions, and therefore describe the mean response of each variable to each paired parameter set.

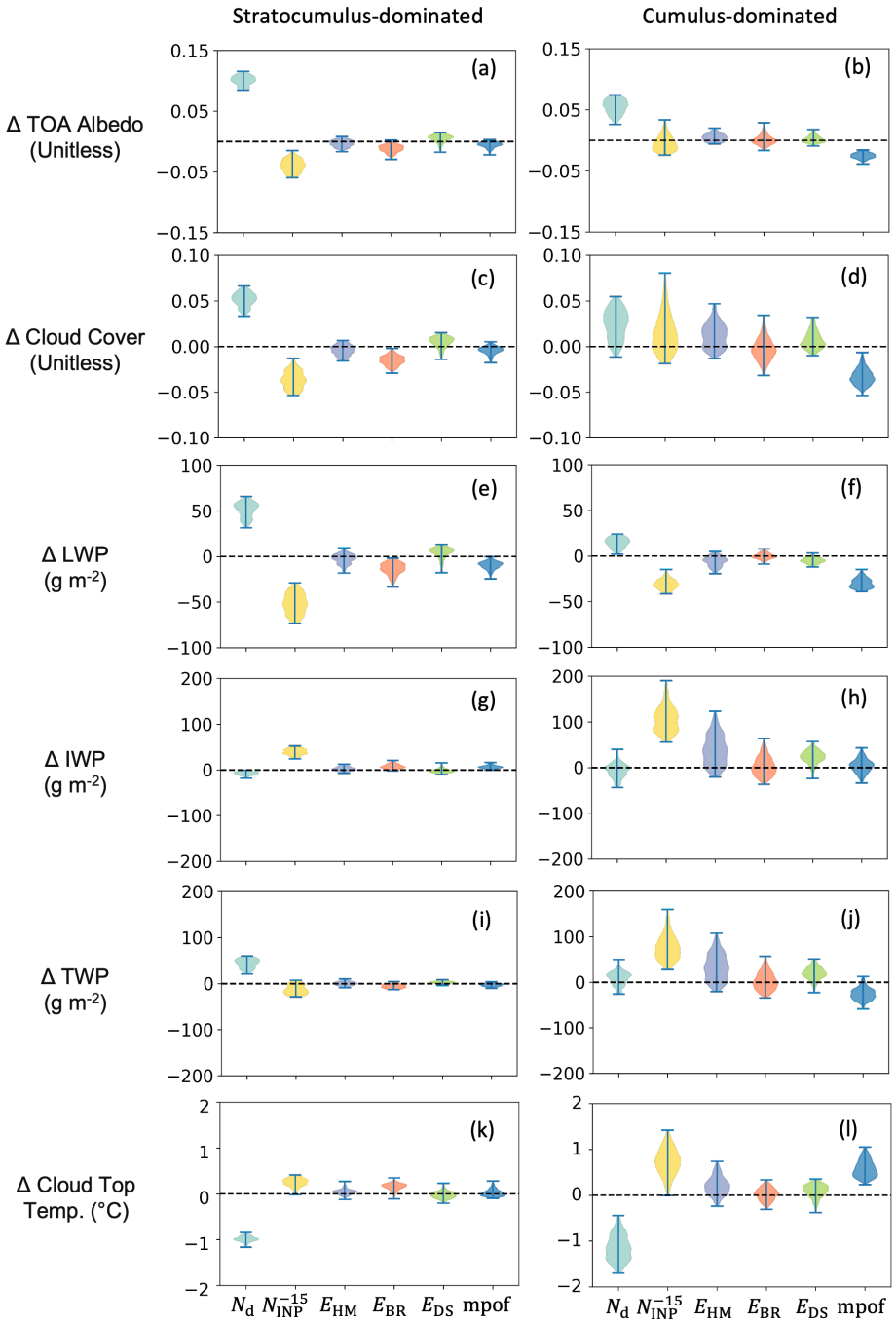


Figure 3.9: Distributions of the cloud property changes resulting from an increase of individual parameters one-at-a-time (OAT) in multiple OAT tests for: all-sky TOA albedo (a, b), cloud cover (c, d), all-sky LWP (e, f), all-sky IWP (g, h), all-sky TWP (i, j) and cloud top temperature (k, l). The left panel shows the results from the Sc region, and the right panel shows the results from the Cu region. Errors of the GP model are propagated through into these multiple OAT test results, but the errors are generally much smaller than the variations shown here (Appendix 3.3). For the process of performing the multiple OAT test, please refer to the details in Section 3.4.3.

Appendix

A3.1 Deriving a new $n_s(T)$ parameterisation for soil dusts

A recent study by Herbert et al. (2025) has shown that the ice-nucleating ability of dust in the atmosphere is influenced by a mineral component and a biogenic component associated with the surface area of the dust. The authors suggest that soil dusts that have come from arid, desert-like, environments are best represented by the mineral component alone, whereas dusts from biologically productive regions are best represented by the inclusion of both components. The authors refer to these two classes of soil dusts as *desert soils* and *fertile soils*, respectively. Some parameterisations that are commonly used to represent INP concentrations in modelling studies (e.g., Harrison et al., 2019) only account for the mineral component, and therefore may only be representative of desert soils. Here, we present a new empirical parameterisation for the ice-nucleating activity of fertile soils, which is likely more representative of INP measurements in the mid- to high latitudes (Herbert et al., 2025).

Laboratory measurements of soil-dust ice nucleating activities were collated from literature (Barr et al., 2023; King, 2024; O'Sullivan et al., 2014; Paramonov et al., 2018; Porter et al., 2020; Sanchez-Marroquin et al., 2020; Steinke et al., 2020; Thompson, 2024; Steinke et al., 2016). These are studies that have tested the untreated properties of soil dusts that have been sampled in situ or collected from the surface. We purposefully omit measurements from desert soil sources, such as the Sahara desert.

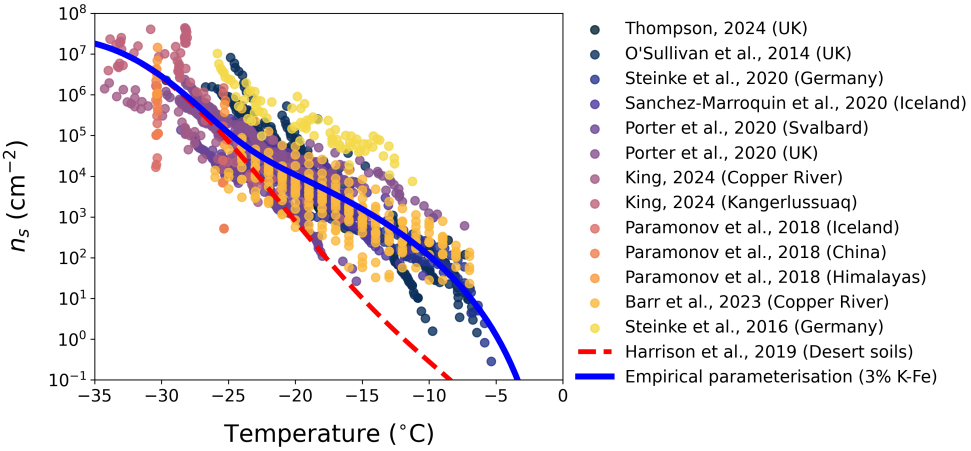


Figure A3.1: Empirical soil-dust parameterisation of $n_{s,\mathrm{soil}}(T)$. Coloured circles show measurements from laboratory studies (references within figure) that have measured the ice-nucleating activity of soil dust sampled from locations around the world. The red dashed line shows the parameterisation for desert soils from Harrison et al. (2019), whilst the solid blue line shows the best fit to the data assuming a K-Fe component (weight percent of 3 %) and a biogenic component described by a power law.

We use the measurements to produce an empirical parameterisation which consists

Table A3.1: Polynomial coefficients used in Eq. A3.1. Values are taken from Harrison et al. (2019).

Polynomial coefficient	**Value**
P_1	-3.25
P_2	-0.793
P_3	-6.91×10^{-2}
P_4	-4.17×10^{-3}
P_5	-1.05×10^{-4}
P_6	-9.08×10^{-7}

of two additive functions, accounting for the two components. For the mineral component, we use a parameterisation from Harrison et al. (2019) that is dependent on the potassium-feldspar (K-Fe) present in the dust (shown separately in Figure A3.1). We use a constant K-Fe content (f_{KFe}) of 0.03, which is representative of a global-mean value (Harrison et al., 2019). For the biogenic component, we use the power law $n_s(T) = -kT^{\alpha}$, which provides a shape consistent with measurements of n_s at high temperatures (Figure A3.1). The variables α and k were systematically varied until the root-mean square error between the measurements and summed contributions of the two functions was minimized. The resulting parameterisation of $n_{s,\mathrm{soil}}(T)$ in cm^{-2} is shown in Figure A3.1, and described by the function

$$n_{s,\mathrm{soil}}(T) = (-kT^{\alpha}) + 10^{(P_1+P_2T+P_3T^2+P_4T^3+P_5T^4+P_6T^5)} f_{\mathrm{KFe}}, \tag{A3.1}$$

where $k = 3.907 \times 10^{-5}$, $\alpha = 6.531$, and the values of P_1 to P_6 are shown in Table A3.1. The temperature T is in °C.

A3.2 Simulated aerosol size distributions during M-Phase

In this section, we produce an INP parameterisation that is representative of the location and time period of the M-Phase campaign. We apply the new $n_{s,\mathrm{soil}}(T)$ parameterisation from Eq. A3.1 to simulated dust concentrations and the marine INP parameterisation ($n_{s,\mathrm{SSA}}(T)$) from McCluskey et al. (2018) to simulated sea-spray aerosol (SSA) concentrations. The concentrations are simulated using a global configuration of the Met Office Unified Model (Brown et al., 2012) version 12.1 which includes Global Atmosphere version 8.0 and Global Land model version 9.0 (Willett et al., 2020). The configuration we use is described in detail by Jones et al. (2022) with the addition of dust in a super-coarse aerosol mode. The emission, advection, and removal of aerosol is simulated by the UK Chemistry and Aerosol (UKCA-mode) model (Mann et al., 2010) which includes a prognostic two-moment aerosol microphysics scheme. In this configuration of UKCA-mode, aerosol components (SSA, sulphate, black carbon, organic carbon, and dust) are represented by log-normally distributed aerosol modes. SSA is present in the accumulation and coarse modes. Dust is present in the accumulation, coarse, and super-coarse modes. Global dust emission parameters ($\mathrm{horiz_d}$, $\mathrm{us_{am}}$, and $\mathrm{sm_{corr}}$) were tuned to global observations of dust aerosol optical depths, dust size distributions, surface dust concentrations, and dust deposition fluxes (Woodward et al., 2022). The resulting values are $\mathrm{horiz_d} = 6.0$, $\mathrm{us_{am}} = 1.45$, and $\mathrm{sm_{corr}} = 0.7$.

A simulation was run from 2018 to 2024, with U and V wind components above the boundary layer nudged to 6-hourly ERA5 reanalysis, and sea surface properties and fluxes represented by observed climatologies of sea surface temperature and sea ice content. The simulated SSA and dust aerosol size distributions were extracted for a region (62.8°W – 51.6°W, 53.1°N – 60.6°N) and time period (23/10/22 – 5/11/22) consistent with the M-Phase campaign. The INP number concentration (N_{INP}) is calculated at each temperature T and in each aerosol size bin i following the singular description (Murray et al., 2012; DeMott et al., 2015; Vali, 2008) using

$$N_{\mathrm{INP_i}}(T) = N_{\mathrm{dust_i}}(1 - e^{n_{s,\mathrm{soil}}(T)\pi d^2}) + N_{\mathrm{SSA_i}}(1 - e^{n_{s,\mathrm{SSA}}(T)\pi d^2}), \tag{A3.2}$$

where $N_{\mathrm{dust_i}}$ and $N_{\mathrm{SSA_i}}$ are the dust and SSA number concentrations in each size bin (L^{-1} of air) and d is the mean diameter of the bin. The bins are summed to obtain the total N_{INP} for each grid box and for each time step (3 hr) of the time series. This is repeated for three model levels (surface, 1 km and 2 km) and a mean taken over the three to provide a concentration that is representative of the vertical cloud structure in the region (92% of Sc clouds and 70% of Cu clouds are below 2 km). A polynomial fit to all values of N_{INP} is used to produce a parameterisation for $N_{\mathrm{INP,M-Phase}}(T)$ which

is described by

$$\log_{10} N_{\mathrm{INP,M-Phase}}(T) = -4.591 - 0.5284T - 3.341\times10^{-2}T^2 - 1.249\times10^{-3}T^3 - 1.579\times10^{-5}T^4, \tag{A3.3}$$

where $N_{\mathrm{INP,M-Phase}}$ has units L^{-1} of air and T is in °C.

The regional model and global model were performed separately, and the use of the global model was solely for providing a temperature-dependent INP parameterisation (Equation A3.3).

A3.3 Kernel selection and evaluation of GP emulators

In this section, we present the results of GP kernel selection and emulator evaluation. We evaluated four stationary kernels using cross-validation on the 66-member training set. In each cross-validation set, 60 points were used for training and 6 for testing. We selected the kernel with the lowest $RMSE$ for each variable, retrained the emulator using all 66 training points, and then evaluated it with an independent 6-member test set generated by Latin hypercube sampling.

Figures A3.2–A3.6 show the standardized error, $\frac{Y_{pred}-Y_{true}}{\sigma_{emulator}}$, together with Q–Q plots, $RMSE$, and R^2. For most cloud variables, the Matérn32 kernel produced the lowest $RMSE$ and was therefore selected. The two exceptions are total water path in the Sc region, for which the RBF kernel performed best, and ice water path in the Cu region, for which the Matérn12 kernel performed best. However, the differences in $RMSE$ relative to the Matérn32 kernel are small in both cases.

All predictions for the testing points have 95% confidence intervals (2σ) that are across the 1:1 line, satisfying the validation criterion suggested from Bastos et al. (2009). We also compared the standard deviation of the test data with the mean standard deviation from emulators across the test points. For all variables, the standard deviation of the test data is higher than the mean standard deviation from emulators across the test points, indicating that the emulators are able to capture the responses and variations of these variables to the perturbations of parameters.

The $RMSE$ values are generally much smaller than the spread of the test data, the 1 million model variants shown in Figure 3.6, and the variations from the multiple OAT tests shown in Figure 3.9. This indicates that the emulators are sufficiently accurate for identifying interactions among the perturbed parameters. However, for ice water path in both regions and total water path in the Cu region, the emulator performance is less satisfactory than the others. This may come from multiple ice production processes interacting and dominating these variables, and hence lead to a greater complexity. Future work is recommended to investigate on the improvement of emulator performance (e.g. testing with different kernels) for these variables, particularly in the Cu region.

To assess whether 66 training points are sufficient, we performed a convergence test (Figure A3.6) using different training sizes (N), with data sampled from the existing 66 training points. For each size with $N < 66$, we randomly selected N training points 30 times and evaluated the emulator against the 6-member test set. The $RMSE$ values for $N = 66$ are identical to those shown in Figures A3.2–A3.6. For most variables, $RMSE$ decreases rapidly up to about 54-60 training points and remains relatively stable thereafter. This suggests that adding simulations beyond 60 will only have small improvements in emulator performance, while requiring substantial additional computational cost. The spread of $RMSE$ across the 30 random subsamples generally

decreases as the number of training points increases, and is smallest at 65 training points. This is consistent with the use of the Latin hypercube sampling method, which was designed for an efficient coverage of the multi-dimensional parameter space.

A more standard convergence test is to compare emulators trained on multiple PPEs of different sizes, each generated independently with the Latin hypercube sampling method. However, such test is not feasible here because of the high computational cost of each simulation in our model setup. Future work with a cheaper model setup (e.g., a smaller domain) is recommended to investigate the number of points needed for robust emulator performance using this approach.

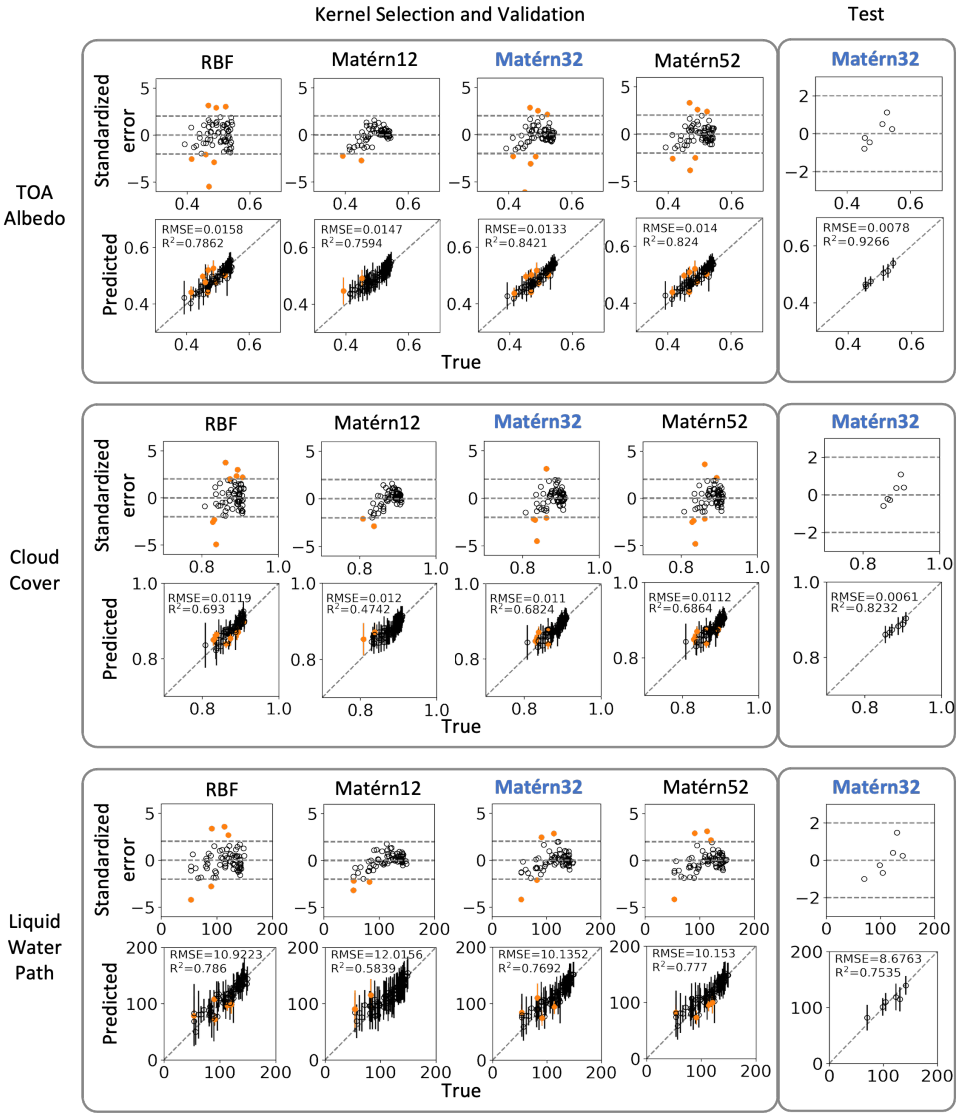


Figure A3.2: Kernel selection and testing results of the GP emulators on TOA albedo, cloud cover, and LWP in the Sc model analysis region. Points in orange indicate a failed emulated point in the standardized error check. The kernel name highlighted in blue indicates that the kernel was selected and the testing results are from comparing the emulator trained with the selected kernel with the testing dataset.

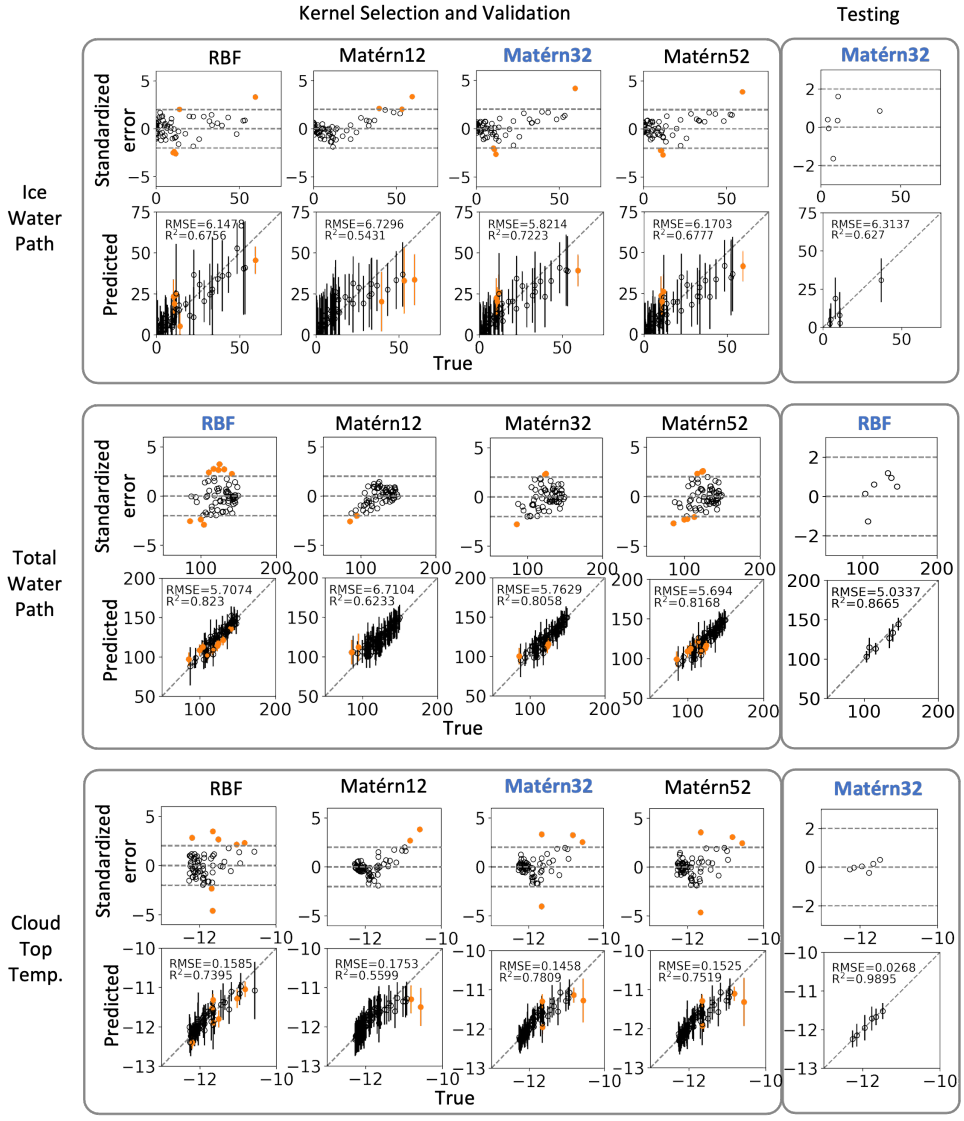


Figure A3.3: Kernel selection and testing results of the GP emulators on IWP, TWP and cloud top temperature in the Sc model analysis region. Points in orange indicate a failed emulated point in the standardized error check. The kernel name highlighted in blue indicates that the kernel was selected and the testing results are from comparing the emulator trained with the selected kernel with the testing dataset.

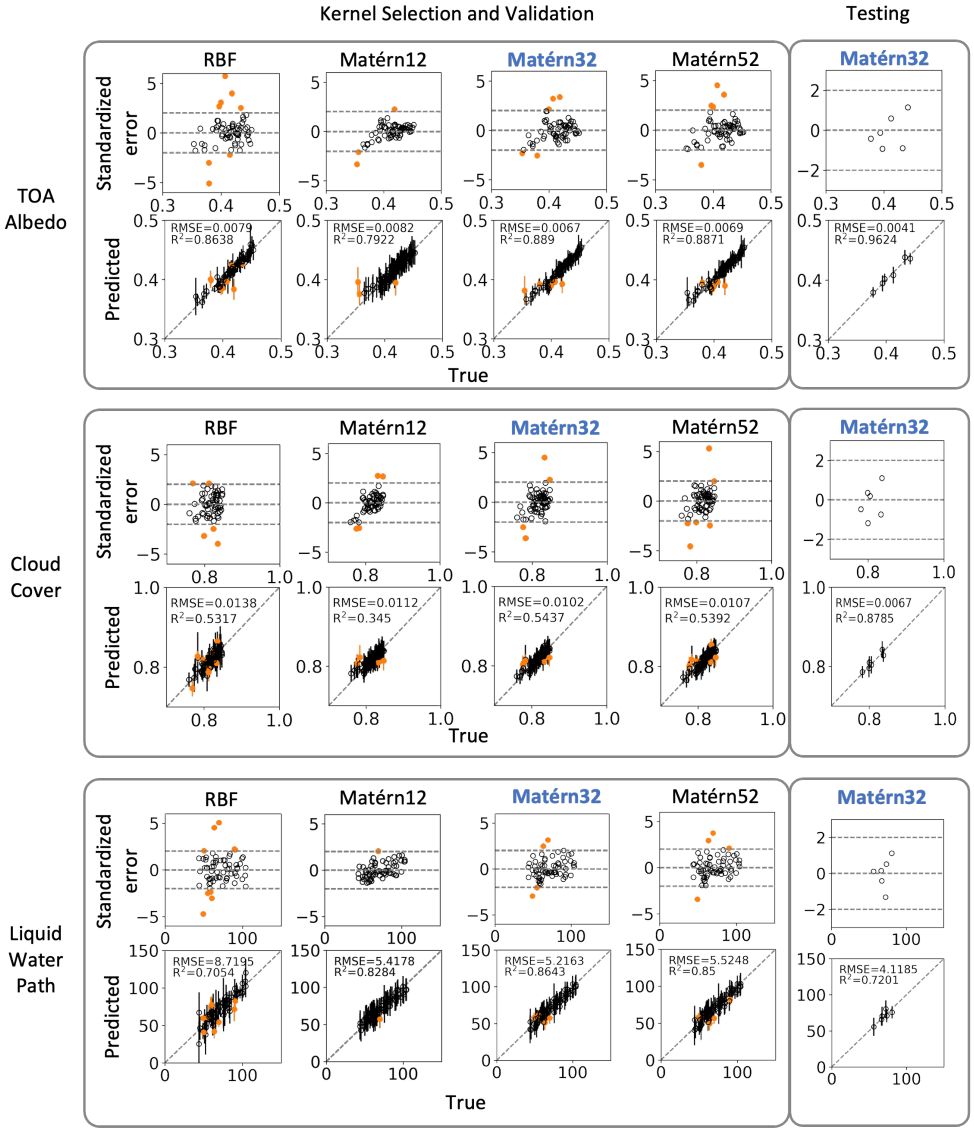


Figure A3.4: Kernel selection and testing results of the GP emulators on TOA albedo, cloud cover, and LWP in the Cu model analysis region. Points in orange indicate a failed emulated point in the standardized error check. The kernel name highlighted in blue indicates that the kernel was selected and the testing results are from comparing the emulator trained with the selected kernel with the testing dataset.

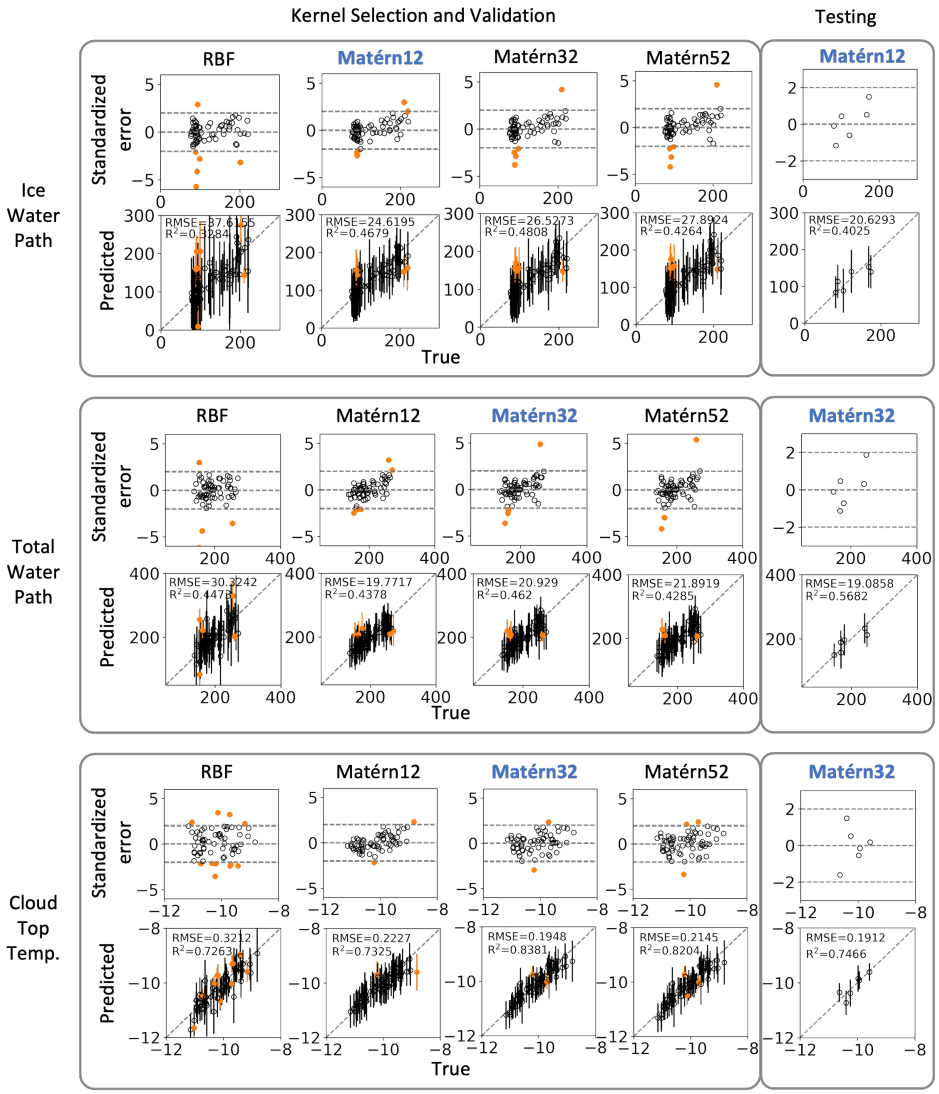


Figure A3.5: Kernel selection and testing results of the GP emulators on IWP, TWP and cloud top temperature in the Cu model analysis region. Points in orange indicate a failed emulated point in the standardized error check. The kernel name highlighted in blue indicates that the kernel was selected and the testing results are from comparing the emulator trained with the selected kernel with the testing dataset.

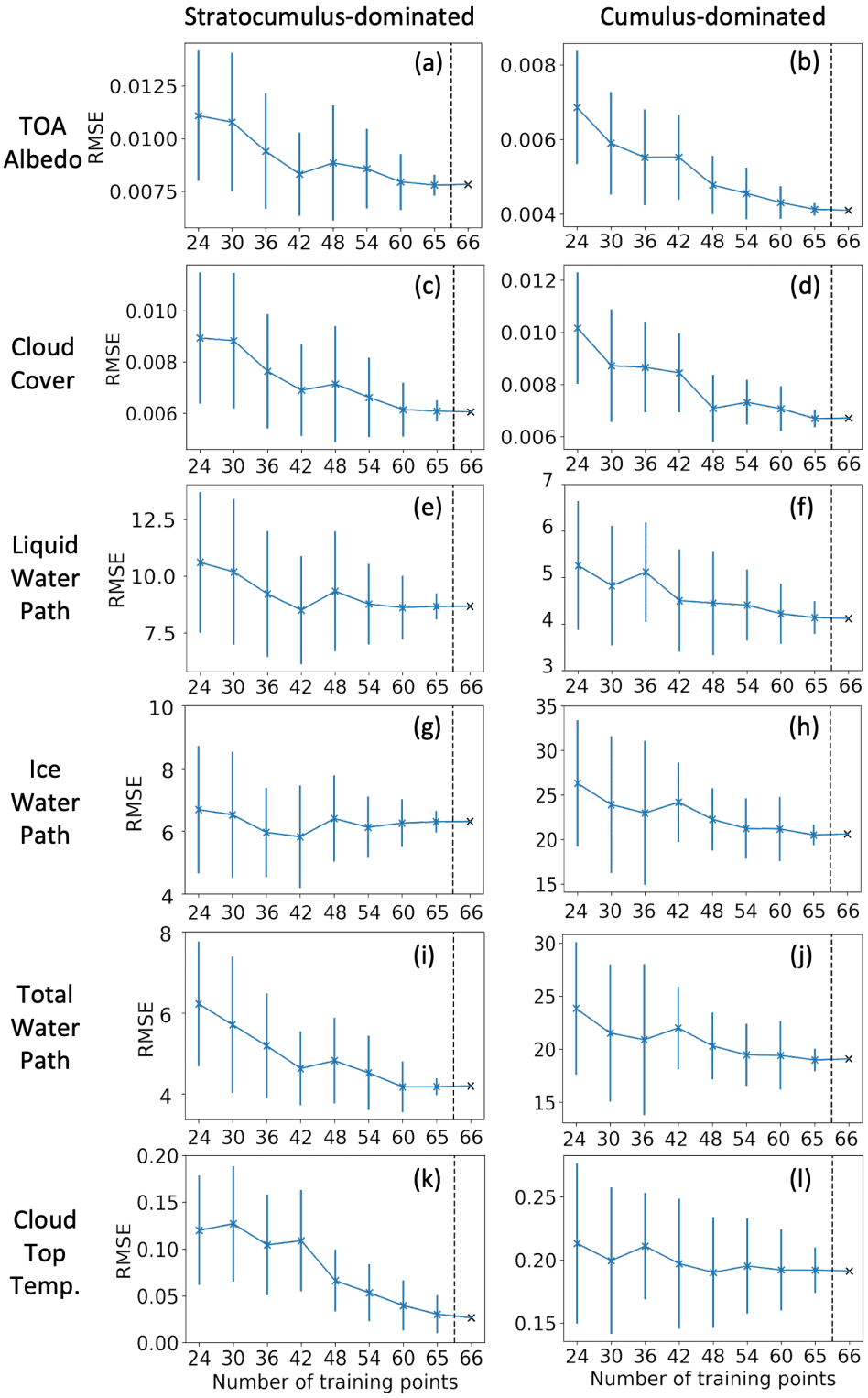


Figure A3.6: Convergence test results ($RMSE$) by using different number of training points over the Sc region (left) and the Cu region (right) for: (a-b) TOA albedo (unitless), (c-d) cloud cover (unitless), (e-f) liquid water path (gm^{-2}), (g-h) ice water path (gm^{-2}), (i-j) total water path (gm^{-2}), and (k-l) cloud top temperature (°C).

A3.4 Flow chart for methods involved in this work

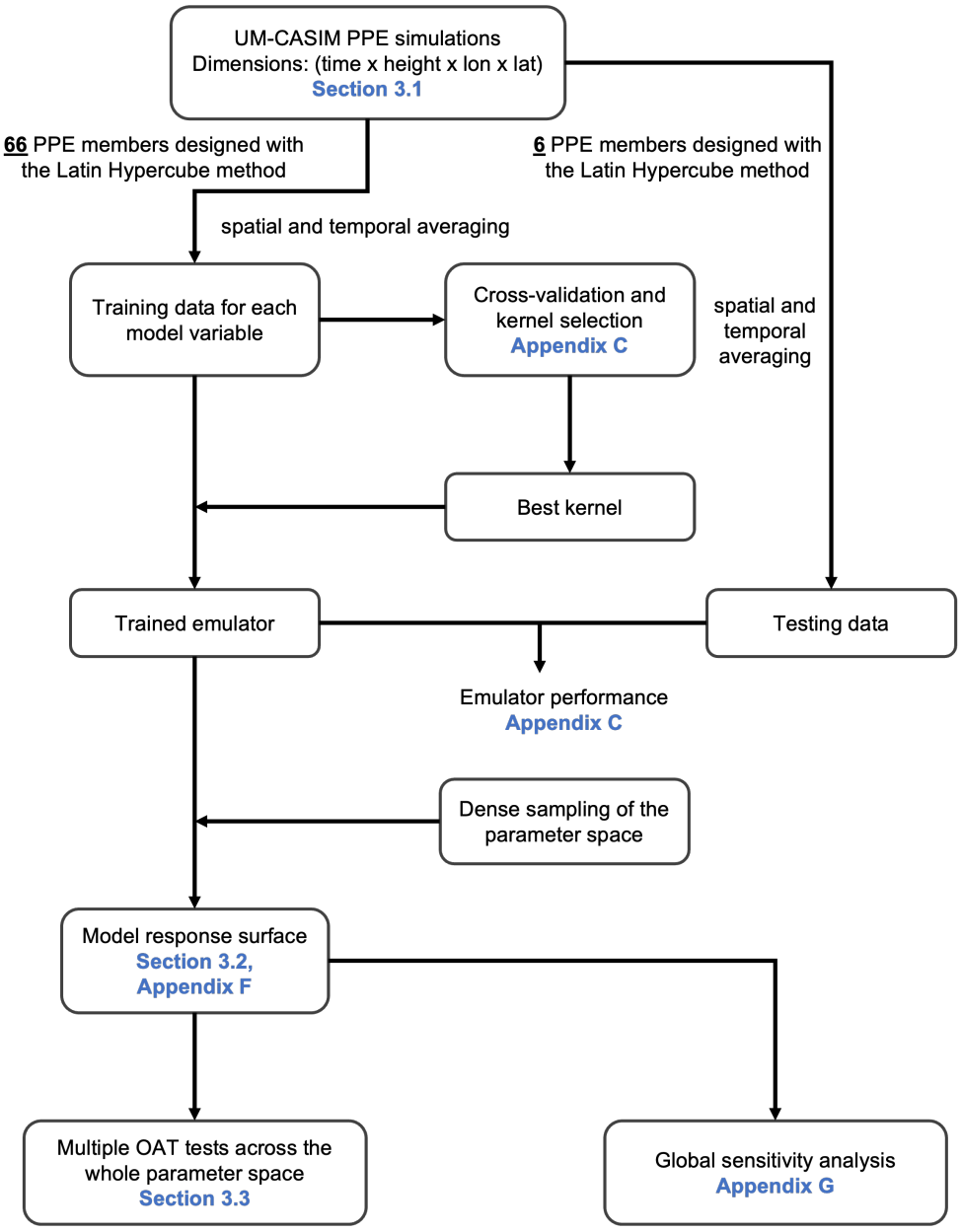


Figure A3.7: Flowchart for methods involved in this work. The sections include the corresponding results are highlighted in blue.

A3.5 Simple illustration of linear and non-linear joint effects between two parameters

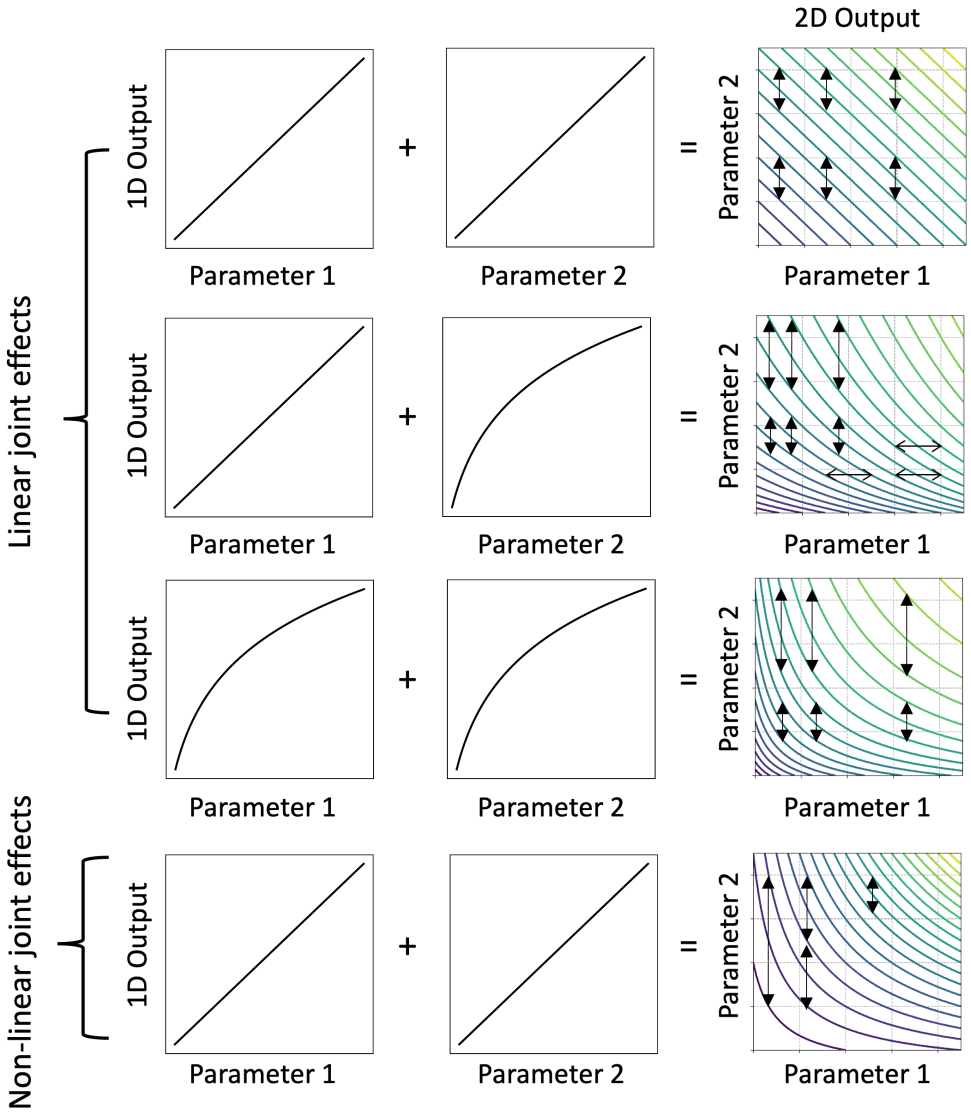


Figure A3.8: A simple illustration of linear and non-linear joint effects between two parameters. This diagram is adapted from Figure 3.3.3 in Sansom (2023). With linear joint effects, the effect of changing one parameter on the model output is independent of the value of the other parameter. With non-linear joint effects, the effect of changing one parameter on the model output is then dependent on the value of the other parameter. The length of the arrows shown in the 2D output represents the variation needed for a parameter to cross three contour lines. All the contour lines shown here are with linear scale.

A3.6 Additional paired-projection figures from GP emulators

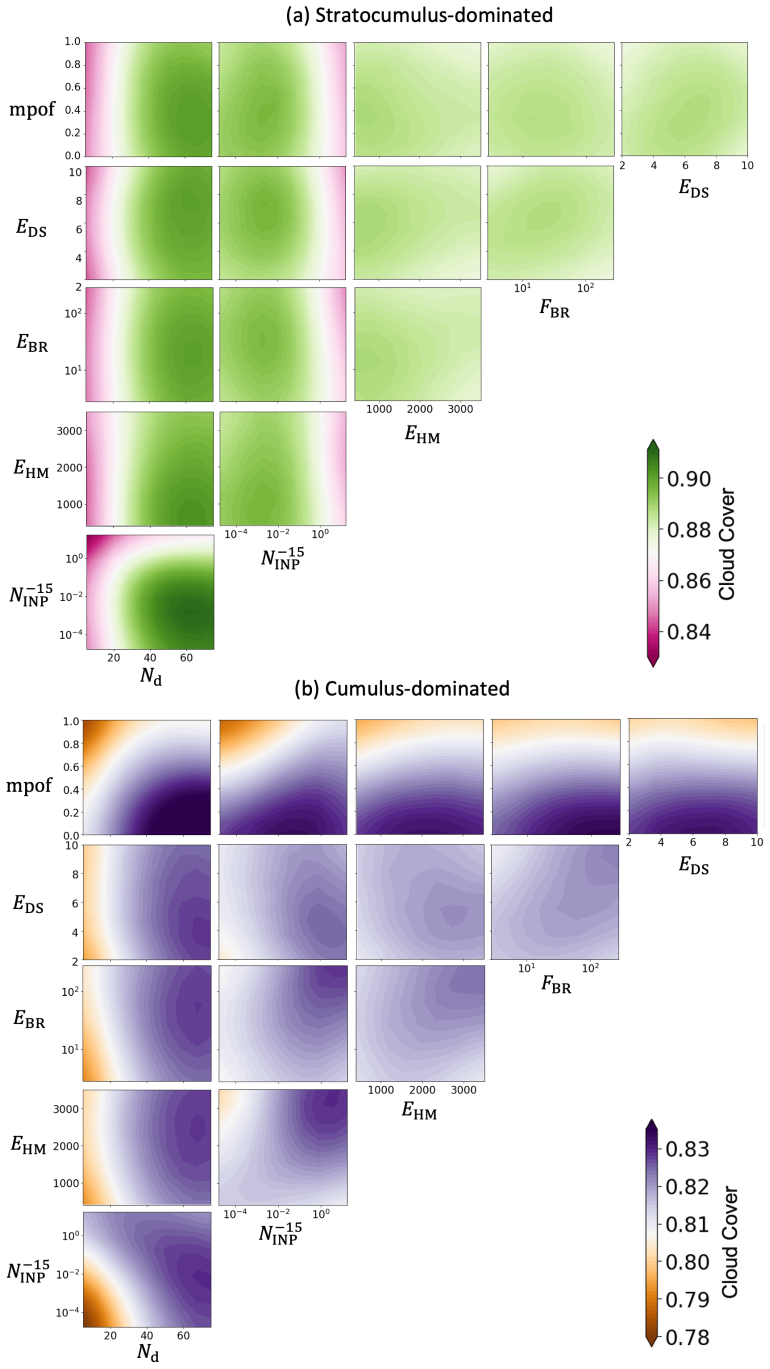


Figure A3.9: Projected mean model responses of cloud cover to paired parameters in (a) the Sc region and (b) the Cu region.

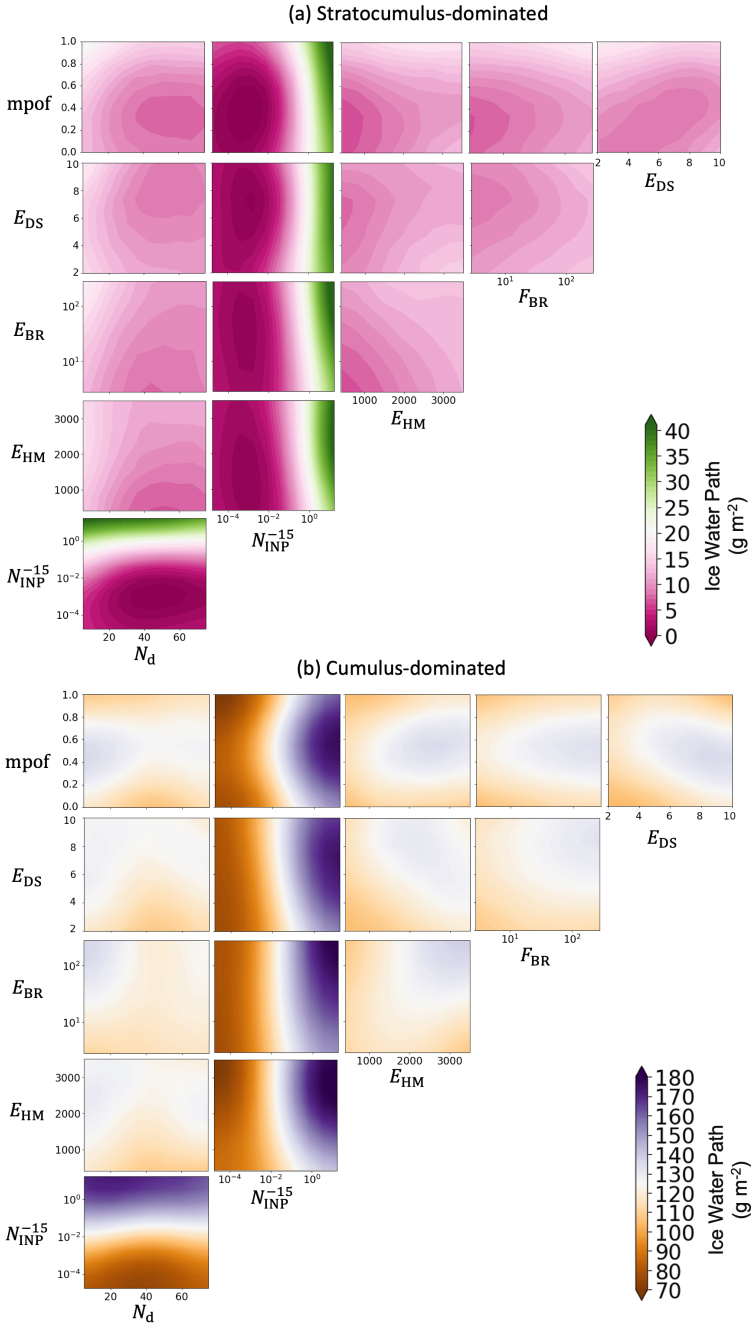


Figure A3.10: Projected mean model responses of all-sky IWP (ice water path) to paired parameters in (a) the Sc region and (b) the Cu region.

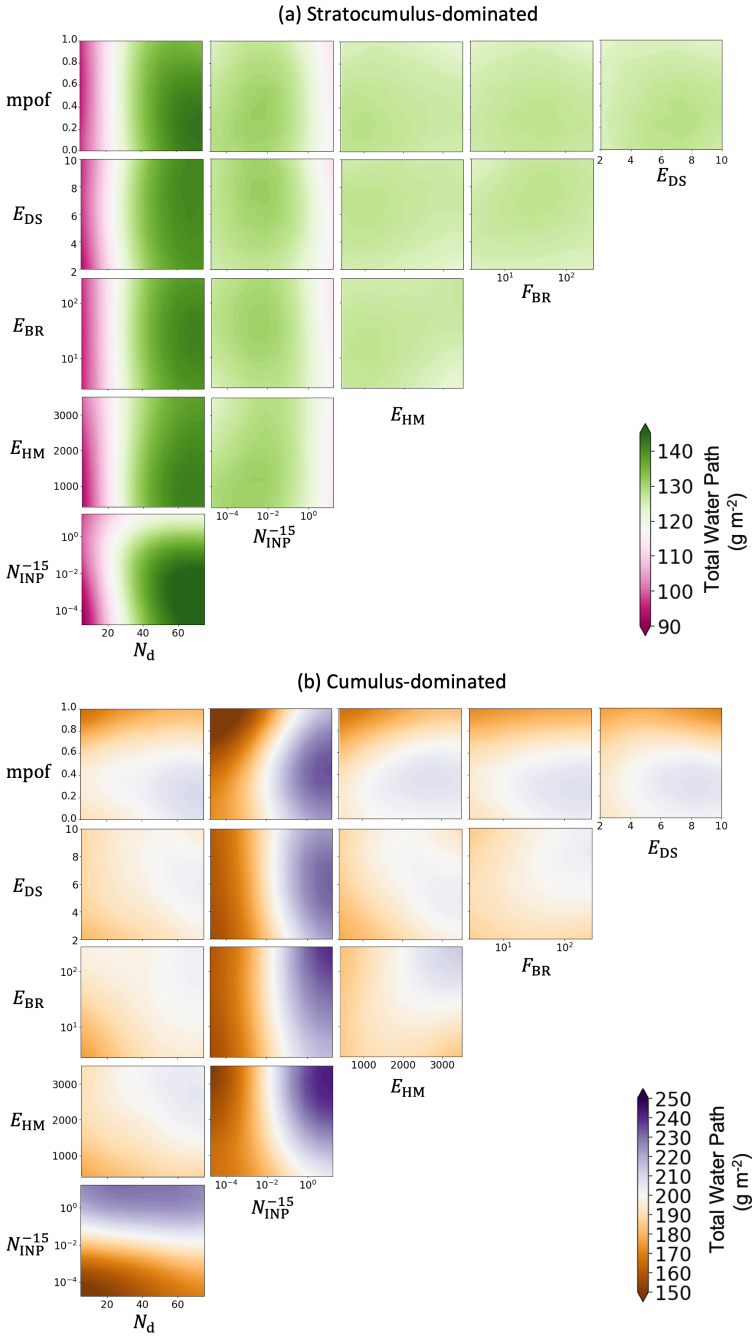


Figure A3.11: Projected mean model responses of all-sky TWP (total water path) to paired parameters in (a) the Sc region and (b) the Cu region.

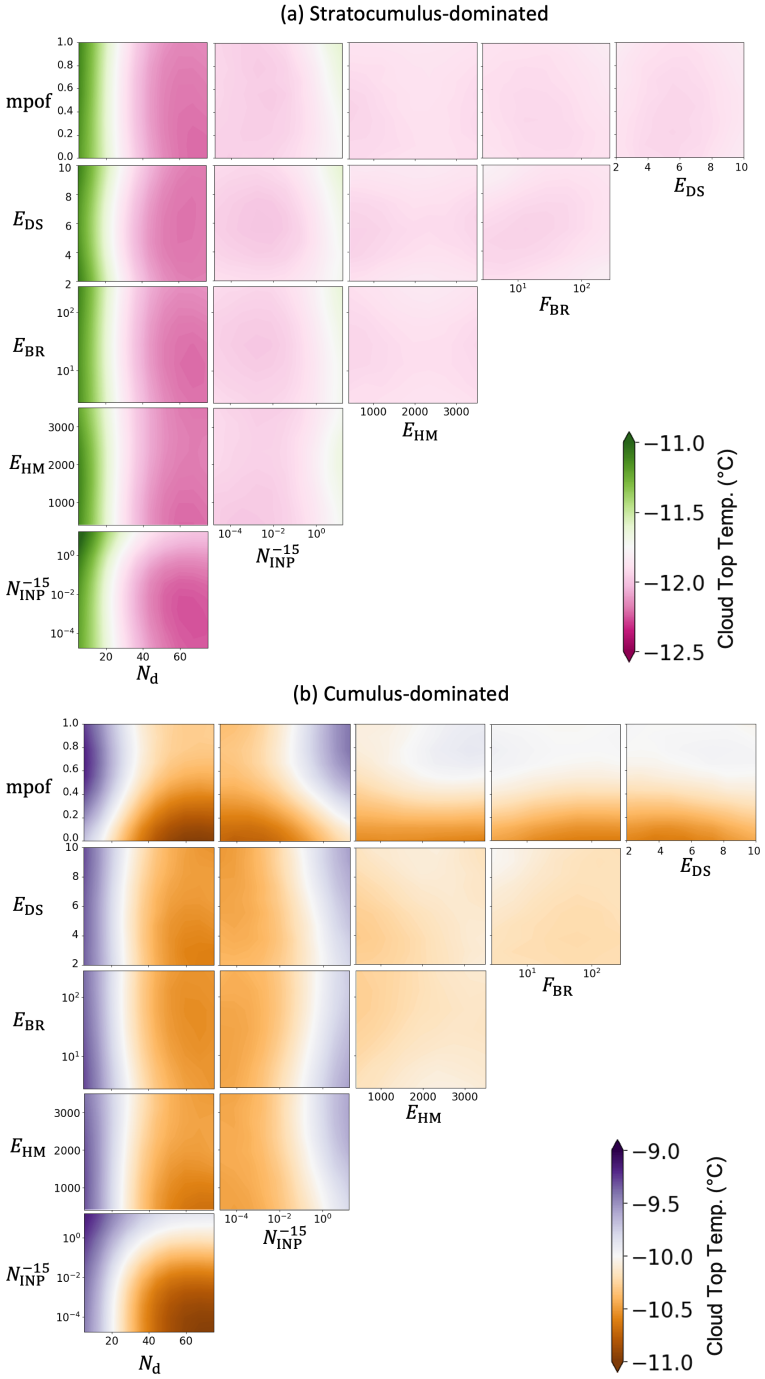


Figure A3.12: Projected mean model responses of cloud top temperature to paired parameters in (a) the Sc region and (b) the Cu region.

A3.7 Results from the global sensitivity analysis

A variance-based sensitivity analysis was also performed to quantify the sensitivities of model variables to the perturbed parameters based on a dense sampling of the emulated parameter space (Saltelli et al., 2000). We used the Sobol' method (Saltelli et al., 2000) with the Python library SALib (Usher et al., 2016) to calculate the sensitivity indices. The first-order sensitivity index measures the main effect of each parameter on a model variable. The total sensitivity index includes both the main effect and any additional effects from interactions with other parameters. Therefore, the difference between the total index and the first-order index indicates how much of a parameter's influence comes from its interactions with other parameters (interactive effects) (Johnson et al., 2015).

Figure A3.13 shows the sensitivity indices over the whole parameter space. This comparison allows us to quantitatively investigate the dominant parameters for the cloud properties in this CAO event over the 6-D parameter space, rather than, as shown in the paired projections, limiting to the values averaged across the parameter space for the non-paired parameters.

In this CAO case, N_{d} dominates the TOA albedo in both regions and exerts strong influences on cloud cover and LWP. In contrast, IWP in both regions has little sensitivity to the perturbations of N_{d}. The strong control of N_{d} over the TOA albedo suggests that an accurate representation of N_{d} and associated processes, including background aerosol fields, droplet activation of CCN and in-cloud processing of CCN, is essential to accurately represent these mixed-phase clouds in simulations.

N_{INP}^{-15} has a strong control of all-sky LWP and IWP in both regions of this CAO case, but its effect on TOA albedo is much weaker compared to N_{d}. In the Cu region, a high N_{INP}^{-15} leads to a reduction in LWP but also an increase in IWP, therefore, its overall influence on TWP is compensated. Although N_{INP}^{-15} strongly influences LWP in both cases, its weaker influence on TOA albedo compared to the influence from N_{d} suggests that, in this CAO case, the Twomey effect associated with perturbations in N_{d} plays a more dominant role in determining the radiative properties of CAO clouds. As a result, TOA albedo exhibits more sensitivity to perturbations of N_{d} than to N_{INP}^{-15}. It is also worth noting here that because the cloud temperature in our case is warm (with a cloud top temperature around -15 °C), the INP concentrations are generally low. Most of the perturbed N_{INP}^{-15} is below 1 L^{-1}, which is smaller than the threshold suggested from Vergara-Temprado et al. (2018) for INP to have a strong effect on TOA albedo.

In this CAO case, all SIP parameters (E_{HM}, E_{BR} and E_{DS}) have generally weak influence on the cloud radiative properties in both regions, compared to other parameters. Comparing the different regions shows that the influence from SIP processes on

cloud properties is relatively enhanced in the Cu region, as the clouds deepen and IWP increases with more snow and graupel formations. Most of their influences on cloud cover are interactive effects, suggesting an additional dependency on other parameters. Among the three SIP parameters, E_{HM} has the strongest influence on LWP, IWP and TWP. This occurs because most cloud temperatures in this case (ranging from -5 to -15 °C) are warmer than the peak temperature for the ice-ice collision (-21 °C) and droplet shattering (-15 °C) processes, but within the temperature range for the HM process (-7.5 °C to -2.5 °C) which peaks at -5 °C. Therefore, the sensitivities of cloud properties to the parameters shown here are case specific; this point will be further discussed in the Discussion and Conclusion section.

The influences of mpof are weak in the Sc region, but become much stronger in the Cu region for cloud cover and LWP, where IWP increased a lot compared to the ones in the Sc region. Its effects on TOA albedo are also enhanced in the Cu region, but much weaker compared to the those from N_{d}. The explanation is similar to N_{INP}^{-15}, as in this case, the radiative properties of CAO clouds are dominated by the Twomey effect associated with perturbations in N_{d}, rather than the change in LWP. The mpof parameter controls the extent to which liquid and ice hydrometeors interact with each other, and our results suggest that for cloud cover and LWP in the Cu region, it is important to have a good representation of the degree of overlap between ice and liquid hydrometeors. However, mpof remains poorly constrained in models (Abel et al., 2017; Korolev et al., 2022; Evans et al., 2025) and can lead to large uncertainties in estimating mixed-phase cloud behaviours under the warming climate and their influences to the Earth's energy budget.

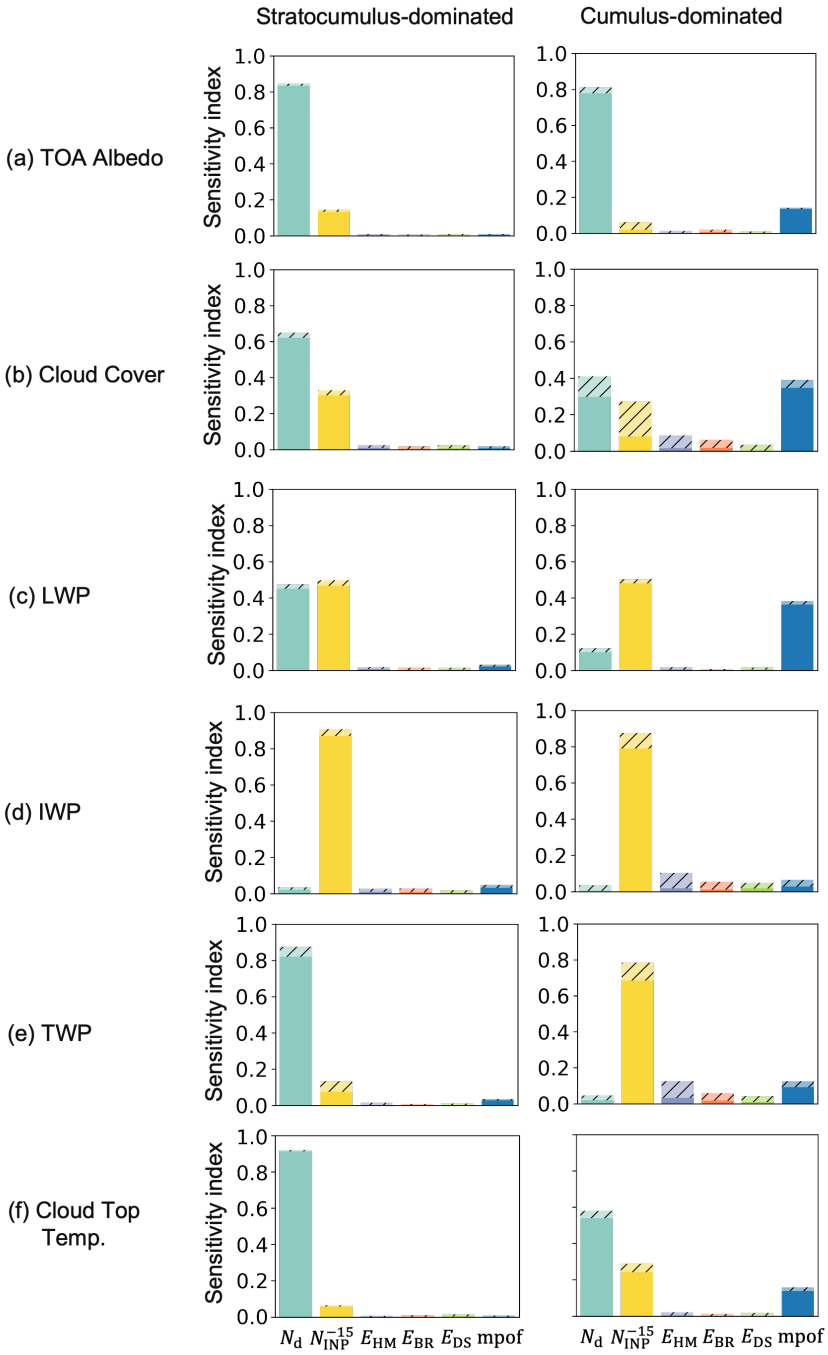


Figure A3.13: Sensitivity indices of all the perturbed parameters for TOA albedo (unitless), cloud cover (unitless), all-sky LWP ($g\,m^{-2}$), all-sky IWP ($g\,m^{-2}$), all-sky TWP ($g\,m^{-2}$) and cloud top temperature (°C). Each sensitivity index consists of the first-order, main effect (solid fill) and the second-order, interactive effects (dashed). Indices are shown separately for the Sc (left column) and Cu (right column) regions.

References

Abel, S. J., Boutle, I. A., Waite, K., Fox, S., Brown, P. R. A., Cotton, R., Lloyd, G., Choularton, T. W., and Bower, K. N. (2017). "The Role of Precipitation in Controlling the Transition from Stratocumulus to Cumulus Clouds in a Northern Hemisphere Cold-Air Outbreak". In: *Journal of the Atmospheric Sciences* 74.7, pp. 2293–2314.

Albrecht, B. A. (1989). "Aerosols, Cloud Microphysics, and Fractional Cloudiness". In: *Science* 245.4923, pp. 1227–1230.

Baran, A. J., Manners, J., Field, P. R., Furtado, K., and Hill, A. (2025). "A consistent coupling of two-moment microphysics and bulk ice optical properties, and its impact on radiation in a regional weather model". In: *Quarterly Journal of the Royal Meteorological Society* 151.772, e5025.

Barr, S. L., Wyld, B., McQuaid, J. B., Neely III, R. R., and Murray, B. J. (2023). "Southern Alaska as a source of atmospheric mineral dust and ice-nucleating particles". In: *Science Advances* 9.33, eadg3708.

Bastos, L. S. and O'Hagan, A. (2009). "Diagnostics for Gaussian Process Emulators". In: *Technometrics* 51.4, pp. 425–438.

Bergeron, T. (1935). "On the physics of clouds and precipitation". In: *Proces Verbaux de l'Association de Météorologie*, pp. 156–178.

Beven, K. (2006). "A manifesto for the equifinality thesis". In: *Journal of Hydrology* 320.1, pp. 18–36.

Bigg, E. K. (1953). "The formation of atmospheric ice crystals by the freezing of droplets". In: *Quarterly Journal of the Royal Meteorological Society* 79.342, pp. 510–519.

Bodas-Salcedo, A., Mulcahy, J. P., Andrews, T., Williams, K. D., Ringer, M. A., Field, P. R., and Elsaesser, G. S. (2019). "Strong Dependence of Atmospheric Feedbacks on Mixed-Phase Microphysics and Aerosol-Cloud Interactions in HadGEM3". In: *Journal of Advances in Modeling Earth Systems* 11.6, pp. 1735–1758.

Brown, A., Milton, S., Cullen, M., Golding, B., Mitchell, J., and Shelly, A. (2012). "Unified Modeling and Prediction of Weather and Climate: A 25-Year Journey". In: *Bulletin of the American Meteorological Society* 93.12, pp. 1865–1877.

Brümmer, B. (1996). "Boundary-layer modification in wintertime cold-air outbreaks from the Arctic sea ice". In: *Boundary-Layer Meteorology* 80.1, pp. 109–125.

— (1999). "Roll and Cell Convection in Wintertime Arctic Cold-Air Outbreaks". In: *Journal of the Atmospheric Sciences* 56.15, pp. 2613–2636.

Bush, M., Flack, D. L. A., Lewis, H. W., Bohnenstengel, S. I., Short, C. J., Franklin, C., Lock, A. P., Best, M., Field, P., McCabe, A., Van Weverberg, K., Berthou, S., Boutle, I., Brooke, J. K., Cole, S., Cooper, S., Dow, G., Edwards, J., Finnenkoetter, A., Furtado, K., Halladay, K., Hanley, K., Hendry, M. A., Hill, A., Jayakumar,

A., Jones, R. W., Lean, H., Lee, J. C. K., Malcolm, A., Mittermaier, M., Mohandas, S., Moore, S., Morcrette, C., North, R., Porson, A., Rennie, S., Roberts, N., Roux, B., Sanchez, C., Su, C.-H., Tucker, S., Vosper, S., Walters, D., Warner, J., Webster, S., Weeks, M., Wilkinson, J., Whitall, M., Williams, K. D., and Zhang, H. (2025). "The third Met Office Unified Model–JULES Regional Atmosphere and Land Configuration, RAL3". In: *Geoscientific Model Development* 18.12, pp. 3819–3855.

Carslaw, K. S., Regayre, L. A., Proske, U., Gettelman, A., Sexton, D. M. H., Qian, Y., Marshall, L. R., Wild, O., van Lier-Walqui, M., Oertel, A., Peatier, S., Yang, B., Johnson, J. S., Li, S., McCoy, D. T., Sanderson, B. M., Williamson, C. J., Elsaesser, G. S., Yamazaki, K., and Booth, B. B. B. (2026). "Opinion: The importance and future development of perturbed parameter ensembles in climate and atmospheric science". In: *Atmospheric Chemistry and Physics* 26.7, pp. 4651–4667.

Ceppi, P., Brient, F., Zelinka, M. D., and Hartmann, D. L. (2017). "Cloud feedback mechanisms and their representation in global climate models". In: *WIREs Climate Change* 8.4, e465.

Clarke, S. J., Abel, S. J., Nott, G. J., Raif, E. N., Tarn, M. D., Biggart, M., Wu, H., Ashmore, D. W., Barr, S. L., Barrett, P. A., Bower, K. N., Bowles, J., Connolly, P. J., Cotton, R., Evans, M. D., Flynn, M., Foster, P. B., Fox, S., Gallagher, M. W., Hu, K., Kent, J., Lloyd, G., Marsden, N. A., McQuaid, J. B., Robinson, J., Tiddeman, D., Wilson, A., Wivell, K., Field, P. R., Choularton, T. W., and Murray, B. J. (2025). "Marine cold-air outbreaks over the Norwegian-Barents and Labrador seas: observational datasets from the ACAO and M-Phase aircraft campaigns". Manuscript submitted for publication.

Conen, F., Stopelli, E., and Zimmermann, L. (2016). "Clues that decaying leaves enrich Arctic air with ice nucleating particles". In: *Atmospheric Environment* 129, pp. 91–94.

Creamean, J. M., Cross, J. N., Pickart, R., McRaven, L., Lin, P., Pacini, A., Hanlon, R., Schmale, D. G., Ceniceros, J., Aydell, T., Colombi, N., Bolger, E., and DeMott, P. J. (2019). "Ice Nucleating Particles Carried From Below a Phytoplankton Bloom to the Arctic Atmosphere". In: *Geophysical Research Letters* 46.14, pp. 8572–8581.

Creamean, J. M., Kirpes, R. M., Pratt, K. A., Spada, N. J., Maahn, M., de Boer, G., Schnell, R. C., and China, S. (2018). "Marine and terrestrial influences on ice nucleating particles during continuous springtime measurements in an Arctic oilfield location". In: *Atmospheric Chemistry and Physics* 18.24, pp. 18023–18042.

de Roode, S. R., Frederikse, T., Siebesma, A. P., Ackerman, A. S., Chylik, J., Field, P. R., Fricke, J., Gryschka, M., Hill, A., Honnert, R., Krueger, S. K., Lac, C., Lesage, A. T., and Tomassini, L. (2019). "Turbulent Transport in the Gray Zone: A Large Eddy Model Intercomparison Study of the CONSTRAIN Cold Air Outbreak Case". In: *Journal of Advances in Modeling Earth Systems* 11.3, pp. 597–623.

DeMott, P. J., Prenni, A. J., McMeeking, G. R., Sullivan, R. C., Petters, M. D., Tobo, Y., Niemand, M., Möhler, O., Snider, J. R., Wang, Z., and Kreidenweis, S. M. (2015). "Integrating laboratory and field data to quantify the immersion freezing ice nucleation activity of mineral dust particles". In: *Atmospheric Chemistry and Physics* 15.1, pp. 393–409.

DeMott, P. J., Hill, T. C. J., McCluskey, C. S., Prather, K. A., Collins, D. B., Sullivan, R. C., Ruppel, M. J., Mason, R. H., Irish, V. E., Lee, T., Hwang, C. Y., Rhee, T. S., Snider, J. R., McMeeking, G. R., Dhaniyala, S., Lewis, E. R., Wentzell, J. J. B., Abbatt, J., Lee, C., Sultana, C. M., Ault, A. P., Axson, J. L., Diaz Martinez, M., Venero, I., Santos-Figueroa, G., Stokes, M. D., Deane, G. B., Mayol-Bracero, O. L., Grassian, V. H., Bertram, T. H., Bertram, A. K., Moffett, B. F., and Franc, G. D. (2016). "Sea spray aerosol as a unique source of ice nucleating particles". In: *Proceedings of the National Academy of Sciences* 113.21, pp. 5797–5803.

Elsaesser, G. S., van Lier-Walqui, M., Yang, Q., Kelley, M., Ackerman, A. S., Fridlind, A. M., Cesana, G. V., Schmidt, G. A., Wu, J., Behrangi, A., Camargo, S. J., De, B., Inoue, K., Leitmann-Niimi, N. M., and Strong, J. D. O. (2025). "Using Machine Learning to Generate a GISS ModelE Calibrated Physics Ensemble (CPE)". In: *Journal of Advances in Modeling Earth Systems* 17.4, e2024MS004713.

Evans, M. D., Abel, S. J., Field, P. R., Finney, D. L., Lloyd, G., Cotton, R. J., Smith, D. K., Murray, B. J., and Huang, X. (2025). "Characterising the spatial overlap between liquid and ice in mixed-phase clouds". In: *Quarterly Journal of the Royal Meteorological Society*, e5041.

Field, P. R., Cotton, R. J., McBeath, K., Lock, A. P., Webster, S., and Allan, R. P. (2014). "Improving a convection-permitting model simulation of a cold air outbreak". In: *Quarterly Journal of the Royal Meteorological Society* 140.678, pp. 124–138.

Field, P. R., Brožková, R., Chen, M., Dudhia, J., Lac, C., Hara, T., Honnert, R., Olson, J., Siebesma, P., de Roode, S., Tomassini, L., Hill, A., and McTaggart-Cowan, R. (2017). "Exploring the convective grey zone with regional simulations of a cold air outbreak". In: *Quarterly Journal of the Royal Meteorological Society* 143.707, pp. 2537–2555.

Field, P. R., Hill, A., Shipway, B., Furtado, K., Wilkinson, J., Miltenberger, A., Gordon, H., Grosvenor, D. P., Stevens, R., and Van Weverberg, K. (2023). "Implementation of a Double Moment Cloud Microphysics Scheme in the UK Met Office Regional Numerical Weather Prediction Model". In: *Quarterly Journal of the Royal Meteorological Society*.

Findeisen, W. (1938). "Kolloid-meteorologische Vorgänge bei Niederschlagsbildung". In: *Meteorologische Zeitschrift* 55, pp. 121–133.

Findeisen, W. and Findeisen, E. (1943). "Untersuchungen über die Eissplitterbildung an Reifschichten (Ein Beitrag zur Frage der Entstehung der Gewitterelektrizität

und zur Mikrostruktur der Cumulonimben)". In: *Meteorologische Zeitschrift* 60, pp. 145–154.

Fletcher, J., Mason, S., and Jakob, C. (2016a). "The Climatology, Meteorology, and Boundary Layer Structure of Marine Cold Air Outbreaks in Both Hemispheres". In: *Journal of Climate* 29.6, pp. 1999–2014.

Fletcher, J. K., Mason, S., and Jakob, C. (2016b). "A Climatology of Clouds in Marine Cold Air Outbreaks in Both Hemispheres". In: *Journal of Climate* 29.18, pp. 6677–6692.

Forster, P., Storelvmo, T., Armour, K., Collins, W., Dufresne, J. L., Frame, D., Lunt, D. J., Mauritsen, T., Palmer, M. D., Watanabe, M., Wild, M., and Zhang, H. (2021). "The Earth's Energy Budget, Climate Feedbacks, and Climate Sensitivity". In: *Climate Change 2021: The Physical Science Basis. Contribution of Working Group I to the Sixth Assessment Report of the Intergovernmental Panel on Climate Change*. Ed. by V. Masson-Delmotte, P. Zhai, A. Pirani, S. L. Connors, C. Péan, S. Berger, N. Caud, Y. Chen, L. Goldfarb, M. I. Gomis, M. Huang, K. Leitzell, E. Lonnoy, J. B. R. Matthews, T. K. Maycock, T. Waterfield, O. Yelekçi, R. Yu, and B. Zhou. Cambridge, United Kingdom and New York, NY, USA: Cambridge University Press. Chap. 7.

Glassmeier, F., Hoffmann, F., Johnson, J. S., Yamaguchi, T., Carslaw, K. S., and Feingold, G. (2019). "An emulator approach to stratocumulus susceptibility". In: *Atmospheric Chemistry and Physics* 19.15, pp. 10191–10203.

Grosvenor, D. P., Sourdeval, O., Zuidema, P., Ackerman, A., Alexandrov, M. D., Bennartz, R., Boers, R., Cairns, B., Chiu, J. C., Christensen, M., Deneke, H., Diamond, M., Feingold, G., Fridlind, A., Hünerbein, A., Knist, C., Kollias, P., Marshak, A., McCoy, D., Merk, D., Painemal, D., Rausch, J., Rosenfeld, D., Russchenberg, H., Seifert, P., Sinclair, K., Stier, P., van Diedenhoven, B., Wendisch, M., Werner, F., Wood, R., Zhang, Z., and Quaas, J. (2018). "Remote Sensing of Droplet Number Concentration in Warm Clouds: A Review of the Current State of Knowledge and Perspectives". In: *Reviews of Geophysics* 56.2, pp. 409–453.

Hallett, J. and Mossop, S. C. (1974). "Production of secondary ice particles during the riming process". In: *Nature* 249, pp. 26–28.

Harrison, A. D., Lever, K., Sanchez-Marroquin, A., Holden, M. A., Whale, T. F., Tarn, M. D., McQuaid, J. B., and Murray, B. J. (2019). "The ice-nucleating ability of quartz immersed in water and its atmospheric importance compared to K-feldspar". In: *Atmospheric Chemistry and Physics* 19.17, pp. 11343–11361.

Hartmann, M., Adachi, K., Eppers, O., Haas, C., Herber, A., Holzinger, R., Hünerbein, A., Jäkel, E., Jentzsch, C., van Pinxteren, M., Wex, H., Willmes, S., and Stratmann, F. (2020). "Wintertime Airborne Measurements of Ice Nucleating Particles in the High Arctic: A Hint to a Marine, Biogenic Source for Ice Nucleating Particles". In: *Geophysical Research Letters* 47.13, e2020GL087770.

Hartmann, M., Gong, X., Kecorius, S., van Pinxteren, M., Vogl, T., Welti, A., Wex, H., Zeppenfeld, S., Herrmann, H., Wiedensohler, A., and Stratmann, F. (2021). "Terrestrial or marine – indications towards the origin of ice-nucleating particles during melt season in the European Arctic up to 83.7° N". In: *Atmospheric Chemistry and Physics* 21.15, pp. 11613–11636.

Hawker, R. E., Miltenberger, A. K., Johnson, J. S., Wilkinson, J. M., Hill, A. A., Shipway, B. J., Field, P. R., Murray, B. J., and Carslaw, K. S. (2021). "Model emulation to understand the joint effects of ice-nucleating particles and secondary ice production on deep convective anvil cirrus". In: *Atmospheric Chemistry and Physics* 21.23, pp. 17315–17343.

Herbert, R. J., Sanchez-Marroquin, A., Grosvenor, D. P., Pringle, K. J., Arnold, S. R., Murray, B. J., and Carslaw, K. S. (2025). "Gaps in our understanding of ice-nucleating particle sources exposed by global simulation of the UK Earth System Model". In: *Atmospheric Chemistry and Physics* 25.1, pp. 291–325.

Huang, X., Field, P. R., Murray, B. J., Grosvenor, D. P., van den Heuvel, F., and Carslaw, K. S. (2025). "Different responses of cold-air outbreak clouds to aerosol and ice production depending on cloud temperature". In: *Atmospheric Chemistry and Physics* 25.18, pp. 11363–11406.

Igel, A. L., van den Heever, S. C., and Johnson, J. S. (2018). "Meteorological and Land Surface Properties Impacting Sea Breeze Extent and Aerosol Distribution in a Dry Environment". In: *Journal of Geophysical Research: Atmospheres* 123.1, pp. 22–37.

Irish, V. E., Hanna, S. J., Willis, M. D., China, S., Thomas, J. L., Wentzell, J. J. B., Cirisan, A., Si, M., Leaitch, W. R., Murphy, J. G., Abbatt, J. P. D., Laskin, A., Girard, E., and Bertram, A. K. (2019). "Ice nucleating particles in the marine boundary layer in the Canadian Arctic during summer 2014". In: *Atmospheric Chemistry and Physics* 19.2, pp. 1027–1039.

Johnson, J. S., Cui, Z., Lee, L. A., Gosling, J. P., Blyth, A. M., and Carslaw, K. S. (2015). "Evaluating uncertainty in convective cloud microphysics using statistical emulation". In: *Journal of Advances in Modeling Earth Systems* 7.1, pp. 162–187.

Johnson, J. S., Regayre, L. A., Yoshioka, M., Pringle, K. J., Turnock, S. T., Browse, J., Sexton, D. M. H., Rostron, J. W., Schutgens, N. A. J., Partridge, D. G., Liu, D., Allan, J. D., Coe, H., Ding, A., Cohen, D. D., Atanacio, A., Vakkari, V., Asmi, E., and Carslaw, K. S. (2020). "Robust observational constraint of uncertain aerosol processes and emissions in a climate model and the effect on aerosol radiative forcing". In: *Atmospheric Chemistry and Physics* 20.15, pp. 9491–9524.

Johnson, J. S., Regayre, L. A., Yoshioka, M., Pringle, K. J., Lee, L. A., Sexton, D. M. H., Rostron, J. W., Booth, B. B. B., and Carslaw, K. S. (2018). "The importance of comprehensive parameter sampling and multiple observations for robust constraint of aerosol radiative forcing". In: *Atmospheric Chemistry and Physics* 18.17, pp. 13031–13053.

Jones, A. C., Hill, A., Hemmings, J., Lemaitre, P., Quérel, A., Ryder, C. L., and Woodward, S. (2022). "Below-cloud scavenging of aerosol by rain: a review of numerical modelling approaches and sensitivity simulations with mineral dust in the Met Office's Unified Model". In: *Atmospheric Chemistry and Physics* 22.17, pp. 11381–11407.

Karalis, M., Sotiropoulou, G., Abel, S. J., Bossioli, E., Georgakaki, P., Methymaki, G., Nenes, A., and Tombrou, M. (2022). "Effects of secondary ice processes on a stratocumulus to cumulus transition during a cold-air outbreak". In: *Atmospheric Research* 277, p. 106302.

King, L. (2024). "Using a small expansion chamber to characterise ice nucleation by high-latitude mineral dusts and volcanic ash". phd. University of Leeds.

Kolstad, E. W. and Bracegirdle, T. J. (2008). "Marine cold-air outbreaks in the future: an assessment of IPCC AR4 model results for the Northern Hemisphere". In: *Climate Dynamics* 30.7, pp. 871–885.

Kolstad, E. W., Bracegirdle, T. J., and Seierstad, I. A. (2009). "Marine cold-air outbreaks in the North Atlantic: temporal distribution and associations with large-scale atmospheric circulation". In: *Climate Dynamics* 33.2, pp. 187–197.

Korolev, A., McFarquhar, G., Field, P. R., Franklin, C., Lawson, P., Wang, Z., Williams, E., Abel, S. J., Axisa, D., Borrmann, S., Crosier, J., Fugal, J., Krämer, M., Lohmann, U., Schlenczek, O., Schnaiter, M., and Wendisch, M. (2017). "Mixed-Phase Clouds: Progress and Challenges". In: *Meteorological Monographs* 58, pp. 5.1–5.50.

Korolev, A. and Milbrandt, J. (2022). "How Are Mixed-Phase Clouds Mixed?" In: *Geophysical Research Letters* 49.18, e2022GL099578.

Lee, L. A., Carslaw, K. S., Pringle, K. J., and Mann, G. W. (2012). "Mapping the uncertainty in global CCN using emulation". In: *Atmospheric Chemistry and Physics* 12.20, pp. 9739–9751.

Lee, L. A., Carslaw, K. S., Pringle, K. J., Mann, G. W., and Spracklen, D. V. (2011). "Emulation of a complex global aerosol model to quantify sensitivity to uncertain parameters". In: *Atmospheric Chemistry and Physics* 11.23, pp. 12253–12273.

Lee, L. A., Pringle, K. J., Reddington, C. L., Mann, G. W., Stier, P., Spracklen, D. V., Pierce, J. R., and Carslaw, K. S. (2013). "The magnitude and causes of uncertainty in global model simulations of cloud condensation nuclei". In: *Atmospheric Chemistry and Physics* 13.17, pp. 8879–8914.

Lee, L. A., Reddington, C. L., and Carslaw, K. S. (2016). "On the relationship between aerosol model uncertainty and radiative forcing uncertainty". In: *Proceedings of the National Academy of Sciences* 113.21, pp. 5820–5827.

Leisner, T., Pander, T., Handmann, P., and Kiselev, A. (2014). "Secondary ice processes upon heterogeneous freezing of cloud droplets". In: *Proceedings of the 14th Conference on Cloud Physics 14th Conference on Atmospheric Radiation*. Presented

Monday, 7 July 2014, 11:00 AM, Essex Center/South (Westin Copley Place). American Meteorological Society. Boston, MA, USA.

Li, X.-Y., Wang, H., Chen, J., Endo, S., Kirschler, S., Voigt, C., Crosbie, E., Ziemba, L. D., Painemal, D., Cairns, B., Hair, J. W., Corral, A. F., Robinson, C., Dadashazar, H., Sorooshian, A., Chen, G., Ferrare, R. A., Kleb, M. M., Liu, H., Moore, R., Scarino, A. J., Shook, M. A., Shingler, T. J., Thornhill, K. L., Tornow, F., Xiao, H., and Zeng, X. (2023). "Large-Eddy Simulations of Marine Boundary Layer Clouds Associated with Cold-Air Outbreaks during the ACTIVATE Campaign. Part II: Aerosol–Meteorology–Cloud Interaction". In: *Journal of the Atmospheric Sciences* 80.4, pp. 1025–1045.

Lock, A. P., Brown, A. R., Bush, M. R., Martin, G. M., and Smith, R. N. B. (2000). "A New Boundary Layer Mixing Scheme. Part I: Scheme Description and Single-Column Model Tests". In: *Monthly Weather Review* 128.9, pp. 3187–3199.

Loeppky, J. L., Sacks, J., and Welch, W. J. (2009). "Choosing the Sample Size of a Computer Experiment: A Practical Guide". In: *Technometrics* 51.4, pp. 366–376.

Mann, G. W., Carslaw, K. S., Spracklen, D. V., Ridley, D. A., Manktelow, P. T., Chipperfield, M. P., Pickering, S. J., and Johnson, C. E. (2010). "Description and evaluation of GLOMAP-mode: a modal global aerosol microphysics model for the UKCA composition-climate model". In: *Geoscientific Model Development* 3.2, pp. 519–551.

Manners, J., Edwards, J. M., Hill, P., and Thelen, J.-C. (2023). *SOCRATES Technical Guide Suite Of Community RAdiative Transfer codes based on Edwards and Slingo*. Met Office, FitzRoy Rd, Exeter EX1 3PB.

Marshall, L., Johnson, J. S., Mann, G. W., Lee, L., Dhomse, S. S., Regayre, L., Yoshioka, M., Carslaw, K. S., and Schmidt, A. (2019). "Exploring How Eruption Source Parameters Affect Volcanic Radiative Forcing Using Statistical Emulation". In: *Journal of Geophysical Research: Atmospheres* 124.2, pp. 964–985.

Mason, R. H., Si, M., Chou, C., Irish, V. E., Dickie, R., Elizondo, P., Wong, R., Brintnell, M., Elsasser, M., Lassar, W. M., Pierce, K. M., Leaitch, W. R., MacDonald, A. M., Platt, A., Toom-Sauntry, D., Sarda-Estève, R., Schiller, C. L., Suski, K. J., Hill, T. C. J., Abbatt, J. P. D., Huffman, J. A., DeMott, P. J., and Bertram, A. K. (2016). "Size-resolved measurements of ice-nucleating particles at six locations in North America and one in Europe". In: *Atmospheric Chemistry and Physics* 16.3, pp. 1637–1651.

McCluskey, C. S., Niu, Q., Hannay, C., Nusbaumer, J. M., Medeiros, B., McFarquhar, G. M., Chapman, W., Fowler, M. D., Stephens, B., Wang, D., Protat, A., and Mace, G. G. (2024). "Mixed Phase Aerosol-Cloud Interactions over the Southern Ocean". In: *AGU Fall Meeting Abstracts*. Vol. 2024. AGU Fall Meeting Abstracts, A54C-01, A54C–01.

McCluskey, C. S., Ovadnevaite, J., Rinaldi, M., Atkinson, J., Belosi, F., Ceburnis, D., Marullo, S., Hill, T. C. J., Lohmann, U., Kanji, Z. A., O'Dowd, C., Kreidenweis,

S. M., and DeMott, P. J. (2018). "Marine and Terrestrial Organic Ice-Nucleating Particles in Pristine Marine to Continentally Influenced Northeast Atlantic Air Masses". In: *Journal of Geophysical Research: Atmospheres* 123.11, pp. 6196–6212.

McCoy, I. L., Wood, R., and Fletcher, J. K. (2017). "Identifying Meteorological Controls on Open and Closed Mesoscale Cellular Convection Associated with Marine Cold Air Outbreaks". In: *Journal of Geophysical Research: Atmospheres* 122.21, pp. 11678–11702.

Mitchell, J. F. B., Senior, C. A., and Ingram, W. J. (1989). "C02 and climate: a missing feedback?" In: *Nature* 341.6238, pp. 132–134.

MODIS Characterization Support Team (MCST) (2017). *MODIS 1km Calibrated Radiances Product*. MODIS Adaptive Processing System, Goddard Space Flight Center, USA.

Morrison, H., van Lier-Walqui, M., Fridlind, A. M., Grabowski, W. W., Harrington, J. Y., Hoose, C., Korolev, A., Kumjian, M. R., Milbrandt, J. A., Pawlowska, H., Posselt, D. J., Prat, O. P., Reimel, K. J., Shima, S.-I., van Diedenhoven, B., and Xue, L. (2020). "Confronting the Challenge of Modeling Cloud and Precipitation Microphysics". In: *Journal of Advances in Modeling Earth Systems* 12.8, e2019MS001689.

Murray, B. J., Carslaw, K. S., and Field, P. R. (2021). "Opinion: Cloud-phase climate feedback and the importance of ice-nucleating particles". In: *Atmospheric Chemistry and Physics* 21.2, pp. 665–679.

Murray, B. J., O'Sullivan, D., Atkinson, J. D., and Webb, M. E. (2012). "Ice nucleation by particles immersed in supercooled cloud droplets". In: *Chemical Society Reviews* 41.19, pp. 6519–6554.

Murray, B. J. and the M-Phase Team (2024). "Ice production in northern hemisphere cold air-outbreak clouds: two contrasting aircraft campaigns". In: EGU General Assembly 2024, Vienna, Austria, 14–19 Apr 2024, EGU24-11598.

Murray-Watson, R. J., Gryspeerdt, E., and Goren, T. (2023). "Investigating the development of clouds within marine cold-air outbreaks". In: *Atmospheric Chemistry and Physics* 23.16, pp. 9365–9383.

Niu, Q., McCluskey, C., and McFarquhar, G. M. (2025). "Marine Boundary Layer Cloud Condensation Nuclei Bias Over the Southern Ocean: Comparisons Between the Community Atmosphere Model 6 and Field Observations". In: *Journal of Geophysical Research: Atmospheres* 130.8, e2024JD042734.

O'Sullivan, D., Murray, B. J., Malkin, T. L., Whale, T. F., Umo, N. S., Atkinson, J. D., Price, H. C., Baustian, K. J., Browse, J., and Webb, M. E. (2014). "Ice nucleation by fertile soil dusts: relative importance of mineral and biogenic components". In: *Atmospheric Chemistry and Physics* 14.4, pp. 1853–1867.

O'Hagan, A. (2006). "Bayesian analysis of computer code outputs: A tutorial". In: *Reliability Engineering and System Safety* 91.10, pp. 1290–1300.

Oakley, J. and O'Hagan, A. (2002). "Bayesian inference for the uncertainty distribution of computer model outputs". In: *Biometrika* 89.4, pp. 769–784.

Paramonov, M., David, R. O., Kretzschmar, R., and Kanji, Z. A. (2018). "A laboratory investigation of the ice nucleation efficiency of three types of mineral and soil dust". In: *Atmospheric Chemistry and Physics* 18.22, pp. 16515–16536.

Park, J. M., van den Heever, S. C., Igel, A. L., Grant, L. D., Johnson, J. S., Saleeby, S. M., Miller, S. D., and Reid, J. S. (2020). "Environmental Controls on Tropical Sea Breeze Convection and Resulting Aerosol Redistribution". In: *Journal of Geophysical Research: Atmospheres* 125.6, e2019JD031699.

Phillips, V. T. J., Yano, J.-I., and Khain, A. (2017). "Ice Multiplication by Breakup in Ice–Ice Collisions. Part I: Theoretical Formulation". In: *Journal of the Atmospheric Sciences* 74.6, pp. 1705–1719.

Pinder, T. and Dodd, D. (2022). "GPJax: A Gaussian Process Framework in JAX". In: *Journal of Open Source Software* 7.75, p. 4455.

Porter, G. C. E., Sikora, S. N. F., Adams, M. P., Proske, U., Harrison, A. D., Tarn, M. D., Brooks, I. M., and Murray, B. J. (2020). "Resolving the size of ice-nucleating particles with a balloon deployable aerosol sampler: the SHARK". In: *Atmospheric Measurement Techniques* 13.6, pp. 2905–2921.

Porter, G. C. E., Adams, M. P., Brooks, I. M., Ickes, L., Karlsson, L., Leck, C., Salter, M. E., Schmale, J., Siegel, K., Sikora, S. N. F., Tarn, M. D., Vüllers, J., Wernli, H., Zieger, P., Zinke, J., and Murray, B. J. (2022). "Highly Active Ice-Nucleating Particles at the Summer North Pole". In: *Journal of Geophysical Research: Atmospheres* 127.6, e2021JD036059.

Possner, A., Pfannkuch, K., and Ramadoss, V. (2024). "Cloud-Resolving ICON Simulations of Secondary Ice Production in Arctic Mixed-Phase Stratocumuli Observed during M-PACE". In: *Journal of the Atmospheric Sciences* 81.2, pp. 417–434.

Prévost, L. M. C., Regayre, L. A., Johnson, J. S., McNeall, D., Milton, S., and Carslaw, K. S. (2025). "Detection of structural deficiencies in a global aerosol model to explain limits in parametric uncertainty reduction". In: *EGUsphere* 2025, pp. 1–65.

Proske, U., Ferrachat, S., Klampt, S., Abeling, M., and Lohmann, U. (2023). "Addressing Complexity in Global Aerosol Climate Model Cloud Microphysics". In: *Journal of Advances in Modeling Earth Systems* 15.5, e2022MS003571.

Proske, U., Ferrachat, S., Neubauer, D., Staab, M., and Lohmann, U. (2022). "Assessing the potential for simplification in global climate model cloud microphysics". In: *Atmospheric Chemistry and Physics* 22.7, pp. 4737–4762.

Pruppacher, H. and Klett, J. (1996). *Microphysics of Clouds and Precipitation*. Atmospheric and Oceanographic Sciences Library. Springer Netherlands.

Raif, E. N., Barr, S. L., Tarn, M. D., McQuaid, J. B., Daily, M. I., Abel, S. J., Barrett, P. A., Bower, K. N., Field, P. R., Carslaw, K. S., and Murray, B. J. (2024). "High ice-

nucleating particle concentrations associated with Arctic haze in springtime cold-air outbreaks". In: *EGUsphere* 2024, pp. 1–38.

Regayre, L. A., Deaconu, L., Grosvenor, D. P., Sexton, D. M. H., Symonds, C., Langton, T., Watson-Paris, D., Mulcahy, J. P., Pringle, K. J., Richardson, M., Johnson, J. S., Rostron, J. W., Gordon, H., Lister, G., Stier, P., and Carslaw, K. S. (2023). "Identifying climate model structural inconsistencies allows for tight constraint of aerosol radiative forcing". In: *Atmospheric Chemistry and Physics* 23.15, pp. 8749–8768.

Regayre, L. A., Pringle, K. J., Booth, B. B. B., Lee, L. A., Mann, G. W., Browse, J., Woodhouse, M. T., Rap, A., Reddington, C. L., and Carslaw, K. S. (2014). "Uncertainty in the magnitude of aerosol-cloud radiative forcing over recent decades". In: *Geophysical Research Letters* 41.24, pp. 9040–9049.

Regayre, L. A., Johnson, J. S., Yoshioka, M., Pringle, K. J., Sexton, D. M. H., Booth, B. B. B., Lee, L. A., Bellouin, N., and Carslaw, K. S. (2018). "Aerosol and physical atmosphere model parameters are both important sources of uncertainty in aerosol ERF". In: *Atmospheric Chemistry and Physics* 18.13, pp. 9975–10006.

Regayre, L. A., Pringle, K. J., Lee, L. A., Rap, A., Browse, J., Mann, G. W., Reddington, C. L., Carslaw, K. S., Booth, B. B. B., and Woodhouse, M. T. (2015). "The Climatic Importance of Uncertainties in Regional Aerosol–Cloud Radiative Forcings over Recent Decades". In: *Journal of Climate* 28.17, pp. 6589–6607.

Renfrew, I. A. and Moore, G. W. K. (1999). "An Extreme Cold-Air Outbreak over the Labrador Sea: Roll Vortices and Air–Sea Interaction". In: *Monthly Weather Review* 127.10, pp. 2379–2394.

Saltelli, A., Chan, K., and Scott, E. (2000). *Sensitivity Analysis*. Vol. 134.

Sanchez-Marroquin, A., Arnalds, O., Baustian-Dorsi, K. J., Browse, J., Dagsson-Waldhauserova, P., Harrison, A. D., Maters, E. C., Pringle, K. J., Vergara-Temprado, J., Burke, I. T., McQuaid, J. B., Carslaw, K. S., and Murray, B. J. (2020). "Iceland is an episodic source of atmospheric ice-nucleating particles relevant for mixed-phase clouds". In: *Science Advances* 6.26, eaba8137.

Sansom, R. W. N., Johnson, J. S., Regayre, L. A., Lee, L. A., and Carslaw, K. S. (2025). "Strong control of the stratocumulus-to-cumulus transition time by aerosol: analysis of the joint roles of several cloud-controlling factors using Gaussian process emulation". In: *EGUsphere* 2025, pp. 1–30.

Sansom, R. (2021). "Demystifying the complex nature of stratocumulus clouds with machine learning". In: *Weather* 76.6, pp. 185–191.

— (2023). "Statistical methods to understand and visualise the complex behaviour of clouds in the climate system". Unpublished.

Sansom, R. W. N., Carslaw, K. S., Johnson, J. S., and Lee, L. (2024). "An Emulator of Stratocumulus Cloud Response to Two Cloud-Controlling Factors Accounting

for Internal Variability". In: *Journal of Advances in Modeling Earth Systems* 16.9, e2023MS004179.

Sherwood, S. C., Webb, M. J., Annan, J. D., Armour, K. C., Forster, P. M., Hargreaves, J. C., Hegerl, G., Klein, S. A., Marvel, K. D., Rohling, E. J., Watanabe, M., Andrews, T., Braconnot, P., Bretherton, C. S., Foster, G. L., Hausfather, Z., von der Heydt, A. S., Knutti, R., Mauritsen, T., Norris, J. R., Proistosescu, C., Rugenstein, M., Schmidt, G. A., Tokarska, K. B., and Zelinka, M. D. (2020). "An Assessment of Earth's Climate Sensitivity Using Multiple Lines of Evidence". In: *Reviews of Geophysics* 58.4, e2019RG000678.

Si, M., Evoy, E., Yun, J., Xi, Y., Hanna, S. J., Chivulescu, A., Rawlings, K., Veber, D., Platt, A., Kunkel, D., Hoor, P., Sharma, S., Leaitch, W. R., and Bertram, A. K. (2019). "Concentrations, composition, and sources of ice-nucleating particles in the Canadian High Arctic during spring 2016". In: *Atmospheric Chemistry and Physics* 19.5, pp. 3007–3024.

Sotiropoulou, G., Sullivan, S., Savre, J., Lloyd, G., Lachlan-Cope, T., Ekman, A. M. L., and Nenes, A. (2020). "The impact of secondary ice production on Arctic stratocumulus". In: *Atmospheric Chemistry and Physics* 20.3, pp. 1301–1316.

Steinke, I., Funk, R., Busse, J., Iturri, A., Kirchen, S., Leue, M., Möhler, O., Schwartz, T., Schnaiter, M., Sierau, B., Toprak, E., Ullrich, R., Ulrich, A., Hoose, C., and Leisner, T. (2016). "Ice nucleation activity of agricultural soil dust aerosols from Mongolia, Argentina, and Germany". In: *Journal of Geophysical Research: Atmospheres* 121.22, pp. 13559–13576.

Steinke, I., Hiranuma, N., Funk, R., Höhler, K., Tüllmann, N., Umo, N. S., Weidler, P. G., Möhler, O., and Leisner, T. (2020). "Complex plant-derived organic aerosol as ice-nucleating particles – more than the sums of their parts?" In: *Atmospheric Chemistry and Physics* 20.19, pp. 11387–11397.

Storelvmo, T., Tan, I., and Korolev, A. V. (2015). "Cloud Phase Changes Induced by CO2 Warming—a Powerful yet Poorly Constrained Cloud-Climate Feedback". In: *Current Climate Change Reports* 1.4, pp. 288–296.

Sullivan, S. C., Barthlott, C., Crosier, J., Zhukov, I., Nenes, A., and Hoose, C. (2018). "The effect of secondary ice production parameterization on the simulation of a cold frontal rainband". In: *Atmospheric Chemistry and Physics* 18.22, pp. 16461–16480.

Takahashi, T., Nagao, Y., and Kushiyama, Y. (1995). "Possible High Ice Particle Production during Graupel–Graupel Collisions". In: *Journal of Atmospheric Sciences* 52.24, pp. 4523–4527.

Tarn, M., Foster, P., McQuaid, J., Robinson, J., Clarke, S., Raif, E., Choularton, T., Gallagher, M., Bower, K., Field, P., and Murray, B. (2025). *Ice-nucleating particle measurements from the M-Phase 2022 flight campaign.*

Thompson, K. A. (2024). "The ice-nucleating activity of fertile soils and crop pathogens". phd. University of Leeds.

Tornow, F., Ackerman, A. S., and Fridlind, A. M. (2021). "Preconditioning of overcast-to-broken cloud transitions by riming in marine cold air outbreaks". In: *Atmospheric Chemistry and Physics* 21.15, pp. 12049–12067.

Twomey, S. (1977). "The Influence of Pollution on the Shortwave Albedo of Clouds". In: *Journal of Atmospheric Sciences* 34.7, pp. 1149–1152.

Usher, W., Herman, J., Whealton, C., Hadka, D., Rios, F., Mutel, C., and van Engelen, J. (2016). *SALib/SALib: Launch!* Version v1.0.0.

Vali, G. (2008). "Repeatability and randomness in heterogeneous freezing nucleation". In: *Atmospheric Chemistry and Physics* 8.16, pp. 5017–5031.

Van Weverberg, K., Giangrande, S., Zhang, D., Morcrette, C. J., and Field, P. R. (2023). "On the Role of Macrophysics and Microphysics in Km-Scale Simulations of Mixed-Phase Clouds During Cold Air Outbreaks". In: *Journal of Geophysical Research: Atmospheres* 128.11, e2022JD037854.

Van Weverberg, K., Morcrette, C. J., and Boutle, I. (2021a). "A Bimodal Diagnostic Cloud Fraction Parameterization. Part II: Evaluation and Resolution Sensitivity". In: *Monthly Weather Review* 149.3, pp. 859–878.

Van Weverberg, K., Morcrette, C. J., Boutle, I., Furtado, K., and Field, P. R. (2021b). "A Bimodal Diagnostic Cloud Fraction Parameterization. Part I: Motivating Analysis and Scheme Description". In: *Monthly Weather Review* 149.3, pp. 841–857.

Vergara-Temprado, J., Miltenberger, A. K., Furtado, K., Grosvenor, D. P., Shipway, B. J., Hill, A. A., Wilkinson, J. M., Field, P. R., Murray, B. J., and Carslaw, K. S. (2018). "Strong control of Southern Ocean cloud reflectivity by ice-nucleating particles". In: *Proceedings of the National Academy of Sciences* 115.11, pp. 2687–2692.

Walters, D., Boutle, I., Brooks, M., Melvin, T., Stratton, R., Vosper, S., Wells, H., Williams, K., Wood, N., Allen, T., Bushell, A., Copsey, D., Earnshaw, P., Edwards, J., Gross, M., Hardiman, S., Harris, C., Heming, J., Klingaman, N., Levine, R., Manners, J., Martin, G., Milton, S., Mittermaier, M., Morcrette, C., Riddick, T., Roberts, M., Sanchez, C., Selwood, P., Stirling, A., Smith, C., Suri, D., Tennant, W., Vidale, P. L., Wilkinson, J., Willett, M., Woolnough, S., and Xavier, P. (2017). "The Met Office Unified Model Global Atmosphere 6.0/6.1 and JULES Global Land 6.0/6.1 configurations". In: *Geoscientific Model Development* 10.4, pp. 1487–1520.

Wegener, A. (1911). *Thermodynamik der Atmosphäre*. Leipzig: J. A. Barth. 331 pp.

Wellmann, C., Barrett, A. I., Johnson, J. S., Kunz, M., Vogel, B., Carslaw, K. S., and Hoose, C. (2018). "Using Emulators to Understand the Sensitivity of Deep Convective Clouds and Hail to Environmental Conditions". In: *Journal of Advances in Modeling Earth Systems* 10.12, pp. 3103–3122.

Wellmann, C., Barrett, A. I., Johnson, J. S., Kunz, M., Vogel, B., Carslaw, K. S., and Hoose, C. (2020). "Comparing the impact of environmental conditions and

microphysics on the forecast uncertainty of deep convective clouds and hail". In: *Atmospheric Chemistry and Physics* 20.4, pp. 2201–2219.

Welti, A., Bigg, E. K., DeMott, P. J., Gong, X., Hartmann, M., Harvey, M., Henning, S., Herenz, P., Hill, T. C. J., Hornblow, B., Leck, C., Löffler, M., McCluskey, C. S., Rauker, A. M., Schmale, J., Tatzelt, C., van Pinxteren, M., and Stratmann, F. (2020). "Ship-based measurements of ice nuclei concentrations over the Arctic, Atlantic, Pacific and Southern oceans". In: *Atmospheric Chemistry and Physics* 20.23, pp. 15191–15206.

Willett, M. R., Graham, T., Brooks, M., and Copsey, D. (2020). *GC4 and GA8GL9 acceptance report*. Tech. rep. Uk Met Office.

Woodward, S., Sellar, A. A., Tang, Y., Stringer, M., Yool, A., Robertson, E., and Wiltshire, A. (2022). "The simulation of mineral dust in the United Kingdom Earth System Model UKESM1". In: *Atmospheric Chemistry and Physics* 22.22, pp. 14503–14528.

Wu, P. and Ovchinnikov, M. (2022). "Cloud Morphology Evolution in Arctic Cold-Air Outbreak: Two Cases During COMBLE Period". In: *Journal of Geophysical Research: Atmospheres* 127.10, e2021JD035966.

Young, G., Lachlan-Cope, T., O'Shea, S. J., Dearden, C., Listowski, C., Bower, K. N., Choularton, T. W., and Gallagher, M. W. (2019). "Radiative Effects of Secondary Ice Enhancement in Coastal Antarctic Clouds". In: *Geophysical Research Letters* 46.4, pp. 2312–2321.

Zelinka, M. D., Myers, T. A., McCoy, D. T., Po-Chedley, S., Caldwell, P. M., Ceppi, P., Klein, S. A., and Taylor, K. E. (2020). "Causes of Higher Climate Sensitivity in CMIP6 Models". In: *Geophysical Research Letters* 47.1, e2019GL085782.

Chapter 4

Identification of model inconsistencies using perturbed parameter ensembles and aircraft observations of mixed-phase cold-air outbreak clouds

Chapter 4 is based on the paper developed and formatted to be submitted to the *Journal of Geophysical Research: Atmospheres*: Huang, X., Field, P. R., Murray, B. J., Grosvenor, D. P., van den Heuvel, F., and Carslaw, K. S. Identification of model inconsistencies using perturbed parameter ensembles and aircraft observations of mixed-phase cold-air outbreak clouds.

Authors: Xinyi Huang[1], Paul R. Field[1,2], Benjamin J. Murray[1], Daniel P. Grosvenor[1,2], Floortje van den Heuvel[3], and Kenneth S. Carslaw[1]

[1]Institute for Climate and Atmospheric Science, School of Earth and Environment, University of Leeds, Leeds LS2 9JT, UK

[2]Met Office, Exeter EX1 3PB, UK

[3]British Antarctic Survey, Cambridge CB3 0ET, UK

4.1 Abstract

Mixed-phase clouds in marine cold-air outbreaks (CAOs) remain a major source of shortwave radiative bias in climate models over high-latitude oceans. Previous evaluations of CAO clouds have typically varied one model parameter at a time and compared models independently with either aircraft or satellite observations, limiting assessment of compensating model effects. Here, we evaluate perturbed parameter ensembles of regional simulations of a Labrador Sea CAO using aircraft observations from the M-Phase campaign and an implausibility measure based on the history-matching method. Particular attention is paid to the representation uncertainty introduced by sparse spatial aircraft sampling, which is large at some model levels and therefore reduces the ability of the observations to constrain the ensemble members. Observational constraints from different *in-situ* cloud variables identify inconsistent subsets of plausible ensemble members, and constraining models with one observed variable does not generally improve agreement with other variables. Although not all the important model parameters were perturbed, such inconsistencies may indicate structural deficiencies in the model. These inconsistencies are much less apparent when evaluating bulk cloud properties, indicating that using satellite-retrieved liquid water path or albedo to assess the modelled CAO clouds may be inadequate, as it can obscure compensating effects or inconsistencies among other cloud properties. Multiple lines of evidence suggest that our model systematically overestimates liquid water content in the mixed-phase clouds of this CAO case, contrary to findings from previous studies. This study highlights the importance of accounting for parameter interactions and compensating model effects when evaluating model representations of mixed-phase clouds.

4.2 Introduction

During marine cold-air outbreak (CAO) events, cold and dry airmass travels from polar regions, mid- or high-latitude continents to open and warm ocean, producing strong turbulent fluxes of heat and moisture from the ocean to the atmosphere and leading to rapid boundary layer deepening and extensive cloud formation (Brümmer, 1996; Kolstad et al., 2008; Kolstad et al., 2009; Fletcher et al., 2016a; Fletcher et al., 2016b). Due to low ambient temperature, the clouds formed during CAO events are typically in a mixed-phase state, where both liquid and ice exist at the same time. These mixed-phase CAO clouds have been identified as a major source of radiative bias over the Southern Ocean in climate models, associated with the underestimated cloud fraction and albedo (Bodas-Salcedo et al., 2012; Bodas-Salcedo et al., 2014; Bodas-Salcedo et al., 2016).

It has been highlighted in several studies that the underestimation of cloud albedo in mixed-phase CAO clouds is associated with an underestimation of liquid water path (LWP) compared to observations (Klein et al., 2009; Field et al., 2014; Abel et al., 2017; Vergara-Temprado et al., 2018; Van Weverberg et al., 2023). Many studies have suggested that aerosol-cloud interactions and ice formation processes play a key role in simulating the LWP of mixed-phase CAO clouds (Klein et al., 2009; Field et al., 2014; Abel et al., 2017; Vergara-Temprado et al., 2018; de Roode et al., 2019; Tornow et al., 2021; Karalis et al., 2022; Possner et al., 2024; Huang et al., 2025, Chapter 2). Prohibiting ice formation or adjusting to a lower temperature for initial ice formation can effectively increase the liquid water content in mixed-phase clouds (Field et al., 2014; Abel et al., 2017; de Roode et al., 2019). Simulating mixed-phase CAO clouds with a better representation of ice-nucleating particles (INPs), which are a subset of aerosols and catalyse ice formation, has been shown to improve the agreement of modelled LWP and SW reflectance with satellite retrievals (Vergara-Temprado et al., 2018). Modelling studies have also suggested that CCN (cloud condensation nuclei) or in-cloud droplet number concentration, and secondary ice formation processes can strongly modulate LWP and albedo of mixed-phase CAO clouds (de Roode et al., 2019; Karalis et al., 2022; Possner et al., 2024; Huang et al., 2025, Chapter 2). However, many of these studies use the one-at-a-time (OAT) test approach, perturbing one parameter or model process individually and missing the joint effects of these parameters and processes on mixed-phase CAO clouds (Huang et al., 2026, Chapter 3). Identification of the cause of model bias and an assessment of model skill may therefore be incomplete or over-confident using the OAT test approach.

Different combinations of model parameters with compensating effects among model processes can lead to the problem of equifinality when using observations to test model performance, in order to isolate the causes of model biases (Beven, 2006; Lee et al., 2016;

Carslaw et al., 2026). In our previous work of using perturbed parameter ensemble (PPE) simulations to identify interactions among parameters in mixed-phase CAO clouds (Huang et al., 2026, Chapter 3), we found that many different combinations of parameters can produce similar values of LWP or cloud albedo. This result suggests that, although a better agreement with observed cloud LWP or albedo may indicate an improved model performance in simulating mixed-phase clouds, it does not necessarily imply that the relevant physical processes and other cloud properties are also correctly represented. The risk of compensating effects among parameters is especially acute for mixed-phase clouds, where complex interactions occur between liquid droplets and ice crystals, and the bulk cloud properties and behaviours are strongly dependent on the properties of these hydrometeors (Pruppacher et al., 1996). Therefore, in this study, we use simulations from our previous work (Huang et al., 2026, Chapter 3) to account for parameter interactions, and evaluate model performance for a CAO case over the Labrador Sea using multiple observed *in-situ* cloud properties from the M-Phase aircraft campaign and satellite retrievals.

Although aircraft observations provide direct, *in-situ* measurements of cloud properties, they are subject to a representativeness issue when compared with model output (Vaillancourt et al., 2003; Zhang et al., 2007; Bulgin et al., 2022). Aircraft data are of high resolution, sampling along a one-dimensional flight track, while model fields represent grid-box means with different resolutions. Previous studies tended to overcome this mismatch by averaging the aircraft observations across time to approximate a grid-box-mean quantity (e.g., Zhang et al., 2007; Evans et al., 2025), but little work has examined how well the sparse aircraft observations sample individual model grid box. In addition, a point-by-point comparison that collocates each observation with the model grid box along the flight track has also been shown difficult for model-observation comparison of cloud properties (Vaillancourt et al., 2003; Zhang et al., 2007), as the modelled meteorological systems cannot be expected to reproduce the observed conditions exactly (Vaillancourt et al., 2003) and cloud fields are heterogeneous (Zhang et al., 2007). Previous studies tended to overcome this issue by comparing vertical profiles of *in-situ* cloud properties over a certain model region corresponding to the flight leg, assuming that the sampled clouds in that region are representative for the whole region (e.g. Zhang et al., 2007; Field et al., 2014; Smith et al., 2025). However, the incomplete sampling from aircraft over a region may also lead to representation uncertainty of aircraft measurements for the composite vertical profiles.

Representation uncertainty is highlighted as a major challenge in ruling out parameter space using observational constraints, as shown in Johnson et al. (2020) using a history matching method. The same challenge exists in this study, where model-observation discrepancy in PPE simulations is assessed with sparse aircraft observations. In history matching, an implausibility measure is usually used (e.g., Williamson

et al., 2013; Johnson et al., 2020), which evaluates the model-observation discrepancy relative to different sources of uncertainty, to rule out observationally implausible model variants. If the representation uncertainty is not well evaluated in the implausibility measure, then an ensemble member may be ruled out because of uncertainty arising from the comparison rather than because of its genuinely implausible model behaviour. This problem was highlighted by Johnson et al. (2020), who showed that observational constraints on aerosol radiative forcing were limited by both parameter compensating effects and the large, poorly defined representativeness uncertainty associated with comparing point measurements with a coarse global model. We therefore evaluate the representation uncertainty associated with the sparse aircraft observations in this study, and then account for this representation uncertainty when applying observational constraints to rule out ensemble members.

The aim of this study is to assess the consistency of constraining PPE simulations with multiple cloud variables using a statistical model-observation comparison metric, with particular attention paid to the representation uncertainty introduced by sparse spatial sampling from aircraft observations. Specifically, we address the following research questions: (1) how representative are the *in-situ* aircraft observations used for model-observation comparison; (2) when representation uncertainty is accounted for, do observational constraints on different *in-situ* cloud variables keep a consistent subset of ensemble members; (3) do observational constraints on *in-situ* different cloud properties provide consistent constraints on the simulated bulk cloud properties (e.g. LWP and albedo). Based on these research questions, this paper is structured as follows. In Section 4.3, we describe the CAO case, aircraft measurements, model simulations, satellite retrievals and model-observation comparison metric used in this study, as well as the preprocessing of both aircraft observations and model output before model-observation comparison. In Section 4.4, we present and discuss the results of assessing the representativeness of aircraft observations, comparing vertical profiles of in-cloud variables between aircraft observations and model output, and effects of constraining one cloud variable on the other variables and on the bulk cloud properties. In Section 4.5, we conclude our results and answer the research questions.

4.3 Methods and Data

4.3.1 Campaign and case description

This work focuses on a marine CAO event over the Labrador Sea on 24 October 2022, which coincided with two flights (C322 and C323) during the M-Phase aircraft campaign (Murray et al., 2024; Clarke et al., 2025). The M-Phase aircraft campaign took place between 18 October 2022 and 5 November 2022, aiming at reducing uncertainties in the mixed-phase cloud response to a warming climate (Murray et al., 2024; Clarke et

al., 2025). A detailed description on the M-Phase aircraft campaign and observational datasets can be found in Clarke et al. (2025).

Figure 4.1 shows the satellite imagery for the CAO event investigated in this study from the MODIS (Moderate Resolution Imaging Spectroradiometer) instrument onboard the Aqua satellite (MODIS Characterization Support Team (MCST), 2017), with flight tracks and domains used for regional model simulations and model-observation analysis. The model simulations are described in Section 4.3.3. There was a northwesterly flow over the Labrador Sea, with clouds forming and aligning with the wind direction. The cloud field evolves from a stratiform, closed-cellular organisation to open-cellular and broken cumulus structures downstream, which is a typical structure of cloud field for CAO events (Brümmer, 1999). Both flights were performed with the FAAM (Facility for Airborne Atmospheric Measurements) BAe-146 (British Aerospace-146) aircraft. Flight C322 measured the stratocumulus-dominated region with sawtooth profiles of clouds (Figure 4.2a), with the cloud measurements starting from 13:30 UTC to 14:30 UTC. Flight C323 measured the cumulus-dominated region using a single sawtooth at the beginning followed by a more level flight track, with cloud measurements made from 18:40 UTC to 19:40 UTC (Figure 4.2b). The measurements made on both flights are described in the next section.

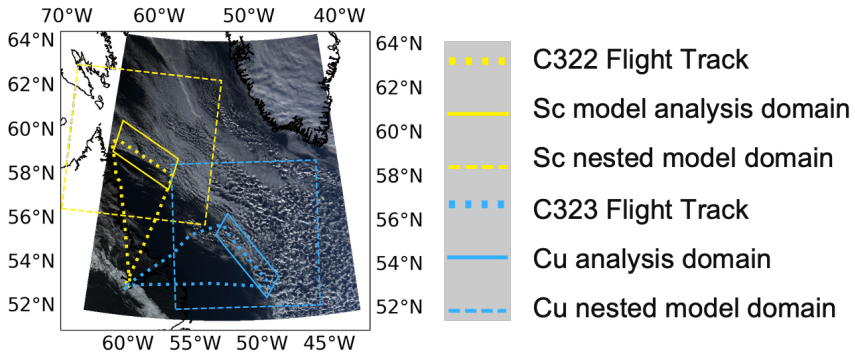


Figure 4.1: Flight tracks (dotted lines), nested model domains (dashed lines) and model analysis domain (solid lines) for Flight C322 (yellow) and Flight C323 (blue) in the M-Phase aircraft campaign. The satellite imagery was obtained from the MODIS (Moderate Resolution Imaging Spectroradiometer) instrument onboard the Aqua satellite (MODIS Characterization Support Team (MCST), 2017).

4.3.2 Aircraft measurements

The aircraft measurements of clouds used in this study include liquid water content (LWC) and ice water content (IWC) from a Nevzorov probe (Korolev et al., 1998), droplet number concentration (N_{CDP}) from a Cloud Droplet Probe (CDP) (Lance et al., 2010), and ice crystal concentration in the high-irregularity category (N_{HI}) defined

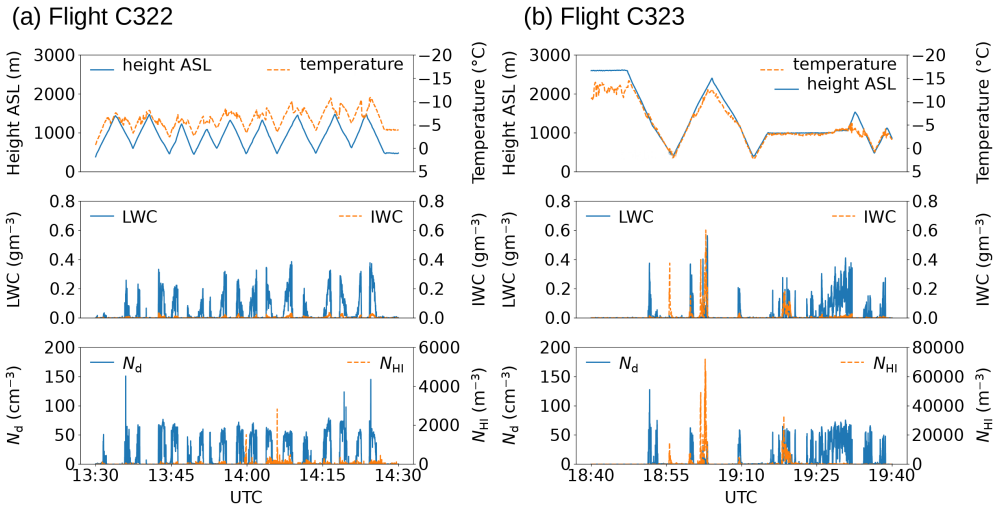


Figure 4.2: Time-series of measurements during Flight C322 and Flight C323 in the M-Phase aircraft campaign: (a) measurements during Flight C322, and (b) measurements during Flight C323. The presented measurements include height ASL (above sea level), ambient temperature, LWC (liquid water content), IWC (ice water content), N_{d} (droplet number concentration) and N_{HI} (high irregular ice crystal number concentration).

by circularity (Crosier et al., 2011) from a Two-Dimensional Stereoscopic (2D-S) probe (Lawson et al., 2006). Figure 4.2a and Figure 4.2b show the time series of these measurements during Flight C322 and Flight C323 respectively.

The Nevzorov probe measures the cloud total water content (TWC) and LWC using constant-temperature hot-wire sensors. Water contents are derived by measuring the excess energy required to maintain the heated collector in cloud, as cloud hydrometeors collide with the collector and evaporate or sublimate (Korolev et al., 1998). IWC is then obtained as the difference between TWC and LWC. A detailed description and discussion on deriving IWC from TWC and LWC can be found in Evans et al. (2025).

The CDP measures cloud droplet size distribution using forward light scattering. As droplets pass through a focused laser beam, the intensity of the scattered light by the droplets is detected to derive droplet diameter based on the Mie scattering theory. Each detected particle is then assigned to a size bin over a diameter range of approximately 2 μm to 50 μm, producing a droplet number size distribution (Lance et al., 2010). N_{CDP} used in this study was calculated by integrating the number concentrations over all measured bins.

The 2D-S probe is an optical array imaging probe and measures the size, concentration and shape of cloud hydrometeors. It consists of two identical orthogonal optical channels. Each channel uses a laser beam that illuminates a linear array of 128 photodiodes. As a cloud hydrometeor passes through the laser beam, it casts shadow images onto the photodiode arrays, allowing the hydrometeor size and shape to be recon-

structed in two dimensions. The effective pixel resolution is 10 μm, which results in a measurable size range from 10 μm to 1280 μm (Lawson et al., 2006). The raw data from the 2D-S probe was further processed using the Optical Array Shadow Imaging Software (OASIS) from the National Centre for Atmospheric Science (NCAS) and Droplet Measurement Technologies (DMT) (Crosier et al., 2011) to obtain the hydrometeor size distribution and categorization based on particle circularities. A detailed description on the processing of 2D-S raw data can be found in Biggart et al. (2026).

For ice crystal number concentration (N_{ice}) in this study, we selected only the ice crystal number concentration from the high-irregularity (HI) category, because the medium-irregularity (MI) category may contain poorly-imaged liquid droplets (Biggart et al., 2026). Using only the HI category reduces the number concentration by approximately 10% relative to the combined HI and MI categories over the M-Phase campaign (Biggart et al., 2026). As the model-observation comparison of ice crystal number is made on a logarithmic scale, using only the HI category for ice crystal number concentration (N_{HI}) is considered acceptable in this study. In addition, only particles larger than 100 μm were used to calculate the total N_{HI}, because out-of-focus liquid droplets may be erroneously identified as ice crystals (Lawson et al., 2006; Biggart et al., 2026).

4.3.3 Model simulations

The model output used in this study is from the perturbed parameter ensemble (PPE) simulations of Huang et al. (2026, Chapter 3). The simulations were performed with the UK Met Office Unified Model (UM) (Brown et al., 2012) version 13.0 using the Regional Atmosphere and Land configuration 3.2 (Bush et al., 2025), coupled to the Cloud AeroSol Interacting Microphysics scheme (CASIM) (Field et al., 2023). CASIM is a double-moment bulk microphysics scheme that predicts both the mass mixing ratios and the number concentrations of cloud hydrometeors (Field et al., 2023). The regional model was driven by hourly boundary conditions from a global simulation (N216, with a grid spacing of approximately 60 km in the mid-latitudes) using the Global Atmosphere and Land configuration 6.1 (Walters et al., 2017). The cloud parameterisation in the nested model was from the bimodal cloud scheme, which uses the subgrid turbulent kinetic energy to diagnose the subgrid humidity distribution and hence cloud fraction in a model grid box (Van Weverberg et al., 2021b; Van Weverberg et al., 2021a).

Two nested regional domains were configured to simulate different stages of the CAO cloud field. The upstream domain captured the early-stage and stratocumulus region and was centred at 60 °N, 60.5 °W, covering the flight track of C322. The downstream domain captured the cumulus region and was centred at 56 °N, 51 °W, covering the flight track of C323. Each nested domain contained 500 × 500 grid points with a horizontal grid spacing of 1.5 km. The regional model had 90 vertical levels extending to 40 km, with 16 levels below 1 km and 28 levels below 3 km. Simulations

were initialised at 00:00 UTC on 24 October 2022 and run for 24 hours. The first 12 h of model output were excluded from the analysis to allow for model spin-up.

The PPE perturbed six parameters simultaneously and contained 66 simulations for each regional domain. The combinations of the six parameters were designed using the Latin hypercube sampling method. The six parameters are the fixed in-cloud droplet number concentration (N_{d}), the INP concentration referenced to -15 °C (N_{INP}^{-15}), the efficiency of the Hallett-Mossop process (E_{HM}), the coefficient controlling the efficiency of the ice-ice collisional breakup (E_{BR}), the efficiency of the droplet-shattering process (E_{DS}), and the mixed-phase overlap factor ($mpof$) which controls the extent of spatial overlap between cloud liquid and ice in a model grid box. A detailed description on the parameters and their perturbed ranges can be found in Huang et al. (2026, Chapter 3).

For the comparison with each flight, we used instantaneous model output from a single snapshot for each flight: 14:00 UTC for C322 region and 19:00 UTC for C323 region, corresponding approximately to the midpoint of the cloud measurements on each flight. Each flight sampled clouds over approximately one hour. Model output from a single snapshot is considered appropriate here because the large-scale CAO cloud field evolved slowly relative to the one-hour measurement period (Feingold et al., 2025). For comparison in each flight, we composited the observations into mean vertical profiles and compared them with the domain-mean vertical profiles from the model (Section 4.3.4), instead of comparing the model with the aircraft point-by-point along the track. The model analysis domains (solid lines in Figure 4.1) were selected manually to capture the flight track within each nested domain.

4.3.4 Preprocessing of aircraft measurements and model output

The cloud properties used for model-observation comparison include the cloud fractions (total, liquid and ice) which is defined as the volume fraction of a model grid box covered by cloud, the in-cloud LWC and IWC, and in-cloud ice number concentration (N_{ice}). This section describes the preprocessing of both aircraft measurements and model output to make the two datasets comparable.

4.3.4.1 Mismatch in spatial resolution between aircraft observations and model simulations

The aircraft observations are point measurements along a narrow flight track, sampled at 1 Hz which corresponds to a mean horizontal spacing of approximately 120 m at the mean aircraft speed of 120 m s^{-1}). The model output consists of instantaneous grid-box mean values, so there is a mismatch in time and spatial resolution between the two datasets. The temporal mismatch is considered secondary in this study as the large-scale CAO cloud field evolved slowly relative to the temporal resolution of aircraft

measurements (Feingold et al., 2025).

To address the spatial mismatch, previous studies have averaged aircraft observations to match the model grid spacing (e.g., Van Weverberg et al., 2021b; Fast et al., 2022; Evans et al., 2025). However, because one aim of this study is to characterise sampling density of aircraft observations relative to the model resolution, we instead first collocated each 1 Hz aircraft measurement to the nearest model grid box based on latitude, longitude and height above sea level (ASL), and then averaged all measurements within each model grid box to represent observed model-grid-box mean. This introduces a representation uncertainty of using sparse point measurements from aircraft observations to compare with model grid-box-mean values.

4.3.4.2 Compositing vertical profiles

In addition to the mismatch in spatial resolution, Vaillancourt et al. (2003) noted that a point-by-point comparison, in which model output is sampled along the flight track, is a severe test. This is because the modelled meteorological systems cannot be expected to reproduce the observed conditions exactly (Vaillancourt et al., 2003). Such point-by-point comparison has been shown difficult for comparing modelled cloud properties to the observations because of the heterogeneity of cloud fields (Zhang et al., 2007).

Following a similar approach of previous studies (e.g., Zhang et al., 2007; Field et al., 2014), we used domain-mean vertical profiles of cloud properties composited from the collocated and averaged aircraft measurements in each flight. Figure 4.3 shows the domain-mean vertical profiles from the aircraft measurements. The corresponding modelled vertical profiles were averaged from the model analysis domains as shown in Figure 4.1. Using vertical profiles from sparse aircraft observations to compare with modelled vertical profiles introduces another representation uncertainty, because the aircraft track only partially sampled the model analysis domain and may not capture the full spatial variability of cloud properties within the model domain.

4.3.4.3 Deriving measured cloud fractions from aircraft observations

Cloud fractions are direct model diagnostics from the bimodal cloud scheme (Van Weverberg et al., 2021b; Van Weverberg et al., 2021a), which is defined as the volume fraction of a model grid box covered by cloud. Because the aircraft did not measure cloud fraction directly, we derived cloud fraction from other measurements. We defined the measured cloud fraction as the proportion of in-cloud measurements among all measurements within a model grid box. The difference between our approach to the approach in Wood et al. (2000) is that they defined cloud fraction as the fraction of time/distance spent in cloud for a given horizontal aircraft run, which is over two-dimensional area, while our definition here is over three-dimensional volume, in order

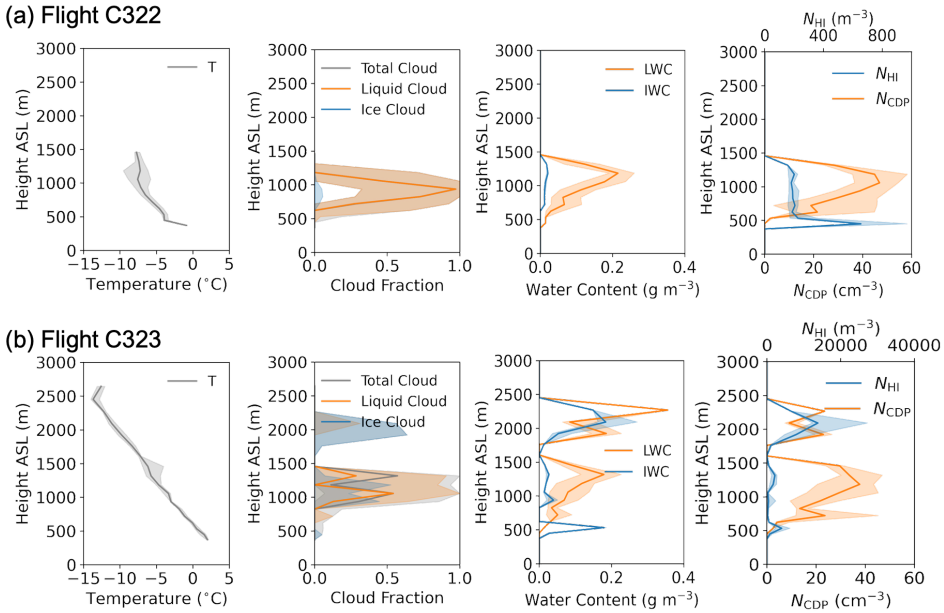


Figure 4.3: Domain-mean vertical profiles of ambient temperature, cloud fractions, in-cloud cloud water contents, N_{CDP}, and N_{HI} from aircraft measurements for (a) Flight C322, (b) Flight C323. The solid lines represent the median values of the variables, and the shaded areas are central 50% interval from 25% to 75%. The aircraft data used for compositing vertical profiles here are the collocated and averaged aircraft measurements, in order to match the model grid spacing.

to be consistent with the cloud fraction diagnostics from the model.

Liquid-cloudy measurements were identified with $N_{\mathrm{CDP}} > 2$ cm^{-3}, and ice-cloudy measurements were identified with $N_{\mathrm{HI}} > 140$ m^{-3}, as in Evans et al. (2025). Cloudy measurements were identified with either $N_{\mathrm{CDP}} > 2$ cm^{-3}, $N_{\mathrm{HI}} > 140$ m^{-3} or both. This number concentration approach identified more measurements as cloudy measurements compared with an identification with LWC and IWC using a threshold of 0.01 g m^{-3}, as shown in Figure A4.1.

Instrument simulators for model variables

Instruments have detection limits. For example, N_{HI} from the 2D-S probe only included particle sizes between 100 μm and 1280 μm, while the modelled ice number concentrations were integrated over the full particle size distribution (PSD). To compare measured and simulated values, we built instrument simulators.

For in-cloud LWC and IWC, we applied a detection threshold for model variables. The detection threshold is set to 0.01 g m^{-3}, consistent with Abel et al. (2017) and Evans et al. (2025). Aircraft measurements and model grid boxes with in-cloud LWC and IWC less than 0.01 g m^{-3} were removed before the vertical profile composition and comparison. For the ice number concentration, we applied a partial integration of

the modelled PSD over the instrument size range of 100 μm to 1280 μm. This required the slope parameter of the modelled PSD to be calculated from the in-cloud number concentration and mass mixing ratio of ice hydrometeors, because the shape parameter is fixed in the implementation of CASIM in UM (Field et al., 2023). As our model used a fixed in-cloud droplet number concentration setup, no further preprocessing was applied.

Throughout this paper we distinguish four hydrometeor number concentrations. N_{CDP} is the droplet number concentration measured by the CDP, and N_{HI} is the high-irregular ice crystal concentration measured by the 2D-S probe. N_{d} denotes the fixed in-cloud droplet number concentration, which is a prescribed parameter in our model (Section 4.3.3). N_{ice} denotes the modelled in-cloud ice number concentration integrated over the instrument size range. In the model-observation comparison below, N_{d} and N_{ice} are used.

4.3.5 Implausibility measure for model-observation comparison

Following the method in Johnson et al. (2020), the implausibility metric (I) is used in model-observation comparison for each cloud variable

$$I = \frac{O - M}{\sqrt{Var(O) + Var(R)}} \tag{4.1}$$

where M is the modelled cloud variable and O is the observed value from aircraft measurements after preprocessing. Var(O) is the variance in measurement from instrument uncertainty. For in-cloud LWC and IWC from the Nevzorov probe and N_{d} from the CDP, an instrument uncertainty of 20% is assumed (Schwarzenboeck et al., 2009; Lance et al., 2010). For N_{HI}, an instrument uncertainty of 50% is assumed (Baumgardner et al., 2017). Var(R) is the variance from representation uncertainty. For Var(R), we only estimated the one associated with compositing vertical profiles using sparse aircraft measurements. Estimating the representation uncertainty associated with using sparse aircraft measurements to approximate grid-box-mean values is beyond the scope of this study, because it would require knowledge of the true sub-grid spatial variability within each model grid box. Two other types of uncertainties were excluded here but included in Johnson et al. (2020), which are Var(M) and Var(S). Var(M) represents the uncertainty associated with using an emulator to estimate model output, but cloud variable from PPE simulations was directly used here, so Var(M) is set to 0. Var(S) is the structural uncertainty associated with potential structural deficiency in the model. We set Var(S) also to 0 as we do not have a way to estimate the structural uncertainty at this stage.

To account for the representation uncertainty associated with compositing domain-

mean vertical profiles, we estimated this uncertainty for each ensemble member using a subsampling approach. At each model level in the model domain, the model grid boxes were randomly sampled 10,000 times, with the size of each sample set was set equal to the number of observed grid boxes at that model level. The mean of the cloud variable within each sample was then calculated, producing a distribution of possible model means that would be obtained if the model were sparsely sampled with the aircraft. The variance from the possible model means is used as $\mathrm{Var}(R)$ for each ensemble member.

In Section 4.4.2, we use $|I| > 2$ as a threshold to identify ensemble members with large model–observation discrepancies. We refer to a member as plausible for a given cloud variable at a given model level if $|I| \leq 2$, and as ruled out otherwise. $|I| > 2$ indicates that the large model–observation discrepancy is unlikely to arise solely from the instrument and representation uncertainties considered in this study.

We also emphasise that this analysis differs from a full, emulator-based history-matching study (e.g., Williamson et al., 2013; Johnson et al., 2020; Regayre et al., 2023; Prévost et al., 2025). History matching usually rules out regions of a continuous parameter space using an emulator to interpolate model behaviour, but here we evaluate only the 66 discrete ensemble members from a sparse Latin hypercube sample. Identifying a member with a large $|I|$ therefore identifies that sampled ensemble member as inconsistent with the observations under the implausibility metric in this study, but it does not rule out the corresponding region of parameter space. The absence of an ensemble member satisfying all constraints does not prove that no other parameter combination exists.

4.3.6 Satellite retrievals

Satellite retrievals were used to support the model-observation comparison in addition to aircraft measurements. The satellite products used include RGB composites using band 1 (610-670 nm), band 3 (459–479 nm), and band 4 (545–565 nm) from the MODIS (Moderate Resolution Imaging Spectroradiometer) Level 1B Calibrated Radiances Product (Collection 6.1) (MODIS Characterization Support Team (MCST), 2017) shown in Figure 4.1, the all-sky liquid water path (LWP) from the AMSR-2 (Advanced Microwave Scanning Radiometer) columnar cloud liquid water product (version 8.2) (Wentz et al., 2014), the single scanner footprint (SSF) of top-of-atmosphere (TOA) shortwave (SW) flux from the CERES (Clouds and the Earth's Radiant Energy System) instrument (Edition 4A) (Su et al., 2015a; Su et al., 2015b). Evaluation of the control simulation against these satellite retrievals can be found in our previous work (Huang et al., 2025, Chapter 2). Here, we derived the TOA albedo as the ratio of the outgoing to the incoming SW flux from CERES, rather than comparing the outgoing SW flux directly as in Huang et al. (2025, Chapter 2).

4.4 Results and Discussion

4.4.1 Representativeness of aircraft measurements

Before comparing the observed and modelled vertical profiles, we first assess how representative the aircraft observations are of the model variables using two metrics shown in Figure 4.4, which capture different aspects of the sampling. The first is the number of aircraft point measurements per model grid box, which relates to the uncertainty in deriving grid-box mean values from aircraft point measurements. The second is the number of model grid boxes containing aircraft measurements per model height level, which relates to the horizontal coverage of the composited profiles. For the C322 region, the results are shown against height normalized by the boundary layer depth (z/z_{BL}), following the approach in Wood (2012). The use of z/z_{BL} was because a bias in temperature profiles produced a deeper boundary layer in most of the ensemble members, as shown in Figure A4.2a. The boundary layer heights of PPE members and the observed profile in the C322 region were identified as the lowest level where $d\theta/dz \geq 0.005$ Km^{-1}.

For each cloud variable, the number of valid aircraft measurements within a collocated model grid box is a measure of the sampling density of the aircraft observations. For cloud fractions, this quantity is equivalent to the total number of aircraft measurements per grid box. In both regions, the number of cloud fraction measurements mostly ranges between 5 and 15 per model grid box, corresponding to a relative sampling uncertainty of approximately 25% – 45% for the sampled mean, assuming that uncertainty scales as $1/\sqrt{n}$ (where n is the number of measurements). For in-cloud properties, the relative uncertainty increases substantially, because fewer measurements remain after non-cloudy measurements are removed. The number of measurements for N_{CDP} and in-cloud LWC is typically around 6 to 8 at the heights where most clouds occur. However, the number decreases to only 2–3 near the top and bottom of the profiles, corresponding to a much larger relative uncertainty of approximately 55% – 70%. The sampling density for N_{HI} in the C322 region is particularly limited, with most of the vertical profile represented by only 2–3 valid measurements per model grid box. We use the $1/\sqrt{n}$ only as an approximate guide, because it assumes that the measurements are statistically independent. At a 1 Hz sampling rate and a spacing of approximately 120 m, adjacent measurements are likely to be autocorrelated, particularly in the stratocumulus region, so the effective number of independent samples may be smaller than the actual number of measurements and therefore the uncertainties could be even larger.

These results suggest that substantial sampling uncertainty is associated with using aircraft point measurements to represent model grid-box-mean cloud properties, particularly for in-cloud properties and in regions where only a small number of measurements are available. Therefore, although the aircraft measurements were collocated

to the nearest model grid box, the limited number of valid measurements in many grid boxes means that the derived observational grid-box mean may still be strongly affected by sampling noise. This limitation weakens the conclusions drawn from the model–observation comparison, especially for in-cloud microphysical properties.

It is important to distinguish this sampling uncertainty from the representation uncertainty associated with using sparse point measurements to estimate a grid-box-mean value. The sampling uncertainty estimated here quantifies the uncertainty of the aircraft-derived mean to the available measurements, but it does not fully quantify the representation uncertainty associated with sub-grid variability within each model grid box. Estimating that component would require additional information about the variability of cloud properties within a model grid box, which is not available from the aircraft observations alone. We therefore do not include this sampling uncertainty as a representation uncertainty term in the implausibility measure. One approach to estimate this representation uncertainty would be using model output from a higher resolution model, such as from large-eddy simulations, to assess the sub-grid heterogeneity of the cloud properties. Similar approaches of using high-resolution model as ground truth have been applied to quantify representativeness of observations in evaluating climate simulations (e.g., Schutgens et al., 2017).

When compositing vertical profiles, the aircraft sampling is generally uneven with height, with the densest sampling around the main cloud layer and fewer valid samples near cloud base and cloud top. The design of flight paths strongly influences the horizontal sampling. The sawtooth flight path in the C322 region (Figure 4.2a) provides a better representation of cloud profiles than the C323 path, which consisted of a single and deep sawtooth followed by a mostly level flight leg (Figure 4.2b). The single and deep sawtooth path at the beginning of the C323 flight resulted in fewer than five valid grid boxes for in-cloud properties above 2000 m ASL, while the subsequent level path led to most of the observations centred around 1000 m ASL.

The representation uncertainty associated with this sparse horizontal sampling is estimated using the subsampling approach described in Section 4.3.4, and the resulting uncertainties are shown in Figures A4.3 and A4.4. A smaller number of sampled grid boxes at a model level generally leads to a larger uncertainty in the composited mean vertical profiles. This uncertainty can directly affect the implausibility measure as it appears in the denominator. When this representation uncertainty is large, the same model-observation difference produces a smaller absolute implausibility value, reducing the ability of the observational constraint to rule out ensemble members. If horizontal sampling were denser, the representation uncertainty would decrease substantially, as shown in Figures A4.5 and A4.6. Therefore, the sparse and uneven aircraft sampling in this case may limit the strength of observational constraints, which is shown in the next section.

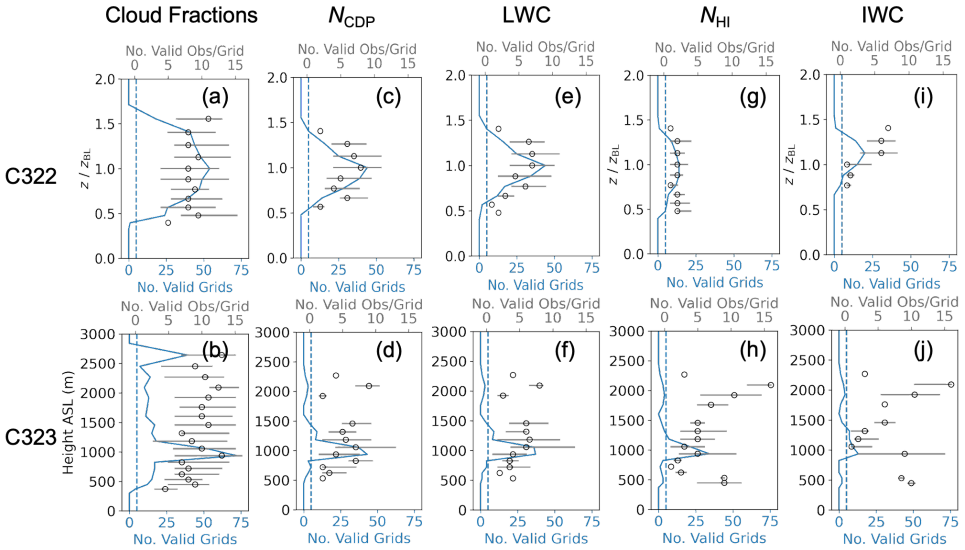


Figure 4.4: The number of aircraft measurements per model grid box (black unfilled circle for median, gray solid line for the central 50% range) and the number of valid grid boxes per model height level (blue solid line) for cloud properties assessed in this work for Flight C322 (top panel) and Flight C323 (bottom panel). The assessed cloud properties include (a, b) cloud fractions, (c, d) N_{CDP} (droplet number concentration measured by CDP), (e, f) in-cloud LWC (liquid water content), (g, h) N_{HI} (high irregular ice crystal number concentration), and (i, j) in-cloud IWC (ice water content). Dashed blue lines represents the number of valid grid boxes as 5, which is a loose threshold used in this work to assess whether enough points were there for calculating the mean cloud properties over the corresponding model height level.

4.4.2 Inconsistency in model-observation comparison

In this section, we aim to identify plausible ensemble members using the implausibility measure and assess the consistency of observational constraints on ensemble members across model levels and across cloud variables. Here, consistency means that the same ensemble members are identified as plausible by different observational constraints. Inconsistency means that different model levels or different cloud variables have different plausible ensemble members. As noted in Section 4.3.5, the usage of the implausibility measure here follows the concept of history matching (Craig et al., 1996; Williamson et al., 2013; Johnson et al., 2020), but is applied here to a sparse set of discrete ensemble members rather than to an emulated parameter space. Therefore, ruling out ensemble members should not be interpreted as ruling out continuous regions of parameter space. Emulators of *in-situ* cloud variables are with high uncertainties (not shown) and hence not used in this study.

4.4.2.1 Inconsistency across vertical levels for individual cloud variables

Figures 4.5 and 4.6 show the distributions of the implausibility measure (I) across all ensemble members for the Sc region and the Cu region respectively, along with the number of plausible ensemble members. Model levels with fewer than five sampled

model grid boxes were excluded from the I calculation and were therefore not used to rule out ensemble members. For N_{d}, we use the model-observation bias value rather than I, because N_{d} is prescribed as a fixed value in each ensemble member and is not subject to the representation uncertainty as the cloud variables in compositing vertical profiles. When applying the N_{d} constraint, we therefore identify plausible ensemble members for which the prescribed N_{d} is within one standard deviation of the observed N_{d}.

The number of plausible ensemble members varies substantially with model level for most cloud properties, indicating that the strength of observational constraint on individual cloud variables is not vertically consistent. Applying observational constraints on cloud fractions and cloud liquid variables in the Sc region (Figure 4.5), more ensemble members are identified as plausible in the middle and upper parts of the cloud layer than near the cloud base. At some model levels, the plausible members can be more than half of the ensemble members, suggesting a weak constraint from observations. This is because a substantial higher representation uncertainty in compositing vertical profiles with these model levels (Figure A4.3) strongly limits the effect of observational constraints. This is also seen for the Cu region (Figure 4.6), that the number of plausible members are strongly correlated with the representation uncertainty (Figure A4.4). The large representation uncertainty broadens the range of acceptable model-observation discrepancy in the implausibility measure and should be interpreted with caution as evidence of good model performance.

The number of plausible ensemble members is not just affected by the magnitude of representation uncertainty alone, but also the model-observation discrepancy. For example, no ensemble members are retained near cloud base in either region with the in-cloud LWC constraints. The values of I are strongly negative, meaning that the mean observed in-cloud LWC is significantly lower than the modelled values. This suggests that the PPE systematically fails to reproduce the observed lower-cloud LWC, and the model overestimation of in-cloud LWC at these model levels is unlikely to be explained by the considered representation and instrument uncertainties alone. This points to a systematic model bias that may not be resolved by perturbing the six parameters here. One possible cause is that the model prescribes a fixed droplet number concentration and therefore cannot represent processes such as aerosol or CCN scavenging, which could reduce droplet number concentrations near cloud base and reduce the in-cloud LWC. Previous studies have also shown the boundary layer scheme and additional cloud microphysical parameters can affect the simulation of liquid water content in mixed-phase CAO clouds (Field et al., 2014; Van Weverberg et al., 2023). Testing the sensitivity to additional cloud and boundary layer schemes would require additional parameter to be tested, while replacing prescribed N_{d} with aerosol-derived N_{d} would require a structural change to the model configuration. Both extensions are beyond

the scope of this study, but they are recommended for future work.

Constraints on in-cloud IWC also lead to strong negative values of I in both regions. The model-observation discrepancy is particularly pronounced in the Cu region, where no ensemble members are identified as plausible, indicating a systematic overestimation of in-cloud IWC across the examined model levels. Together with the in-cloud LWC discrepancy, this suggests that the model tends to overestimate in-cloud cloud condensate amount for both ice and liquid, and that this overestimation is not resolved by the tested parameters, even though these parameters have previously been shown important to in-cloud LWC and IWC in mixed-phase clouds (Tornow et al., 2021; Karalis et al., 2022; Possner et al., 2024; Huang et al., 2025, Chapter 2).

To further illustrate the inconsistency of observational constraints across vertical levels for individual cloud variables, binary (plausible/ implausible) maps for ensemble members are shown in Figures A4.7 and A4.8 for individual observational constraints. These maps show whether each ensemble member is identified as plausible at each model level when a single observational constraint is used. For both regions, no single ensemble member is identified as plausible at all model levels when total, liquid, or ice cloud fraction are used individually as the constraint. The parameter distributions from plausible ensemble members consequently differ across model levels (Figures A4.9 - A4.12). This means that an ensemble member identified as plausible at one model level is not necessarily as plausible at another model level for the same observational constraint. This inconsistency is similar to the level-2 structural inconsistency described by Prévost et al. (2025), where the constrained parts of parameter space by multiple constraints do not overlap.

Only a few ensemble members are identified as plausible for some in-cloud properties across all available model levels, such as in-cloud IWC in the Sc region (Figure A4.7), and in-cloud N_{d}/LWC, in-cloud N_{ice} and N_{ice}/IWC in the Cu region (Figure A4.8). In particular, the two ensemble members identified as plausible by in-cloud N_{ice} constraint in the Cu region have N_{INP}^{-15} parameter values of 0.08 L^{-1} and 0.05 L^{-1}, which are close to the two observed N_{INP}^{-15} values from the M-Phase C323 measurements (0.02 L^{-1} and 0.08 L^{-1}). This suggests that in-cloud N_{ice} constraint may provide useful information about INP concentrations in the Cu region. However, the values of N_{INP}^{-15} associated with plausible ensemble members from other observational constraints do not agree with the observed N_{INP}^{-15}. That is, constraint on one cloud variable does not necessarily imply that the same set of ensemble members can reproduce other cloud variables or constrain the parameters in a consistent way. The consistency of observational constraints across different cloud variables is assessed in the next section.

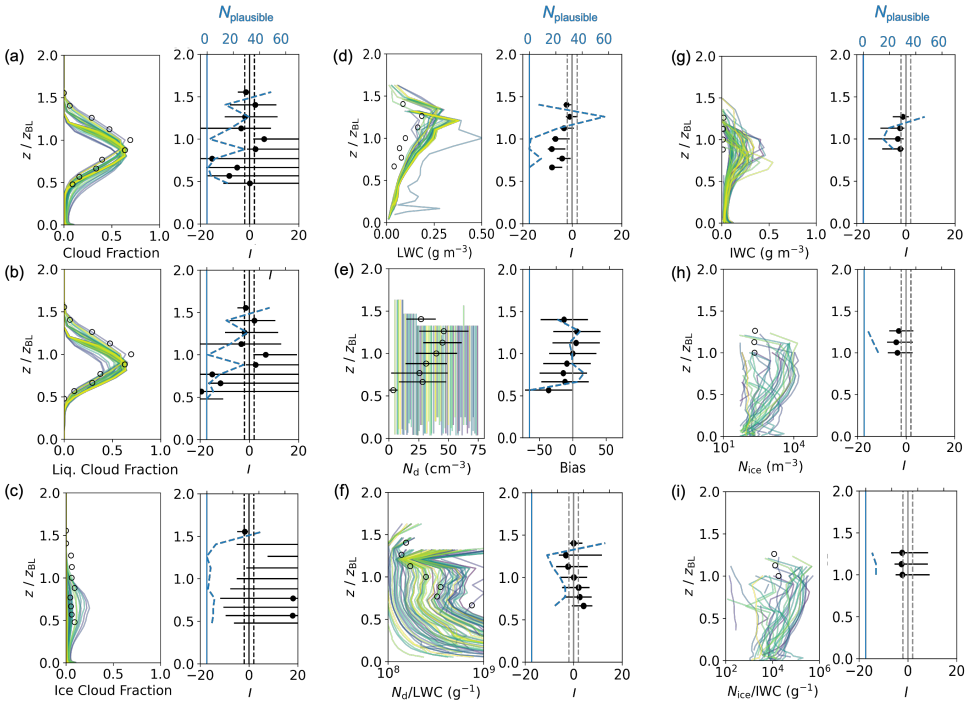


Figure 4.5: Vertical profiles in the C322 Sc region for cloud properties from aircraft observations and model output, along with the distribution of I and the number of plausible ensemble members with $|I| \leq 2$ for: (a) cloud fraction (unitless), (b) liquid cloud fraction (unitless), (c) ice cloud fraction (unitless), (d) in-cloud LWC (g m^{-3}), (e) in-cloud N_{d} (cm^{-3}), (f) in-cloud N_{d}/LWC (g^{-1}), (g) in-cloud IWC (g m^{-3}), (h) in-cloud N_{ice} (m^{-3}) and (i) in-cloud N_{ice}/IWC (g^{-1}). Lines in profiles for cloud properties represent the mean from each ensemble member over the whole model analysis domain in Figure 4.1. The unfilled circles in profiles for cloud properties represent the mean from the aircraft observations in each flight. Filled circles and bars in the distribution of I represent the median and central 90% interval of I from all ensemble members. Dashed vertical lines in the distribution of I represent $I = -2$ and $I = 2$. Blue dashed lines represent the number of plausible ensemble members.

4.4.2.2 Inconsistency in constraints across *in-situ* cloud variables

The analysis above shows inconsistency across vertical levels when individual cloud properties are used to rule out PPE simulations against aircraft observations. We next examine whether similar inconsistencies occur among multiple cloud variables in this section. For this analysis, we select model levels where there are plausible ensemble members for all or most of the examined cloud variables. The selected model level for the Sc region is at a normalised height of approximately 1.12 relative to the boundary layer depth, and is the only level with retained ensemble members for all cloud properties. The selected level for the Cu region is at approximately 937 m ASL. The in-cloud LWC and in-cloud IWC are excluded from this analysis at this level for the Cu region because their systematic biases leave no model level available for analysis in this region.

The binary (plausible/ implausible) maps of ensemble members by applying obser-

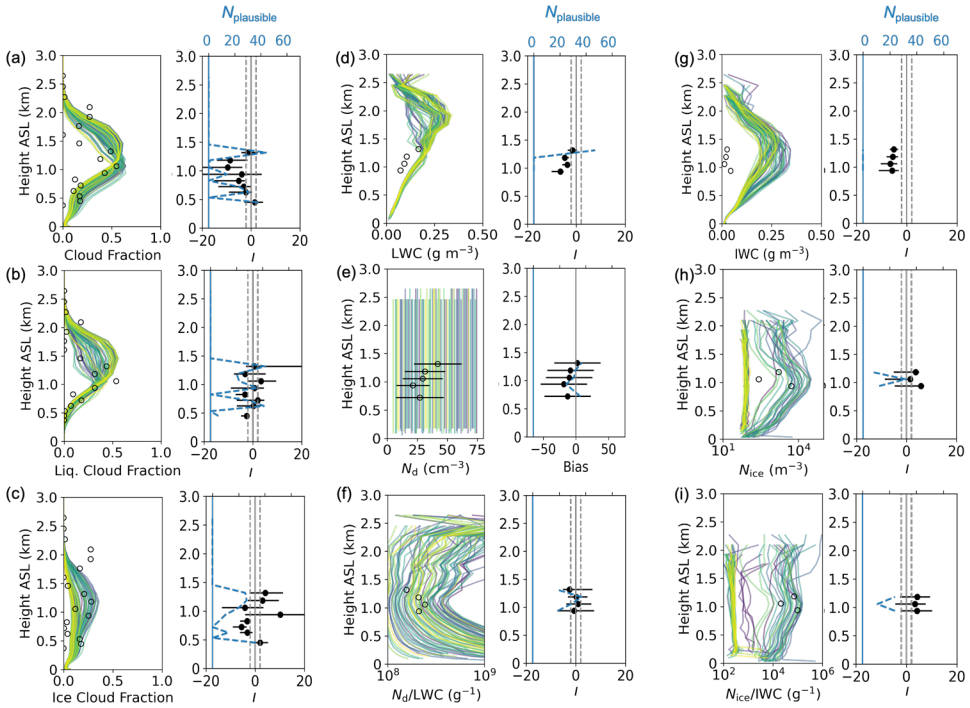


Figure 4.6: Vertical profiles in the C323 Cu region for cloud properties from aircraft observations and model output, along with the distribution of I and the number of plausible ensemble members with $|I| \leq 2$ for: (a) cloud fraction (unitless), (b) liquid cloud fraction (unitless), (c) ice cloud fraction (unitless), (d) in-cloud LWC (g m^{-3}), (e) in-cloud N_{d} (cm^{-3}), (f) in-cloud N_{d}/LWC (g^{-1}), (g) in-cloud IWC (g m^{-3}), (h) in-cloud N_{ice} (m^{-3}) and (i) in-cloud N_{ice}/IWC (g^{-1}). Lines in profiles for cloud properties represent the mean from each ensemble member over the whole model analysis domain in Figure 4.1. The unfilled circles in profiles for cloud properties represent the mean from the aircraft observations in each flight. Filled circles and bars in the distribution of I represent the median and central 90% interval of I from all ensemble members. Dashed vertical lines in the distribution of I represent $I = -2$ and $I = 2$. Blue dashed lines represent the number of plausible ensemble members.

vational constraints on different cloud variables are shown in Figure 4.7 for the Sc region and Figure 4.8 for the Cu region, together with the corresponding parameter distributions from plausible ensemble members. Inconsistencies are also evident when multiple observational constraints are used to identify ensemble members simultaneously.

First, there is no ensemble member that simulates plausible values of all cloud properties. That is, in this 6-parameter PPE, there is no combination of the parameters that produces a skilful model across all the observations. Individual ensemble members are consistent with only a small subset of the cloud variables, which is on average 2.14 out of 9 variables (23.7%) in the Sc region and 2.09 out of 7 variables (29.9%) in the Cu region. Note that the inconsistency identified here is highly dependent on the representation and instrument uncertainties considered in the implausibility measure, which are small enough to identify inconsistency here. If the representation uncertainties are large (e.g. including the representation uncertainties in using point

measurements to represent grid-box-mean values), the observational constraint will be weaker and the ability to identify model inconsistencies will be reduced.

Second, the parameter ranges constrained by some cloud properties do not always agree with the observed N_{d} and N_{INP}^{-15} from the aircraft campaign. For example, ensemble members identified as plausible with cloud fraction constraint in the Cu region generally have higher N_{d} values than observed at this model level, and lower N_{INP}^{-15} values than observed. Similarly, in the Sc region, in-cloud IWC has strongly contrasting constraint on N_{INP}^{-15}, compared to the constrained N_{INP}^{-15} ranges from N_{ice} and N_{ice}/IWC. N_{INP}^{-15} values from in-cloud IWC constraint are near the lower end of the N_{INP}^{-15} perturbed range, whereas N_{INP}^{-15} values from N_{ice} and N_{ice}/IWC constraints are near the upper end. Neither of the constrained ranges of N_{INP}^{-15} overlaps with the observed N_{INP}^{-15} values.

The ability to identify model inconsistencies with observations depends strongly on the estimated representation uncertainties. Figure 4.9 shows how different multiples of the representation uncertainty affect both the percentage of variables that are consistent per ensemble member and the number of ensemble members that are consistently constrained by all observational variables. When the representation uncertainty increases, the model consistency also increases, as indicated by a higher percentage of consistent variables per ensemble member. Once the representation uncertainty is sufficiently large, approximately by a factor of 10 of the original estimate in the Sc region and 100 in the Cu region, at least one plausible ensemble member can now be identified that is consistent with all observational constraints.

However, the percentage of consistent variables does not reach 100% in either region. This is partly because the N_{d} constraint is not affected by the representation uncertainty in this analysis due to our model setup. In addition, not all ensemble members produce N_{ice} that are measurable by the 2D-S probe. Therefore, regardless of how large the representation uncertainty becomes, these ensemble members cannot reproduce the observed N_{ice} or N_{ice}/IWC constraints.

One limitation here is that only the PPE simulations are used for comparison with the aircraft observations. These simulations provide a sparse sampling of the six-dimensional parameter space, meaning that ruling out individual ensemble members is not equivalent to ruling out regions of parameter space, as it would be in emulator-based history matching studies (e.g., Williamson et al., 2013; Johnson et al., 2020; Regayre et al., 2023; Prévost et al., 2025). Other untested combinations of parameters may exist that would make consistent model-observation comparison. For this reason, inconsistencies in this study are not assessed solely by whether a single ensemble member can satisfy all observational constraints simultaneously as shown above. We also examine whether ruling out ensemble members with one cloud variable (constrained variable)

improves or degrades the performance with the other cloud variables (affected variables), using the absolute change in the mean $|I|$ ($|\Delta I|$) of the affected variables. The change in mean $|I|$ is calculated between the full ensemble and the plausible ensemble members.

The changes in mean $|I|$ of the affected cloud variables with constraints on different constrained variables are shown in Figure 4.10. The size of each circle indicates the reduction in the spread of the affected cloud variable from the full ensemble to the plausible PPE subset. A reduction in mean $|I|$ (green) indicates that the ensemble members identified plausible with the constraint are on average closer to the aircraft observations for the affected variable. A larger circles indicates a stronger narrowing of the simulated range and hence a stronger constraint of the affected variable. The analysis in this section uses the same model levels as above.

The diagonal elements are generally large and green, as constraining one variable should reduce its discrepancy and narrow its simulated range. However, constraining one cloud variable does not lead to uniformly improved agreement across all other cloud variables, and the direction and magnitude of these effects differ between the two regions. For example, in the Sc region, constraining total cloud fraction improves the mean performance of the plausible ensemble members for the other cloud fraction diagnostics, N_{d}/LWC, N_{ice} and N_{ice}/IWC, but degrades the mean agreement for in-cloud IWC. In contrast, in the Cu region, constraining the total cloud fraction only improves the model-observation agreement from the plausible PPE subset for N_{d}/LWC, while degrading the model performance for the other variables. Such inconsistencies across variables are similar to the level-1 inconsistency described by Prévost et al. (2025), in which constraining the model with one variable does not improve model performance against the other variables.

Constraining in-cloud LWC degrades the agreement of the plausible ensemble members with the aircraft measurements for all other variables in the Sc region. This provides further evidence that the model has a systematic bias in in-cloud LWC. Applying LWC constraint selects ensemble members that agree less with the other cloud variables. Because in-cloud LWC is commonly used for evaluating mixed-phase cloud simulations, this result here demonstrates that agreement with in-cloud LWC alone is not necessarily sufficient to indicate a general improvement of other mixed-phase cloud properties.

A strong constraint is not always associated with improved model-observation agreement. For example, constraining in-cloud IWC in the Sc region substantially narrows the retained PPE range for both ICF (ice cloud fraction) and N_{ice}/IWC, as shown by the large circles in Figure 4.10a. However, this narrowing is accompanied by a substantial degradation in the mean agreement with the aircraft observations for ICF

and N_{ice}/IWC. This suggests that selecting members that better match in-cloud IWC does not simultaneously improve the representation of the other in-cloud ice properties. Similarly, in the Cu region (Figure 4.10b), constraining CF (bulk cloud fraction) results in strong constraints on ICF, N_{ice} and N_{ice}/IWC, but also leads to a strong degradation in the agreement of these variables with observations.

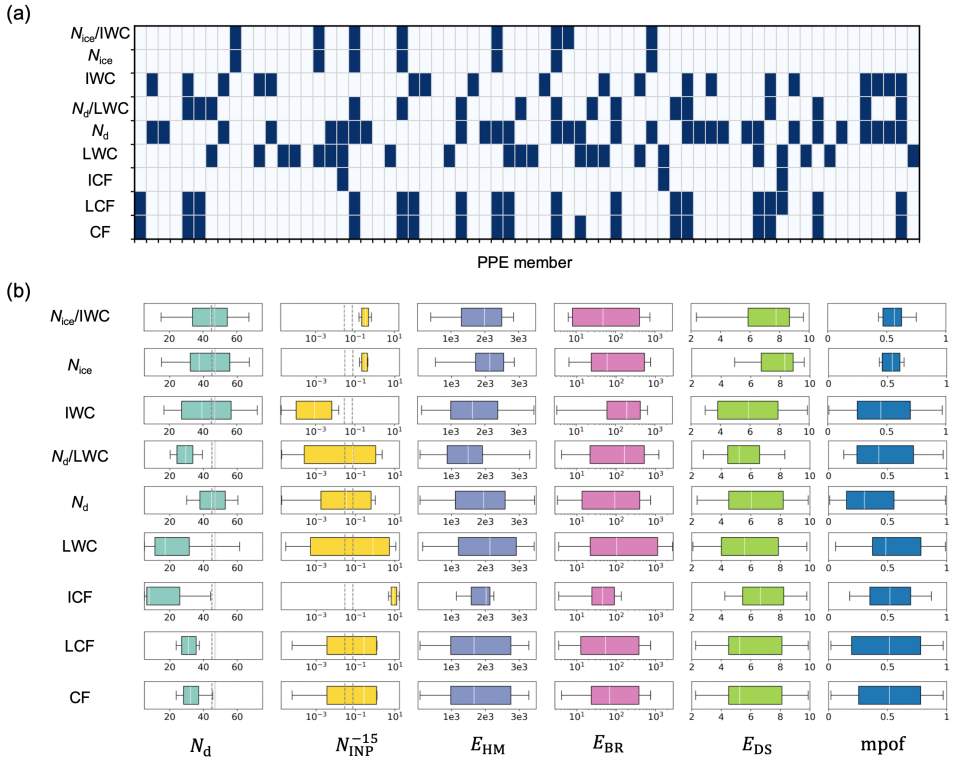


Figure 4.7: Comparison of using different observational constraints in the C322 Sc region:(a) Binary retention map for all ensemble members using different cloud variables as constraints and (b) the distributions of parameter ranges from the remaining ensemble members for the C322 Sc region. Ensemble members that are ruled out for each observational constraint are shown in light blue in the retention map, and that are retained are shown in dark blue in the retention map. The horizontal length of the subplot with distributions of constrained parameter ranges represents the perturbed range of the corresponding parameter. The analysis is based on a model level at a normalised height of approximately 1.12 relative to the boundary layer depth for this C322 Sc region. The dashed gray line in the N_d plots represents the median of N_d measured by CDP and the solid light gray line represents the mean of N_d measured by CDP. The two dashed gray lines in the N_{INP}^{-15} represents the INP concentrations at -15 °C from two runs of INP measurements during Flight C322.

4.4.3 Effects of constraining *in-situ* cloud variables on bulk cloud properties

In this section, we assess the effects on how constraining ensemble members using *in-situ* aircraft observations affects the simulated bulk cloud properties (Figure 4.11). The bulk cloud properties include cloud cover, all-sky liquid water path (LWP), and top-of-the-atmosphere (TOA) albedo. Satellite retrievals of LWP and TOA albedo are also

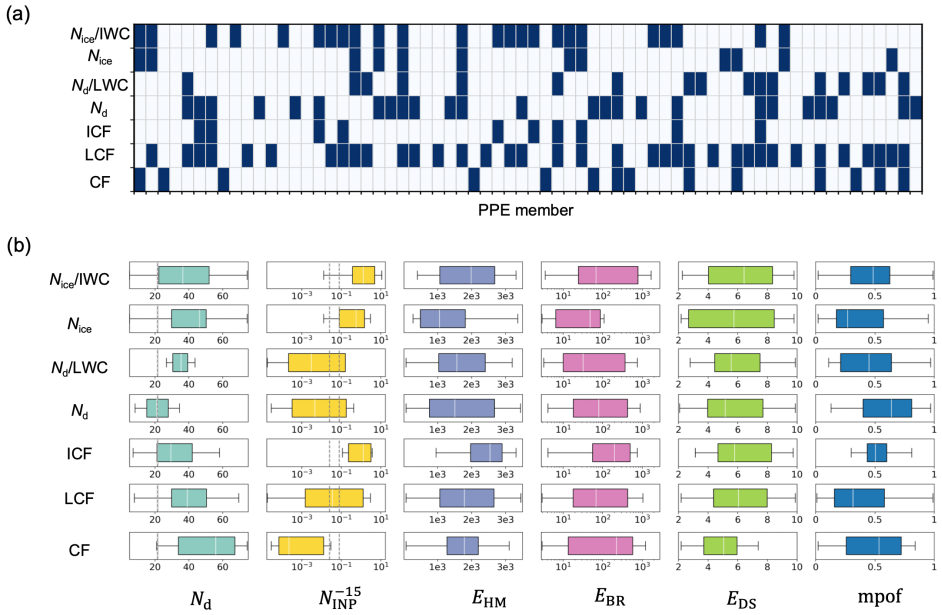


Figure 4.8: Comparison of using different observational constraints in the C323 Cu region: Binary (plausible / implausible) map for all ensemble members using different cloud variables as constraints and (b) the distributions of parameter ranges from the remaining ensemble members for the C323 Cu region. Ensemble members that are ruled out for each observational constraint are shown in light blue in the retention map, and that are retained are shown in dark blue in the retention map. The horizontal length of the subplot with distributions of constrained parameter ranges represents the perturbed range of the corresponding parameter. The analysis is based on a model level at approximately 937 m ASL for this C323 Cu region. The dashed gray line in the N_d plots represents the median of N_d measured by CDP and the solid light gray line represents the mean of N_d measured by CDP. The two dashed gray lines in the N_{INP}^{-15} represents the INP concentrations at -15 °C from two runs of INP measurements during Flight C323.

included for comparison with the modelled values. For the C322 Sc region, both the LWP from the AMSR-2 and the grid-box mean LWC measured by the Nevzorov probe is used.

The observational constraints from *in-situ* variables on the bulk cloud properties are more coherent than those found among the *in-situ* variables themselves (Figure 4.11). In the Sc region, for example, constraining different ice properties (IWC, N_{ice} and N_{ice}/IWC) produces similar effects on cloud cover (medians around 0.9) and TOA albedo (medians around 0.5), even though these ice properties show strong inconsistencies in their effects on the other microphysical properties in Section 4.4.2. This is because different cloud variables are sensitive to different parameters. The *in-situ* ice microphysical properties, such as N_{ice} and IWC, are sensitive to N_{INP}^{-15}, but they have strongly different constrained ranges of N_{INP}^{-15} (Figure 4.7b). In contrast, the bulk cloud properties examined here are dominated by N_d in this CAO case, as shown in our previous work (Huang et al., 2026, Chapter 3), and the ranges of N_d constrained by these *in-situ* ice properties are relatively similar (Figure 4.7b). In addition, constraining to-

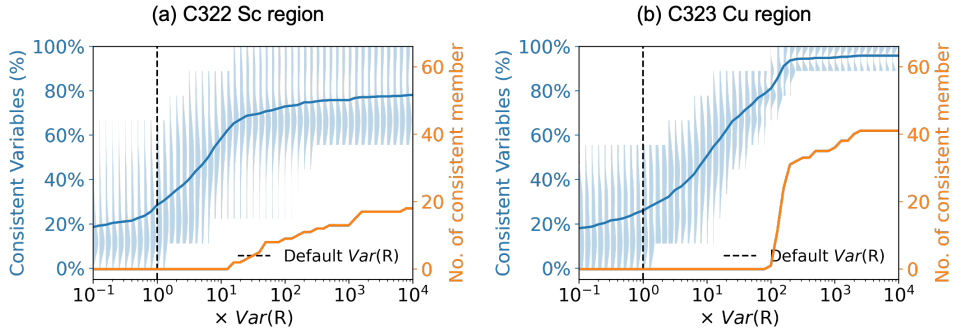


Figure 4.9: Percentage of constrained variables that are consistent with observations for each ensemble member (blue) and number of ensemble members that are consistent with all observational constraints (orange), against different multiples of the original representation uncertainty (Var(R)) for (a) the C322 Sc region and (b) the C323 Cu region. The solid blue line shows the mean percentage of consistent variables across ensemble members, and each half, blue violin plot shows the spread in this percentage at the corresponding multiple of representation uncertainty. The selected model level for the Sc region is at a normalised height of approximately 1.12 relative to the boundary layer depth, and the selected level for the Cu region is at approximately 937 m ASL.

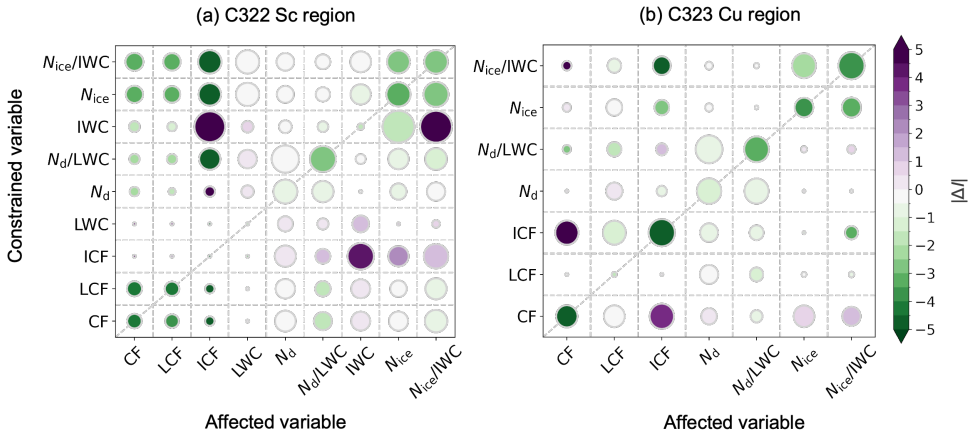


Figure 4.10: Effects of applying observational constraint on one cloud variable (constrained variable) to other cloud variables (affected variable) for (a) the C322 Sc region and (b) the C323 Cu region. The absolute change in the mean I ($\Delta|I|$) of the affected variables is calculated between the full ensemble and the subset ensemble members identified as plausible by constraining the constrained variable. A negative $\Delta|I|$ (green) indicates that the retained ensemble members are on average closer to the aircraft observations for the affected variable. The size of each circle indicates the reduction in the spread of the affected cloud variable from the full ensemble to the retained subset. Larger circles therefore indicate a stronger narrowing of the simulated range and hence a stronger constraining effect on the affected variable.

tal and liquid cloud fractions in the C322 Sc region, and N_d in the C323 Cu region, produce a better agreement of modelled TOA albedo with the observed value, but these constraints do not simultaneously improve agreement of other in-cloud variables with aircraft observations. This shows that apparent agreement of a model with satellite-retrieved cloud properties does not guarantee that the underlying cloud microphysical

properties are correctly simulated. Therefore, using bulk properties such as LWP or TOA albedo alone to constrain or tune model parameters can be inadequate, as it may obscure compensating effects or inconsistencies among other cloud properties.

The comparison of LWP provides further evidence that the model tends to overestimate liquid water in both regions. Most ensemble members have higher LWP than the satellite-retrieved LWP. In the Sc region, applying the in-cloud LWC constraint shifts the LWP bias from positive (+30 g m^{-2}) to negative (-15 g m^{-2}) relative to the satellite-retrieved LWP. This is likely because the LWC constraint is applied at a single model level, whereas LWP is a vertically integrated column quantity. Improved agreement at one level therefore does not necessarily imply improved agreement in the column-integrated liquid water. However, satellite-retrieved LWP is also subject to retrieval uncertainty, and the LWP estimated by vertically integrating the Nevzorov LWC measurements is approximately 10 g m^{-2} lower than the satellite-retrieved LWP, giving better agreement with the LWC-constrained model values. Nevertheless, the aircraft LWC profiles, the LWP comparison, and the inconsistencies introduced by the in-cloud LWC constraint together provide multiple lines of evidence that the model overestimates liquid water in this CAO case. This contrasts with the low liquid water bias reported in previous evaluations of modelled mixed-phase clouds (Klein et al., 2009; Field et al., 2014; Abel et al., 2017; Van Weverberg et al., 2023), which may arise from structural changes and tuning applied between the model versions used in earlier studies and the one used here.

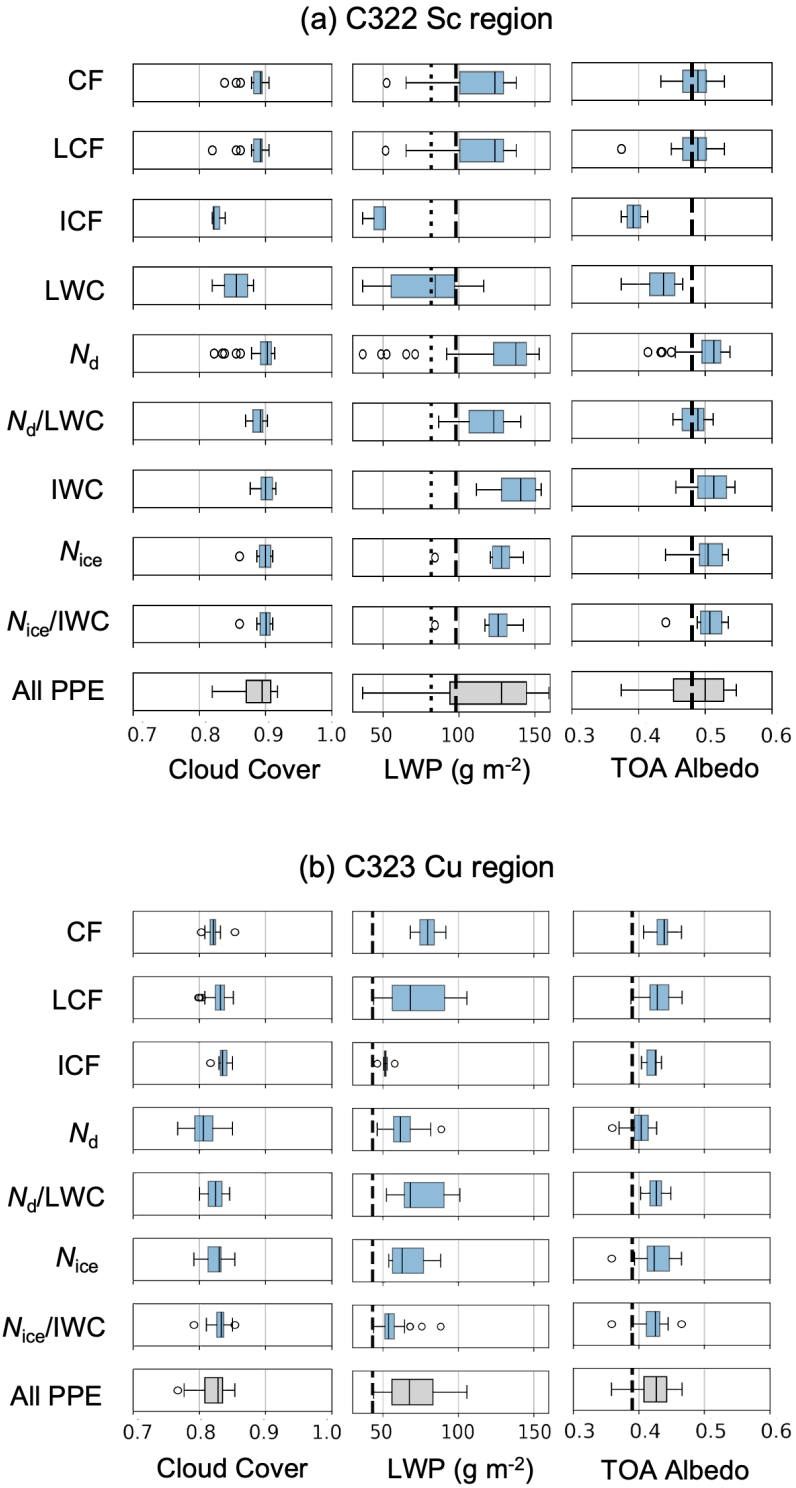


Figure 4.11: Effects of applying observational constraint on one *in-situ* cloud variable to bulk cloud properties including cloud cover, all-sky LWP (liquid water path) and TOA (top-of-the-atmosphere) albedo in: (a) the C322 Sc region and (b) the C323 Cu region. The dashed black lines in LWP and TOA albedo panels represent satellite retrieved values of these two properties. The dotted black line in LWP of the C322 Sc region represents the LWP derived using grid-box mean LWC profiles measured by the Nevzorov probe.

4.5 Conclusions

Mixed-phase cold-air outbreak (CAO) clouds remain a major source of uncertainty in climate models, and previous model evaluations have often used a one-at-a-time approach that cannot fully account for compensating effects among model parameters and processes. Building on our previous work showing that different combinations of parameters can produce similar bulk cloud properties (Huang et al., 2026, Chapter 3), this study evaluated perturbed parameter ensemble simulations (PPE) of a Labrador Sea CAO case against M-Phase aircraft observations (Clarke et al., 2025). We applied an implausibility measure based on the history-matching method (Craig et al., 1996; Williamson et al., 2013; Johnson et al., 2020), with particular attention to the representation uncertainty introduced by sparse aircraft sampling. The evaluation was performed separately for an upstream stratocumulus (Sc) region sampled by flight C322 and a downstream cumulus (Cu) region sampled by flight C323.

The aircraft observations in this case provide sparse and uneven sampling of the CAO cloud field. Most model grid boxes generally contain only a small number of cloud microphysical measurements, ranging from approximately 6-8 points per model grid box for liquid microphysical properties to fewer than 3 points per model grid box for ice microphysical properties. The limited sampling can introduce substantial uncertainty in how well the aircraft point measurements represent grid-box-mean cloud properties. The sparse horizontal sampling density of aircraft measurements at each model level is strongly dependent on the design of flight path, and introduces representation uncertainties in compositing domain-mean vertical profiles from aircraft measurements for model-observation comparison. A smaller number of model grid boxes with observations can lead to a higher representation uncertainty in comparing domain-mean vertical profiles, limiting the effect of observational constraints.

Observation-based constraints derived from different *in-situ* cloud variables identify inconsistent subsets of plausible ensemble members. No ensemble member simulates plausible values for all observed cloud properties across all model levels, indicating that none of the investigated parameter combinations produces a model that is skilful across all observations. Even with a single observational constraint, the plausible ensemble members vary with model height level, suggesting vertical inconsistency when applying observational constraints to cloud profiles. At model levels where more than one ensemble member is identified as plausible for each cloud variable, individual ensemble members are consistent with only a small subset of the cloud variables, which is on average 2.14 out of 9 variables (23.7%) in the stratocumulus region and 2.09 out of 7 variables (29.9%) in the cumulus region.

Model inconsistencies are also evident when ensemble members constrained by one cloud variable are evaluated against the other cloud variables. Constraining one cloud

variable does not consistently improve model-observation agreement for the other cloud variables. In some cases, an observational constraint substantially narrows the simulated range of another cloud variable, indicating a strong constraint on that affected variable. However, the strong narrowing does not always improve model-observation agreement of the affected variable. This inconsistency demonstrates that apparent improvement in one property of the modelled clouds can occur without a consistent improvement of all the other cloud properties.

The observational constraints from *in-situ* variables on the bulk cloud properties, including cloud cover, LWP and TOA albedo, are more coherent than those found among the *in-situ* variables themselves. However, inconsistencies are still identified in the constrained ranges of bulk cloud properties with different observational constraints. For example, in the Sc region, in-cloud LWC constraint leads to a median value of LWP around 84 g m^{-2}, while in-cloud IWC constraint leads to a median value of LWP around 140 g m^{-2}. Even if some observational constraints produced similar ranges of the bulk cloud properties, they did not necessarily have consistent constraints on the other *in-situ* cloud properties. This suggests that agreement in bulk cloud properties does not guarantee that the underlying cloud microphysics are correctly represented. Therefore, improved model agreement with bulk cloud properties should be interpreted with caution when assessing the representation of mixed-phase clouds in models.

Multiple lines of evidence suggest that our model systematically overestimated liquid water content in both regions of this CAO case, in contrast to the low liquid-water bias suggested in previous studies on mixed-phase CAO clouds (Klein et al., 2009; Field et al., 2014; Abel et al., 2017). The mean observed in-cloud LWC is significantly lower than the values from PPE at cloud base in the Sc region and across all model levels in the Cu region, and this bias cannot be explained by the representation and instrument uncertainties alone. In addition, constraining the ensemble members using in-cloud LWC as constraint in the Sc region degrades model-observation agreement for all other in-cloud properties, suggesting that improving agreement with LWC alone does not necessarily improve the overall representation of mixed-phase microphysics. The contrast of our results on LWP bias with previous studies may reflect changes in model structure and tuning between model versions.

The inconsistencies identified using multiple observational constraints may indicate potential structural deficiencies in the model, but this interpretation depends strongly on the uncertainties included in the implausibility measure and the selection of model parameters and structure. The instrument and representation uncertainties estimated in this study are small enough for model inconsistencies to be identified. If larger representation uncertainties were included, for example those associated with using sparse aircraft point measurements to represent model grid-box-mean values, the observational constraints would be weaker and the ability to identify model inconsistencies

would be reduced. In addition, the PPE does not span the full set of processes and parameters that may influence mixed-phase cloud properties. A more comprehensive and systematic assessment of model performance for mixed-phase clouds should therefore expand the set of tested parameters and processes, including those controlling boundary-layer structure, the cloud-fraction scheme, and additional cloud microphysical processes (Field et al., 2014; Van Weverberg et al., 2023). The PPE simulations also provide only a sparse sampling of the six-dimensional parameter space. Therefore, the model inconsistencies identified here should be interpreted as inconsistencies within the sampled ensemble members, rather than as evidence that no acceptable parameter combinations exist.

Our findings suggest that evaluating mixed-phase CAO clouds using a single observed variable, or using only bulk properties that can be retrieved by satellite, can lead to inadequate conclusions on the representation of these clouds in the models. Multiple observational constraints are needed, especially for comparison against PPE simulations where compensating effects from parameters are accounted for. However, it may not be possible to achieve consistent constraint across multiple observations without altering the model structure (Prévost et al., 2025). Therefore, consistent, tight observational constraint and a reduced model uncertainty will likely require a process of model development coupled with constraint steps attempted in this study, as proposed by Prévost et al. (2025). Future work should extend this approach using larger, emulated parameter spaces with CAO cases spanning various environmental conditions and locations. A better quantification of representation uncertainty in using aircraft observations for model-observation comparison is also needed, especially on using aircraft point measurements to represent model grid-box-mean cloud properties.

Appendix

(a) C322 liquid cloud measurements

LWC / N_{CDP}	Yes	No
Yes	1029	207
No	24	2341

(c) C323 liquid cloud measurements

LWC / N_{CDP}	Yes	No
Yes	649	139
No	25	288

(b) C322 ice cloud measurements

IWC / N_{HI}	Yes	No
Yes	54	234
No	137	3176

(d) C323 ice cloud measurements

IWC / N_{HI}	Yes	No
Yes	291	258
No	37	3015

Figure A4.1: Comparison of using different measurements from aircraft observations to identify in-cloud measurements for (a) liquid cloud measurements in the C322 Sc region, (b) ice cloud measurements in the C322 Sc region, (c) liquid cloud measurements in the C323 Cu region, and (d) ice cloud measurements in the C323 Cu region. The thresholds of measurement being identified as in-cloud measurements are: $N_{\mathrm{CDP}} > 2$ cm^{-3}, LWC $> 10^{-5}$ g m^{-3}, $N_{\mathrm{HI}} > 140$ m^{-3}, IWC $> 10^{-5}$ g m^{-3}. Numbers highlighted with blue shading represent the number of points counted as in-cloud measurements for each region and each cloud type.

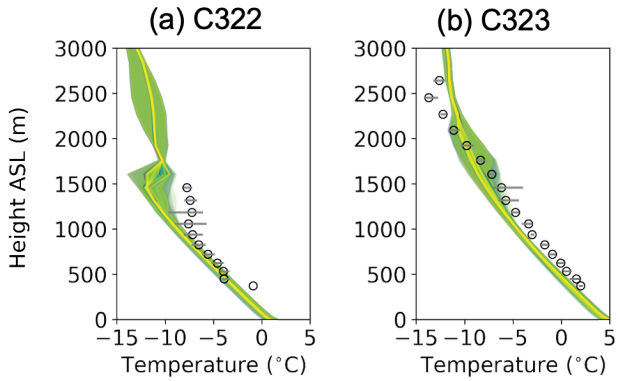


Figure A4.2: Comparison in vertical profiles of ambient temperatures from aircraft measurements and PPE simulations for (a) the C322 Sc region, and (b) the C323 Cu region. Line and shaded area represent the median and central 90% interval from each PPE member over the model analysis domain shown Figure A4.1(a). Unfilled circles and bars represent the median and central 90% interval from the aircraft measurements in each flight.

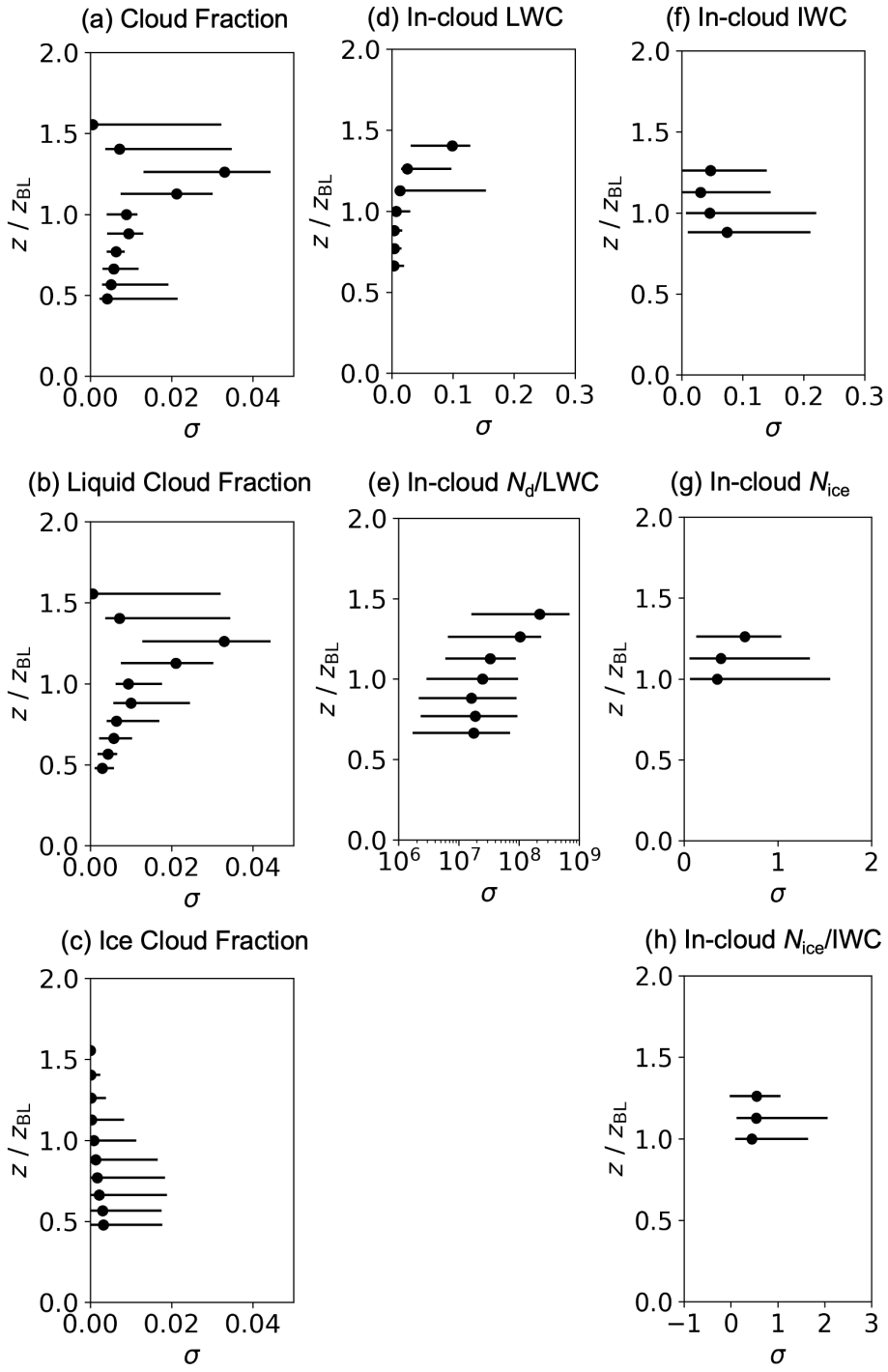


Figure A4.3: Representation uncertainties in compositing domain-mean vertical profiles in the C322 Sc region: (a) cloud fraction (unitless), (b) liquid cloud fraction (unitless), (c) ice cloud fraction (unitless), (d) in-cloud LWC (g m^{-3}), (e) in-cloud N_d/LWC (g^{-1}), (f) in-cloud IWC (g m^{-3}), (g) in-cloud N_{ice} (m^{-3}) and (h) in-cloud N_{ice}/IWC (g^{-1}). Circles and bars represent the median and central 90% interval of sampling uncertainties from all PPE members at that model level, except for N_d. The circles represent the standard deviation of observed N_d from CDP at each model level.

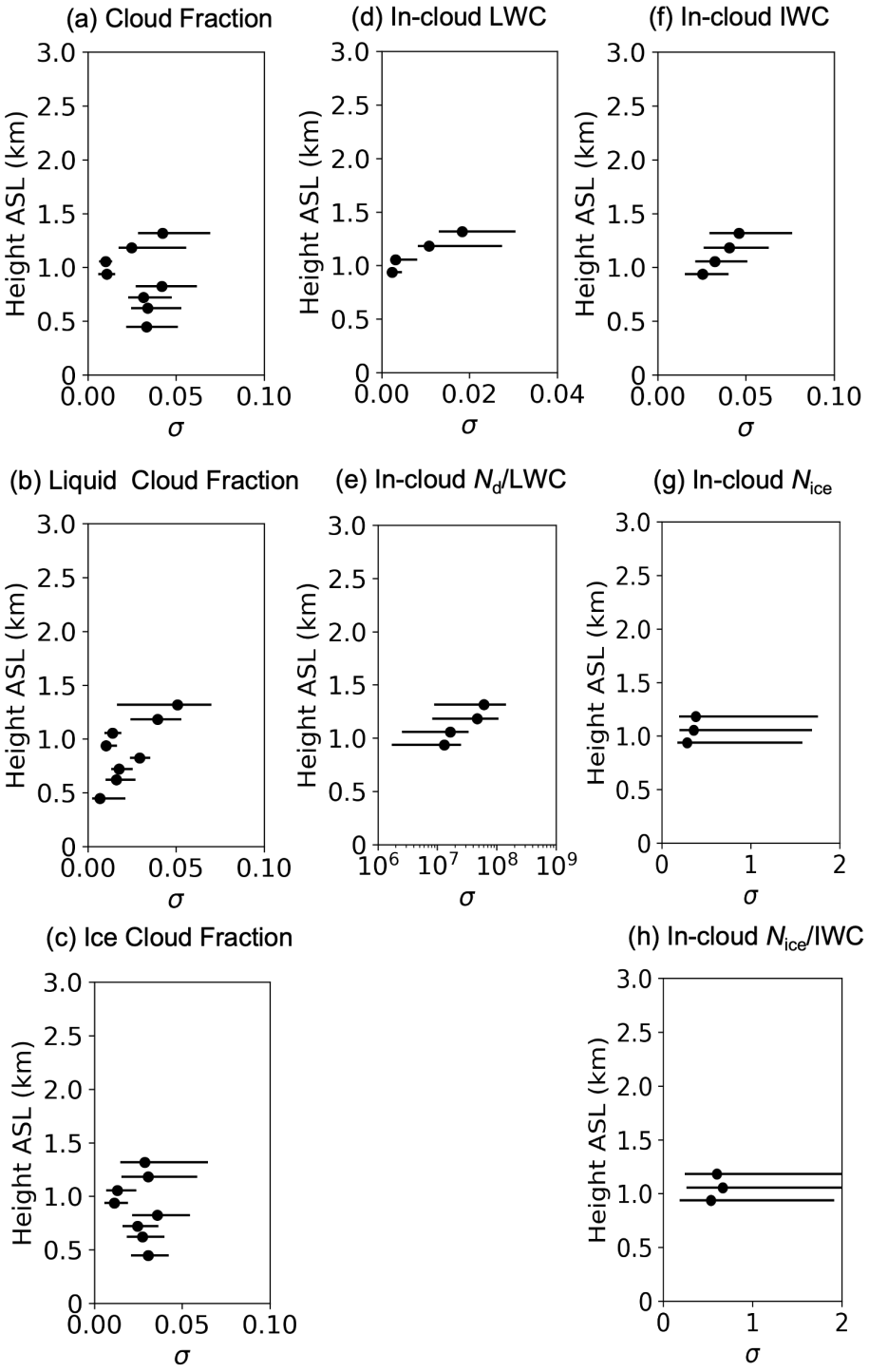


Figure A4.4: Representation uncertainties in compositing domain-mean vertical profiles in the C323 Cu region: (a) cloud fraction (unitless), (b) liquid cloud fraction (unitless), (c) ice cloud fraction (unitless), (d) in-cloud LWC (g m^{-3}), (e) in-cloud N_d/LWC (g^{-1}), (f) in-cloud IWC (g m^{-3}), (g) in-cloud N_{ice} (m^{-3}) and (h) in-cloud N_{ice}/IWC (g^{-1}). Circles and bars represent the median and central 90% interval of sampling uncertainties from all PPE members at that model level, except for N_d. The circles represent the standard deviation of observed N_d from CDP at each model level.

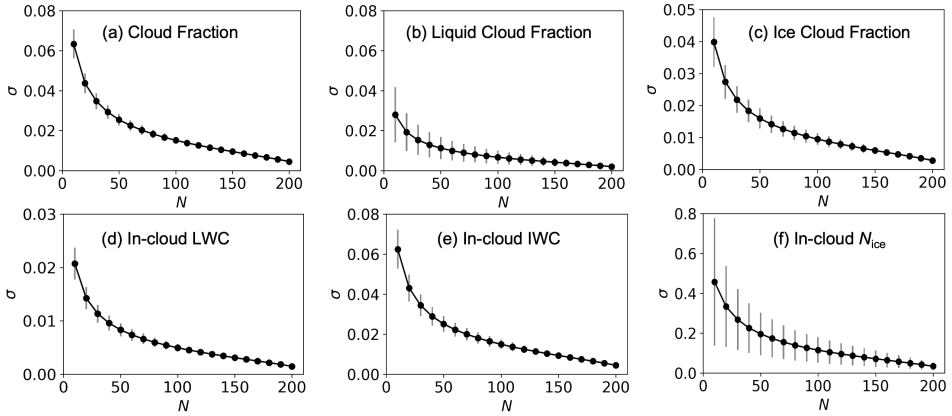


Figure A4.5: Dependency of representation uncertainty (σ) in compositing domain-mean vertical profiles on the number of valid model grid boxes at one model level in the C322 Sc region: (a) cloud fraction (unitless), (b) liquid cloud fraction (unitless), (c) ice cloud fraction (unitless), (d) in-cloud LWC (g m^{-3}), (e) in-cloud IWC (g m^{-3}), and (f) in-cloud N_{ice} (m^{-3}). The model level selected for the analysis is at a normalised height of 1.0 relative to the boundary layer depth. The circles and bars represent the mean and mean ± one standard deviation of sampling uncertainties from all PPE members.

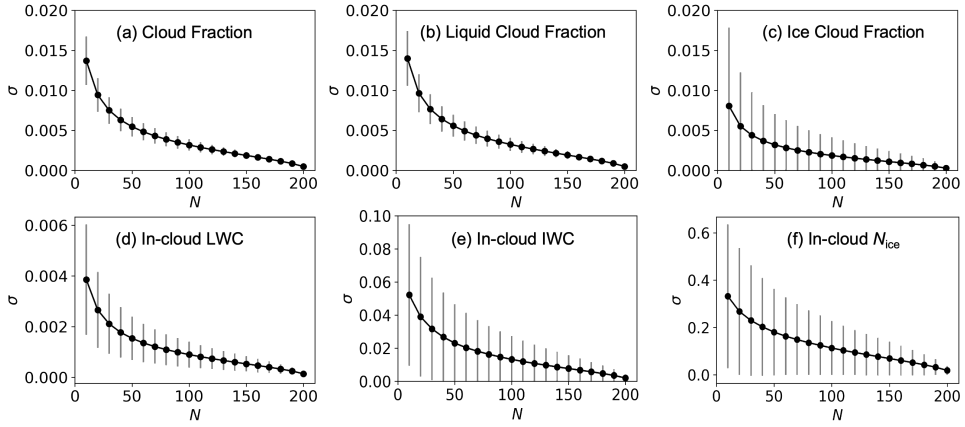


Figure A4.6: Dependency of representation uncertainty (σ) in compositing domain-mean vertical profiles on the number of valid model grid boxes at one model level in the C323 Cu region: (a) cloud fraction (unitless), (b) liquid cloud fraction (unitless), (c) ice cloud fraction (unitless), (d) in-cloud LWC (g m^{-3}), (e) in-cloud IWC (g m^{-3}), and (f) in-cloud N_{ice} (m^{-3}). The model level selected for the analysis is at approximately 1450 m above sea level. The circles and bars represent the mean and mean ± one standard deviation of sampling uncertainties from all PPE members.

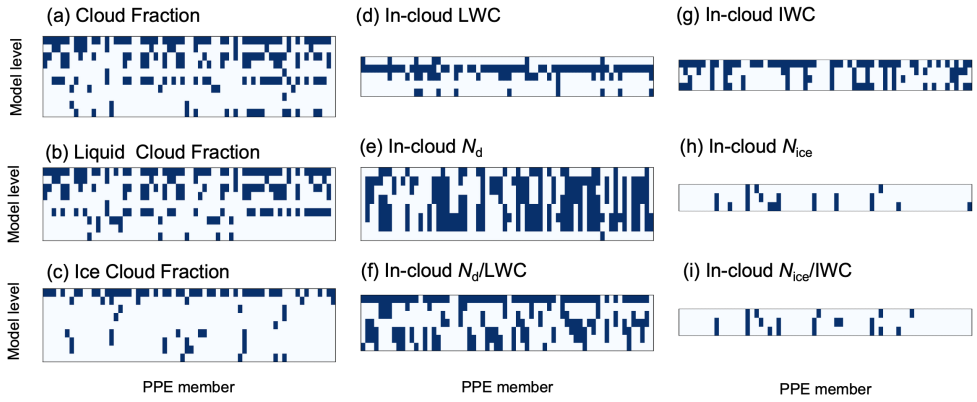


Figure A4.7: Binary (plausible/ implausible) maps for PPE members with observational constraints on different cloud properties in the C322 Sc region: (a) cloud fraction, (b) liquid cloud fraction, (c) ice cloud fraction, (d) in-cloud LWC, (e) in-cloud N_{d}, (f) in-cloud N_{d}/LWC, (g) in-cloud IWC, (h) in-cloud N_{ice} and (j) in-cloud N_{ice}/IWC (g^{-1}). PPE members that are ruled out for each observational constraint are shown in light blue in the binary map, and that are identified as plausible are shown in dark blue in the binary map.

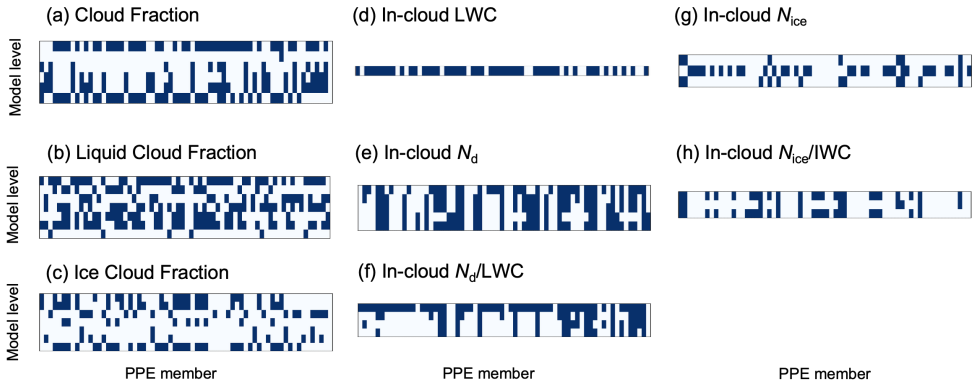


Figure A4.8: Binary (plausible/ implausible) maps for PPE members with observational constraints on different cloud properties in the C323 Cu region: (a) cloud fraction, (b) liquid cloud fraction, (c) ice cloud fraction, (d) in-cloud LWC, (e) in-cloud N_{d}, (f) in-cloud N_{d}/LWC, (g) in-cloud IWC, (h) in-cloud N_{ice} and (j) in-cloud N_{ice}/IWC (g^{-1}). PPE members that are ruled out for each observational constraint are shown in light blue in the binary map, and that are identified as plausible are shown in dark blue in the binary map.

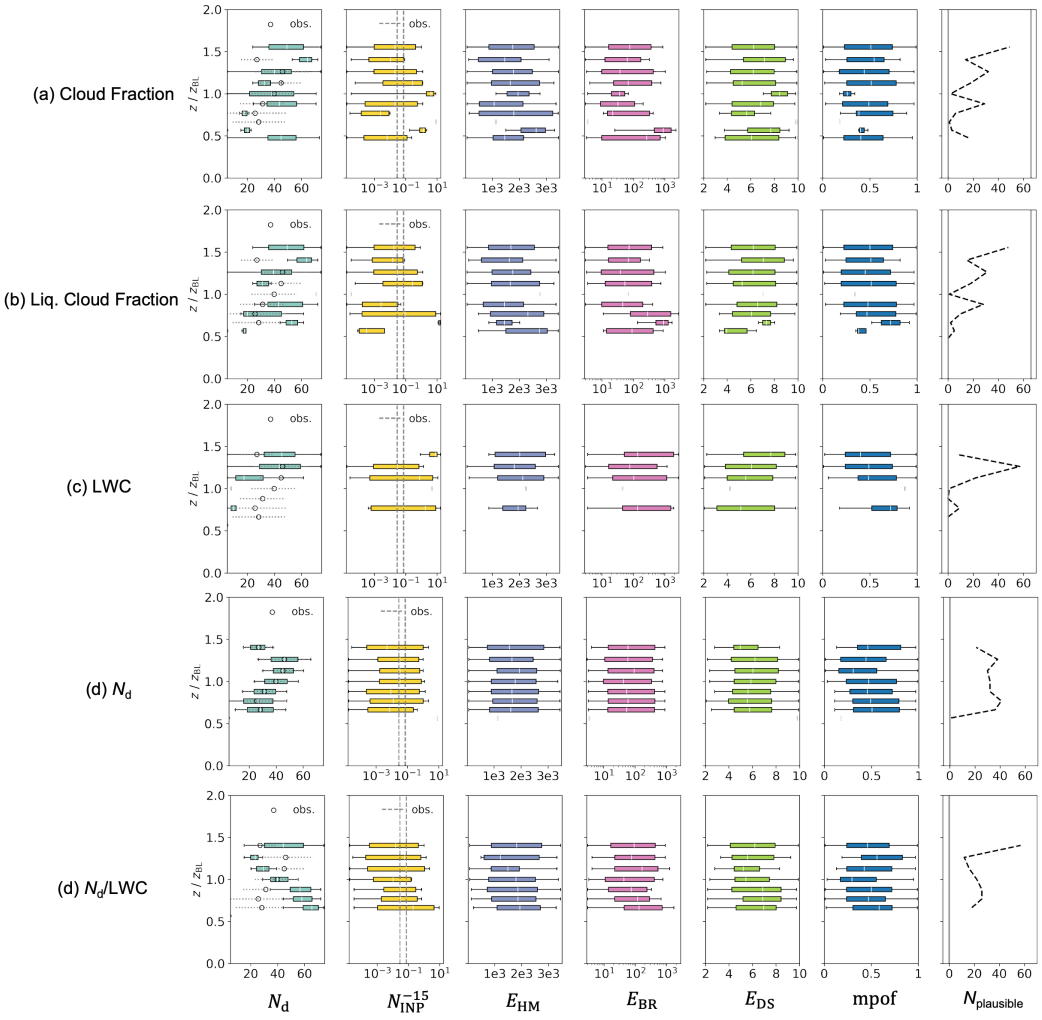


Figure A4.9: Distributions of parameter ranges from the PPE members retained by observational constraints on different cloud properties in the C322 Sc region: (a) cloud fraction, (b) liquid cloud fraction, (c) in-cloud LWC, and (d) in-cloud N_d, and (e) in-cloud N_d/LWC. The number of retained PPE members at each model level is shown in right panel.

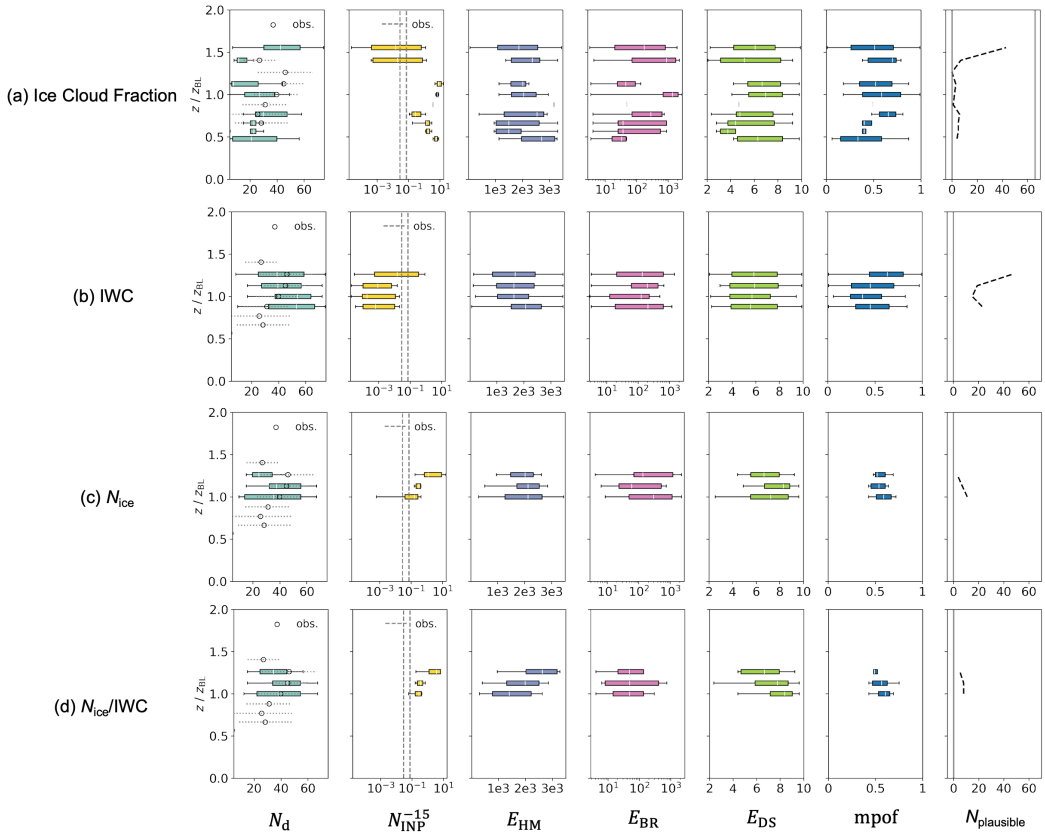


Figure A4.10: Distributions of parameter ranges from the PPE members retained by observational constraints on different cloud properties in the C322 Sc region: (a) ice cloud fraction, (b) in-cloud IWC, (c) in-cloud N_{ice}, and (d) in-cloud N_{ice}/IWC. The number of retained PPE members at each model level is shown in right panel.

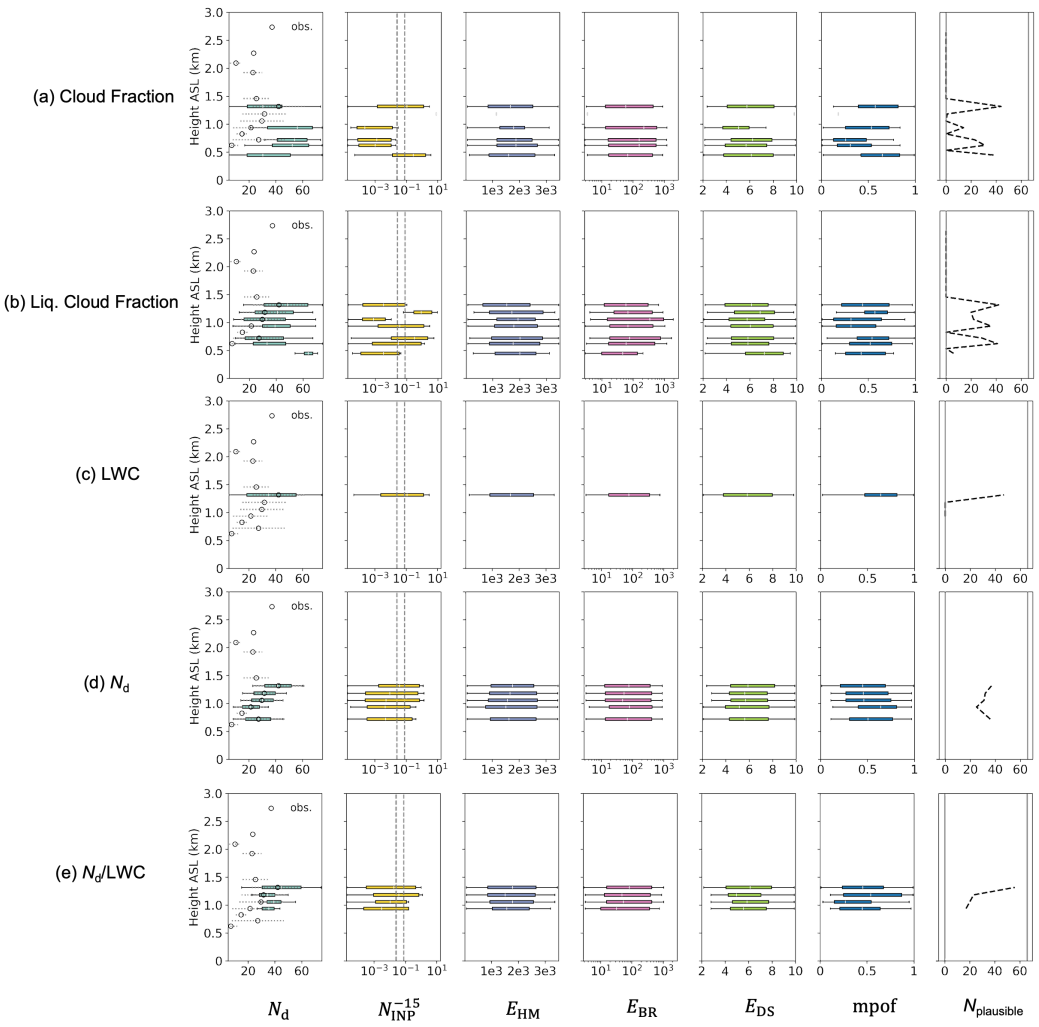


Figure A4.11: Distributions of parameter ranges from the PPE members retained by observational constraints on different cloud properties in the C323 Cu region: (a) cloud fraction, (b) liquid cloud fraction, (c) in-cloud N_d, and (d) in-cloud N_d/LWC. The number of retained PPE members at each model level is shown in right panel.

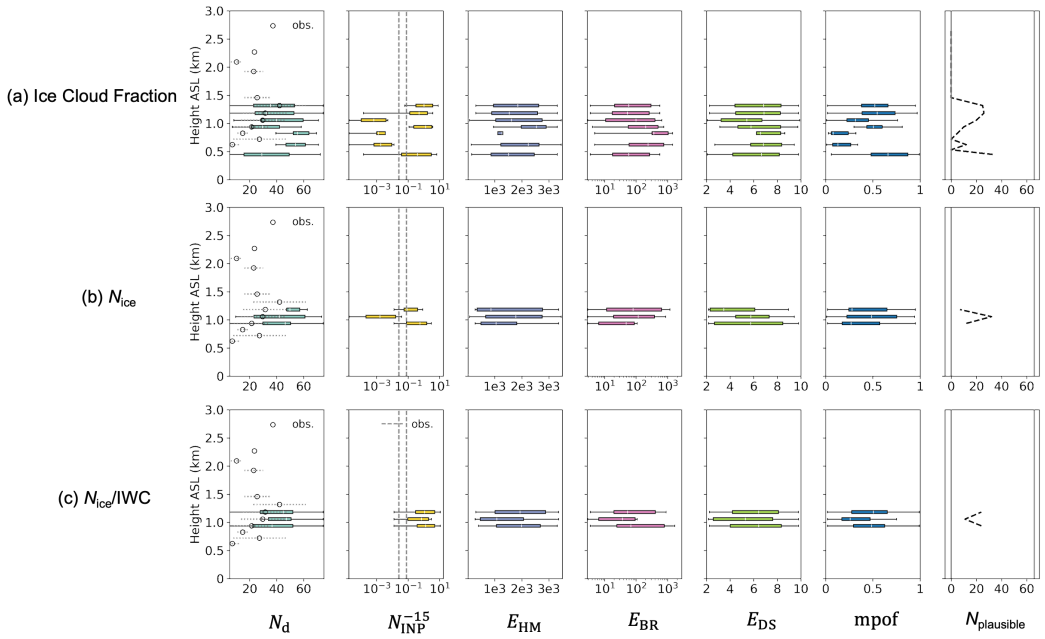


Figure A4.12: Distributions of parameter ranges from the PPE members retained by observational constraints on different cloud properties in the C323 Cu region: (a) ice cloud fraction, (b) in-cloud N_{ice}, and (c) in-cloud N_{ice}/IWC. The number of retained PPE members at each model level is shown in right panel.

References

Abel, S. J., Boutle, I. A., Waite, K., Fox, S., Brown, P. R. A., Cotton, R., Lloyd, G., Choularton, T. W., and Bower, K. N. (2017). "The Role of Precipitation in Controlling the Transition from Stratocumulus to Cumulus Clouds in a Northern Hemisphere Cold-Air Outbreak". In: *Journal of the Atmospheric Sciences* 74.7, pp. 2293–2314.

Baumgardner, D., Abel, S. J., Axisa, D., Cotton, R., Crosier, J., Field, P., Gurganus, C., Heymsfield, A., Korolev, A., Kraemer, M., Lawson, P., McFarquhar, G., Ulanowski, Z., Um, J., Vochezer, P., and Wendisch, M. (2017). "Cloud Ice Properties: In Situ Measurement Challenges". In: *Meteorological Monographs* 58, pp. 9.1–9.23.

Beven, K. (2006). "A manifesto for the equifinality thesis". In: *Journal of Hydrology* 320.1, pp. 18–36.

Biggart, M., Choularton, T. W., Gallagher, M. W., Bower, K. N., Lloyd, G., Connolly, P. J., Murray, B. J., Tarn, M. D., Raif, E. N., and Abel, S. J. (2026). "Secondary ice production within shallow, mixed-phase clouds in cold air outbreaks over the Labrador Sea". In: *EGUsphere* 2026, pp. 1–41.

Bodas-Salcedo, A., Andrews, T., Karmalkar, A. V., and Ringer, M. A. (2016). "Cloud liquid water path and radiative feedbacks over the Southern Ocean". In: *Geophysical Research Letters* 43.20, pp. 10938–10946.

Bodas-Salcedo, A., Williams, K. D., Field, P. R., and Lock, A. P. (2012). "The Surface Downwelling Solar Radiation Surplus over the Southern Ocean in the Met Office Model: The Role of Midlatitude Cyclone Clouds". In: *Journal of Climate* 25.21, pp. 7467–7486.

Bodas-Salcedo, A., Williams, K. D., Ringer, M. A., Beau, I., Cole, J. N. S., Dufresne, J.-L., Koshiro, T., Stevens, B., Wang, Z., and Yokohata, T. (2014). "Origins of the Solar Radiation Biases over the Southern Ocean in CFMIP2 Models". In: *Journal of Climate* 27.1, pp. 41–56.

Brown, A., Milton, S., Cullen, M., Golding, B., Mitchell, J., and Shelly, A. (2012). "Unified Modeling and Prediction of Weather and Climate: A 25-Year Journey". In: *Bulletin of the American Meteorological Society* 93.12, pp. 1865–1877.

Brümmer, B. (1996). "Boundary-layer modification in wintertime cold-air outbreaks from the Arctic sea ice". In: *Boundary-Layer Meteorology* 80.1, pp. 109–125.

— (1999). "Roll and Cell Convection in Wintertime Arctic Cold-Air Outbreaks". In: *Journal of the Atmospheric Sciences* 56.15, pp. 2613–2636.

Bulgin, C. E., Thomas, C. M., Waller, J. A., and Woolliams, E. R. (2022). "Representation Uncertainty in the Earth Sciences". In: *Earth and Space Science* 9.6, e2021EA002129.

Bush, M., Flack, D. L. A., Lewis, H. W., Bohnenstengel, S. I., Short, C. J., Franklin, C., Lock, A. P., Best, M., Field, P., McCabe, A., Van Weverberg, K., Berthou, S.,

Boutle, I., Brooke, J. K., Cole, S., Cooper, S., Dow, G., Edwards, J., Finnenkoetter, A., Furtado, K., Halladay, K., Hanley, K., Hendry, M. A., Hill, A., Jayakumar, A., Jones, R. W., Lean, H., Lee, J. C. K., Malcolm, A., Mittermaier, M., Mohandas, S., Moore, S., Morcrette, C., North, R., Porson, A., Rennie, S., Roberts, N., Roux, B., Sanchez, C., Su, C.-H., Tucker, S., Vosper, S., Walters, D., Warner, J., Webster, S., Weeks, M., Wilkinson, J., Whitall, M., Williams, K. D., and Zhang, H. (2025). "The third Met Office Unified Model–JULES Regional Atmosphere and Land Configuration, RAL3". In: *Geoscientific Model Development* 18.12, pp. 3819–3855.

Carslaw, K. S., Regayre, L. A., Proske, U., Gettelman, A., Sexton, D. M. H., Qian, Y., Marshall, L. R., Wild, O., van Lier-Walqui, M., Oertel, A., Peatier, S., Yang, B., Johnson, J. S., Li, S., McCoy, D. T., Sanderson, B. M., Williamson, C. J., Elsaesser, G. S., Yamazaki, K., and Booth, B. B. B. (2026). "Opinion: The importance and future development of perturbed parameter ensembles in climate and atmospheric science". In: *Atmospheric Chemistry and Physics* 26.7, pp. 4651–4667.

Clarke, S. J., Abel, S. J., Nott, G. J., Raif, E. N., Tarn, M. D., Biggart, M., Wu, H., Ashmore, D. W., Barr, S. L., Barrett, P. A., Bower, K. N., Bowles, J., Connolly, P. J., Cotton, R., Evans, M. D., Flynn, M., Foster, P. B., Fox, S., Gallagher, M. W., Hu, K., Kent, J., Lloyd, G., Marsden, N. A., McQuaid, J. B., Robinson, J., Tiddeman, D., Wilson, A., Wivell, K., Field, P. R., Choularton, T. W., and Murray, B. J. (2025). "Marine cold-air outbreaks over the Norwegian-Barents and Labrador seas: observational datasets from the ACAO and M-Phase aircraft campaigns". Manuscript submitted for publication.

Craig, P. S., Goldstein, M., Seheult, A. H., and Smith, J. A. (1996). "Bayes Linear Strategies for Matching Hydrocarbon Reservoir History". In: *Bayesian Statistics 5: Proceedings of the Fifth Valencia International Meeting*. Ed. by J. M. Bernardo, J. O. Berger, A. P. Dawid, A. F. M. Smith, J. M. Bernardo, J. O. Berger, A. P. Dawid, and A. F. M. Smith. Oxford University Press.

Crosier, J., Bower, K. N., Choularton, T. W., Westbrook, C. D., Connolly, P. J., Cui, Z. Q., Crawford, I. P., Capes, G. L., Coe, H., Dorsey, J. R., Williams, P. I., Illingworth, A. J., Gallagher, M. W., and Blyth, A. M. (2011). "Observations of ice multiplication in a weakly convective cell embedded in supercooled mid-level stratus". In: *Atmospheric Chemistry and Physics* 11.1, pp. 257–273.

de Roode, S. R., Frederikse, T., Siebesma, A. P., Ackerman, A. S., Chylik, J., Field, P. R., Fricke, J., Gryschka, M., Hill, A., Honnert, R., Krueger, S. K., Lac, C., Lesage, A. T., and Tomassini, L. (2019). "Turbulent Transport in the Gray Zone: A Large Eddy Model Intercomparison Study of the CONSTRAIN Cold Air Outbreak Case". In: *Journal of Advances in Modeling Earth Systems* 11.3, pp. 597–623.

Evans, M. D., Abel, S. J., Field, P. R., Finney, D. L., Lloyd, G., Cotton, R. J., Smith, D. K., Murray, B. J., and Huang, X. (2025). "Characterising the spatial overlap

between liquid and ice in mixed-phase clouds". In: *Quarterly Journal of the Royal Meteorological Society*, e5041.

Fast, J. D., Bell, D. M., Kulkarni, G., Liu, J., Mei, F., Saliba, G., Shilling, J. E., Suski, K., Tomlinson, J., Wang, J., Zaveri, R., and Zelenyuk, A. (2022). "Using aircraft measurements to characterize subgrid-scale variability of aerosol properties near the Atmospheric Radiation Measurement Southern Great Plains site". In: *Atmospheric Chemistry and Physics* 22.17, pp. 11217–11238.

Feingold, G., Glassmeier, F., Zhang, J., and Hoffmann, F. (2025). "Opinion: Inferring process from snapshots of cloud systems". In: *Atmospheric Chemistry and Physics* 25.18, pp. 10869–10885.

Field, P. R., Cotton, R. J., McBeath, K., Lock, A. P., Webster, S., and Allan, R. P. (2014). "Improving a convection-permitting model simulation of a cold air outbreak". In: *Quarterly Journal of the Royal Meteorological Society* 140.678, pp. 124–138.

Field, P. R., Hill, A., Shipway, B., Furtado, K., Wilkinson, J., Miltenberger, A., Gordon, H., Grosvenor, D. P., Stevens, R., and Van Weverberg, K. (2023). "Implementation of a Double Moment Cloud Microphysics Scheme in the UK Met Office Regional Numerical Weather Prediction Model". In: *Quarterly Journal of the Royal Meteorological Society*.

Fletcher, J., Mason, S., and Jakob, C. (2016a). "The Climatology, Meteorology, and Boundary Layer Structure of Marine Cold Air Outbreaks in Both Hemispheres". In: *Journal of Climate* 29.6, pp. 1999–2014.

Fletcher, J. K., Mason, S., and Jakob, C. (2016b). "A Climatology of Clouds in Marine Cold Air Outbreaks in Both Hemispheres". In: *Journal of Climate* 29.18, pp. 6677–6692.

Huang, X., Field, P. R., Herbert, R. J., Murray, B. J., van den Heuvel, F., Grosvenor, D. P., Sansom, R. W. N., and Carslaw, K. S. (2026). "Interacting effects of droplet number and ice formation processes on mixed-phase cold-air outbreak clouds". In: *EGUsphere* 2026, pp. 1–49.

Huang, X., Field, P. R., Murray, B. J., Grosvenor, D. P., van den Heuvel, F., and Carslaw, K. S. (2025). "Different responses of cold-air outbreak clouds to aerosol and ice production depending on cloud temperature". In: *Atmospheric Chemistry and Physics* 25.18, pp. 11363–11406.

Johnson, J. S., Regayre, L. A., Yoshioka, M., Pringle, K. J., Turnock, S. T., Browse, J., Sexton, D. M. H., Rostron, J. W., Schutgens, N. A. J., Partridge, D. G., Liu, D., Allan, J. D., Coe, H., Ding, A., Cohen, D. D., Atanacio, A., Vakkari, V., Asmi, E., and Carslaw, K. S. (2020). "Robust observational constraint of uncertain aerosol processes and emissions in a climate model and the effect on aerosol radiative forcing". In: *Atmospheric Chemistry and Physics* 20.15, pp. 9491–9524.

Karalis, M., Sotiropoulou, G., Abel, S. J., Bossioli, E., Georgakaki, P., Methymaki, G., Nenes, A., and Tombrou, M. (2022). "Effects of secondary ice processes on a stratocumulus to cumulus transition during a cold-air outbreak". In: *Atmospheric Research* 277, p. 106302.

Klein, S. A., McCoy, R. B., Morrison, H., Ackerman, A. S., Avramov, A., de Boer, G., Chen, M., Cole, J. N. S., Del Genio, A. D., Falk, M., Foster, M. J., Fridlind, A., Golaz, J.-C., Hashino, T., Harrington, J. Y., Hoose, C., Khairoutdinov, M. F., Larson, V. E., Liu, X., Luo, Y., McFarquhar, G. M., Menon, S., Neggers, R. A. J., Park, S., Poellot, M. R., Schmidt, J. M., Sednev, I., Shipway, B. J., Shupe, M. D., Spangenberg, D. A., Sud, Y. C., Turner, D. D., Veron, D. E., von Salzen, K., Walker, G. K., Wang, Z., Wolf, A. B., Xie, S., Xu, K.-M., Yang, F., and Zhang, G. (2009). "Intercomparison of model simulations of mixed-phase clouds observed during the ARM Mixed-Phase Arctic Cloud Experiment. I: single-layer cloud". In: *Quarterly Journal of the Royal Meteorological Society* 135.641, pp. 979–1002.

Kolstad, E. W. and Bracegirdle, T. J. (2008). "Marine cold-air outbreaks in the future: an assessment of IPCC AR4 model results for the Northern Hemisphere". In: *Climate Dynamics* 30.7, pp. 871–885.

Kolstad, E. W., Bracegirdle, T. J., and Seierstad, I. A. (2009). "Marine cold-air outbreaks in the North Atlantic: temporal distribution and associations with large-scale atmospheric circulation". In: *Climate Dynamics* 33.2, pp. 187–197.

Korolev, A. V., Strapp, J. W., Isaac, G. A., and Nevzorov, A. N. (1998). "The Nevzorov Airborne Hot-Wire LWC–TWC Probe: Principle of Operation and Performance Characteristics". In: *Journal of Atmospheric and Oceanic Technology* 15.6, pp. 1495–1510.

Lance, S., Brock, C. A., Rogers, D., and Gordon, J. A. (2010). "Water droplet calibration of the Cloud Droplet Probe (CDP) and in-flight performance in liquid, ice and mixed-phase clouds during ARCPAC". In: *Atmospheric Measurement Techniques* 3.6, pp. 1683–1706.

Lawson, R. P., O'Connor, D., Zmarzly, P., Weaver, K., Baker, B., Mo, Q., and Jonsson, H. (2006). "The 2D-S (Stereo) Probe: Design and Preliminary Tests of a New Airborne, High-Speed, High-Resolution Particle Imaging Probe". In: *Journal of Atmospheric and Oceanic Technology* 23.11, pp. 1462–1477.

Lee, L. A., Reddington, C. L., and Carslaw, K. S. (2016). "On the relationship between aerosol model uncertainty and radiative forcing uncertainty". In: *Proceedings of the National Academy of Sciences* 113.21, pp. 5820–5827.

MODIS Characterization Support Team (MCST) (2017). *MODIS 1km Calibrated Radiances Product*. MODIS Adaptive Processing System, Goddard Space Flight Center, USA.

Murray, B. J. and the M-Phase Team (2024). "Ice production in northern hemisphere cold air-outbreak clouds: two contrasting aircraft campaigns". In: EGU General Assembly 2024, Vienna, Austria, 14–19 Apr 2024, EGU24-11598.

Possner, A., Pfannkuch, K., and Ramadoss, V. (2024). "Cloud-Resolving ICON Simulations of Secondary Ice Production in Arctic Mixed-Phase Stratocumuli Observed during M-PACE". In: *Journal of the Atmospheric Sciences* 81.2, pp. 417–434.

Prévost, L. M. C., Regayre, L. A., Johnson, J. S., McNeall, D., Milton, S., and Carslaw, K. S. (2025). "Detection of structural deficiencies in a global aerosol model to explain limits in parametric uncertainty reduction". In: *EGUsphere* 2025, pp. 1–65.

Pruppacher, H. and Klett, J. (1996). *Microphysics of Clouds and Precipitation*. Atmospheric and Oceanographic Sciences Library. Springer Netherlands.

Regayre, L. A., Deaconu, L., Grosvenor, D. P., Sexton, D. M. H., Symonds, C., Langton, T., Watson-Paris, D., Mulcahy, J. P., Pringle, K. J., Richardson, M., Johnson, J. S., Rostron, J. W., Gordon, H., Lister, G., Stier, P., and Carslaw, K. S. (2023). "Identifying climate model structural inconsistencies allows for tight constraint of aerosol radiative forcing". In: *Atmospheric Chemistry and Physics* 23.15, pp. 8749–8768.

Schutgens, N., Tsyro, S., Gryspeerdt, E., Goto, D., Weigum, N., Schulz, M., and Stier, P. (2017). "On the spatio-temporal representativeness of observations". In: *Atmospheric Chemistry and Physics* 17.16, pp. 9761–9780.

Schwarzenboeck, A., Mioche, G., Armetta, A., Herber, A., and Gayet, J.-F. (2009). "Response of the Nevzorov Hot Wire Probe in Clouds Dominated by Droplet Conditions in the Drizzle Size Range". In: *Atmospheric Measurement Techniques* 2, pp. 779–788.

Smith, D. K. E., Renfrew, I. A., van den Heuvel, F., Lachlan-Cope, T., Crawford, I., Bower, K., Flynn, M., Evans, M. D., Abel, S. J., and Field, P. (2025). "The Impact of Mixed-Phase Cloud Processes on Simulating Southern Ocean Clouds and Their Radiative Effect". In: *Journal of Geophysical Research: Atmospheres* 130.23, e2025JD044452.

Su, W., Corbett, J., Eitzen, Z., and Liang, L. (2015a). "Next-generation angular distribution models for top-of-atmosphere radiative flux calculation from CERES instruments: methodology". In: *Atmospheric Measurement Techniques* 8.2, pp. 611–632.

— (2015b). "Next-generation angular distribution models for top-of-atmosphere radiative flux calculation from CERES instruments: validation". In: *Atmospheric Measurement Techniques* 8.8, pp. 3297–3313.

Tornow, F., Ackerman, A. S., and Fridlind, A. M. (2021). "Preconditioning of overcast-to-broken cloud transitions by riming in marine cold air outbreaks". In: *Atmospheric Chemistry and Physics* 21.15, pp. 12049–12067.

Vaillancourt, P. A., Tremblay, A., Cober, S. G., and Isaac, G. A. (2003). "Comparison of Aircraft Observations with Mixed-Phase Cloud Simulations". In: *Monthly Weather Review* 131.4, pp. 656–671.

Van Weverberg, K., Giangrande, S., Zhang, D., Morcrette, C. J., and Field, P. R. (2023). "On the Role of Macrophysics and Microphysics in Km-Scale Simulations of Mixed-Phase Clouds During Cold Air Outbreaks". In: *Journal of Geophysical Research: Atmospheres* 128.11, e2022JD037854.

Van Weverberg, K., Morcrette, C. J., and Boutle, I. (2021a). "A Bimodal Diagnostic Cloud Fraction Parameterization. Part II: Evaluation and Resolution Sensitivity". In: *Monthly Weather Review* 149.3, pp. 859–878.

Van Weverberg, K., Morcrette, C. J., Boutle, I., Furtado, K., and Field, P. R. (2021b). "A Bimodal Diagnostic Cloud Fraction Parameterization. Part I: Motivating Analysis and Scheme Description". In: *Monthly Weather Review* 149.3, pp. 841–857.

Vergara-Temprado, J., Miltenberger, A. K., Furtado, K., Grosvenor, D. P., Shipway, B. J., Hill, A. A., Wilkinson, J. M., Field, P. R., Murray, B. J., and Carslaw, K. S. (2018). "Strong control of Southern Ocean cloud reflectivity by ice-nucleating particles". In: *Proceedings of the National Academy of Sciences* 115.11, pp. 2687–2692.

Walters, D., Boutle, I., Brooks, M., Melvin, T., Stratton, R., Vosper, S., Wells, H., Williams, K., Wood, N., Allen, T., Bushell, A., Copsey, D., Earnshaw, P., Edwards, J., Gross, M., Hardiman, S., Harris, C., Heming, J., Klingaman, N., Levine, R., Manners, J., Martin, G., Milton, S., Mittermaier, M., Morcrette, C., Riddick, T., Roberts, M., Sanchez, C., Selwood, P., Stirling, A., Smith, C., Suri, D., Tennant, W., Vidale, P. L., Wilkinson, J., Willett, M., Woolnough, S., and Xavier, P. (2017). "The Met Office Unified Model Global Atmosphere 6.0/6.1 and JULES Global Land 6.0/6.1 configurations". In: *Geoscientific Model Development* 10.4, pp. 1487–1520.

Wentz, F., T. Meissner, C., Gentemann, K., and Hilburn, J. S. (2014). *Remote Sensing Systems GCOM-W1 AMSR2 Environmental Suite on 0.25 deg grid*. Remote Sensing Systems, Santa Rosa, CA.

Williamson, D., Goldstein, M., Allison, L., Blaker, A., Challenor, P., Jackson, L., and Yamazaki, K. (2013). "History matching for exploring and reducing climate model parameter space using observations and a large perturbed physics ensemble". In: *Climate Dynamics* 41.7, pp. 1703–1729.

Wood, R. (2012). "Stratocumulus Clouds". In: *Monthly Weather Review* 140.8, pp. 2373–2423.

Wood, R. and Field, P. R. (2000). "Relationships between Total Water, Condensed Water, and Cloud Fraction in Stratiform Clouds Examined Using Aircraft Data". In: *Journal of the Atmospheric Sciences* 57.12, pp. 1888–1905.

Zhang, J., Gong, W., Leaitch, W. R., and Strapp, J. W. (2007). "Evaluation of modeled cloud properties against aircraft observations for air quality applications". In: *Journal of Geophysical Research: Atmospheres* 112.D10.

Chapter 5

The importance of aerosols and ice formation for the response of mixed-phase clouds to warming

Chapter 5 is based on the paper developed and formatted to be submitted to the *Proceedings of the National Academy of Sciences*: Huang, X., Field, P. R., Murray, B. J., Grosvenor, D. P., van den Heuvel, F., and Carslaw, K. S. The importance of aerosols and ice formation for the response of mixed-phase clouds to warming.

Authors: Xinyi Huang[1], Paul R. Field[1,2], Benjamin J. Murray[1], Daniel P. Grosvenor[1,2], Floortje van den Heuvel[3], and Kenneth S. Carslaw[1]

[1]Institute for Climate and Atmospheric Science, School of Earth and Environment, University of Leeds, Leeds LS2 9JT, UK

[2]Met Office, Exeter EX1 3PB, UK

[3]British Antarctic Survey, Cambridge CB3 0ET, UK

5.1 Abstract

Uncertainty in how clouds respond to warming is a major challenge in estimating how sensitive the climate is to greenhouse gases. For mixed-phase clouds containing both ice and liquid water, climate models suggest that the liquid-ice partitioning plays an important role. However, liquid-ice partitioning alone does not capture the effects of complex cloud microphysical processes. In this study, we develop statistical models (emulators) of cloud properties using simulations from a high-resolution model that represents mixed-phase clouds formed during marine cold-air outbreaks. The simulations explore a joint distribution of seven environmental factors and five cloud microphysical parameters that influence cloud behaviour. Using this approach, we analyse thousands of cloud cases under present-day (2020s) and future warmer (2090s) climates. We find that cloud properties and radiative effects are highly sensitive to droplet concentrations and ice production processes. While droplet concentrations are most important for present-day conditions, ice formation processes dominate the changes of both shortwave and longwave cloud radiative effects (CREs) to warming, introducing large uncertainties. The best-estimated change in net CRE between the 2020s and the 2090s in the Northern Hemisphere ranges between -1.65 W m^{-2} and -1.07 W m^{-2}, with a median value of -1.35 W m^{-2}. The uncertainty is increased further by almost a factor of 2 with the inclusion of future changes in aerosols, which influence droplet concentration and primary ice formation, in combination with changes in environmental conditions. Overall, this study highlights that cloud microphysics and aerosols play a critical role in determining how mixed-phase clouds respond to climate change, and they are a major source of uncertainty in climate predictions.

5.2 Introduction

Cloud feedbacks remain one of the dominant sources of uncertainty in projections of future global warming (Forster et al., 2021). Estimates of equilibrium climate sensitivity (ECS) increased substantially in many Coupled Model Intercomparison Project Phase 6 (CMIP6) models compared to those in CMIP5, with cloud feedbacks playing a central role in this increase (Zelinka et al., 2020). One major reason for the increase in ECS is the positive shift of extratropical low-cloud feedback associated with the representation of supercooled liquid water in mixed-phase clouds (Zelinka et al., 2020). Although substantial progress has been made in understanding mixed-phase cloud feedbacks, large uncertainties remain, and the poor representation of cloud microphysics in climate models is still one of the major sources of uncertainties (Ceppi et al., 2017; Sherwood et al., 2020).

Aerosol-cloud interactions and ice formation processes are among the major sources of uncertainty in the representation of cloud microphysics in climate models (Khain et al., 2015; Korolev et al., 2017; Morrison et al., 2020). Aerosol can act as cloud condensation nuclei (CCN) and ice-nucleating particles (INPs), and plays an important role in the properties of mixed-phase clouds. The effects of CCN and INP on mixed-phase cloud properties such as cloud cover and cloud albedo have been extensively investigated in previous studies. Generally, it is understood that higher CCN concentrations enhance cloud reflectivity through the Twomey effect (Twomey, 1977) and subsequent cloud adjustments (Albrecht, 1989; Ackerman et al., 2004), similar to warm shallow clouds (Lohmann et al., 2005). Higher INP concentrations can reduce the supercooled liquid water and hence reduce cloud albedo (e.g., Vergara-Temprado et al., 2018; Smith et al., 2025), although CCN and INP can have interactive effects such that for some conditions the change in cloud albedo may not follow this simple picture (Huang et al., 2026, Chapter 3). In addition to primary ice production through INPs, secondary ice production (SIP), which can strongly enhance ice number concentrations, has also been shown to affect the lifetime and radiative effects of mixed-phase clouds (Field et al., 2017a; Atlas et al., 2022; Pasquier et al., 2022; Karalis et al., 2022).

Using observational constraints on climate models improves the representation of supercooled liquid water fraction in present-day mixed-phase clouds, leading to a weaker negative cloud feedback and a corresponding higher ECS (Tan et al., 2016). However, the liquid-ice partitioning in mixed-phase clouds results from many interactive, complex but poorly constrained cloud microphysical processes. Murray et al. (2021) suggests that the strength and even sign of cloud-phase feedback can vary with different present-day INP concentrations and potential changes in INP in future. However, no studies so far have examined how aerosols and ice formation affect the change of mixed-phase cloud properties in the warming climate, i.e., how aerosols affect the strength of cloud

feedback. This distinction is important as the processes controlling the states of present-day mixed-phase clouds are not necessarily the same as those that control the cloud responses to warming.

Quantifying the role of aerosols and ice formation in mixed-phase cloud feedback is challenging. Global climate models (GCMs) provide the primary framework for estimating cloud feedbacks, but the coarse resolution and simplified cloud microphysics limit their ability to resolve the cloud-scale processes that are vital to mixed-phase clouds (Ceppi et al., 2017; Sherwood et al., 2020). High-resolution regional simulations, such as cloud-resolving models and large-eddy simulations, can represent these processes more explicitly (Bretherton, 2015), but their computational cost means that they are usually restricted to case studies. Case studies are far from adequate when the effects of cloud microphysical assumptions vary substantially across a range of environmental conditions. To fully understand the interactions of multiple microphysical and environmental factors, perturbed parameter ensemble (PPE) with a large number of simulations is required (Carslaw et al., 2026), which can further increase the requirement of computational resource.

To address this challenge, we trained statistical emulators using a set of idealised high-resolution PPE simulations with a horizontal grid spacing of 1.5 km. The PPE was designed to sample a wide range of environmental conditions of marine cold-air outbreak (CAO) clouds in both present-day climate and globally warmed climate under the SSP3-7.0 (Shared Socioeconomic Pathway 3-7.0) scenario. Marine CAO events were selected here because extensive mixed-phase clouds form when cold and dry airmasses flow over the warm ocean during these events (Brümmer, 1999; Renfrew et al., 1999; Fletcher et al., 2016b; Murray-Watson et al., 2023), providing a strongly forced meteorological condition to simulate mixed-phase clouds of importance to climate (Bodas-Salcedo et al., 2014).

The overall workflow is as follows. First, marine CAO environmental conditions were sampled from the UK Earth System Model (UKESM) output under the SSP3-7.0 scenario for both the 2020s (2020–2029) and 2090s (2090–2099), with the 2090s corresponding to an approximate +4 K increase in global-mean sea surface temperature relative to the 2020s. These sampled conditions were used to define the ranges of seven environmental cloud-controlling factors (Figure A5.1). Second, in total 150 PPE simulations were performed using combinations of these environmental factors and five cloud microphysical parameters: droplet number concentration (N_{d}), INP concentration (N_{INP}), and the efficiencies of three SIP processes (Table A5.8). Note that aerosol effects were not investigated explicitly, but were represented indirectly through prescribed perturbations to N_{d} and N_{INP} in the model cloud microphysics scheme. Each PPE simulation used a two-day idealised forcing by a prescribed time-varying SST, representing the advection of the air mass over an increasingly warmer sea surface during

marine CAOs.

The PPE simulations were then used to train statistical emulators of multiple cloud radiative properties. The same trained emulators were applied to both present-day and future climate conditions. For each climate, several thousands of marine CAOs were sampled. For each sampled marine CAO, 18,750 combinations of the microphysical parameters controlling N_d, N_{INP}, and SIP efficiencies were further sampled. Figure 5.1 shows a simplified illustration of the sampling of environmental factors and cloud microphysical parameters, and Figure A5.1 shows the distributions of these environmental conditions.

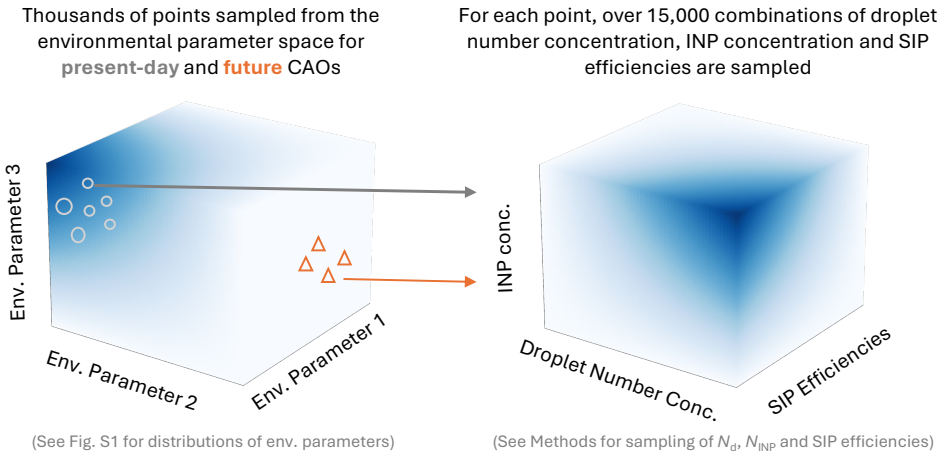


Figure 5.1: A simplified illustration of sampling environmental factors and cloud microphysical parameters over the parameter space. The emulator of cloud properties (blue shading) was trained on a set of 150 idealised high-resolution regional model simulations. The gray circles represent the present-day (2020s) CAOs and the orange triangles represent future (2090s) CAOs. See Materials and Methods for a detailed description on the sampling of environmental conditions in marine CAOs and the sampling of droplet number concentration (N_d), INP concentration (N_{INP}) and efficiencies of SIP processes.

5.3 Results and Discussion

The results presented below first assess the effects and relative importance of aerosols and ice formation processes on cloud states in the present-day and future climates, and on changes in cloud states between these climates. This is followed by an analysis quantifying the controls of these processes on the response of cloud radiative effect (CRE) to warming. The effect of including future changes in aerosols on the CRE response is then examined at the end of the section.

Changes in marine CAO environmental conditions between the 2020s and the 2090s are much larger in the Northern Hemisphere (NH) than the Southern Hemisphere (SH) (Figure A5.1). In particular, the mean of SSTs at the beginning of CAO events in the NH increases on average by about 4 K, but only 0.5 K in the SH. This is because

most SH CAO events initialise from sea-ice edge, where the SST is around 272.5 K, while more CAO events initialise from coastlines in the NH (Fletcher et al., 2016a) and experience a stronger increase of SST at the beginning of CAO events in the warming climate. In general, cloud cover and cloud albedo reduce in the 2090s as the strength of CAO events (M_{850}, CAO index at 850 hPa) becomes weaker in both hemispheres (Figure A5.1c and Figure A5.1k), with the reduction of M_{850} much stronger in the NH. These changes of cloud properties to a reduction in M_{850} are consistent with findings from previous study (Fletcher et al., 2016b).

5.3.1 Effect of aerosols on cloud albedo, cover and longwave radiation

Figure 5.2 and Figure 5.3 show how N_{d} and S_{INP} affect cloud cover (f_{cld}), cloud albedo (α_{cld}) and cloud longwave (LW) flux ($R_{\mathrm{LW,cld}}$) under present-day and warmer climate conditions, as well as the change in cloud properties between these two climate states. By "climate state" we mean the joint distribution of the 7 environmental parameters under present-day and future marine CAO conditions. We perturbed S_{INP}, the scaling factor of the temperature-dependent INP concentration from Cooper (1986), here instead of N_{INP}, as N_{INP} varies with temperature and the sampled CAO cases span a wide range of cloud temperatures. Each of the 375 grid cells in the N_{d} vs. S_{INP} contour plots represents the mean cloud property over several thousand CAO cases (i.e., over 1 million model realisations in total). The effects of SIP perturbations have been averaged here and are examined separately in Section 5.3.3. To calculate the change in cloud properties between climate states, we also assume that the mean N_{d} and S_{INP} remain unchanged. The effect of accounting for possible changes in aerosols is discussed in Section 5.3.5.

Averaged over several thousand CAOs, these emulator response surfaces show some well-understood effects of aerosols on cloud properties in the present-day climate. In Figures 5.2(a) and 5.2(b), cloud albedo and cloud fraction increase with increasing N_{d}, with greatest sensitivity at low N_{d}, which is the typical aerosol-cloud interaction Twomey effect with cloud adjustments (Twomey, 1977; Albrecht, 1989). An increase in N_{INP} (larger S_{INP}) causes reductions in albedo and cloud cover, as found in several previous modelling studies (e.g., Vergara-Temprado et al., 2018; Smith et al., 2025). Although it has been shown that cloud albedo could also increase with N_{INP} (Huang et al., 2025, Chapter 2) under very cold CAO conditions, the mean effect over both the NH and SH CAO ensembles is a decrease in cloud albedo and fraction.

The effects of N_{d} and S_{INP} on cloud properties are different in the warmer climate. While the effect of N_{d} is approximately the same as in the present climate, the effect of S_{INP} in the warmer climate is slightly weaker in the SH and much weaker in the NH. This weakening can be understood in terms of the general reduction in temperature-dependent N_{INP} in the warmer NH clouds, while SH clouds are only slightly warmer in

2090 than in 2020s (Figure A5.1d and Figure A5.1l).

The general changes in cloud fraction and cloud albedo with warming are also similar to what has been predicted for shallow warm clouds (Qu et al., 2015; Myers et al., 2016; McCoy et al., 2017a), and the changes are much larger over the NH where the change in SST is much greater than over the SH. In the NH, cloud cover decreases by 0.09 (12%) averaged across the range of N_{d} and S_{INP} that we sampled, cloud albedo decreases by 0.02 (4.8%), and cloud LW flux increases by 9.50 W m^{-2} (3.8%) as SST increases in the warmer climate. The decreases in cloud cover and albedo are the typical thermodynamically driven responses of cloud thinning seen in other shallow clouds (e.g., Sansom et al., 2024; Sansom et al., 2025, and many others) - i.e., reduction in liquid water path affecting albedo and hastened cloud break up with warmer SSTs reducing the average cloud cover in CAOs.

Our results show that these changes in cloud properties with warming are strongly affected by N_{d} and S_{INP} (Figures 5.2d and 5.3d). For the NH clouds, the change in cloud cover across all N_{d} and S_{INP} has a central 90% range (5% to 95%) of -0.07 to -0.10 (approximately 0.33 times the mean, as shown in the distribution of df_{cld} in Figure 5.3d), the change in albedo is -0.006 to -0.036 (approximately 1.5 times the mean change, as shown in PDF of $d\alpha_{\mathrm{cld}}$ in Figure 5.3d), and the change in cloud LW flux is 10.13 W m^{-2} to 8.34 W m^{-2} (approximately 0.15 times the mean change, as shown in PDF of $dR_{\mathrm{LW,cld}}$ in Figure 5.3d). For the SH, these changes are -0.008 to -0.014 for cloud cover (approximately 0.6 times the mean, as shown in PDF of df_{cld} in Figure 5.2d), -0.0016 to -0.0027 for cloud albedo (approximately 0.55 times the mean, as shown in PDF of $d\alpha_{\mathrm{cld}}$ in Figure 5.2d), and 1.46 W m^{-2} to 1.13 W m^{-2} (approximately 0.25 times the mean change, as shown in PDF of $dR_{\mathrm{LW,cld}}$ in Figure 5.2d) for cloud LW flux. Note that the magnitude of these ranges depends on the perturbation ranges of the microphysical parameters.

The contour plots in Figs 5.2d and 5.3d show that N_{d} and S_{INP} affect the change in cloud properties differently to how they affect these properties in either the present day or warmer climate. While the investigated cloud properties in the present-day and future climates are most sensitive to N_{d} in both hemispheres, the change in cloud albedo from present-day to future ($\Delta\alpha_{cld}$) is most sensitive to S_{INP}. This difference in sensitivities to S_{INP} for the cloud state and the change in cloud state occurs with warming because INP concentration is temperature dependent, as assumed aerosols remain the same in the warming climate, fewer INPs become active and the cloud properties become less sensitive to the variations of S_{INP}. Such a strong change of sensitivity in the warming climate leads to a strong dependency of the change of cloud properties on S_{INP}. In contrast, the sensitivity to N_{d} is similar in present-day and future climates, so these sensitivities largely cancel when the change in cloud properties is calculated.

How N_{INP} levels influence cloud responses to climate change is similar to the "cloud phase feedback" (Tan et al., 2016; Ceppi et al., 2017; Murray et al., 2021). In that picture defined by supercooled water fraction, higher ice content in the present-day leads to a stronger change in SW reflection with warming because there is a stronger transition from ice-dominated to liquid-dominated clouds which are more reflective. In our simulations, we interpret this as a change in sensitivity to present-day N_{INP} with warming. In both hemispheres, we find that a higher present-day N_{INP} (a higher S_{INP}), therefore a higher ice fraction in present-day clouds, leads to less reduction in cloud albedo in the warming climate, consistent with the findings from Tan et al. (2016).

5.3.2 Effect of aerosols on SW and LW cloud radiative effects

To understand how these changes in cloud cover and cloud albedo affect SW cloud radiative effect (CRE) at the top of the atmosphere (TOA), we decomposed the contributions to SWCRE, R^{SW}_{CRE}, and the partial contributions to the change in CRE with warming, dR^{SW}_{CRE}, at a particular location as follows:

$$\begin{aligned} R^{SW}_{CRE} &= R^{SW\downarrow} f_{cld}(\alpha_{cld} - \alpha_{clr}) \\ dR^{SW}_{CRE} &= R^{SW\downarrow}(f_{cld}(d\alpha_{cld} - d\alpha_{clr}) + (\alpha_{cld} - \alpha_{clr})df_{cld}) \end{aligned} \tag{5.1}$$

where α_{cld} and α_{clr} are the cloudy and clear-sky albedos. The value of α_{clr} is set to 0.1 and remains unchanged in the warmer climate, so $d\alpha_{clr}$ is 0 in the equation. For a given N_{d} and S_{INP}, the change in cloud albedo with warming ($d\alpha_{cld}$) will be caused by thermodynamic effects on cloud thickness with fixed N_{d} and S_{INP}. This term will vary with N_{d} and S_{INP} if they affect the strength of these physical cloud responses. The change in cloud cover with warming (df_{cld}) will be caused by the thermodynamic effects of increased SST and changes in atmospheric stability. This term will also vary with N_{d} and S_{INP} if there are changes in aerosol-cloud adjustments in the warmer climate.

Similarly for the LWCRE (R^{LW}_{CRE}):

$$\begin{aligned} R^{LW}_{CRE} &= f_{cld}(R_{cld} - R_{clr}) \\ dR^{LW}_{CRE} &= f_{cld}(dR_{cld} - dR_{clr}) + (R_{cld} - R_{clr})df_{cld} \end{aligned} \tag{5.2}$$

The second term is a simple change in LWCRE caused by a change in cloud cover (df_{cld}). The first term is the change in the LW emission contrast between the surface and the cloud, which can be caused by a change in lapse rate (at constant cloud height), a change in cloud top height, or a change in emissivity of the cloud caused by a change in cloud thickness and N_{d}. We did not separate the change in lapse rate and cloud top height, as a separate emulator on cloud top height is required. The latter effect is very small except for very thin clouds in the Arctic or for cirrus.

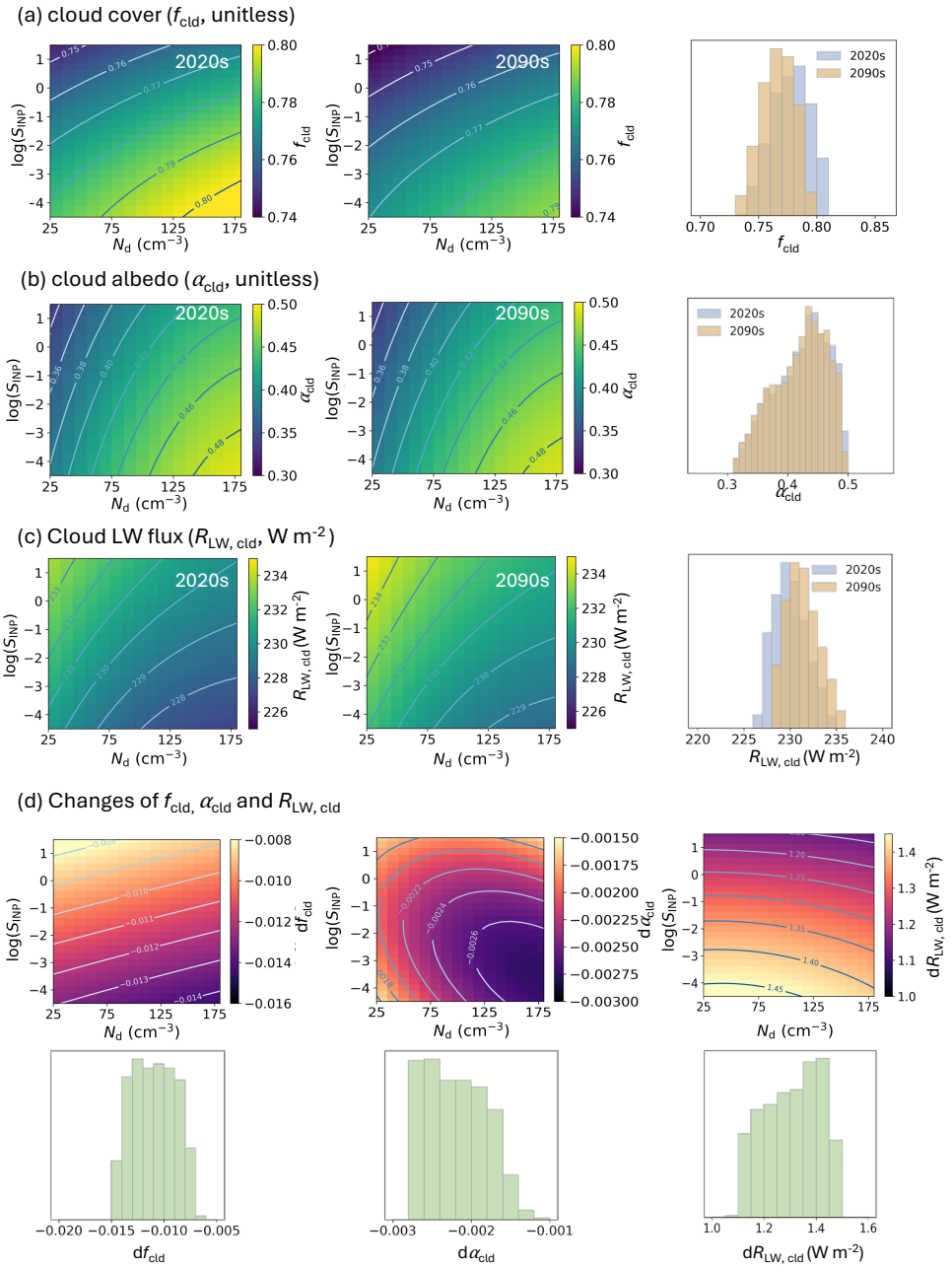


Figure 5.2: Effects of N_d and S_INP in the SH on (a) cloud cover (f_{cld}, unitless), (b) cloud albedo (α_{cld}, unitless), (c) cloud longwave (LW) flux ($R_{LW,cld}$, W m^{-2}), and (d) changes of these three cloud properties between the warming climate (2090s) and present-day climate (2020s). The $log(S_\mathrm{INP})$ is used here to show the scaling of the temperature-dependent N_INP, which is the Cooper parameterization (Cooper, 1986) in this work.

The dependencies of these terms on N_d and S_INP and the distributions of their values are shown in Figure 5.4. The $df_\mathrm{cld}(\alpha_\mathrm{cld} - \alpha_\mathrm{clr})$ term is a combination of a strong dependence of the present-day albedo on N_d (Figure 5.2b and Figure 5.3b) and a strong dependence of df_{cld} on S_INP. Thus, the magnitude of $df_\mathrm{cld}(\alpha_\mathrm{cld} - \alpha_\mathrm{clr})$ increases with N_d primarily because the cloud cover of higher-albedo clouds is reduced in the warmer

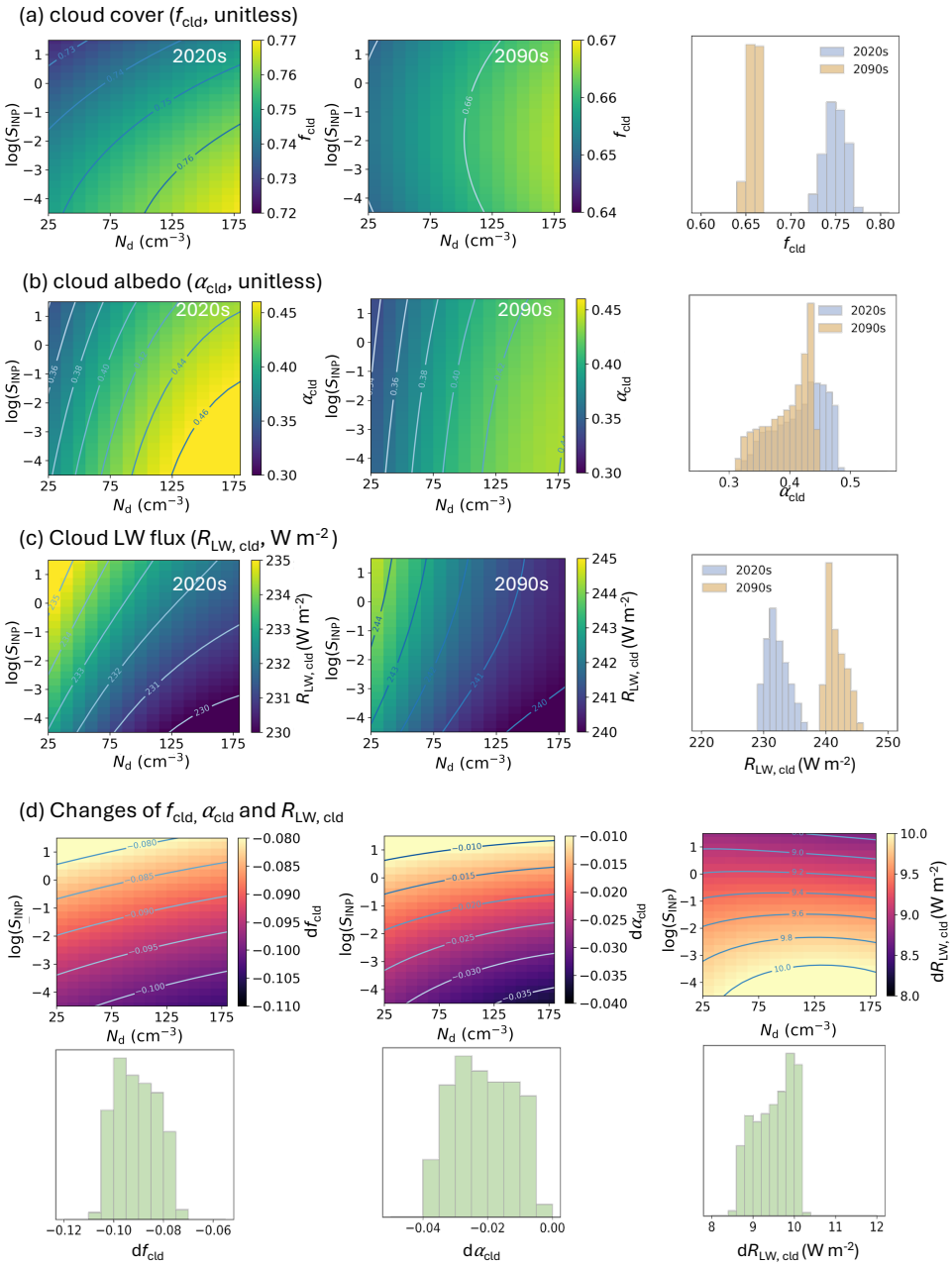


Figure 5.3: Effects of N_d and S_{INP} in the NH on (a) cloud cover (f_{cld}, unitless), (b) cloud albedo (α_{cld}, unitless), (c) cloud longwave (LW) flux ($R_{LW,cld}$, W m^{-2}), and (d) changes of these three cloud properties between the warming climate (2090s) and present-day climate (2020s). The $log(S_{INP})$ is used here to show the scaling of the temperature-dependent N_{INP}, which is the Cooper parameterization (Cooper, 1986) in this work.

climate (i.e., dependence on the initial state) and partly because the effect of S_{INP} on cloud cover changes with temperature (dependence on the change in state).

In contrast, the $f_{cld}(d\alpha_{cld} - d\alpha_{clr})$ term is dominated by the S_{INP} sensitivity of $d\alpha_{cld}$ with only a weak effect of N_d. It is a factor of 2 weaker than $df_{cld}(\alpha_{cld} - \alpha_{clr})$ over both

hemispheres. Similarly, S_{INP} dominates the variations for both LWCRE terms in both hemispheres.

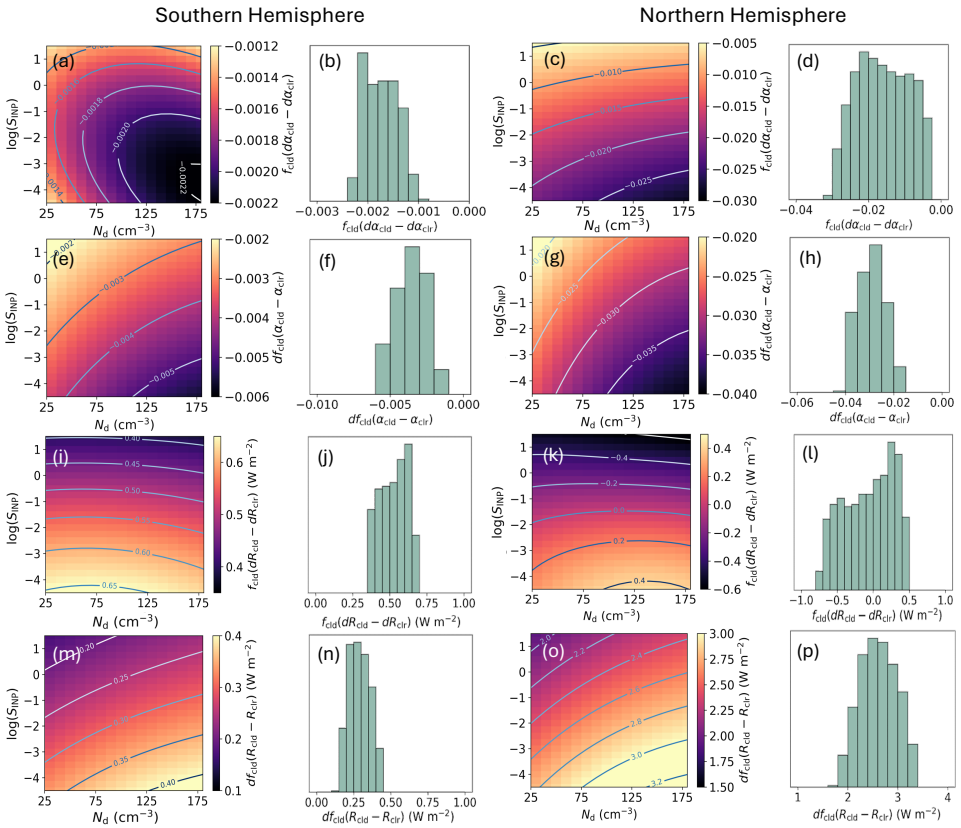


Figure 5.4: Effects of N_{d} and N_{INP} on the decomposition terms for SWCRE and LWCRE: (a-d) by a change in cloud albedo for SWCRE ($f_{\mathrm{cld}}(d\alpha_{\mathrm{cld}} - d\alpha_{\mathrm{clr}})$, unitless), (e-h) by a change in cloud cover for SWCRE ($df_{\mathrm{cld}}(\alpha_{\mathrm{cld}} - \alpha_{\mathrm{clr}})$, unitless), (i-l) by a change in cloud LW flux for LWCRE ($f_{\mathrm{cld}}(dR_{\mathrm{cld}} - dR_{\mathrm{clr}})$, W m^{-2}), and (m-p) by a change in cloud cover for LWCRE ($df_{\mathrm{cld}}(R_{\mathrm{cld}} - R_{\mathrm{clr}})$, W m^{-2}). Terms for SH are shown in the left two columns and for NH are shown in the right two columns.

5.3.3 Importance of secondary ice production

Secondary ice production (SIP) is a substantial cause of uncertainty in the properties of present-day mixed-phase clouds (Field et al., 2017a; Atlas et al., 2022; Pasquier et al., 2022), both in terms of which mechanisms operate under different conditions as well as the rates of ice particle production within each mechanism (Field et al., 2017a). To evaluate the importance of SIP on cloud properties and the changes of them in the warmer climate, we included three mechanisms (rime-splintering - HM, ice-ice breakup - BR and frozen droplet shattering - DS) and perturbed appropriate parameters over a realistic range (see our previous work (Huang et al., 2026, Chapter 3) and Materials and Methods for a detailed description). We consider SIP to be a model uncertainty, which we compare to the effect on cloud properties caused by the assumed ranges of

N_d and S_{INP}.

Figure 5.5 compares the effects of the SIP uncertainty with the range in the decomposition terms across the sampled range of N_d and S_{INP}. To make the sensitivities to the three quantities comparable, we calculate the linear slope between the decomposition terms and the standardized value (range from 0 to 1) of each parameter to show their effects. Using the slopes of linear fits directly compares the dependencies of the decomposition terms on the parameters. The spreads of variables (90%) caused by varying each parameter with the other parameters unchanged are shown in Figure A5.2 for the SH and Figure A5.3 for the NH. Figure A5.4 shows the linear fits for the cloud properties and the change of cloud properties from present-day to future climates.

A stronger influence of S_{INP} and SIP processes on the changes in cloud properties to warming compared to the influence of N_d is reflected in the sensitivities of the decomposition terms (Figure 5.5). The term associated with the change in cloud albedo ($d\alpha_{cld}f_{cld}$) is most sensitive to SIP processes in the SH, particularly the Hallett-Mossop (HM) rime-splintering process. In the NH, this term is most sensitive to S_{INP}, although the sensitivities to SIP processes remain substantial. A strong sensitivity to SIP processes is also found for the term associated with the change in cloud LW flux ($dR_{cld}f_{cld}$) in the SH. By contrast, the terms associated with changes in cloud cover ($R_{cld}df_{cld}$ and $\alpha_{cld}df_{cld}$) show weaker sensitivities to SIP processes.

These sensitivities arise because parameters that most strongly control cloud properties are not necessarily those that dominate the changes in those cloud properties (Figure A5.4). For example, N_d has the largest effect on NH cloud albedo under both present-day and future climates. However, because its effects are similar in the two climates, its contribution to the change in cloud albedo from present-day to future is small (Figure A5.4b and Figure A5.4e). By contrast, S_{INP} and all SIP processes have weaker effects on NH cloud albedo in each individual climate, but their sensitivities change substantially under the warming climate. As a result, S_{INP} and all SIP processes exert a much stronger influence on the change in NH cloud albedo (Figure A5.4e). The sensitivities of cloud albedo to SIP processes are more dominant in the SH as the small temperature change limits the effects from S_{INP} variations, but shifts in cloud regimes still occur in the warming climate. For cloud cover, SIP processes, especially the HM process, strongly influence the cloud covers in each climate, which is similar to our previous work on a case study (Huang et al., 2025, Chapter 2), but their effects on changes in cloud cover are much weaker than those from S_{INP}.

Overall, SIP uncertainty has a complex but important effect on cloud properties and changes in cloud properties with warming, especially for cloud albedo in both hemispheres. Given current understanding of SIP processes and the challenge of quantifying its effect across diverse environments (Field et al., 2017a), the large contribution

to uncertainty in the feedback processes may be irreducible.

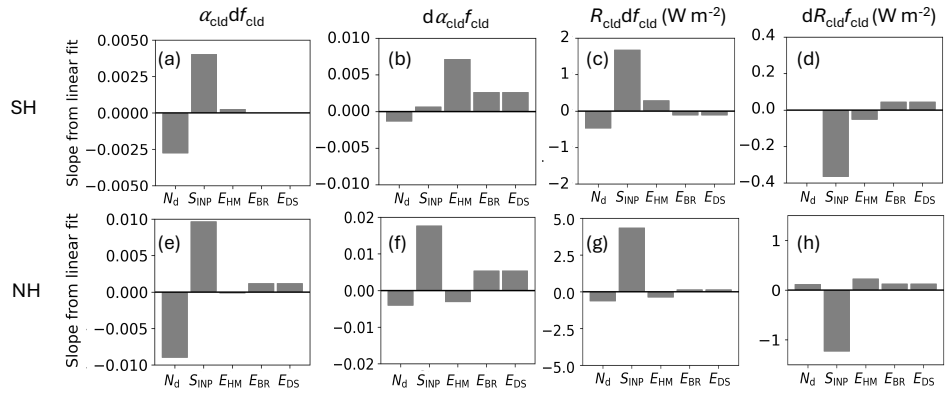


Figure 5.5: Effects from N_d, S_{INP} and three SIP parameters (E_{HM}, E_{BR} and E_{DS}) using slope from linear fit between the decomposition terms and standardized values of parameters on (a, e) $\alpha_{cld}df_{cld}$, (b, f) $d\alpha_{cld}f_{cld}$, (c, g) $R_{cld}df_{cld}$ (W m^{-2}), and (d, h) $dR_{cld}f_{cld}$. Figures for the SH are shown in the top panel and in the bottom panel for the NH.

5.3.4 The cloud microphysical component of feedback uncertainty

In the previous section we showed that cloud properties relevant to cloud feedback depend on cloud microphysical factors - N_d, S_{INP} and SIP processes. In this section we translate these warming-induced changes in cloud properties into changes in radiative flux. In the 2090s climate, the distribution of CAOs is different to 2020s, with generally less occurrence and a shift poleward (Figure A5.16). The change in the distribution of cloud regimes is a component of the global cloud feedback - for example, replacement of CAOs with a different cloud regime could cause an important radiative change. However, our focus here is the extent to which, averaged across CAO clouds, cloud microphysics modulates the strength of the feedback. We refer to the combined effect of aerosol (N_d and S_{INP}) and SIP uncertainty as the *microphysical component* of cloud feedback in contrast to the spatial component caused by changes in the spatial distribution of different cloud regimes. The changes in CREs (with a unit of W m^{-2}) are used here to infer the feedback associated with the responses of mixed-phase CAO clouds, and the calculation of feedback (with a unit of W m^{-2} K^{-1}) simply uses a global mean SST +4 K warmer.

Figure 5.6 shows the 2020s–to–2090s changes in SW, LW and net CREs, as well as the first-order sensitivity indices for N_d, S_{INP} and all three SIP processes shown together. The first-order sensitivity index quantifies the fraction of variance in the CRE response that can be attributed to changes in each factor independently. We restricted our analysis to marine CAOs occurring within the latitude bands of 60 °S – 70 °S in the SH and 55 °N – 60 °N in the NH, as these bands contained a sufficient number of marine CAOs in both climates for a meaningful statistical comparison.

In both hemispheres, the change in SWCRE ($\Delta R_{\mathrm{CRE}}^{\mathrm{SW}}$) is negative to the warmer climate from the present-day climate (a positive feedback), while the change in LWCRE ($\Delta R_{\mathrm{CRE}}^{\mathrm{LW}}$) is positive (a negative feedback). The change in net CRE ($\Delta R_{\mathrm{CRE}}^{\mathrm{net}}$) is positive in the SH (an overall negative feedback), while $\Delta R_{\mathrm{CRE}}^{\mathrm{net}}$ is negative in the NH (an overall positive feedback). This difference in the sign of $\Delta R_{\mathrm{CRE}}^{\mathrm{net}}$ between the two hemispheres is mainly because the incoming SW flux weakens at higher latitudes, which dampens the magnitude of $\Delta R_{\mathrm{CRE}}^{\mathrm{SW}}$. This effect from incoming SW flux on $\Delta R_{\mathrm{CRE}}^{\mathrm{SW}}$ is also evident in Figure A5.5 and Figure A5.6, where the decomposition terms and change of CREs are shown for each 5-degree latitude band. For example, the largest $\Delta R_{\mathrm{CRE}}^{\mathrm{SW}}$ occur in early spring (September for the SH, March for the NH) and late autumn (April for the SH and October for the NH). The dependency of $\Delta R_{\mathrm{CRE}}^{\mathrm{SW}}$ on the incoming SW flux suggests that, for clouds that occur at higher latitudes and during seasons with weak incoming SW radiation, $\Delta R_{\mathrm{CRE}}^{\mathrm{LW}}$ associated with future cloud changes cannot be neglected and should be carefully treated as an important component of cloud feedback.

The strength of the feedback is very strongly affected by cloud microphysics. Table A5.1 compares key statistics for changes in CREs and the ranges caused by cloud microphysics in both hemispheres. In the NH, the median $\Delta R_{\mathrm{CRE}}^{\mathrm{SW}}$ is -4.11 W m^{-2} (a positive feedback) with a central 90% interval of 3.35 W m^{-2} caused by aerosols (via our N_{d} and S_{INP} choices) and SIP processes. This is equivalent to a range in feedback of 0.84 W m^{-2} K^{-1} for the SST +4 K warmer climate. For $\Delta R_{\mathrm{CRE}}^{\mathrm{LW}}$, the median is +2.74 W m^{-2} (a negative feedback) and the central 90% interval is 2.06 W m^{-2} (0.52 W m^{-2} K^{-1} for SST +4 K). The median of $\Delta R_{\mathrm{CRE}}^{\mathrm{net}}$ is -1.38 W m^{-2} (an overall positive feedback) with the central 90% interval of $\Delta R_{\mathrm{CRE}}^{\mathrm{net}}$ 1.57 W m^{-2} (0.39 W m^{-2} K^{-1} for SST +4 K). These results show that the feedback of mixed-phase CAO cloud is very strongly modulated by cloud microphysical processes. In the SH, the ranges caused by aerosols and SIP processes are much weaker than the ones in the NH, where CAO clouds undergo weaker changes driven by much less increases in SST. Here, the median and central 90% interval of $\Delta R_{\mathrm{CRE}}^{\mathrm{net}}$ are +0.40 W m^{-2} (an overall negative feedback) and 0.65 W m^{-2} (0.16 W m^{-2} K^{-1} for SST +4 K).

The ranges of ΔR_{CRE} have different causes in each hemisphere. In the SH, changes on all the assessed CREs are dominated by ice formation processes (Figures 5.6b–d). Based on the first-order sensitivity indices, SIP processes contribute to more than 97% of the variation in $\Delta R_{\mathrm{CRE}}^{\mathrm{SW}}$, 27% of the variation in $\Delta R_{\mathrm{CRE}}^{\mathrm{LW}}$ and 62% of the variation in $\Delta R_{\mathrm{CRE}}^{\mathrm{net}}$. S_{INP} contribute to 70% of the variation in $\Delta R_{\mathrm{CRE}}^{\mathrm{LW}}$ and 36% of the variation in $\Delta R_{\mathrm{CRE}}^{\mathrm{net}}$. The contribution from N_{d} is very limited for all three ΔR_{CRE} values. In the NH, S_{INP} most strongly influences both $\Delta R_{\mathrm{CRE}}^{\mathrm{SW}}$ (76%) and $\Delta R_{\mathrm{CRE}}^{\mathrm{LW}}$ (90%), but has a substantially reduced effect on $\Delta R_{\mathrm{CRE}}^{\mathrm{net}}$ (35%). This reduction results from compensation between $\Delta R_{\mathrm{CRE}}^{\mathrm{SW}}$ and $\Delta R_{\mathrm{CRE}}^{\mathrm{LW}}$ to variations in S_{INP}, as shown in Figure A5.9. A higher S_{INP} leads to less negative reduction in $\Delta R_{\mathrm{CRE}}^{\mathrm{SW}}$, but also a less positive

increase in $\Delta R^{\mathrm{LW}}_{\mathrm{CRE}}$. A similar compensation, but in the opposite direction, occurs for N_{d} as well. However, the effect from N_{d} on $\Delta R^{\mathrm{LW}}_{\mathrm{CRE}}$ is much weaker than its effect on $\Delta R^{\mathrm{SW}}_{\mathrm{CRE}}$. Therefore, for the change in net CRE in the NH, N_{d} exerts a stronger influence than N_{INP} with a total contribution of 51%. Contributions from SIP processes in the NH are much weaker (less than 10%) compared to their influences in the SH ΔR_{CRE}.

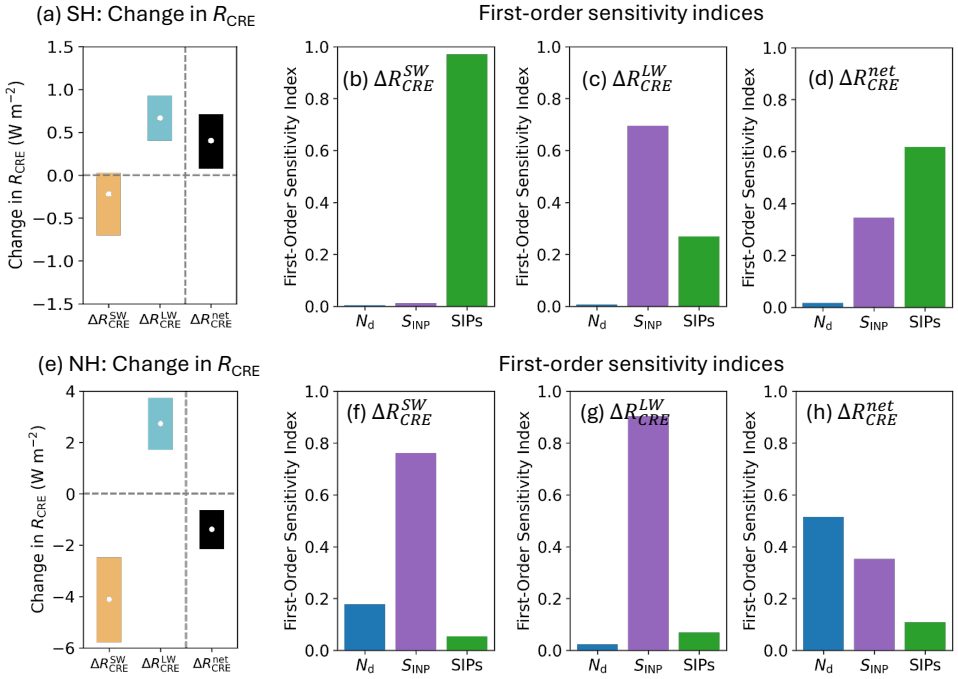


Figure 5.6: The central 90% range of changes in SWCRE ($\Delta R^{\mathrm{SW}}_{\mathrm{CRE}}$), LWCRE ($\Delta R^{\mathrm{LW}}_{\mathrm{CRE}}$) and net CRE ($\Delta R^{\mathrm{net}}_{\mathrm{CRE}}$) by sampling N_{d}, N_{INP} and all three SIP uncertainties, and the first-order sensitivities on the changes of CREs from these parameters for (a-d) SH, and (e-h) NH.

5.3.5 Effect from changes in aerosol in the future climate

We next ask how the magnitude and range of the feedback depends on the assumed range of present-day and future N_{d} and S_{INP}. There are two important effects to consider. Firstly, the range of N_{d} and S_{INP} in the present-day can be constrained to a narrower range than so far assumed based on observations, which will reduce the feedback ranges calculated above. However, there is uncertainty in these concentrations that needs to be accounted for. Secondly, N_{d} and S_{INP} may change in future. The emulators provide a means to calculate the effects of all potential combinations of N_{d} and S_{INP} in the present-day and future climates averaged across the thousands of CAOs without having to repeat any simulations.

For the present-day SH CAOs, we assume $N_{\mathrm{d}} = 50 \pm 10$ cm^{-3} and $log_{10}(S_{\mathrm{INP}})$ = -2 $\pm$ 0.5 based on observations from the Southern Ocean Clouds (SOC) campaign (Smith et al., 2025). For the present-day NH CAOs, we assume $N_{\mathrm{d}} = 100 \pm 10$ cm^{-3} and

$log_{10}(S_{\mathrm{INP}})$ = -1 ± 0.5 based on the observations from the Arctic Cold-Air Outbreak (ACAO) (Raif et al., 2024) and M-Phase aircraft campaigns (Clarke et al., 2025; Huang et al., 2026, Chapter 3). Note that the seasonal cycle is not represented as we are using the mean over each climate state and only marine CAOs are considered here, so the constraining here is not representative for the entire hemispheres. For potential changes in aerosols between the 2020s and the 2090s, we assume that N_{d} could increase or decrease by up to 20 cm^{-3} in both hemispheres and that N_{INP} could increase or decrease by up to a factor of 10 ($log_{10}(S_{\mathrm{INP}}) = \pm 1$). That is, for every combination of present-day N_{d} and S_{INP}, we calculated ΔR_{CRE} from all possible future combinations of N_{d} and S_{INP}.

Figure 5.7 shows the ranges of $\Delta R^{\mathrm{net}}_{\mathrm{CRE}}$ with different assumptions about how aerosols could change in both hemispheres, using our simplified approach here of perturbing the N_{d} and S_{INP}. The ranges for $\Delta R^{\mathrm{SW}}_{\mathrm{CRE}}$ and $\Delta R^{\mathrm{LW}}_{\mathrm{CRE}}$ are shown in Figure A5.7 and Figure A5.8. Tables A5.2–A5.7 show the statistics on the change of CREs with different aerosol assumptions and constraints.

Using observational constraints on N_{d} and N_{INP} from CAO campaigns, the range of $\Delta R^{\mathrm{net}}_{\mathrm{CRE}}$ in the NH can be reduced by 63%. However, the constraining strength on the range of $\Delta R^{\mathrm{net}}_{\mathrm{CRE}}$ in the SH is very limited, as the dominated source of uncertainties is SIP processes in the SH (Figure 5.6(d)).

There is a substantial increase in the uncertainty in feedback (change in $\Delta R^{\mathrm{net}}_{\mathrm{CRE}}$) when we account for changes in aerosols with warming. Here we used the estimates with observational constraints on current N_{d} and N_{INP}, which is our best estimates with the known information for marine CAOs, to show the increase in the uncertainty. In the SH, allowing for potential increases or decreases between the 2020s and the 2090s leads to 56% increase in the central 90% interval of the net CRE change. In the NH, the range of the net CRE changes increases almost by a factor of 2 (+183%).

With the emulators, we also separate the effects of different combinations of increases and decreases. For example, if we assume that N_{d} increases by 20 cm^{-3} between the 2020s and the 2090s, but still allow for both increases or decreases in N_{INP} by a factor of 10, then the positive feedback is weakened in the NH and the negative feedback is strengthened in the SH. This change represents a combination of feedback and cloud adjustments driven by the increase in N_{d} (i.e., a radiative forcing) which is negative. However, we cannot cleanly separate feedback and forcing when N_{d} changes with climate because adjustments are usually calculated at fixed SST.

The effect of increases and decreases in N_{INP} in the 2090s are different between the NH and the SH. The changes have a weak effect in the NH regardless of what is assumed about changes in N_{d} because the much warmer 2090s conditions weaken the sensitivity of the clouds to N_{INP}. However, in the SH, where changes in SST are

much less than in the NH, an increase in N_{INP} partly offsets the effect of increasing N_{d} because it reduces cloud albedo and fraction (Figure 5.2). This is a form of INP-driven radiative forcing through cloud adjustments.

Overall, there is great variability in the strength of feedbacks across all the potential changes in aerosol that we have analysed. An increase of N_{d} combined with a decrease of N_{INP} leads to the smallest reduction of SWCRE in the NH future climate, and the biggest increase of SWCRE in the SH future climate; while the opposite change (a decrease of N_{d} with an increase of N_{INP}) leads to the largest opposite changes (Figure A5.7). Similar effects can be found on $\Delta R_{\mathrm{CRE}}^{\mathrm{LW}}$ (Figure A5.8). The differences from different combinations of N_{d} and N_{INP} changes in the future results in a difference of $\Delta R_{\mathrm{CRE}}^{\mathrm{net}}$ between the median values about 1.07 W m^{-2} (0.27 W m^{-2} K^{-1} for SST +4 K) in the NH and about 0.49 W m^{-2} (0.12 W m^{-2} K^{-1} for SST +4 K) in the SH. These results show that it is important to constrain both the magnitude and the sign of aerosol (CCN and INP) changes in the warming climate to reduce uncertainties in cloud feedback from mixed-phase clouds.

Future changes in N_{d} and N_{INP} are difficult to predict and are likely to be spatially variable. Over the NH, we can expect a decrease in N_{d} driven by reductions in anthropogenic aerosol emissions. Over the SH, decadal changes in CCN of locally up to 85% and more widely 22% have been calculated based on known changes in zonal wind speeds and assumed increases in sea spray emission (Korhonen et al., 2010). Other changes in natural aerosol sources cannot be ruled out (Carslaw et al., 2010). Changes in INP concentrations are less well understood. Dust is the main INP source in the NH and is non-negligible over the SH (Herbert et al., 2025). Recent analysis shows that dust in the atmosphere decreased by about 5% per decade (Gupta et al., 2026) over recent decades. However, INPs are mostly not represented in dust mass loading and optical measurements, and their concentration may be susceptible to other poorly understood processes (Herbert et al., 2025). We essentially have a very limited understanding of how INP might change in future, but our results show that any changes could have a large effect on the response of mixed-phase clouds to the warming climate.

5.4 Conclusions

The response of mixed-phase clouds to warming is often considered through the change of cloud phase, which is the transition from ice crystals to more reflective liquid droplets (Tan et al., 2016; Ceppi et al., 2017; Murray et al., 2021). However, the liquid-ice partitioning, as well as cloud extent and lifetime in mixed-phase clouds are strongly controlled by complex and uncertain cloud microphysics processes, including aerosol-cloud interaction, primary ice production through INP and secondary ice production (SIP). The poor representation of cloud microphysics remain a key source of uncertainties in

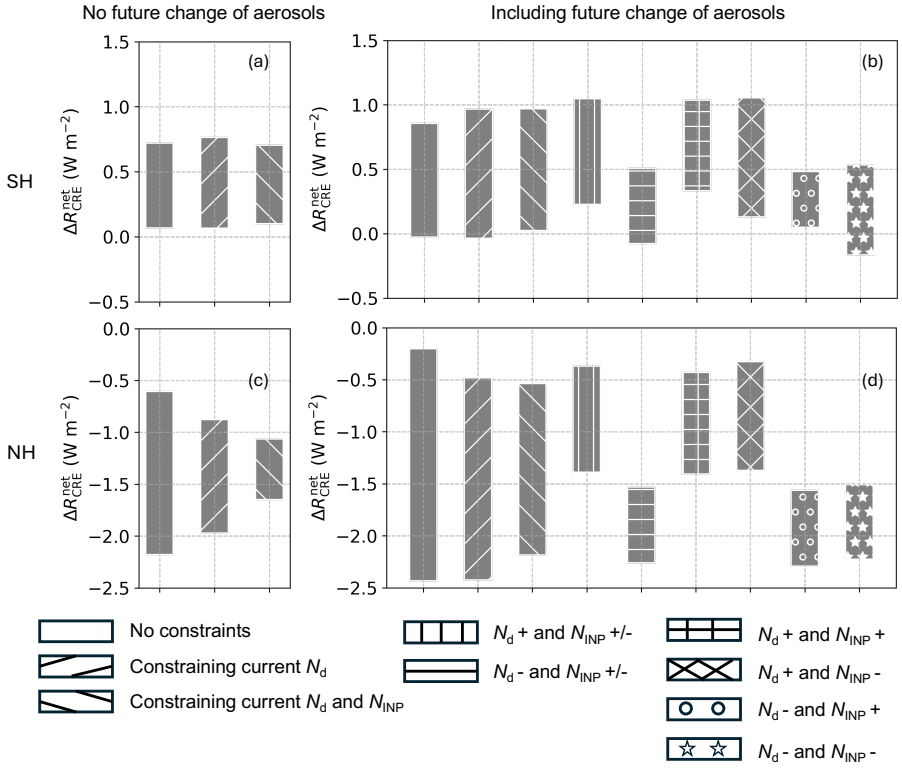


Figure 5.7: Comparison of the central 90% range of the changes in net CRE ($\Delta R^{\mathrm{net}}_{\mathrm{CRE}}$) for (a, c) no future changes of aerosols, and (b, d) including future changes of aerosols in the warmer climate, along with different constraints on present-day and future N_{d} and N_{INP}. Figures for the SH are shown in the top panel and in the bottom panel for the NH. Ranges for changes in SWCRE and LWCRE are shown in Figure A5.7 and Figure A5.8.

estimating cloud feedback of mixed-phase clouds (Sherwood et al., 2020).

In this work, we sampled several thousands of cold-air outbreak (CAO) events from present-day (2020s) and approximately 4 K warmer (2090s) climates from a climate model, and used statistical emulators trained on high-resolution simulations to represent properties of mixed-phase clouds formed during these CAO events. For each sampled CAO, 18,750 combinations of the cloud microphysical parameters, including N_{d} (droplet number concentration), N_{INP} (INP concentration) and efficiencies of three SIP processes, were used to quantify the role of cloud microphysics in controlling both mixed-phase cloud states and change of cloud states under warming.

Our simulations show that, in a warmer climate, CAO cloud fraction and albedo both decrease with weaker CAO strengths and with warmer SSTs that accelerate the transition from stratocumulus to cumulus clouds, similar to shallow warm clouds (e.g., Bretherton et al., 2013). These responses of CAO clouds to warming are much stronger in the Northern Hemisphere (NH), which warms more than the Southern Hemisphere (SH). However, the strength of feedback of mixed-phase CAO clouds depends on cloud microphysics. Using the change of net cloud radiative effect ($\Delta R^{\mathrm{net}}_{\mathrm{CRE}}$) at the top-of-

the-atmosphere, we find that the range (central 90% interval) of $R_{\mathrm{CRE}}^{\mathrm{net}}$ caused by N_{d}, N_{INP} and SIP processes is 0.65 W m^{-2} (0.16 W m^{-2} K^{-1} for SST +4 K) in the SH, and even larger in the NH with 1.57 W m^{-2} (0.39 W m^{-2} K^{-1} for SST +4 K).

Another key finding is that the sensitivity of cloud states to a microphysics parameter can be different from the sensitivity of the change in cloud states. That is, the processes that most strongly control mixed-phase cloud properties are not necessarily those that dominate the change in those cloud properties under warming. For example, N_{d} strongly modulates cloud albedo in both present-day and future climates over both hemispheres, but its effects on the change of cloud albedo in the warming climate are much reduced. This is because the sensitivities of cloud albedo to N_{d} are similar in both climates, so the sensitivities largely cancel for the change of cloud albedo. This suggests that constraining present-day mixed-phase cloud properties alone is not sufficient to reduce the uncertainties in the responses of these clouds to warming. We need to quantify the effects in present-day mixed-phase clouds across a wide range of environmental conditions that might partially represent some future environmental conditions.

Ice formation, including primary ice production through INP and SIP, is important for the responses of mixed-phase clouds and therefore the change of cloud radiative effects (CREs) under warming. These processes are strongly temperature-dependent, so the sensitivities of cloud properties to INP and SIP differ substantially between present-day and future climates. Using cloud albedo in the NH as an example, the contributions from N_{INP} and SIPs based on first-order sensitivity indices are less than 20% to present-day and future states of cloud albedo, but over 95% to the change of cloud albedo in the warming climate. It is also important to understand SIP not just as an important factor in present-day clouds, but also how it changes with warming. Although SIP mechanisms are associated with specific temperature regimes, their effect on cloud feedback is not straightforward because SIP interacts with cloud hydrometeors in a complex way. As the current observational and theoretical constraints on SIP mechanisms and rates are limited (Field et al., 2017a; Morrison et al., 2020), process-level observations and substantial model development are needed to constrain SIP uncertainties.

Extensive measurements in a small number of CAOs (e.g. M-Phase and ACAO aircraft campaign) in the Arctic enable the range of $\Delta R_{\mathrm{CRE}}^{\mathrm{net}}$ in the NH to be narrowed much more (63% reduction) than would have been possible a few years ago, enabling feedback uncertainties to be narrowed as well. However, the observational constraints on N_{d} and N_{INP} are much less effective in the SH, as the dominant source of uncertainties is from SIP which is still poorly represented in models. In addition, there are other model microphysics and dynamics uncertainties that will further inflate the ranges we calculated. It may be feasible to constrain some of these uncertainties using calibration and history matching (e.g., Johnson et al., 2020; Regayre et al., 2023) applied to *in-situ*

and remote cloud observations. However, some of these observational constraints may not effectively narrow the uncertainty in $\Delta R^{\mathrm{net}}_{\mathrm{CRE}}$, just as aerosol measurements do not effectively constrain uncertainty in aerosol forcing (e.g. Lee et al., 2016). Future work is needed to assess which uncertainties could be constrained, and how they help to narrow the microphysical component of cloud feedback uncertainty that we have quantified.

Allowing aerosol states to change in the future can substantially increase the uncertainties of the change in CREs from mixed-phase clouds under warming. Constraining both the magnitude and sign of the aerosol change in the future is important to reduce the uncertainties. This represents a combination of forcing (cloud adjustments) with feedback, which have traditionally been treated separately by definition (forcing at constant SST). We need to better understand how aerosol-driven adjustments are affected by the environment. In addition, aerosol is not just important for forcing, it also modulates feedback, and hence introduces large uncertainty.

This study focused on mixed-phase clouds in CAO events and the results show that this approach works well for single cloud regimes to quantify the role of cloud microphysics in the responses of clouds to warming. Having quantified the importance of aerosol-cloud interactions, ice formation processes and future changes in aerosols, it is now needed to find ways to include the effects in global models so that these effects can be combined with changes in the spatial distribution of cloud regimes. Nevertheless, this study demonstrates the importance of aerosols and ice formation for the responses of mixed-phase clouds to a warming climate, the strong control of these processes on feedback, and the need of quantifying uncertainties from cloud microphysics systematically and thoroughly in the assessment of cloud feedback and climate sensitivity.

5.5 Materials and Methods

5.5.1 Identification of cold-air outbreak initialising points in CMIP6

To identify present-day (2020s: 2020–2029) and future (2090s: 2090–2099) marine cold-air outbreak (CAO) cases, we selected one ensemble member (r1i1p1f2) from the CMIP6 (Coupled Model Intercomparison Project Phase 6) ScenarioMIP (Scenario Model Intercomparison Project) SSP3-7.0 (Shared Socioeconomic Pathway) experiment with the UKESM (UK Earth System Model) version 1.0 (Sellar et al., 2020). The SSP3-7.0 is closer to the cloud feedback simulations with sea surface temperature (SST) in the future +4 K.

Daily-mean potential temperatures at 850 hPa and open-ocean surface temperature were used to calculate the cold-air outbreak index at 850 hPa (M_{850}). Sea grid points with $M_{850} > 0$ K were considered as CAO grid points. As air masses in CAO events come off from a cold continental region or over sea ice, we used land-sea mask and sea-

ice concentration to create an edge map (green dots in Figure A5.10). CAO initialising points were identified by sorting the CAO grid points ($M_{850} > 0$ K) next to the edge and then selecting the highest M_{850} CAO grid points with the selected grids at least 5° away from each other to avoid identifying more than one point from the same CAO event. As the focus of our work is on the high-latitude CAO events, CAO grid points lower than 50° were excluded. Figure A5.10 shows examples of CAO initialising points identified in the Northern Hemisphere (NH, 2025-01-01) and the Southern Hemisphere (SH, 2025-07-02) in the selected ensemble member simulation.

5.5.2 Model configuration

Idealised simulations were performed using the Limited-Area Model (LAM) configuration of the Met Office Unified Model (Brown et al., 2012) version 13.9, coupled with a double-moment bulk Cloud AeroSol Interacting Microphysics (CASIM) scheme (Shipway et al., 2012; Grosvenor et al., 2017; Field et al., 2023). The LAM domain was set to bicyclic (east-west and north-south cyclic) and the surface type was set to sea for all model grids. There were 64 x 64 grid points horizontally with a grid spacing of 1.5 km, spanning an area of 96 km x 96 km. Such choice of grid spacing has been shown sufficient to reproduce the general features of the CAO cloud system (e.g. the stratus and cumulus regions) (Field et al., 2017b) and was aimed to keep consistent with the grid spacing used in our previous studies (Huang et al., 2025, Chapter 2). There were 80 levels vertically in the LAM up to 38.5 km. The time step was set to 60 s. The idealised simulations were run for 48 hours with the first 6 hours excluded from analysis due to model spin-up.

The simulations were initialised with profiles for dry potential temperature (θ), relative humidity (RH), and horizontal wind components (u, v) as piecewise linear functions of height above sea level. The design and perturbation of the initial profiles are further discussed in the next section. Surface pressure was set to 1000 hPa for all simulations. External forcings including the sea surface temperature (SST), geostrophic forcing (u_{geo}, v_{geo}) and large-scale subsidence (w) forcing were also applied through the model run time, with the SST varying with time while the rest of the external forcings remained the same during the model run time. The time-varying SST was defined by the initial SST (SST_0) and the total increase in SST over the 48-hour simulation (ΔSST). In each simulation, the SST was held constant at SST_0 for the first 3 hours and then increased linearly to $SST_0 + \Delta SST$ by the end of the simulation at 48 hours. This time-varying SST represents the air mass being advected over a progressively warmer sea surface during a marine CAO. These external forcings were also perturbed in the PPE (perturbed parameter ensemble) simulations, which is further discussed in the next section. Figure A5.12 shows an example of the time-series of model output for a one-at-a-time sensitivity test on the initial SST (SST_0).

5.5.3 Design of perturbed parameter ensemble

To investigate how aerosol-cloud interactions and cloud microphysics processes affect the radiative properties of CAO clouds in both present-day and future CAO events, we selected 7 environmental parameters and 5 cloud microphysics parameters in our perturbed parameter ensemble (PPE) simulations. The parameters, their definitions and perturbed ranges are shown in Table A5.8. The seven environmental parameters were selected based on expert elicitation and previous studies investigating the cloud-controlling factors for CAO clouds (Fletcher et al., 2016b; McCoy et al., 2017b; Wu et al., 2022; Chen et al., 2022; Murray-Watson et al., 2023; Wu et al., 2025; Klingebiel et al., 2025). The perturbed ranges of the environmental parameters were selected based on the characteristics of CAO events at both present-day and future climates. The perturbed range of droplet number concentration was selected based on observations from the M-Phase (Clarke et al., 2025; Huang et al., 2026, Chapter 3), the ACAO (Arctic Cold-Air Outbreak) (Raif et al., 2024) and the SOC (Southern Ocean Clouds) campaigns (Smith et al., 2025). The perturbed ranges of INP concentration using S_{INP} which is a scaling parameter of the temperature-dependent N_{INP} parameterisation, and the three parameters controlling the efficiencies of SIP processes follow the values in our previous work (Huang et al., 2026, Chapter 3). Initial profiles and external forcings for the control simulation are shown in Figure A5.11.

There were 150 PPE simulations performed by perturbing all 12 parameters simultaneously using the Latin Hypercube sampling (LHS) method, and the output of these simulations were used later for training the Gaussian Process (GP) emulators. In addition to the 150 PPE simulations, another smaller set of 20 simulations designed by LHS were performed to generate the testing dataset.

5.5.4 Preprocessing of albedo in idealised simulations

The idealised simulations use time-varying SST to represent the downstream evolution of CAO clouds. As a result, model time should be interpreted as the distance travelled by the clouds toward the warmer ocean. However, albedo (α), which is defined as the ratio of outgoing (R_{out}) to incoming shortwave (R_{in}) radiation, is strongly influenced by the solar zenith angle (SZA), which varies with model time (i.e. time of day). A limitation of this time-dependent albedo is that the value at a single model hour cannot be considered representative of the mean daytime albedo at a given distance travelled by the clouds. For example, using albedo at a high SZA hour can overestimate the daily-mean albedo at this location, while using albedo at a low SZA hour can underestimate the daily-mean albedo. In addition, when incoming solar radiation is low (SZA $> 65°$), albedo cannot be derived directly from the model output.

To overcome the SZA effects on albedo, we use clear-sky albedo (α_{clr}) as a proxy to

adjust the cloud albedo (α_{cld}), as the clear-sky albedo remains the same (approximately 0.1 with minimal effects from wind speeds) through each simulation. The cloud albedo was calculated using top-of-the-atmosphere (TOA) albedo (α_{TOA}) and cloud cover (f_{cld}). At each model time, we calculated the ratio of the hourly clear-sky albedo to the daily-mean clear-sky albedo and then divided the hourly cloud albedo by the calculated ratio. In this method, we ignored the differences of the optical path between sea surface and clouds. Figure A5.13(a) shows an example of the comparison between raw and adjusted albedos of clear-sky and cloud with PPE member 30.

$$\begin{aligned} \alpha_{TOA} &= \alpha_{cld} f_{cld} + \alpha_{clr}(1 - f_{cld}) \\ \alpha_{cld} &= (\alpha_{TOA} - \alpha_{clr}(1 - f_{cld}))/f_{cld} \end{aligned} \tag{5.3}$$

To fill the gaps where the albedo was not available due to high SZA and little incoming SW radiation, we applied ridge regression for the adjusted cloud albedo in each PPE simulation using in-cloud liquid water path (LWP), in-cloud ice water path (IWP), and cloud cover. The ridge regression model is specific to each PPE simulation as the fixed in-cloud N_{d} is different in the simulations, which strongly affects the cloud albedo. Although the cloud albedo should not be affected by the cloud cover, we used cloud cover to add information about the cloud regime as the cloud albedo can be different between stratus clouds and cumulus clouds even with the same in-cloud LWP and IWP.

Figure A5.13(b) shows an example of LWP, IWP, cloud cover, and the predicted cloud albedo (PPE member 30). Note that hours beyond 42 hours were not included due to poor performance of the ridge regression on cumulus-dominated regions. We also performed leave-one-out validation for the ridge regression method. The mean RMSE (root mean squared error) for predicting cloud albedo using ridge regression is 0.02, the mean MAE (mean absolute error) is 0.03 and the mean R^2 score (coefficient of determination) is 0.76.

5.5.5 Gaussian Process emulation

Based on the decomposition of CREs shown in the main text, four variables were chosen for building the Gaussian Process (GP) emulator (Oakley et al., 2002; O'Hagan, 2006; Lee et al., 2011; Johnson et al., 2015): cloud cover (f_{cld}), cloud albedo (α_{cld}) and cloud LW flux ($R_{\mathrm{LW,cld}}$) and clear-sky LW flux ($R_{\mathrm{LW,clr}}$). The clear-sky albedo (α_{clr}) is assumed to be 0.1 and remains unchanged under warming. All these variables were averaged spatially (over 96 km x 96 km) and temporally (from 6 hour to 36 hour model time).

The testing results of GP emulators for these variables are shown in Figure A5.14 with RMSE, NRMSE (normalised root mean squared error using the range between the maximum and the minimum values), MAE, R^2 and pass rate. The emulator passes with a testing member by crossing the 1-1 line using the 95% confidence intervals from the GP emulators. In general, GP emulators perform reasonably fine on these variables, but the uncertainties from emulators cannot be ignored.

We further validated the emulators by computing the ratio between the standard deviation of the predicted mean values at the testing points and the mean of the predicted standard deviations at those points. For all three emulators, the ratios exceed 1, which suggests the emulator uncertainties are sufficiently small to capture meaningful variation in these variables.

5.5.6 Sampling of N_d, S_{INP} and SIP processes for each CAO event

To understand how N_d, S_{INP} and SIP processes affect the cloud cover, cloud albedo and cloud LW flux, we performed dense regular-interval sampling of the N_d (20 points from 5 to 200 cm^{-3}) and S_{INP} parameter space (29 points from 10^{-5} to 10^2). In addition, for each N_d-S_{INP} point, 50 points were sampled using Latin Hypercube Sampling (LHS) within the three-dimensional parameter space of the SIP parameters. For each CAO event, the seven environmental parameters were fixed. Therefore, the total number of samples generated from each emulator for one CAO case was 20×29×50=29,000. Figure A5.15 shows the sampling values for all five parameters.

Because regular-interval sampling may reach or approach the boundaries of the parameter space, where emulator uncertainties are higher, we excluded points with N_d less than 25 cm^{-3} or higher than 175 cm^{-3}, and points with S_{INP} less than $10^{-4.5}$ or higher than $10^{1.5}$ for the analysis. After this filtering, the total number of points being used for analysis from each emulator for one CAO case is 375 x 50 = 18,750.

Note that not all identified CAO initialization points from the selected CMIP6 simulation were included in the analysis. This is because some points had initial conditions outside the perturbed parameter range, particularly those with low wind speeds. We selected 5 m s^{-1} as the minimum wind speed for our simulations, as weaker winds lead to reduced mixing and minimal cloud formation.

5.5.7 Calculation of SW fluxes

We binned the CAO events by month and by latitude (5 degree interval from 60 to 90 in both hemispheres). For the analysis of changes in TOA fluxes, only 60-70 S and 55-60 N latitude bands were selected here for the analysis of the change of CREs, because the other latitude bins do not contain enough valid CAO events in the future climate for robust statistical analysis (Figure A5.16). The change in SW flux was calculated by

using daily-mean incoming SW flux, which accounts for the influence of daylight length compared to using the daytime-mean flux alone.

Appendix

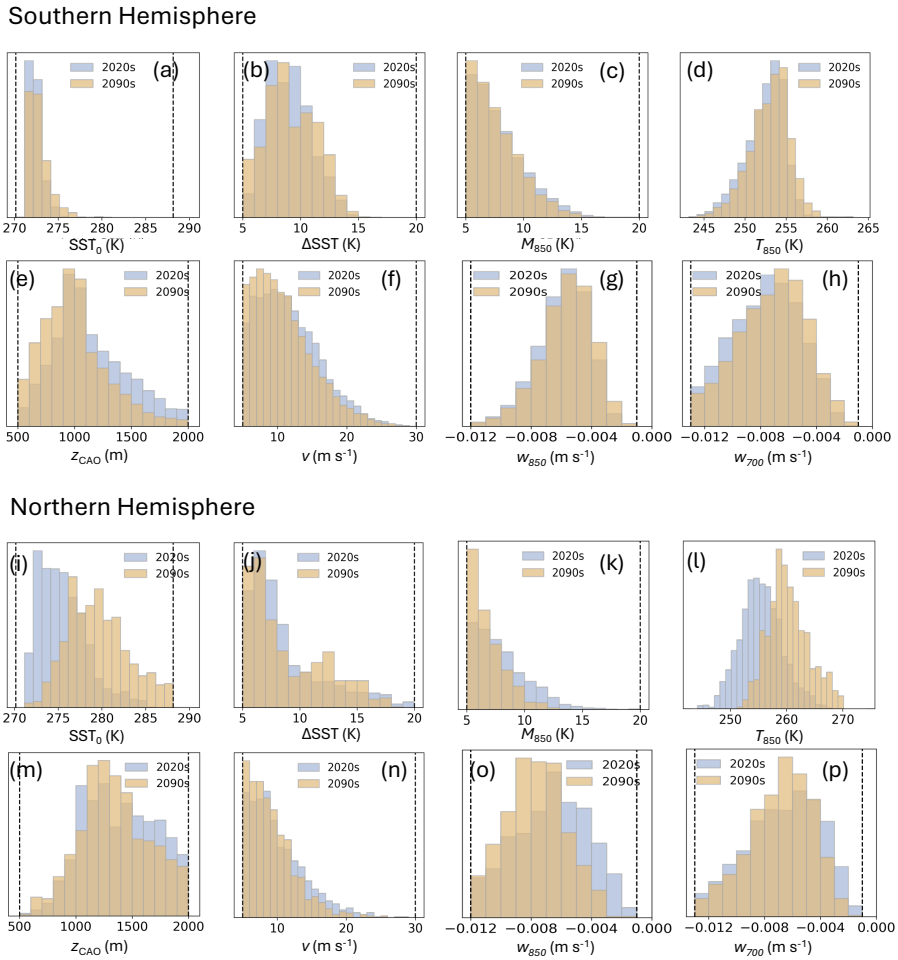


Figure A5.1: Distributions of environmental conditions in CAO events in present-day climate (2020s) and warmer climate (2090s) for the Southern Hemisphere (top) and Northern Hemisphere (bottom): (a, i) SST (sea surface temperature) at the beginning of CAO event (initial SST, K); (b, j) change of SST in 48 hours (the length of the simulation) (Δ SST, K); (c, k) CAO index at 850 hPa (M_{850}, K); (d, l) temperature at 850 hPa (T_{850}, K) - this is not a parameter perturbed in this study; (e, m) CAO depth (m); (f, n) wind speed (m s^{-1}); (g, o) subsidence rates at 850 hPa (W_{850}, m s^{-1}); and (h, p) subsidence rates at 700 hPa (W_{700}, m s^{-1}). Environmental conditions were extracted from one ensemble member (r1i1p1f2) from the CMIP6 (Coupled Model Intercomparison Project Phase 6) ScenarioMIP (Scenario Model Intercomparison Project) SSP3-7.0 (Shared Socioeconomic Pathway) experiment with the UKESM (UK Earth System Model) version 1.0.

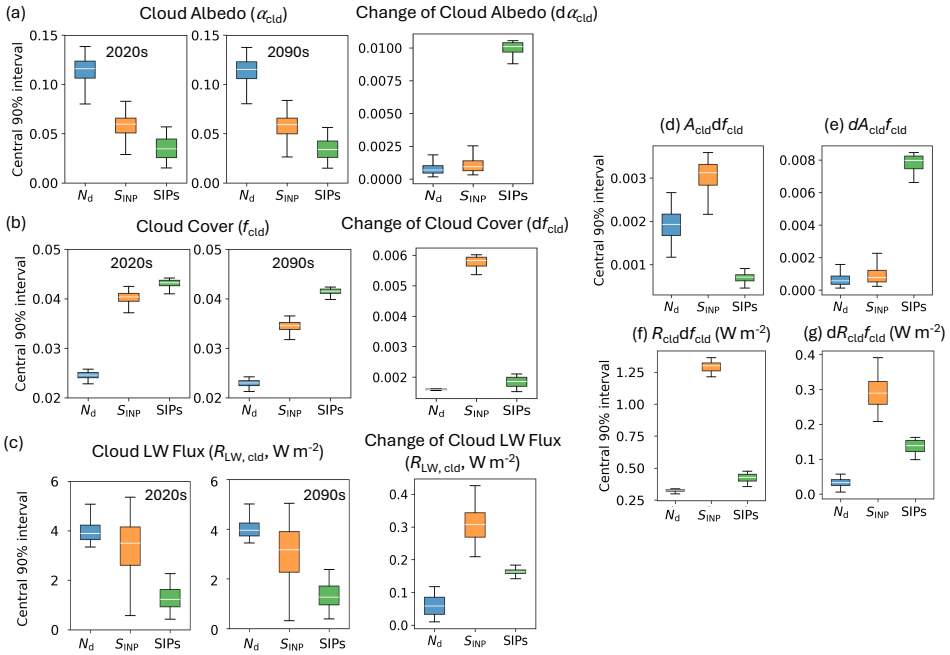


Figure A5.2: Distributions from varying N_{d} (blue), N_{INP} (orange) and SIP processes (green) on the variations of cloud-state variables and the change of cloud states in the SH for: (a) cloud cover (f_{cld}, unitless), (b) cloud albedo (α_{cld}, unitless), and (c) cloud LW flux ($R_{\mathrm{LW,cld}}$, W m^{-2}). Feedback decomposition terms are also shown here for (d) $\alpha_{cld}df_{cld}$ (unitless), (e) $d\alpha_{cld}f_{cld}$ (unitless), (f) $R_{\mathrm{LW,cld}}df_{\mathrm{cld}}$ (W m^{-2}), (g) $dR_{\mathrm{LW,cld}}f_{\mathrm{cld}}$ (W m^{-2}). Each value used for producing a box plot is the central 90% interval (5% to 95%) by varying the parameter under a fixed combination of the other two parameters. Terms related to clear-sky albedo and clear-sky LW flux are not shown here as these two are not affected by cloud microphysics.

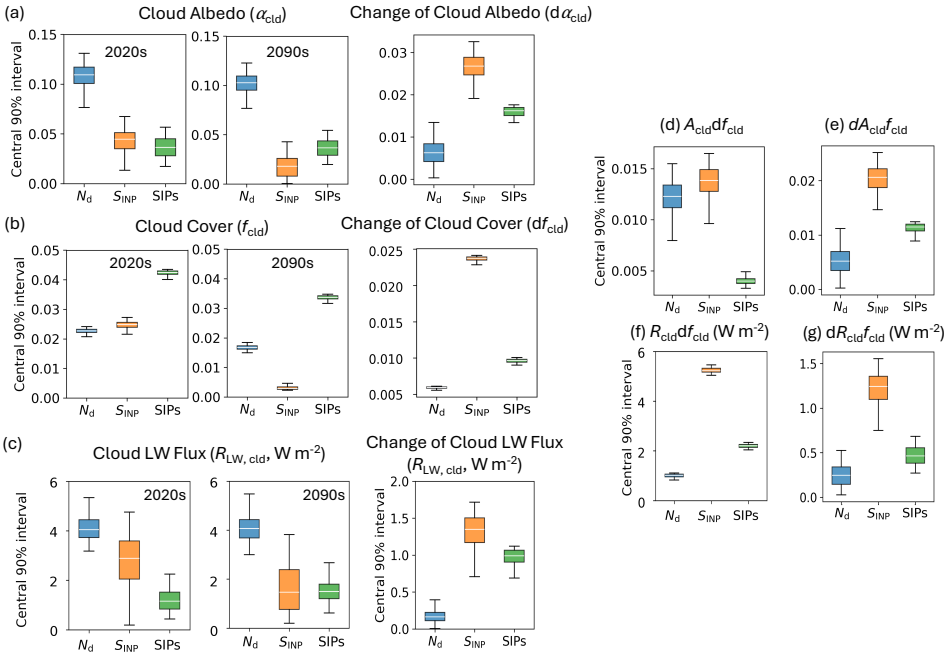


Figure A5.3: Distributions from varying N_{d} (blue), N_{INP} (orange) and SIP processes (green) on the variations of cloud-state variables and the change of cloud states in the NH for: (a) cloud cover (f_{cld}, unitless), (b) cloud albedo (α_{cld}, unitless), and (c) cloud LW flux ($R_{\mathrm{LW,cld}}$, W m^{-2}). Feedback decomposition terms are also shown here for (d) $\alpha_{cld}df_{cld}$ (unitless), (e) $d\alpha_{cld}f_{cld}$ (unitless), (f) $R_{\mathrm{LW,cld}}df_{\mathrm{cld}}$ (W m^{-2}), (g) $dR_{\mathrm{LW,cld}}f_{\mathrm{cld}}$ (W m^{-2}). Each value used for producing a box plot is the central 90% interval (5% to 95%) by varying the parameter under a fixed combination of the other two parameters. Terms related to clear-sky albedo and clear-sky LW flux are not shown here as these two are not affected by cloud microphysics.

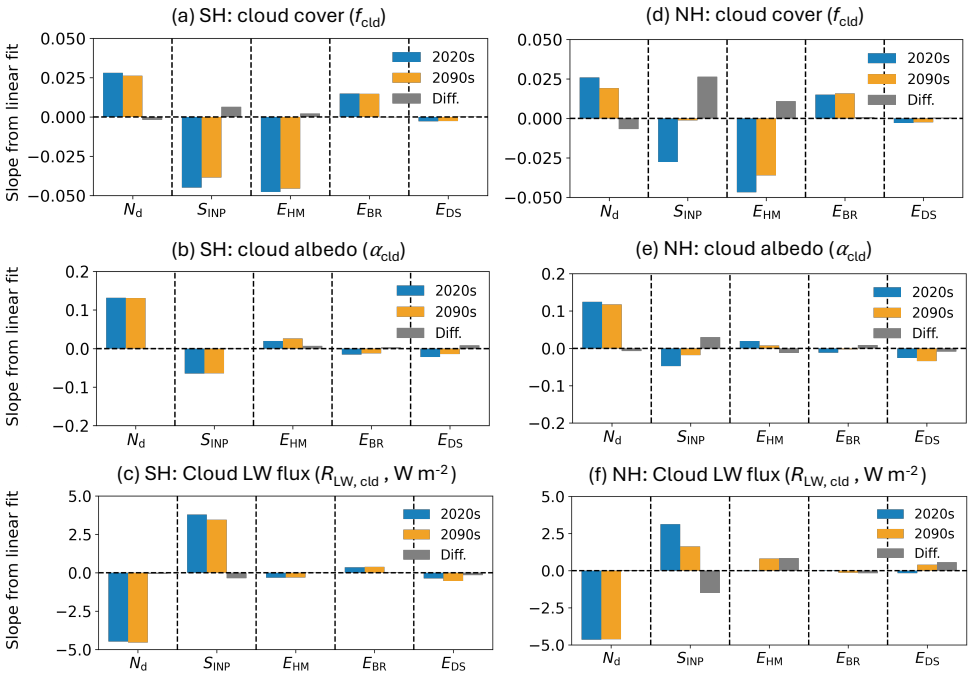


Figure A5.4: Effects from N_{d}, N_{INP} and three SIP parameters (E_{HM}, E_{BR} and E_{DS}) using slope from linear fit between the cloud properties and standardized values of parameters on (a, d) cloud cover (f_{cld}, unitless), (b, e) cloud albedo (α_{cld}, unitless), and (c, f) cloud longwave (LW) flux ($R_{LW,cld}$, W m^{-2}). Figures for the SH are shown in the left and in the right for the NH. Values for present-day (2020s) are shown in blue, the warmer climate (2090s) in orange and the difference between climates in gray.

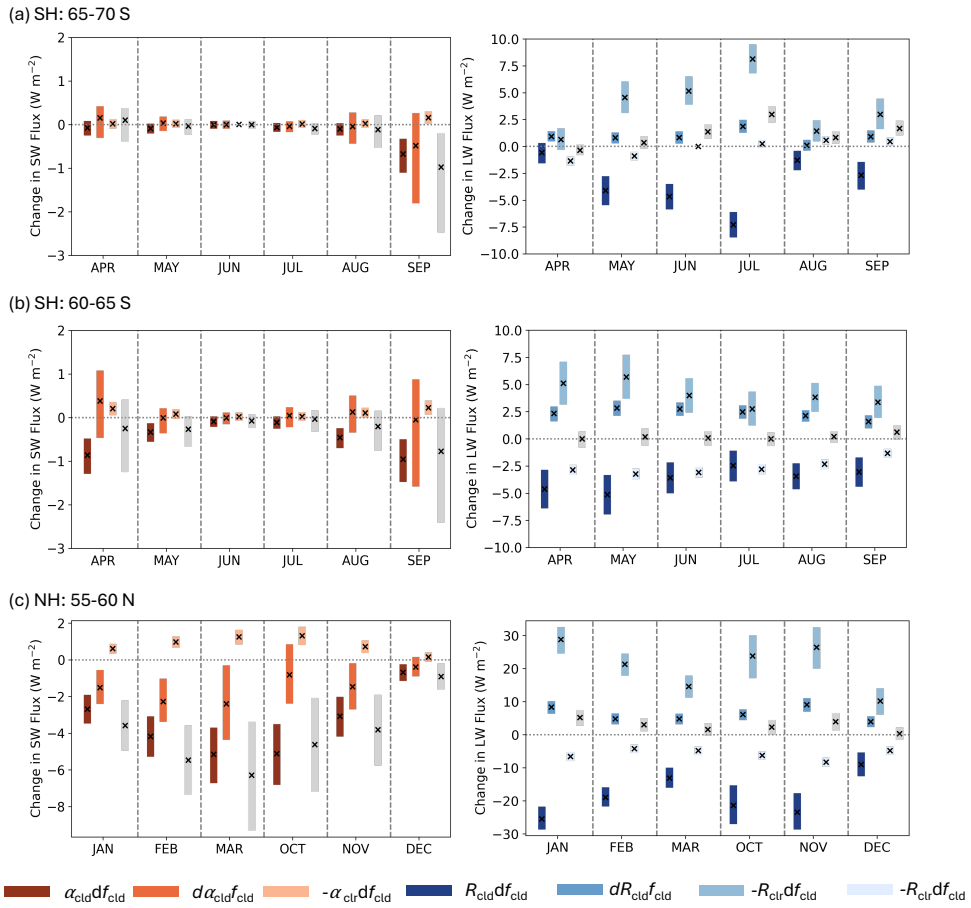


Figure A5.5: Monthly ranges (5% quantile, median and 95% quantile) of the feedback decomposition terms for (a) 65-70 S in the SH, (b) 60 - 65 S in the SH and (c) 55 - 60 N in the NH, by varying N_d, N_{INP} and SIP processes across the parameter space. The cross represents the median value and the gray bars are the sum of the feedback decomposition terms.

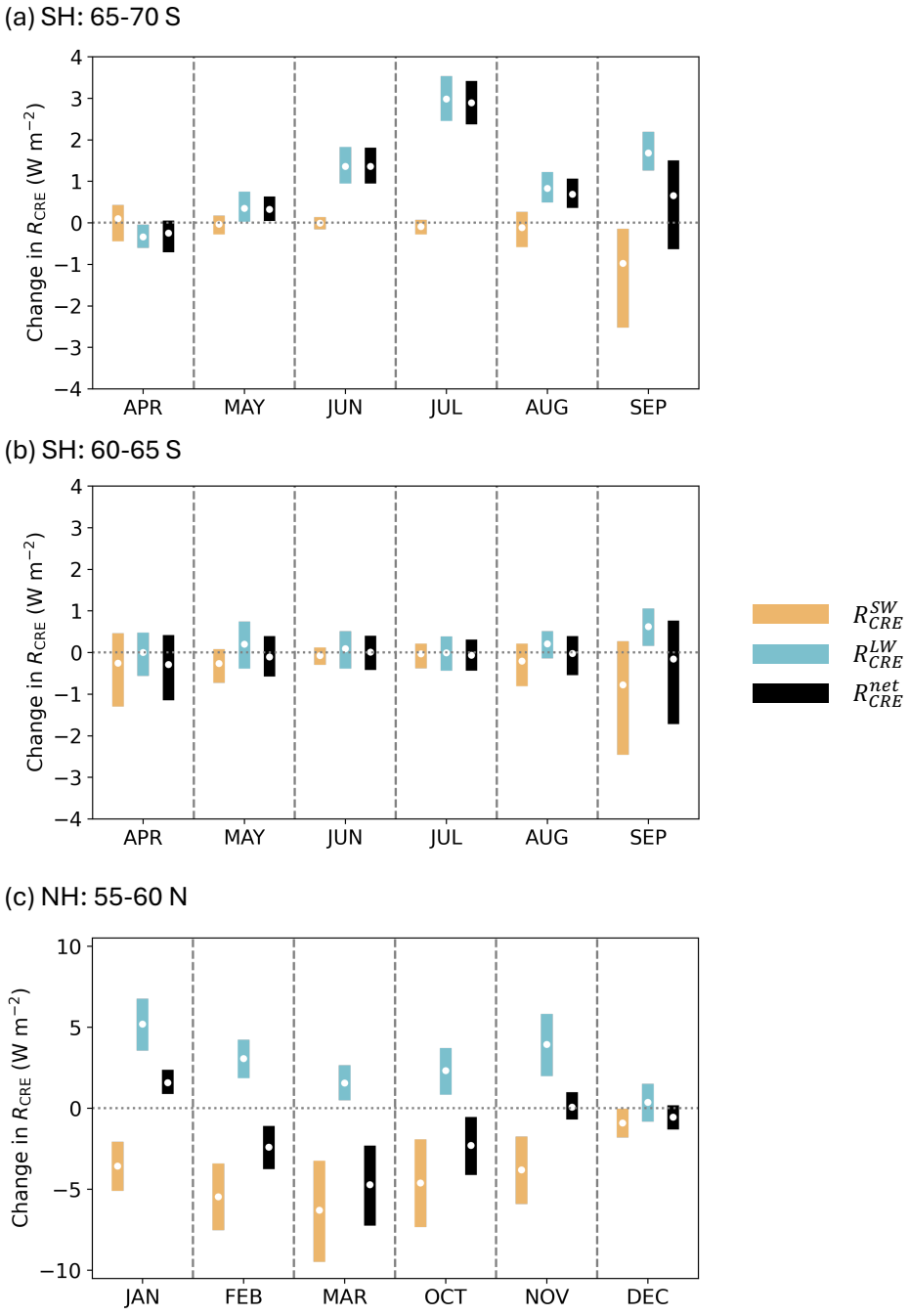


Figure A5.6: Distributions of SW, LW and net fluxes changes by varying N_{d}, N_{INP} and SIP processes across the parameter space for: monthly distributions at (a) 65-70 S In the SH, (b) 60 - 65 S in the SH and (c) 55 - 60 N in the NH.

Table A5.1: Statistics for ΔR_{CRE} between present-day (2020s) and warmer (2090s) climates

	Median	Central 90% interval	Central 90% interval for SST +4 K
SH $\Delta R_{\mathrm{CRE}}^{\mathrm{SW}}$	$-0.22\ \mathrm{W\,m^{-2}}$	$0.73\ \mathrm{W\,m^{-2}}$	$0.18\ \mathrm{W\,m^{-2}\,K^{-1}}$
SH $\Delta R_{\mathrm{CRE}}^{\mathrm{LW}}$	$+0.67\ \mathrm{W\,m^{-2}}$	$0.54\ \mathrm{W\,m^{-2}}$	$0.14\ \mathrm{W\,m^{-2}\,K^{-1}}$
SH $\Delta R_{\mathrm{CRE}}^{\mathrm{net}}$	$+0.40\ \mathrm{W\,m^{-2}}$	$0.65\ \mathrm{W\,m^{-2}}$	$0.16\ \mathrm{W\,m^{-2}\,K^{-1}}$
NH $\Delta R_{\mathrm{CRE}}^{\mathrm{SW}}$	$-4.11\ \mathrm{W\,m^{-2}}$	$3.35\ \mathrm{W\,m^{-2}}$	$0.84\ \mathrm{W\,m^{-2}\,K^{-1}}$
NH $\Delta R_{\mathrm{CRE}}^{\mathrm{LW}}$	$+2.74\ \mathrm{W\,m^{-2}}$	$2.06\ \mathrm{W\,m^{-2}}$	$0.52\ \mathrm{W\,m^{-2}\,K^{-1}}$
NH $\Delta R_{\mathrm{CRE}}^{\mathrm{net}}$	$-1.38\ \mathrm{W\,m^{-2}}$	$1.57\ \mathrm{W\,m^{-2}}$	$0.39\ \mathrm{W\,m^{-2}\,K^{-1}}$

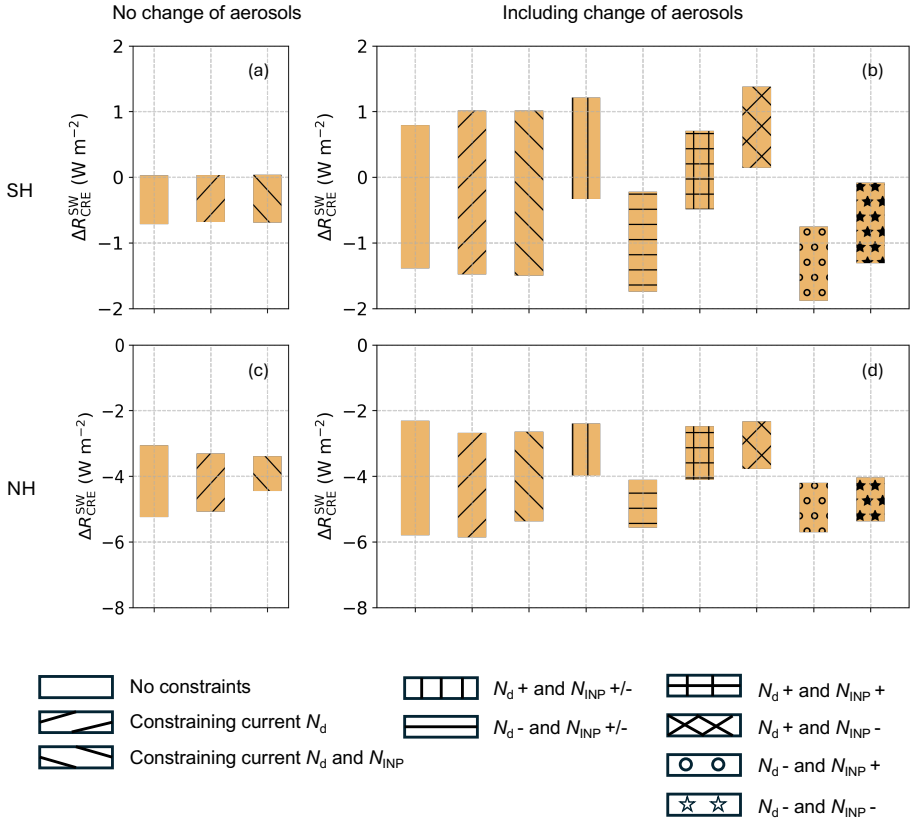


Figure A5.7: Comparison of the central 90% range of the changes in SWCRE ($\Delta R_{\mathrm{CRE}}^{\mathrm{SW}}$) for (a, c) no future changes of aerosols, and (b, d) including future changes of aerosols in the warmer climate, along with different constraints on present-day and future N_{d} and N_{INP}.

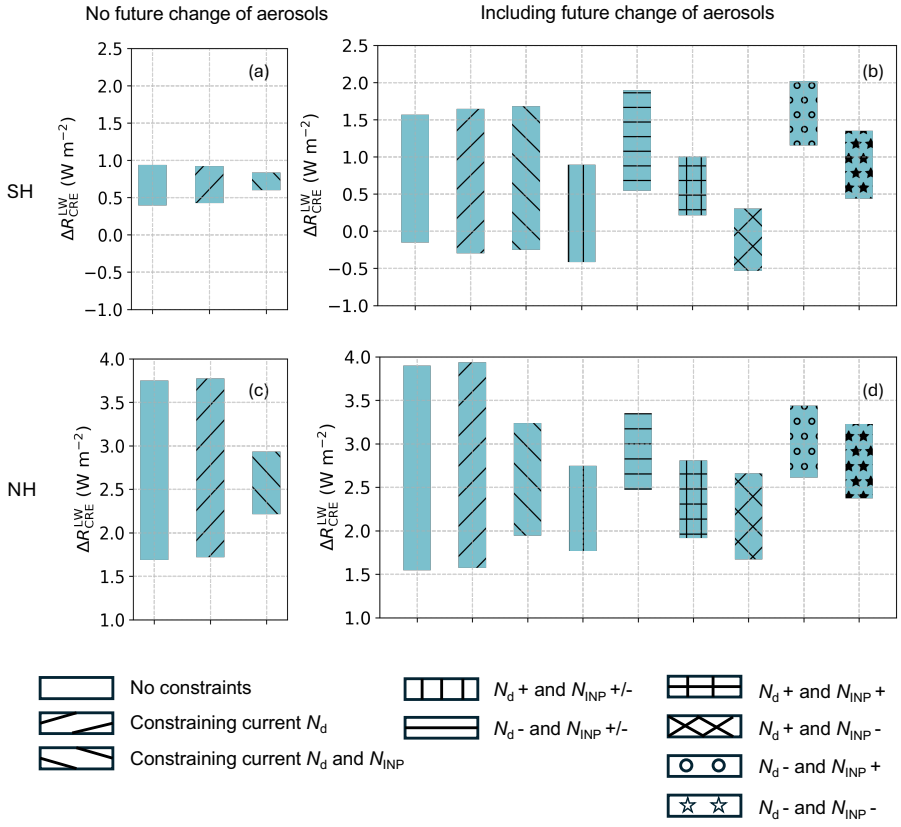


Figure A5.8: Comparison of the central 90% range of the changes in LWCRE ($\Delta R_{\mathrm{CRE}}^{\mathrm{LW}}$) for (a, c) no future changes of aerosols, and (b, d) including future changes of aerosols in the warmer climate, along with different constraints on present-day and future N_{d} and N_{INP}.

Table A5.2: Statistics for $\Delta R_{\mathrm{CRE}}^{\mathrm{SW}}$ between present-day (2020s) and warmer (2090s) climates for different aerosol assumptions in the SH

Aerosol assumption	**Median**	**Central 90% interval**	**Central 90% interval for SST +4 K**
No future changes + No constraints	$-0.22\ \mathrm{W\,m^{-2}}$	$0.73\ \mathrm{W\,m^{-2}}$	$0.18\ \mathrm{W\,m^{-2}\,K^{-1}}$
No future changes + current N_{d} constrained	$-0.20\ \mathrm{W\,m^{-2}}$	$0.70\ \mathrm{W\,m^{-2}}$	$0.18\ \mathrm{W\,m^{-2}\,K^{-1}}$
No future changes + current N_{INP} constrained	$-0.21\ \mathrm{W\,m^{-2}}$	$0.73\ \mathrm{W\,m^{-2}}$	$0.18\ \mathrm{W\,m^{-2}\,K^{-1}}$
Future changes included + No constraints	$-0.30\ \mathrm{W\,m^{-2}}$	$2.14\ \mathrm{W\,m^{-2}}$	$0.53\ \mathrm{W\,m^{-2}\,K^{-1}}$
Future changes included + current N_{d} constrained	$-0.19\ \mathrm{W\,m^{-2}}$	$2.47\ \mathrm{W\,m^{-2}}$	$0.62\ \mathrm{W\,m^{-2}\,K^{-1}}$
Future changes included + current N_{INP} constrained	$-0.20\ \mathrm{W\,m^{-2}}$	$2.52\ \mathrm{W\,m^{-2}}$	$0.63\ \mathrm{W\,m^{-2}\,K^{-1}}$
N_{d} + and N_{INP} ±	$+0.44\ \mathrm{W\,m^{-2}}$	$1.55\ \mathrm{W\,m^{-2}}$	$0.39\ \mathrm{W\,m^{-2}\,K^{-1}}$
N_{d} - and N_{INP} ±	$-0.98\ \mathrm{W\,m^{-2}}$	$1.52\ \mathrm{W\,m^{-2}}$	$0.38\ \mathrm{W\,m^{-2}\,K^{-1}}$
N_{d} + and N_{INP} +	$+0.12\ \mathrm{W\,m^{-2}}$	$1.19\ \mathrm{W\,m^{-2}}$	$0.30\ \mathrm{W\,m^{-2}\,K^{-1}}$
N_{d} + and N_{INP} -	$+0.74\ \mathrm{W\,m^{-2}}$	$1.24\ \mathrm{W\,m^{-2}}$	$0.31\ \mathrm{W\,m^{-2}\,K^{-1}}$
N_{d} - and N_{INP} +	$-1.26\ \mathrm{W\,m^{-2}}$	$1.13\ \mathrm{W\,m^{-2}}$	$0.28\ \mathrm{W\,m^{-2}\,K^{-1}}$
N_{d} - and N_{INP} -	$-0.66\ \mathrm{W\,m^{-2}}$	$1.23\ \mathrm{W\,m^{-2}}$	$0.31\ \mathrm{W\,m^{-2}\,K^{-1}}$

Table A5.3: Statistics for $\Delta R_{\mathrm{CRE}}^{\mathrm{SW}}$ between present-day (2020s) and warmer (2090s) climates for different aerosol assumptions in the NH

Aerosol assumption	**Median**	**Central 90% interval**	**Central 90% interval for SST +4 K**
No future changes + No constraints	$-4.11\ \mathrm{W\,m^{-2}}$	$3.35\ \mathrm{W\,m^{-2}}$	$0.84\ \mathrm{W\,m^{-2}\,K^{-1}}$
No future changes + current N_{d} constrained	$-4.22\ \mathrm{W\,m^{-2}}$	$2.98\ \mathrm{W\,m^{-2}}$	$0.75\ \mathrm{W\,m^{-2}\,K^{-1}}$
No future changes + current N_{INP} constrained	$-3.97\ \mathrm{W\,m^{-2}}$	$1.06\ \mathrm{W\,m^{-2}}$	$0.27\ \mathrm{W\,m^{-2}\,K^{-1}}$
Future changes included + No constraints	$-4.23\ \mathrm{W\,m^{-2}}$	$4.24\ \mathrm{W\,m^{-2}}$	$1.06\ \mathrm{W\,m^{-2}\,K^{-1}}$
Future changes included + current N_{d} constrained	$-4.26\ \mathrm{W\,m^{-2}}$	$4.09\ \mathrm{W\,m^{-2}}$	$1.02\ \mathrm{W\,m^{-2}\,K^{-1}}$
Future changes included + current N_{INP} constrained	$-4.00\ \mathrm{W\,m^{-2}}$	$2.73\ \mathrm{W\,m^{-2}}$	$0.68\ \mathrm{W\,m^{-2}\,K^{-1}}$
N_{d} + and N_{INP} ±	$-3.23\ \mathrm{W\,m^{-2}}$	$1.59\ \mathrm{W\,m^{-2}}$	$0.40\ \mathrm{W\,m^{-2}\,K^{-1}}$
N_{d} - and N_{INP} ±	$-4.86\ \mathrm{W\,m^{-2}}$	$1.46\ \mathrm{W\,m^{-2}}$	$0.37\ \mathrm{W\,m^{-2}\,K^{-1}}$
N_{d} + and N_{INP} +	$-3.36\ \mathrm{W\,m^{-2}}$	$1.64\ \mathrm{W\,m^{-2}}$	$0.41\ \mathrm{W\,m^{-2}\,K^{-1}}$
N_{d} + and N_{INP} -	$-3.11\ \mathrm{W\,m^{-2}}$	$1.45\ \mathrm{W\,m^{-2}}$	$0.36\ \mathrm{W\,m^{-2}\,K^{-1}}$
N_{d} - and N_{INP} +	$-4.99\ \mathrm{W\,m^{-2}}$	$1.50\ \mathrm{W\,m^{-2}}$	$0.38\ \mathrm{W\,m^{-2}\,K^{-1}}$
N_{d} - and N_{INP} -	$-4.73\ \mathrm{W\,m^{-2}}$	$1.33\ \mathrm{W\,m^{-2}}$	$0.33\ \mathrm{W\,m^{-2}\,K^{-1}}$

Table A5.4: Statistics for $\Delta R_{\mathrm{CRE}}^{\mathrm{LW}}$ between present-day (2020s) and warmer (2090s) climates for different aerosol assumptions in the SH

Aerosol assumption	**Median**	**Central 90% interval**	**Central 90% interval for SST +4 K**
No future changes + No constraints	$+0.67\ \mathrm{W\,m^{-2}}$	$0.54\ \mathrm{W\,m^{-2}}$	$0.14\ \mathrm{W\,m^{-2}\,K^{-1}}$
No future changes + current N_{d} constrained	$+0.68\ \mathrm{W\,m^{-2}}$	$0.50\ \mathrm{W\,m^{-2}}$	$0.12\ \mathrm{W\,m^{-2}\,K^{-1}}$
No future changes + current N_{INP} constrained	$+0.73\ \mathrm{W\,m^{-2}}$	$0.24\ \mathrm{W\,m^{-2}}$	$0.06\ \mathrm{W\,m^{-2}\,K^{-1}}$
Future changes included + No constraints	$+0.68\ \mathrm{W\,m^{-2}}$	$1.72\ \mathrm{W\,m^{-2}}$	$0.43\ \mathrm{W\,m^{-2}\,K^{-1}}$
Future changes included + current N_{d} constrained	$+0.63\ \mathrm{W\,m^{-2}}$	$1.94\ \mathrm{W\,m^{-2}}$	$0.49\ \mathrm{W\,m^{-2}\,K^{-1}}$
Future changes included + current N_{INP} constrained	$+0.69\ \mathrm{W\,m^{-2}}$	$1.93\ \mathrm{W\,m^{-2}}$	$0.48\ \mathrm{W\,m^{-2}\,K^{-1}}$
N_{d} + and N_{INP} ±	$+0.26\ \mathrm{W\,m^{-2}}$	$1.31\ \mathrm{W\,m^{-2}}$	$0.33\ \mathrm{W\,m^{-2}\,K^{-1}}$
N_{d} - and N_{INP} ±	$+1.23\ \mathrm{W\,m^{-2}}$	$1.35\ \mathrm{W\,m^{-2}}$	$0.34\ \mathrm{W\,m^{-2}\,K^{-1}}$
N_{d} + and N_{INP} +	$+0.58\ \mathrm{W\,m^{-2}}$	$0.79\ \mathrm{W\,m^{-2}}$	$0.20\ \mathrm{W\,m^{-2}\,K^{-1}}$
N_{d} + and N_{INP} -	$-0.08\ \mathrm{W\,m^{-2}}$	$0.84\ \mathrm{W\,m^{-2}}$	$0.21\ \mathrm{W\,m^{-2}\,K^{-1}}$
N_{d} - and N_{INP} +	$+1.54\ \mathrm{W\,m^{-2}}$	$0.87\ \mathrm{W\,m^{-2}}$	$0.22\ \mathrm{W\,m^{-2}\,K^{-1}}$
N_{d} - and N_{INP} -	$+0.89\ \mathrm{W\,m^{-2}}$	$0.91\ \mathrm{W\,m^{-2}}$	$0.23\ \mathrm{W\,m^{-2}\,K^{-1}}$

Table A5.5: Statistics for $\Delta R_{\mathrm{CRE}}^{\mathrm{LW}}$ between present-day (2020s) and warmer (2090s) climates for different aerosol assumptions in the NH

Aerosol assumption	**Median**	**Central 90% interval**	**Central 90% interval for SST +4 K**
No future changes + No constraints	$+2.74\ \mathrm{W\,m^{-2}}$	$2.06\ \mathrm{W\,m^{-2}}$	$0.52\ \mathrm{W\,m^{-2}\,K^{-1}}$
No future changes + current N_{d} constrained	$+2.78\ \mathrm{W\,m^{-2}}$	$2.05\ \mathrm{W\,m^{-2}}$	$0.51\ \mathrm{W\,m^{-2}\,K^{-1}}$
No future changes + current N_{INP} constrained	$+2.62\ \mathrm{W\,m^{-2}}$	$0.71\ \mathrm{W\,m^{-2}}$	$0.18\ \mathrm{W\,m^{-2}\,K^{-1}}$
Future changes included + No constraints	$+2.76\ \mathrm{W\,m^{-2}}$	$2.35\ \mathrm{W\,m^{-2}}$	$0.59\ \mathrm{W\,m^{-2}\,K^{-1}}$
Future changes included + current N_{d} constrained	$+2.79\ \mathrm{W\,m^{-2}}$	$2.36\ \mathrm{W\,m^{-2}}$	$0.59\ \mathrm{W\,m^{-2}\,K^{-1}}$
Future changes included + current N_{INP} constrained	$+2.63\ \mathrm{W\,m^{-2}}$	$1.29\ \mathrm{W\,m^{-2}}$	$0.32\ \mathrm{W\,m^{-2}\,K^{-1}}$
N_{d} + and N_{INP} ±	$+2.34\ \mathrm{W\,m^{-2}}$	$0.98\ \mathrm{W\,m^{-2}}$	$0.24\ \mathrm{W\,m^{-2}\,K^{-1}}$
N_{d} - and N_{INP} ±	$+2.95\ \mathrm{W\,m^{-2}}$	$0.88\ \mathrm{W\,m^{-2}}$	$0.22\ \mathrm{W\,m^{-2}\,K^{-1}}$
N_{d} + and N_{INP} +	$+2.41\ \mathrm{W\,m^{-2}}$	$0.89\ \mathrm{W\,m^{-2}}$	$0.22\ \mathrm{W\,m^{-2}\,K^{-1}}$
N_{d} + and N_{INP} -	$+2.26\ \mathrm{W\,m^{-2}}$	$0.99\ \mathrm{W\,m^{-2}}$	$0.25\ \mathrm{W\,m^{-2}\,K^{-1}}$
N_{d} - and N_{INP} +	$+3.04\ \mathrm{W\,m^{-2}}$	$0.83\ \mathrm{W\,m^{-2}}$	$0.21\ \mathrm{W\,m^{-2}\,K^{-1}}$
N_{d} - and N_{INP} -	$+2.86\ \mathrm{W\,m^{-2}}$	$0.85\ \mathrm{W\,m^{-2}}$	$0.21\ \mathrm{W\,m^{-2}\,K^{-1}}$

Table A5.6: Statistics for $\Delta R^{\mathrm{net}}_{\mathrm{CRE}}$ between present-day (2020s) and warmer (2090s) climates for different aerosol assumptions in the SH

Aerosol assumption	**Median**	**Central 90% interval**	**Central 90% interval for SST +4 K**
No future changes + No constraints	$+0.40\ \mathrm{W\,m^{-2}}$	$0.65\ \mathrm{W\,m^{-2}}$	$0.16\ \mathrm{W\,m^{-2}\,K^{-1}}$
No future changes + current N_{d} constrained	$+0.44\ \mathrm{W\,m^{-2}}$	$0.70\ \mathrm{W\,m^{-2}}$	$0.17\ \mathrm{W\,m^{-2}\,K^{-1}}$
No future changes + current N_{INP} constrained	$+0.49\ \mathrm{W\,m^{-2}}$	$0.60\ \mathrm{W\,m^{-2}}$	$0.15\ \mathrm{W\,m^{-2}\,K^{-1}}$
Future changes included + No constraints	$+0.37\ \mathrm{W\,m^{-2}}$	$0.88\ \mathrm{W\,m^{-2}}$	$0.22\ \mathrm{W\,m^{-2}\,K^{-1}}$
Future changes included + current N_{d} constrained	$+0.43\ \mathrm{W\,m^{-2}}$	$1.00\ \mathrm{W\,m^{-2}}$	$0.25\ \mathrm{W\,m^{-2}\,K^{-1}}$
Future changes included + current N_{INP} constrained	$+0.47\ \mathrm{W\,m^{-2}}$	$0.94\ \mathrm{W\,m^{-2}}$	$0.24\ \mathrm{W\,m^{-2}\,K^{-1}}$
N_{d} + and N_{INP} ±	$+0.71\ \mathrm{W\,m^{-2}}$	$0.82\ \mathrm{W\,m^{-2}}$	$0.20\ \mathrm{W\,m^{-2}\,K^{-1}}$
N_{d} - and N_{INP} ±	$+0.26\ \mathrm{W\,m^{-2}}$	$0.58\ \mathrm{W\,m^{-2}}$	$0.15\ \mathrm{W\,m^{-2}\,K^{-1}}$
N_{d} + and N_{INP} +	$+0.73\ \mathrm{W\,m^{-2}}$	$0.70\ \mathrm{W\,m^{-2}}$	$0.18\ \mathrm{W\,m^{-2}\,K^{-1}}$
N_{d} + and N_{INP} -	$+0.69\ \mathrm{W\,m^{-2}}$	$0.92\ \mathrm{W\,m^{-2}}$	$0.23\ \mathrm{W\,m^{-2}\,K^{-1}}$
N_{d} - and N_{INP} +	$+0.28\ \mathrm{W\,m^{-2}}$	$0.43\ \mathrm{W\,m^{-2}}$	$0.11\ \mathrm{W\,m^{-2}\,K^{-1}}$
N_{d} - and N_{INP} -	$+0.24\ \mathrm{W\,m^{-2}}$	$0.70\ \mathrm{W\,m^{-2}}$	$0.17\ \mathrm{W\,m^{-2}\,K^{-1}}$

Table A5.7: Statistics for $\Delta R^{\mathrm{net}}_{\mathrm{CRE}}$ between present-day (2020s) and warmer (2090s) climates for different aerosol assumptions in the NH

Aerosol assumption	**Median**	**Central 90% interval**	**Central 90% interval for SST +4 K**
No future changes + No constraints	$-1.38\ \mathrm{W\,m^{-2}}$	$1.57\ \mathrm{W\,m^{-2}}$	$0.39\ \mathrm{W\,m^{-2}\,K^{-1}}$
No future changes + current N_{d} constrained	$-1.41\ \mathrm{W\,m^{-2}}$	$1.09\ \mathrm{W\,m^{-2}}$	$0.27\ \mathrm{W\,m^{-2}\,K^{-1}}$
No future changes + current N_{INP} constrained	$-1.35\ \mathrm{W\,m^{-2}}$	$0.58\ \mathrm{W\,m^{-2}}$	$0.15\ \mathrm{W\,m^{-2}\,K^{-1}}$
Future changes included + No constraints	$-1.52\ \mathrm{W\,m^{-2}}$	$2.23\ \mathrm{W\,m^{-2}}$	$0.56\ \mathrm{W\,m^{-2}\,K^{-1}}$
Future changes included + current N_{d} constrained	$-1.46\ \mathrm{W\,m^{-2}}$	$1.94\ \mathrm{W\,m^{-2}}$	$0.49\ \mathrm{W\,m^{-2}\,K^{-1}}$
Future changes included + current N_{INP} constrained	$-1.41\ \mathrm{W\,m^{-2}}$	$1.65\ \mathrm{W\,m^{-2}}$	$0.41\ \mathrm{W\,m^{-2}\,K^{-1}}$
N_{d} + and N_{INP} ±	$-0.92\ \mathrm{W\,m^{-2}}$	$1.02\ \mathrm{W\,m^{-2}}$	$0.25\ \mathrm{W\,m^{-2}\,K^{-1}}$
N_{d} - and N_{INP} ±	$-1.94\ \mathrm{W\,m^{-2}}$	$0.73\ \mathrm{W\,m^{-2}}$	$0.18\ \mathrm{W\,m^{-2}\,K^{-1}}$
N_{d} + and N_{INP} +	$-0.96\ \mathrm{W\,m^{-2}}$	$0.98\ \mathrm{W\,m^{-2}}$	$0.24\ \mathrm{W\,m^{-2}\,K^{-1}}$
N_{d} + and N_{INP} -	$-0.88\ \mathrm{W\,m^{-2}}$	$1.04\ \mathrm{W\,m^{-2}}$	$0.26\ \mathrm{W\,m^{-2}\,K^{-1}}$
N_{d} - and N_{INP} +	$-1.95\ \mathrm{W\,m^{-2}}$	$0.73\ \mathrm{W\,m^{-2}}$	$0.18\ \mathrm{W\,m^{-2}\,K^{-1}}$
N_{d} - and N_{INP} -	$-1.92\ \mathrm{W\,m^{-2}}$	$0.72\ \mathrm{W\,m^{-2}}$	$0.18\ \mathrm{W\,m^{-2}\,K^{-1}}$

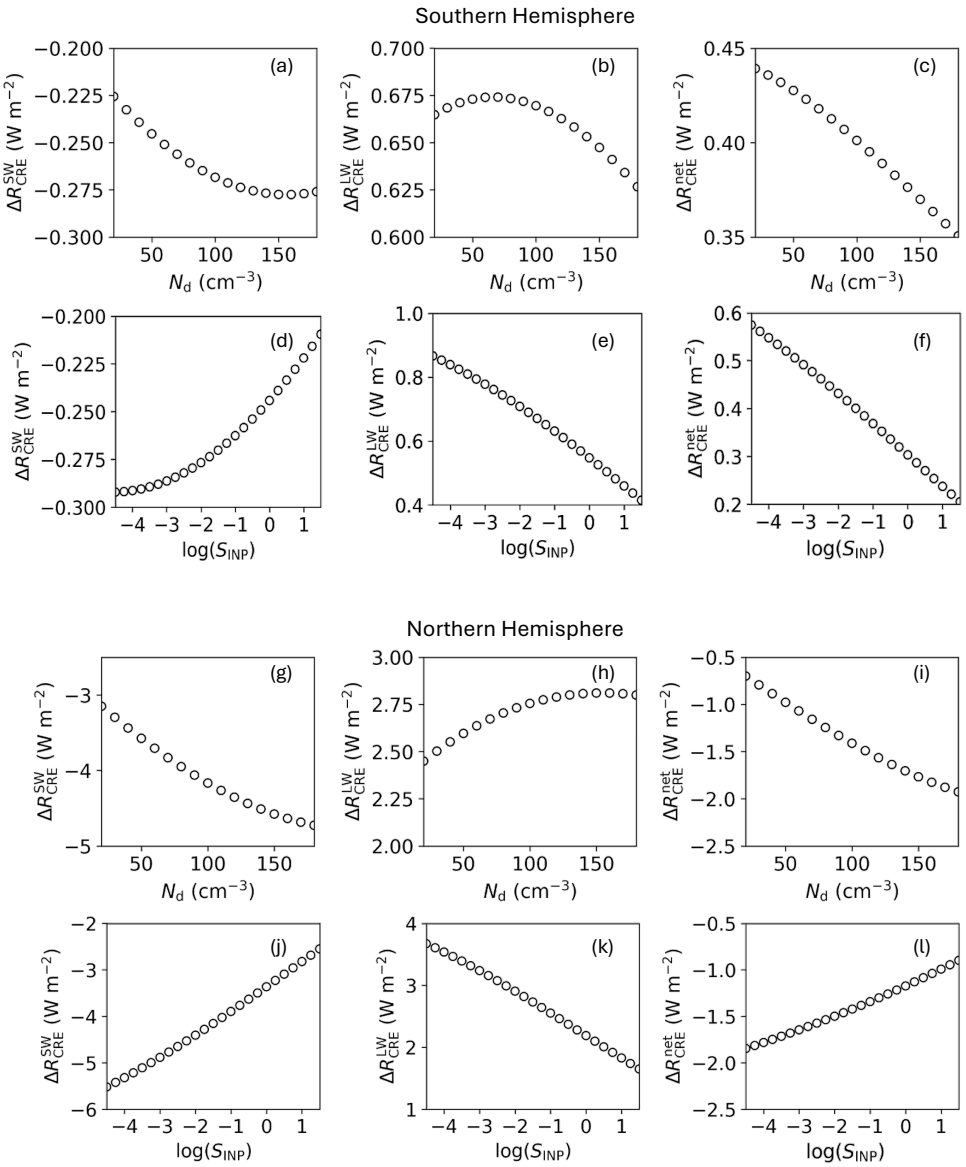


Figure A5.9: Scatter plots of changes in SWCRE (left), LWCRE (middle) and net CRE (right) against N_d and $log(S_\mathrm{INP})$ for the Southern Hemisphere (top) and Northern Hemisphere (bottom).

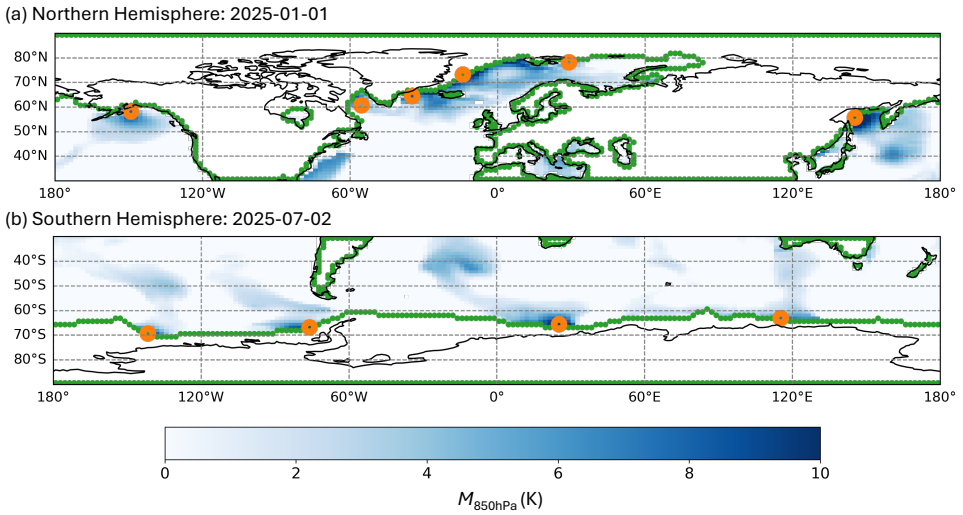


Figure A5.10: Examples of CAO initialising points identified over the (a) Northern Hemisphere (2025-01-01) and (b) the Southern Hemisphere (2025-07-02) in the selected ensemble member simulation. Green points are the edge points identified using land-sea mask and sea-ice concentration.

Table A5.8: Parameters perturbed and their descriptions

Parameter	Definition	Perturbed range	Control value
SST_0	Initial SST (K)	270.15–288.15	273.15
ΔSST	Change in SST over 48 hours (K)	5–20	10
M_{850}	CAO index at 850 hPa (K)	5–20	10
z_{CAO}	CAO depth, defined as the height at which the potential temperature equals the sea-surface potential temperature (m)	500–2000	1000
v	Meridional wind component ($m\,s^{-1}$)	5–30	10
w_{850}	Subsidence at 850 hPa ($m\,s^{-1}$)	-0.0120–-0.0010	-0.0050
w_{700}	Subsidence at 700 hPa ($m\,s^{-1}$)	-0.0170–-0.0013	-0.0065
N_d	Fixed in-cloud droplet number concentration (cm^{-3})	5–200	100
S_{INP}	Scaling of the default INP parameterisation	10^{-5}–10^{2}	10^{0}
E_{HM}	Efficiency of the Hallett–Mossop process (mg^{-1})	35–3500	350
E_{BR}	Coefficient controlling the efficiency of ice–ice collisional breakup	28–2800	280
E_{DS}	Efficiency of the droplet-shattering process	2–10	5

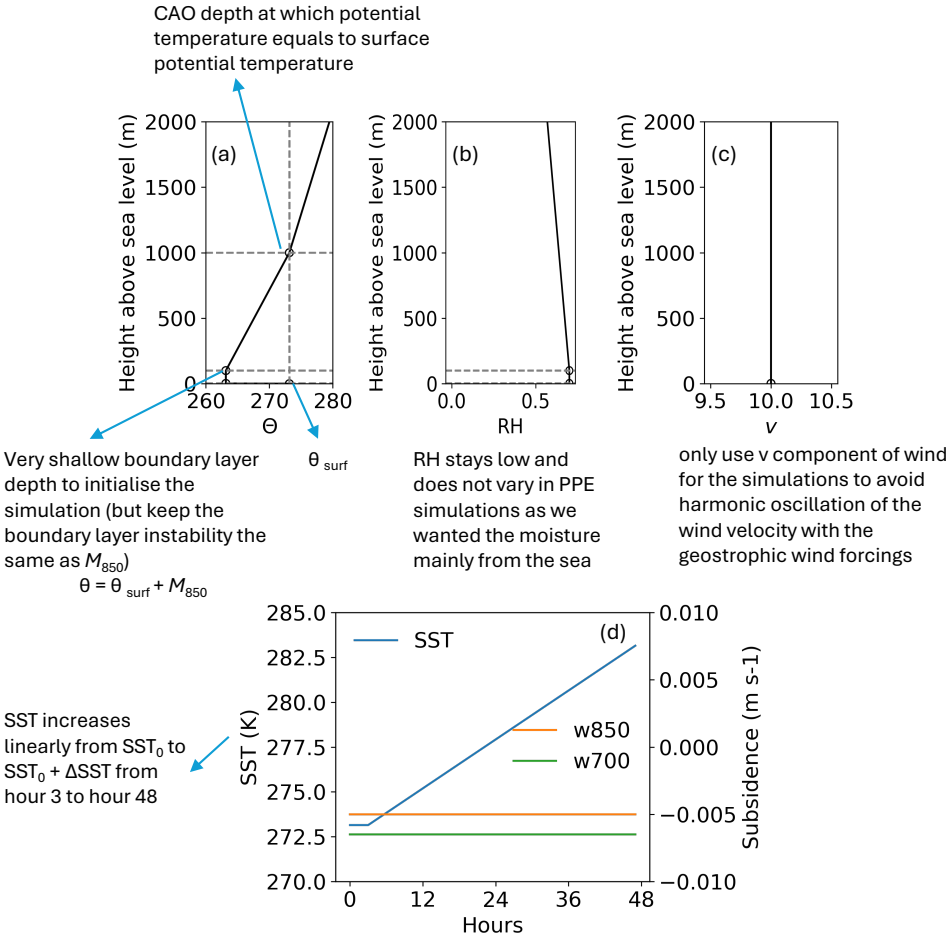


Figure A5.11: Initial profiles and external forcings for the control simulation: (a) potential temperature (θ, K) profile, (b) relative humidity (RH) profile, (c) v component of wind (m s-1) profile, and (d) time-varying sea surface temperature (SST, K), and constant subsidence rates at 850 hPa (w_{850}) and 700 hPa (w_{700}).

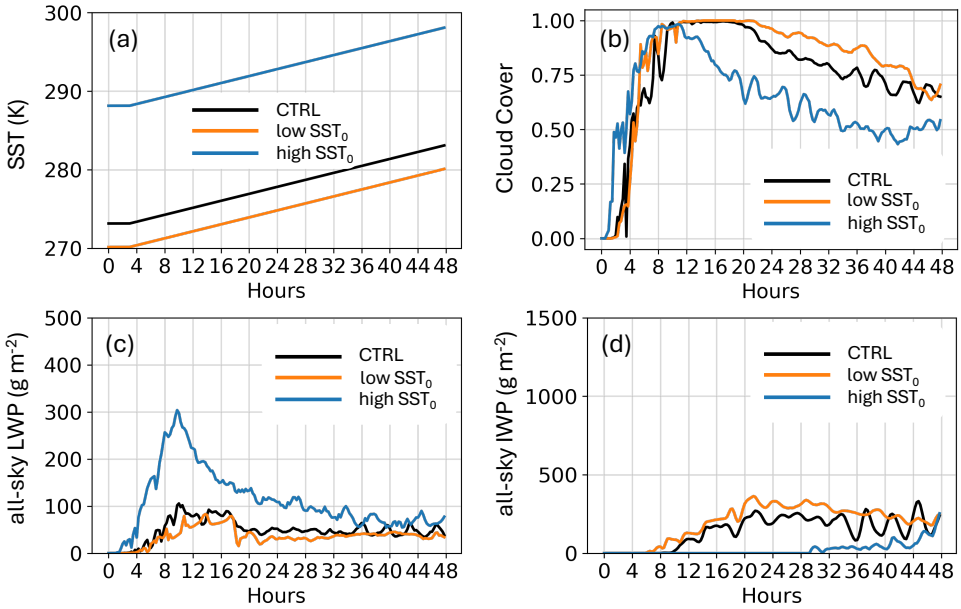


Figure A5.12: Time-series of model output in the one-at-a-time sensitivity test for using different initial SSTs (SST_0): (a) SST (K), (b) cloud cover (unitless), (c) all-sky LWP (liquid water path, g m^{-2}) and (d) all-sky IWP (ice water path, g m^{-2}).

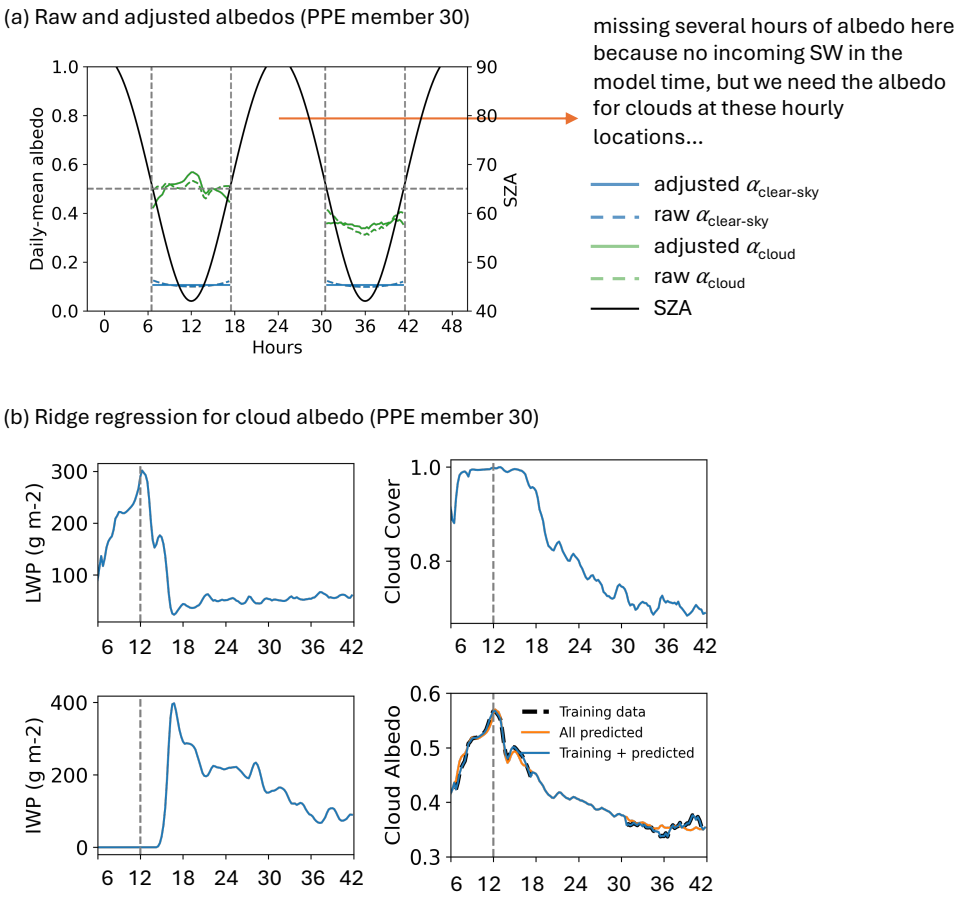


Figure A5.13: Examples of (a) raw and adjusted albedos, and (b) the predicted cloud albedo using ridge regression from PPE member 30.

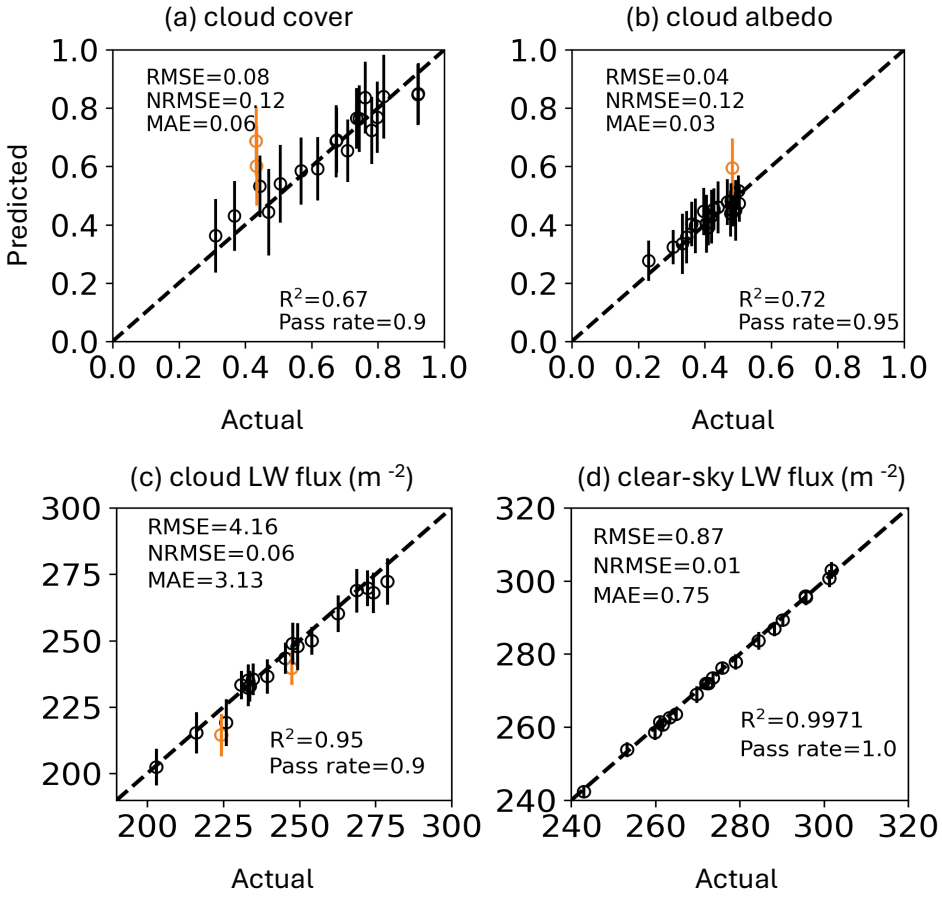


Figure A5.14: Testing results for GP emulators of (a) cloud cover, (b) cloud albedo, (c) cloud LW flux, and (d) clear-sky LW flux.

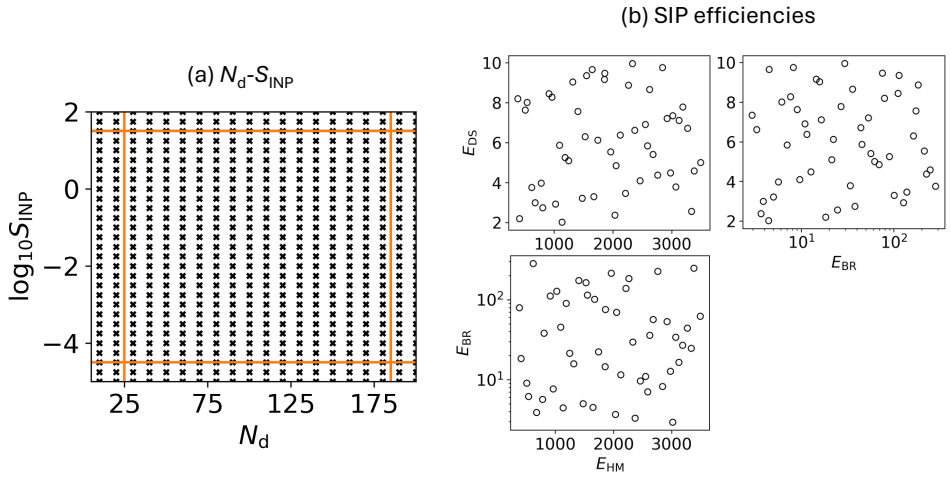


Figure A5.15: Sampling of N_d, S_{INP} and SIP processes over the parameter space: (a) regular-interval sampling of N_d-S_{INP} parameter space, and (b) LHS (Latin Hypercube Sampling) of all three SIP parameters. Values within the orange lines in (a) show the values included for analysis as the uncertainties from emulators can be high near the boundaries.

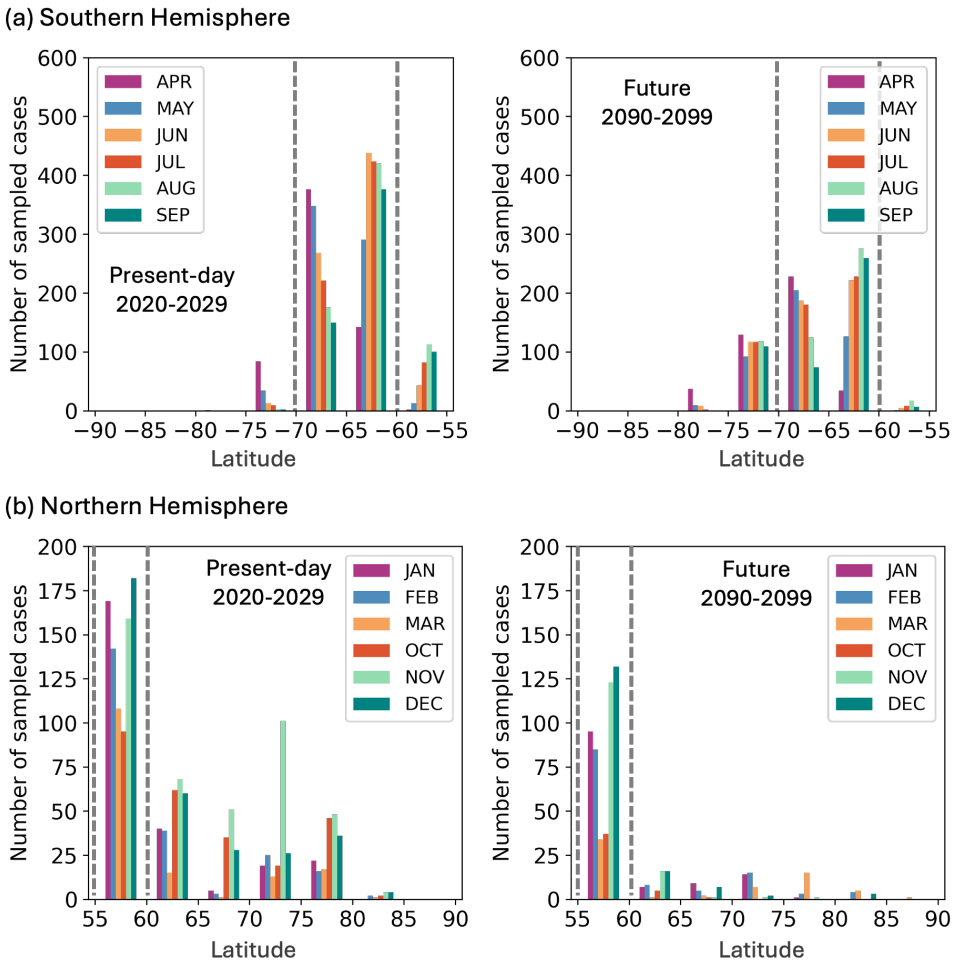


Figure A5.16: Number of valid CAO cases for analysis in each latitude-month bin for (a) the Southern Hemisphere and (b) the Northern Hemisphere.

References

Ackerman, A. S., Kirkpatrick, M. P., Stevens, D. E., and Toon, O. B. (2004). "The impact of humidity above stratiform clouds on indirect aerosol climate forcing". In: *Nature* 432.7020, pp. 1014–1017.

Albrecht, B. A. (1989). "Aerosols, Cloud Microphysics, and Fractional Cloudiness". In: *Science* 245.4923, pp. 1227–1230.

Atlas, R. L., Bretherton, C. S., Khairoutdinov, M. F., and Blossey, P. N. (2022). "Hallett-Mossop Rime Splintering Dims Cumulus Clouds Over the Southern Ocean: New Insight From Nudged Global Storm-Resolving Simulations". In: *AGU Advances* 3.2, e2021AV000454.

Bodas-Salcedo, A., Williams, K. D., Ringer, M. A., Beau, I., Cole, J. N. S., Dufresne, J.-L., Koshiro, T., Stevens, B., Wang, Z., and Yokohata, T. (2014). "Origins of the Solar Radiation Biases over the Southern Ocean in CFMIP2 Models". In: *Journal of Climate* 27.1, pp. 41–56.

Bretherton, C. S. (2015). "Insights into low-latitude cloud feedbacks from high-resolution models". In: *Philosophical Transactions of the Royal Society A: Mathematical, Physical and Engineering Sciences* 373.2054, p. 20140415.

Bretherton, C. S. and Blossey, P. N. (2013). "Low cloud reduction in a greenhouse-warmed climate: Results from Lagrangian LES of a subtropical marine cloudiness transition". In: *Journal of Advances in Modeling Earth Systems* 6.1, pp. 91–114.

Brown, A., Milton, S., Cullen, M., Golding, B., Mitchell, J., and Shelly, A. (2012). "Unified Modeling and Prediction of Weather and Climate: A 25-Year Journey". In: *Bulletin of the American Meteorological Society* 93.12, pp. 1865–1877.

Brümmer, B. (1999). "Roll and Cell Convection in Wintertime Arctic Cold-Air Outbreaks". In: *Journal of the Atmospheric Sciences* 56.15, pp. 2613–2636.

Carslaw, K. S., Boucher, O., Spracklen, D. V., Mann, G. W., Rae, J. G. L., Woodward, S., and Kulmala, M. (2010). "A review of natural aerosol interactions and feedbacks within the Earth system". In: *Atmospheric Chemistry and Physics* 10.4, pp. 1701–1737.

Carslaw, K. S., Regayre, L. A., Proske, U., Gettelman, A., Sexton, D. M. H., Qian, Y., Marshall, L. R., Wild, O., van Lier-Walqui, M., Oertel, A., Peatier, S., Yang, B., Johnson, J. S., Li, S., McCoy, D. T., Sanderson, B. M., Williamson, C. J., Elsaesser, G. S., Yamazaki, K., and Booth, B. B. B. (2026). "Opinion: The importance and future development of perturbed parameter ensembles in climate and atmospheric science". In: *Atmospheric Chemistry and Physics* 26.7, pp. 4651–4667.

Ceppi, P., Brient, F., Zelinka, M. D., and Hartmann, D. L. (2017). "Cloud feedback mechanisms and their representation in global climate models". In: *WIREs Climate Change* 8.4, e465.

Chen, J., Wang, H., Li, X., Painemal, D., Sorooshian, A., Thornhill, K. L., Robinson, C., and Shingler, T. (2022). "Impact of Meteorological Factors on the Mesoscale Morphology of Cloud Streets during a Cold-Air Outbreak over the Western North Atlantic". In: *Journal of the Atmospheric Sciences* 79.11, pp. 2863–2879.

Clarke, S. J., Abel, S. J., Nott, G. J., Raif, E. N., Tarn, M. D., Biggart, M., Wu, H., Ashmore, D. W., Barr, S. L., Barrett, P. A., Bower, K. N., Bowles, J., Connolly, P. J., Cotton, R., Evans, M. D., Flynn, M., Foster, P. B., Fox, S., Gallagher, M. W., Hu, K., Kent, J., Lloyd, G., Marsden, N. A., McQuaid, J. B., Robinson, J., Tiddeman, D., Wilson, A., Wivell, K., Field, P. R., Choularton, T. W., and Murray, B. J. (2025). "Marine cold-air outbreaks over the Norwegian-Barents and Labrador seas: observational datasets from the ACAO and M-Phase aircraft campaigns". Manuscript submitted for publication.

Cooper, W. (1986). "Ice Initiation in Natural Clouds". In: *Precipitation Enhancement—A Scientific Challenge, Meteorological Monographs.*

Field, P. R., Lawson, R. P., Brown, P. R. A., Lloyd, G., Westbrook, C., Moisseev, D., Miltenberger, A., Nenes, A., Blyth, A., Choularton, T., Connolly, P., Buehl, J., Crosier, J., Cui, Z., Dearden, C., DeMott, P., Flossmann, A., Heymsfield, A., Huang, Y., Kalesse, H., Kanji, Z. A., Korolev, A., Kirchgaessner, A., Lasher-Trapp, S., Leisner, T., McFarquhar, G., Phillips, V., Stith, J., and Sullivan, S. (2017a). "Secondary Ice Production: Current State of the Science and Recommendations for the Future". In: *Meteorological Monographs* 58, pp. 7.1–7.20.

Field, P. R., Brožková, R., Chen, M., Dudhia, J., Lac, C., Hara, T., Honnert, R., Olson, J., Siebesma, P., de Roode, S., Tomassini, L., Hill, A., and McTaggart-Cowan, R. (2017b). "Exploring the convective grey zone with regional simulations of a cold air outbreak". In: *Quarterly Journal of the Royal Meteorological Society* 143.707, pp. 2537–2555.

Field, P. R., Hill, A., Shipway, B., Furtado, K., Wilkinson, J., Miltenberger, A., Gordon, H., Grosvenor, D. P., Stevens, R., and Van Weverberg, K. (2023). "Implementation of a Double Moment Cloud Microphysics Scheme in the UK Met Office Regional Numerical Weather Prediction Model". In: *Quarterly Journal of the Royal Meteorological Society.*

Fletcher, J., Mason, S., and Jakob, C. (2016a). "The Climatology, Meteorology, and Boundary Layer Structure of Marine Cold Air Outbreaks in Both Hemispheres". In: *Journal of Climate* 29.6, pp. 1999–2014.

Fletcher, J. K., Mason, S., and Jakob, C. (2016b). "A Climatology of Clouds in Marine Cold Air Outbreaks in Both Hemispheres". In: *Journal of Climate* 29.18, pp. 6677–6692.

Forster, P., Storelvmo, T., Armour, K., Collins, W., Dufresne, J. L., Frame, D., Lunt, D. J., Mauritsen, T., Palmer, M. D., Watanabe, M., Wild, M., and Zhang, H. (2021). "The Earth's Energy Budget, Climate Feedbacks, and Climate Sensitivity".

In: *Climate Change 2021: The Physical Science Basis. Contribution of Working Group I to the Sixth Assessment Report of the Intergovernmental Panel on Climate Change*. Ed. by V. Masson-Delmotte, P. Zhai, A. Pirani, S. L. Connors, C. Péan, S. Berger, N. Caud, Y. Chen, L. Goldfarb, M. I. Gomis, M. Huang, K. Leitzell, E. Lonnoy, J. B. R. Matthews, T. K. Maycock, T. Waterfield, O. Yelekçi, R. Yu, and B. Zhou. Cambridge, United Kingdom and New York, NY, USA: Cambridge University Press. Chap. 7.

Grosvenor, D. P., Field, P. R., Hill, A. A., and Shipway, B. J. (2017). "The relative importance of macrophysical and cloud albedo changes for aerosol-induced radiative effects in closed-cell stratocumulus: insight from the modelling of a case study". In: *Atmospheric Chemistry and Physics* 17.8, pp. 5155–5183.

Gupta, A. K., Kok, J. F., Amiridis, V., Gkikas, A., Rizos, K., Proestakis, E., Logothetis, S., Marinou, E., and Pérez García-Pando, C. (2026). "A global decline in atmospheric dust during the 21st century". In: *Research Square*. Preprint, Version 1.

Herbert, R. J., Sanchez-Marroquin, A., Grosvenor, D. P., Pringle, K. J., Arnold, S. R., Murray, B. J., and Carslaw, K. S. (2025). "Gaps in our understanding of ice-nucleating particle sources exposed by global simulation of the UK Earth System Model". In: *Atmospheric Chemistry and Physics* 25.1, pp. 291–325.

Huang, X., Field, P. R., Herbert, R. J., Murray, B. J., van den Heuvel, F., Grosvenor, D. P., Sansom, R. W. N., and Carslaw, K. S. (2026). "Interacting effects of droplet number and ice formation processes on mixed-phase cold-air outbreak clouds". In: *EGUsphere* 2026, pp. 1–49.

Huang, X., Field, P. R., Murray, B. J., Grosvenor, D. P., van den Heuvel, F., and Carslaw, K. S. (2025). "Different responses of cold-air outbreak clouds to aerosol and ice production depending on cloud temperature". In: *Atmospheric Chemistry and Physics* 25.18, pp. 11363–11406.

Johnson, J. S., Cui, Z., Lee, L. A., Gosling, J. P., Blyth, A. M., and Carslaw, K. S. (2015). "Evaluating uncertainty in convective cloud microphysics using statistical emulation". In: *Journal of Advances in Modeling Earth Systems* 7.1, pp. 162–187.

Johnson, J. S., Regayre, L. A., Yoshioka, M., Pringle, K. J., Turnock, S. T., Browse, J., Sexton, D. M. H., Rostron, J. W., Schutgens, N. A. J., Partridge, D. G., Liu, D., Allan, J. D., Coe, H., Ding, A., Cohen, D. D., Atanacio, A., Vakkari, V., Asmi, E., and Carslaw, K. S. (2020). "Robust observational constraint of uncertain aerosol processes and emissions in a climate model and the effect on aerosol radiative forcing". In: *Atmospheric Chemistry and Physics* 20.15, pp. 9491–9524.

Karalis, M., Sotiropoulou, G., Abel, S. J., Bossioli, E., Georgakaki, P., Methymaki, G., Nenes, A., and Tombrou, M. (2022). "Effects of secondary ice processes on a stratocumulus to cumulus transition during a cold-air outbreak". In: *Atmospheric Research* 277, p. 106302.

Khain, A. P., Beheng, K. D., Heymsfield, A., Korolev, A., Krichak, S. O., Levin, Z., Pinsky, M., Phillips, V., Prabhakaran, T., Teller, A., van den Heever, S. C., and Yano, J.-I. (2015). "Representation of microphysical processes in cloud-resolving models: Spectral (bin) microphysics versus bulk parameterization". In: *Reviews of Geophysics* 53.2, pp. 247–322.

Klingebiel, M., Ehrlich, A., Gryschka, M., Risse, N., Maherndl, N., Schirmacher, I., Rosenburg, S., Hörnig, S., Moser, M., Jäkel, E., Schäfer, M., Deneke, H., Mech, M., Voigt, C., and Wendisch, M. (2025). "Airborne observations of cloud properties during their evolution from organized streets to isotropic cloud structures along an Arctic cold-air outbreak". In: *Atmospheric Chemistry and Physics* 25.17, pp. 9787–9801.

Korhonen, H., Carslaw, K. S., Forster, P. M., Mikkonen, S., Gordon, N. D., and Kokkola, H. (2010). "Aerosol climate feedback due to decadal increases in Southern Hemisphere wind speeds". In: *Geophysical Research Letters* 37.2.

Korolev, A., McFarquhar, G., Field, P. R., Franklin, C., Lawson, P., Wang, Z., Williams, E., Abel, S. J., Axisa, D., Borrmann, S., Crosier, J., Fugal, J., Krämer, M., Lohmann, U., Schlenczek, O., Schnaiter, M., and Wendisch, M. (2017). "Mixed-Phase Clouds: Progress and Challenges". In: *Meteorological Monographs* 58, pp. 5.1–5.50.

Lee, L. A., Carslaw, K. S., Pringle, K. J., Mann, G. W., and Spracklen, D. V. (2011). "Emulation of a complex global aerosol model to quantify sensitivity to uncertain parameters". In: *Atmospheric Chemistry and Physics* 11.23, pp. 12253–12273.

Lee, L. A., Reddington, C. L., and Carslaw, K. S. (2016). "On the relationship between aerosol model uncertainty and radiative forcing uncertainty". In: *Proceedings of the National Academy of Sciences* 113.21, pp. 5820–5827.

Lohmann, U. and Feichter, J. (2005). "Global indirect aerosol effects: a review". In: *Atmospheric Chemistry and Physics* 5.3, pp. 715–737.

McCoy, D. T., Eastman, R., Hartmann, D. L., and Wood, R. (2017a). "The Change in Low Cloud Cover in a Warmed Climate Inferred from AIRS, MODIS, and ERA-Interim". In: *Journal of Climate* 30.10, pp. 3609–3620.

McCoy, I. L., Wood, R., and Fletcher, J. K. (2017b). "Identifying Meteorological Controls on Open and Closed Mesoscale Cellular Convection Associated with Marine Cold Air Outbreaks". In: *Journal of Geophysical Research: Atmospheres* 122.21, pp. 11678–11702.

Morrison, H., van Lier-Walqui, M., Fridlind, A. M., Grabowski, W. W., Harrington, J. Y., Hoose, C., Korolev, A., Kumjian, M. R., Milbrandt, J. A., Pawlowska, H., Posselt, D. J., Prat, O. P., Reimel, K. J., Shima, S.-I., van Diedenhoven, B., and Xue, L. (2020). "Confronting the Challenge of Modeling Cloud and Precipitation Microphysics". In: *Journal of Advances in Modeling Earth Systems* 12.8, e2019MS001689.

Murray, B. J., Carslaw, K. S., and Field, P. R. (2021). "Opinion: Cloud-phase climate feedback and the importance of ice-nucleating particles". In: *Atmospheric Chemistry and Physics* 21.2, pp. 665–679.

Murray-Watson, R. J., Gryspeerdt, E., and Goren, T. (2023). "Investigating the development of clouds within marine cold-air outbreaks". In: *Atmospheric Chemistry and Physics* 23.16, pp. 9365–9383.

Myers, T. A. and Norris, J. R. (2016). "Reducing the uncertainty in subtropical cloud feedback". In: *Geophysical Research Letters* 43.5, pp. 2144–2148.

O'Hagan, A. (2006). "Bayesian analysis of computer code outputs: A tutorial". In: *Reliability Engineering and System Safety* 91.10, pp. 1290–1300.

Oakley, J. and O'Hagan, A. (2002). "Bayesian inference for the uncertainty distribution of computer model outputs". In: *Biometrika* 89.4, pp. 769–784.

Pasquier, J. T., Henneberger, J., Ramelli, F., Lauber, A., David, R. O., Wieder, J., Carlsen, T., Gierens, R., Maturilli, M., and Lohmann, U. (2022). "Conditions favorable for secondary ice production in Arctic mixed-phase clouds". In: *Atmospheric Chemistry and Physics* 22.23, pp. 15579–15601.

Qu, X., Hall, A., Klein, S. A., and DeAngelis, A. M. (2015). "Positive tropical marine low-cloud cover feedback inferred from cloud-controlling factors". In: *Geophysical Research Letters* 42.18, pp. 7767–7775.

Raif, E. N., Barr, S. L., Tarn, M. D., McQuaid, J. B., Daily, M. I., Abel, S. J., Barrett, P. A., Bower, K. N., Field, P. R., Carslaw, K. S., and Murray, B. J. (2024). "High ice-nucleating particle concentrations associated with Arctic haze in springtime cold-air outbreaks". In: *EGUsphere* 2024, pp. 1–38.

Regayre, L. A., Deaconu, L., Grosvenor, D. P., Sexton, D. M. H., Symonds, C., Langton, T., Watson-Paris, D., Mulcahy, J. P., Pringle, K. J., Richardson, M., Johnson, J. S., Rostron, J. W., Gordon, H., Lister, G., Stier, P., and Carslaw, K. S. (2023). "Identifying climate model structural inconsistencies allows for tight constraint of aerosol radiative forcing". In: *Atmospheric Chemistry and Physics* 23.15, pp. 8749–8768.

Renfrew, I. A. and Moore, G. W. K. (1999). "An Extreme Cold-Air Outbreak over the Labrador Sea: Roll Vortices and Air–Sea Interaction". In: *Monthly Weather Review* 127.10, pp. 2379–2394.

Sansom, R. W. N., Johnson, J. S., Regayre, L. A., Lee, L. A., and Carslaw, K. S. (2025). "Strong control of the stratocumulus-to-cumulus transition time by aerosol: analysis of the joint roles of several cloud-controlling factors using Gaussian process emulation". In: *EGUsphere* 2025, pp. 1–30.

Sansom, R. W. N., Carslaw, K. S., Johnson, J. S., and Lee, L. (2024). "An Emulator of Stratocumulus Cloud Response to Two Cloud-Controlling Factors Accounting for Internal Variability". In: *Journal of Advances in Modeling Earth Systems* 16.9, e2023MS004179.

Sellar, A. A., Walton, J., Jones, C. G., Wood, R., Abraham, N. L., Andrejczuk, M., Andrews, M. B., Andrews, T., Archibald, A. T., de Mora, L., Dyson, H., Elkington, M., Ellis, R., Florek, P., Good, P., Gohar, L., Haddad, S., Hardiman, S. C., Hogan, E., Iwi, A., Jones, C. D., Johnson, B., Kelley, D. I., Kettleborough, J., Knight, J. R., Köhler, M. O., Kuhlbrodt, T., Liddicoat, S., Linova-Pavlova, I., Mizielinski, M. S., Morgenstern, O., Mulcahy, J., Neininger, E., O'Connor, F. M., Petrie, R., Ridley, J., Rioual, J.-C., Roberts, M., Robertson, E., Rumbold, S., Seddon, J., Shepherd, H., Shim, S., Stephens, A., Teixiera, J. C., Tang, Y., Williams, J., Wiltshire, A., and Griffiths, P. T. (2020). "Implementation of U.K. Earth System Models for CMIP6". In: *Journal of Advances in Modeling Earth Systems* 12.4, e2019MS001946.

Sherwood, S. C., Webb, M. J., Annan, J. D., Armour, K. C., Forster, P. M., Hargreaves, J. C., Hegerl, G., Klein, S. A., Marvel, K. D., Rohling, E. J., Watanabe, M., Andrews, T., Braconnot, P., Bretherton, C. S., Foster, G. L., Hausfather, Z., von der Heydt, A. S., Knutti, R., Mauritsen, T., Norris, J. R., Proistosescu, C., Rugenstein, M., Schmidt, G. A., Tokarska, K. B., and Zelinka, M. D. (2020). "An Assessment of Earth's Climate Sensitivity Using Multiple Lines of Evidence". In: *Reviews of Geophysics* 58.4, e2019RG000678.

Shipway, B. J. and Hill, A. A. (2012). "Diagnosis of systematic differences between multiple parametrizations of warm rain microphysics using a kinematic framework". In: *Quarterly Journal of the Royal Meteorological Society* 138.669, pp. 2196–2211.

Smith, D. K. E., Renfrew, I. A., van den Heuvel, F., Lachlan-Cope, T., Crawford, I., Bower, K., Flynn, M., Evans, M. D., Abel, S. J., and Field, P. (2025). "The Impact of Mixed-Phase Cloud Processes on Simulating Southern Ocean Clouds and Their Radiative Effect". In: *Journal of Geophysical Research: Atmospheres* 130.23, e2025JD044452.

Tan, I., Storelvmo, T., and Zelinka, M. D. (2016). "Observational constraints on mixed-phase clouds imply higher climate sensitivity". In: *Science* 352.6282, pp. 224–227.

Twomey, S. (1977). "The Influence of Pollution on the Shortwave Albedo of Clouds". In: *Journal of Atmospheric Sciences* 34.7, pp. 1149–1152.

Vergara-Temprado, J., Miltenberger, A. K., Furtado, K., Grosvenor, D. P., Shipway, B. J., Hill, A. A., Wilkinson, J. M., Field, P. R., Murray, B. J., and Carslaw, K. S. (2018). "Strong control of Southern Ocean cloud reflectivity by ice-nucleating particles". In: *Proceedings of the National Academy of Sciences* 115.11, pp. 2687–2692.

Wu, P. and Ovchinnikov, M. (2022). "Cloud Morphology Evolution in Arctic Cold-Air Outbreak: Two Cases During COMBLE Period". In: *Journal of Geophysical Research: Atmospheres* 127.10, e2021JD035966.

Wu, P., Ovchinnikov, M., Xiao, H., Lackner, C. P., Geerts, B., Tornow, F., and Elsaesser, G. (2025). "Effect of Ice Number Concentration on the Evolution of Bound-

ary Layer Clouds During Arctic Marine Cold-Air Outbreaks". In: *Journal of Geophysical Research: Atmospheres* 130.3, e2024JD041282.

Zelinka, M. D., Myers, T. A., McCoy, D. T., Po-Chedley, S., Caldwell, P. M., Ceppi, P., Klein, S. A., and Taylor, K. E. (2020). "Causes of Higher Climate Sensitivity in CMIP6 Models". In: *Geophysical Research Letters* 47.1, e2019GL085782.

Chapter 6

Conclusions and Future Work

This thesis has advanced our understanding on the role of aerosol–cloud interactions and ice formation processes in mixed-phase cold-air outbreak (CAO) clouds. In Chapter 2, different responses of mixed-phase CAO clouds to perturbations in droplet number concentration, INP concentration and the Hallett-Mossop (HM) process efficiency were shown by simulating mixed-phase clouds in two CAO events under different environmental conditions with a high-resolution regional model. In Chapter 3, the interacting effects among cloud microphysical processes and parameters were identified using perturbed parameter ensemble (PPE) simulations and model emulation. Chapter 4 further assessed how well these clouds are represented in the model and identified model inconsistencies by evaluating simulated mixed-phase CAO clouds from PPEs against aircraft observations. Chapter 5 extended our analysis beyond individual studies and present-day climate conditions to study the role of aerosol–cloud interactions and ice formation processes in modulating the response of mixed-phase CAO clouds to the warming climate using emulators trained with idealised regional simulations. The main findings of the thesis are summarised below in response to the research objectives and questions presented in Section 1.6. Implications and recommendations for future studies from each chapter are discussed in Section 6.2.

6.1 Summary of main findings

6.1.1 Chapter 2: Different responses of cold-air outbreak clouds to aerosol and ice production depending on cloud temperature

(a) *How do aerosol-cloud interactions and ice formation processes affect the properties of mixed-phase CAO clouds under different environmental conditions?*

The effects of aerosol-cloud interactions and ice formation processes on mixed-phase CAO clouds are strongly dependent on the environmental conditions. In

particular, this chapter shows that cloud temperature strongly modulates the liquid-ice partitioning of mixed-phase CAO clouds, which then affects how these clouds respond to perturbations in cloud microphysical processes.

In a warm October CAO over the Labrador Sea, where the mean cloud top temperature is around −15 °C, the simulated CAO clouds are dominated by liquid water in the control simulation. In this liquid-dominated October case, increasing INP concentration enhances ice formation and precipitation, strongly depletes liquid water, and consequently reduces cloud cover and top-of-the-atmosphere (TOA) albedo. A reduction in liquid water is also found when the droplet number concentration is lower, or when the HM process is more efficient.

In a cold March case over the Labrador Sea, where the mean cloud-top temperature is around −35 °C, the simulated CAO clouds are instead dominated by ice in the control simulation. In this ice-dominated March case, increasing INP concentration produces the opposite response to that in the liquid-dominated October case. Although a higher INP concentration enhances ice formation and further depletes liquid water, it also increases cloud cover and TOA albedo, with the strongest response occurring in the cumulus cloud region. This contrasting behaviour arises because little liquid water remains in the control simulation of the cold March case, so a further depletion of liquid water is limited. Meanwhile, increasing INP concentration produces a larger number of ice hydrometeors, reduces their mean size and fall speed, slows snow autoconversion, and therefore weakens precipitation removal of cloud water. As a result, more cloud water is retained in the cloud, leading to increased cloud cover and TOA albedo. No strong effects from the perturbation of droplet number concentration and HM process efficiency are seen in this case.

These contrasting responses demonstrate that the impact of INPs on mixed-phase CAO cloud properties is not universal, but depends on the initial cloud state, especially the liquid-ice partitioning which is strongly controlled by cloud temperature and ambient INP concentrations.

(b) *What is the relative importance of droplet number concentration, INP concentration and the Hallett-Mossop SIP process on mixed-phase CAO clouds in a one-at-a-time test?*

INP concentration has a strong influence on mixed-phase CAO clouds in both warm and cold cases, whereas the relative importance of droplet number concentration and the efficiency of the HM process is much greater in the warm October case than in the cold March case. Changes in droplet number concentration have a stronger influence in the warm October case because more liquid water is available for liquid-phase aerosol-cloud interactions. In contrast, in the cold March

case, where the clouds are already ice-dominated and contain little liquid water, perturbing droplet number concentration has only a small effect. Similarly, perturbing the HM process efficiency has its strongest influence in the warm October case, particularly in the cumulus-dominated region, because cloud temperatures more frequently fall within the active temperature range of the HM process and sufficient liquid water is available for riming. In the cold March case, cloud temperatures are generally too low for the HM process, so changing its efficiency has little influence on the simulated CAO clouds.

These results show that the relative importance of aerosol-cloud interactions and ice formation processes depends strongly on the initial cloud state and the environmental conditions of CAOs. Therefore, understanding how these processes affect mixed-phase CAO clouds and how they may influence the responses of these CAO clouds to a warming climate, requires a broad sampling range of CAO conditions rather than relying on a small number of case studies.

6.1.2 Chapter 3: Interacting effects of droplet number and ice formation processes on mixed-phase cold-air outbreak clouds

(a) *What is the effect on the properties of mixed-phase CAO clouds of simultaneously perturbing parameters controlling aerosol-cloud interactions and ice formation processes?*

In Chapter 3, six parameters were investigated, which are prescribed droplet number concentration, INP concentration, efficiencies of three SIP processes, and the mixed-phase overlap factor. Perturbing these investigated parameters simultaneously reveals strong interacting effects (non-linear joint effects) on the properties of mixed-phase CAO clouds. This means that the response of mixed-phase CAO clouds to the perturbation of one parameter is dependent on the values of the other parameters, which is an effect that cannot be detected using the one-at-a-time test. For example, in the stratocumulus region, the responses of LWP to an increase in droplet number concentration range from +31 g m^{-2} to +65 g m^{-2} depending on the values of the other parameters, resulting in a difference of 34 g m^{-2} in the magnitude of the LWP response. The interactions among parameters can also affect the direction (or sign) of the cloud response to a parameter. For example, increasing INP concentration in the cumulus region does not always lead to a reduction of the TOA albedo.

These interacting effects also lead to equifinality, where different combinations of parameters can produce similar cloud properties through compensating effects. Across the 1 million model variants generated using the emulator, over 70,000 model variants can produce a TOA albedo agreeing with the observed

TOA albedo in the Sc region and over 90,000 in the Cu region. The number of model variants consistent with observations would likely increase further if uncertainties of observations were included. This demonstrates the importance of accounting for parameter interactions and compensating effects when evaluating the representation of mixed-phase clouds in models against observations, and using a one-at-a-time approach to tune parameter values against observations may fall into the problem of equifinality.

(b) *What is the relative importance of these parameters in controlling the properties of mixed-phase CAO clouds over the whole parameter space?*

The relative importance of the investigated parameters varies between cloud regimes. In the stratocumulus-dominated region, droplet number concentration and INP concentration are the dominant controls on cloud radiative properties, indicating the importance of aerosols acting as cloud condensation nuclei and as INPs during the early stage of the CAO cloud field. In the cumulus-dominated region, droplet number concentration remains a primary control, while the mixed-phase overlap factor exerts a stronger influence on cloud properties than it does in the stratocumulus region. The clouds in the studied CAO event show relatively weak sensitivity to perturbations in all three secondary ice production parameters. However, this weak sensitivity does not imply that SIP processes are unimportant in general, but indicates that the simulated clouds in this particular case are relatively insensitive to the values of these SIP parameters.

The relative importance of these parameters may be substantially different in other CAO events, as Chapter 2 shows that the responses of mixed-phase CAO clouds to these cloud microphysical parameters are strongly dependent on environmental conditions. Therefore, strong sensitivity of a cloud property to a parameter in this case does not imply that the same parameter is universally important under all CAO conditions. By limiting the analysis to a single CAO case, this study examines the sensitivity and interactions of cloud microphysical parameters without the additional confounding effects of varying environmental conditions. The results in Chapter 3 demonstrate the importance of exploring the full parameter space to fully understand the factors controlling cloud properties.

6.1.3 Chapter 4: Identification of model inconsistencies using perturbed parameter ensembles and aircraft observations of mixed-phase cold-air outbreak clouds

(a) *Do aircraft measurements, which are sparse point data, provide enough information for model–observation comparison against model output, which are grid-box mean data?*

Aircraft observations used in Chapter 4 were obtained from Flights C322 and C323 during the M-Phase aircraft campaign, which sampled cloud properties during the CAO event on 24 October 2022 over the Labrador Sea.

The sparse and uneven sampling of aircraft observations in this case introduces substantial representation uncertainties into the model-observation comparison. Many model grid boxes contain only a small number of valid aircraft measurements, particularly for in-cloud microphysical properties. The sampling density within a model grid box ranges from approximately 6-8 points for liquid microphysical properties to fewer than 3 points for ice microphysical properties. This limited sampling in a model grid box introduces uncertainty in how well the mean from the aircraft point measurements represent grid-box-mean cloud variables. However, without further information about the true subgrid variability of cloud properties, this representation uncertainty associated with using sparse point measurements to estimate grid-box mean cannot be quantified in this study.

Sparse horizontal sampling by aircraft introduces an additional representation uncertainty when measurements are composited into domain-mean vertical profiles for model-observation comparison. Because this uncertainty depends on the number of sampled grid boxes at each model level, sparsely sampled levels generally have larger representation uncertainties associated with composing domain-mean vertical profiles from observations. Increase in this representation uncertainty affects the implausibility measure, reducing the ability of identifying model inconsistencies with observations.

Therefore, although aircraft measurements provide valuable information on *in-situ* cloud properties for evaluating modelled mixed-phase CAO clouds, representation uncertainties arising from sparse sampling can limit the ability of using aircraft measurements to constrain ensemble members and identify model inconsistencies.

(b) *Can the model simultaneously simulate all cloud properties well?*

Observational constraints from aircraft measurements identify inconsistent subsets of plausible ensemble members. No ensemble member simulates plausible values for all observed cloud properties across all model levels. Even when a single cloud variable is used as the constraint, the plausible ensemble members vary with height, indicating vertical inconsistency in the simulated cloud profiles. At model levels where more than one ensemble member is identified as plausible for each cloud variable, individual ensemble members are consistent with only a small subset of the cloud variables, which is on average 2.14 out of 9 variables (23.7%) in the stratocumulus region and 2.09 out of 7 variables (29.9%) in the cumulus region.

Inconsistencies are also evident when ensemble members constrained by one cloud variable are evaluated against the other cloud variables. Constraining one cloud variable does not consistently reduce model-observation discrepancy for the other cloud variables. In some cases, an observational constraint substantially narrows the simulated range of another variable, but this stronger constraint does not necessarily improve agreement with the observations. Therefore, apparent improvement in one cloud property does not necessarily correspond to an overall improvement in the simulated mixed-phase cloud state.

Bulk cloud properties, such as cloud cover, LWP and TOA albedo, show more coherent responses to the *in-situ* observational constraints than the *in-situ* microphysical variables themselves. For example, in the Sc region, constraining different ice properties, including IWC, N_{ice} and N_{ice}/IWC, produces similar ranges of cloud cover, with medians around 0.9, and TOA albedo, with medians around 0.5. This coherence contrasts with the strong inconsistencies in how these same constraints affect the other *in-situ* microphysical properties, suggesting that apparent agreement in bulk cloud properties does not guarantee that the underlying cloud microphysics are correctly represented. In addition, inconsistencies remain evident in the constrained ranges of some bulk cloud properties, further illustrating the model inconsistencies. For example, in the Sc region, constraining in-cloud LWC leads to a median LWP of around 84 g m^{-2}, whereas constraining in-cloud IWC leads to a median LWP of around 140 g m^{-2}. Similarly, in the Cu region, constraining the bulk cloud fraction leads to a median LWP of around 79 g m^{-2}, whereas constraining ice cloud fraction leads to a median LWP of around 51 g m^{-2}.

The model also shows systematic positive biases in in-cloud LWC with multiple lines of evidence. In both regions, the mean observed in-cloud LWC is significantly lower than the values from the ensemble members, and this bias cannot be explained by the representation and instrument uncertainties alone. In both regions, the ensemble members also show positive LWP biases when modelled LWP is compared with satellite-retrieved LWP. In addition, constraining ensemble members with in-cloud LWC in the stratocumulus region also degrades model-observation agreement for all other in-cloud properties, indicating that improving agreement with LWC in the model does not necessarily improve the overall representation of mixed-phase cloud microphysics.

The model inconsistencies identified here may suggest potential model structural deficiency, but the identified inconsistencies are highly dependent on the uncertainties included in the implausibility measure in this study and on the limited set of parameters perturbed in this study. For example, once the representation uncertainty is sufficiently large, approximately by a factor of 10 of the original

estimate in the Sc region and 100 in the Cu region for the examined model levels, at least one plausible ensemble member can then be identified that is consistent with all observational constraints. In addition, other model parameters, processes and structural choices may strongly affect mixed-phase clouds. Therefore, a more systematic assessment of model representation should include additional important parameters and improved quantification of representation uncertainties in model-observation.

6.1.4 Chapter 5: The importance of aerosols and ice formation for the response of mixed-phase clouds to warming

(a) *How do environmental conditions change for CAO events in the warming climate?*

Under the Shared Socioeconomic Pathway SSP3-7.0 scenario in the 2090s, CAO events in both the Southern Hemisphere (SH) and Northern Hemisphere (NH) experience an increase in sea surface temperature (SST), and a reduction in the CAO strength indicated with the CAO index at 850 hPa and wind speed. These environmental changes are stronger in the NH than in the SH. This hemispheric difference arises because most SH CAOs form near the sea-ice edge in both the present-day and future climates, where SSTs remain close to 0 °C and leads to only about +0.5 °C change in SST at the beginning of SH CAOs. In contrast, some NH CAOs form along coastlines and therefore experience larger increases in SST, which leads to a mean increase about 4 °C for NH CAOs in the warming climate. The shift towards warmer and weaker CAO conditions leads to reductions in cloud cover and cloud albedo in both hemispheres.

(b) *How do aerosols and ice formation processes affect the response of mixed-phase CAO clouds to the warming climate?*

Aerosols and ice formation processes strongly modulate the response of mixed-phase CAO clouds to warming, leading to substantial uncertainty in the associated changes in cloud radiative effects (CREs). This is reflected in the central 90% intervals of the change in net CRE, which span 1.57 W m^{-2} in the NH and 0.65 W m^{-2} in the SH.

Droplet number concentration strongly controls cloud albedo and cloud cover in both present-day and future climates, but its effect on the change in cloud properties with warming is much reduced because the sensitivities of cloud properties are similar in both climates and therefore largely cancel in the difference of cloud states. In contrast, INP concentration and SIP processes have stronger effects on the change in cloud properties because their effects on cloud properties are temperature and cloud-regime dependent and change substantially between the present-day and future climates.

Ice formation processes are therefore particularly important in controlling the response of mixed-phase CAO clouds to warming. The first-order sensitivity indices show that INP concentration dominates the variance in the NH shortwave and longwave CRE responses, explaining 76% and 90% of their variance respectively. The contribution to the change in net CRE from INP concentration is smaller, because the shortwave and longwave responses partly compensate each other. In the SH, SIP processes dominate the uncertainties in the CRE responses, explaining 62% of the variance in the change in net CRE. This likely occurs because the warming is weaker in the SH CAOs, but the change of cloud regimes still occurs, allowing SIP processes to strongly influence the cloud radiative responses.

These results show that the processes controlling present-day mixed-phase cloud properties are not necessarily the same as those controlling the responses of mixed-phase clouds to warming. Therefore, constraining present-day cloud states alone is not sufficient for understanding cloud feedback and the sensitivity of mixed-phase clouds to aerosol and ice formation processes must also be understood across the environmental conditions relevant to both present-day and future climates.

(c) *How much do changes in aerosol in the future climate affect the response of mixed-phase CAO clouds to the warming climate?*

Including changes in aerosols in the future climate substantially increases the uncertainty in the response of mixed-phase CAO clouds to warming. When present-day droplet number concentration and INP concentration are constrained using observations, the uncertainty range in the change of net cloud radiative effect in the NH is reduced substantially by 63%, from 1.57 W m^{-2} to 0.58 W m^{-2}. However, allowing droplet number concentration and INP concentration to change between the 2020s and 2090s greatly broadens the range of change in the constrained net CRE. In the SH, allowing for potential increases or decreases between 2020s and 2090s leads to 56% increase in the central 90% interval of the net CRE change. In the NH, the range of the net CRE changes increases almost by a factor of 2 (+183%).

The sign of changes in future aerosols is also important. An increase in droplet number concentration combined with a decrease in INP concentration produces the smallest reduction in shortwave CRE in the NH and shifts the change of shortwave CRE in the SH from negative to positive. Across the different combinations of changes in future droplet number concentration and INP concentration, the median net CRE response varies by about 1.07 W m^{-2} in NH and 0.49 W m^{-2} in SH. These results show that uncertainties in both the magnitude and sign in changes of future aerosol can strongly affect estimates of mixed-phase cloud feedback, and that changes in aerosol should be considered as part of the uncertainty

in responses of mixed-phase clouds to warming.

6.2 Implications and Recommendations for future studies

The different responses of mixed-phase CAO clouds to change in INP found in Chapter 2 suggest that the widely reported reduction in shortwave reflectivity with increasing INP concentration (e.g. Vergara-Temprado et al., 2018) is not a universal behaviour of mixed-phase CAO clouds. Instead, it depends on the liquid–ice partitioning of the initial cloud state, which can be strongly affected by cloud temperature and the ambient INP concentration. Future studies are recommended to sample mixed-phase CAO cases across the full range of cloud top temperatures to better understand how aerosol-cloud interactions and ice formation processes vary across different cloud regimes. The two CAO cases examined in Chapter 2 had cloud top temperatures near the warmer and colder ends of the cloud top temperature range during CAO events. Cases with intermediate cloud top temperatures, which occupy a large fraction of the CAO population, were therefore not examined. Sampling across the full cloud top temperature range will improve our understanding of how liquid-phase, ice-phase, and mixed-phase processes interact under different environmental conditions, and how these interactions control the sensitivity of mixed-phase CAO clouds to aerosol and ice-formation perturbations.

It is also recommended to identify the transition between regimes in which enhanced INP concentrations reduce cloud cover and albedo and in which they increase cloud cover and albedo. Chapter 2 identified opposite responses of mixed-phase CAO clouds to increases in INP concentration, but did not determine the conditions under which this sign reversal occurs. Extending this analysis to a wider set of CAO cases, and to other models or microphysics schemes, would allow the regime-dependent INP response identified here to be generalised and its controlling mechanisms to be more clearly established.

Chapter 3 shows the existence of non-linear, interacting effects between model parameters. Using the method of an OAT test, which is applied in many previous studies, may be insufficient to understand the importance and effects of these parameters. The equifinality found in Chapter 3 also suggests that tuning parameters to match with observations may also give the right answer for the wrong reasons, which is also seen in global models (e.g. Lee et al., 2016; Regayre et al., 2018). Future studies are recommended to apply the PPE and model emulation approach to a wider range of CAO conditions and include a broader set of model parameters and processes. In addition to the parameters investigated in this thesis, other cloud microphysical parameters such as those controlling snow deposition rates (Van Weverberg et al., 2023) and parameters in the boundary-layer scheme (Field et al., 2014), have also been shown to affect mixed-phase CAO clouds. It is also recommended to use aerosol-aware approaches and

to include aerosol processing for a better representation of cloud condensation nuclei and ice-nucleating particles in mixed-phase clouds. Assessing mixed-phase CAO clouds under different environmental conditions using PPEs that span a more complete set of relevant parameters, together with multiple observational datasets, will provide a more systematic evaluation of model performance on mixed-phase clouds.

Chapter 4 identified the inconsistencies in identifying plausible PPE members using multiple observations. However, the ability of identifying inconsistencies is strongly dependent on the representation uncertainties considered in the implausibility measure, which has been shown to be a major challenge when ruling out parameter space (Johnson et al., 2020). Representation uncertainties in model-observation comparison should be better quantified in future studies to improve the strength and reliability of observational constraints. Specifically, future work is recommended to investigate the uncertainty associated with using point measurements to estimate grid-box-mean cloud properties, identify the criteria of sampling density for robust model-observation comparison, and develop guidance for measurement strategies specifically for model-observation comparison.

Finally, Chapter 5 shows that the microphysical processes controlling present-day mixed-phase cloud properties are not the same as those controlling the cloud response to warming. In particular, uncertainties in ice formation processes, including INP concentration and SIP processes, can lead to large uncertainties in predicting the response of mixed-phase CAO clouds to warming, while future changes in aerosols widen these uncertainties even further. Constraining the present-day cloud state alone is therefore not sufficient to constrain the mixed-phase cloud feedback. However, the regional simulations used in Chapter 5 limit the ability to apply the radiative-kernel method (Zelinka et al., 2012a; Zelinka et al., 2012b) for diagnosing cloud feedbacks, and do not account for the combined effects of microphysical responses and changes in the spatial distribution of cloud regimes. Future studies are therefore recommended to combine the cloud microphysical controls with the changes in the spatial distribution of cloud regimes. This would advance our quantification of uncertainties in mixed-phase cloud feedback and provide a more systematic basis for identifying key sources of uncertainties to be constrained in future studies.

The findings of this thesis show that quantifying and reducing uncertainty in the mixed-phase cloud feedback requires cloud microphysical uncertainties to be sampled across the parameter space, and models to be evaluated against multiple observations with well-quantified uncertainties. Applying the approach of using PPEs, statistical emulation and multiple observational constraints to a wider range of CAO conditions and in other models would improve our understanding of the processes that control the response of mixed-phase clouds to warming, and help identify where observational constraints can most effectively reduce the uncertainty in estimating the mixed-phase

cloud feedback.

References

Field, P. R., Cotton, R. J., McBeath, K., Lock, A. P., Webster, S., and Allan, R. P. (2014). "Improving a convection-permitting model simulation of a cold air outbreak". In: *Quarterly Journal of the Royal Meteorological Society* 140.678, pp. 124–138.

Johnson, J. S., Regayre, L. A., Yoshioka, M., Pringle, K. J., Turnock, S. T., Browse, J., Sexton, D. M. H., Rostron, J. W., Schutgens, N. A. J., Partridge, D. G., Liu, D., Allan, J. D., Coe, H., Ding, A., Cohen, D. D., Atanacio, A., Vakkari, V., Asmi, E., and Carslaw, K. S. (2020). "Robust observational constraint of uncertain aerosol processes and emissions in a climate model and the effect on aerosol radiative forcing". In: *Atmospheric Chemistry and Physics* 20.15, pp. 9491–9524.

Lee, L. A., Reddington, C. L., and Carslaw, K. S. (2016). "On the relationship between aerosol model uncertainty and radiative forcing uncertainty". In: *Proceedings of the National Academy of Sciences* 113.21, pp. 5820–5827.

Regayre, L. A., Johnson, J. S., Yoshioka, M., Pringle, K. J., Sexton, D. M. H., Booth, B. B. B., Lee, L. A., Bellouin, N., and Carslaw, K. S. (2018). "Aerosol and physical atmosphere model parameters are both important sources of uncertainty in aerosol ERF". In: *Atmospheric Chemistry and Physics* 18.13, pp. 9975–10006.

Van Weverberg, K., Giangrande, S., Zhang, D., Morcrette, C. J., and Field, P. R. (2023). "On the Role of Macrophysics and Microphysics in Km-Scale Simulations of Mixed-Phase Clouds During Cold Air Outbreaks". In: *Journal of Geophysical Research: Atmospheres* 128.11, e2022JD037854.

Vergara-Temprado, J., Miltenberger, A. K., Furtado, K., Grosvenor, D. P., Shipway, B. J., Hill, A. A., Wilkinson, J. M., Field, P. R., Murray, B. J., and Carslaw, K. S. (2018). "Strong control of Southern Ocean cloud reflectivity by ice-nucleating particles". In: *Proceedings of the National Academy of Sciences* 115.11, pp. 2687–2692.